

FLEXsense

FLEX Sentinel Tandem Campaign: Technical Assistance for airborne measurements during the FLEX Sentinel Tandem Experiment

ESA Contract No. 4000125402/18/NL/NA

FINAL REPORT

D3 of the FlexSense Campaign



Max Planck Institute
for Biogeochemistry



HYPER SPECTRAL
DEVICES



Universität
Zürich^{UZH}



29 July 2021

Final Version

Table of contents

1	Executive Summary	10
2	Background.....	13
3	Specific campaign objectives.....	14
4	Instrumentation and processing	15
4.1	Sentinel-3B	15
4.1.1	Operation of Sentinel-3 satellites during the campaign IOP.....	15
4.1.2	OLCI data in the reprogrammed FLEX like mode	15
4.1.2.1	Rationale of the FLEX mode experiment.....	15
4.1.2.2	Processing of the OLCI FLEX mode data	16
4.1.2.3	Future analysis of the Sentinel-3B “FLEX mode” dataset.....	20
4.2	Airborne imaging spectrometer <i>HyPlant</i>	21
4.2.1	Processing of <i>HyPlant</i> data.....	22
4.2.1.1	SIF retrieval according to the SVD.....	26
4.2.1.2	SIF retrieval using the iFLD method.....	26
4.2.1.3	SIF retrieval algorithm according to novel SFM algorithm with soil-correction	26
4.3	Airborne thermal imager TASI.....	35
4.3.1	Processing of TASI data	36
4.4	Airborne LiDAR	38
4.4.1	Processing LiDAR data	38
4.5	Ground-based FloX System	39
4.5.1	Stationary FloX systems to record long time series	40
4.5.2	The mobile FloX system for covering the spatial diversity within and across fields	41
4.5.3	Processing of FloX system data	42
4.6	Novel reference targets for future Cal / Val activities.....	43
4.7	The quantification of biochemical and structural vegetation properties	44
4.8	Eddy covariance: acquisition and processing of surface fluxes and the calculation of GPP .	46
4.8.1	Selhausen, Germany.....	46
4.8.2	Grosseto, Italy.....	47
4.8.3	Majadas, Spain	49
5	Quality assessment and validation of the retrieval of sun-induced fluorescence	50
5.1	Quantitative evaluation of the fluorescence maps from the novel SFM algorithm	50
5.2	Comparison between iFLD and SFM maps.....	65
5.3	Comparison and validation of airborne fluorescence products using ground-based measurements.....	69

5.4	Comparison of airborne fluorescence products recorded from different flight altitudes....	78
6	Defining operational quality flags and retrieval uncertainty for airborne SIF products	81
6.1	Quality Flags	81
6.1.1	Solar Zenith Angle (SZA)	84
6.1.2	View Zenith Angle (VZA)	84
6.1.3	Surface elevation	86
6.1.4	Cloud Mask	87
6.1.5	Non-fluorescence reference surface	89
6.1.6	Signal to Noise Ratio (SNR)	90
6.2	Per-pixel SIF retrieval uncertainty	94
6.2.1	iFLD	95
6.2.2	SFM	96
7	Site-specific results for the better understanding of SIF and its potential to track dynamic changes in photosynthesis and detect vegetation stress early.....	100
7.1	Grosseto, Italy.....	100
7.1.1	Linking sun-induced fluorescence, biophysical canopy parameters, and carbon and water fluxes	102
7.1.2	Midday depression of gross primary productivity and SIF in alfalfa (<i>Medicago sativa</i> L.) 108	
7.1.3	Diverse agricultural land-use and its relation to the regional diversity of sun-induced fluorescence	111
7.1.4	Comparison of reflectance-based indices and fluorescence metrics.....	115
7.1.5	Variability in wavelength position of the red and far-red peaks.....	117
7.1.6	Diurnal dynamics of airborne measured SIF and canopy temperature	119
7.1.7	Outcomes of the SurfSense campaign 2018 in Grosseto, Italy (summary of main findings) 123	
7.2	Selhausen and Jülich, Germany.....	131
7.2.1	Mapping the spatial variability of sun-induced fluorescence and canopy traits in a large agricultural region	133
7.2.2	Understanding spatial heterogeneity of SIF from the single pixel to the field	139
7.2.3	Linking eddy based GPP fluxes to SIF maps – determining the right spatial scale to register dynamically changing footprints of carbon fluxes to SIF	149
7.3	Campus Klein-Altendorf, Germany.....	156
7.3.1	Understanding the dynamics of photosynthesis of plants grown under future, elevated CO ₂ concentrations using passive and active fluorescence approaches.....	157
7.3.2	Mapping and understanding the diurnal dynamics of sun-induced fluorescence in agricultural plants.....	163
7.3.3	Measuring sun-induced fluorescence from a novel UAV-based SIF system	168

7.4	Majadas de Tietar, Spain	171
7.4.1	Correlations between ground and airborne measured SIF of the herbaceous layers and the tree canopy	172
7.4.2	The case study of the 2018 heat-wave in the Iberian Peninsula – heat stress effects on SIF and GPP.....	176
7.4.3	Monitoring functional diversity with sun-induced fluorescence	179
7.5	OHP, France	179
7.5.1	Mapping of structural, bio-chemical and physiological traits of the ecosystem of the OHP Plateau.....	183
7.5.2	Influence of variations in atmospheric CO ₂ concentrations on plant performance ...	194
7.6	Laegeren, Switzerland	196
7.6.1	Assessment of site data.....	196
7.6.2	Contextual information to judge scientific suitability of collected data.....	199
7.6.3	Concluding remarks.....	200
7.7	Greifensee, Switzerland and Tyrrhenian open water site.....	201
7.7.1	Site characteristics.....	201
7.7.2	First evaluation of radiometric measurements over aquatic sites.....	202
7.7.3	Retrieval of algal fluorescence from in-situ to airborne to satellite scale	203
7.7.4	Follow up activities and concluding remarks	204
8	Synthesis of 2018 campaign data and recommendation for future use.....	207
8.1	SIF retrieval: from SVD and iFLD to the Spectral Fitting Method (SFM) – the proposed retrieval method for the FLEX satellite mission.....	207
8.2	Quality and uncertainties of airborne SIF products – current status and steps forward ...	207
8.3	SIF as an early stress indicator and its potential to improve forward modelling of gross primary productivity.....	209
8.4	Measuring and understanding SIF from open waters.....	210
8.5	Towards a Cal / Val concept for the FLEX satellite mission.....	210
9	References.....	213
10	Data storage and organization	222
11	Quality Flags	225
12	Scientific publications that resulted from this campaign.....	243
12.1	Publication I: Vila-Guerau de Arellan et al. (2020) - CloudRoots: integration of advanced instrumental techniques and process modelling of sub-hourly and sub-kilometre land–atmosphere interactions.....	244
12.2	Publication II: Martini et al. (submitted to <i>New Phytologist</i>) - Heat wave effect on SIF and GPP on the Iberian dehesa ecosystem	275
12.3	Publication III: Siegmann et al. (submitted to <i>Remote Sensing of Environment</i>) - Dynamics of diurnal courses of SIF in agricultural systems	276

	Doc.: Final Report		
	Date: 29 July 2021	Issue: 2	Revision: 1
	Ref.: ESA Contract No. 4000125402/18/NL/NA		Page: 5 / 288

12.4	Publication IV: Scharr et al. (submitted to <i>Remote Sensing of Environment</i>) - Effect of the point-spread function of SIF retrieval	277
12.5	Publication V: Di Cicco et al. (2020) - “Flex 2018” Cruise: an opportunity to assess phytoplankton chlorophyll fluorescence retrieval at different observational scales	278

Reference Documents (RD)

- [RD-01] FLEX Sentinel Tandem Campaign: Technical Assistance for airborne measurements during the FLEX Sentinel Tandem Experiment 2018, CIP: Campaign Implementation Report, ESA Contr. No. 4000125402/18/NL/NA
- [RD-02] FLEX Sentinel Tandem Campaign: Technical Assistance for Airborne measurements during the FLEX Sentinel Tandem Experiment 2018, DAR: Data Acquisition Report, ESA Contr. No. 4000125402/18/NL/NA
- [RD-03] Technical Note: Data Organization for FLEXSense Campaign
- [RD-04] SurfSense: Technical Assistance for airborne and ground measurements during the High Spatio-Temporal Resolution Land Surface Temperature (SurfSense) Experiment 2018, Final Report, ESA Contr. No. 4000125840/18/NL/LF
- [RD-05] SARSense: Technical Assistance for Airborne Measurements during the SAR Sentinel Experiment, CIP & DAR, ESA Contr. No. 4000125444/18/NL/LF
- [RD-06] Photoproxy: Technical Assistance for the Photosynthetic-Proxy Experiment, Photosynthesis Report 1 - 3, ESA Contr. No. 4000125731/19/NL/LF
- [RD-07] SurfSense: Technical Assistance for airborne and ground measurements during the High Spatio-Temporal Resolution Land Surface Temperature (SurfSense) Experiment 2018, DAR: Data Acquisition Report, ESA Contr. No. 4000125840/18/NL/LF
- [RD-08] Technical Assistance for the Development of Ground-based Systems for Long-term measurements of Red and Far-red Sun Induced Chlorophyll Fluorescence (DEFLOX). CCN extension, Deliverable 2, ESA Contr. No. 4000120771/17/NL/MP/mg
- [RD-09] ATMOFLEX: Technical Assistance for the Deployment of Ground-based Instruments for Long term measurements of Red and Far-red Sun-Induced chlorophyll Fluorescence (ATMOFLEX), Final Report, ESA Contr. No. 4000122454/17/NL/FF/mg
- [RD-10] Technical Assistance for the Deployment of an advanced hyperspectral imaging sensor during HYFLEX, CCN1 – CCN4, DAR & Final Report, ESA Contr. No. 4000107143/12/NL/FF/lf
- [RD-11] ATMOFLEX: Technical Assistance for the Deployment of Ground-based Instruments for Long term measurements of Red and Far-red Sun Induced chlorophyll Fluorescence (ATMOFLEX), CCN1, Final Report, ESA Contr. No. 4000122454/17/NL/FF/mg
- [RD-12] FLEX/Sentinel-3 Tandem Mission - FLEX Bridge Study; Final Report, January 2016; ESA ESTEC Contract No. 4000112341/14/NL/FF/gp
- [RD-13] HyPlant Processing Experiment (HYPER); Final Report, ESA Contract No. 4000112890/14/NL/FF/gp

People who contributed to the report:

Team Germany

Uwe Rascher
Bastian Siegmann
Vera Krieger
Maria Matveeva
Juan Quiros Vargas
Onno Muller
Patrick Rademske
David Herrera
Stephani Baum

Team Italy

Franco Miglietta
Lorenzo Genesio
Roberto Colombo
Marco Celesti
Marin Tudoroiu
Sergio Cogliati
Federico Carotenuto
Benjamino Gioli
Andrea Genangelli

Team Czech Republic

Jan Hanus
Karel Holous

Team Spain

Mirco Migliavacca
David Martini
M Pilar Martin
Arnaud Carrara
Gerardo Moreno
Rosario Gonzales_Cascon
Tarek El-Madany
Javier Pacheco-Labrador

Team Switzerland

Alexander Damm
Rifat Ahmed
Remika Gupana
Eugenie Paul-Limoges

Team France

Ilja Reiter
Irène Xueref-Remy
Jean-Philippe Mevy
Mathieu Santonja

Team Tasmania

Juliane Bending
Zbynek Malenovsky

Team JB Hyperspectral

Tommaso Julitta
Andreas Burkart

Abbreviations

agl	Above Ground Level
AOT	Aerosol optical thickness
APAR	Absorbed Photosynthetically Active Radiation
ASTER	Advanced Spaceborne Thermal Emission and Reflection Radiometer
ATCOR	Atmospheric and Topographic CORrection
BRDF	Bidirectional Reflectance Distribution Function
Cal / Val	Calibration and Validation
CKA	Campus Klein-Altendorf
DAS	Days after sowing
DEM	Digital Elevation Model
DSM	Digital Surface Model
EC	Eddy Covariance
EO	Earth Observation
ESA	European Space Agency
ET	Evapotranspiration
f_{APAR}	Fraction of Absorbed Photosynthetic Active Radiation
F_{687}	Fluorescence at 687 nm
F_{760}	Fluorescence at 760 nm
FLEXsense	'appreciation for this campaign activity'
FLH	Fluorescence Line Height
FLORIS	FLuORescence Imaging Spectrometer
FWHM	Full Width at Half Maximum
GLT	Geometric Lookup Table
GNDALT	Ground elevation
GPP	Gross primary production
GPP_{DT}	Gross primary production day time partitioning
GSD	Ground Sample Distance
H	Sensible Heat Flux
ICOS	Integrated Carbon Observation System
iFLD	Improved Fraunhofer line depth
IOP	Intensive Observation Period
LAI	Leaf Area Index
LCC	Leave Chlorophyll Content
LE	Latent Heat Flux
LIFT	Laser-induced fluorescence transient
LLL	Land leaving radiance

LST	Land Surface Temperature
LUEp	Light Use Efficiency of Photosynthesis
MMD	Maximum-Minimum Difference
NDVI	Normalized difference vegetation index
NEE	Net Ecosystem Exchange
NETR	Net Radiation
NIRv	Near-Infrared Reflectance of Vegetation
NPQ	Non-Photochemical Quenching
OLCI	Ocean and Land Color Instrument
PAR	Photosynthetically active radiance
PRI	Photochemical Reflectance Index
PSF	Point Spread Function
ROI	Region of interests
RT	Radiative Transfer
SFM	Spectral Fitting Method
SIF	Sun-Induced Fluorescence
SNR	Signal-to-Noise
SPR	Atmospheric pressure
SVD	Singular Vector Decomposition
SZA	Solar Zenith Angle
T _{air}	Air Temperature
TES	Temperature and Emissivity Separation
TIR	Thermal Infrared
TOA	Top-of-Atmosphere
TOC	Top-of-canopy
TR32	Transregional Collaborative Research Centre 32
UAV	Unmanned aerial vehicle
VPD	Vapor pressure deficient
VZA	Viewing zenith angles

1 Executive Summary

The 2018 Fluorescence Explorer Sense (FLEXSense) campaign combined various field activities in preparation for the FLEX satellite mission. Two months of campaign activities were undertaken at six sites across Europe, which included the opportunity to measure and interpret the fluorescence signal across various scales (from leaf level to satellite data). The focus of these activities was the recording of complete FLEX-like data sets, which include all relevant elements that are needed for the preparation of the FLEX satellite mission. The data set of this campaign has proven to be complete, providing almost all elements that are needed to develop and validate the data products of the FLEX and Sentinel missions, i.e. including ground based characterization of the structural and functional plant traits, recording of time series of top-of-canopy reflectance, fluorescence and atmospheric properties¹, extensive airborne mapping with the high-resolution imaging spectrometer *HyPlant*, the TASI thermal imager and an airborne LiDAR system, as well as satellite based imagery from Sentinel-2, Sentinel-3 and Sentinel-3B in a reprogrammed mode during commissioning phase.

The main outcomes and findings of this activity are structured in five main chapters and can be summarized as follows:

- **Chapter 4** gives an extensive overview on the instruments and data that were used in this campaign activity. During this campaign, we relied on some well-established airborne and ground-based sensors. The airborne package consisting of the high-resolution imaging spectrometer *HyPlant* (hyperspectral surface reflectance and sun-induced fluorescence (SIF)), TASI (surface temperature) and a LiDAR system (surface and canopy structure) were used from an aircraft and built the backbone of these campaign activities. Data from this sensor package were recorded over diverse ecosystems (including agriculture, natural forests, agroforestry, grasslands, coastal regions and inland and offshore waters) and 342 flight lines of combined data were recorded, processed and quality-checked. The airborne data were combined with extensive ground-based measurements of plant function, detailed atmospheric characterization, and on several ‘golden days’ with synchronous overpasses of the Sentinel-3A and 3B tandem constellation during the commissioning phase, when Sentinel-3B data were provided in a special ‘reprogrammed high-resolution mode’.
- **Chapter 5** describes the retrieval of SIF according to the spectral fitting method (SFM), which is the nominal retrieval method of the FLEX satellite mission. We used the campaign data to develop and carefully test the SFM for *HyPlant* imagery. While in previous activities the SFM retrieval scheme was already applied to selected *HyPlant* data, we have now consolidated the retrieval, have performed a sensitivity analysis on the impact of atmospheric parameters, have implemented an empirical constraint of the method and have finally implemented quantitative quality flags with the SIF data products. The retrieval uses bare soil pixels to constrain the atmospheric radiative transfer (RT) and thus can be used to obtain robust and accurate estimations of fluorescence for a variety of atmospheric and environmental conditions without a strict need of external auxiliary information (i.e., sun photometer), as requested by previous versions of the algorithm. The proposed fluorescence retrieval method was successfully adapted for the use with parallel computing techniques, facilitating for the first time the retrieval of SIF from a large number of flight lines (approx. 100 flight lines in 11 hours). The outcome of the new retrieval method is compared to established retrieval methods, such as the iFLD and the SVD and we could show that the SFM delivers high-quality SIF products for

¹ Synergies with the AtmoFlex activity, which focused on the characterization, standardization and operation of the FLOX systems across different sites covering a time period of 14 months.

both fluorescence peaks (SIF₆₈₇ and SIF₇₆₀). The uncertainty of the SIF products from *HyPlant* data was $< 0.3 \text{ mW m}^{-2} \text{ sr}^{-1} \text{ nm}^{-1}$ and thus is close to the nominal uncertainty target of the FLEX satellite mission. [see also publication IV for a novel module within the *HyPlant* retrieval on the PSF deconvolution]

- **Chapter 6** describes the operational quality flags that were developed during this campaign and which is now implemented for the operational processing of *HyPlant* data. The quality flags give a visual and quantitative overview on key parameters of the level-1c data (e.g. solar zenith angles (SZAs), view geometry, surface elevation and cloud coverage) and also calculates signal-to-noise (SNR) values for automatically selected vegetation units. These uncertainty estimates are tested on some representative flight lines and are now implemented as additional data layers with the *HyPlant* data products. With these new quantitative uncertainty parameters, we provide the basis for a more elaborate quantitative error estimate of *HyPlant* imagery and other airborne fluorescence sensors and open the path for further considerations including *HyPlant* imagery in future Calibration and Validation (Cal / Val) concepts.
- **Chapter 7** highlights the site-specific findings that could be drawn from the campaign data, which can be summarized as follows:
 - A complete diurnal course of maps of SIF, vegetation temperature and reflectance were recorded from a large and diverse agricultural research campus (Campus Klein-Altendorf, Germany). These data were used to develop and test an empirical down-scaling approach, which allows to quantitatively separate structural and functional influences on diurnal canopy SIF measurements of various crop systems. [see chapter 7.3.2 and publication III]
 - The relationship between gross primary productivity (GPP) and SIF was re-examined at various ecosystems. Diurnal and seasonal dynamics were described and interpreted showing that a linear relationship between GPP and SIF only exists on aggregated seasonal data, when changes in canopy chlorophyll content determines GPP. Under stressful conditions, when photosynthesis operates below its potential maximum, the linear relationship breaks down and SIF is the only remote sensing parameter that is able to track stress-induced down regulation of photosynthesis. [see chapters 7.1.1, 7.1.2, 7.2.3]
 - The relationship between GPP and SIF was analyzed in more detail in a nutrient manipulation experiment in a Mediterranean agroforestry, which experienced extreme high temperatures during the campaign activity. We could show that reflectance-based vegetation indices such as the chlorophyll content index (CCI), enhanced vegetation index (EVI), normalized difference vegetation index (NDVI) and near-infrared reflectance of vegetation (NIRv) did not show any significant response to the heatwave. The functionally based parameters, namely photochemical reflectance index (PRI) and SIF were clearly affected by the extreme temperatures that caused a functional downregulation of photosynthesis. The relationship between GPP and SIF was thus reversed demonstrating the potential of SIF to serve as an early stress indicator. [see chapter 7.4.2 and publication II]
 - Larger scale *HyPlant* maps and mobile FloX system measurements were used to investigate the spatio-temporal variations of SIF across different functional plant types. In this context, large agricultural areas in Germany and Italy and diverse Mediterranean forest ecosystems were mapped while on ground the biochemical and photosynthetic characteristics of the diverse vegetation were recorded. These data built the bases to better understand the link between functional diversity of plants and the dynamics in the

	Doc.: Final Report		
	Date: 29 July 2021	Issue: 2	Revision: 1
	Ref.: ESA Contract No. 4000125402/18/NL/NA		Page: 12 / 288

- SIF signal and in reflectance. [see sections 7.1.3, 7.1.4, 7.2.1, 7.3.1, 7.4.3, 7.5 and publication I]
- Several *HyPlant* flight lines were acquired over open inland and coastal waters to test the possibility to retrieve SIF from FLEX like satellite data. The data were spatially binned to increase the SNR ratio of level-1c data and then SIF was successfully retrieved from these images. This demonstrates that SIF can also be retrieved from water ecosystem, even though the low radiance signal in combination with the lower fluorescence signal of open waters will require some concepts to improve SNR. [see section 7.7 and publication V]

The project required a coordination effort of a large number of institutional players and scientists. Most of the objectives have been achieved and a very a large dataset has been put together by assembling field measurements, airborne & satellite acquisitions, and in-depth scientific evaluation of the data. Using data from this extensive campaign, five scientific publications have already been published or were submitted for publication (see section 12), data from this campaign activity have been requested by several group and according to our knowledge, 8 scientific peer-review publication are submitted or published using and acknowledging the data from this campaign². The results of this campaign activity in combination with the outcomes of the synergistic activities ATMOFLEX, SurfSense and Sarsense are particularly relevant for pursuing fruitful interactions with the Flex L2 Project. The FLEXsense campaign provides the most complete and reliable database of high-quality reflectance and SIF data that shall be used to further develop and validate the performance of the L2 retrievals and to be used in the Flex Cal / Val strategy and the FLEX measurements validation protocol.

² Counted according to best knowledge by July 2021

	Doc.: Final Report		
	Date: 29 July 2021	Issue: 2	Revision: 1
	Ref.: ESA Contract No. 4000125402/18/NL/NA		Page: 13 / 288

2 Background

Within the framework of its Earth Observation Envelope Program, the European Space Agency (ESA) carries out a number of different activities to support geophysical algorithm development, calibration, validation, and the simulation of future space borne earth observation missions. The overall goals are derived from the general scientific objectives of several upcoming missions in the context of future Earth Observation (EO) programs and their users. Furthermore, the objectives are relevant for validation campaigns, which are prepared and conducted as part of the current missions in orbit or under development.

The special focus of these campaign activities is on supporting the upcoming Earth Explorer 8 Fluorescence Explorer (FLEX) satellite mission, which comprises a tandem mission between the newly developed FLEX satellite instrument (also referred as FLORIS) and the operational Sentinel-3 satellite mission. The FLEX mission will be the first mission designed to monitor the photosynthetic activity of terrestrial vegetation by using a novel technique to measure the chlorophyll fluorescence signal that originates from the core of photosynthetic machinery. This will open up new possibilities to assess the dynamics of photosynthesis through SIF, which represents a great advancement compared with current conventional land surface monitoring satellites, which can only detect potential photosynthesis derived from passive reflectance measurements using conventional land surface monitoring satellites. The objective of the FLEX satellite mission is to provide global maps of actual photosynthesis and plant health status by measuring the fluorescence signal vegetation on a 300 m x 300 m resolution and a global revisiting time of 10 - 25 days.

The specific FLEX objectives are:

- To support the identification of optimal management strategies (plant growth and stress resistance) in the context of crop production and food security.
- To provide an early pre-visual identification of stress effects to help track resilience and recovery of plant photosynthetic function, to delimit vegetation sites compromised by biotic and abiotic stresses, and to identify vegetation stands affected by insect or disease in order to schedule measures to salvage a harvest.
- To better understand and describe processes related to the dynamics of plant photosynthesis, aiming at more accurate estimates of GPP to improve the implementation of carbon assimilation into dynamic vegetation models.
- To increase our knowledge about carbon and water cycle-coupling, thus improving the predictive capability of current model systems.

3 Specific campaign objectives

The basic setup of the FLEXSense campaign activities focused on collecting relevant airborne data over representative monitoring sites, concurrent with ground-based measurements for time intervals compatible with the FLEX / Sentinel-3 space-borne missions over a longer period (approx. two months) to sample spatio-temporal variability in vegetation, soils, and the atmosphere. In order to study tradeoffs and synergies between different ground and airborne approaches, high frequency sampling was conducted during intensive observation periods (IOP) to simulate temporal and spatial sampling with repeated flyovers. To cover the above-mentioned analyses, strong collaboration was required among different communities to build on the experience from previously planned activities in the context of mission development and Cal / Val activities for the existing Sentinel-2 and Sentinel-3, and the future FLEX mission.

These activities focused on quantifying the structural and functional status of vegetation by exploiting SIF, land surface temperature (LSE), and the bio-physical characteristics of vegetation, such as e.g. chlorophyll content or canopy water content. Despite the focus on terrestrial vegetation, we expect that the data from this campaign activity will also prove useful for coastal and atmospheric related applications.

To achieve these objectives, several airborne and ground actions in combination with the relevant data processing, scientific data analysis, data storage, and dissemination activities were conducted during the vegetation period 2018 covering six sites in Germany, Italy, France, Spain and Switzerland with the aim to:

- Record a high-quality reference data set of experimental real-world data that span the spatial scales from (i) ground-based measurements of leaf and canopy fluorescence emission (SIF), selected biophysical vegetation parameters and quantitative measurements of vegetation functioning; (ii) a detailed characterization of atmospheric properties; (iii) high-resolution airborne measurements of surface reflectance and SIF, as well as (iv) satellite data from Sentinel-2 and Sentinel-3.
- Process these data to higher-level data products using retrieval schemes that are currently being developed in preparation of the FLEX satellite mission.
- Test and validate the different data products across the spatial scales using the various data collected during this campaign.

The outcome of this campaign will be used for other FLEX-related activities and in the wider context of ESAs Earth Observatory initiative. Concretely, the data from this campaign will be used in:

- The L2-study of ESA, which aims to deliver level-2 product retrieval schemes for the future FLEX satellite mission. Currently, these retrievals are developed on modelled data from the E2E simulator only. In the next upcoming steps, the campaign data from this activity will build the basis to test and evaluate the level-2 retrievals based on real experimental data.
- Additionally, data from this campaign will be embedded in future Cal / Val concepts for FLEX and other optical satellite missions. The goal is to develop a Cal / Val concept that uses fiducial reference measurements to link Cal / Val of different satellite missions. The data from this campaign may provide an example for a fiducial reference measurement concept for fluorescence measurements .

4 Instrumentation and processing

4.1 Sentinel-3B

4.1.1 Operation of Sentinel-3 satellites during the campaign IOP

The Copernicus Sentinel-3 mission comprises a series of four separate satellites in constellation. Two out of four satellites are already in orbit. Sentinel-3A was launched in 2016 and Sentinel-3B in 2018, respectively. Both satellites are equipped with two optical instruments i) ocean and land colour instrument (OLCI) and ii) sea and land surface temperature radiometer (SLSTR). Furthermore, they carry a synthetic aperture radar altimeter (SRAL) and a microwave radiometer (MWR). The objective of the Sentinel-3 mission is to monitor the ocean and land surfaces and their temperatures as part of the Global Monitoring for Environment and Security (GMES) program. The satellites are equipped with three precise orbit determination (POD) systems: i) a Doppler orbit radio positioning system (DORIS), ii) a GPS receiver, providing precise orbit determination and tracking multiple satellites simultaneously (GNSS) and iii) a laser retro-reflector system (LRR). The approx. lifetime of both satellites is seven years. They are operating at an altitude of 814.5 km and cover the whole earth every two days.

Concurrent with the 2018 FLEXsense campaign, Sentinel-3A and Sentinel-3B were operated in constellation as part of the tandem commissioning phase. This presented a unique opportunity to acquire FLEX-like data simulating the tandem mission concept between Sentinel-3 and FLEX. The tandem commissioning phase consists of three phases:

Drift phase 1 (25 April – 6 June 2018): Initial drift of Sentinel-3B to reach Sentinel-3A

On 25 April 2018, Sentinel-3B was launched into a 10 km higher orbit than Sentinel-3A and was allowed to drift back to Sentinel-3A to reach its position during the tandem phase. The drift phase was completed on 6 June 2018.

Tandem phase (6 June – 16 October 2018): Sentinel 3A and Sentinel 3B constellation

During the tandem phase, Sentinel-3B took its position 30 s in front of Sentinel-3A. Both satellites are located at an angle of 180° to each other. At the end of June, first data from Sentinel-3B instruments OLCI and SRAL were obtained. At the beginning of September, SLSTR provided its first data. Furthermore, MWR data were available before drift phase 2 had started.

Drift phase 2 (16 October – 27 November 2018): Drift of Sentinel-3B to operational orbit

In drift phase 2, Sentinel-3B was maneuvered from an angle of 180° to Sentinel-3A to 140°. After the completion of the second drift phase, all Sentinel-3B instruments were performing normally.

4.1.2 OLCI data in the reprogrammed FLEX like mode

4.1.2.1 *Rationale of the FLEX mode experiment*

During the tandem phase of the Sentinel-3A and -3B tandem mission, it was possible to perform a dedicated FLEX campaign re-programming the OLCI band settings on the B unit for a limited time. Hence, this mimicked as much as possible the future Sentinel-3 and FLEX mission concept.

The main constraints for this campaign were the following:

- the time period during which OLCI on Sentinel-3B could be operated in FLEX mode was eight weeks (from 14 June 2018 to 14 August 2018);
- each OLCI acquisition in “FLEX mode” was limited to a total length of 6500 frames (i.e.,

~1950 km on ground ~286 s) per orbit. Orbit, start and stop time were selected in advance in order to acquire over the ATMOFLEX / FLEXSense sites;

- in total, 45 bands were available at a spectral resolution of ≈ 1.25 nm in the spectral range 389 - 1040 nm.

Given the constraints outlined above, two main scientific objectives were identified that are directly linked to the development of the FLEX level-1B to level-2 processor:

1. Measurements to test the FLEX level-1B to level-2A processing, in particular spatial co-registration, spectral cross-calibration, and final ortho-rectification.
2. Measurements to test the atmospheric characterization using the measurements from Sentinel-3A, the sub-sequent atmospheric correction and surface reflectance retrieval in all spectral channels including the ones from the re-programmed OLCI-B.

Data acquisition was performed over the ATMOFLEX / FLEXSense sites in Germany, Italy, France, Switzerland, Spain and Nebraska (USA). This yielded in total nine acquisitions over the entire sensing window during which we were able to record “complete data sets” in which all components from ground, airborne and satellite measurements and simultaneous atmospheric measurements were available (Table 1). On these flight lines, the quality of *HyPlant* and Sentinel-3A data was carefully checked. Sentinel-3B level-0 data were processed to L-1B calibrated top-of-atmosphere (TOA) radiances within the context of the MULTI-FLEX Living Planet Fellowship research project carried out by Marco Celesti³. The entire dataset of level-1B TOA radiances is available through the ESA repository (<https://eo4society.esa.int/projects/multi-flex-towards-a-strategy-for-fluorescence-monitoring-at-multiple-scales-within-the-context-of-the-flex-s-3-tandem-mission/>).

4.1.2.2 Processing of the OLCI FLEX mode data

The final spectral configuration selected for the “FLEX mode” OLCI-B data is reported in Figure 1. This spectral configuration was selected in order to represent some key elements of the low-resolution FLORIS module (FLORIS-LR) and of the high-resolution one (FLORIS-HR). It covers the key spectral regions in an optimal way given the constraints of minimal bandwidth and total number of possible bands. Moreover, the configuration adds some bands for optimal spectral / radiometric processing and consistency check. One of the calibration setups of OLCI, the S09 calibration mode, was modified to achieve this configuration.

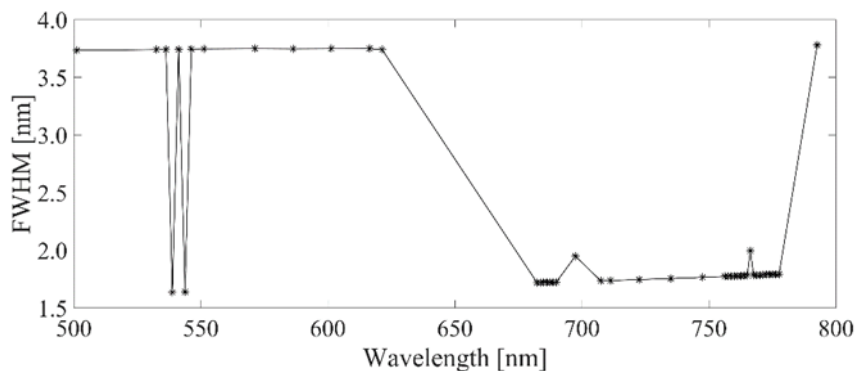


Figure 1: Spectral configuration (central wavelength and Full Width at Half Maximum, or FWHM) of the 45 bands in the OLCI sensor onboard Sentinel-3B reconfigured in “FLEX mode” during the commissioning phase.

³ <https://eo4society.esa.int/projects/multi-flex-towards-a-strategy-for-fluorescence-monitoring-at-multiple-scales-within-the-context-of-the-flex-s-3-tandem-mission/>

Since there was no ground processor capable of processing data up to level-1B (i.e., from raw data to TOA radiances), a specific processing chain had to be developed. Within the collaboration between the Sentinel-3 Mission Performance Centre (ESA/Contract No. 400011836/14/I-LG) and a Living Planet Fellowship project (MULTI-FLEX, ESA/Contract No. 4000125442/18/I-NS), the “FLEX mode” data was adapted to the standard EO mode format. Hence, they were ingested into the standard level-1 OLCI processor (OL1). In particular, 45 bands of level-0 products were split into three separate products, each with spectral subsets of 21 bands (Figure 2). Besides, additional adaptations were made to the header in order to mimic the EO mode data. Moreover, full sets of calibration (OL_1_CAL_AX), instrument specifications (OL_1_INS_AX) and programming (OL_1_PRG_AX) ancillary data files (ADFs) were produced in order to feed the OL1 processor. Every spectral subset was successfully processed up to level-1B and formatted as a standard OLCI level-1B product (Figure 3). Afterwards, the data were quality checked to ensure consistency in the processing of the different spectral subsets.

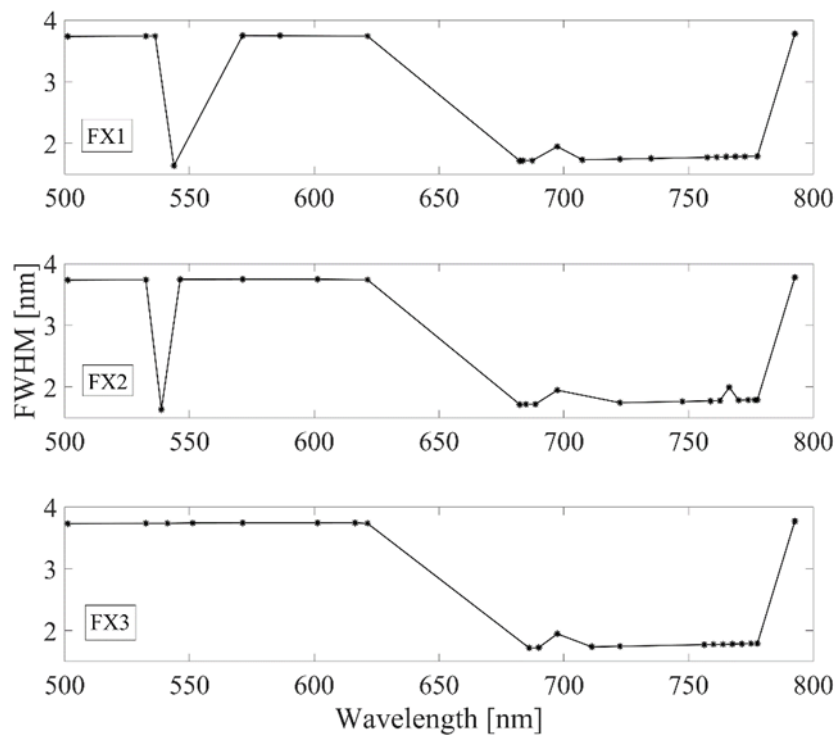


Figure 2: Central wavelength and FWHM of the three spectral subsets (FX1, FX2 and FX3) of the “FLEX mode” OLCI data.

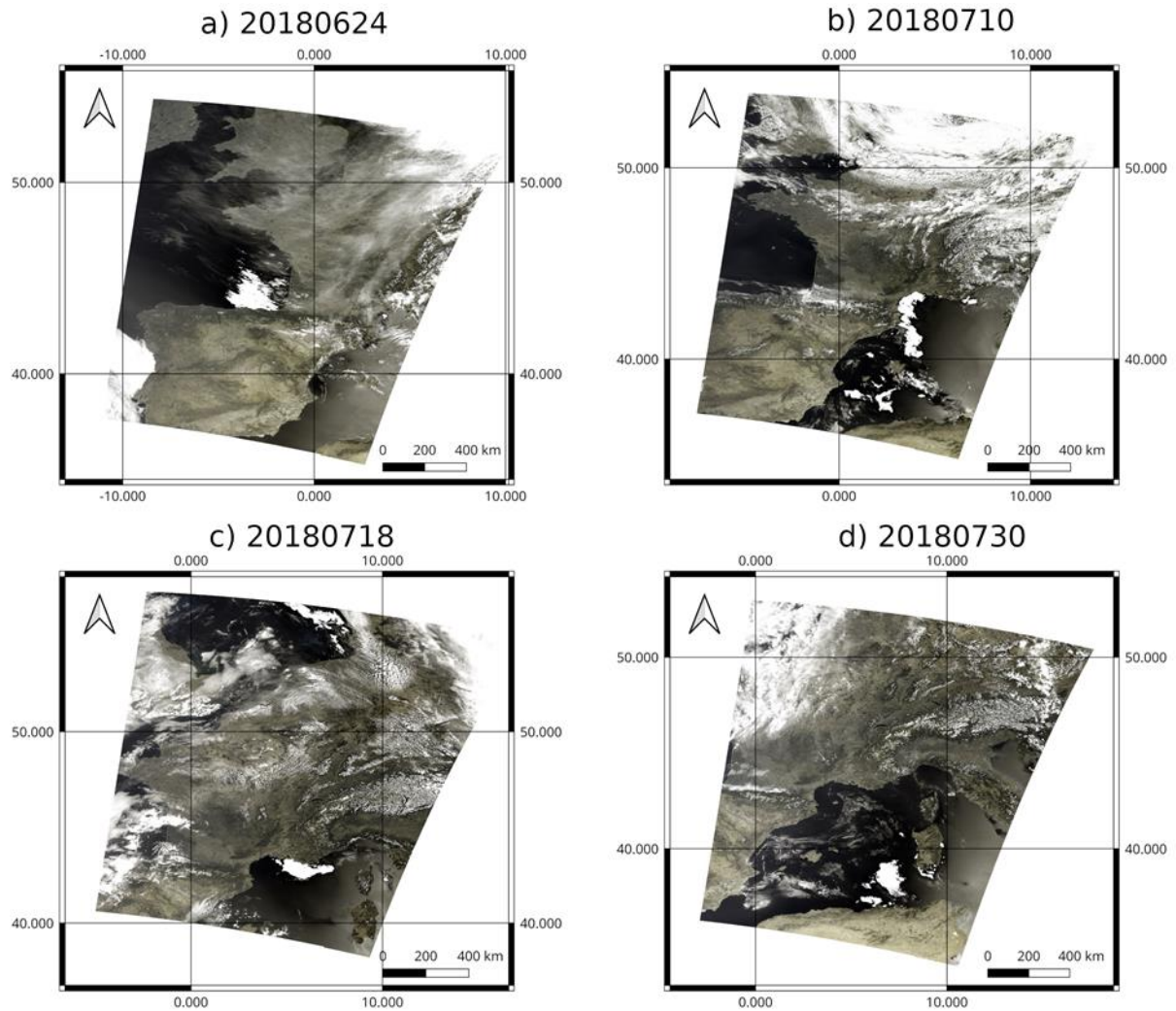


Figure 3: Four Sentinel-3B OLCI FLEX mode level-1B TOA radiance products (“tristimulus” RGB composite) from the selected dataset, acquired on 24 June 2018 (a), 10 July 2018 (b), 18 July 2018 and 30 July 2018. Data were projected in WGS84 using the SNAP ESA software. The entire dataset of level-1B TOA radiances is available through the ESA Earth Online repository (<https://eo4society.esa.int/projects/multi-flex-towards-a-strategy-for-fluorescence-monitoring-at-multiple-scales-within-the-context-of-the-flex-s-3-tandem-mission/>)

Table 1: List of “FLEX mode” acquisitions with OLCI onboard Sentinel-3B during the FLEXsense IOP. These data were manually selected as their complete data (including airborne, atmospheric and ground-based measurements) are available.

#	Site	Coordinates	Date and S3Br time (2018)	S3A	S3Br	HyPlant (low/high fly)	CIMEL	FloX	S3r camera	Target	Turps, VegParam, Atmo...
SP1	Spain (Majadas)	39.939644 N, 5.77175556 E	24 June (start time 10:22:52, end time 10:28:30)	Yes	Yes	YY	Y	Y		Savannah	
FR1	France (OHP)	43.932067 N, 5.715636° E	10 July (start time 10:08:02, end time 10:13:40)	Yes	Yes	YY	N	Y	4	Oak Forest	Lidar
IT1	Italy (Grosseto Crop - Braccagni)	N 42.830842, E 11.070136	07 July (start time 09:45:52, end time 09:51:38)	Yes	Yes	YY	Y	Y	4	Alfa alfa	
IT2	Italy (Grosseto Crop - Braccagni)	N 42.830842, E 11.070136	18 July (start time 09:59:30, end time 10:05:08)	Yes	Yes	NY	N	Y		Corn	
IT3	Italy (Grosseto Crop - Braccagni)	N 42.830842, E 11.070136	30 July (start time 09:49:27.233, end time 09:55:06.913)	Yes	Yes	NY	N	Y	4	Corn	
GE1	Germany (Selhausen)	N 50.869293, E 6.450168	02 July (start time 10:13:29, end time 10:19:07)	Yes	Yes	NY	Y (FZJ)	Y	4	Grass	MFRSR
GE2	Germany (Selhausen)	N 50.869293, E 6.450168°	02 August (start time 10:09:41.290, end time 10:15:20.970)	Yes	Yes	YY	Y (FZJ)	Y		Grass	MFRSR
SW1	Switzerland (Lägeren)	47.478576 N, 8.343082° E	13 July		No	YY	TBC	Y		Mixed Forest	
SW1	Switzerland (Lägeren)	47.478576 N, 8.343082° E	18 July (start time 09:59:30, end time 10:05:08)	Yes	Yes	NN	TBC	Y		Mixed Forest	

4.1.2.3 Future analysis of the Sentinel-3B “FLEX mode” dataset

Although there are inherent discrepancies in the spectral resolution, spectral characterization and SNR between OLCI and FLORIS, with these “FLEX mode” data we obtained for the first time a collection of satellite images with relatively high spectral resolution in the oxygen absorption bands (O₂-A and O₂-B) without compromising the spatial resolution compared to the future FLEX data. This is of utmost relevance within the context of future FLEX Cal / Val activities, both for testing sampling strategies and for learning lessons related to the future coupling of ground, airborne and satellite scale data. The Sentinel-3B “FLEX mode” dataset, in fact, provides an observational playground to test algorithms and procedures for the upcoming FLEX / Sentinel-3 tandem mission. Preliminary efforts in this direction are being undertaken, particularly toward the comparison of airborne and satellite products. Figure 4a shows an RGB synthesis of the surface reflectance mosaic obtained from *HyPlant* DUAL images in Braccagni (Italy) on 30 July 2018. *HyPlant* surface reflectance was coupled to a simulation of the atmospheric properties (MODTRAN RT model) and convoluted to the Sentinel-3B “FLEX mode” spectral resolution to generate a map of simulated TOA radiance. Figure 4b shows the spectral coefficient of correlation between *HyPlant* and Sentinel-3B “FLEX mode” TOA radiance, highlighting an overall very good agreement between the two products. Further analysis will be carried out, including a comparison of top-of-canopy (TOC) reflectance and fluorescence products as soon as a proper atmospheric correction of the Sentinel-3B “FLEX mode” data is performed.

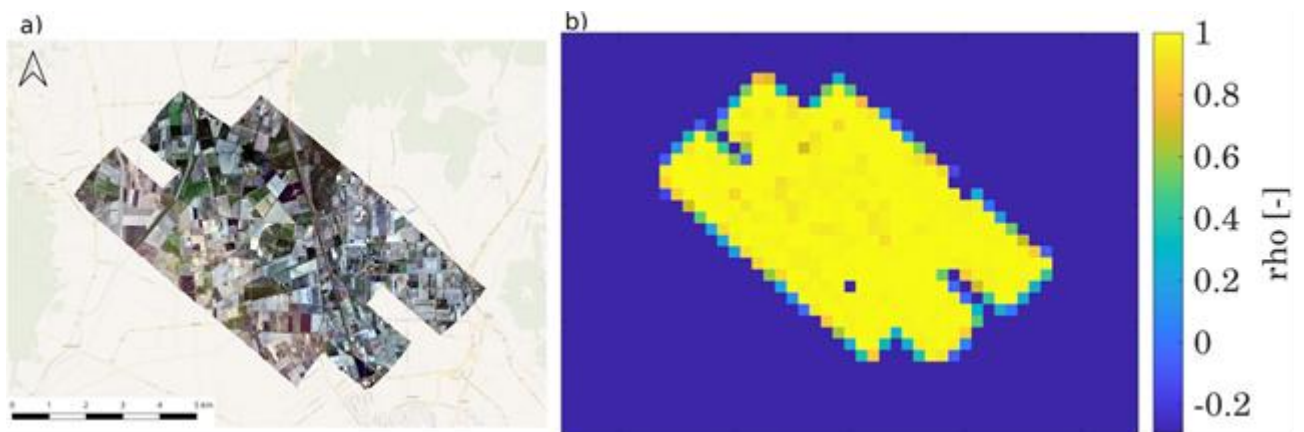


Figure 4: a) RGB synthesis of *HyPlant* surface reflectance in Braccagni (Italy) on 30 July 2018; b) coefficient of correlation between *HyPlant* and Sentinel-3B “FLEX mode” TOA radiance spectra.

A critical aspect related to increasing the increased usefulness of the Sentinel-3B “FLEX mode” data for quantitative analysis is the characterization of the uncertainty of the level-1B products. By comparing data acquired during the tandem phase in operational mode, Lamquin et al. (2020) reported an overall very good consistency between the Sentinel-3A and Sentinel-3B OLCI instruments, with radiometric deviation between the two of about 1-2%. Nevertheless, the performance of OLCI in “FLEX mode” cannot be quantified in such a straightforward way, since it is not directly possible to reconstruct standard OLCI bands by means of the “FLEX mode” microbands. The ESA project “SF-tape” being undertaken with FU Berlin is currently exploiting state of the art RT modeling and numerical optimization approaches to quantitatively characterize the uncertainty in the Sentinel-3B “FLEX mode” TOA radiance data. Preliminary results show a very good agreement with Sentinel-3A OLCI data after accounting for the different spectral configuration of the two OLCI instruments (i.e. the “FLEX mode” vs the standard operational OLCI mode), with discrepancies in the same order of magnitude as those reported by Lamquin et al. (2020). This is encouraging for the future exploitation of these data, as it confirms the stable performance of the OLCI level-1 processor when dealing with the high resolution “FLEX mode” spectral configuration.

4.2 Airborne imaging spectrometer *HyPlant*

The *HyPlant* sensor is a high-performance airborne instrument consisting of two sensor modules: The DUAL module, which contains two push broom imaging line scanners providing spectral information from 380 nm to 2500 nm, and the FLUO module, which produces data at high spectral resolution (0.25 nm) in the spectral region between 670 nm and 780 nm. Both modules are connected to an Oxford 3052 GPS / INS unit, which provides, synchronously with the image data, aircraft position and orientation information for image rectification and geo-referencing. Both imagers (DUAL and FLUO modules) are mounted in a single platform with the mechanical capability to align the field of view (FOV) (see Siegmann et al. 2019 for a detailed technical description of the *HyPlant* sensor).

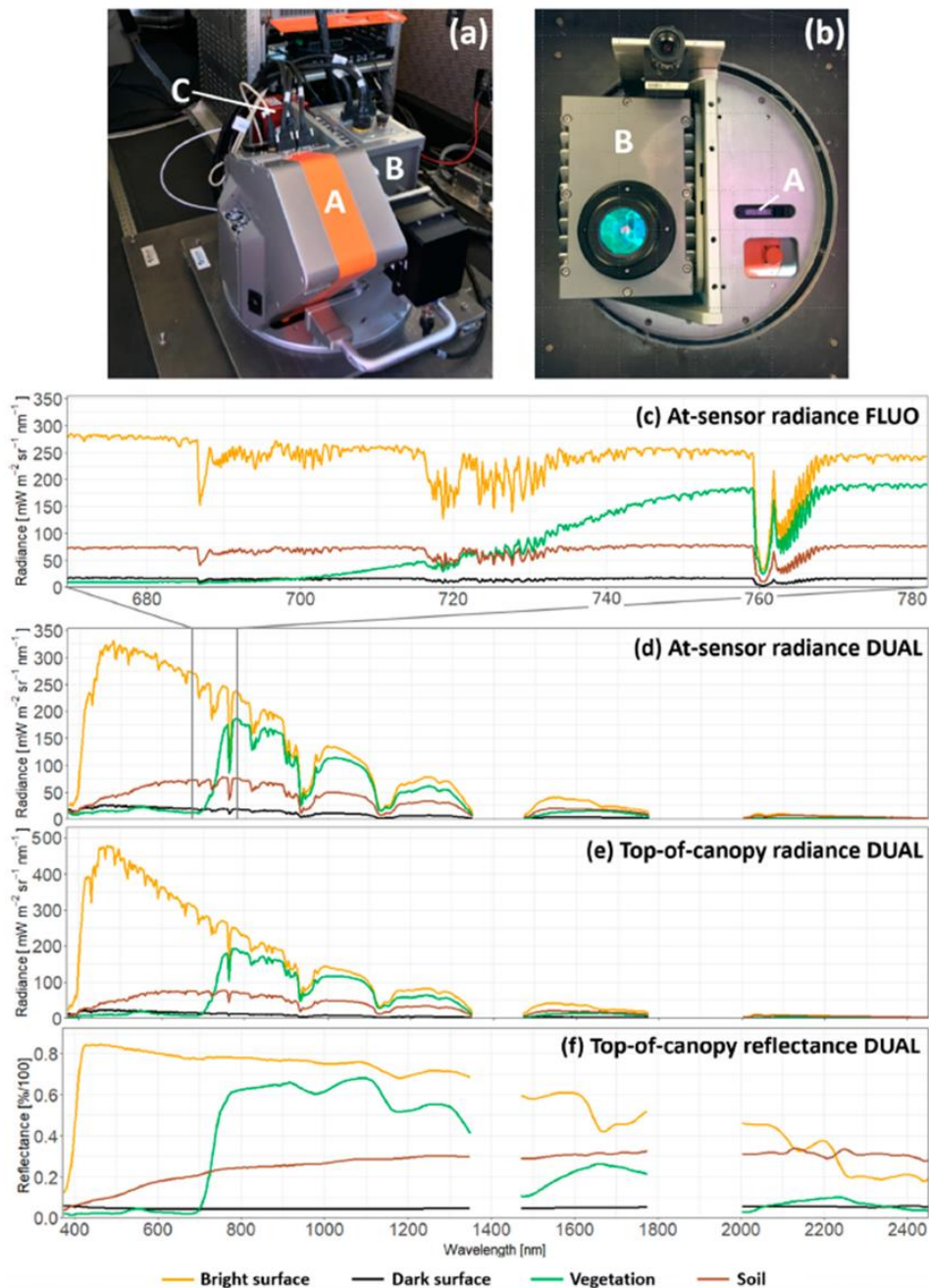


Figure 5: *HyPlant* airborne imaging spectrometer: a) installation of the sensor system in the aircraft, consisting of the broadband DUAL module (A), high-resolution FLUO module (B) and GPS / INS unit (C); b) *HyPlant* DUAL (A) and FLUO (B) module installed in the hatch of the aircraft (image taken from below the aircraft); c) *HyPlant* FLUO at-sensor radiance; d) *HyPlant* DUAL at-sensor radiance; e) *HyPlant* DUAL TOC radiance; f) *HyPlant* DUAL TOC reflectance of selected surfaces (figure taken from Siegmann et al. 2019).

	Doc.: Final Report		
	Date: 29 July 2021	Issue: 2	Revision: 1
	Ref.: ESA Contract No. 4000125402/18/NL/NA		Page: 22 / 288

The *HyPlant* airborne imaging spectrometer was developed as a cooperative endeavor between Germany's FZJ and the Finnish company SPECIM. As the core reference instrument and demonstrator for the FLEX satellite mission, *HyPlant* was the first airborne sensor optically optimized to retrieve the fluorescence full-spectrum, taking advantage of the oxygen absorption and fluorescence near 687 nm and 760 nm. Since the initial testing in 2012, research has confirmed the possibility to retrieve SIF in the O₂-A and O₂-B bands (Rascher et al. 2015; Siegmann et al. 2019). Since then, *HyPlant* data have been used in various activities and to date 19 scientific publications that use *HyPlant* fluorescence products have been released (Rascher et al. 2015, Rossini et al. 2015, Simmer et al. 2015, Wieneke et al. 2016, Drusch et al. 2017, Middleton et al. 2017, Colombo et al. 2018, Gerhards et al. 2018, von Hebel et al. 2018, Bandopadhyay et al. 2019, Gamon et al. 2019, Liu et al. 2019, Siegmann et al. 2019, Tagliabue et al. 2019, Yang et al. 2019, Pinto et al. 2020, Tagliabue et al. 2020, Vila-Guerau de Arellan et al. 2020, and Hornero et al. 2021).

The first *HyPlant* system has been continuously updated and the optical path, the detector unit and the read-out electronics have been continuously improved. Since the 2018 FLEXSense campaign activities, the *HyPlant* sensor reached a consolidated status and the system is now labeled *HyPlant* 3. *HyPlant* 3 is annually calibrated and calibration data have shown a stable and comparable performance of the sensor since 2018. No sensor or data artifact are known from the laboratory calibration and we thus assume that the currently used *HyPlant* 3 sensor version is a consolidated airborne sensor for optical reflectance and fluorescence measurements, which provides radiometrically stable and reproducible data with a geo-accuracy better than one pixel (Siegmann et al. 2019).

4.2.1 Processing of *HyPlant* data

The *HyPlant* processing chain gives an overview about the single processing steps of the DUAL and FLUO module, from raw data to final products, such as TOC radiance, vegetation indices and fluorescence maps (Figure 6). The processing chain consists of four clusters, whereas the first cluster describes the transfer of raw data, associated navigation and header files, and calibration data to the two processing lines of the DUAL and FLUO module. The second cluster explains the procession of the DUAL data while the third and fourth cluster deals with the processing of the FLUO data and the retrieval of SIF according to four different SIF-retrieval methods (Figure 6).

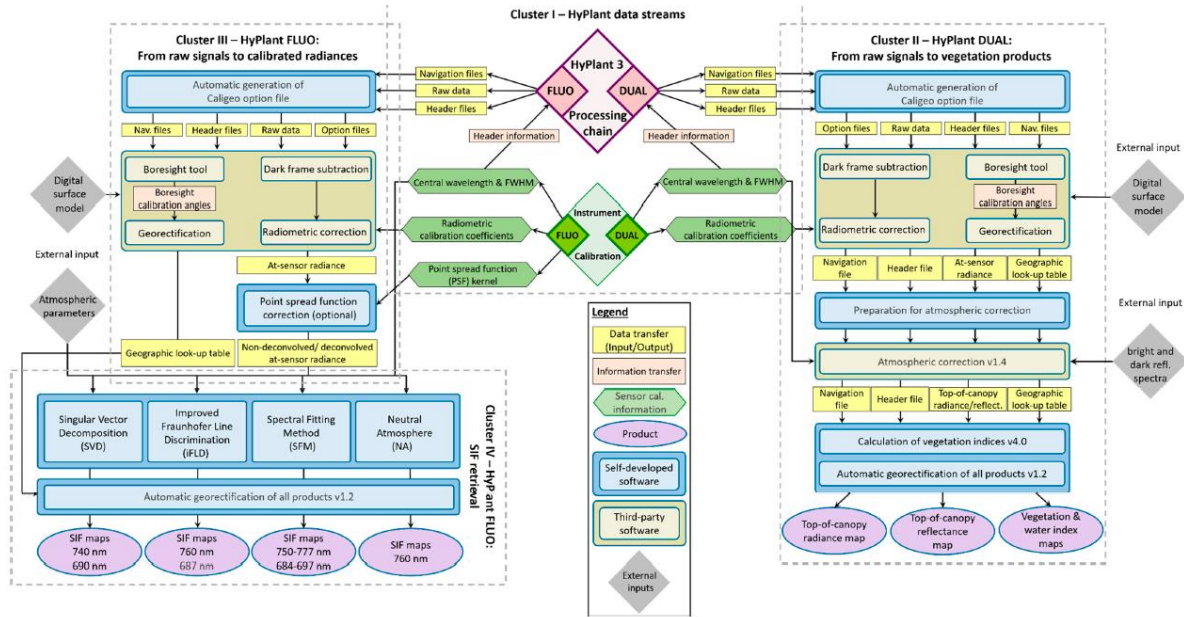


Figure 6: Overview of the *HyPlant* processing chain consisting of four processing clusters. Figure taken from Siegmann et al. (2019).

The following paragraphs provide an overview on the processing of the DUAL and FLUO data (further details can be found in Siegmann et al. 2019).

DUAL module

Raw data from the *HyPlant* DUAL module are processed to at-sensor radiance using the program CaliGeoPRO and the most recent radiometric calibration provided by Specim. Geometric lookup table (GLT) and MapLoc files of the georectification produced with CaliGeo are stored on the server. Atmospheric correction was performed with the commercial software Atmospheric & Topographic Correction algorithm (ATCOR). Generated TOC reflectance and radiance data were georectified using the stored GLT files.

Ten vegetation indices that are related to chlorophyll content, water content, leaf area index (LAI), photosynthesis and non-photochemical quenching are calculated from the TOC reflectance data as a default from *HyPlant* DUAL data (Siegmann et al. 2019).

FLUO module

Another part of the *HyPlant* processing chain describes the procedure of converting FLUO raw data to at-sensor radiance (Figure 6). For this purpose, the CaliGeoPro software is used with the most recent radiometric calibration data that are provided by Specim within the frame of the annual calibration procedure. As the result of this pre-processing, the user receives the at-sensor radiance and the GLT file similar to the DUAL processing. In contrast to the DUAL module, the radiometric correction of the FLUO module can optionally be extended by the application of a custom-made point spread function (PSF) deconvolution procedure. Ideally, an imaging spectrometer looking at a monochromatic point source should produce a single pixel response. In real systems, however this is not the case, and the resulting signal spreads in the sensor matrix around this pixel. This distribution of light across the sensor is called instantaneous PSF and in the case of fluorescence retrieval may substantially affect the magnitude of the fluorescence signal. The sensitivity of the retrieved fluorescence products to an imperfect PSF was first described by Alonso et al. (2008) and then further evaluated by Scharr et al (submitted). Now it is established that the PSF should be minimized or corrected during preprocessing.

	Doc.: Final Report		
	Date: 29 July 2021	Issue: 2	Revision: 1
	Ref.: ESA Contract No. 4000125402/18/NL/NA		Page: 24 / 288

In *HyPlant 3*, the PSF is optimized and *HyPlant 3* operates with a greatly improved PSF. Based on some forward studies, we know that the impact of the PSF on fluorescence products is less than 20% for normal measurement settings, but nevertheless we have implemented a deconvolution routine that follows the Van Cittert approach (Jähne 2005), which can be switched on or off by the user (Siegmann et al. 2019).

The main processing steps are labelled in the file name of the flight line (Table 2). Each file name contains the acquisition date, area and local time of the data acquisition, as well as information about the flight altitude from which the ground pixel size can be concluded. The basic information recorded was the name of the flight line, heading of the aircraft during data acquisition, and the module (DUAL or FLUO) from which the flight line was recorded. After the radiometric and wavelength calibration, the label 'radiance' is added. TOC radiance files are stored with the 'img_surfrad' label. The TOC reflectance files are additionally spectral polished and smile corrections are applied (these files are labelled with 'img_atm_polish_smcorr' in the file name). From TOC reflectance, vegetation indices are calculated and vegetation index files are labelled with 'indices_up'.

For the FLUO module, the label 'deconv_i1' indicates that the deconvolution was applied using the PSF. The label 'Fs_linear_v2' indicates that the fluorescence maps were calculated with the singular value decomposition (SVD) method. The label 'FIXDEM_V5' shows that the maps were calculated with the Improved Fraunhofer line depth (iFLD) method. The fluorescence maps calculated with the SFM are stored in two different files, marked with the label 'SIFO₂A' and 'SIFO₂B' for the two absorption bands. *HyPlant* flight lines labelled with the suffix 'rect' indicate that the calculated product was georectified.

Table 2: The file names for the different *HyPlant* products using data acquisition at the Selhausen test site in Germany as an example. Final products are marked in bold.

Acquisition date	Acquisition area	Recording time (local)	Flight altitude	Module of the sensor	Processing steps DUAL	Processing steps FLUO
YYYYMMDD	-SEL (Selhausen)	-hh:mm	-0600 (1 m x 1 m pixel)	-FLUO	-radiance (radiometric calibration file of SPECIM was applied)	-radiance (radiometric calibration file of SPECIM was applied)
				-DUAL	-img_surfrad (atmospherically corrected radiance data)	-deconv_i1 (deconvolution of the spectra to correct the point spread function)
					-img_atm_polish_smcrr (atmospherically corrected reflectance data, with applied spectral polishing and smile correction)	-FIXDEM_V5 (fluorescence maps calculated with brightness correction of the iFLD method)
					-indices_up (calculation of selected vegetation indices)	-Fs_linear_v2 (fluorescence maps calculated with the SVD method)
					-rect (georectification using the GLT file)	-SIFO2A and -SIFO2B (fluorescence maps calculated with the SFM)
						-rect (georectification using the GLT file)

	Doc.: Final Report		
	Date: 29 July 2021	Issue: 2	Revision: 1
	Ref.: ESA Contract No. 4000125402/18/NL/NA		Page: 26 / 288

Three different fluorescence retrieval methods have been developed since 2012, the iFLD, the SVD and the SFM. The iFLD method was applied to all flight lines to retrieve fluorescence. Only a few flight lines could not be processed because of missing non-vegetated pixels, which is a requirement of the iFLD method. Additionally, the SVD and the SFM method were applied to selected core flight lines as well as to the flight lines that could not be processed by the iFLD method.

4.2.1.1 SIF retrieval according to the SVD

The so-called SVD retrieval method is a form of spectral fitting method for fluorescence retrieval (Guanter et al. 2012, 2013; Joiner et al. 2013). It also represents the at-sensor radiance as the sum of the radiance reflected by the surface and the fluorescence contribution. The reflected radiance is constructed as the product of a spectrally smooth surface reflectance (modeled as a polynomial in wavelength) and the atmospheric absorption. However, instead of using explicit RT modeling to calculate atmospheric absorption along the spectral fitting window, this is modeled as a linear combination of orthogonal spectral functions derived from the data through singular vector decomposition (similar to principal component analysis) (Siegmann et al. 2019). The SVD method for *HyPlant* imagery was established in 2014 and is used since then for retrieving SIF from the FLUO data.

4.2.1.2 SIF retrieval using the iFLD method

The iFLD, as part of the *HyPlant* processing chain, is based on the iFLD method initially proposed by Alonso et al. (2008) which was adapted to allow SIF retrievals from the FLUO module of *HyPlant* (Rascher et al. 2015). The SIF signal is retrieved at two wavelengths: the oxygen absorption band at 687 nm (O₂-B) and 760 nm (O₂-A).

All required atmospheric transfer functions are obtained from MODTRAN5 (Berk et al. 2005) simulations, in combination with the MODTRAN5 interrogation technique (Damm et al. 2015, Verhoef et al. 2003, 2003a, 2007). For the airborne data, an empirical constraint based on non-vegetated reference surfaces is additionally implemented to account for uncertainties in the characterization of the atmosphere and remaining sensor artifacts (i.e., spectral shifts and detector miscalibration). The details of this approach can be found in Damm et al. (2014). The iFLD method can only be applied with sufficient non-vegetated reference pixels across track along the whole flight line (Siegmann et al. 2019).

4.2.1.3 SIF retrieval algorithm according to novel SFM algorithm with soil-correction

This section introduces the novel fluorescence retrieval algorithm developed for the *HyPlant* sensor (and generally for similar airborne imaging spectrometers, e.g. SPECIM IBIS), including discussion of motivations, theoretical foundations and technical implementations. This type of fluorescence retrieval is of special interest as a similar retrieval approach is currently being developed for the FLEX satellite mission. Given the potential synergies between this airborne retrieval and the proposed satellite retrieval, their exploitation is intended.

Airborne fluorescence retrieval based on the SFM (Cogliati et al. 2018) is a physically-based approach aiming at quantifying the filling-in of canopy F within the O₂ absorption bands (Cogliati et al. 2015a). The red and far-red fluorescence peaks are retrieved from *HyPlant* data by analyzing narrow spectral windows centered at the two O₂-B and O₂-A bands, respectively. For the moment, the airborne F retrieval is limited to providing fluorescence maps at the O₂ bands only, and it is not yet intended to retrieve the full F spectrum. However, this would be possible by a more sophisticated spectral fitting

	Doc.: Final Report		
	Date: 29 July 2021	Issue: 2	Revision: 1
	Ref.: ESA Contract No. 4000125402/18/NL/NA		Page: 27 / 288

algorithm that is developed for ground-based measurements (Cogliati et al. 2019) and currently under development for the FLEX satellite mission.

Technically, the current airborne fluorescence retrieval consists of three main processing blocks:

- 1) in-flight characterization of the instrument spectral response functions (SPECCAL);
- 2) modeling of the atmospheric transfer functions;
- 3) decoupling of the canopy fluorescence and reflectance (Spectral Fitting Method- SFM).

The algorithm relies on forward simulation of at-sensor radiance spectra at the O₂ bands by means of coupled surface / atmosphere RT calculations. The surface is characterized by a spectrally smooth behavior that can be modelled with simple parametric functions (i.e., polynomials for reflectance; peak-like functions for fluorescence) within the SFM technique. Conversely, the propagation of radiation through the atmosphere is performed by using the MODTRAN® (MODerate resolution atmospheric TRANsmission) computer code. The atmospheric model is parametrized according with the approach under development within the FLEX L-2 retrieval module study. Indeed, the *HyPlant* fluorescence airborne retrieval algorithm geared to be equivalent (or as similar as possible) to the official algorithm that is developed for the FLEX satellite mission. This would promote reciprocal knowledge between airborne campaigns activities and the satellite mission E2E simulation studies. In fact, algorithms employed to process airborne campaigns imagery can take advantage of the analysis developed in the FLEX theoretical studies. Additionally, a hypothesis implemented within the FLEX E2E mission simulator can be tested and validated by means of campaign experimental data. However, these positive feedbacks need somehow to consider limitations that arise from the intrinsic difference between *HyPlant* and FLEX in terms of observation scale / geometry (boundary layer vs. TOA) and specific instrument technical performances (SNR, dual-view capability, etc.). In practice, the FLEX retrieval algorithm cannot be used directly for the processing of *HyPlant* imagery, but parts of the algorithm or some key hypothesis can be adopted for airborne processing in a similar way. In this regard, the set of atmospheric model input parameters used to compute the at-sensor radiance, is one of the common points between satellite and airborne retrievals. Specifically, the parameters used to describe scattering and absorption effects of the atmosphere are: i) the aerosol optical thickness (AOT); ii) atmospheric profile and aerosols models, the Angstrom extinction exponent (ASTMX), asymmetry factor of the scattering phase function (G); iii) column water vapour (H₂OSTR); iv) atmospheric pressure (SPR); v) as well the Line Of Sight (LOS) parameters required to describe the sun-target-sensor geometry (Table 3). The *HyPlant* fluorescence retrieval code does not implement internal estimations of the atmospheric variables as it is typically done in a more sophisticated airborne and satellite atmospheric correction algorithm (i.e., FLEX retrieval algorithm). This fact is due to the characteristics of the *HyPlant* FLUO instrument, which is specialized for detecting canopy fluorescence (670 nm - 800 nm), but not for retrieving aerosols by observing wavelengths in the extended VNIR spectral region including the blue spectral region wavelengths. Typically, aerosol retrieval is done in the visible and near-infrared (VIS-NIR) wavelengths (mainly 400 - 800 nm) because the aerosol effect is larger at shorter wavelengths (blue green) while it decreases at longer wavelengths. The aerosol retrieval from FLUO (650 - 800 nm) is very challenging as reported in few papers in the past for atmospheric chemistry satellites (Frankenberg et al. 2011). Conversely, aerosol retrieval would be much more efficient from DUAL data which covers an extended spectral range. FLUO and DUAL are not exactly co-registered and on the same spatial grid to allow a direct exploitation of DUAL to support FLUO data processing. Applying a co-registration algorithm between FLUO and DUAL would be a direct solution. Otherwise, macropixels i.e. 10 x 10pixels could be considered as it happens in the FLEX processor to overcome the spatial mismatch between the two sensors. This could be a challenge to develop for the future with a direct benefit for the SIF retrieval and the further matching of spectral indices related to biophysical parameters (spectral vegetation indices) and SIF.

Consequently, the atmospheric model input variables need to be supplied to the retrieval code in the form of external a-priori information. Two options are envisaged: i) in-situ sun photometer

measurements are typically considered as a reference standard for remote sensing and ii) by exploiting widely used “atmospheric correction” algorithms for hyperspectral imagery (i.e. ATCOR).

Table 3: Atmospheric model inputs parameters used in the *HyPlant* retrieval algorithm.

Parameter	RTM code	Source	Type
<i>Aerosol Optical Thickness (550 nm)</i>	AOT550	Sunphotometer, ATCOR	Atmospheric status
<i>Atmosphere Model</i>	MODEL	standard model (Tropical, Mid-Latitude summer, Mid-Latitude winter etc.)	
<i>Aerosol Model</i>	IHAZE	standard model (Rural, Maritime, Urban etc.)	
<i>Angstrom Extinction Exponent</i>	ASTMX	Sunphotometer, ATCOR	
<i>Column Water Vapour</i>	H2OSTR	Sunphotometer, ATCOR	
<i>Surface Pressure</i>	SPR	meteo	
<i>Henyey-Greenstein parameter</i>	G	sunphotometer	
<i>Sensor altitude</i>	H1	navigation file	Line-Of-Sight Geometry
<i>View Zenith Angle</i>	VZA	navigation file	
<i>Surface altitude a.s.l.</i>	GNDALT	base reference maps	
<i>Solar Zenith Angle</i>	SZA	internally computed	

Generally, sun photometer measurements are collected at the same time as *HyPlant* observations during intensive airborne campaigns, but it might not always be the case. Alternatively, permanent sun photometer stations belonging to the Aeronet international network located closely to the survey area (in the range of few kilometres) can be exploited, under the assumption of local homogeneous atmospheric conditions. The sun photometer offers reliable estimations for most of the parameters necessary to characterize the optical properties, especially parameters related to atmospheric scattering (i.e. AOT, A, G) and broadband absorption features (i.e. water vapour). Conversely, these observations do not provide information about other narrow band features, e.g. related to the molecular absorption of atmospheric gases such as oxygen. This limitation is intrinsically related to the sun photometer instrument design and the fact that the measurements are done in few discrete broad spectral bands (6 - 11 bands) located in the spectral region characterized by atmospheric scattering. On the other hand, remote sensing of fluorescence strongly relies on accurate modeling of the radiance spectrum inside the O₂ bands, where additional atmospheric properties can play a relevant role. Primary, the O₂ absorption bands depend on the amount of oxygen molecules in the air column, which can be derived considering: i) path length along the atmosphere; and ii) atmospheric pressure as a proxy of the O₂ molecule concentration. Therefore, the modeling of the atmospheric RT at the O₂ bands requires additional variables beyond the parameters typically used for the atmospheric correction of multispectral data.

Alternatively, key atmospheric composition variables can be derived from “atmospheric correction” algorithms (ACOR). In this case, the ATCOR software is applied to the hyperspectral imagery collected by the DUAL sensor (400 - 2500 nm). Thus, the parameters obtained can be used as input parameters for the fluorescence retrieval. This approach has similar limitations as the sun photometer since the atmospheric variable estimated only concerns scattering and broadband absorption features only (i.e., aerosols and water vapor). The information related to narrow band features such as the O₂ bands are not provided with this approach. However, the ATCOR approach offers two main advantages: i) atmospheric parameters are estimated in a more consistent way because they are derived directly from airborne measurements and the same MODTRAN code can be used for the fluorescence retrieval; and ii) all the information can be obtained from the airborne data and no other auxiliary field measurements are needed.

	Doc.: Final Report		
	Date: 29 July 2021	Issue: 2	Revision: 1
	Ref.: ESA Contract No. 4000125402/18/NL/NA		Page: 29 / 288

Practically, the atmospheric model input parameters used in the *HyPlant* fluorescence retrieval are derived from external information as follows:

- i) the AOT, A, G, H₂OSTR parameters are obtained from the sun photometer or ATCOR;
- ii) atmospheric and aerosol models are selected among the standard models available in MODTRAN (typically mid-latitude summer and rural, respectively);
- iii) the atmospheric pressure is derived from meteorological stations nearby the study area;
- iv) finally, the LOS parameters are computed from the digital elevation model (DEM) and the *HyPlant* navigation data (Table 3).

Basically, a wide and heterogeneous variety of external information are needed to run the code.

Once the model input variables are provided, the atmospheric transfer functions (i.e. direct / diffuse transmittance, path radiance and spherical albedo) are computed and extracted from MODTRAN by means of the Modtran Interrogation Technique (MIT). The atmospheric functions are further combined according to the T18 system proposed by Verhoef et al. (2018) and, afterwards they are employed to simulate the *HyPlant* at-sensor radiance (L). The forward model relies on the four-stream RT theory (Verhoef and Bach, 2012), which represents an accurate and efficient approach for describing the RT interactions between surface and atmosphere (eq. 1).

$$\begin{aligned}
L = & \rho_{so} \frac{E_s^0 \cos \theta_s}{\pi} \\
& + \left[\frac{\tau_{ss} r_{so} E_s^0 \cos \theta_s}{\pi} + F_{so} + \frac{(\tau_{sd} + \tau_{ss} \overline{r_{sd}} \rho_{dd}) E_s^0 \cos \theta_s / \pi + \overline{F_{hem}} \rho_{dd} r_{do}}{1 - r_{dd} \rho_{dd}} r_{do} \right] \tau_{oo} \\
& + \left[\frac{(\tau_{sd} \overline{r_{dd}} + \tau_{ss} \overline{r_{sd}}) E_s^0 \cos \theta_s / \pi + \overline{F_{hem}}}{1 - r_{dd} \rho_{dd}} \right] \tau_{do}
\end{aligned} \tag{eq. 1}$$

The L spectrum is composed by three additive terms that are referred to as atmospheric path radiance, target's surface radiance and adjacency contributions, respectively. The surface reflectance is modelled by four-terms: r_{so} is the target bi-directional reflectance factor, r_{do} the target directional reflectance for diffuse incidence, $\overline{r_{sd}}$ the average surroundings diffuse reflectance for solar irradiance, and $\overline{r_{dd}}$ the average surroundings diffuse reflectance for diffuse incidence. The ρ_{so} is the atmospheric bi-directional reflectance and the ρ_{dd} the spherical albedo of the atmosphere. The τ_{ss} is the direct atmospheric transmission in the direction of the sun, τ_{oo} the direct atmospheric transmittance in the viewing direction, τ_{sd} diffuse atmospheric transmittance for solar incidence, τ_{do} directional atmospheric transmittance for diffuse incidence. The E_s^0 is the extra-terrestrial solar spectral irradiance on a plan perpendicular to the sunrays, and θ_s is the local SZA. The F_{so} is the SIF radiance of the target in the observer's direction and $\overline{F_{hem}}$ the hemispherical fluorescence flux of the surrounding. The over bar indicates the spatial filtering of the terms related to the infinitely extended surrounding area. Currently, eq. 1 is employed under the Lambertian assumption for both reflectance and fluorescence, which means that the different reflectance $r_{so}, r_{do}, r_{sd}, r_{dd}$ and fluorescence F_{so}, F_{hem} terms are considered equal. To process *HyPlant* imagery, the Spectral Fitting approach uses the 750 nm - 780 nm and 684 nm - 697 nm spectral windows for O₂-A and O₂-B bands, respectively. The fluorescence spectral behavior is modeled as a computationally fast pseudo-Voigt, implemented as a linear combination of Lorentzian and Gaussian peak functions. The reflectance spectrum is instead represented by a third order polynomial function at the O₂-A band or a piecewise cubic spline for the

	Doc.: Final Report		
	Date: 29 July 2021	Issue: 2	Revision: 1
	Ref.: ESA Contract No. 4000125402/18/NL/NA		Page: 30 / 288

O₂-B. This version of the algorithm (hereafter defined “classic”) has been developed and successfully employed to process airborne imagery collected in previous FLEX campaigns i.e., SOYFLEX etc.

Although full physical retrieval is generally preferred, at the current stage a semi-empirical approach is beneficial for several reasons: to overcome some current uncertainties to set up all the atmospheric model input parameters required; and to fulfil the FLEXsense 2018 campaign objectives. Specially, when the algorithm is employed to process a large set of airborne data collected during extensive campaigns, the following applies:

- The option of using the retrieval method is strictly subject to the availability of external (independent) information about atmospheric characteristics (i.e., sun photometer).
- The external sun photometer information does not provide all the essential variables to model the atmospheric RT within the O₂ bands properly. For some flight lines, this required some “manual” tuning of few key atmospheric parameters to properly “scale” the absolute value of fluorescence maps within the requested accuracy.
- Since the atmospheric parameters strongly affect the accuracy of the final fluorescence maps product, it must be considered that the “quality” of the atmospheric measurements is heterogeneous (e.g. because they come from different instruments).
- The overall practical workflow to set up all the input parameters required to run the SFM retrieval code is not fully automated, but it requires some “manual” time consuming action. The latter is not practical and efficient when many flight lines need to be processed, as it was the case in the current FLEXsense 2018 campaign.

Therefore, it was necessary to design a different airborne fluorescence retrieval scheme that overcomes such limitations and allows the practical objectives of the campaign to be fulfilled. The new methodology adopts an image-based solution to obtain a more robust characterization of the atmospheric variables. Consequently, we obtain improved modeling of the spectra inside the O₂ bands, by exploiting the spectral information from bare soil pixels. The widely used iFLD method that has been implemented for *HyPlant* for a few years is a similar concept (Rascher et al. 2015; Siegmann et al. 2019). In practice, the novel retrieval algorithm introduces an additional processing step to refine the value of atmospheric model input parameters from their initial first guess values available from external sources (i.e., sun photometer).

A sensitivity analysis was performed to investigate the impact of the atmospheric parameters on the depth of the O₂ absorption bands. The band depth ratio is evaluated considering at-sensor radiance spectrum computed by the atmospheric RT model considering a pixel with reflectance equal to 1 (Figure 7 and Figure 8).

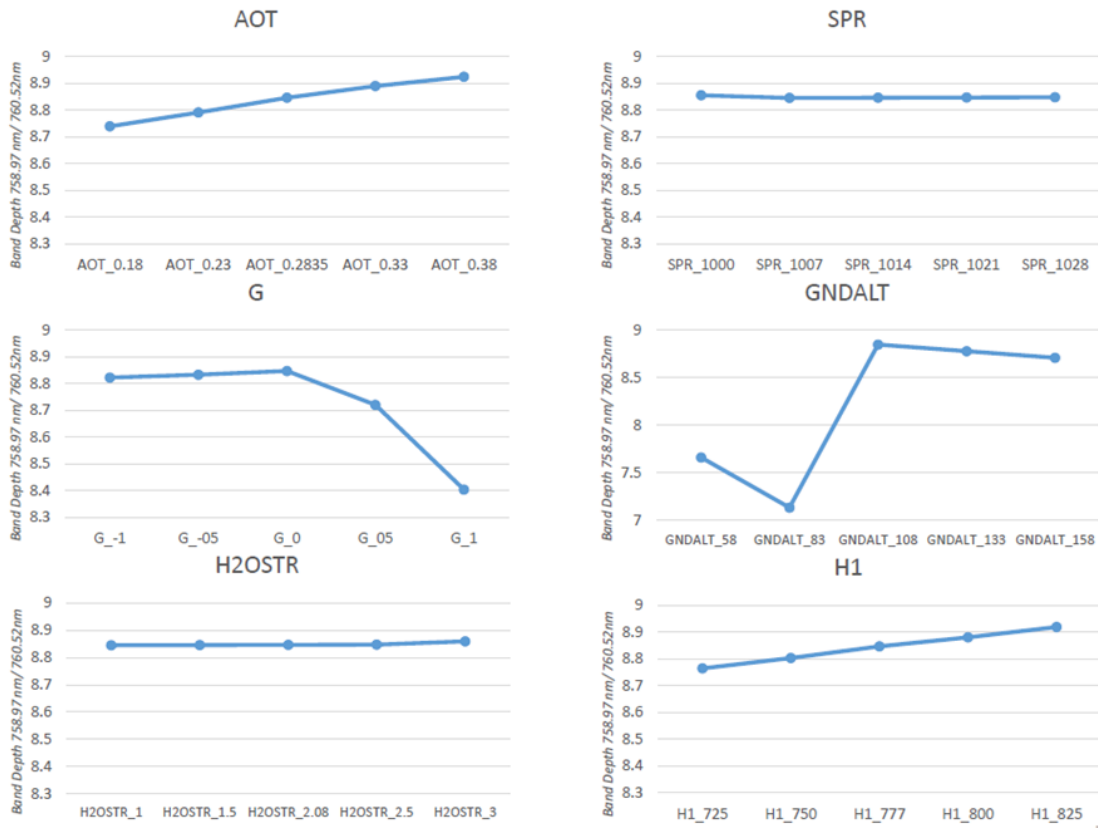


Figure 7: O₂-A band depth (ratio between wavelengths 758.87 nm / 760.52 nm) considering a range of values for the different atmospheric model inputs: AOT, SPR, G, ground elevation (GNDALT), column water content (H₂O) and sensor height (H1).

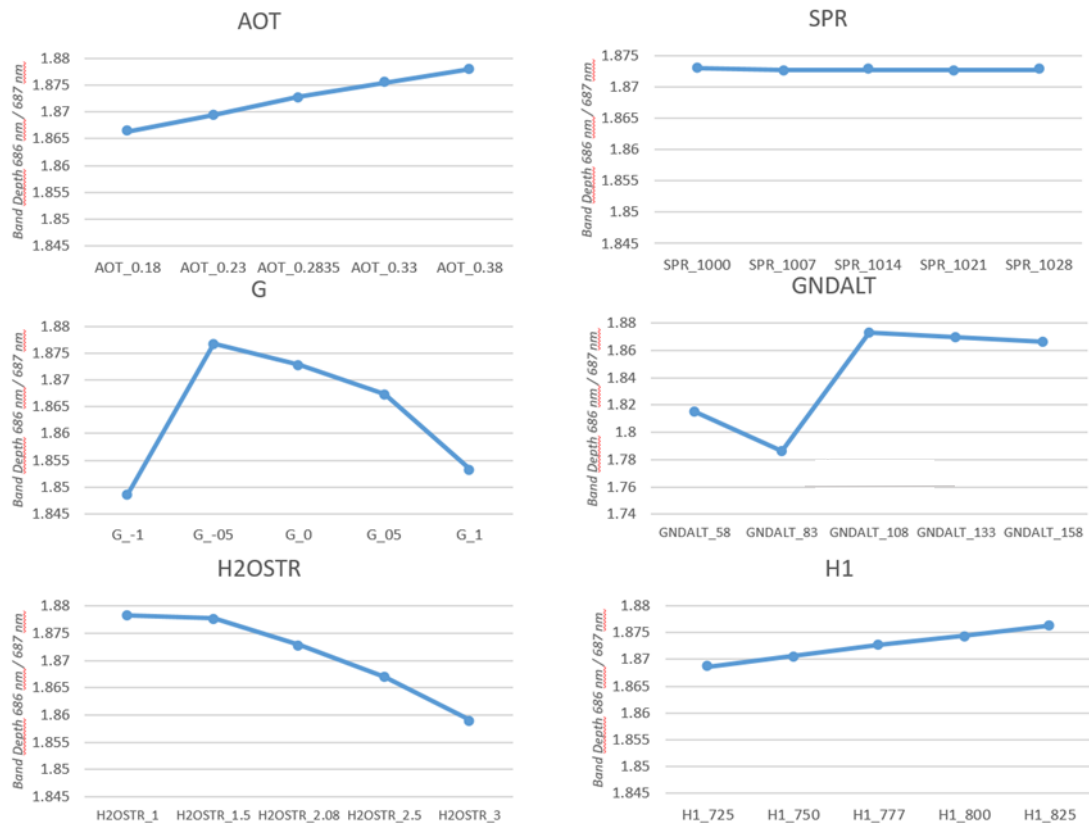


Figure 8: O₂-B band depth (ratio between 686 nm and 687 nm) considering a range of values for the different atmospheric model input parameters: AOT, SPR, G, GNDALT, column water content (H₂O) and sensor height (H1).

Omitting a physical interpretation about the effect caused by the different variables, the clear outcome from Figure 7 and Figure 8 is the strong impact of geometric parameters (i.e., H1, GNDALT) on both O₂ bands. Apparently, SPR does not show a substantial contribution which is caused by the fact that atmospheric pressure is not a direct input of MODTRAN, but rather indirectly considered by changing the geometric distance between GNDALT and observer elevation (H1). This approach indirectly reproduces the effect of lower / higher atmospheric pressure values (i.e., different amounts of absorbing O₂ molecules) by varying the surface-observer path length. The increase of surface-observer distance implicitly means larger O₂ absorption, as occurs when SPR increases. Practically, this workaround is implemented by “adjusting” the surface and observer elevations, according to the actual atmospheric pressure (meteorological station). This is achieved by means of the isobaric equation. Currently, there is no agreement about the proper implementation of equations used to correct surface and sensor elevations. Furthermore, we are not confident the isobaric equation is fully consistent with the vertical P-T profiles available in MODTRAN.

Therefore, the novel fluorescence retrieval algorithm employs an internal estimation of the “effective” surface-sensor distance, with the aim of limiting uncertainty about H1 parameter. The “effective” distance is not equivalent to the geometric distance, but rather interpreted as the geometric distance that produces an effect on the RT variables (i.e., O₂ absorption) equivalent to a defined change in atmospheric pressure.

Operatively, this concept was implemented within the novel *HyPlant* fluorescence retrieval code in the following main processing steps:

i) **Identifying non-vegetated pixels:** The NDVI map is internally computed and stored as an output product to help the interpretation of fluorescence maps. The NDVI map is thus exploited to obtain a “binary classification” of the imagery between two classes: vegetated and non-vegetated pixels. This is done by using a threshold corresponding to a value between $0 < \text{NDVI} < 0.15$. Only non-vegetated pixels located at nadir are considered in this analysis. This is required to prevent any changes in O₂ absorption depth caused by different sensor viewing angles (between 0 and $\pm 16^\circ$). In fact, different viewing angles correspond to slightly different surface-sensor path lengths and, consequently, a different amount of O₂ absorption. To avoid uncertainties, only non-vegetated pixels that are in the central columns of the image are considered (± 30 pixels that correspond to a viewing angle of $\pm 1.2^\circ$). Finally, the average at-sensor radiance spectrum of non-vegetated pixels is computed. An example of the procedure implemented is reported in Figure 9.

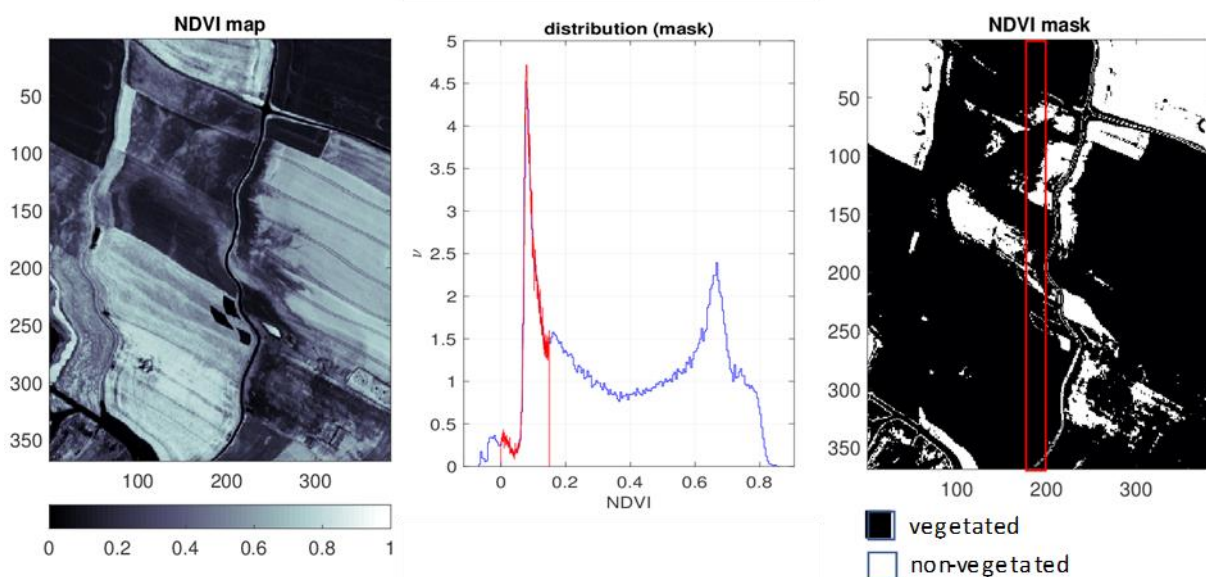


Figure 9: (left) NDVI map; (middle) frequency distribution of NDVI values for the entire image (blue line) and distribution of pixels in the range $0 < \text{NDVI} < 0.15$ (red line) and (right) NDVI binary mask considering a threshold value of 0.15.

ii) **Estimation of “effective” surface-sensor distance:** The MODTRAN calculations are repeated a few times considering different values of H1 (sensor height, Figure 10), while keeping the ground elevation constant. As described before, the effect caused by different values of atmospheric pressure can be simulated by changing the geometric surface-sensor distance. The MODTRAN simulation is stored in an internal Look-up-Table (LUT). Fluorescence is computed from the average at-sensor distance (estimated in the previous point) considering different H1 values. Thereafter, the “effective” H1 is derived under the assumption that $F = 0$ (null fluorescence) for non-vegetated pixels. In practice, the linear regression model between fluorescence and H1 values is estimated, and the “effective” H1 value, which corresponds to $F=0$, is computed (Figure 11).

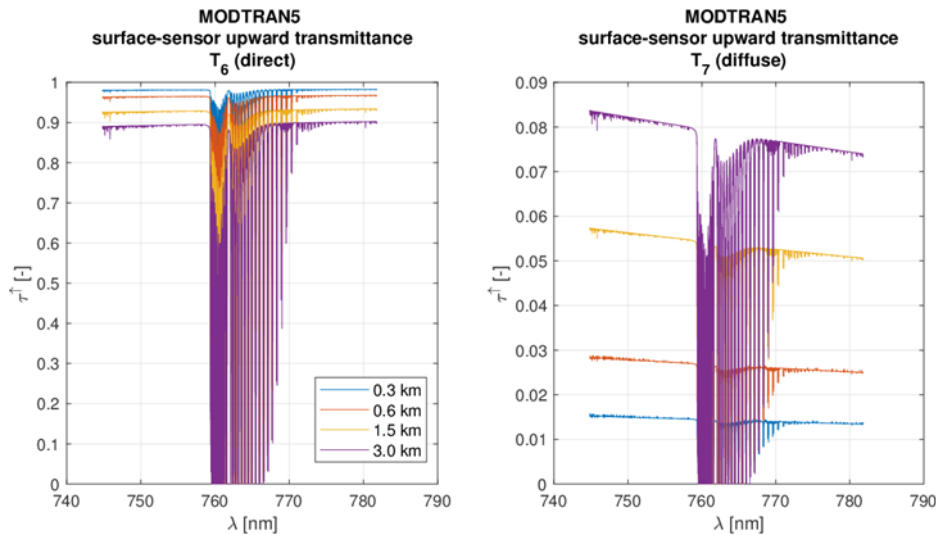


Figure 10: Example of surface to sensor direct (left) and diffuse (right) transmittance spectra computed by MODTRAN5 (spectral resolution of 0.1 cm^{-1}) considering different H1 values.

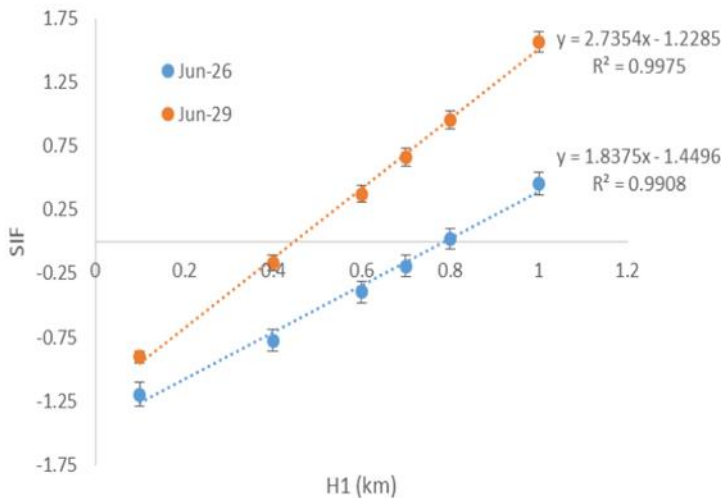


Figure 11: Example of fluorescence values ($\text{mWm}^{-2}\text{sr}^{-1}\text{nm}^{-1}$) computed from the non-vegetated averaged radiance signature derived in the previous steps considering different sensor heights above ground level (agl). The two data series refers to flight lines collected in two different days (26 and 29 June 2018).

iii) **Atmospheric RT calculations with different viewing-angles:** The atmospheric transfer functions are computed with MODTRAN considering the “effective” H1 value estimated in the previous step. The atmospheric RT calculations are performed twice considering nadir and off-nadir view-angles (i.e., 0° and 16° , respectively). This expedient allows a better retrieval of fluorescence at the edges of the image

(off-nadir), because atmospheric functions result more accurate also in this part of the imagery. Technically, the off-nadir viewing-angle value of 16° is considered sufficiently accurate for the purposes of the RT calculations because the roll angles registered from the IMU is typically lower than 1° in most of the flight lines. Finally, the atmospheric transfer functions for each column of the image are computed by means of a linear interpolation, considering nadir and off-nadir MODTRAN simulations as boundary conditions. The assumption of a linear variation between nadir and off-nadir might be not very accurate, but for the moment, it is considered a good compromise between complexity and retrieval accuracy.

To summarize the number of processing steps implemented in the novel version of the algorithm, the overall flow-chart is reported in Figure 12. It consists of several consecutive processing steps that recall the main structure of the “classic” algorithm, with some additions. The first block, common to the standard processing algorithm, deals with a first rough estimation of the instrument ISRF in terms of bandwidth and wavelengths position (both parameters are estimated for each image column). Afterwards, the atmospheric functions are computed a few times considering different H1 values; the fluorescence is retrieved over non-vegetated pixels; and H1 “effective” value is estimated (with assumption $F=0$). The “effective” value is thus used to re-compute the atmospheric functions, and we also consider the different view zenith angles $[0, 16]$. Finally, the SFM is applied per pixel and the fluorescence maps are computed.

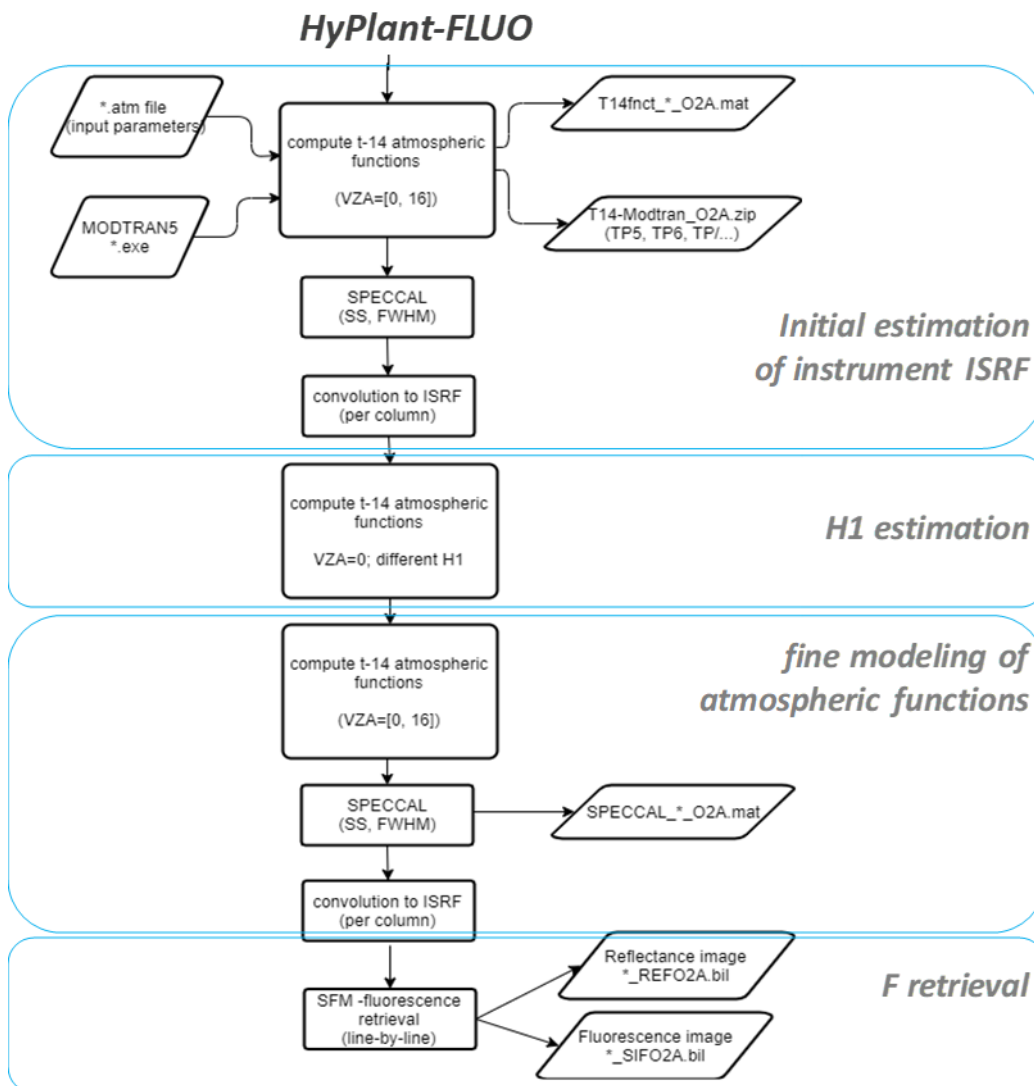


Figure 12: Flow chart of the novel SFM retrieval algorithm with soil-correction (HYPLANT-SFM-NVR).

	Doc.: Final Report		
	Date: 29 July 2021	Issue: 2	Revision: 1
	Ref.: ESA Contract No. 4000125402/18/NL/NA		Page: 35 / 288

Practically, this novel approach offers a few advances: i) to obtain more robust and accurate fluorescence estimations for the entire variety of atmospheric and environmental conditions observed during the extensive FLEXSense 2018 campaign (June to August at several sites across Europe); and ii) to provide airborne fluorescence products without a strict need of accurate external auxiliary information (i.e., sun photometer, as required by the previous versions of the algorithm).

The fluorescence retrieval code is implemented in MATLAB exploiting a parallel computing technique (OpenMP). The code can run either on Windows desktops or on high-performance Linux-based IT infrastructure. The latter was used to process the large number of flight lines collected during the FLEXSense campaign 2018, in order to support the project with high-performance infrastructure and simplify the processing activity. Several Linux bash scripts were implemented to simplify the following activities: i) preparation of the scheduler submission scripts (Slurm files); and ii) review and reporting of the information stored in the output log files from the scheduler. This software / hardware infrastructure permitted gaining a high level of performance (computational time), in fact about 100 *HyPlant* flight lines were processed in about 11 hours.

The fluorescence retrieval algorithm software code project is implemented in MATLAB and is hosted on the GitLab online service (<https://gitlab.com/cogliatisergio/HYPLANT-SFM>) to provide simple and fast access and track changes in the latest and updated version of the software code between the teams involved in development and testing (i.e., University of Milano-Bicocca and Forschungszentrum Jülich). Specifically, the fluorescence retrieval algorithm code is referred to the development branch called “hypsometric_2_SPR_INV_VZA” (https://gitlab.com/cogliatisergio/HYPLANT-SFM/-/tree/hypsometric_2_SPR_INV_VZA). Currently, access to the software code can be granted upon request to the PI of the algorithm development project and in agreement with ESA project technical officer.

Limitations, open points and recommendations for future developments:

The fluorescence retrieval algorithm implemented for the FLEXSense 2018 campaign permitted the processing of the complete set of flight lines indicated in the high priority list (among one hundred flight lines) while also considering a large variety of environmental (surface / atmosphere) conditions. However, there are still some limitations that can be overcome in the future:

- perfect knowledge of the atmospheric optical properties (i.e., scattering) should be implemented on the basis of the external data from sun photometer observations;
- the topography effect in terms of surface elevation, slope and aspect is not implemented;
- the fine scale surface elevation (i.e., digital surface model (DSM)) is not yet considered in the retrieval scheme. This is an additional topic that will be investigated more in the future: One aim is to understand its impact on the “accuracy of the fluorescence maps”. Yet another is to understand whether to use ATCOR atmospheric parameters instead of sun photometer measurements.

4.3 Airborne thermal imager TASI

TASI-600 is a push broom hyperspectral thermal sensor system designed specifically for airborne use by the Canadian company Itres. The TASI is sensitive to wavelengths in the long-wave infrared (LWIR) part of the electromagnetic spectrum. This instrument measures the intensity of emitted radiance from the imaged target across 32 spectral bands in the range of 8 to 11.5 microns. The TASI-600 collects an image swath of 600 pixels ‘across track’ by 1 pixel ‘along track’. The raw imagery from the TASI has a data depth of 14-bits (0 - 16,383). The TASI used in this study is equipped by on-board dual black body calibration, which enables radiometric calibration for each flight line during the flight and improve radiometric accuracy. As a thermal sensor, TASI could be used for a number of applications i.e. forest or agriculture ecosystem monitoring as well as for archaeological or urban heat islands detection. Within the activities connected to the SurfSense project, TASI was used for periodical data

	Doc.: Final Report		
	Date: 29 July 2021	Issue: 2	Revision: 1
	Ref.: ESA Contract No. 4000125402/18/NL/NA		Page: 36 / 288

acquisition over the Grosseto area (approx. 25 km²). Acquired data were used mainly for Land Surface Temperature (LST) calculations.

4.3.1 Processing of TASI data

Several methods exist for the retrieval of LST from thermal infrared (TIR) remote sensed data. In this section, LST and LSE are obtained by using the temperature and emissivity separation (TES) algorithm (Gillespie et al. 1998), which requires at least four or five thermal bands.

TES algorithm

The TES algorithm was developed by Gillespie et al. (1998), and is used to produce the standard products of LST and LSE from the advanced spaceborne thermal emission and reflection radiometer (ASTER) data. The TES algorithm provides simultaneously LST and emissivity data, and requires at least four or five TIR bands. As input, it uses the land-leaving radiances (LLL) and the downwelling atmospheric radiance, and it is composed of three different modules: NEM (normalized emissivity method), RATIO, and MMD (maximum-minimum difference). The NEM module provides a first guess of the surface temperature and emissivity using an iterative procedure. The RATIO module normalizes the surface emissivity providing the so-called beta spectrum and the MMD module recovers the final surface emissivity and temperature using a semi-empirical relationship between minimum emissivity (e_{min}) and spectral contrast (MMD), $e_{min}=a+b \cdot MMD^c$. The TES algorithm was adapted to TASI characteristics (more info of e_{min} MMD relation).

Radiometric corrections

Radiometric corrections of measured data were carried out in the RadCorr (Itres Ltd) program. For the radiometric calibration of the TASI-600 data, calibration coefficients derived from two calibration black bodies scanned during the flight were used. Calibration coefficients were specified for each flight line separately. The values of the final image data are given in radiometric units [$\mu W cm^{-2} sr^{-1} nm^{-1}$].

Georeferencing

Georeferencing was carried out by means of a parametric geocoding method using data acquired by the GNSS / IMU unit and the digital terrain model in the GeoCor (Itres Ltd.) program. In one step, geometric corrections, orthorectification, and data georeferencing were performed. For resampling of the data into the coordinate system, the nearest neighbor method was used. Hyperthermal data was georeferenced into the UTM coordinate system (zone 30/31/32/33N, WGS-84, depending on locality).

Atmospheric corrections and calculations of temperature characteristics

Radiometric calibrations deliver image data containing radiation from the surface $\varepsilon B(T)$, attenuated by atmosphere plus radiation from the atmosphere along the line of sight. Thus, the measured radiance at sensor level L consists mainly of radiance emitted from the land surface $\varepsilon B(T)$, downwelling atmospheric radiance $L_{\downarrow atm}$ reflected by the surface, and atmospheric upwelling radiance $L_{\uparrow atm}$. The sum of all these components is expressed by a radiative transfer equation (RTE):

$$L = \tau \varepsilon B(T) + \tau (1 - \varepsilon) L_{\downarrow atm} + L_{\uparrow atm} \quad \text{eq. 2}$$

B(T) is the radiance of the surface at temperature T according to Planck's law, ϵ is the surface's emissivity and τ is atmospheric transmittance. It is important to emphasize that all elements in the equation are wavelength dependent but notation for this is omitted for the sake of clarity. Since the sensor is of finite bandwidth, quantities in the RTE equation are replaced by band-effective equivalents. Kirchhoff's law of thermal radiation implies that reflectivity can be rewritten as $(1 - \epsilon)$ for opaque materials. RTE can be used under the assumption of cloud-free atmosphere under local thermodynamic equilibrium.

The quantities $L_{\downarrow atm}$, $L_{\uparrow atm}$ and τ was modeled using the MODTRAN 5.3 RT model, which was parametrized by sources mentioned in Table 4. Compensating for atmospheric transmittance and upwelling atmospheric radiance led to LLL:

$$LLL = \epsilon B(T) + (1 - \epsilon) L_{\downarrow atm} \quad \text{eq. 3}$$

LLL is the sum of the radiance emitted by the surface and the reflected radiance. Taking the downwelling atmospheric radiation $L_{\downarrow atm}$ into account is not possible without knowing the emissivity of the surface. Eliminating the influence of downwelling atmospheric radiance was part of the calculation of temperature T and emissivity ϵ of the surface – this was performed by TES. From TES, the noisiest bands (1, 2, 3, 4, 5, 14, 15, and 16) are excluded so that the final products have 24 bands. Using the radiance leaving the surface LLL, it was possible to calculate the brightness temperature that approximates the temperature T. The brightness temperature calculation was based on the inversion of the Planck's law assuming emissivity equals one. The brightness temperature was calculated from the average of all the spectral bands and is, therefore, less affected by noise.

Table 4: Sources of atmospheric parameters of MODTRAN-5.3 (atmospheric correction of TASI data).

France	MODIS	MODIS / Aqua Temperature and Water Vapor Profiles 5-Min L2 Swath 5 km
Germany	Radiosonde	10410 EDZE Essen; 10548 Meiningen; 10618 ETGI Idar-Oberstein
Italy	Radiosonde	16245 LIRE Pratica Di Mare
Spain	MODIS	MODIS / Aqua Temperature and Water Vapor Profiles 5-Min L2 Swath 5 km
Switzerland	MODIS	MODIS / Aqua Temperature and Water Vapor Profiles 5-Min L2 Swath 5 km

Summary of TASI data processing:

- 1) Radiometric calibration – RadCorr software delivered by sensor producer
- 2) Geo-ortho rectification - GeoCorr software delivered by sensor producer
- 3) Parametrization of MODTRAN-5.3
- 4) TES algorithm and atmospheric corrections (AC)

Outputs:

- Image data showing the kinetic temperature (T); **LST** [K] (land surface temperature)
- Image data showing emissivity; **LSE** [-] (land surface emissivity)
- Image data showing the radiation leaving the surface LLL; **LLL** [$\text{W m}^{-2} \text{sr}^{-1} \text{m}^{-1}$] (land-leaving radiance)
- Image data showing brightness temperature; **BBT** [K] (broadband brightness temperature); spatial pixel resolution: 3.6 m
- Image data showing the measured radiance at sensor level; **RAD** [$\mu\text{W cm}^{-2} \text{sr}^{-1} \text{nm}^{-1}$]

4.4 Airborne LiDAR

LMS-Q780 is a long-range airborne laser scanner with capability of full-waveform echo digitalization and analysis designed by the Austrian company Riegl. The LMS-Q780 is equipped with a rotating polygon mirror, which leads to straight parallel scan lines and enables an equally dense laser footprint pattern on the ground. Advantageously, the FOV of the laser scanner is 60° broad compared with *HyPlant* and TASI. This will lead to a high overlap of parallel LiDAR scan lines and higher point density. The Riegl LMS-Q780 is able to distinguish up to ten simultaneous pulses in the air, which results in a dense laser footprint pattern even in rugged areas without the need to follow terrain. This is important with regard to the FLEXSense flight planning, which is driven by the actual sun azimuth and other objectives.



Figure 13: TASI-600 and laser scanner (LiDAR) Riegl LMS-Q780 mounted in the aircraft together with the *HyPlant* sensor.

4.4.1 Processing LiDAR data

Trajectory calculation

To calculate the flight trajectory, the POSPac 7.1 software was used. It is followed by the conversion of trajectories in the Riegl – POIImport 1.7.3. software. The input data are GNSS and IMU data recorded at a frequency of 200 Hz. The output is a flight trajectory in the UTM coordinate system. For further processing in the SW RiPROCESS, we had to convert the trajectory in the POIImport program to the *.pof format.

Georeferencing

The following software from the company Riegl Laser Measurement System GmbH was used to adjust the laser data:

RiPROCESS 1.8.4 – software for computations of adjustment of data from laser scanners

RiANALYZE 6.2.2 – full waveform data analysis software

RiWORLD 5.1.3 – software for georeferencing of data from a laser scanner

GeoSysManager 2.0.8 – management of a database of coordinate systems and projections

Export

The resulting laser data was usually exported as a point cloud in LAZ format (UTM coordinate system, zone 30\31\32\33N, WGS-84) including the so-called Riegl extra bytes that assign the information from full-waveform analysis (amplitude and pulse width) to each of the points. Heights were exported as orthometric. Conversion from ellipsoidal heights (WGS-84) to orthometric heights was based on Earth Gravitational Model 1996 (EGM96).

DEM

The point clouds exported from RiPROCESS were used as input data for DEMs calculations in LAS Tools software from rapidlasso GmbH. For the DEM calculation, the processing is the following:

- 1) LiDAR flight lines were merged together for one locality;
- 2) merged point cloud was divided into tiles;
- 3) noise filtering was performed for each tile;
- 4) classification to ground and non-ground points was performed;
- 5) digital terrain model (DTM) was calculated via the TIN of ground points;
- 6) DSM was calculated via the TIN of ground and non-ground points; and
- 7) the normalized digital surface model (nDSM) , known as the canopy height model, was calculated as the difference of DSM and DTM.

Table 5: Flights used for DEMs calculations of each area.

	Area	Flights
France	OHP, SP3	10.07.2018 OHP
Germany	TR32, SP3	26.06.2018 TR32
	Campus Klein-Altendorf (CKA)	02.08.2018 CKA
	SEL	27.06.2018 SEL
Italy	Grosseto, SP3	20.07.2018 SP3
Spain	Madajas, SP3	24.06.2018 SP3
Switzerland	Laegeren	13.07.2018 Laegeren

4.5 Ground-based FloX System

The FloX system is a field spectroscopy system manufactured by JB Hyperspectral Devices UG and it is made for high temporal frequency acquisition of continuous TOC optical properties with a focus on SIF estimates. The system is equipped with two spectrometers: i) Ocean Optics FLAME S, covering the full range of VIS-NIR; and ii) Ocean Optics QEPro, with high spectral resolution (FWHM - of 0.3 nm) in the range of the fluorescence emission 650 nm - 800 nm. Each spectrometer optical input is split to two fiber optics which lead to 1) a cosine receptor measuring the solar irradiance and 2) a bare fiber measuring the target reflected radiance. Spectrometers are housed in a thermally regulated Peltier box, which keeps the internal temperature lower than 25°C in order to reduce dark current drift.



Figure 14: The FloX system. (Left) The temperature controlled and sealed central unit of the FloX system with the four-fiber optics that collect incoming and upwelling radiance on the two spectrometers. (Right) The FloX system as it is installed in a winter wheat field in Selhausen. The fiber optics are placed in the NADIR position about two meters above the canopy, continuously collecting light for fluorescence retrieval.

	Doc.: Final Report		
	Date: 29 July 2021	Issue: 2	Revision: 1
	Ref.: ESA Contract No. 4000125402/18/NL/NA		Page: 40 / 288

Moreover, the thermoelectric cooler (TEC) of the QE-Pro is set to 20°C to provide stable measurement conditions. The signal is automatically optimized for each channel at the beginning of each measurement cycle and two associated dark spectra are collected as well. Metadata such as the spectrometer temperature, the detector temperature and the humidity, GPS position and time are also stored in the SD memory of the system. The measurements are fully automatic; after setup and activation, no further user input is required. The FloX system is optimized for low power consumption and remote installation with multiple interfaces for data storage and transmission. The basic routines of FloX are based on SPECY (Forschungszentrum Jülich, IBG-2: Plant Sciences).

4.5.1 Stationary FloX systems to record long time series

The FloX system is designed for continuous operation to record the time series of single vegetation patches from TOC orientation. Thus, the fiber optics are generally installed a few meters TOC measuring the incoming and upwelling radiation every five minutes. The signal is automatically optimized for each channel at the beginning of each measurement cycle; two associated dark spectra are collected as well. Metadata such as spectrometer temperature, detector temperature and humidity, GPS position and time are also stored in the SD memory of the system ([RD-09]).

During the 2018 FLEXsense campaign, the following FloX systems were installed:

- One at ICOS tower in Jülich, Germany [N 50.91, E 6.41]
- One at Selhausen, Germany [N 50.87, E 6.45]
- One at ICOS tower (100 m height) and one on the ground in OHP, France [N 43.93, E 5.71]
- Two FloX systems at the Rogaie site, Italy [N 50.87, E 6.45]
- Two in Spain over two trees [N 39.94, E 5.77]
- One on an Eddy tower in Laegeren, Switzerland [N 47.48, E 8.34]

Several publications are already online in which data from the FloX systems above were used (Wieneke et al. 2018, Martini et al. 2019; Campbell et al. 2019, Cogliati et al. 2019, Wohlfahrt et al. 2018).

Data from the FloX systems (upwelling and downwelling radiance, reflectance and related quality flags) are currently available at the JB server:

- JB-009-ESA⁴: In the period 21 February 2018 until 31 August 2018 approx. 115,000 Measurement cycle have been acquired.
- JB-001-MM: In the period 21 February 2018 until 31 July 2018 approx. 20500 Measurement cycle have been acquired.
- JB-013-ESA⁵: In the period 17 July 2018 until 26 August 2018 approximately 34,000 measurement cycles were acquired.
- JB-012-ESA: In the period 10 November 2017 until of 9 May 2019 approximately 320,000 measurement cycles were acquired.
- JB-010-ESA⁶: In the period 1 December 2017 until 17 September 2019 approximately 460,000 measurement cycles were acquired.
- JB-015-AD: In the period 14 June 2018 until 14 October 2018 approximately 80,000 measurement cycles were acquired.

⁴ QE failure from November 2018

⁵ QE failure from August 2018

⁶ Defective shutter not properly working in some days in June, July and August 2018

- JB-003-MM: In the period 14 June 2018 until 14 August 2018 approximately 100,000 measurement cycles were acquired.
- JB-016-MM: In the period 14 June 2018 until 14 August 2018 approximately 35,000 measurement cycles were acquired.

4.5.2 The mobile FloX system for covering the spatial diversity within and across fields

During the 2018 FLEXSense campaign, we first time tested the mobile use of the FloX system to record the spatial variability of vegetation at the time of airborne mapping. For this newly tested measurement protocol, we used two nearly identical and intercalibrated FloX systems. A first device, termed the ‘mobile’ device, was fitted with a provisional backpack harness from RuckPac Ltd. A lightweight tripod was combined with a horizontal extension arm and a gimbal device for the fiber optics. The optic fibers were connected to the gimbal ensuring constant levelling of the system. A counter balance was attached to the opposite side of the horizontal arm. The combination of a backpack-carried FloX and a tripod with stabilization enabled operation by a single person, who recorded the exact time of arrival and departure at each location. Additionally, each location was marked with a handheld GPS unit (Garmin). The FOV of the optical fibers was $\sim 25^\circ$ and the FOV of the FloX systems was approximately 1 m (Figure 15).

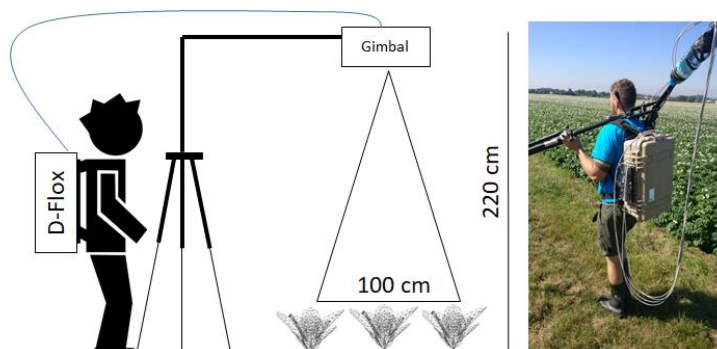


Figure 15 The mobile FloX system, which was tested for the first time in the Selhausen region during the 2018 FLEXSense campaign.

The mobile device was used to measure SIF along predefined transects in selected fields in the Selhausen area. To minimize crop damage, we used the tractor tracks nearest to the predefined transects to relocate the system. At each location, the tripod was set to face south to avoid shadows and avoid anisotropy effects. The optic fibers were 2.20 m above the ground although the height varied depending on the slope or local conditions on the ground. The second ‘reference’ FloX was installed on a permanent position in proximity to the measurement field. The installation height was matched to the height of the mobile device (height 220 cm). To minimize bi-directional effects and avoid shadowing from the tripod, the mobile and the stationary setup faced southwards (Figure 16).

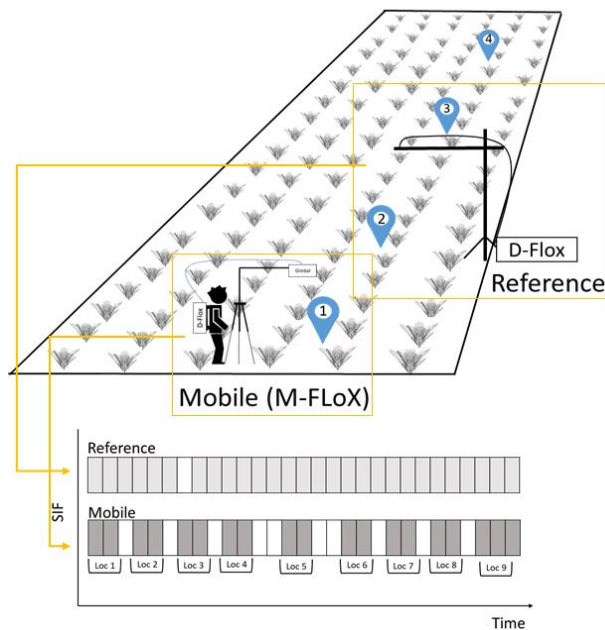


Figure 16 Measurement transects of the mobile FloX system that were performed during the time windows of the *HyPlant* overpasses in the Selhausen area.

4.5.3 Processing of FloX system data

The FloX data-processing is entirely based on the open source R software (R Core Team, 2017). The core functions of the data-processing are contained in two R packages (FieldSpectroscopyCC and FieldSpectroscopyDP) openly available on GitHub platform at <https://github.com/tommasojulitta> and released under the license GNU v3.0 (Julitta et al. 2017). The Graphical User Interface is provided to FloX customers as an R script to facilitate the analysis of the data collected, although the source code is available to JB customers and adaptable to user's needs.

The concept behind the processing was specifically adapted to ESA requirements in the contest of the ESA ATMOFLEX project following a specific workflow:

1. Reading of input files (raw data, see Raw Data)
2. Conversion of raw data to radiance data (using the JB provided calibration files)
3. Calculation of apparent reflectance factors
4. Calculation of Reflectance based Spectral Vegetation Indices (SVIs)
5. Sun-Induced Chlorophyll Fluorescence retrieval (Cogliati et al. 2019)
6. Calculation of QA / QC routines

The data-processing procedure is illustrated in the following diagram (from raw to level-2 product) ([RD-09]).

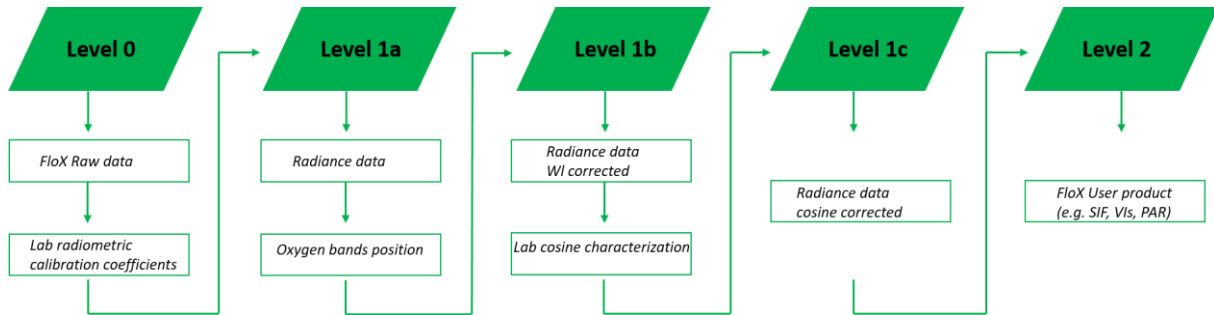


Figure 17: Scheme of the data-processing structure of the FloX system.

The raw data (level-0) are stored as digital counts. One measurement cycle is stored within six lines, whereas the first line is the header containing metadata. Since the upward looking and downward-looking channels have different integration times to achieve an optimal use of the dynamic range, they may be affected by different dark currents. This is accounted for by acquiring two dark current measurements with the two different integration times. The instrument measures twice the upward-looking channel to quantify the stability of illumination during the measurement. Both spectrometers store 1024 pixels for each spectrum. The metadata within the header of each measurement contains essential data for processing, such as GPS, integration time, the actual time of the measurement, temperature, and humidity.

The level-1a product result from the conversion of raw data (digital counts) to radiance ($\text{Wm}^{-2}\text{nm}^{-1}\text{sr}^{-1}$). The radiance conversion is applied to all the measurements acquired by FloX during the field deployment.

The spectral shift of the FloX is evaluated with regard to the position of the oxygen absorption bands in level-1a product. The position of the oxygen bands atmospheric feature is used as a reference to establish the spectral shift of the full range spectrometer. The average of the spectral shift detected both in $\text{O}_2\text{-B}$ and $\text{O}_2\text{-A}$ band is then applied to correct the full spectrum spectrometer measurements (upwelling and downwelling radiance) based on a linear interpolation. The level-1b product contains the spectral shift corrected radiances for the full range spectrometer.

Cosine diffusers mounted on the upward looking fibers of the FloX are opaline glass CC3 (Ocean Optics) and the cosine response has been characterized in the lab. The diffuser cosine response matrix is given at an interval of a five-degree angle and resampled at 1 nm spectral resolution. Based on the correction matrix, the compensation is applied to the downwelling radiance.

The level-2 product includes higher-level products derived from downwelling and upwelling radiance. Photosynthetically active radiance (PAR), reflectance-based vegetation indices and SIF estimates are part of the level-2 product calculated on the FloX data, but not delivered in the ATMOFLEX framework.

While in the framework of ATMOFLEX, the focus was on the downwelling and upwelling radiance. The FLEXsense project also involved the retrieval of fluorescence in order to validate *HyPlant* SIF maps. Therefore, particular attention was paid to fluorescence retrieval made by applying SFM and Specfit algorithm, following Cogliati et al. (2019).

4.6 Novel reference targets for future Cal / Val activities

Active references panels were designed and built to support Cal / Val efforts for the future FLEX earth explorer mission. The references were planned and manufactured to fit within the demands of the *HyPlant* airborne sensor. Two LED types with a center wavelength of 680 nm and 750 nm and a lens with a homogenous angular emission field of about 40° were used. The spectral emission

characteristics of the combined LEDs were chosen to mimic the actual spectral shape of the chlorophyll fluorescence. Their functioning was also successfully tested during an outdoor field deployment. The indoor calibration routine was developed and radiometric calibration coefficients of the panels in the two requested configurations were produced and analyzed. The outdoor test was successfully performed together with an in-field assessment of the panel emission matching the expected indoor calibration ([RD-01]). These new reference targets were technically tested in the campaign under field conditions. A detailed evaluation of the characteristics and performance of the reference targets was done in the 2019 campaign activities; detailed results for the new reference targets will be provided with the 2019 campaign activity reports.

4.7 The quantification of biochemical and structural vegetation properties

During the times of the overflights, various plant traits and biophysical parameters were determined: for the sites Selhausen and CKA in Germany, the study site in Italy, and the study site at OHP, France. Leaf chlorophyll and carotenoid contents were determined destructively. The protocols for these measurements were compared prior to the campaign to facilitate comparability of the data; however, sampling and measurement protocols may vary slightly between the sites. Thus, more detail will be given in the following chapters with the site descriptions.

The general data acquisition and measurement procedure for classical leaf and canopy traits – German sites

Samples were taken at two main locations that are overseen by the Jülich Research Centre. One is located in Klein-Altendorf, Germany and the other is located close to Selhausen, Germany. The plant measurements and sample acquisitions in Selhausen were done in crop cultures with the permission of local farmers. In Klein-Altendorf, crops that were planted for research purposes were analyzed. The cultures sampled were sugar beet, pea, maize, potato, and wheat. Sampling was done in the end of July and the beginning of August 2018 each time in parallel or concurrently with the airborne data acquisition. The parameters and traits acquired in the field were the developmental stage using the Biologische Bundesanstalt für Land- und Forstwirtschaft, Bundessortenamt und Chemische Industrie (BBCH) scale, plant height, sowing density for both sites and chlorophyll content using a SPAD-502Plus Chlorophyll meter (Konika Minolta Inc., Japan) only in Selhausen. For the SPAD measurements, the average of ten leaf measurements was determined. Additionally, one plant was harvested at each measurement location and stored in a plastic bag in order to determine the fresh weight on the same day at the Jülich Research Centre. The leaf area was measured using a Li-3200C Area Meter (LI-COR, USA). The samples were then stored at 65°C in a drying cabinet until they were completely dried in order to determine dry weight and water content. Knowing the sowing density (the distance between single plants) as well as the row spacing at each sampling location allowed us to upscale the measurements for one plant (LAI, dry weight) to one square meter.

For the determination of the chlorophyll and carotenoid content, fresh green leaves were sampled in the field. Using a leaf tissue puncher, 3 - 5 leaf disks with a diameter of 8 mm (CKA) and 9 mm (Selhausen) were randomly punched out of the upper green leaves of a plant. The leaf disks were transferred into 2-mL micro centrifuge tubes, immediately frozen in liquid nitrogen, and transported to the Jülich Research Centre. There, the samples were then stored at -80°C.

	Doc.: Final Report		
	Date: 29 July 2021	Issue: 2	Revision: 1
	Ref.: ESA Contract No. 4000125402/18/NL/NA		Page: 45 / 288

Sample preparation and analysis (chlorophyll and carotenoid) – all sites

All plant pigments, chlorophylls and carotenoids, are fat-soluble compounds. They can be extracted from water-containing living plant tissue by organic solvents such as acetone. An additional step of extraction with 100% acetone is needed to guarantee complete extraction.

The absorption maxima of chlorophylls are found in the red and blue regions of the visible spectrum. The absorption in the red and blue maxima is highest in freshly isolated chlorophylls. Therefore, quantitative chlorophyll determinations should be carried out immediately after extraction. In the case of chlorophyll-a, values between 1 and 3.7 per mgg^{-1} fresh weight are available, which can also be attributed to the different types of plants (sugar beet, maize, potato, pea and wheat). For chlorophyll-b, lower values of 0.1 to 1 mgg^{-1} fresh weight are observed. The absorbance in the blue region is stronger than in the red region, which is documented by a continuous decrease of the values.

All chloroplast carotenoids exhibit a typical absorption spectrum that is characterized by two maxima with one shoulder (lutein and 3-carotene) in the blue spectral region. The wavelength position of the absorption maxima of carotenoids also depends on the type of solvent and its water content. The sum of carotenoids can be determined in a total leaf or chloroplast pigment extract together with chlorophylls by measuring the absorbance not only in the absorption maxima of chlorophyll-a and b, but additionally at a wavelength where carotenoids show good absorption, e.g., at 470 nm. The absorbance of the pigment extract measured at 470 nm happens mainly due to light absorption by carotenoids; a smaller amount is absorbed by chlorophyll-b, whereas chlorophyll-a contributes very little to the absorption at this wavelength. Therefore, the concentration of total carotenoids can be determined by deduction of the relative absorption of chlorophyll-a and -b by the absorption coefficient of total carotenoids at 470 nm. The resulting values are lower than those of chlorophyll-a and -b and lie in a range of 0.1 to 1.1 mgg^{-1} fresh weight.

The leaf disk samples acquired in the field and stored at -80°C were weighed into 2-mL micro centrifuge tubes with a weight between 10 mg and 20 mg. The extraction of chlorophyll A, chlorophyll B and carotenoids was performed with 100% acetone buffered with magnesium hydroxide carbonate ($\sim 4 \text{ MgCO}_3 \text{ Mg(OH)}_2 \cdot 5 \text{ H}_2\text{O}$). 10 g of magnesium hydroxide carbonate were mixed with 500 ml of acetone and stored at 4°C . 250 μl of the described buffer were added to the previously weighed leaf disks including a metal sphere. Homogenization was done using the swing mill MM 400 (Retsch, Germany) for 60 s at a frequency of 30 s^{-1} . The metal ball was removed using a magnet and washed three times with a 250 μl acetone buffer that was captured in the micro centrifuge tube. The tubes were then centrifuged at 4°C at 4100 rpm for 5 min.

250 μl of the supernatant were transferred into a Cuvette and mixed with 750 μl of acetone 100% (dilution 1:4). Absorption was measured with a Specord 200 Plus spectrophotometer (Analytik Jena AG, Germany). The measurements were performed at the wavelengths 470 nm, 645 nm, 662 nm, and 710 nm. During all steps, the tubes were exposed to as little light as possible and continuously stored on ice until measurement.

For the determination of the chlorophyll and carotenoid content, the absorbance values in the following equations as described in Lichtenthaler and Buschmann (2001) and Lichtenthaler (1987) were substituted with the acquired values:

$$\text{Chl}_A = 11.24 (A_{662} - A_{710}) - 2.04 (A_{645} - A_{710})$$

$$\text{Chl}_B = 20.13 (A_{645} - A_{710}) - 4.19 (A_{662} - A_{710})$$

$$\text{Chl}_{A+B} = 7.05 (A_{662} - A_{710}) - 18.09 (A_{645} - A_{710})$$

$$\text{Bulk Carotenoids} = (1000 (A_{470} - A_{710}) - 1.9 \text{ Chl}_A - 63.14 \text{ Chl}_B) / 214$$

Relationship of relative chlorophyll content to absolute chlorophyll content – OHP, France

Leaves of the upper sun crown were harvested at the O₃HP shortly after the overflight campaign on the 18 July 2018, and analysed by HPLC with a protocol tuned to Downy oak at the CEA-Cadarache c/o Michel Havaux. The conversion factor from chlorophyll mass per leaf dry mass to chlorophyll mass per unit leaf area is leaf mass per area, which is about $108 \pm 8 \text{ g DM m}^{-2}$. This is to say that the $3492 \text{ ng chlorophyll g}^{-1} \text{ dry mass}$ (Figure 18) are about $377 \text{ mg chlorophyll m}^{-2}$, and correspond to a relative chlorophyll content of 40.5 ± 3.6 (SPAD) for the trees of the O₃HP core plot. This relationship is quite similar to previous studies on oak and other tree species (e.g. Percival et al. 2008, Richardson et al. 2002, Bielinis et al. 2015).

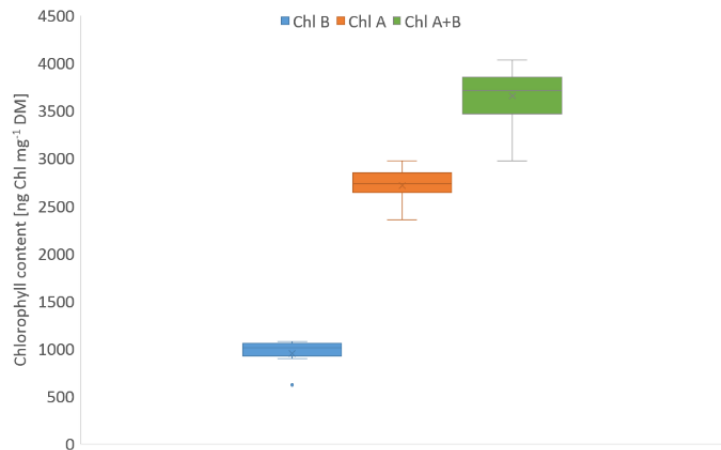


Figure 18 : Chlorophyll content related to leaf dry mass of $n=14$ trees at the O₃HP core plot. Data provided by Michel Havaux, CEA Cadarache.

4.8 Eddy covariance: acquisition and processing of surface fluxes and the calculation of GPP

4.8.1 Selhausen, Germany

In the Selhausen study site, two eddy towers were installed in the study region providing surface flux data during the period of the campaign. These eddy towers are integrated in the framework of the Integrated Carbon Observation System (ICOS), where several Eddy Covariance (EC) towers are positioned across Germany. This is the German contribution for the European network infrastructure of the monitoring system ICOS. In Germany, the EC towers are meant for atmospheric measurements of CO₂, CH₄ and N₂O. The EC tower was equipped with a three-dimensional sonic anemometer (Model CSAT-3, Campbell Scientific Inc., Logan, Utah, USA) and an open-path infrared gas analyzer (Model LI-7500, Li-Cor Inc. Biosciences, Lincoln, Nebraska, USA). The analyser was calibrated every three months in the lab. Both instruments were mounted 2.5 m above the surface. EC measured turbulent fluxes were calculated as 30-min averages using the software package TK3.11 (Foken et al. 2004). The test field was additionally equipped with meteorological measurements like air temperature (HMP45C, Vaisala Inc., Helsinki, Finland) precipitation (Thies Clima type tipping bucket, distributed by Ecotech, Bonn, Germany), and radiation (NR01, Hukseflux and Delft, Netherlands). Up to four self-calibrating soil heat-flux plates (HFPO1, Hukseflux Thermal Sensors, Delft, Netherlands) were installed at a depth of 0.08 m. Soil water content (SWC, CS616, Campbell Scientific, Inc., Logan, USA) and soil temperature (TCAV, Campbell Scientific, Inc., Logan, USA) were sampled in the layer above the heat flux plates. Beside the flux measurements and typical climate parameters, the phenological development of the crops and farming activities were recorded as well. The two EC towers used in Selhausen, Germany,

	Doc.: Final Report		
	Date: 29 July 2021	Issue: 2	Revision: 1
	Ref.: ESA Contract No. 4000125402/18/NL/NA		Page: 47 / 288

were located in a winter wheat and a sugar beet field during the 2018 vegetation period (see Figure 108 for the exact location of the two eddy towers in the Selhausen region).

Data from the EC towers were processed to produce half-hourly values of GPP estimated from the Net Ecosystem Exchange (NEE) measurements using a daytime data-based flux-partitioning algorithm after Lasslop et al. (2010), implemented with the gap-filling and source partitioning software REddyProc (REddyProc Team, 2014). Data gaps in the time series of the meteorological driver variables (taken from the climate station of the Selhausen site) required for modelling GPP were filled before partitioning with a variant of the data interpolating empirical orthogonal functions method (Beckers and Rixen 2003, Graf et al. 2017). The REddyProc package provides both night-time and day-time partitioning. The day-time partitioning approach models GPP with a rectangular hyperbolic light-response curve with additional consideration of the vapour pressure deficit limitation of photosynthesis. GPP day-time partitioning (GPP_{DT}) should correlate better with SIF and vegetation indices because in a way some remote sensing information is already embedded in the modelled GPP. Night-time partitioning might be problematic if there are large changes in temperature from day to night or in the presence of heat waves, as the technique relies on modeling ecosystem respiration on the basis of its temperature dependency.

4.8.2 Grosseto, Italy

Two EC stations were installed and managed “ad hoc” in the ATMOFLEX site in Central Italy (Le Rogaie, Grosseto). Those stations were provided by the University of Bonn (D) and were managed by FCS, including data retrieval and regular maintenance (Figure 19). One EC station was installed on irrigated corn within the pivot area; the second was installed on alfalfa in the proximity of the pivot area (Figure 19). A full description of the EC stations installed in Le Rogaie is given in the ATMOFLEX CCN final report ([RD-11]).

Vertical and horizontal CO_2 and water vapor concentration profiles were also made in the Le Rogaie site in Italy, at periodic intervals to finally obtain relevant data to retrieve surface fluxes (f_{CO_2} , and γE , latent heat flux). To this aim, the site was be equipped with a temporary mast installation as well as with a portable / mobile integrated equipment to obtain horizontal scalar concentration profiles. The mobile system consisted of a vertical mast carrying a GPS antenna and an infrared open-path gas analyzer (Li7500, Licor, USA) that were connected to a central datalogger (Campbell, CR 1000) that acquired the position of the sampling as well as air temperature, atmospheric pressure and CO_2 / water vapour concentrations 1Hz frequency. Credible estimates of f_{CO_2} (carbon flux), LE (latent heat), H (sensible heat fluxes) and u^* (momentum flux) were obtained using standard processing packages and the classical CarboEurope procedures for flux estimations. Estimates of GPP over the alfalfa and corn crops in Italy and other crops in Germany was made throughout the duration of the FLEXsense campaign and beyond. Half-hourly values of GPP were estimated from the measured CO_2 flux using the day-time partitioning (Lasslop et al. 2010) implemented in the REddyProc software (REddyProc Team 2014). In addition, all computations have been made using ECpack. ECpack is a program to process eddy-covariance data stored in NetCDF files. and `ec_ncdf` which were initially developed by Arjan van Dijk et al. (2004), and now maintained and further developed by Arnold Moene (arnold.moene@wur.nl). More information about the software and computations can be found at <http://www.met.wur.nl/projects/jep/>. The header of the output table is explained below (Table 6). For more information, see the ATMOFLEX CCN1 report ([RD-11]).

Table 6: Explanation of the output parameters.

Short name	Measurement Unit	Long name
DOY	-	Day of Year
Hr	-	Hour
Mn	-	Minute
DOY	-	Day of Year
Hr	-	Hour
Mn	-	Minute
Dir	[degr]	Wind Direction
d(dir)	[degr]	Wind Direction Tolerance
Mean(vectorU)	[m/s]	Mean Wind Speed
dMean(vectorU)	[m/s]	Mean Wind Speed Tolerance
Mean(TSon)	[K]	Mean Sonic Air Temperature
dMean(TSon)	[K]	Mean Sonic Air Temperature Tolerance
Mean(q)	[kg/kg]	Specific Humidity
dMean(q)	[kg/kg]	Specific Humidity Tolerance
H	[W/m ²]	Sensible Heat Flux
Tol(H)	[W/m ²]	Sensible Heat Flux Tolerance
LE	[W/m ²]	Latent Heat
dLE	[W/m ²]	Latent Heat Tolerance
UStar	[m/s]	Friction Velocity
dUStar	[m/s]	Friction Velocity Tolerance
FCO ₂	[μm/m ² /s ⁻¹]	CO ₂ Flux
dFCO ₂	[μm/m ² /s ⁻¹]	CO ₂ Flux Tolerance



Figure 19: Left side: EC station with vertical wind profiles and net radiometer installed in the corn area at Le Rogaie site (Italy). Two EC stations were installed in Le Rogaie on two different crops (corn and alfalfa) for all the duration of the experiment. Right side: Localization of the EC stations at Le Rogaie site (Italy) in 2018.

4.8.3 Majadas, Spain

Three ecosystem EC towers operated at the site and during the flight overpass, two of them are used in the FLEXSENSE project. The long-term FLUXNET site Majadas de Tiétar (ES-LMa in FLUXNET, since 2003) serves as the control treatment (CT), and the plot fertilized with nitrogen in 2014 named ES-LM1 [the NT plot]. Each tower is equipped with a R3-50 sonic anemometer (Gill Instruments Limited, Lyngington, UK) to measure three-dimensional wind components and sonic temperature, and a LI-7200 infra-red gas analyzer (Licor Bioscience, Lincoln, Nebraska, USA) to measure CO₂ and H₂O mixing ratios. The measurement height is 15 m above ground for all towers.

EC data and meteorological data were collected and the processing of the raw high-frequency data was conducted using EddyPro v 6.2.0. Calculated CO₂ fluxes were storage corrected from seven-point profile measurements. The friction velocity (u^*) threshold was determined following the FLUXNET procedure. The estimated threshold is 0.16 ms⁻¹ and all data with u^* values below the established threshold were removed from further analysis. The gap-filling of missing and bad quality data [QC values > 1 according to Foken et al. 2004] was then performed (Reichstein et al. 2005). Subsequently, flux partitioning of NEE into GPP and Reco was conducted by applying both the nighttime and daytime flux partitioning method (Reichstein et al. 2005). In the plots presented in the following, we report only GPP derived with daytime partitioning. All post-processing was conducted using the R package REddyProc v 1.2.2 (Wutzler et al. 2018). The details of the full processing including statistics on the number of gaps for the individual fluxes are provided in El-Madany et al. (2018 and 2020).

5 Quality assessment and validation of the retrieval of sun-induced fluorescence

5.1 Quantitative evaluation of the fluorescence maps from the novel SFM algorithm

Part of this chapter that refers to the influence of the PSF are used for a scientific publication. More details on this topic and an extended scientific discussion can be found in this publication (attachment 12.4).

Scharr H., Rademske P., Alonso L., Cogliati S. & Rascher U. Spatio-spectral deconvolution for high resolution spectral imaging with an application to the estimation of sun-induced fluorescence. *Remote Sensing of Environment*, submitted 7 March 2021.

The novel fluorescence retrieval algorithm has been used to process a large number of *HyPlant* flight lines collected during the FLEXSense 2018 campaign. For the first time, it was possible to process among one hundred different lines because i) the *HyPlant* fluorescence retrieval code was implemented on high-performance computer (HPC) infrastructure available from UNMIB; and ii) an ad-hoc bash scripts were prepared to automatize the processing chain regarding the submission-processing and quality check of the fluorescence maps.

Specifically, more than three hundred *HyPlant* flight lines were collected over the selected tests sites across Europe during the FLEXSense 2018 campaign. A subset was selected as “high-priority” data set, according to a number of criteria encompassing clear-sky conditions, flight lines patterns simultaneous to Sentinel3-B satellite in FLEX reconfigured mode overpasses and scientific interests from local site managers. A synthetic list of the flight lines processed is reported in Table 7, including the acquisition date, time, flight altitude and the overall flight lines identification code.

In summary:

- flight flight-lines corresponding to Sentinel-3B reconfigured overpasses are processed for all the tests sites (Italy, Switzerland, Germany, Spain and France),
- flight lines collected in Grosseto (IT) were processed along the campaign extent, starting from beginning of June until end of July (10 June, 18 July, 20 July, 30 July, 31 July),
- flight lines in the CKA and SEL sites in Germany were processed (large number of lines), according to the field experiments. The TR32 mosaic was also processed.

Table 7: List of flight lines processed with the SFM airborne retrieval code.

ACQUISITION DATE (YYYYMMDD)	LINE CODE	LOCAL TIME (HHMM)	FLIGHT ALTITUDE (M)	LINE #
20180610	GRO	1037	600	L6
20180610	GRO	1347	600	L6
20180610	GRO	1621	600	L6
20180610	S3IT	1305	3050	L4
20180610	S3IT	1309	3050	L3
20180610	S3IT	1314	3050	L2
20180610	S3IT	1319	3050	L1
20180624	MAJ	1241	1015	L1

20180624	MAJ	1245	1015	L2
20180624	MAJ	1249	1015	L3
20180624	MAJ	1253	1015	L4
20180624	MAJ	1257	1015	L5
20180624	S3ESP	1222	3050	L1
20180624	S3ESP	1226	3050	L2
20180624	S3ESP	1230	3050	L3
20180624	S3ESP	1234	3050	L4
20180626	SEL	1522	600	L6
20180626	SEL	1526	600	L5
20180626	SEL	1530	600	L4
20180626	SEL	1537	600	L3
20180626	SEL	1543	600	L2
20180626	SEL	1548	600	L1
20180626	TR32	1306	1800	L17
20180626	TR32	1314	1800	L16
20180626	TR32	1322	1800	L15
20180626	TR32	1330	1800	L14
20180626	TR32	1338	1800	L13
20180626	TR32	1346	1800	L12
20180626	TR32	1354	1800	L11
20180626	TR32	1401	1800	L10
20180626	TR32	1409	1800	L9
20180626	TR32	1416	1800	L8
20180626	TR32	1424	1800	L7
20180626	TR32	1430	1800	L6
20180626	TR32	1437	1800	L5
20180626	TR32	1443	1800	L4
20180626	TR32	1449	1800	L3
20180626	TR32	1455	1800	L2
20180626	TR32	1502	1800	L1
20180627	SEL	1046	600	L4
20180627	SEL	1051	600	L3
20180629	CKA	1110	600	L4
20180629	CKA	1115	600	L3
20180629	CKA	1119	600	L2
20180629	CKA	1123	600	L1
20180629	CKA	1225	600	L4
20180629	CKA	1229	600	L3
20180629	CKA	1233	600	L2
20180629	CKA	1237	600	L1

20180629	CKA	1242	350	L2
20180629	CKA	1246	350	L1
20180629	CKA	1435	600	L4
20180629	CKA	1440	600	L3
20180629	CKA	1443	600	L2
20180629	CKA	1446	600	L1
20180629	CKA	1451	350	L1
20180629	CKA	1454	350	L2
20180629	CKA	1547	600	L1
20180629	CKA	1550	600	L2
20180629	CKA	1554	600	L3
20180629	CKA	1558	600	L4
20180702	S3GER	1219	3050	L1
20180702	S3GER	1223	3050	L2
20180702	S3GER	1228	3050	L3
20180702	S3GER	1233	3050	L4
20180713	S3SWI	1355	3050	L4
20180713	S3SWI	1402	3050	L3
20180713	S3SWI	1407	50	L2
20180713	S3SWI	1411	3050	L1
20180719	S3IT	1246	3050	L1
20180719	S3IT	1251	3050	L2
20180719	S3IT	1256	3050	L3
20180719	S3IT	1301	3050	L4
20180730	S3IT	1135	3050	L1
20180730	S3IT	1140	3050	L2
20180730	S3IT	1145	3050	L3
20180730	S3IT	1149	3050	L4
20180730	S3IT	1154	3050	L3
20180730	S3IT	1159	3050	L2
20180731	S3IT	1301	3050	L1
20180731	S3IT	1306	3050	L2
20180731	S3IT	1311	3050	L3
20180731	S3IT	1316	3050	L4
20180802	CKA	1310	600	L4
20180802	CKA	1314	600	L3
20180802	CKA	1318	600	L2
20180802	CKA	1322	600	L1
20180802	CKA	1326	350	L1
20180802	CKA	1329	350	L2
20180802	S3GER	1204	3050	L1

20180802	S3GER	1208	3050	L2
20180802	S3GER	1212	3050	L3
20180802	S3GER	1217	3050	L4
20180802	SEL	1227	600	L1
20180802	SEL	1233	600	L2
20180802	SEL	1238	600	L3
20180802	SEL	1244	600	L4
20180802	SEL	1249	600	L5
20180802	SEL	1254	600	L6

The flight lines processed include a large variety of observation conditions:

- flight altitude (i.e., 350 m, 600 m, 1800 m, 3050 m), resulting in different pixel sizes;
- geographical locations;
- time of the day (morning / noon / afternoon, the SZA);
- atmospheric conditions (AOT, A, H₂O etc.)
- type of ecosystems (different crops and natural vegetation).

The variability of the atmospheric parameters during the extension of the campaign for all the processed flight is reported in Figure 20. The AOT, the ASTMX, and the column water vapor (H₂O) values are derived from sun photometer measurements or from the ATCOR inversion of the DUAL imagery. The sun photometer data include either measurements collected within the field with hand-held photometers (i.e., Microtops II) or more sophisticated robotic instrument measurements belonging to the Aeronet network. In general, Aeronet data are preferred over the to in-field instrumental measurements for a couple of reasons: i) the accuracy of the camel instrument is better; and ii) Aeronet data are processed according to well-established algorithms. In the case of the data being extracted from Aeronet, processing level-1.5 is used. The Henyey–Greenstein asymmetry phase function (G) parameter is not provided directly by typical sun photometer processing. Rather, it is available from more advanced aerosol products disseminated by the Aeronet network. In particular, the phase function asymmetry factor is only available within advanced data processing levels i.e., aerosol inversion (v3) products. Unfortunately, G is available only for *HyPlant* flight lines near Aeronet stations, whereas a “standard” value of 0.8 is assumed for the other flight lines.

The atmospheric parameters described before are extracted from external sources, whereas sensor elevation (H1) is directly estimated from the image by using the current version of the retrieval algorithm. In particular, the non-vegetated pixels are used to refine the atmospheric RT modeling on the base of H1 parameter. Figure 21 shows the comparison between H1 values from the *HyPlant* navigation system data and the “effective” values estimated for the O₂-B and O₂-A bands (see description in section 4.2.1.3). The discrepancies between the nominal value from the navigation system and those estimated by the retrieval algorithm are caused by a number of factors, including a number of assumptions in the atmospheric modeling (MODTRAN) as well as uncertainties in other parameters derived from the sun photometer (atmospheric scattering).

The “quality” of the fluorescence maps that were produced is evaluated for the large set of processed flight lines by using the following approach:

- First, an automatic screening was used based on the distribution of fluorescence values for the O₂-A and O₂-B bands over the entire image. The fluorescence values shall be within the expected range between 0 – 4 mWm⁻²sr⁻¹nm⁻¹ according with a number of papers in literature where ground-based field spectroscopy measurements are reported and compared from different types of crops / forest

	Doc.: Final Report		
	Date: 29 July 2021	Issue: 2	Revision: 1
	Ref.: ESA Contract No. 4000125402/18/NL/NA		Page: 54 / 288

canopy, such as measurements reported by Rossini et al. (2016) and Marrs, Jones, Allen & Hutyrá (2021). To support the interpretation, the distribution of the NDVI for the whole image is plotted to give a sense of the average content of the scene (if the scene is mainly covered by vegetated pixels, or mixed vegetated non-vegetated pixels etc.).

ii) Second, the airborne fluorescence retrieval is compared with ground-based fluorescence measurements collected by the FloX instruments (section 5.3).

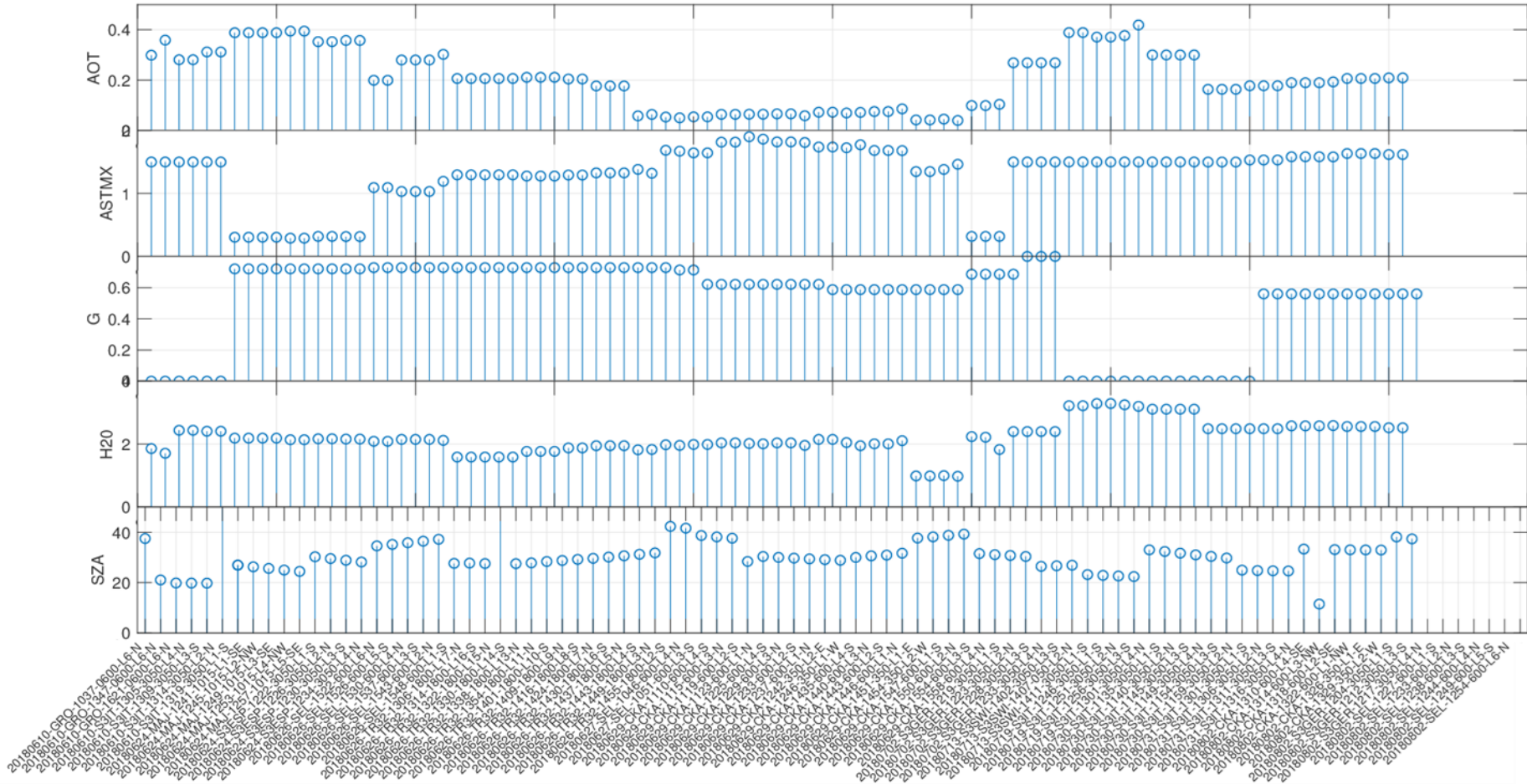


Figure 20: Atmospheric model input parameters in term of AOT, ASTMX, asymmetry of the scattering phase function (G), column water vapor (H₂O) and SZA corresponding to the *HyPlant* flight lines processed during the extension of the FLEXsense 2018 campaign over the different testing sites.

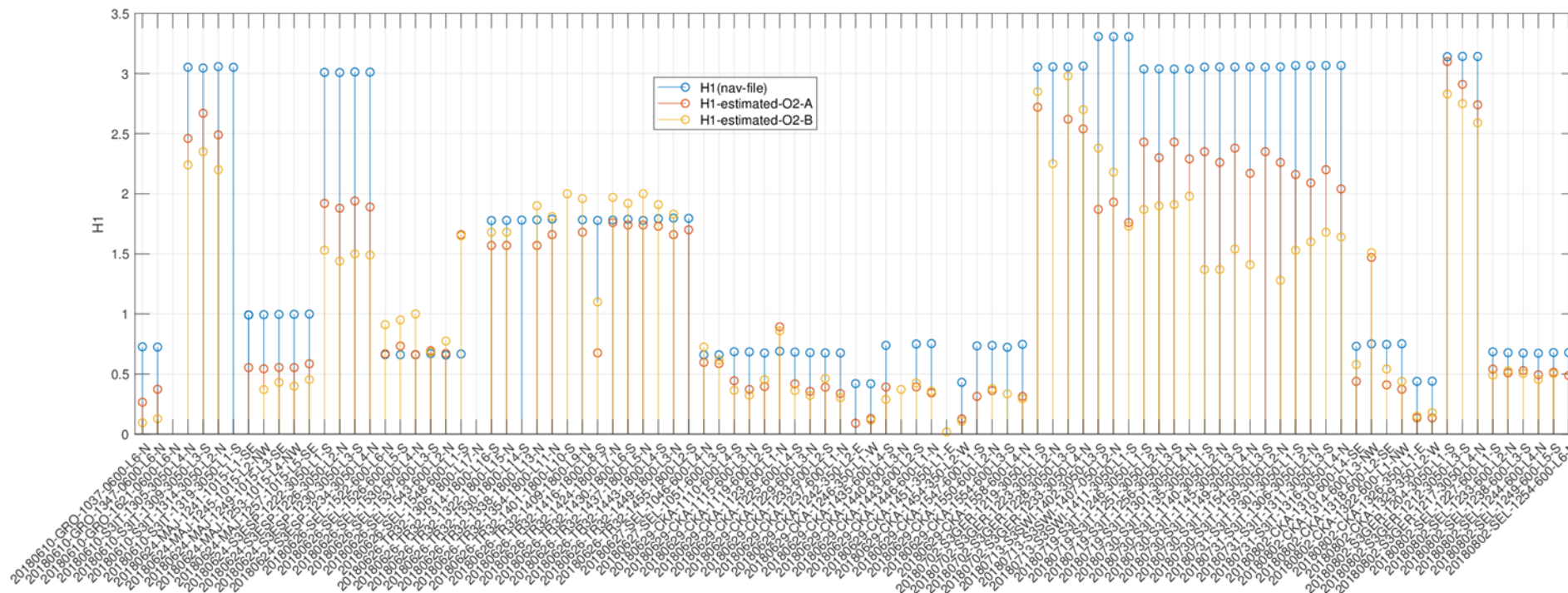


Figure 21: Sensor elevation above the ground surface (H1) from the *HyPlant* navigation file (blue points) and values estimated from the airborne fluorescence retrieval algorithm for O₂-A (orange) and O₂-B (yellow) bands based on non-vegetated pixels correction.

	Doc.: Final Report		
	Date: 29 July 2021	Issue: 2	Revision: 1
	Ref.: ESA Contract No. 4000125402/18/NL/NA		Page: 57 / 288

Some of the F maps at the O₂-b and O₂-A bands computed by the novel fluorescence retrieval algorithm based on the SFM are presented. First, the *HyPlant* Sentinel-3 pattern mosaic of fluorescence is shown in Figure 22 - Figure 25 for Italy, Germany (two mosaics), and Spain, respectively. The NDVI maps retrieved from the FLUO module are reported to provide a reference for the interpretation of the red and far-red F maps.

In general, the overall spatial structure of the NDVI and F maps are consistent: larger fluorescence values are observed for those areas characterized by dense vegetation (higher NDVI); conversely, lower fluorescence values are observed for sparse vegetation and values close to zero for non-vegetated pixels. This is consistent for all the imagery processed. The absolute fluorescence values computed by the retrieval algorithm are in line with the typical values expected from ground-based observations and theoretical models in the range between 0 - 3 mWm⁻²sr⁻¹nm⁻¹. Another improvement of the novel fluorescence maps is the good agreement between overlapped areas of two adjacent images; typical border effects such as “different brightness” are not evident between two consecutive lines. However, there might be some residual brightness effects that could happen. **Brightness difference at the image borders** (i.e., last 80 - 50 pixels to the edge): This effect is corrected in the SFM retrieval code because MODTRAN simulations are done for nadir (0°) and off-nadir (16°) across-track viewing angles of *HyPlant*. The remaining brightness difference between two adjacent flight lines are ‘natural’ and it could be relevant information about the canopy properties (i.e. fluorescence anisotropy). It should be there in the data. In future, this could be further analyzed more into details as follows: i) correcting fluorescence anisotropy by developing a novel bidirectional reflectance distribution function (BRDF) correction algorithm if we want to show homogenous images; ii) exploiting anisotropic behavior of SIF for downstream scientific applications for example developing a hemispherical SIF map. **Brightness difference over the entire image:** Individual flight lines are processed independently, this means that the atmospheric correction is done for every single image (i.e., soil selection etc.). It is surprising how independent flight lines match well most of the times (no brightness difference), considering the complex and complicated retrieval. Some few sparse flight lines result particularly dark/bright because the atmospheric correction for these specific lines did not perform well. The typical causes are relevant changes in the topography or sudden clouds. This few lines would require additional investigations.

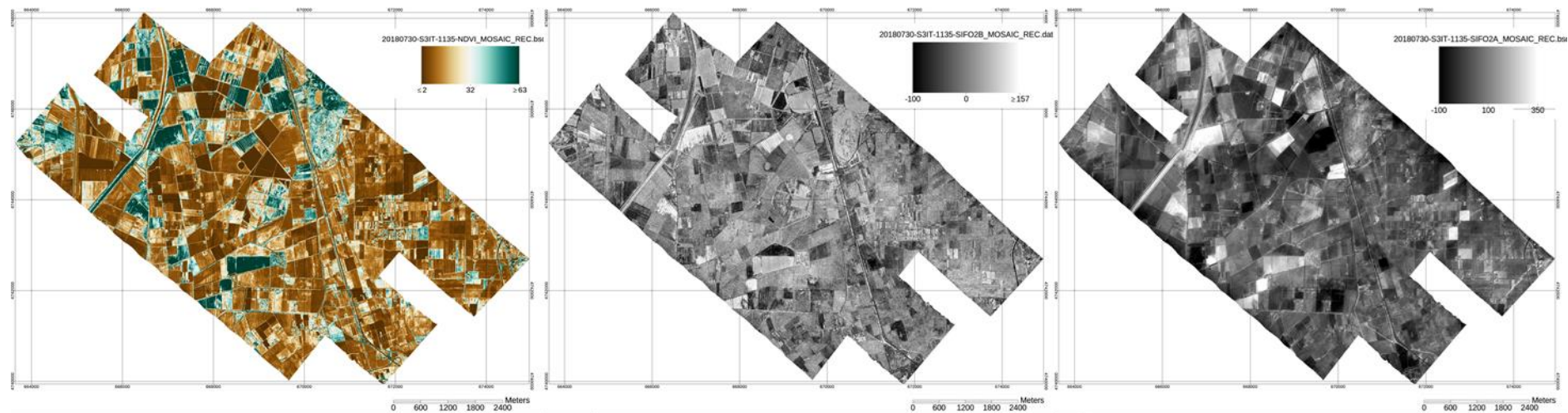


Figure 22: NDVI (left), red F (middle), and far-red F (right) maps of the Sentinel-3 pattern in Grosseto (Italy) collected on 30 July 2018, covering a 5 x 5 km area.

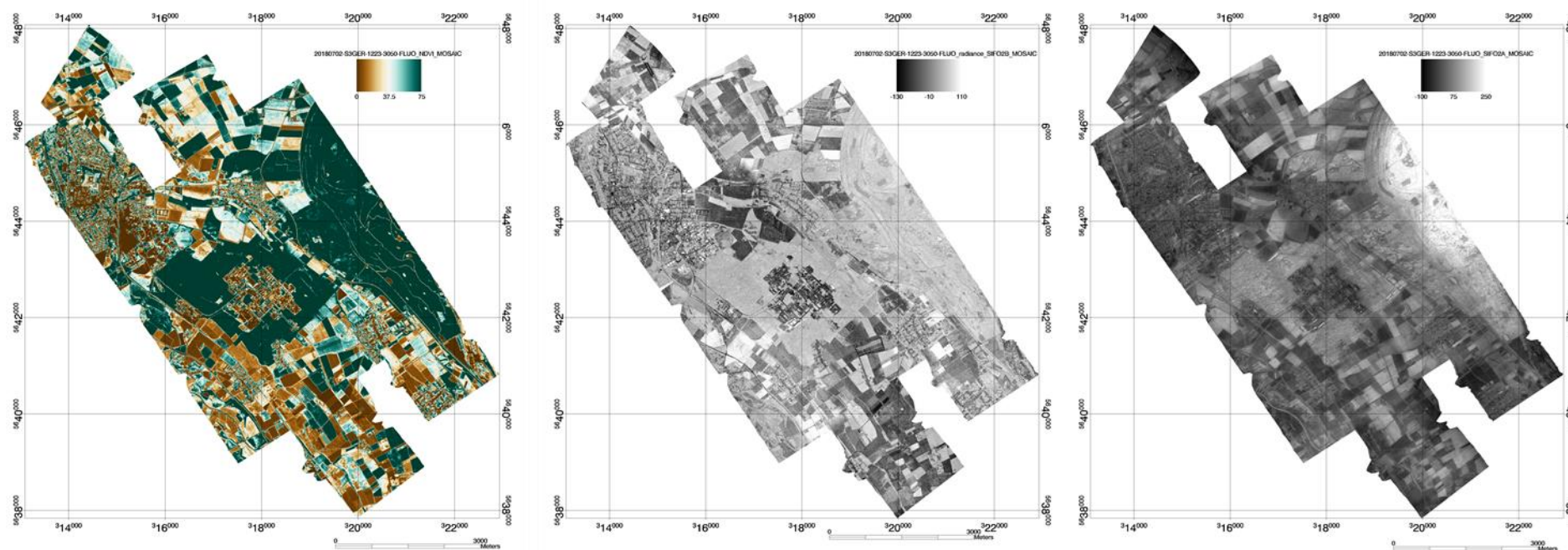


Figure 23: NDVI (left), red fluorescence (middle), and far-red fluorescence (right) Sentinel-3 pattern in Selhausen (Germany) collected on 30 July 2018, covering a 5 x 5 km area.

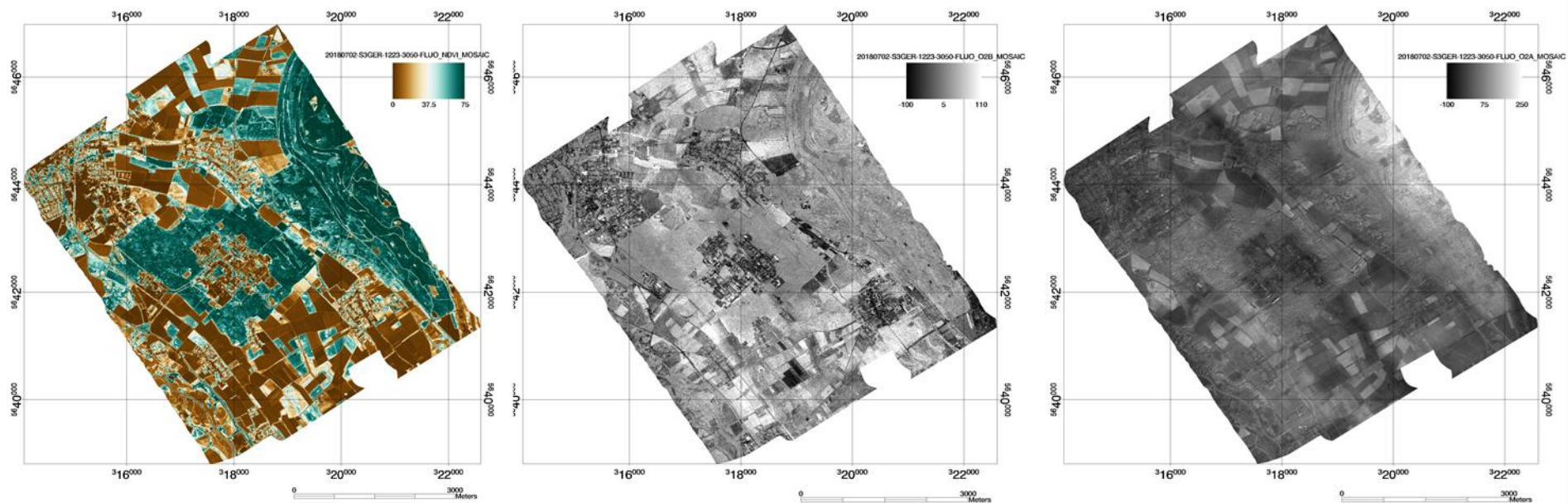


Figure 24: NDVI (left), red fluorescence (middle), and far-red fluorescence (right) Sentinel-3 pattern in CKA (Germany) collected on 30 July 2018, covering a 5 x 5 km area.

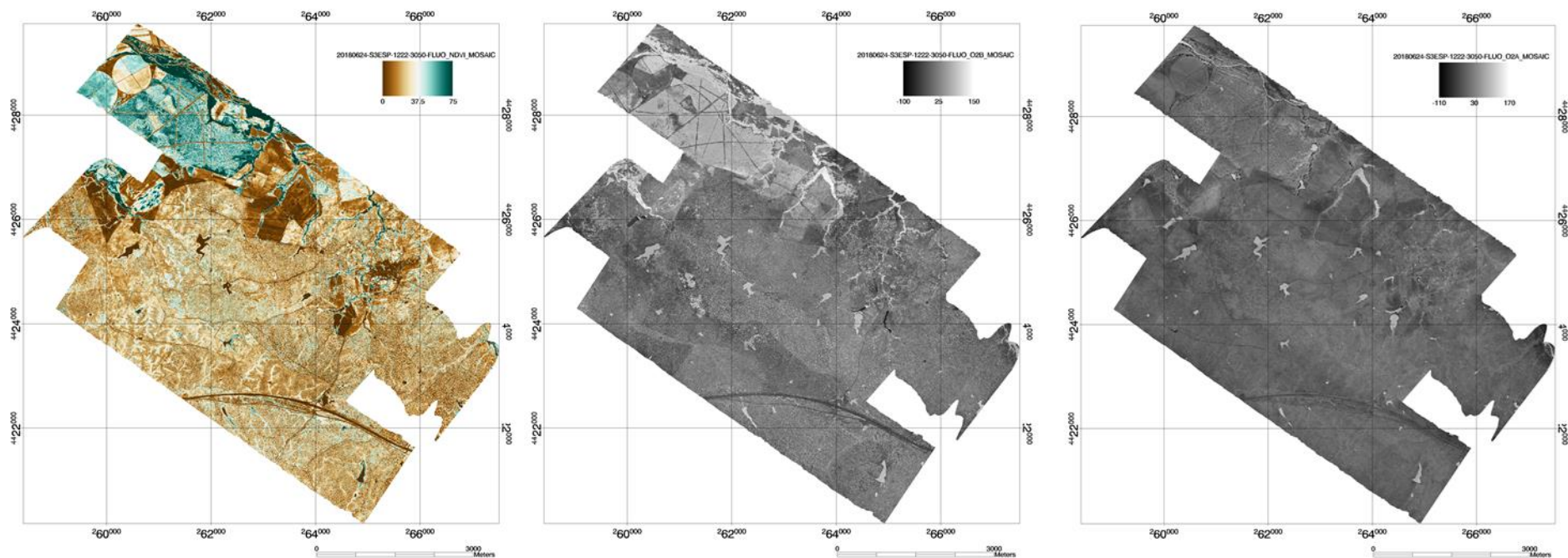


Figure 25: NDVI (left), red fluorescence (middle), and far-red fluorescence (right) Sentinel-3 pattern in Majadas (Spain) collected on 24 June 2018, covering a 5 x 5 km area.

	Doc.: Final Report		
	Date: 29 July 2021	Issue: 2	Revision: 1
	Ref.: ESA Contract No. 4000125402/18/NL/NA		Page: 62 / 288

A quantitative evaluation of the reliability of fluorescence maps produced on the large data set can be performed by analysing the distribution of red and far-red fluorescence values for the entire image. This provides a better understanding about the reliability of the fluorescence absolute values retrieved. A synthetic overview for several flight lines collected at 3050 m, 600 m and 350 m are reported in Figure 26 - Figure 28. In summary, there are a few considerations to take into account:

- Fluorescence values at both the O₂-A and O₂-B bands are always lower than 3 mW m⁻²sr⁻¹nm⁻¹.
- Fluorescence values at O₂-B show slightly larger values than the fluorescence values at O₂-A band; in general, this result is suspicious, but it could occur for sparse vegetation areas in which reabsorption plays a lesser role. Further analysis should be done.
- There is a substantial number of slightly negative values (-1 and 0 mWm⁻²sr⁻¹nm⁻¹) that are related to bare soil pixels. They were substantially improved from previous versions of the retrieval algorithm, but a better understand whether they come from the instrumental noise or the retrieval algorithm is needed.

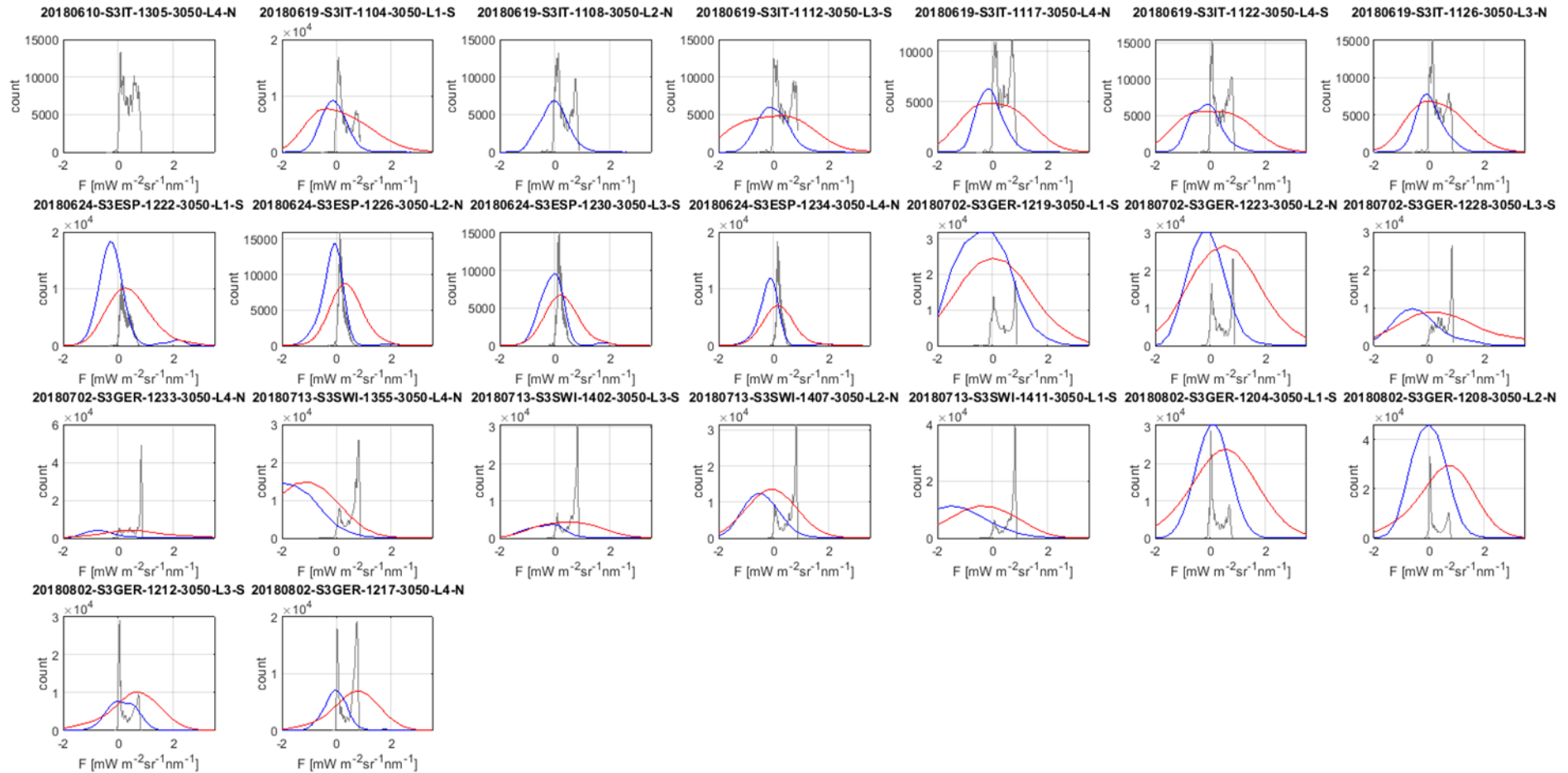


Figure 26: Distribution of red (red line), far-red fluorescence (blue line) values and NDVI (gray line) over the entire image for a number of processed flight lines collected at 3050 m.

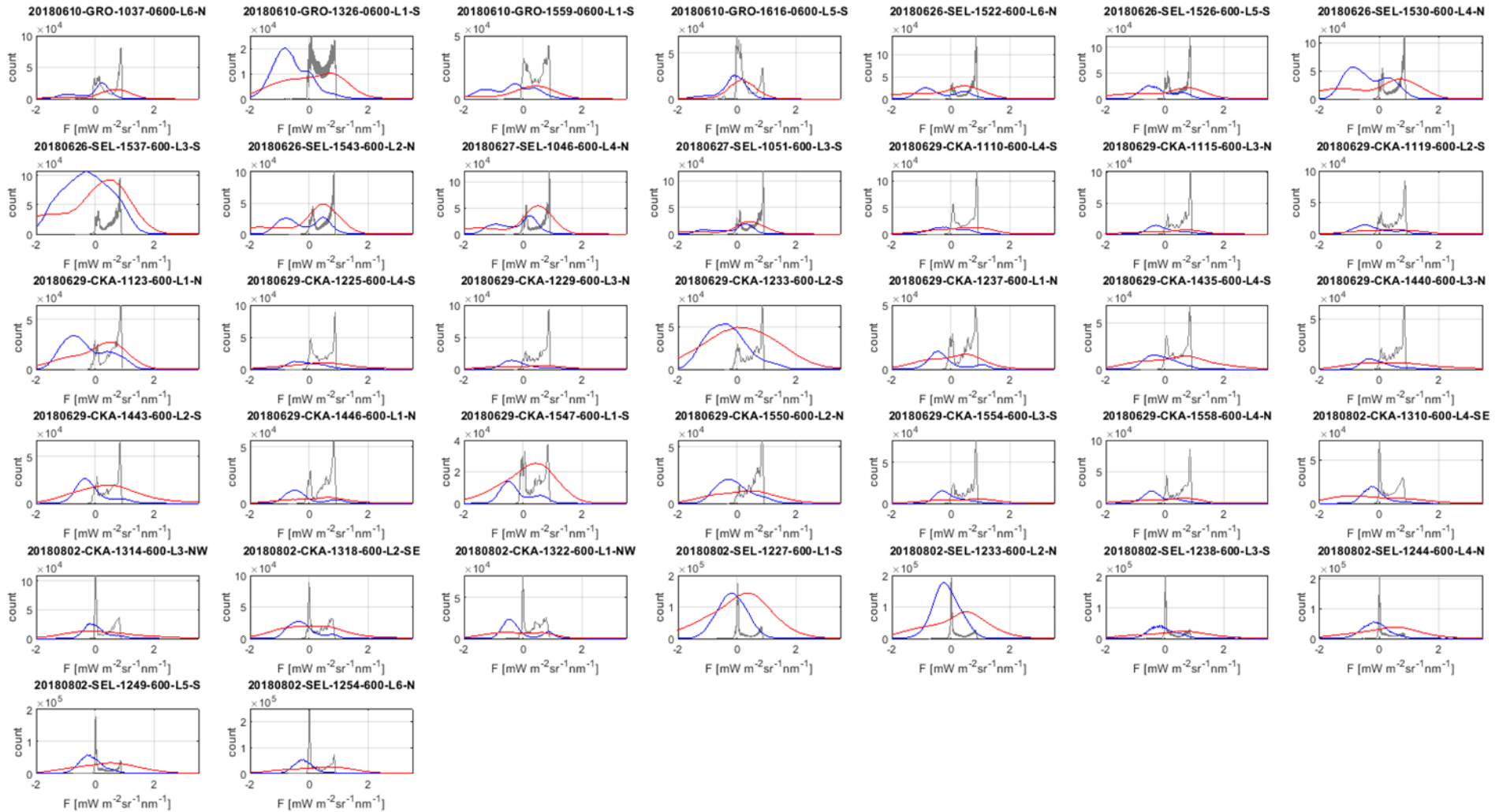


Figure 27: Distribution of red (red line), far-red fluorescence (blue line) values and NDVI (gray line) over the entire image for a number of processed flight lines collected at 600 m.

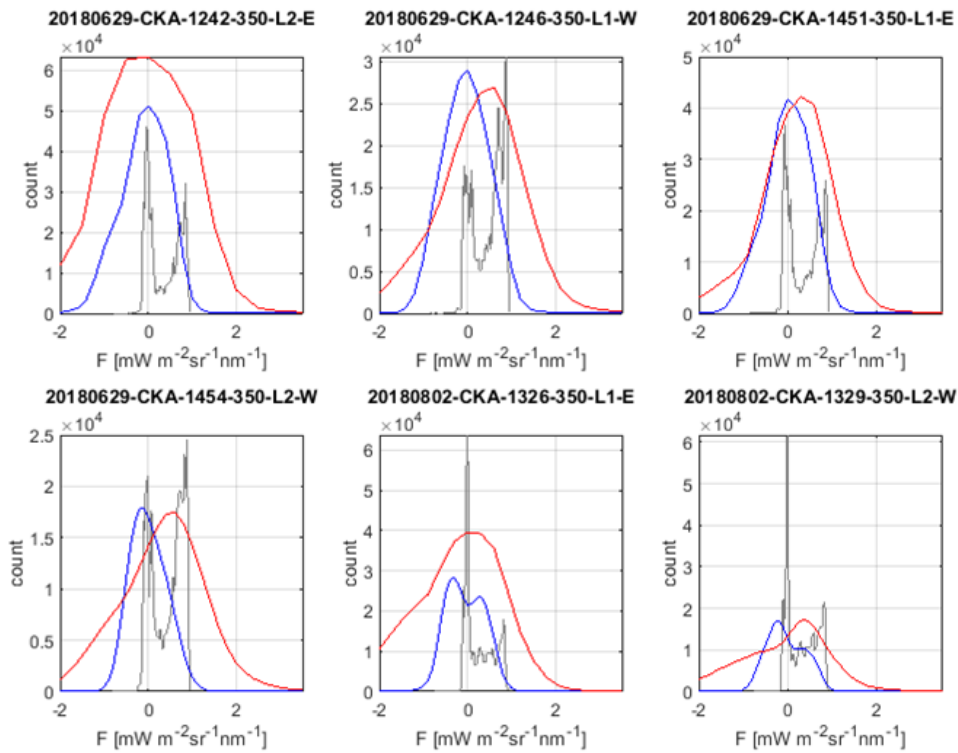


Figure 28: Distribution of red (red line), far-red fluorescence (blue line) values and NDVI (gray line) over the entire image for a number of processed flight lines collected at 350 m.

5.2 Comparison between iFLD and SFM maps

In this section, an additional comparison between the SFM and the iFLD is presented via the average SIF retrieved in eleven crop canopies using a *HyPlant* image collected on 26 June 2018, in Selhausen, Germany (Figure 29).

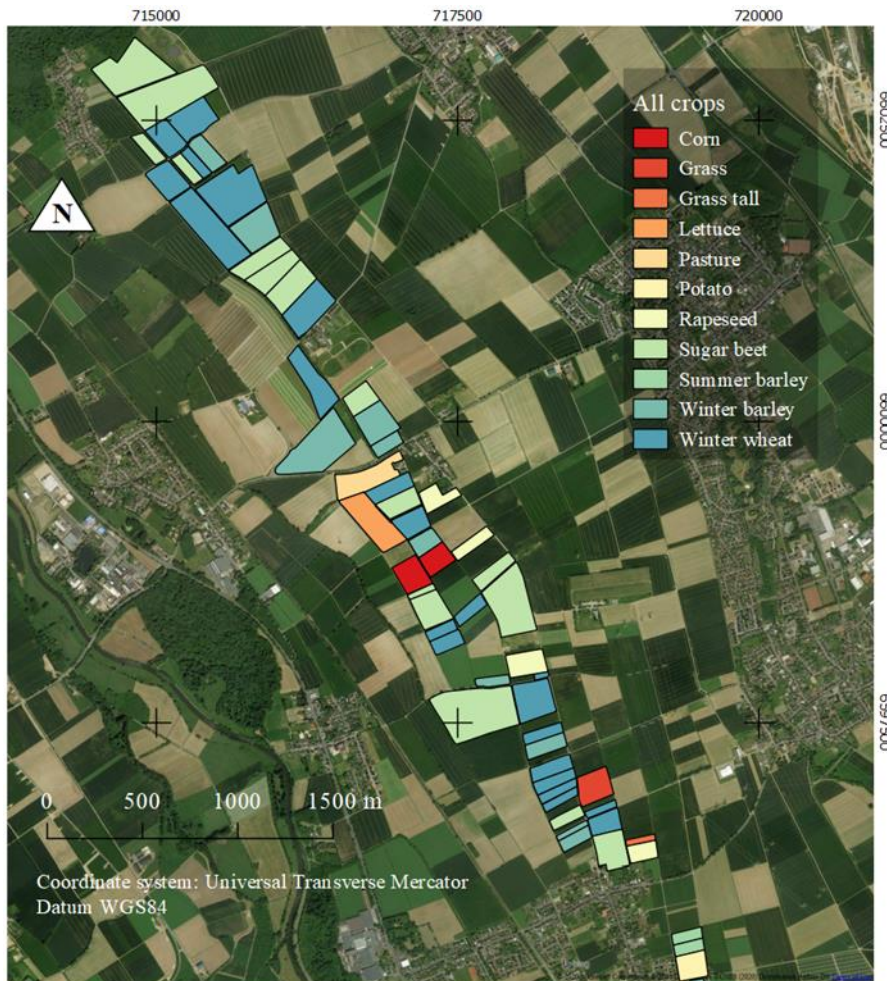


Figure 29: Crop fields used for the comparison between the SFM and the iFLD SIF retrievals using a *HyPlant* image of 26 June 2018 (Selhausen, Germany).

The red and far-red average fluorescence values computed for the different crops are shown in Figure 30. The summer barley was the crop with the higher SIF values retrieved by both methods and absorption bands (iFLD-A = 1.67, and iFLD-B = 0.49; SFM-A = 3.13, SFM-B = 1.42), while the lowest O₂-A SIF was retrieved in grass (iFLD = 0.30; SFM = 0.34; Figure 30). In addition, the lower standard deviation of the barley (winter and summer) indicates the spatial homogeneity of SIF at canopy level within these fields compared with the other crops. A lower O₂-B SIF was recorded for lettuce and sugar beets (iFLD = 0.13 - 0.15; SFM = 0.35 - 0.44). Furthermore, using iFLD, the O₂-A SIF is always higher than O₂-B. Nonetheless, when using the SFM method this is not always true: the average O₂-B SIF retrieved with this method in grass and potato canopies was higher than the O₂-A SIF. A more detailed analysis including the specific phenology stages and stress conditions of each crop field could help to explain the mentioned differences. However, this is not within the scope of the present analysis.

Figure 31 a and b present a zoom to the O₂-A SIF retrieved with both methods over the summer barley field; their respective histograms are shown in Figure 31 c. The data in both cases follow a similar distribution. Nevertheless, less noise is observed in the SFM product. Moreover, the spatial distribution of the discrete classes on the SFM-based map better accords with the spatial distribution of canopy properties derived from other vegetation maps, e.g., vegetation indices.

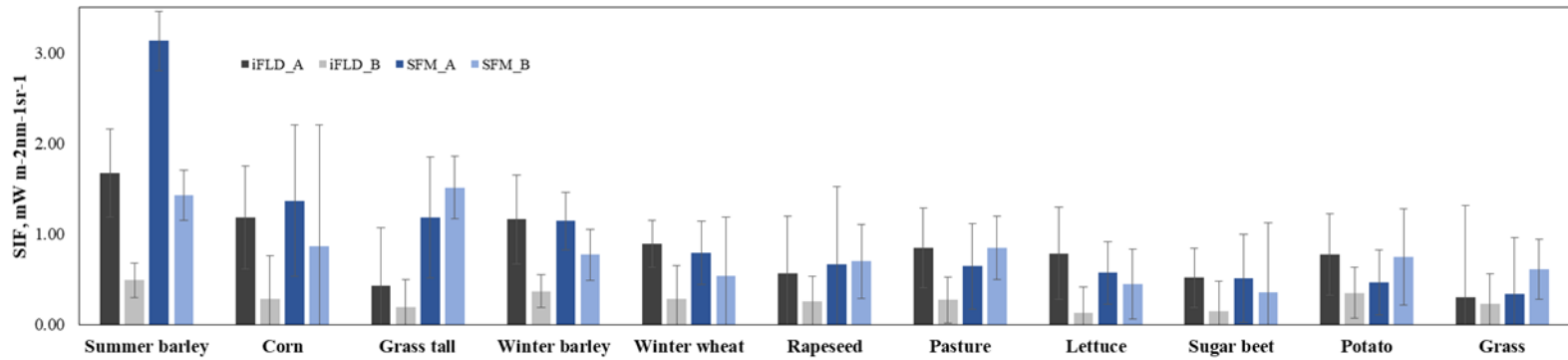


Figure 30: Average SIF retrieved with iFLD and SFM methods at the O₂-A and O₂-B absorption bands over eleven crop canopies. Error bars represent the standard deviation.

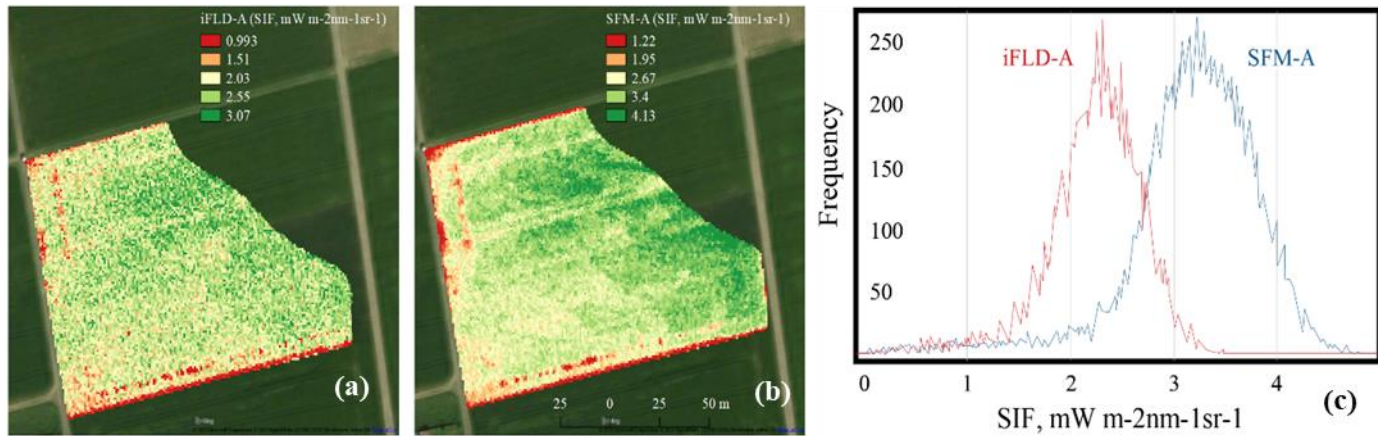


Figure 31: Zoom into the iFLD (a) and SFM (b) O₂-A maps of the summer barley field, and their respective histograms (c).

Figure 32 shows the iFLD and SFM O₂-A and O₂-B outputs from the *HyPlant* overflight on 26 June 2018. At the O₂-A bands, both methods provide better results in the sense that intra- and inter-field variability can be observed with more clarity (Figure 32 a and c). By visual comparison, the best result is perceived in the SFM-A image, which shows stronger contrast among fields and clearer heterogeneity within single fields. The SIF retrieved at O₂-B (Figure 32 b and d) in general provides more noisy results with lower values than those observed in the O₂-A derived SIF maps. The latest might be due to the lower intensity of the chlorophyll fluorescence signal at the O₂-B, regardless of the retrieval method. As shown in the histograms, the iFLD in the sample dataset used for the present analysis retrieved slightly fewer negative values than the SFM at the O₂-A (~3% less) but more at the O₂-B (~4% more). With both methods, the majority of the negative values is observed at O₂-B.

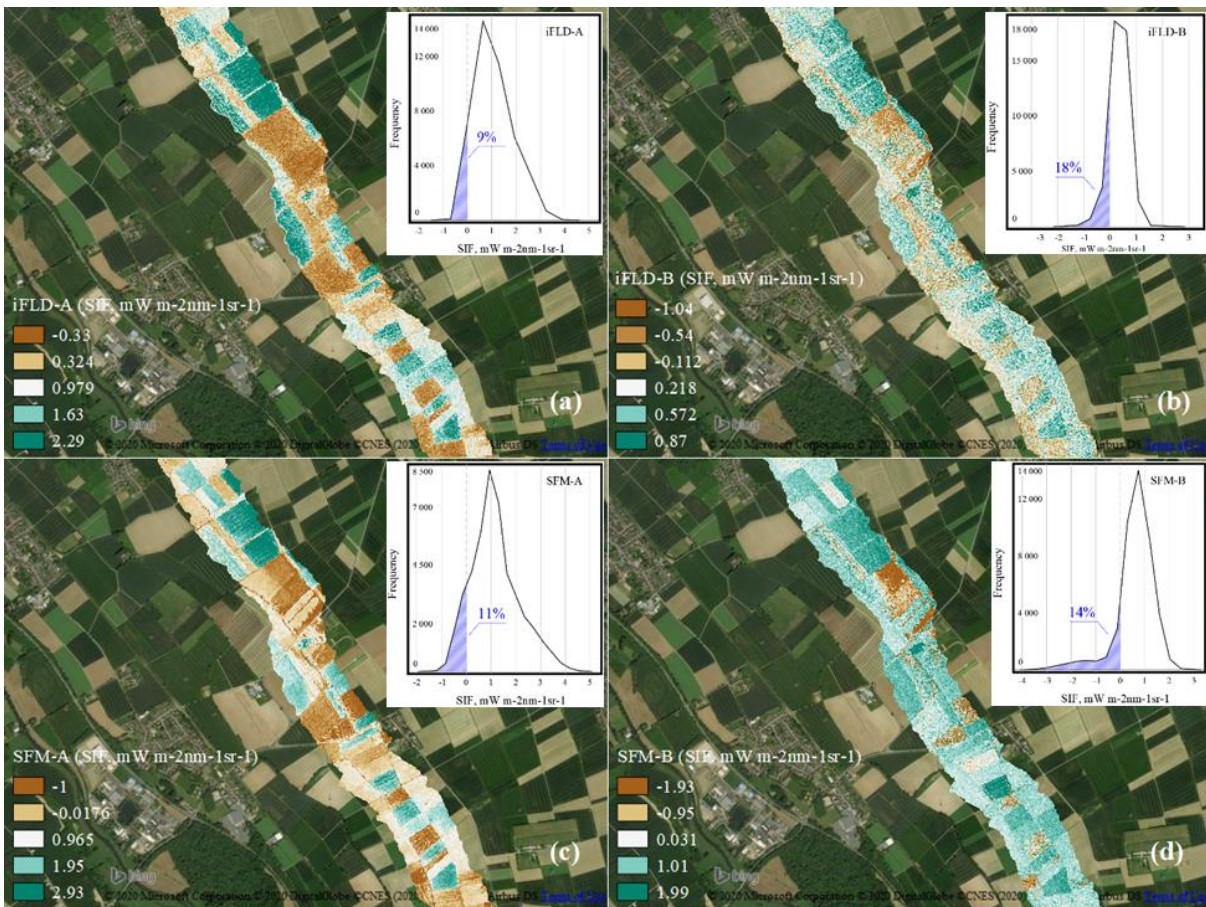


Figure 32: iFLD-A (a), iFLD-B (b), SFM-A (c), and SFM-B (d) retrieval outputs and their histograms obtained from the *HyPlant* 26 June 2018 image processing (Selhausen, Germany).

The general patterns observed in the entire image can be confirmed with the analysis of a single representative field. Figure 33 shows the larger field covered within the study area that correspond to a five-ha winter wheat zone (Figure 33a - d). As mentioned before, the SFM-A output presents the most reasonable values within the expected range, as well as the most congruent spatial distribution of discrete classes. Moreover, the retrievals at O₂-B have a higher variability, especially the SFM-B, which provides negative values down to -3.52 (SFM).

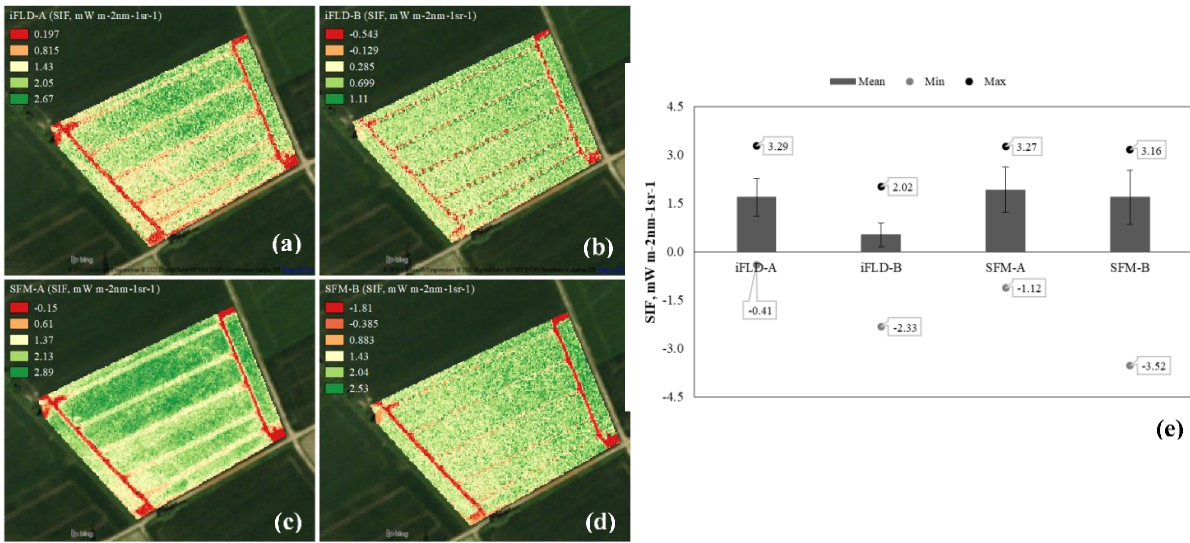


Figure 33: iFLD-A (a), iFLD-B (b), SFM-A (c), and SFM-B (d) retrieval outputs obtained from a 5-ha single winter wheat field, and their respective mean, maximum, and minimum values (e).

5.3 Comparison and validation of airborne fluorescence products using ground-based measurements

A quantitative evaluation of the reliability of the estimated *HyPlant* SIF maps is reported and discussed in this section. The ground-based SIF measurements from FloX instruments are compared with the corresponding values in the SIF maps produced from *HyPlant* imagery. The FloX spectrometer is equipped with a GPS unit. Basically, latitude and longitude are stored in the form of geographical coordinates together with each single spectrum collected by the instrument. Region of interests (ROIs), which correspond to FloX point measurements, are identified within the *HyPlant* imagery. The size of the ROIs is adapted based on the pixel size of the specific *HyPlant* image (i.e. from 0.5 m, 1 m and 4.5 m) and FloX footprint, so that ROIs are representative for the actual footprint of the FloX measurements. Typically, FloX measurements in agricultural areas are collected from a close distance above the canopy, typically ranging from 1 to 3 meters. It corresponds to a sampling area with a circular shape with an approximate diameter of 0.5 to 1.5 m. Therefore, the selection of the ROIs within the *HyPlant* images needs to be considered in order to match the two measurements as far as possible.

The fluorescence ground-based measurements are available from all campaign sites, but tower-based set-ups (i.e., fixed single point measurement) were only recorded in France, Spain and Switzerland. This makes the comparison between ground-based and airborne measurements weak. Conversely, data sets collected in Italy and Germany are much more promising because spatially distributed FloX measurements were recorded simultaneously with the airborne and satellites observations. The analysis presented in this section focuses on these two sites.

Germany, Selhausen

The consistency between ground and airborne SIF retrievals is evaluated by *HyPlant* images collected in Selhausen (Germany), which were recorded from 600 m agl during the vegetation growth peak in 2018. Figure 34 presents the average SIF values retrieved with the SFM from *HyPlant* imagery plotted against the SIF retrieved with the same method from FloX ground measurements (four surface coverages: sugar beet, corn, lawn, and winter wheat).

Sugar beet and corn measurements were collected with a mobile FloX that was carried to the specific points on the field. A tripod was used to measure the upwelling and downwelling radiance at ~2 m agl and a gimbal helped to ensure the perpendicular position of the upwelling-measuring channel over the ground. In the scatterplot, the horizontal 'error bars' of the FloX data correspond to the E stability values per data point. Airborne SIF was retrieved from *HyPlant* images recorded on 26 June (at 15:30 and 15:37, CEST) and 27 June (at 10:46 and 10:51, CEST). The FloX measurements were recorded in a period of 22 and 27 min, respectively, close to the airborne overpasses. On the first day, the largest temporal mismatch between FloX and *HyPlant* measurements was 15 minutes, while on the second day it was 12 minutes. Strong relationships between the airborne and ground measurements were found for the O₂-A ($R^2 = 0.777$, $p < 0.001$) and O₂-B band ($R^2 = 0.850$, $p < 0.001$), respectively. However, compared with the FloX ground-based SIF measurements, SIF retrieved with the SFM from *HyPlant* airborne data was slightly lower for SIF₇₆₀ and higher for SIF₆₈₇. Furthermore, at both scales (ground and airborne level) the highest SIF values were estimated for sugar beets with a notably better agreement on 26 June (*HyPlant* image recorded at 15:37 CEST). On 27 June, the average SIF₇₆₀ retrieved from *HyPlant* collected at 10:46 - 10:51 CEST over sugar beets ranged from 1.07 to 1.36 $\text{mWm}^{-2}\text{sr}^{-1}\text{nm}^{-1}$, while the corresponding FloX measurements varied from 1.61 to 2.03 $\text{mWm}^{-2}\text{sr}^{-1}\text{nm}^{-1}$. In comparison, sugar beet lawn and winter wheat had distinctly lower SIF values recorded at ground and airborne level, including a few negative retrievals from *HyPlant* data (~-0.12). Additionally, the *HyPlant*-based corn SIF₆₈₇ values ($0.48 \text{ mWm}^{-2}\text{sr}^{-1}\text{nm}^{-1}$) closely matched the FloX retrievals ($0.5 \text{ mWm}^{-2}\text{sr}^{-1}\text{nm}^{-1}$). However, the SIF₇₆₀ measurement was underestimated by $0.57 \text{ mWm}^{-2}\text{sr}^{-1}\text{nm}^{-1}$. In this context, the FloX measurement uncertainty has to be considered for this data point, since the E stability factor was the highest among all the measurements (0.74).

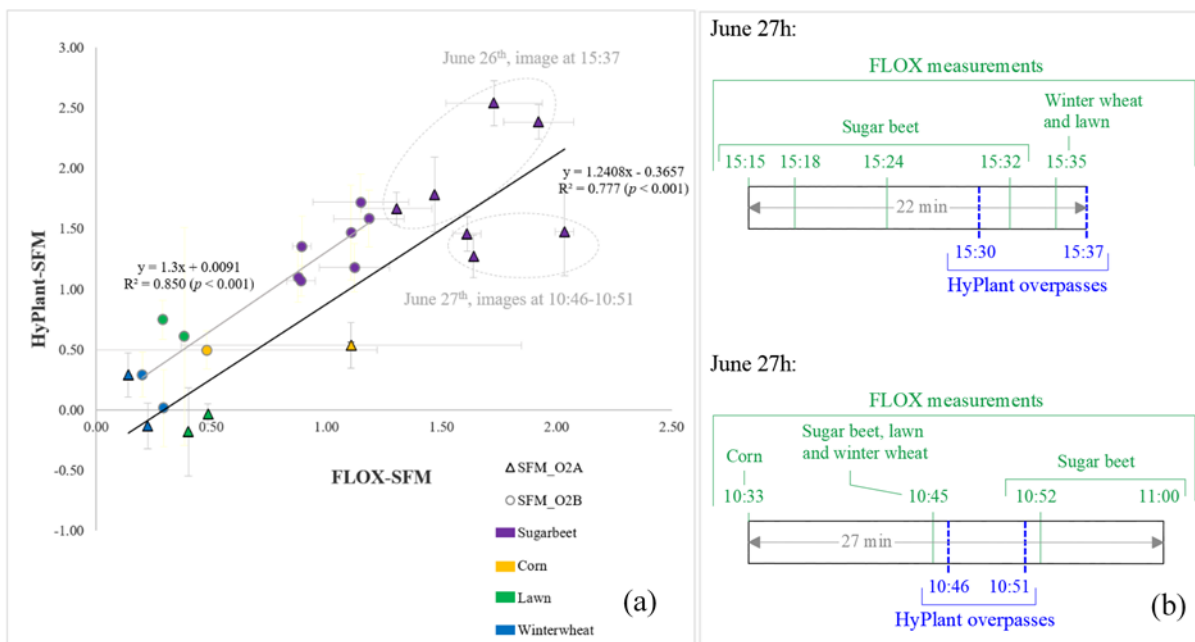


Figure 34: (a) Scatterplot between FloX and *HyPlant* SIF₇₆₀ and SIF₆₈₇ measurements based on the SFM, and (b) a schematic representation of the temporal offsets between the *HyPlant* overpasses and FloX measurements.

Due to the good agreement of the airborne and ground-based SFM retrievals presented in Figure 34, the compatibility of the different airborne retrievals among each other was analyzed. Figure 35 illustrates the analysis comparing the SVD, iFLD and SFM far-red SIF maps of one flight line from 26 June 2018. While panel b) of the figure shows a high correlation between the SFM and iFLD retrieval, panel a) illustrates a distinctly lower agreement between the SVD and iFLD as well as between the SVD and SFM retrieval. In this context, it must be noted that far-red SIF using the SVD method was determined at 740 nm, while the iFLD and SFM

provide far-red SIF derived at 760 nm. In general, the spatial patterns of the iFLD and SFM maps look very similar (panel d) and e)). The value range is slightly different, with on average higher SIF₇₆₀ values retrieved using the SFM.

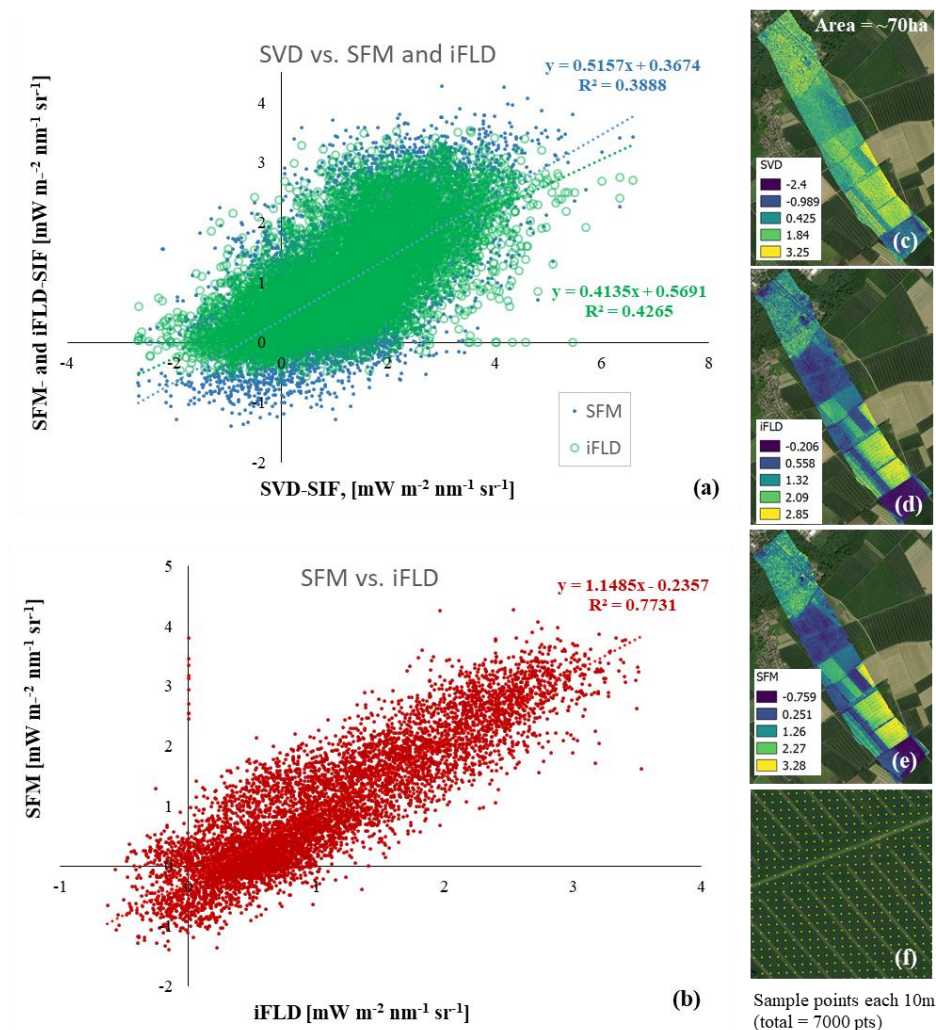


Figure 35: Comparison of the different SIF retrieval methods applied to a *HyPlant* flight line covering the Selhausen area on 26 June 2018. (a) Scatterplot between *HyPlant* SVD SIF₇₆₀ and *HyPlant* SFM and iFLD SIF₇₆₀, respectively. (b) Scatterplot between *HyPlant* iFLD SIF₇₆₀ and *HyPlant* SFM SIF₇₆₀. (c-e) *HyPlant* SIF₇₆₀ retrieved with the SVD, iFLD, and SFM method. (f) Subset of the sampling scheme used for the comparison of the different retrieval methods.

The spatially distributed FloX measurements in Italy were collected on 30 July 2018 (DOY=211), simultaneously with the *HyPlant* and Sentinel-3B reconfigured overpasses. The FloX instrument (serial code: JB-013-ESA) was installed on a tractor (Figure 36) to collect spatially distributed measurements. The instrument box was fixed in the cabin whereas a 5-m long pole was installed to keep the spectrometer fiber optics nadir-looking on the target and far away from the tractor to avoid any contamination of the radiometric measurements. As in the standard measurement procedure, two fibers were used: i) up-looking fiber to measure downwelling irradiance; and ii) down-looking fiber to sample the canopy. The up-looking fiber optics dedicated to measuring downwelling irradiance was installed on a mechanical gimbal to assure accurate measurements (cosine receptors levelled with the ground surface). The tractor set-up was used to move within the pivot cornfields, collecting spatially distributed spectral measurements in a number of different waypoints. Specifically, a few replicates of measurements were recorded of the same point (in a number between 3 - 5) when the tractor reached a defined waypoint without moving the tractor. Once spectral measurements were collected for a certain point, the FloX-tractor moved to the successive waypoint.

This approach would offer a better quality of the field spectral measurements. The ground spectral data were collected between 11:00 to 13:00 local time.

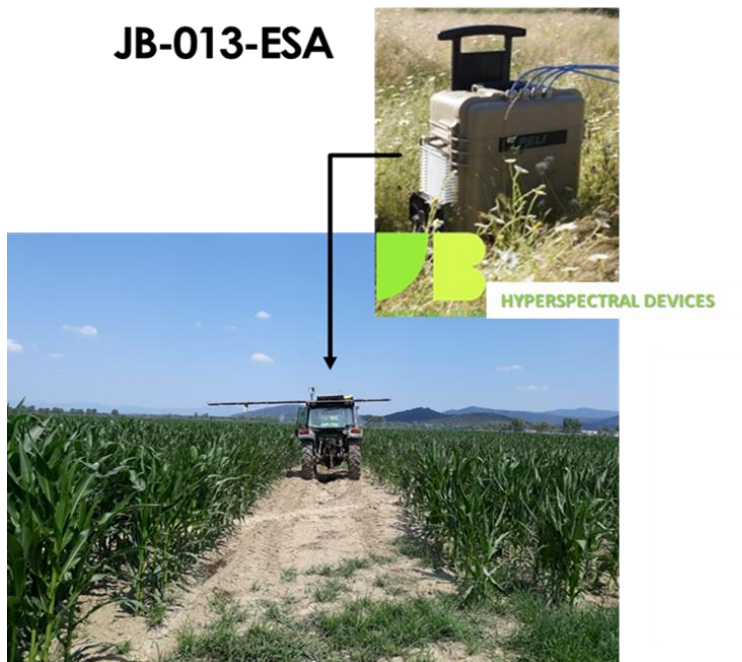


Figure 36: FloX instrument installed on a tractor during the field measurements.

Corn mainly covered the pivot field (1 km diameter). Nevertheless, the entire field is divided in different sectors where corn plants reached a different level of development on 30 July, resulting in different levels of canopy cover. The spectral measurements from the tractor were done in several waypoints. It allowed sampling of the spatial heterogeneity of the field and provided useful information for further airborne and satellite analysis. The locations of the measurements collected by the FloX instrument installed on the tractor are reported in Figure 37, while Figure 38 shows the corn canopy during the ground and airplane measurements.



Figure 37: The location of FloX measurements: In the Google Earth image, the symbols represent the data clusters defined using the FloX GPS information. On the top right, the RGB DUAL image shows the field at the moment of the *HyPlant* acquisition.



Figure 38: Different spots of the pivot cornfield.

The R and F spectra between 670 - 780 nm estimated from the *SpecFit* algorithm are shown in Figure 39. The typical spectral behavior characterized by the lower-red fluorescence peak (caused by the chlorophyll reabsorption) and a larger far-red fluorescence peak is observed for most of the targets. The main difference between the points consists in the large variability within the field caused by the different canopy development and thus canopy fractional cover (background soil effect). Dense vegetation typically exhibits a larger fluorescence in the far-red peak, but it also means larger reabsorption and consequently a lower red peak. The fluorescence observed by the FloX instrument at the O₂-A and O₂-B bands were extracted to compare them with the F values retrieved from the *HyPlant* imagery.

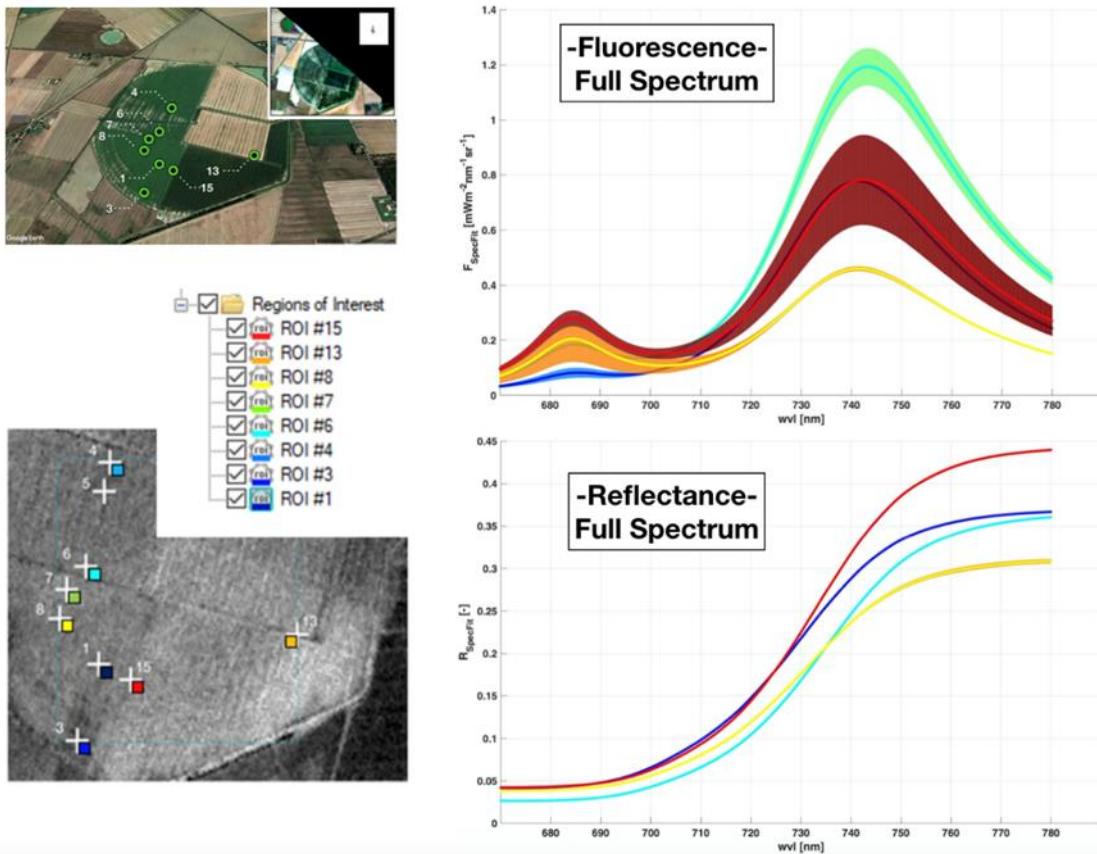


Figure 39: R and fluorescence spectra retrieved by the SpecFit algorithm from different points measured by the FloX: (top right) full fluorescence spectrum; (bottom right) R signature; (top / bottom left) location of FloX measurements on Google Earth and on the F_{760} image, respectively. The white crosses represent the FloX GPS coordinates, while the colored squares, the ROIs (2 x 2 pixels).

The *HyPlant* imagery was collected according to the so-called Sentinel-3 pattern which consists of four adjacent and partially overlapped images collected from a flight altitude of 3050 m above the ground surface. It results in a spatial pixel size of 4.5 m. The FloX measurements were located within the flight line L2 (Figure 40) collected at 11:40 local time (20180730-S3IT-1140-3050-L2-N). The line 20180730-S3IT-1159-3050-L2-N-FLUO collected a few minutes later (11:59 h local time) can be used. However, a cloud appeared close to the pivot area. The details of the two *HyPlant* maps are shown in Table 8. The far-red fluorescence maps (760 nm) retrieved by the iFLD and SFM algorithms are reported in Figure 41.

Table 8: *HyPlant* flight lines collected in Grosseto and matching the FloX measurements.

Flight line name	Local Time	Day	Spatial resolution
20180730-S3IT-1140-3050-L2	11:40	30 July	4.5 m
20180730-S3IT-1159-3050-L2	11:59	30 July	4.5 m

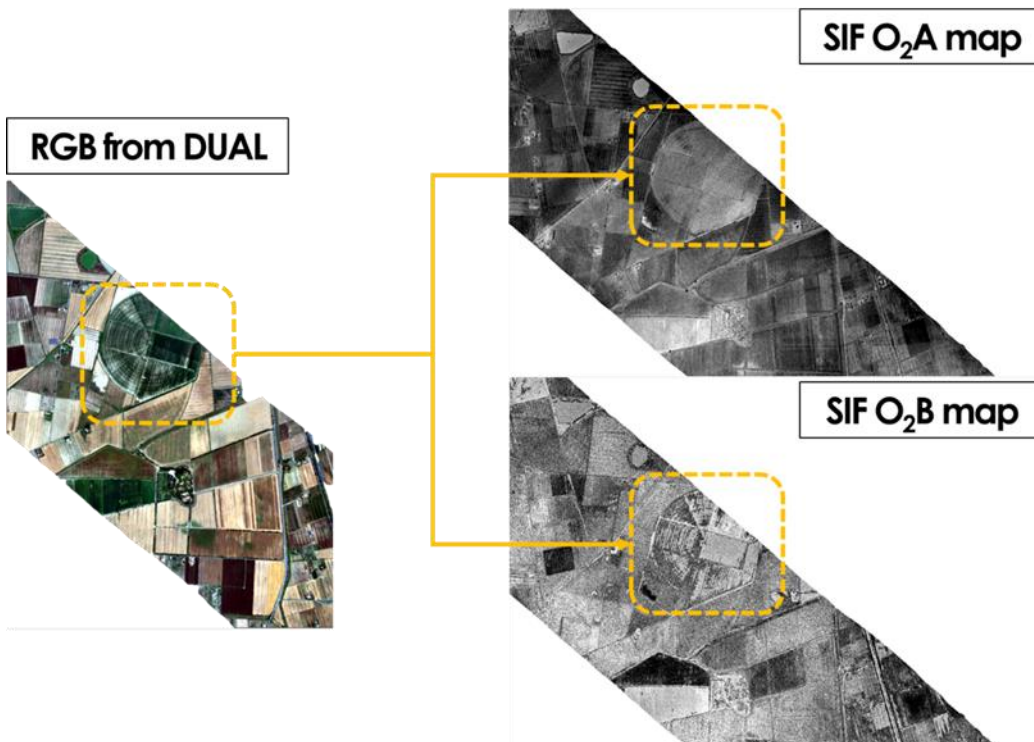


Figure 40: Overview of the pivot field from RGB DUAL (left) and F maps derived from the FLUO module of *HyPlant*.

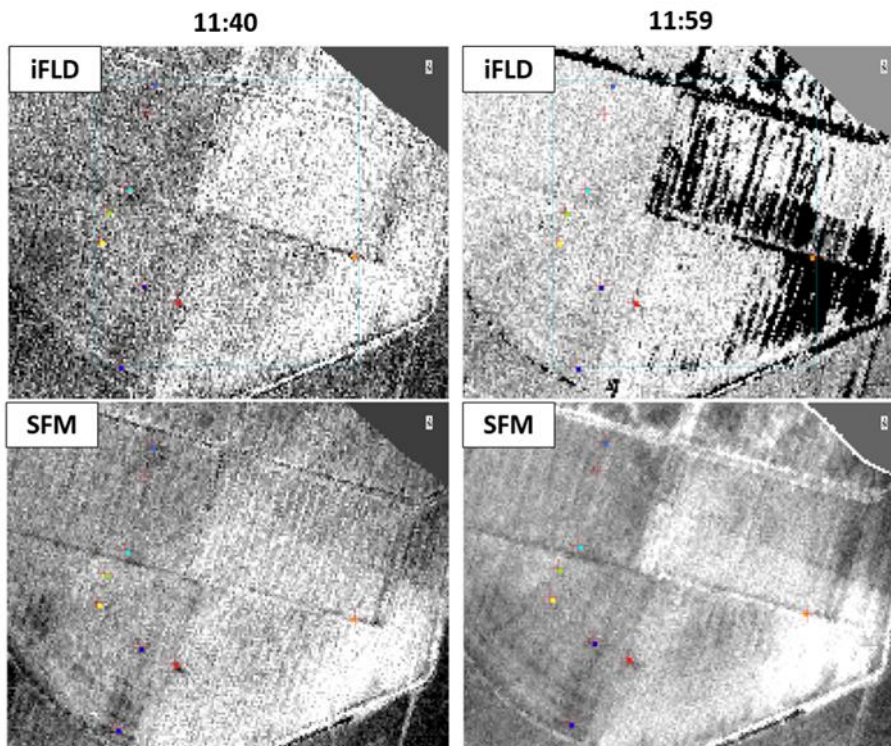


Figure 41: Far-red F maps (760 nm) produced by the iFLD (top) and SFM (bottom) retrieval algorithms from the two *HyPlant* images collected at 11:40 (left) and 11:59 (right) local time.

A quantitative analysis about the consistency of the fluorescence maps follows below. Specifically, the FloX values in both oxygen absorption bands were compared with the *HyPlant* fluorescence maps obtained by using iFLD and SFM retrieval methods. Figure 42 shows scatterplots between FloX and *HyPlant* F retrieved at

the O₂-A by the SFM approach for the two flight lines. The error bars for each point were computed in terms of the standard deviation between successive samples in the same area in case of the FloX measurements and the standard deviation of the ROIs values for the *HyPlant* F data. The ground and airborne measurements show a coefficient of determination of about $R^2 = 0.72$ and $R^2 = 0.62$, the slope of the linear model is close to 1:1 ($m = 0.86$ and $m = 1.03$), and the intercept is close to zero ($q = 0.13$; $q = 0.1$). The Root Mean Square Error (RMSE) is around 0.14 and 0.19 $\text{mW m}^{-2} \text{sr}^{-1} \text{nm}^{-1}$ for the imagery collected at 11:40 and 11:59, respectively. The slightly lower performance of the imagery acquired at 11:59 is probably related to the additional complication caused by unstable sky conditions. Indeed, a cloud suddenly appeared close to the pivot area. Even if the cloud (and its projected shadow) does not directly cover the pixels in the pivot area, a cloud can affect the overall atmosphere radiation transfer and the way that downwelling radiance (from sun, sky and cloud) interacts with the canopy. The amount of diffuse radiation and the direction by which it impinges the canopy can affect the overall amount of fluorescence emitted by the target.

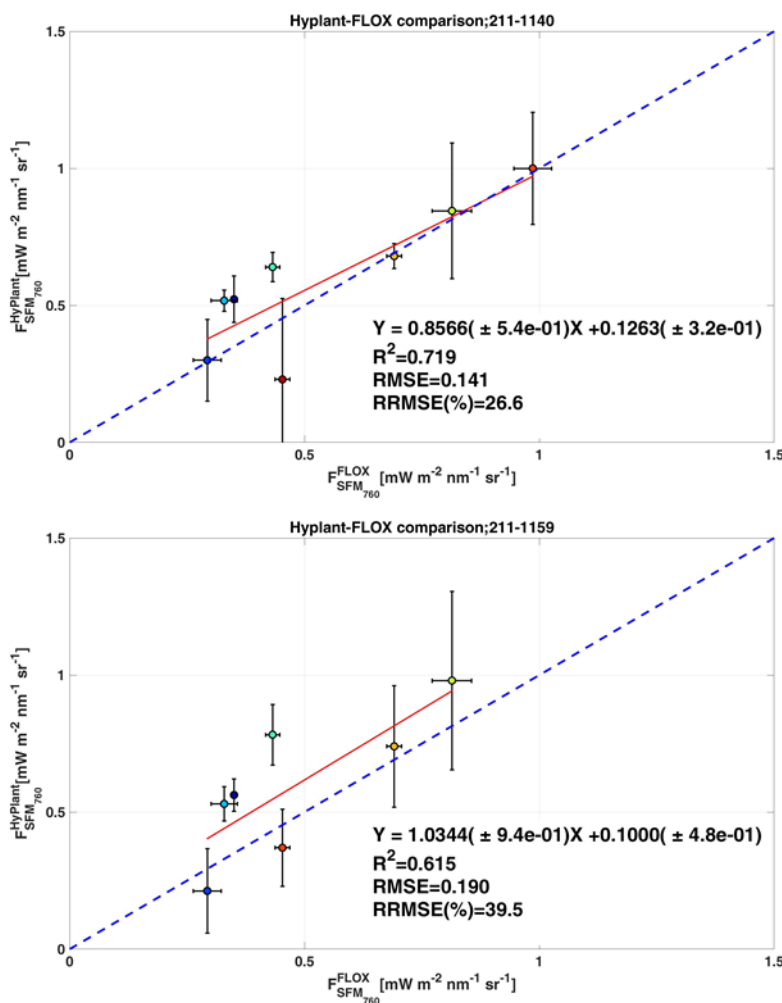


Figure 42: Comparison of fluorescence values at 760 nm from FloX and *HyPlant* using the SFM method and the two flight lines acquired on 30 July; (top) flight line at 11:40; (bottom) line at 11:59 local time.

The fluorescence retrieval at the O₂-B band is generally more critical because of the lower SNR ratio and the sharp spectral behavior of both reflectance and fluorescence. In the present analysis, it seems that the issue is even accentuated by the spatial heterogeneity of the investigated crop field. In fact, the scatterplots related to the red fluorescence (O₂-B) between ground and airborne observation results are largely affected (Figure 43), especially due to the large uncertainty (deviation) of the fluorescence values from the airborne fluorescence products. Other causal factors are the spatial heterogeneity of the field under investigation

(Figure 38) and the fact that parts of the field do not have a full canopy coverage. This entails a larger contribution from the background soil on the overall spectral signal. Therefore, slight mismatches between FloX sampling areas and ROIs selected within *HyPlant* imagery can produce additional noise. However, the values retrieved from *HyPlant* show a generalized overestimation.

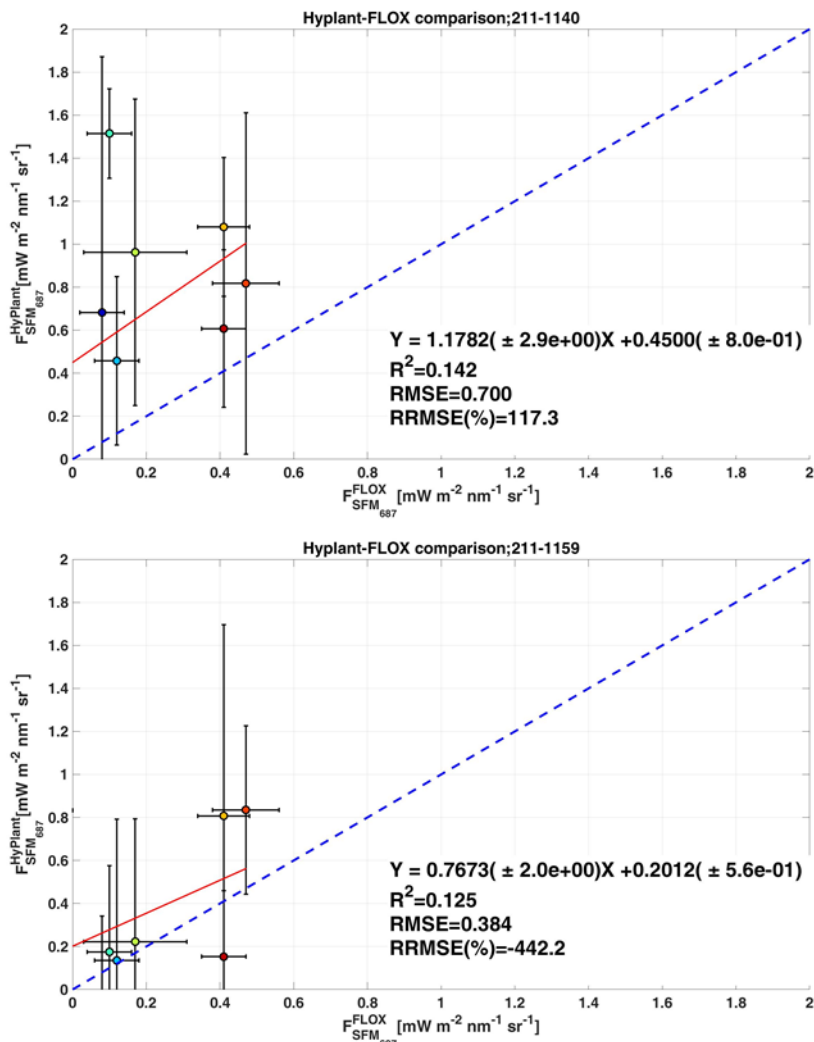


Figure 43: Comparison of F values at 687 nm from FloX and *HyPlant* using the SFM method and the two flight lines acquired on 30 July; (top) flight line at 11:40; (bottom) line at 11:59 local time.

It must be noted, however, that the results over these test sites seems slightly worse (considering the red fluorescence at O₂-B) compared with those reported for the German site. First, it must be considered that only imagery with a 4.5 m spatial resolution was collected on 30 July 2018. Therefore, the spatial match between airborne and ground measurements is more complex and can introduce some additional uncertainty. Second, the investigated canopy (i.e., corn) has a complex geometry in between electrophile and planophile leaf distribution. This plays a relevant role especially when the canopy cover is not full (and leaf distribution is mostly vertical), making the contribution from the background soil larger and introducing additional uncertainties in the analysis.

5.4 Comparison of airborne fluorescence products recorded from different flight altitudes

In order to analyze the influence of the data acquisition altitude on the estimated SIF using the different retrieval methods (iFLD, SFM and SVD), two data sets of the Selhausen site covering the same area were selected, which were recorded at close intervals on 2 August 2018 from two different altitudes. The first data set was acquired at 12:10 CEST from 3050 m agl (Figure 44, right), which resulted in a spatial resolution of 4.5 m. Half an hour later (12:40 CEST), the same area was recorded again with 1 m spatial resolution from 680 m agl (Figure 44, left). In addition, polygons were created that represent the three land cover classes: forest (Fo), fields with photosynthetically active radiation (Fg), and fields with bare soil or harvest residuals (So). The land cover map is illustrated in Figure 44 in the middle. From the three land cover types, it was expected that the classes Fo and Fg provide SIF values higher than zero. For the class So, SIF values around zero were assumed.

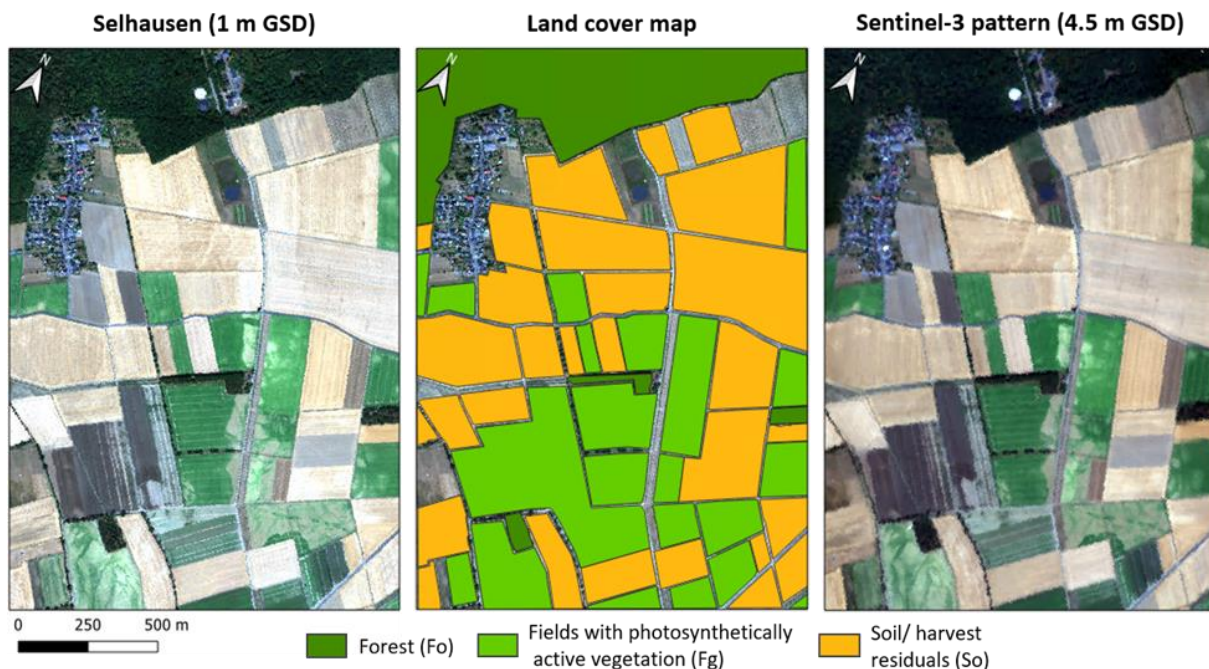


Figure 44: Subset of the Selhausen area recorded with *HyPlant* from 680 m agl at 12:40 local time (left) and from 3050 m agl at 12:10 local time (right). In the middle is an illustration of the land cover map consisting of the three classes.

Figure 45 illustrates the box plots derived from the three land cover classes with the three different retrieval methods for SIF derived from the O₂-A absorption feature. For the two vegetation classes Fo and Fg, the SFM provided the highest SIF values followed by the iFLD and the SVD. While the SIF values derived with the iFLD and SFM were positive and in a reasonable range for both acquisition altitudes, the box plots for the SVD showed median SIF values only slightly higher than zero and in the case of the class Fo the median was even negative. In comparison with the iFLD and SFM, higher SIF values were expected for the SVD method for the two vegetation classes because the SVD derives SIF at 740 nm, which is very close to the emission peak of far-red SIF. Additionally, the SVD results for both acquisition altitudes were characterized by a higher variance for all three classes. For the class So, the three retrieval methods led to SIF values very close to zero. This is realistic because bare soil and harvest residuals should not emit SIF. For both acquisition altitudes, the iFLD provides values only marginally deviating from zero. By contrast, the SFM and SVD were characterized by slightly negative values for the data recorded from 680 m agl and slightly positive values recorded from 3050 m agl. However, it must be further considered that the three methods rely on bare soils to retrieve SIF.

They show small positive/negative differences between low/high altitude flights without a clear systematic pattern. This is caused by few factors that play a different role to the result. First, low/high altitude flights correspond to different pixel sizes and a different contribution of shadow/sunlit parts of the canopy within the pixel which is not simply linear between the two images. Second, SIF retrieval based on soil reference could result corrupted for high altitude flights because bare soils pixels could result mixed with other land cover targets and slightly affecting the overall accuracy of the retrieval. This aspect need further detailed investigation in the future activities.

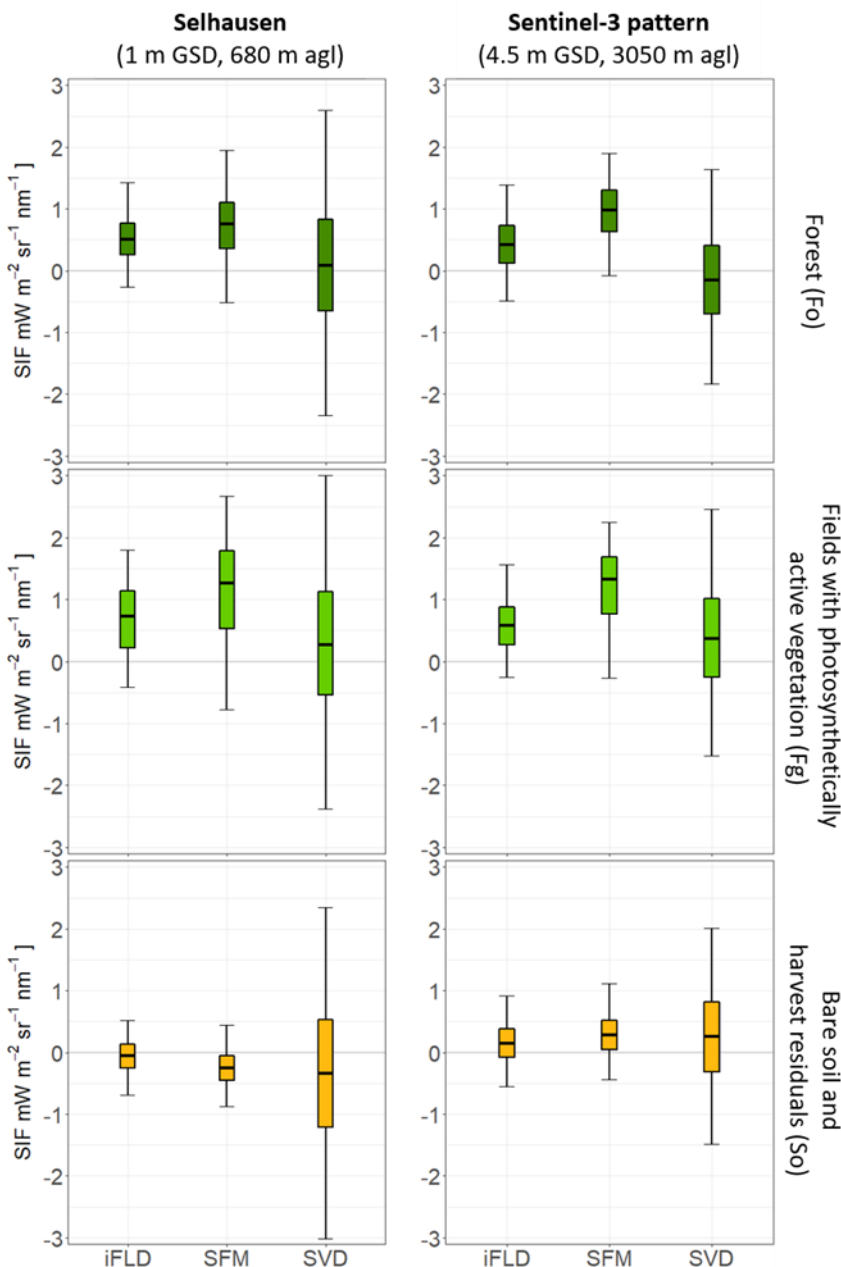


Figure 45: Box plots of the SIF maps derived at 760 nm (iFLD and SFM) and 740 nm (SVD) for the three land cover classes shown in Figure 44. The whiskers correspond to the 2nd and 98th quantile.

Figure 46 shows the box plots of red SIF derived for the three different classes and the two data acquisition altitudes. It is clearly visible that the variance of the SVD results is much higher in comparison with the iFLD and SFM results except for the class Fo in the *HyPlant* image recorded from the lower altitude. As expected, the calculated iFLD and SVD median values for the class for both data acquisition altitudes were close to zero.

By contrast, the determined median values for the SFM results were clearly higher with 0.5 and 1 $\text{mWm}^{-2}\text{nm}^{-1}\text{sr}^{-1}$ for the low and high-altitude data acquisition, respectively. For the class Fg, the results of all retrieval methods and both acquisition altitudes were very similar on average with mainly positive values around 1 $\text{mWm}^{-2}\text{nm}^{-1}\text{sr}^{-1}$. However, compared with the iFLD, the SFM and SVD retrievals led to much more negative SIF values. The class Fo was characterized by very low SIF with median values - around zero when derived with the iFLD and SVD retrieval from the low altitude data set. The SFM provided slightly higher SIF with values of about 0.7 $\text{mWm}^{-2}\text{nm}^{-1}\text{sr}^{-1}$ for the low and 1 $\text{mWm}^{-2}\text{nm}^{-1}\text{sr}^{-1}$ for high data acquisition altitude. While retrieved SIF using the iFLD for the class Fo is similar for both data sets, the SFM retrieval led to slightly and the SVD to distinctly higher SIF retrieved from the data set recorded from 3050 m agl. It seems, therefore, that the data acquisition altitude had an effect on the SIF retrieval based on the SFM and SVD for the Fo class. However, it must be noted that this effect is much more pronounced when using the SVD method.

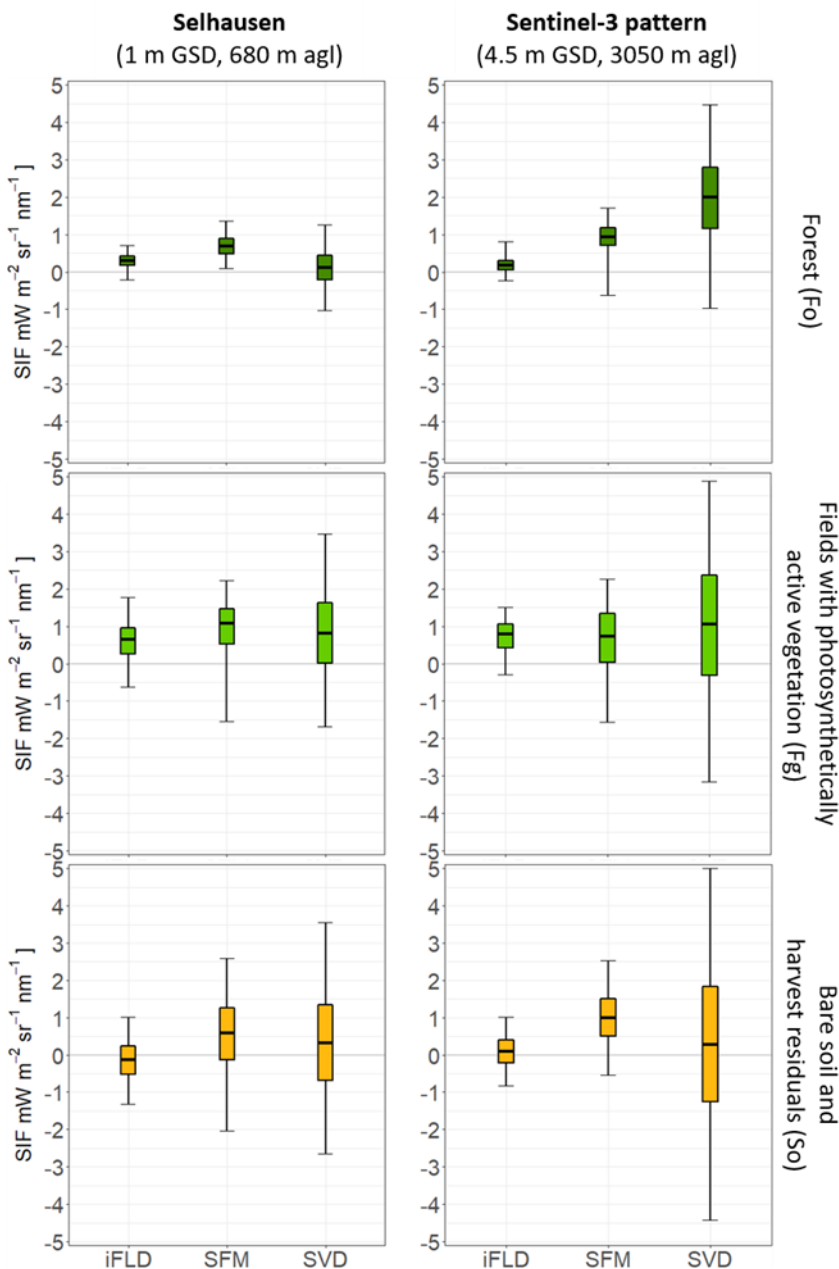


Figure 46: Box plots of the SIF maps derived at 687 nm (iFLD and SFM) and 690 nm (SVD) for the three land cover classes shown in Figure 44. The whiskers correspond to the 2nd and 98th quantile.

6 Defining operational quality flags and retrieval uncertainty for airborne SIF products

The goal of this section is to provide qualitative and quantitative information about the overall quality of *HyPlant* FLUO image data and the retrieved SIF map products. This information is intended to help end-users to better judge the quality of the *HyPlant* FLUO module at-sensor-radiance data (level-1c data) as well as the quality of the associated SIF maps (level-2c data). This section provides a first overview of the quality flags (section 6.1) that are currently being implemented within the processing pipeline of *HyPlant* FLUO image data as well as the concept for uncertainty estimates (section 6.1.6) for the *HyPlant* fluorescence products. In this section, we focus on the definition of the quality flags and retrieval uncertainty for the iFLD (Univ. of Zurich) and SFM (Univ. Milano-Bicocca) fluorescence retrieval algorithms, which are the most widely used algorithm for SIF retrieval for airborne imagery and which are linked to the nominal retrieval scheme for the FLEX satellite mission.

Quality flags for the level-1c data provide information about the meta-data of flight lines as well as data acquisition conditions, such as SZA, VZA, surface topography, cloud cover, the availability of non-fluorescence reference surfaces, and SNR. Some quality flags have a general meaning (SZA, VZA, SNR), while surface topography and non-fluorescence pixels are intended to be used in SIF retrievals (section 6.1).

The full error propagation for the SIF value retrieval uncertainty per pixel cannot be established within this activity. However, we provide an approach for estimating uncertainties either by calculating an error propagation along the SIF product development or by exploiting error matrices within the data products (sections 6.2 and 6.1.6).

6.1 Quality Flags

The quality flags were implemented as a stand-alone routine (Matlab programming) that can be executed independently from the SIF retrieval. Each quality flag is implemented as an individual function that is sequentially called from the main routine (QUALITY_FLAGS.m). The overall workflow of the entire processing chain including quality flags and uncertainty is reported in Figure 47.

The level-1c quality flags are stored within the data files produced by the *HyPlant* processing chain as pixel-level values stored within *HyPlant* product files in the form of additional quality layers (i.e., spectral bands in envi file format). The intent is to offer numeric values for quantitative and automated selection/filtering of the image data for downstream analysis. A data product quality report file (pdf file) is produced with each flight line that summarizes overall quality flags, uncertainties and image statistics.

The procedure is exemplified by two representative flight lines from the 2018 campaign activity. The lines represent a 'good' flight line, i.e. where according to our subjective evaluation measurement conditions were optimal, and a 'challenging' flight line, i.e. where unstable atmospheric conditions makes data processing complicated and where SIF products are expected to be associated with higher uncertainty. Level-1c quality labels as well as the data product quality report file will be included in the data processing pipeline of *HyPlant* imagery starting with the 2019 campaign data.

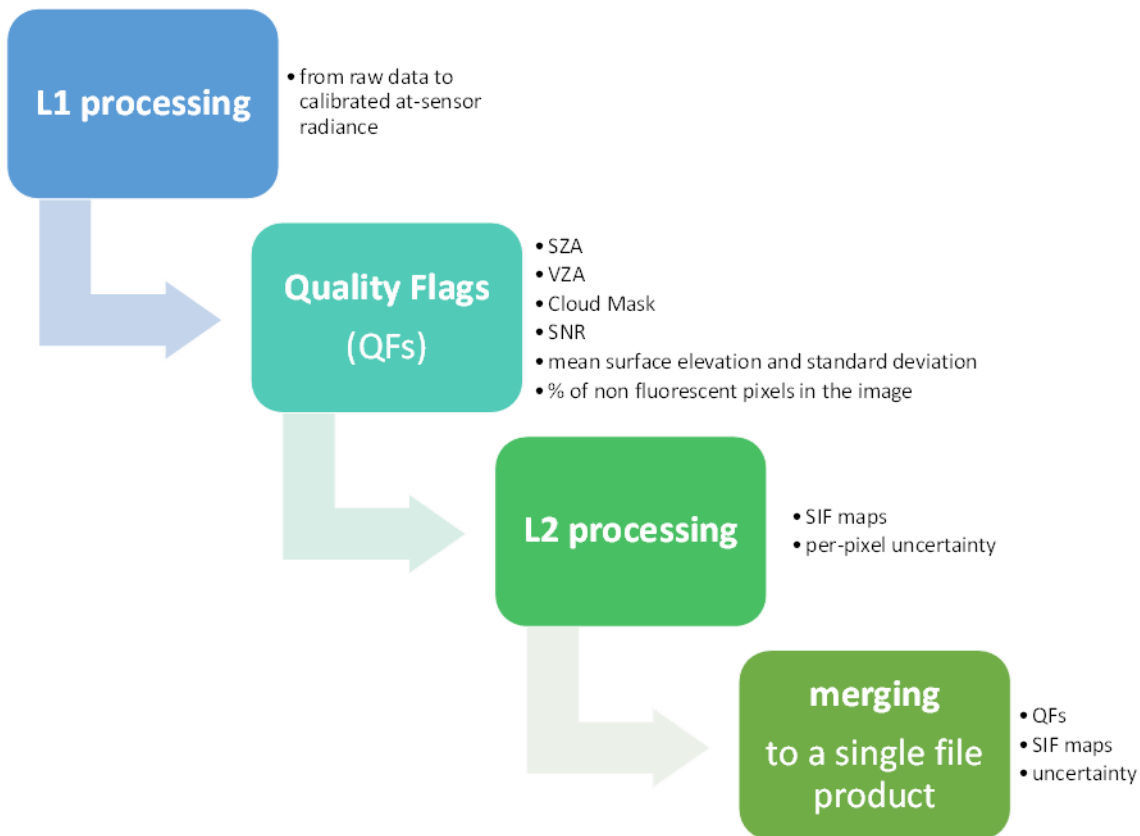


Figure 47: *HyPlant* processing steps including quality flags, uncertainty, and a final reformatting of the output SIF map product.

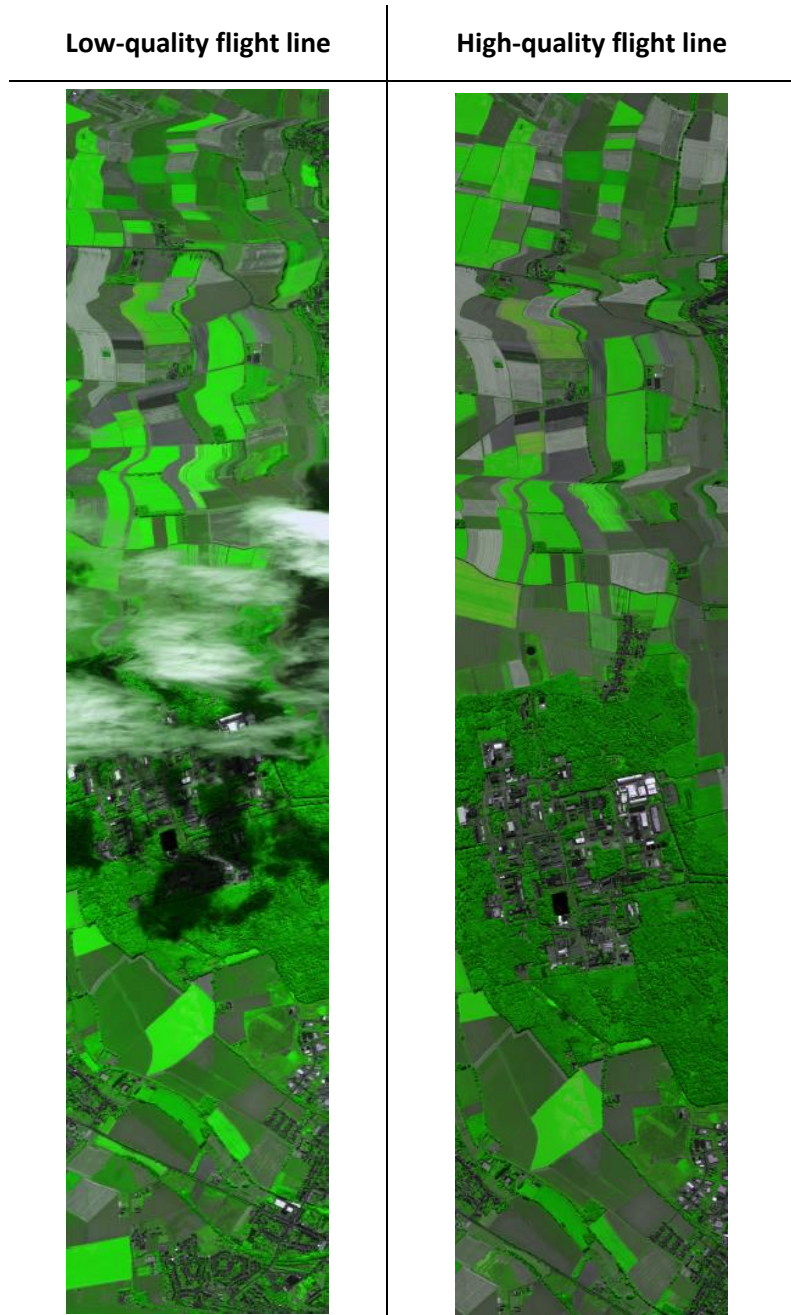
In the following sections, the proposed quality flags are described in detail and accompanied with examples derived from two flight lines covering the same area recorded under different acquisition conditions.

Data set A – low-quality flight line

The first flight line was recorded on 28 June 2018 at 12.17 h local time from 3050 m agl, which led to a spatial resolution of 4.5 m. It covers an agricultural area close to the city of Jülich as well as parts of the research center Jülich. This data set belongs to the “S3 pattern” flight lines and was recorded under non-ideal conditions (partly covered with clouds). In the further course, this data set is referred to as “low-quality flight line”.

Data set B – high quality flight line

The second data set was recorded on 2 July at 12.23 h local time from the same altitude. It covers almost the same area and is also part of the “S3 pattern” flight lines. The data set was recorded under ideal conditions and is therefore referred to as “high quality flight line” below (Figure 48).



Name	20180628-S3GER-1217-3050-L2-N-FLUO	20180702-S3GER-1223-3050-L2-N-FLUO
Acquisition date	20180628	20180702
Acquisition time	1217	1223
Study site	S3GER	S3GER
Flight direction	N	N
Ground sampling distance [m]	4.5	4.5

Figure 48: Non-georectified false color composites showing the at-sensor radiance of the low (left) and high-quality (right) flight line with associated meta information.

6.1.1 Solar Zenith Angle (SZA)

SZA provides information about the overall downwelling irradiance level under clear sky conditions (it is one of the main drivers of SIF intensity), surface BRDF, and shadows. Lower SZA values correspond to higher irradiance and generally have limited BRDF effects (even if it depends on surface characteristics). A single value is used for the entire image. The SZA is computed by using latitude/longitude and GPS time stored within the header file of each *HyPlant* FLUO at-sensor radiance (level-1 product) image. Available standard routines are used to compute SZA.

An indication of the overall quality of the imagery in relation to SZA is given in Table 9 as a guide for non-experienced users (**optimal** = good data quality; **suboptimal** = medium data quality: data shall be used with attention; **non-optimal** = poor data quality: data can't be used).

Table 9: Values assumed by the SZA quality flag.

SZA (deg)	QUALITY
0-50	optimal
51-70	suboptimal
71-90	non-optimal
Output data format	
SIF map product file	
<ul style="list-style-type: none"> SZA[deg] = solar zenith angle in degrees (single value for the entire image) 	
Summary pdf file	
SZA value	

6.1.2 View Zenith Angle (VZA)

The VZA provides information about surface BRDF. Typically, off-nadir pixels can be more affected by surface anisotropy. The VZA maps is not available from the L1 processor (Caligeo, Specim) and therefore a simple script was developed to calculate it. In a first instance, VZA is derived from the GPS/IMU navigation file available for each image. The roll angle for every single image line is used to calculate VZA on pixel basis. Figure 49 illustrates the VZA maps of the two example flight lines. At this stage, surface topography is not considered because the SIF retrieval algorithm is limited to process imagery of flat areas only, though it will be introduced in future developments. An indication of the overall quality of the imagery in relation to VZA is given in Table 10 as a guide for non-experienced users (**optimal** = good data quality; **suboptimal** = data can be used with attention).

Table 10: Values assumed by the VZA quality flag.

VZA (deg)	QUALITY
0-10	optimal
10-20	suboptimal
Output data format	
SIF map product	
<ul style="list-style-type: none"> VZA [deg] = view zenith angle in degrees (image) 	
Summary pdf file	
Max VZA value	

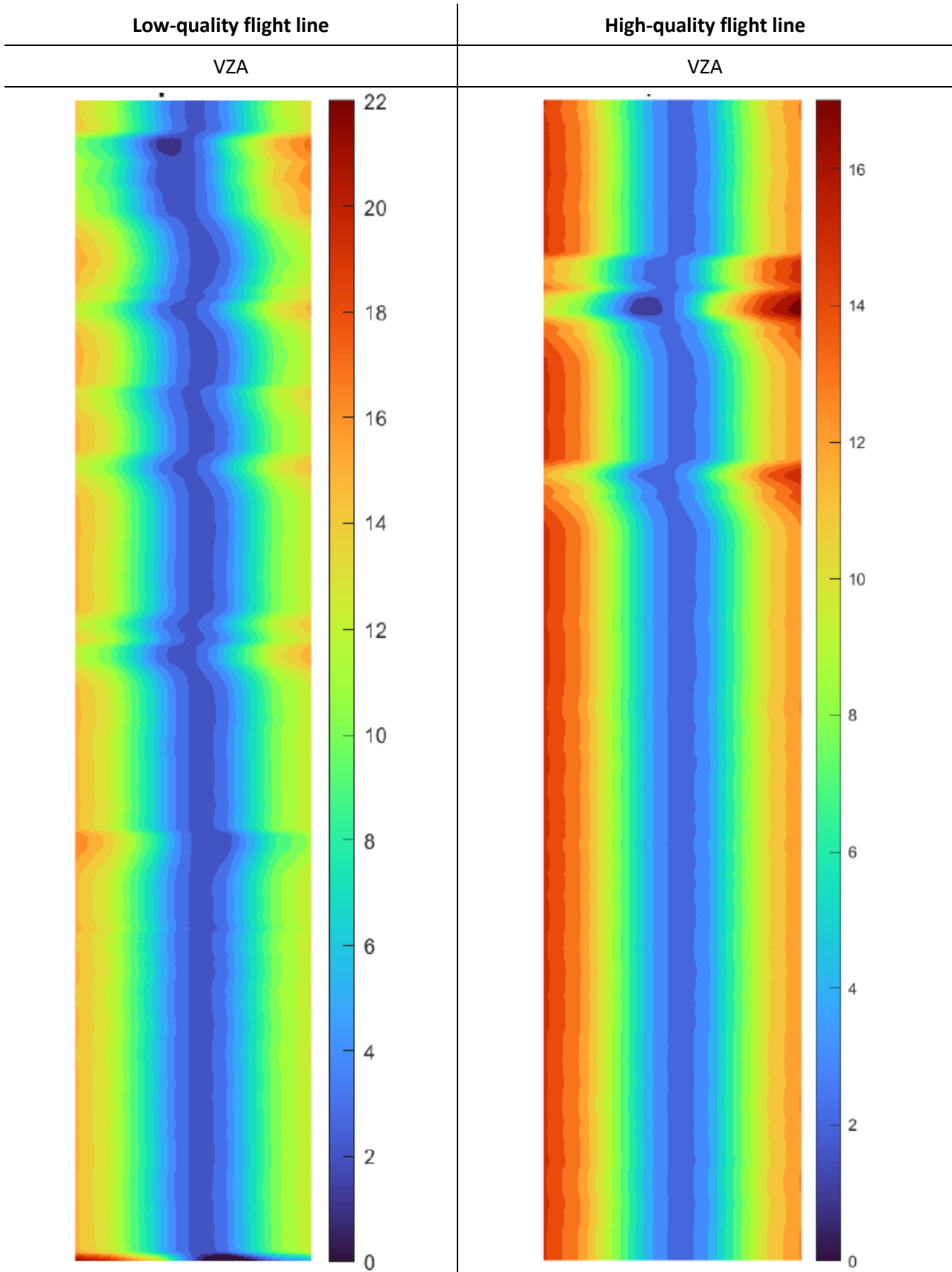


Figure 49: Non-georectified VZA map of the low (left) and high-quality (right) flight line.

6.1.3 Surface elevation

Topographic effects (elevation/slope/aspect) are not considered/corrected within the current iFLD and SFM retrieval algorithms. Hence, SIF maps calculated on rugged terrains or even areas with subtle elevation changes can be affected by errors. Further developments of the SIF retrieval should aim at including topography, but for the moment we defined only a quality flag. This flag is defined as the standard deviation value of the image pixel elevations. Larger standard deviation values indicate varying topography and therefore the expected quality of SIF retrievals is poor.

In practice, the global digital elevation model product from the ASTER available at a spatial resolution of 1 arc second (approximately 30 m horizontal posting at the equator) is used (<https://doi.org/10.5067/ASTER/ASTGTM.003>). The implemented routine enables the automatic download of tiles (<https://lpdaac.earthdata.nasa.gov>) corresponding to the *HyPlant* image and the extraction of values from the area covered by *HyPlant* (Figure 50). The mode and standard deviation values are calculated and stored in the quality flag outputs. This ASTER-DEM is a DEM, which in the strict sense can be considered to be a DSM, since it is calculated from optical stereo images and thus also shows the outer surface of e.g. dense forests (see e.g. the forest surrounding the Forschungszentrum Jülich in our example). This DSM is considered ideal for our analysis as it is related to the surface of the vegetation layer (see <https://doi.org/10.5194/isprs-archives-XLI-B4-143-2016> for more details of this product).

A qualitative indication about the overall quality of the imagery in relation to topography QF is given in Table 11 as a guide for non-experienced users (**optimal** = good data quality; **suboptimal** = medium data quality: data shall be used with caution).

Table 11: Values assumed by the surface elevation quality flag.

Value	QUALITY
> 15 m	suboptimal (rugged terrain)
< 15 m	optimal (flat terrain)
Output data format	
SIF map product	
<ul style="list-style-type: none"> • SURF_ELEVATION_MODE = mode of the elevation values (single value for the entire image) • SURF_ELEVATION_STD layer = standard deviation of the elevation values (single value for the entire image) 	
Summary pdf file	
Mode and standard deviation value	

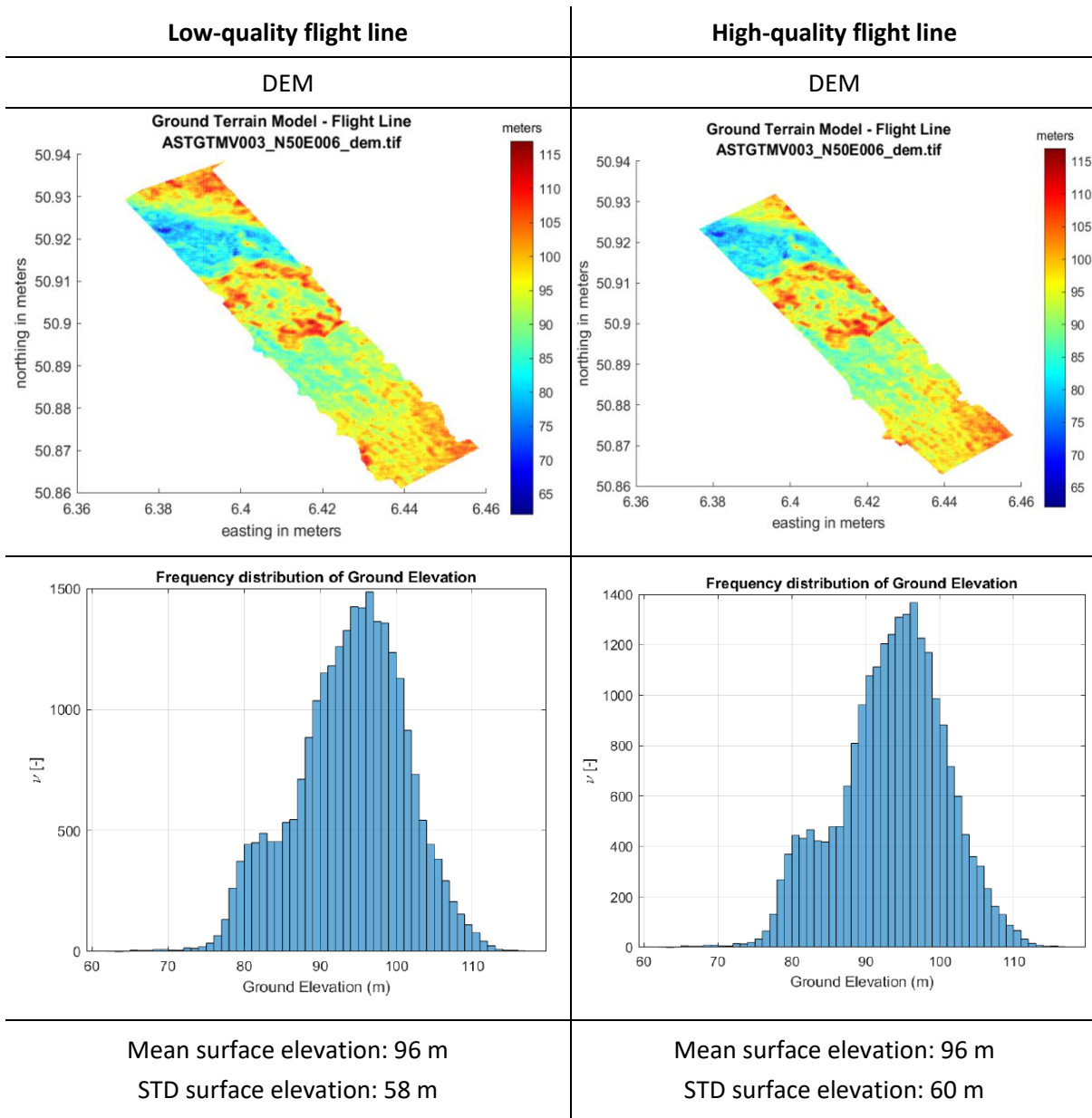


Figure 50: Georectified ASTER-DEM (top), histograms of the height distribution (middle) as well as mean and standard deviation of the surface elevation (bottom) of the area covered by the low-quality (left) and high-quality (right) flight line.

6.1.4 Cloud Mask

Clouds represent one of the most problematic disturbing effects in the SIF retrieval because they severely affect resulting SIF map quality in multiple ways: i) a direct effect occurs in the “atmospheric correction” algorithm when clouds are identified and confused with bare soil; ii) an indirect effect caused by complex radiative effect from clouds that affects the irradiance of surrounding areas.

A new and specifically dedicated algorithm has been prototyped and implemented within the *HyPlant* processor. A binary mask [0, 1] delimitating the area covered by clouds is obtained. The algorithm was newly developed and tested since there are no algorithms available that can be adapted to the spectral configuration of the *HyPlant* FLUO sensor. The complexity arises because the FLUO instrument covers a limited spectral range (650 nm - 800 nm) and some of the key wavelengths typically used in operational satellite cloud mask processors (i.e., cirrus band) are not available. This limitation could be overcome by using *HyPlant* DUAL data in cloud-mask processing. However, this would require substantial re-projections of FLUO and DUAL data because of the two image geometries.

Therefore, a new algorithm was developed that uses the high-resolution observations of the O₂-A band in the FLUO data. The algorithm is mainly inspired by the cloud mask and cloud fraction algorithm fast retrieval scheme for clouds from the oxygen A band (FRESCO and FRESCO+) widely used for atmospheric chemistry satellites (Desmons et al. 2019, Wang et al. 2008). Since FRESCO was designed for satellite data to derive the cloud fraction, it cannot directly be used for high-resolution airborne imagery. For this reason, it was adapted to detect clouds from *HyPlant* FLUO image data.

In practice, the algorithm relies on the analysis of the O₂-A band (i.e., band depth) to gain information about the radiation pathlength (i.e., sun-target-sensor distance or objects height). The O₂-A band depth of cloudy pixels is lower because of the shorter sun-cloud-sensor path length, while the band depth of a lower elevated surface is higher because the optical path is longer. An explanatory description of the algorithm is shown in Figure 51. Potentially, it would be interesting to look at the detection of cloud shadows in the future, since they strongly affect the fluorescence emission. The approach at the O₂ band would be preferred since shadows have exactly opposite behavior than clouds (i.e. deeper band depth). But alternatives approach might be exploit information from other wavelengths to complement the O₂-A i.e., spectral indices not sensitive to shadows.

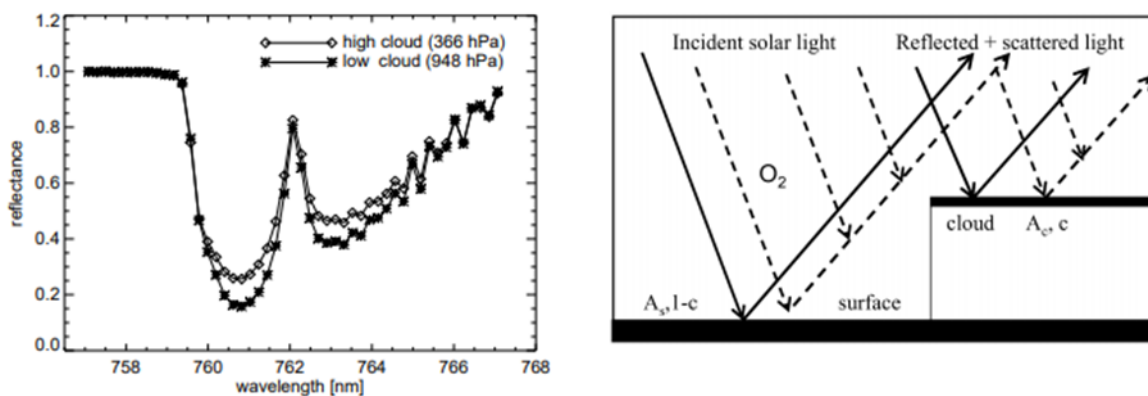


Figure 51: Typical cloud spectra of the O₂-A band measured by GOME. The spectra are normalized at 758 nm to show the relative depth of the band for clouds at different heights (credits: Wang et al. 2008).

In practice, the algorithm was implemented as follows:

- O₂-A band depth is calculated from *HyPlant* FLUO at-sensor radiance;
- K-means unsupervised classification is applied to identify the two classes - clouds and surfaces not covered by clouds

The determined cloud masks for the low-quality and high-quality flight lines are shown in Figure 52.

Table 12: Values assumed by the cloud mask quality flag.

Value	QUALITY
0	cloudy
1	clear
Output data format	
SIF map product	
<ul style="list-style-type: none"> • CLOUD_MASK = binary mask with float values [0, 1] (image) 	
Summary pdf file	
Cloud cover %	

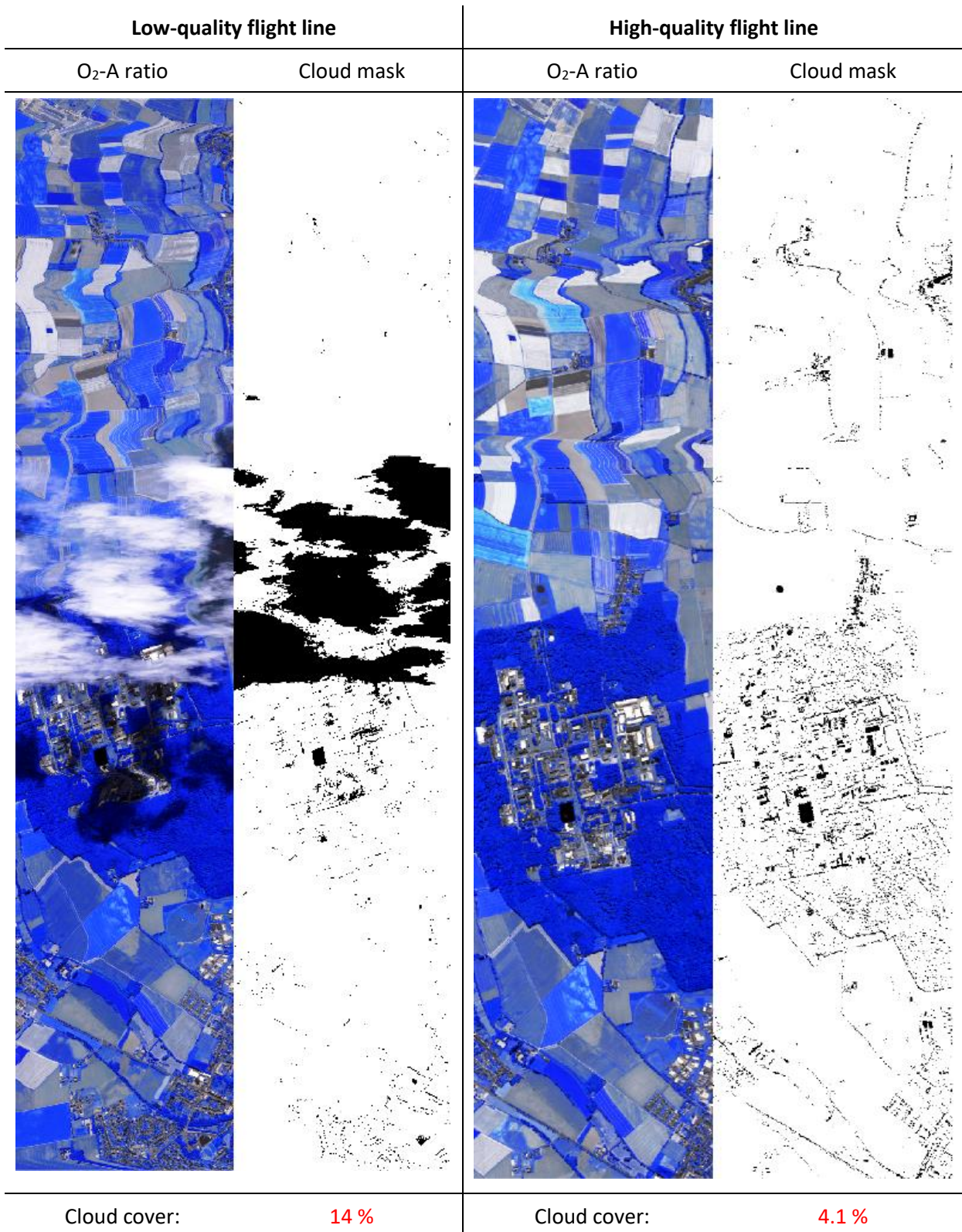


Figure 52: Non-georectified O₂-A ratio and cloud mask map of the low-quality (left) and high-quality (right) flight line with associated information on average cloud cover.

6.1.5 Non-fluorescence reference surface

The IFLD and SFM methods mainly rely on non-fluorescence pixels to constrain the atmospheric correction at the O₂ bands. The existence of non-fluorescence pixels (e.g., bare soil) within the flight line affects the

overall possibility and accuracy of the SIF retrievals. This quality flag reports the overall amount of non-fluorescent pixels (%) at nadir (± 30 pixels) that are used in the SIF retrieval.

Table 13: Values assumed by the non-fluorescence reference surface quality flag.

Value	QUALITY
< 1%	doubtful SIF retrieval
> 1%	meaningful SIF retrieval
Output data format	
SIF map product	
<ul style="list-style-type: none"> • %_NON_FLUO_PIXELS = % of non-fluorescent pixels at nadir (single value for the entire image) 	
Summary pdf file	
Total % of non-fluorescence pixels	

6.1.6 Signal to Noise Ratio (SNR)

The actual at-sensor radiance SNR affects the overall quality of the maps produced by the SIF retrieval algorithm. The SNR is evaluated by means of algorithms based on the analysis of the signal distribution over “homogeneous areas”, considering the intrinsic spatial variability of natural surfaces and the spectral-spatial correlation between adjacent pixels. In particular, the method relies on multiple linear regression (MLR) in which inter-band (spectral) and intra-band (spatial) correlations are exploited to decorrelate the image data. The homogeneous regions division and spectral de-correlation (HRSDSC) method (Fu et al. 2014) was used. The methodology includes a preliminary image segmentation for homogeneous areas (based on a NDVI map); a kernel of limited size is considered around the barycenter of each segmented area. The MLR coefficients (representing spectral-spatial correlation of the adjacent pixels within the kernel) are estimated for each individual area and residuals are used to obtain the noise variance. Afterwards, the SNR for the individual segment and for each waveband of the FLUO spectrometer is determined. This vicarious approach has also been used for analyzing PRISMA (ASI) data. The spectral SNR values obtained were close to the pre-launch characterization measurements performed by Leonardo Aerospace s.p.a. Further analysis of relatively large ROIs on pseudo invariant calibration sites (PICS) also proved the reliability of this algorithm.

Examples of SNR maps are depicted in Figure 53 and Figure 54. The SNR value for each individual segmented area (e.g., crop field) was computed for the pixels around the barycenter and the values used for all the pixels that belong to this segment. Light gray colors indicate higher SNR values while darker gray regions represent lower SNR values.

The SNR values estimated for the different segments highlight the differences between fields. This is normal and expected since the actual SNR is still partially related to the overall signal intensity reaching the sensor (i.e., target’s brightness). The SNR processing is available and integrated in the *HyPlant* “operational” processor. The spectral SNR for each segmented area is computed for all wavelengths, while SNR values at 680 nm, 687 nm, 750 nm, and 760 nm are stored as image maps within the SFM SIF product maps (representatives of the O₂-A and O₂-B bands).

A qualitative indication about the overall quality of the imagery in relation to SNR is given in Table 14 as a guide for non-experienced users (**optimal** = good data quality; **suboptimal** = medium data quality: data shall be used with caution; **non-optimal** = poor data quality: data can’t be used).

Table 14: Values assumed by the SNR quality flag.

SNR	QUALITY
100-300	optimal
50-100	suboptimal
20-50	non-optimal
Output data format	
SIF map product	
<ul style="list-style-type: none"> • SNR680 = signal-to-noise ratio at 680 nm (image) • SNR687 = signal-to-noise ratio at 687 nm (image) • SNR750 = signal-to-noise ratio at 750 nm (image) • SNR760 = signal-to-noise ratio at 760 nm (image) 	
Summary pdf file	
SNR mean value and peak SNR (90-98 percentiles) wavelengths 680, 687, 750, 760 nm	

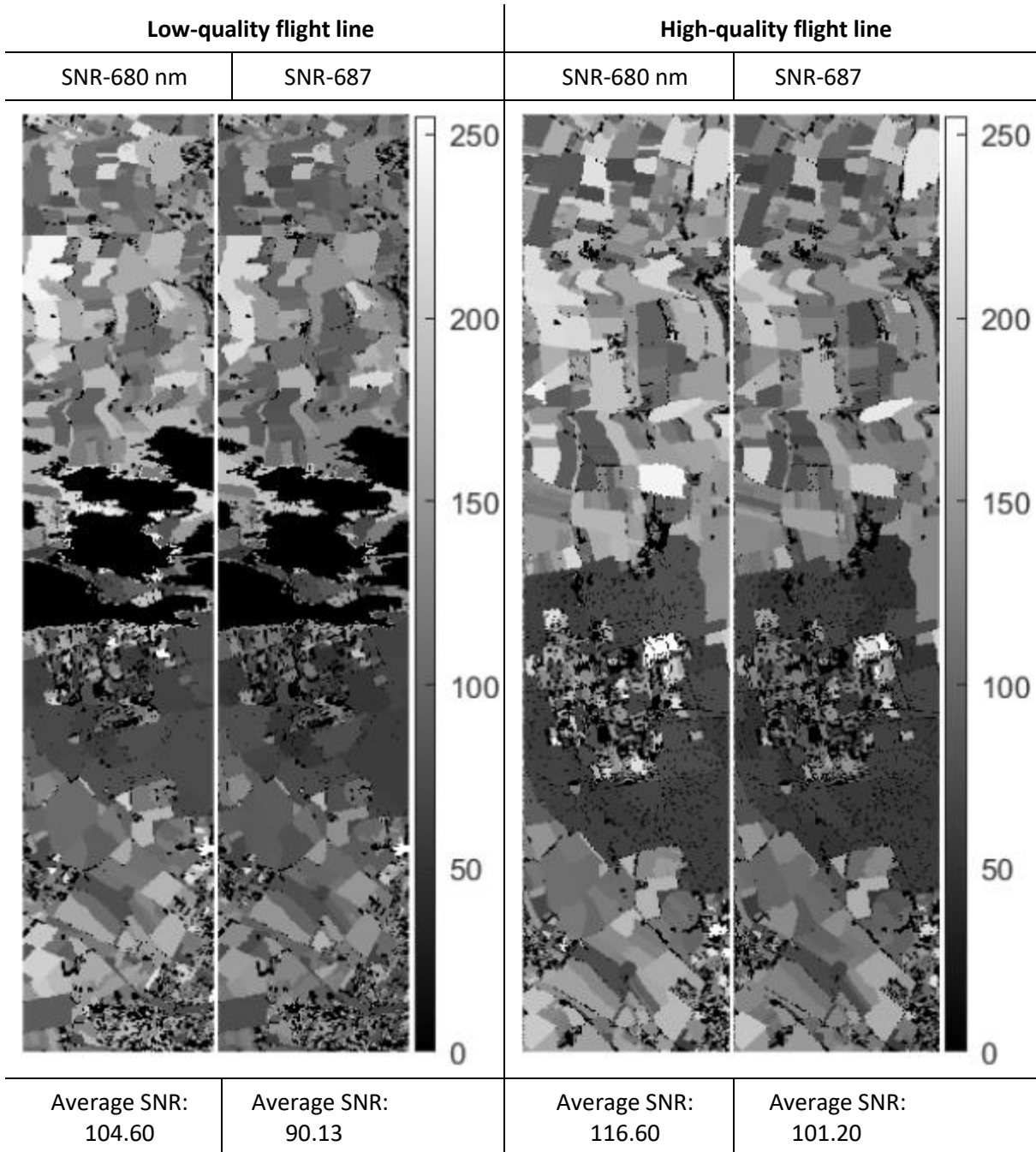


Figure 53: Non-georectified SNR maps at 680 nm and 687 nm of the low-quality (left) and high-quality (right) flight line with associated information on average SNR for each map.

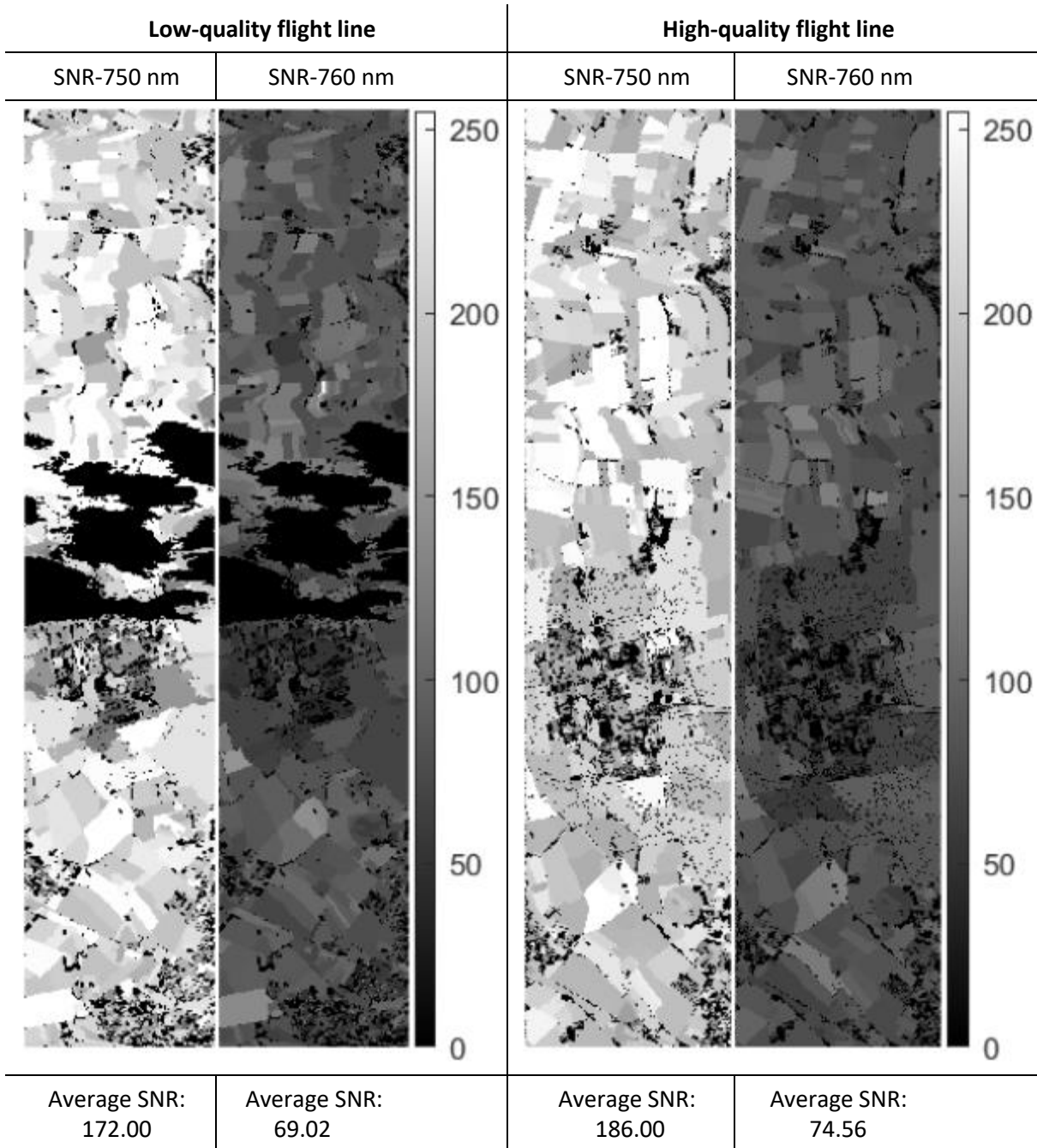


Figure 54: Non-georectified SNR maps at 750 and 760 nm of the low-quality (left) and high-quality (right) flight line with associated information on average SNR for each map.

Figure 55 shows the spectral SNR retrieved from *HyPlant* for the test images: i) the gray lines represent the overall variability for each individual segmented area, and the different magnitude mostly depends on the target brightness; ii) the red line represents the average SNR over the entire image; iii) the blue and cyan lines are the 90th and 98th percentile, respectively, which represents the instrument peak SNR over the entire scene (i.e., considering actual SNR and surface reflectance). As expected, a clear spectral pattern with lower values at the absorption bands can be observed.

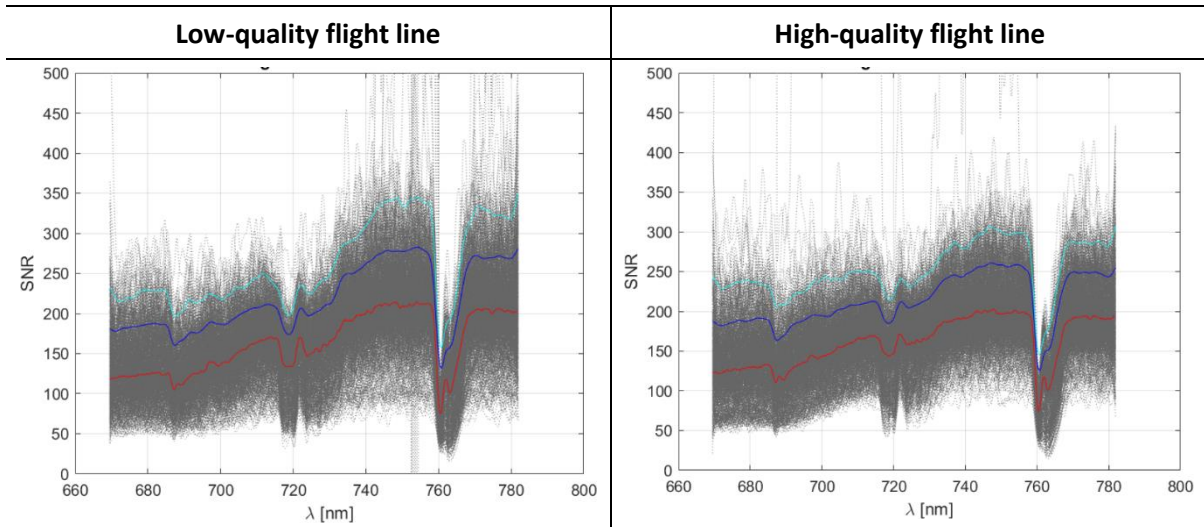


Figure 55: Determined SNR of the low-quality (left) and high-quality (right) flight line. The grey lines represent the SNR values calculated for the classified segments (homogeneous areas) while the red, blue and cyan lines represent the averaged, 90th percentile and 98th percentile SNR per wavelength. The slightly higher percentiles values observed for the low-quality flight line are likely related to the very bright clouds.

6.2 Per-pixel SIF retrieval uncertainty

A complete evaluation of the per-pixel uncertainty in SIF maps is highly complex and would involve complete error budgeting and propagation along the entire processing chain, starting with the characterization of uncertainty from the laboratory calibration, data pre-processing, level-1 products generation and finally the retrieval of level-2 products. Especially, the propagation of errors is a complex task that requires to quantitatively identify all sources of uncertainty.

A treatment of important sources contributing to the overall uncertainty of an airborne observation σ_{ref_meas} is presented in Białek et al. (2020) and includes at least the uncertainties caused by instrumental effects (σ_{ins}), their calibration and processing (σ_{cal}), and the subsequent retrieval of data products (σ_{prod}). When uncertainty contributions are expressed through variances, one can assume that the three errors add linearly and can be expressed as

$$\sigma_{ref_meas}^2 = \sigma_{ins}^2 + \sigma_{cal}^2 + \sigma_{prod}^2 + \sigma_{rep}^2 \quad \text{eq. 4}$$

For the airborne SIF products of *HyPlant*, we can provide a few considerations of which sources should be considered for a forward pixel-based uncertainty estimate:

- Uncertainties due to the instrumental effects of *HyPlant*, such as radiometric non-uniformities or non-linear sensor characteristics, were characterized and described in detail in the HYPER project ([RD-13]). Based on this evaluation, several parts of the *HyPlant* sensor were redesigned and since 2016 the *HyPlant* sensor has operated in a stable optical configuration, which is checked and characterized annually in the calibration facility of Specim (Oulu, Finland) (see Siegmann et al. 2019 for a detailed description of the optical performance of the *HyPlant* sensor as has been used since 2016). For the high-resolution FLUO module, special care is taken to characterize the spectral sensitivity of individual detector elements and their corresponding spatial and spectral PSF. This characterization of the PSF is crucial for the error of the final SIF products. The quantitative evaluation of the PSF, the possibility for deconvolution and the associated error are summarized in a scientific publication (Scharr et al. submitted, see also attachment).

	Doc.: Final Report		
	Date: 29 July 2021	Issue: 2	Revision: 1
	Ref.: ESA Contract No. 4000125402/18/NL/NA		Page: 95 / 288

- Uncertainties caused by L1 data processing occur, while digital signals are converted to radiances using the annual calibration coefficients provided by the manufacturer. We have tracked the laboratory calibration coefficients and parameters for the past years and for *HyPlant*, it was shown that in-flight parameters were very similar to laboratory parameters and no severe deviations were detected thus far. Additionally, we did not see any signs of degradation of the system. Since its last major upgrade, which take place in early 2016, the system has been stable and we thus assume a constant contribution from this uncertainty source. Some uncertainties were addressed in the section above; quantitative data from the operational level-1c quality flags may be used for an uncertainty estimate of *HyPlant* imagery.
- Uncertainties caused by the fluorescence retrievals are either related to uncertainties to disentangle reflected radiance from SIF emissions or by the reliability of the atmospheric compensation, which is particularly crucial for retrievals based on atmospheric absorption bands (i.e. oxygen absorption lines). SIF retrieval approaches differ in their strategies to separate surface reflectance and fluorescence and range from simple estimates based on neighboring wavelengths to complex physical modeling. See Cendrero-Mateo et al. 2019; Mohammed et al. (2019) for comprehensive review on this topic. Atmospheric correction is pivotal for SIF retrievals but requires exact knowledge of the atmospheric state, which is often not measurable and must be estimated from the data itself or auxiliary observations. Such uncertainty estimates are then used to parameterize atmospheric RT models to derive atmospheric transfer functions for SIF retrievals (see Chang et al. (2020) for a recent comparison of different SIF retrieval strategies and how they can compensate for varying atmospheric and illumination conditions).

For estimating uncertainties in *HyPlant* SIF products, we can make some analogies with uncertainty estimates that were made for individual point measurements (Buman et al, submitted). However, a complete error propagation for *HyPlant* SIF products is not feasible within this study and would require a quantitative error estimate that is highly dependent on the actual retrieval scheme and the way how atmospheric parameters (derived either from measurements or model runs) are handled. Thus, for this activity, we focused on the quantification of the overall pixelwise uncertainty of SIF retrievals to reflect the combined error of the individual components discussed above. We conceded the two most important retrieval methods currently used for airborne imagery, namely the iFLD (section 6.2.1) and the SFM (section 6.2.2). Both currently use either atmospheric measurements or estimates of the atmospheric state for an a-priori RT modelling, while the parameterization of atmospheric parameters is constrained by incorporating non-vegetated pixels. Results may serve as good bases for a more detailed error propagation.

6.2.1 iFLD

The iFLD-based SIF retrieval as implemented for *HyPlant* incorporates an empirical correction factor derived from non-fluorescent reference surfaces. This strategy enables the compensation of uncertain knowledge of the atmospheric state in the process of the atmospheric RT modeling and the remaining sensor effects after their compensation (e.g. spectral shift) (see Damm et al. 2014). In general, atmospheric transfer functions (i.e. transmittance, path radiance, spherical albedo) are calculated using a best guess of atmospheric parameters. Afterwards, the upwelling transmittance in the O₂-A and O₂-B bands is empirically corrected (factor k) to achieve zero SIF over reference surfaces. The retrieval of k is based on an iterative process minimizing SIF for reference surfaces by changing k in the RT scheme. k factors obtained for reference surfaces are then extra/interpolated per scan line to retrieve SIF over vegetation surfaces, considering a brightness dependency of k (i.e. exponential increasing k with decreasing brightness). This extra/interpolation causes uncertainties that can be estimated by evaluating resulting SIF over used reference surfaces. Figure 56 visualizes retrieved uncertainties, represented as estimated SIF over surfaces (expecting zero SIF). Uncertainties are considered as baseline uncertainty, which may be valid for vegetated surfaces as well. It is possible that brightness dependencies or structural effects can reduce or increase SIF retrieval uncertainties for vegetation. The resulting uncertainty maps allows the calculation of general

descriptive statistics such as mean uncertainty, standard deviation, etc. In the example below, mean SIF uncertainty is $0.016 \text{ mW m}^{-2} \text{ nm}^{-1} \text{ sr}^{-1}$ with a standard deviation of $0.24 \text{ mW m}^{-2} \text{ nm}^{-1} \text{ sr}^{-1}$ corresponding to a relative uncertainty of $0.8\% \pm 12\%$.

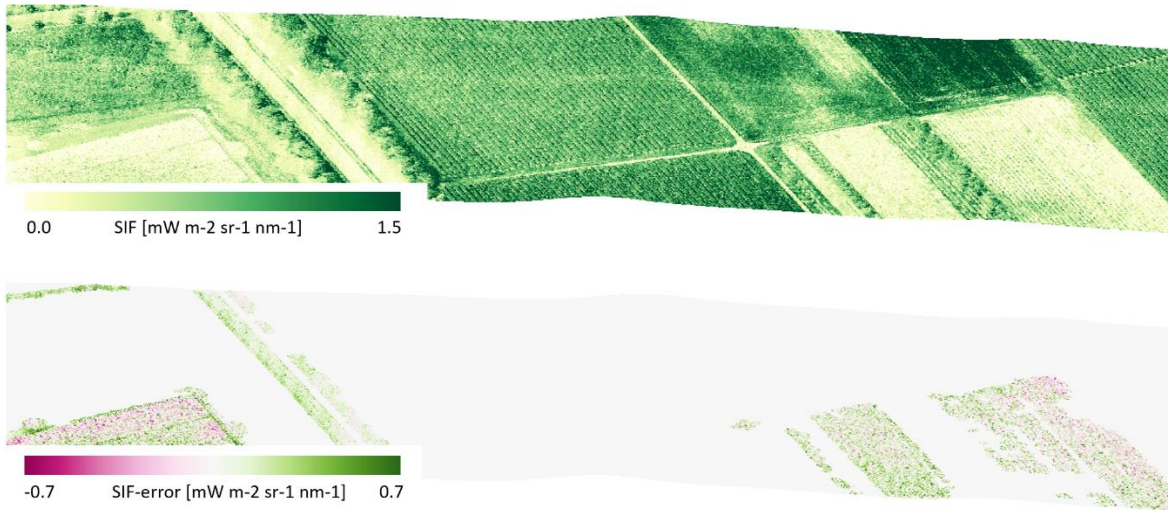


Figure 56: SIF₇₆₀ map (top) and the corresponding SIF₇₆₀ uncertainty for non-vegetated reference surfaces (bottom).

6.2.2 SFM

The SIF retrieval from the SFM algorithm is based on the inversion of the at-sensor radiance spectrum around the O₂ bands, to separate the fluorescence and reflected radiance contributions. An iterative optimization (minimization) technique is used to estimate fluorescence/reflectance, to obtain the best match between observed at-sensor radiance and the one modeled by the SFM. Therefore, a first indication about the successful retrieval of the true parameters is goodness-of-fit, which describes how well SFM fits the observed data. This is quantified from the band-to-band residuals between the two spectra. Moreover, numerical optimization (inversion) is prone to errors because observed data are noisy and the optimization technique might fall into local minima during the cost function minimization when a descent gradient is calculated as a finite difference. The confidence (i.e., stability) of the estimated parameters depends on the local derivatives at the optimal point: the steepest derivatives correspond to unstable solutions and therefore confidence level is larger.

Following these considerations, the SIF uncertainty is implemented according with the standard Matlab routine that computes uncertainty on the base of spectral residuals and the values of Jacobians (J) at the optimal point (the end point of the optimization). The residuals and J enable the determination of the confidence bonds around the optimal solution found from numerical optimization.

A general example of full SIF spectrum retrieval uncertainty from a typical FloX measurement is shown in Figure 57. This figure does not exactly represent the *HyPlant* SIF (retrieved only at the O₂ bands and not along the full SIF spectrum), but it clearly shows the different levels of uncertainty between the red bands (higher) and far-red bands (lower).

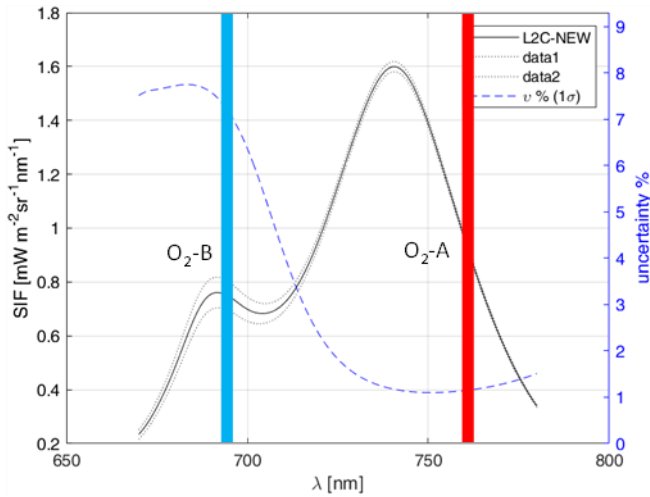


Figure 57: Example of spectral uncertainty from full spectrum SIF retrieval from FloX.

The approach is now implemented with the SFM retrieval for routine and operational processing. The SIF retrieval uncertainty is computed independently for each image pixel during the inversion of the *HyPlant* at-sensor radiance to distinguish SIF and reflectance. The uncertainty is expressed as an absolute value, but the relative value is also stored in the output files. The latter is less affected by overall SIF magnitude and therefore can be compared between targets with different intensity amplitudes (i.e. crop fields with different SIF) and when flight lines collected at different time of the day need to be compared.

Examples of the uncertainty maps obtained from *HyPlant* are reported in Figure 58 and Figure 59.

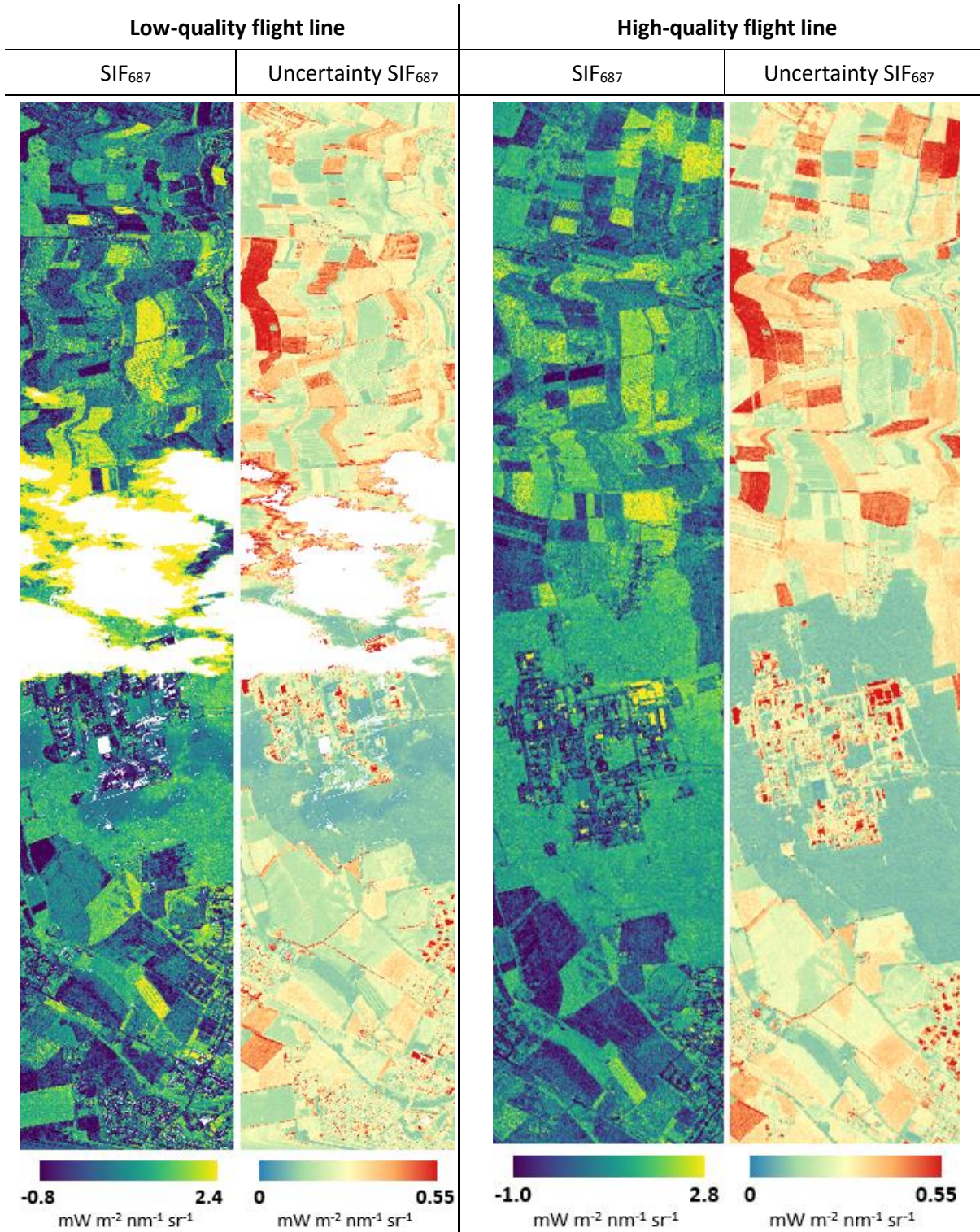


Figure 58: Non-georectified SIF₆₈₇ and corresponding SIF₆₈₇ uncertainty maps derived from the low-quality (left) and high-quality (right) flight line. In the low-quality SIF and SIF uncertainty map, the cloud covered pixels were masked (with areas).

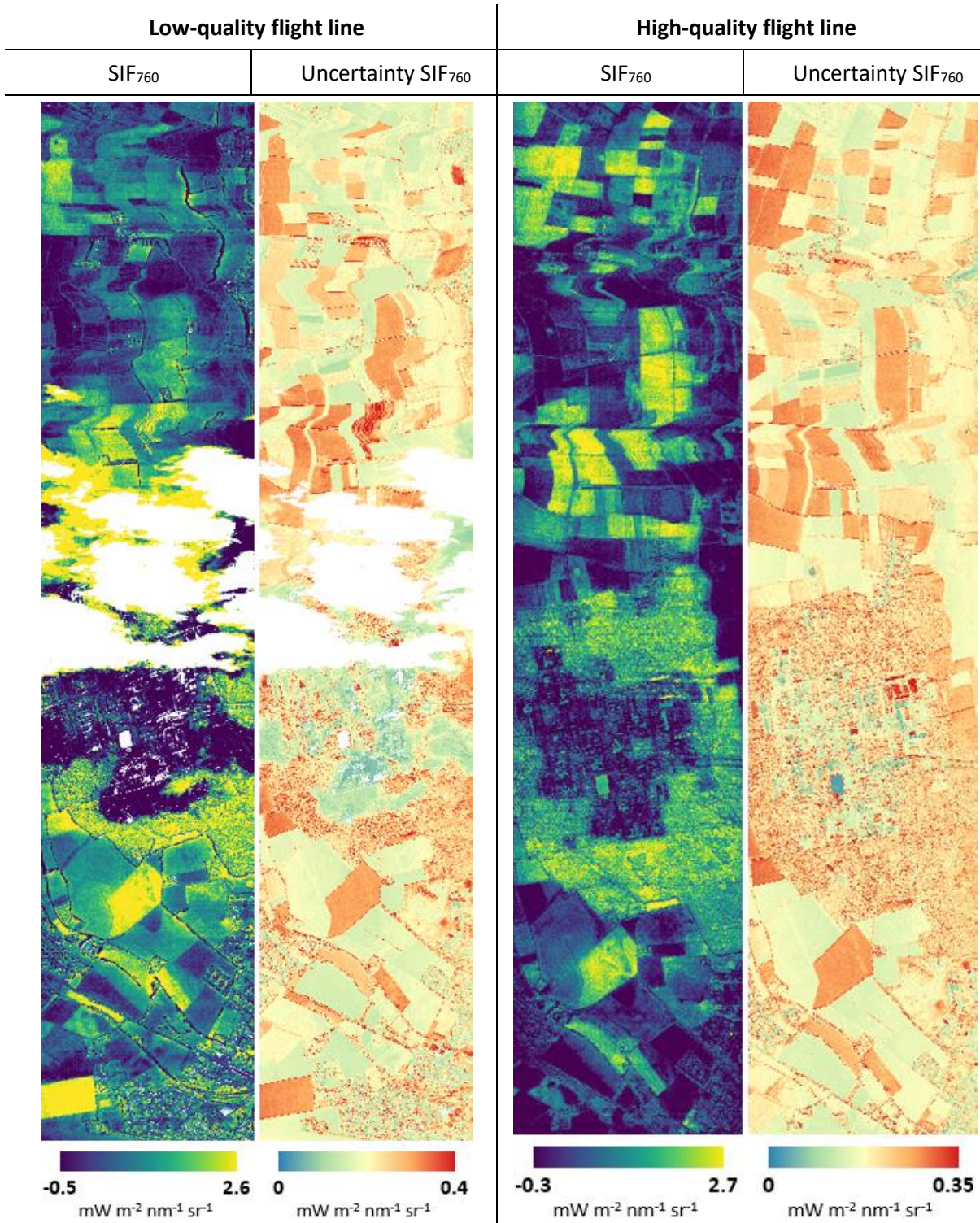


Figure 59: Non-georectified SIF₇₆₀ and the corresponding SIF₇₆₀ uncertainty maps derived from the low-quality (left) and high-quality (right) flight line. In the low-quality SIF and SIF uncertainty map, the cloud covered pixels were masked (with areas).

7 Site-specific results for the better understanding of SIF and its potential to track dynamic changes in photosynthesis and detect vegetation stress early

During the 2018 FLEXsense campaign, more than 400 flight lines were acquired between 7 June and 2 August 2018. Details on the study sites, the flight lines, and the quality of the single flight lines can be found in the data acquisition report of this campaign ([RD-02]). Campaign activities facilitated the integrated measurements from the ground, TOC, and airborne up to the satellite level. We selected several intensive observation periods, where all components were in place to address the objectives of this campaign. The following table gives an overview on the most promising data sets that were used for the scientific analysis presented in this section⁷.

Table 15: Overview of the used data.

Site	Date	Instruments				
		Sentinel	HyPlant	TASI	LiDAR	Ground-based measurement
Grosseto	10 June – 30 July	x	x	x	x	x
Majadas	24 June – 16 July	x	x	x		x
Selhausen	26+27+29 June and 2 Aug	x	x	x	x	x
CKA	26 June – 2 July		x	x		x
OHP	10 July		x			x
Laegeren	13+14 July	x	x			x
Greifensee	14+15 July	x	x			
Tyrrhenian open water site	4 - 10 June	x	x			X (FloX)

7.1 Grosseto, Italy

[42.83N, 11.07E]

This experimental site is located in central Italy at 20 km from the coastline in central Tuscany (Figure 60). The site is part of a milk production farm. It mainly consists of a large irrigated flat area extending over 72 ha. The area has a circular shape with 1 km diameter and is irrigated by a rotating pivot-irrigation system that is normally operated 24 h a day in the period June - August. A full irrigation cycle is completed within four days. The area was cultivated with a grass mixture from January to May 2018 and then entirely planted with corn at the end of May. This crop was grown during the June - September period under full irrigation and fertilization reaching full canopy cover at mid / end July and a maximum height of 2.8 / 3.0 m in mid-August. From June onwards, the area was surrounded by dry grasslands/soils where no ETP is expected to occur.

⁷ All airborne data acquired during this campaign are processed and available within the campaign data package.



Figure 60: Le Rogaie field site.



Figure 61: Flight lines for the experimental site Le Rogaie: Grosseto (A) and the additional line (B) during the 2018 campaign.

During the 2018 campaign, three FloX systems were used JB-001-MM, JB-009-ESA and JB-013-ESA, acquiring high-resolution spectra on different crops approximately from February up to August. High-resolution TOC spectra were systematically collected over several targets, namely forage, alfalfa and corn, from February up to August, in order to cover crops at different growing stages (Figure 62). Nevertheless, not all the data acquired can be used. The days correspond to the ones acquired in clear sky conditions; data in unstable daily illumination conditions were removed.

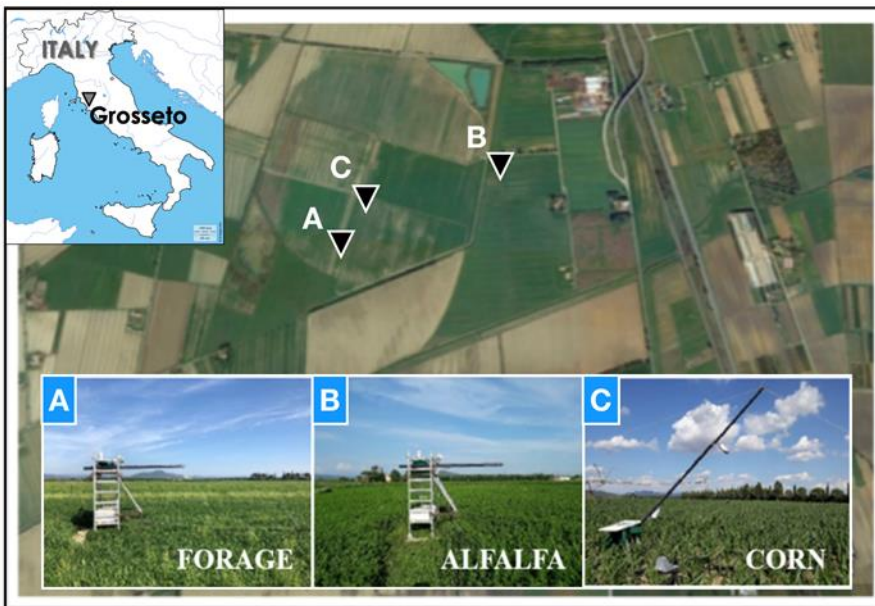


Figure 62: Location of the FloX instruments at the Grosseto sites.

7.1.1 Linking sun-induced fluorescence, biophysical canopy parameters, and carbon and water fluxes

Surface fluxes and fluorescence in Le Rogaie, Grosseto (Italy)

In this section, we report some highlights of the surface flux measurements and fluorescence that were made in Le Rogaie, Grosseto (Italy) in the frame of the FLEXSense and ATMOFLEX campaigns. Some of the data reported here are also included in the ATMOFLEX CCN report ([RD-11]) and will be used for further analysis in the PhotoProxy project ([RD-06]).

Energy and carbon flux from EC stations were calculated using two standardized method, namely the Ec_pack and the EddyPro software packages. Figure 63 - Figure 66 show some diurnal courses of the fluxes in alfalfa and corn at two representative days early and in the middle of the vegetation period. These exemplary diurnal courses highlight the overall match between the data processed using different software packages and illustrate the range of variation that was observed for the two crops at the beginning and at the end of the growing season. Differences between the two methods are visible in night-time measurements, where the EddyPro software clearly gives unrealistic short-term variations in carbon fluxes, which are most likely related to erroneous calculations / assumptions of night-time respiration. Visible checking of the diurnal courses showed realistic data, with overall realistic flux calculations (Figure 63 - Figure 66).

Alfa_alfa DOY 145 (25 May)

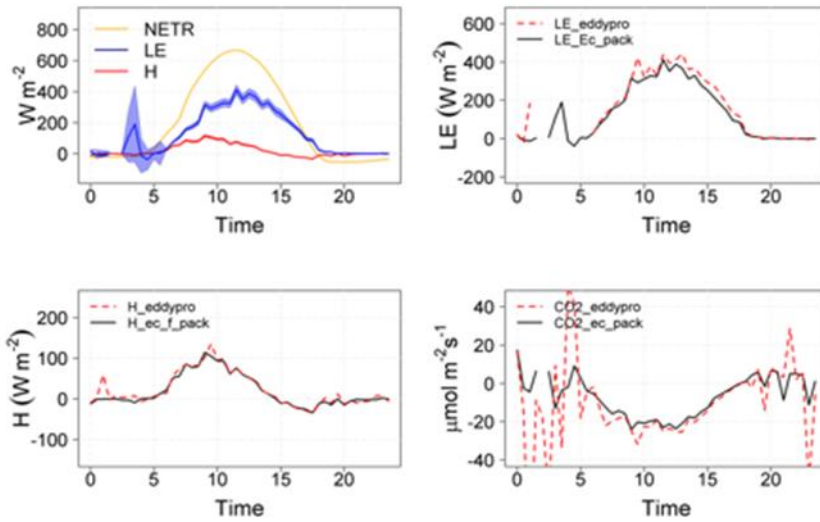


Figure 63: Energy and carbon fluxes measured from the alfalfa field on 25 May. Top left: net radiation (NETR), LE and sensible heat flux (H) measured on a clear, cloudless day. Other panels: comparison of fluxes computed with Ec_pack software (solid black line) and Eddy Pro software (dashed red line): LE – top right, H – bottom left, CO₂ flux – bottom right.

Alfa_alfa DOY 189 (08 Jul)

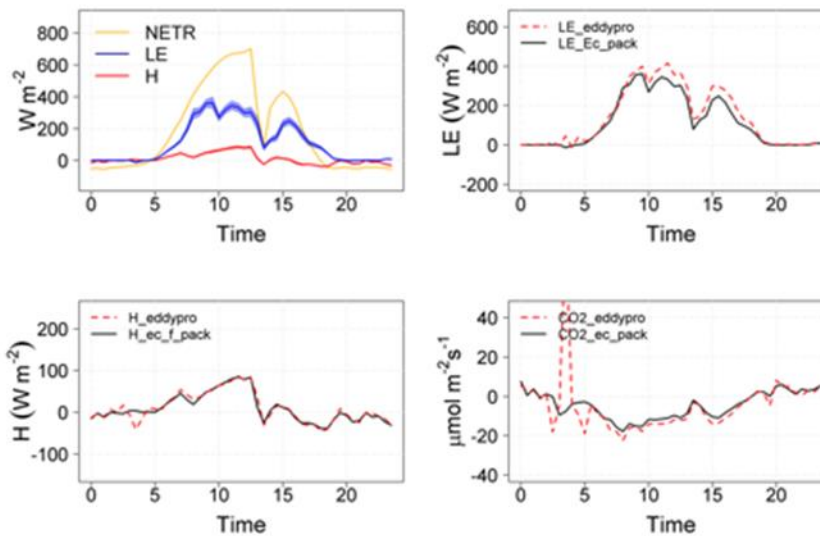


Figure 64: Energy and carbon fluxes measured from the alfalfa field on 8 July. Top left: NETR, LE and sensible heat flux (H). While morning hours had clear-sky conditions, at midday clouds moved in, which clearly affected energy and water fluxes around midday and early afternoon. Other panels: comparison of fluxes computed with Ec_pack software (solid black line) and Eddy Pro software (dashed red line): LE – top right, H – bottom left, CO₂ flux – bottom right.

Corn DOY 213 (01 Aug)

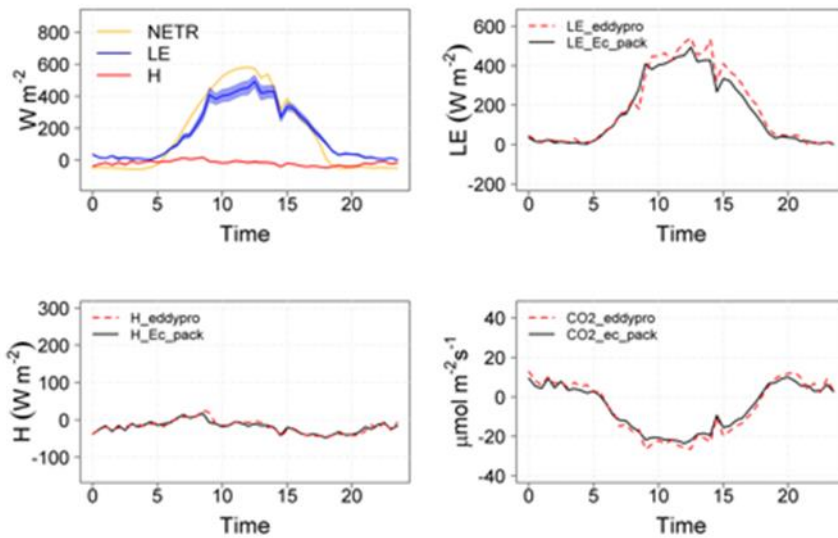


Figure 65: Energy and carbon fluxes measured from the corn field on 1 August. Top left: NETR, LE and sensible heat flux (H). While morning and midday hours had clear-sky conditions, during the afternoon clouds moved in, which affected energy and water fluxes. Other panels: comparison of fluxes computed with Ec_pack software (solid black line) and Eddy Pro software (dashed red line): LE – top right, H – bottom left, CO₂ flux – bottom right.

Corn DOY 239 (27 Aug)

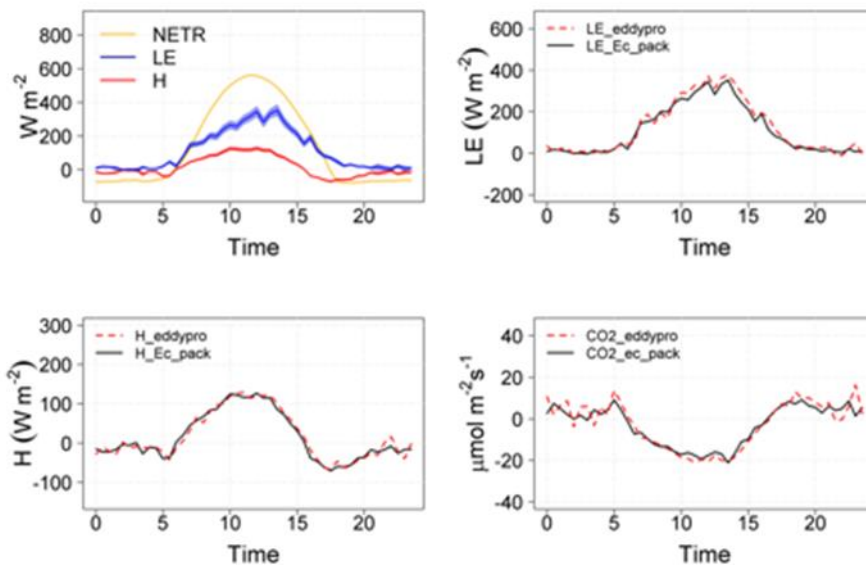


Figure 66: Energy and carbon fluxes measured from the corn field on 27 August. Top left: NETR, LE and sensible heat flux (H) measured at a clear, cloudless day. Other panels: comparison of fluxes computed with Ec_pack software (solid black line) and Eddy Pro software (dashed red line): LE – top right, H – bottom left, CO₂ flux – bottom right.

In addition to visual inspection, we calculated the energy balance closure (EBR) of the EC data and concluded that the energy balance was sufficiently closed for both corn and alfalfa (Figure 67). The good energy balance closure indicates a sufficient measurement of all relevant parameters, i.e. a good model parameterization. The remaining discrepancy reflects the overall mismatch between the EC tower footprint and the footprint of the net radiometer, which hardly extends more than a few meters from the tower position.

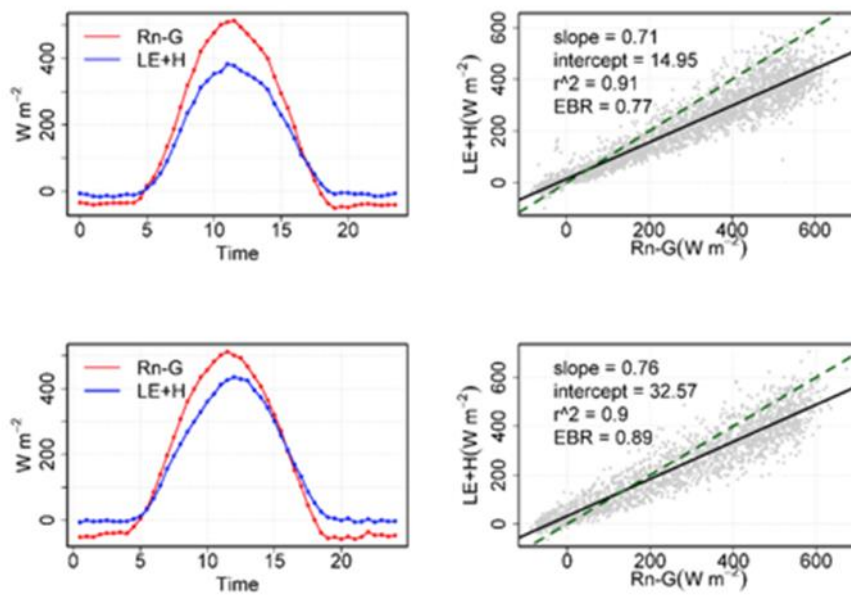


Figure 67: Energy balance closure for the alfalfa (top panels) and the corn field (bottom panels). The left panels show the mean daily course of the difference between the net radiation (Rn-G red line) and the sum of the LE and the sensible heat flux (LE+H blue line) for a representative day (18 June 2018). The right panels show the correlation between the two. The slope, the intercept and the R^2 of the linear regression are shown in the figure, where EBR is the energy balance ratio ($EBR = \text{sum}(LE + H) / \text{sum}(Rn - G)$).

Finally, GPP was calculated using classic flux-partitioning methods, which use night-time respiratory data and their relationship with air temperature. To understand the relationship between SIF and GPP, we used the seasonal cycle of fully closed and photosynthetic active canopy (green leaves dominating the canopy) of half-hour SIF and GPP data and selected clear sky days, only. SIF data were measured by the FloX system which was deployed at short distance from the EC towers.

GPP and SIF both are clearly correlated with absorbed photosynthetically active radiation (APAR) (Figure 68 and Figure 69 right panels) confirming that higher energy absorption in photosynthetic tissues results in higher photosynthetic carbon uptake rates and in higher intensities of SIF. This first order effect was already described by several satellite-based SIF papers that aggregate data over large temporal and spatial scales. Using our seasonal courses, we also show that the correlation between SIF and APAR ($r^2 = 0.85$) is slightly tighter than the correlation between APAR and GPP ($r^2 = 0.62$), which confirms that SIF can serve as an excellent remote sensing parameter for $APAR_{\text{green}}$. We also want to stress that GPP, SIF, and APAR are light-dependent fluxes and thus these parameters track diurnal and seasonal changes in incoming PAR, which is the underlying reason for their tight correlation. Looking at the correlation between GPP and SIF as well as at NDVI (a normalized and light-intensity-independent greenness parameter), the correlation is rather weak. Light-induced variations in SIF and GPP are not reflected in NDVI (Figure 68 and Figure 69 left panels).

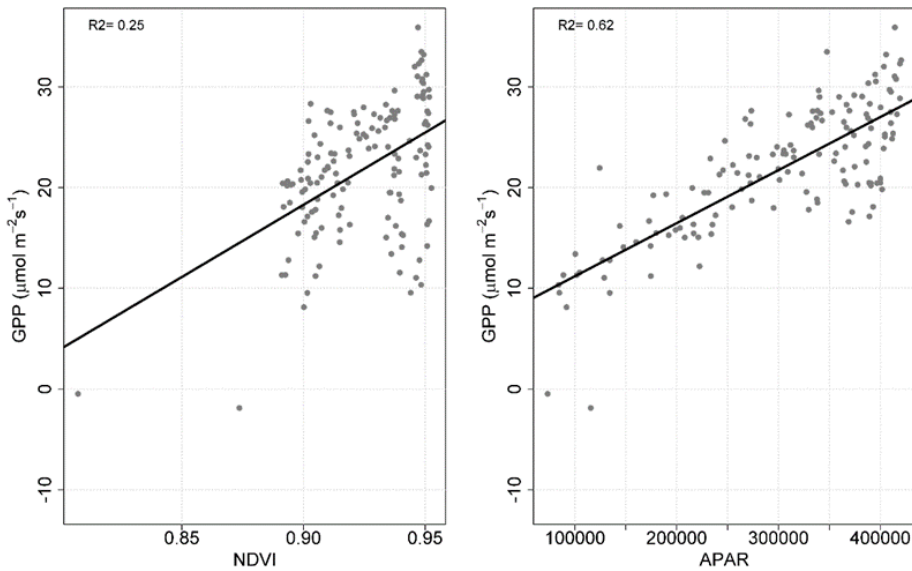


Figure 68: Correlation between GPP and NDVI (left panel) and APAR (right panel) in alfalfa. For this graph, which shows daytime half-hour measurements from June and July 2018, only data from clear cloud free days were selected and plotted. The time period corresponded to the time period where the alfalfa canopy was fully closed but did not show any signs of senescence. Hence, we selected all measurement points from a fully green, photosynthetic active canopy.

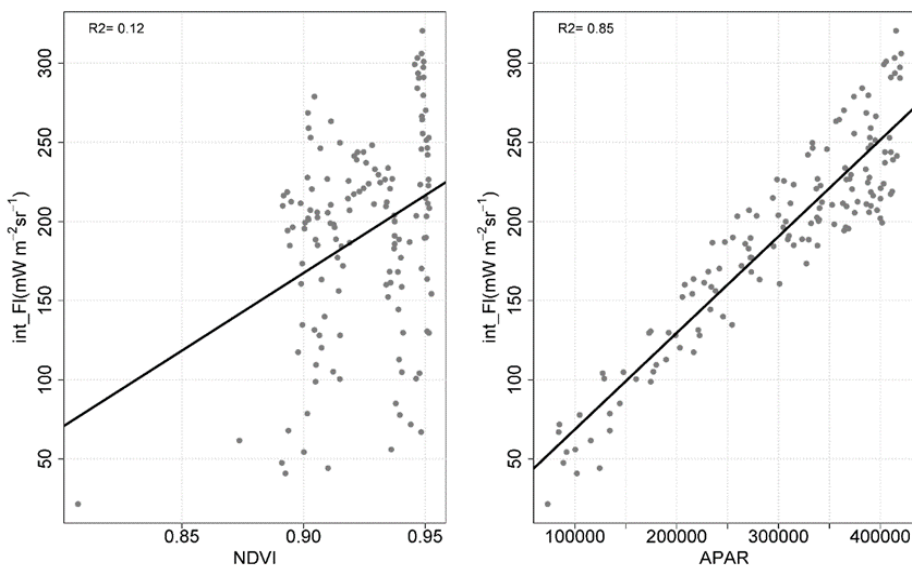


Figure 69: Correlation between GPP and NDVI (left panel) and APAR (right panel) in corn. For this graph, which shows daytime half-hour measurements from June and July 2018, only data from clear cloud free days were selected and plotted. The time period corresponded to the time period where the corn canopy was fully closed but did not show any signs of senescence. Hence, we selected all measurement points from a fully green, photosynthetic active canopy.

Taking the next step in our correlation analysis, we now correlated half-hourly values of GPP with the total integrated fluorescence signal and with SIF₇₆₀ (Figure 70 and Figure 71). Here, we show measurement points that were recorded under clear sky conditions (red symbols in the graphs below) as well as all measurement points (black symbols in the graphs below). It is evident that there is no tight correlation between SIF and GPP. There is clearly substantial variability between the two parameters even though a general positive trend between both parameters remains. This relationship is clearly non-linear in corn if one only looks at the clear

sky measurements. This general finding is seen equally in integrated SIF and in SIF₇₆₀ and no qualitative or quantitative difference between the two fluorescence products is visible (Figure 70 and Figure 71).

We interpret this finding as a clear indication that there are second order effects, which influence GPP and SIF, and that both parameters are influenced by different underlying mechanisms. While GPP most likely shows a strong dependency of temperature and vapour pressure deficit (VPD), which affect respiration and stomatal opening, SIF is most likely affected by the regulatory properties of photosynthetic light reactions and its intrinsic link to non-photochemical energy dissipation and to linear and cyclic electron flow within the photosystems.

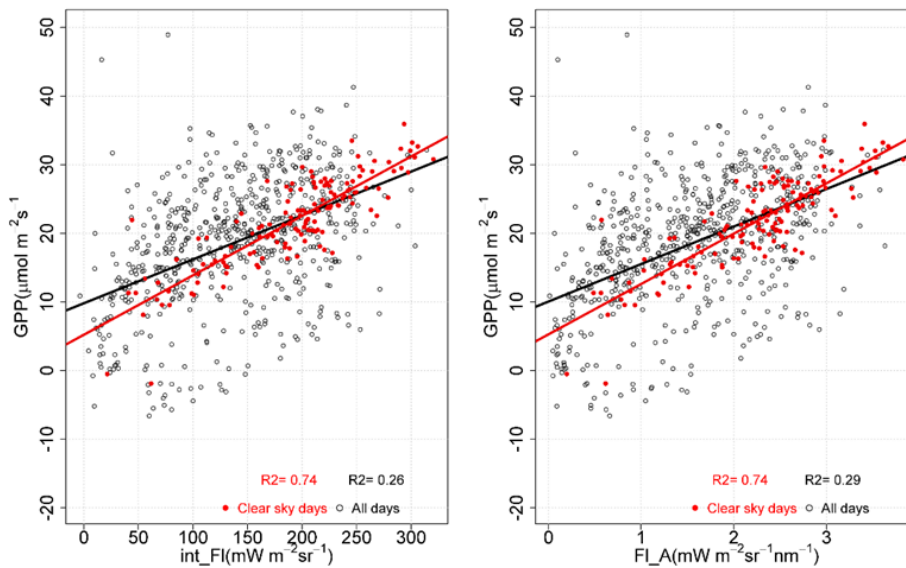


Figure 70: Correlation between GPP and total SIF (left panel) and SIF₇₆₀ (right panel) in alfalfa. Black symbols correspond to all daytime half-hour measurements from the time period between 8 May until 17 September 2018, while red symbols correspond to measurements that were taken under clear, cloud-free conditions.

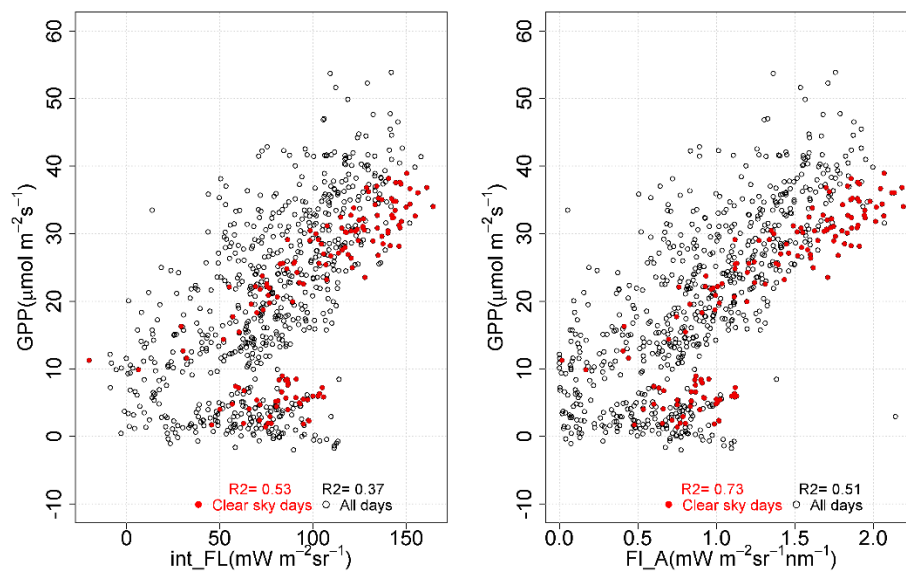


Figure 71: Correlation between GPP and total SIF (left panel) and SIF₇₆₀ (right panel) in corn. Black symbols correspond to all daytime half-hour measurements from the time period 24 May until 17 August 2018, while red symbols correspond to measurements that were taken under clear, cloud free conditions. The time period corresponded to the time period where the corn canopy was fully closed but did not show any signs of senescence. Hence, we selected all measurement points from a fully green, photosynthetic active canopy.

7.1.2 Midday depression of gross primary productivity and SIF in alfalfa (*Medicago sativa* L.)

The content of this section was prepared by Marin Tudoroiu and partly overlaps with the information that was summarized in his final report during his research fellowship at ESA.

In addition to the correlation, which is seen at ‘normal’ days, where presumably the plants were not experiencing stress, the authors also analyzed the diurnal courses on days that were characterized by extreme high temperatures and low soil water availability (Figure 72). At this stressful day, GPP and SIF both showed a distinct midday depression, where carbon uptake rates and SIF were clearly reduced compared with the maximum that was recorded at normal days. This midday depression is likely related to a stress-induced stomatal closure and a functional down-regulation of photosynthetic electron transport and energy use in photosynthetic carbon fixation.

Similar observation were also found in other diurnal courses and could be reproduced in corn (Marin et al. *in prep.*). The data clearly indicate a well detectable decoupling between irradiance and fluorescence under stressful conditions that can likely be interpreted by enhanced photoprotection in the leaves of the stressed canopies. Such an observation is of importance because detectable decoupling between light intensity and fluorescence is a well identifiable sign of physiological adjustment in the leaves, which may outline the importance of fluorescence measurements for the early detection of stress in crop canopies.

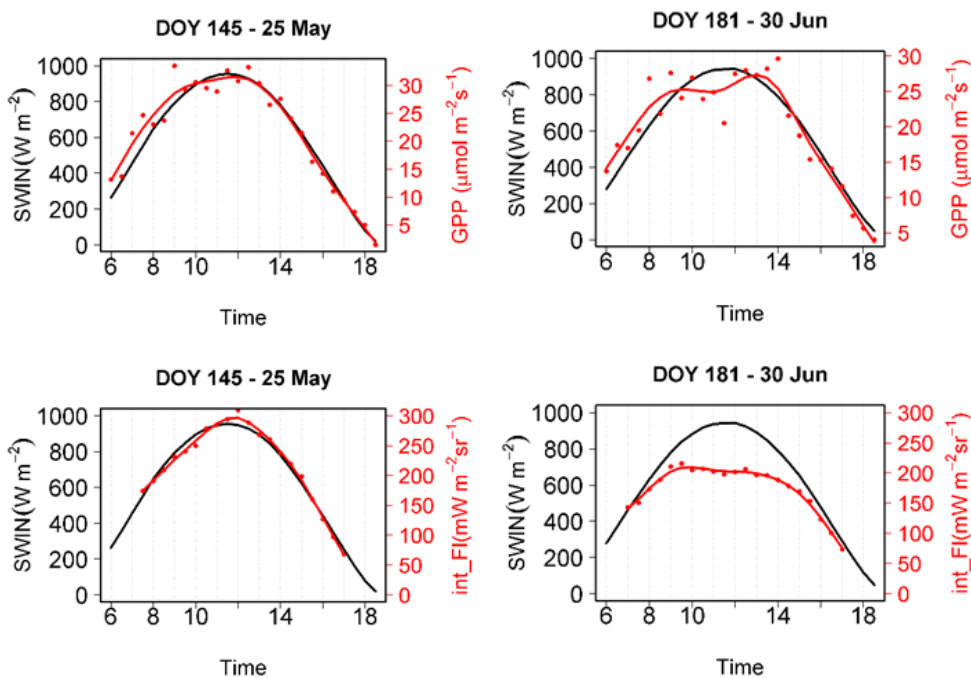


Figure 72: GPP and SIF measured at two representative clear-sky days in alfalfa. The upper panels illustrate the daily course of GPP; the lower panels represent the integral of canopy fluorescence as measured by the FloX. The black line shows the daily course of incoming shortwave radiation. The left panels show the diurnal course of a ‘normal’ day (25 May 2018), where air temperatures were moderate and the plants had ample availability of soil water, following previous rain events. The right panels exemplify a ‘stressful’ day, where air temperatures were high and a soil water resources from the last irrigation cycle were presumably depleted. On this stressful day, GPP and SIF both showed a distinct midday depression, where carbon uptake rates and SIF were clearly reduced compared with the maximum that was recorded at normal days.

This finding could be confirmed using the long-term measurements of the carbon fluxes and the time series of SIF on alfalfa.

The growing season was divided into two periods: period-A, between 25 May and 10 June and period-B, from 29 June to 9 July. Those two periods were separated by a cut of the forage crop that started on 11 June. The canopies were at full cover (LAI >9) during both periods. PAR measured at the surface was also comparable in the two periods. A cosmic neutron probe (Hydroinnova, mod.CRS 1000/B, NM, USA) installed in the proximity of the EC station showed that soil water was more abundant in period A. This is confirmed by the soil water content derived from the Conservative Surface Water Index (CSWI, Nelson et al. 2018) adjusted for the specific soil structural properties. Prolonged drought between the two periods caused significant soil water depletion in the upper soil layers and elsewhere. VPD was lower in period A, and in period B as it reached values >2 kPa around noon (Table 16).

Table 16: Mean values of the main parameters used in the interpretation of the results.

Parameter [UM]	Period A (mean ± standard error)	Period B (mean ± standard error)
PAR [Wm ⁻²]	368.0±5.26	379.3±4.96
SWC [-]	0.421±0.010	0.416±0.007
Neutron Counting rate [-]	0.1533±0.0005	0.1563±0.0009
VPD [kPa]	1.14±0.14	1.99±0.16
GPP [mmol m ⁻² s ⁻¹]	27.32±1.32	22.90±1.35
SIF integral [mW m ⁻² sr ⁻¹]	236.6±13.7	211.7±6.02
SIFy [sr ⁻¹ * 10 ⁻³]	0.64±0.03	0.57±0.01
SIF_Ay [sr ⁻¹ * 10 ⁻³]*	0.01479±0.001	0.01462±0.00039

While the EC technique can provide credible estimates of GPP for every half-hour both in clear sky and overcast days, SIF cannot be reliably retrieved in all circumstances. Rapid changes in irradiance due to clouds may affect the stability of the absorbed PAR during the time of the measurements. Spectral measurements are made, on average, at one-minute frequency but the integration time of the spectrometers may vary depending on the irradiance. If irradiance changes substantially within the integration time of a measurement, wrong estimates of SIF occur. Moreover, the fluorescence emission of leaves and canopies is a very dynamic process because it depends on the velocity of build-up / relaxation of photoprotection (non-photochemical quenching, NPQ) that occur after every and even small change in irradiance. A transition from low to high irradiance causes a short duration increase in fluorescence emission per photon absorbed, defined as fluorescence yield (SIFy) (Murchie and Ruban, 2020). The transition from high to low irradiance causes a reduction in SIFy instead that adjusts over several minutes under low light (Kromdijk et al. 2016). Due to the uneven temporal response of NPQ build-up and relaxation, the presence of scattered clouds unavoidably changes SIFy whose magnitude is also dynamically affected by photosynthetic induction responses (Wyber et al. 2018). SIF retrieval is also problematic for high SZA due to the inaccurate response of the commercial cosine-corrector used in the FloX system (Cogliati et al. 2015). Accordingly, used SIF data were filtered to exclude i) irradiance instability during the integration time of the measurements, ii) periods with frequent and rapid changes in irradiance due to scattered clouds, and iii) an SZA greater than 45°.

SIF and GPP both followed the diurnal cycle of irradiance in period A, while a pronounced variation (GPP and SIF midday depression) occurred during Period B (Figure 73). Three main mechanisms can be invoked to interpret those observations. Two of those would account for more or less transient changes in light absorbance, while the third accounts for changes in energy dissipation with unmodified absorbance:

- 1) A reduction in the content of light-absorbing pigments occurring under water stress conditions may lead to reduced light absorbance thus explaining the concomitant depression of GPP and SIF.
- 2) Changes in canopy architecture due to rapid paraheliotropic leaf movements can lead to a reduction in the fraction of absorbed light. Reed and Travis (1987) observed that such movements do occur during the day in alfalfa under stress conditions.
- 3) Soil water depletion and high evaporative demand cause physiological responses in the plants at both the leaf and canopy scales. Stress-induced stomatal closure can cause a decrease in leaf-scale SIF and it can also translate into an overall reduction of canopy conductance leading to a decrease of GPP due to the diffusional limitation of gas exchange.

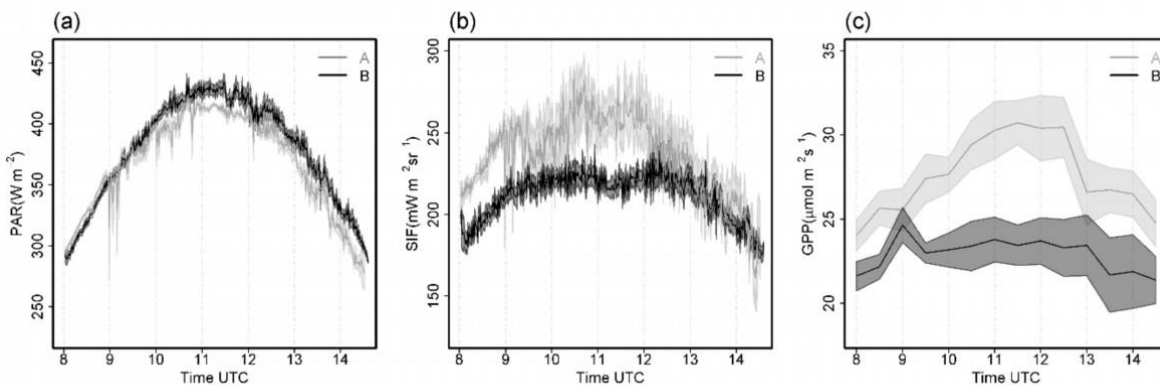


Figure 73: Mean daily course of PAR - (a), integral of SIF - (b) and GPP (c) for period A (grey) and B (black). The solid lines show the mean values while shaded areas indicate the deviation from the mean (standard error). Time is expressed as UTC (Coordinate Universal Time).

Hypotheses I and II are unlikely to provide a reliable interpretation of our observations for a number of reasons: even if a change in the concentrations of light absorbing pigment might have occurred between periods A and B, it is very unlikely that short-term fluctuations in pigment content could occur over the course of the day, as the midday depression of GPP in period B would suggest (Figure 73). Changes in pigment concentrations occur at a much slower pace than a day. Moreover, concomitant reductions of canopy GPP and SIF that would be caused by a decrease in the fraction of light absorbed (hypotheses I and II) would not affect the overall light use efficiency (LUE) of the canopy ($LUE = GPP / APAR$) as well as the SIFy. Instead, the occurrence of increased diffusional limitations to gas exchange in period B compared with A can fully explain the entire set of field observations. Indeed, both LUE and SIFy are decreased under the more stressful conditions of period B and in particular during periods of high irradiance around noon when the canopy conductance is also reduced (Figure 74). A decrease of carboxylation efficiency in the Calvin cycle (Jonard et al. 2020), reduced demand of adenosine triphosphate (ATP) and nicotinamide adenine dinucleotide phosphate (NADPH) lead to a reduction in electron transport (Vanlerberghe et al. 2016) and to proton accumulation in the thylakoids triggering an increase in NPQ and an overall decrease in SIF and SIFy.

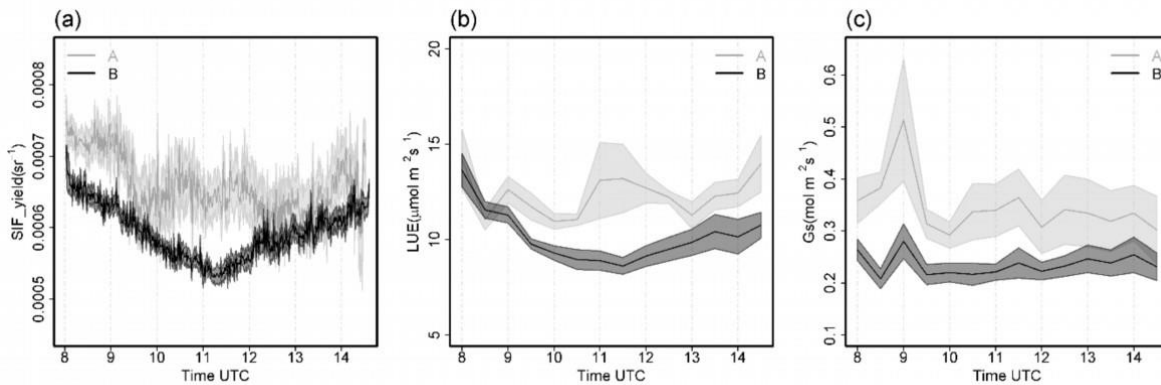


Figure 74: Mean daily courses of SIFy - (a), LUE - (b), and surface conductance (Gs - (c)) for period A (grey) and B (black). The solid lines show the mean values while shaded areas indicate the deviation from the mean (standard error). Time is expressed as UTC (Coordinate Universal Time).

Our conclusion is that an overall decrease in canopy conductance, which is likely driven by a reduction of soil water content, can explain the observed differences in GPP and SIF between the two considered periods (A and B). The concomitant reduction of SIFy and LUE can be therefore considered a reliable indicator of water stress-driven decrease in canopy conductance. The examination of daily courses of both variables confirms that this is the main driver of midday depression of both GPP and SIF. Such depression occurs when the evaporative demand and the radiation load is at its maximum. Those conclusions challenge previous leaf-scale observations that negated a strong association between LUE and SIFy under stress conditions (Helm et al. 2020; Marrs et al. 2020) but confirms the dependency that was shown by Paul-Limoges et al. (2018) in a field scale study. We are aware that our conclusion cannot yet be generalized to other crops than alfalfa. This is why we believe that additional experimentation under field conditions is urgently required to further increase the comprehension of the complex connection between fluorescence emissions and gas exchange of canopies.

7.1.3 Diverse agricultural land-use and its relation to the regional diversity of sun-induced fluorescence

The content of this section is also presented in the ATMOFLEX CCN final report ([RD-11]). There are some differences in the direction of the discussion to meet the specific objectives of the activities. However, major parts of this section are intentionally repeated to facilitate easy access to these results that were acquired using the synergies between the two campaign activities.

The combination of land-use maps that were created in the frame of the ATMOFLEX CCN and the *HyPlant* data acquired during this campaign, obtained interesting and novel information on the fluorescence emissions of specific crop types in Grosseto. The area is characterized by the presence of different summer crops which are mostly irrigated during the period June - September. Some farmers grow corn and sorghum as fodder crops while other grow processing tomato for the food industry (Figure 75).

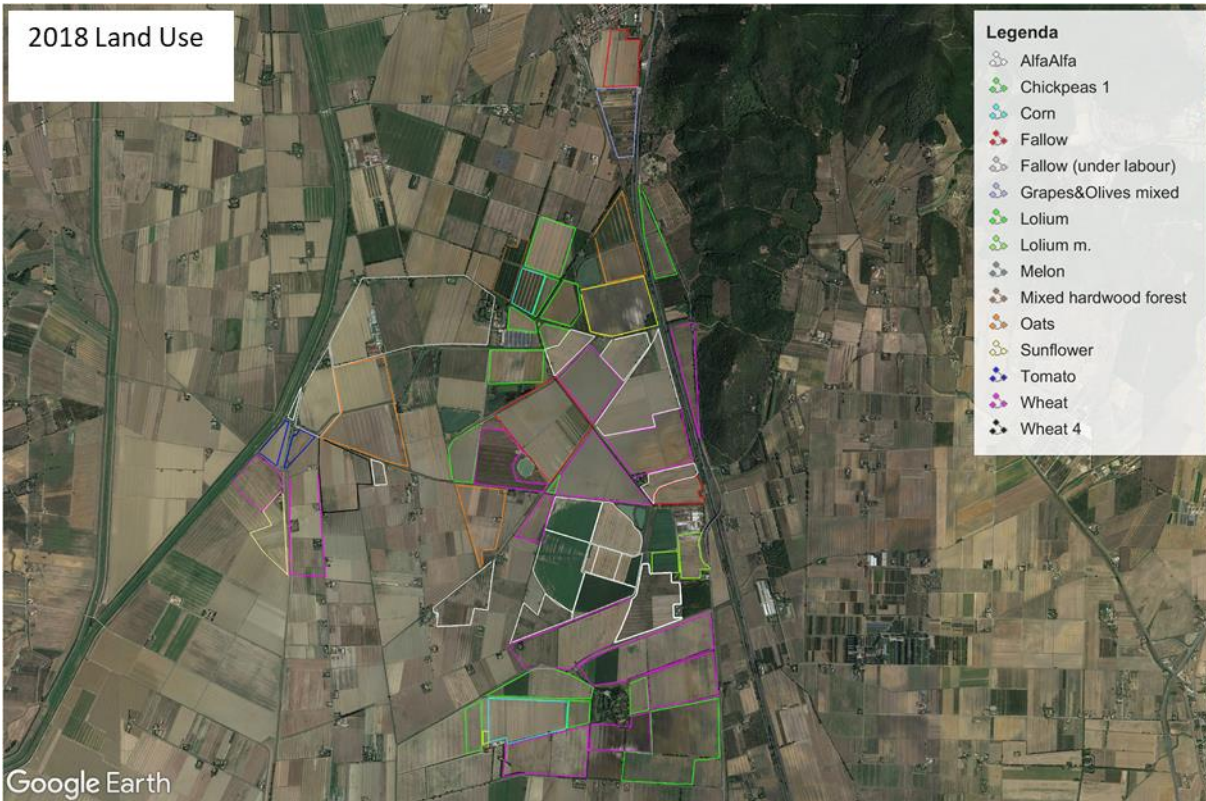


Figure 75: Land-use of the core study site in the Grosseto area during the study period, i.e. July 2018.

The Sentinel-2 image of Figure 76 shows the distribution of the tomato crops at the time of the *HyPlant* flights in the summer of 2018 (white circles). The corn fields are indicated by red outlines.

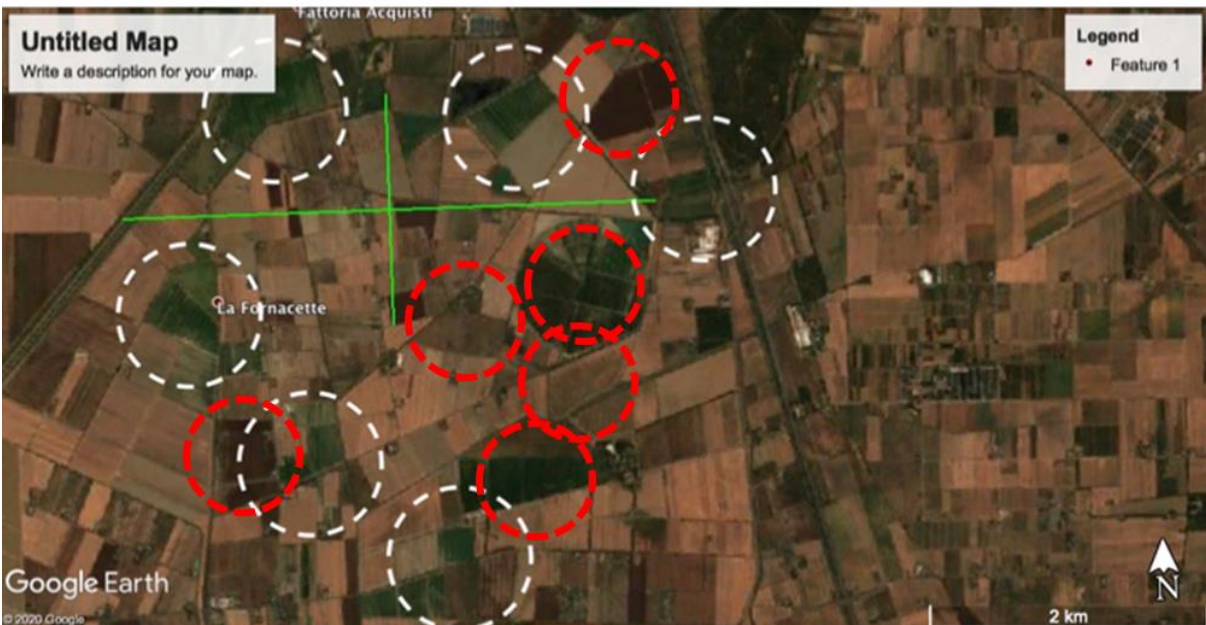


Figure 76: Spatial distribution of corn (red circles) and tomato fields (white circles) in the Grosseto area. The area was surveyed to identify all land-use classes and crop types during the FlexSense2018 campaign.

The following figure (Figure 77) illustrates the NDVI index of the region as calculated by Sentinel-2 instead. The data clearly show that both tomato and corn fields had high NDVI, reflecting the green status of the irrigated vegetation. It is well known that the NDVI index is proportional to the crop leaf area and, with this,

to the light absorption in the PAR region. The index is often used to derive LAI and the fraction of absorbed photosynthetic active radiation (f_{APAR}) values by regression. Yet, it is also well understood that NDVI tends towards saturation for high LAI and f_{APAR} . This likely explains why the NDVI value of the tall and leafy corn fields is not much higher than the NDVI of the tomato crop. While the LAI of irrigated corn was higher in this species at the time of the measurements.



Figure 77: Sentinel-2-derived NDVI map of the same scene shown in Figure 76. Data were acquired on 2 August 2018.

SIF emissions measured by *HyPlant* over corn and tomato fields showed a striking difference. The integral of SIF in tomato is in fact much higher than the SIF of corn in spite of a lower LAI, a lower NDVI, and possibly a lower f_{APAR} . This suggests that the fluorescence yield of tomato exceeds that of corn. Examples of the difference between the *HyPlant*-derived SIF are shown in the following Figure 78, where the NDVI values obtained by the full-range spectrometer of *HyPlant* are compared with the SIF-A obtained by the SFM method.

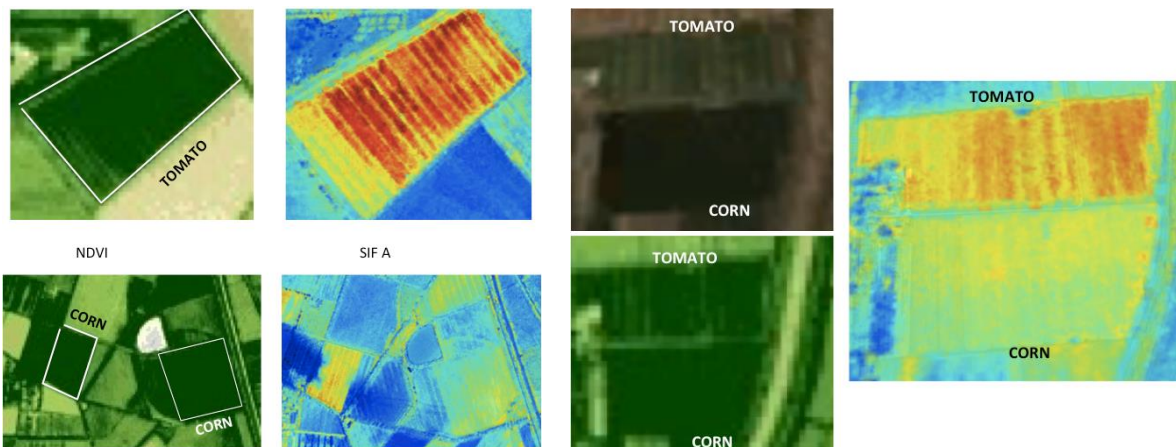


Figure 78: NDVI and SIF-A values of corn and tomato fields are visually compared for selected corn and tomato fields in Grosseto. The large difference in SIF-A between the two crops is clearly detectable visually.

A more detail data analysis reveals that the higher SIF-A values in tomato are due to a significantly lower relative band depth of the apparent reflected radiance at 760 nm. Such difference is shown in Figure 79 below, where the radiances of the two crops shown in the left panel of Figure 78 are highlighted.

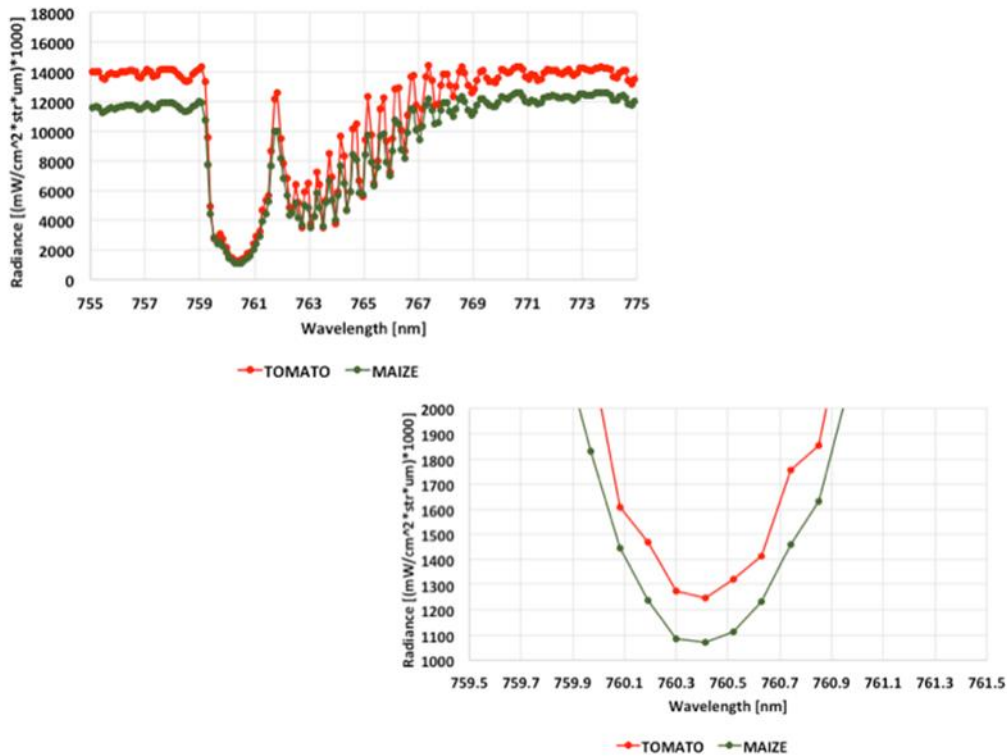


Figure 79: Apparent reflected radiances acquired by *HyPlant* on 30 July 2018 during a clear-sky day overpass of the Grosseto region. The upper panel shows the data for tomato (red line) and for corn (green line) around the center of the O₂-A absorption band of the spectrum. The relative band depth is more shallow in tomato, due to a higher fluorescence infilling of the O₂-A band. This translates into an estimation of higher SIF-A values for this crop compared with corn.

Data interpretation requires a series of considerations. First of all, there is a clear structural difference between a tomato and a corn field. At the end of the month of July, plants of irrigated corn exceed two meters in height and the canopy space is populated by green leaves down to the level of the soil surface. The leaf area density of this crop is large. On the other hand, processing tomato plants tend to cover the surface by laying on the soil surface while growing more in space than in height. When the berries are formed (from mid-July to the end of August) the tomato plants are forming a shallow layer that rarely exceed 30 cm in height. The leaf area density is, therefore, much lower than in corn, and the crop forms a planophyll leaf layer. Now, it is very well understood that structural components of the canopies largely affect the reabsorption of the red light of the first peak of canopy fluorescence, but also the photon escape probability in the near-infrared. In addition, NIR escape is also favored in case of erectophyll (corn) versus planophyll (tomato) leaf angles. The net result of increased SIF-A in tomato compared with corn can then be interpreted to be driven by structural rather than physiological components. Nevertheless, such difference is of importance because it defines some basic and detectable differences between the two crop types that further characterize the whole scene of airborne images taken by *HyPlant* in July 2018. The geographical distribution of tomato fields is clearly detectable in the *HyPlant* SIF-A image as shown in Figure 80. All the tomato fields are well visible in the airborne fluorescence map, where they form a spatial “tomato ring”.

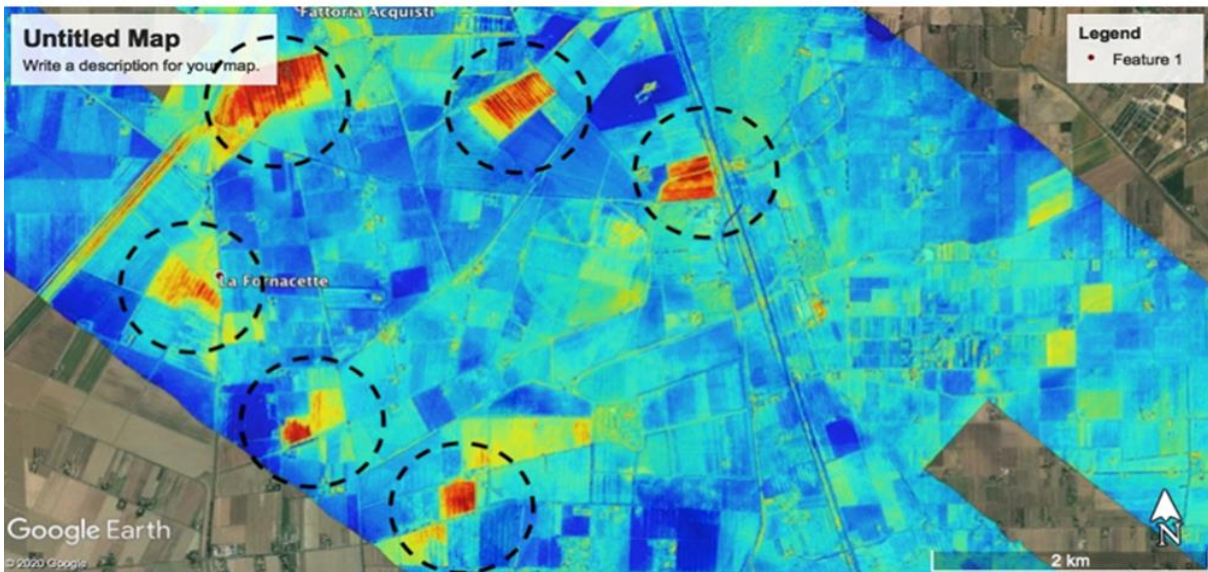


Figure 80: SIF-A map derived from *HyPlant* images taken on 30 July 2018. The tomato fields with a much higher SIF-A values are outlined but are also easily identifiable in the map, where they form a geographically distinguishable “tomato ring”.

The difference between the tomato crops and the rest of the scene was so high that even a downscaling of the SIF-A map to the approximate spatial resolution of FLEX (300 x 300 m) could distinguish the presence of the tomato field. This is illustrated in Figure 81 where the left panel shows the *HyPlant* SIF-A image degraded to the FLEX satellite resolution. The right panel shows the overlap between the full spatial resolution and the degraded image (in transparency).

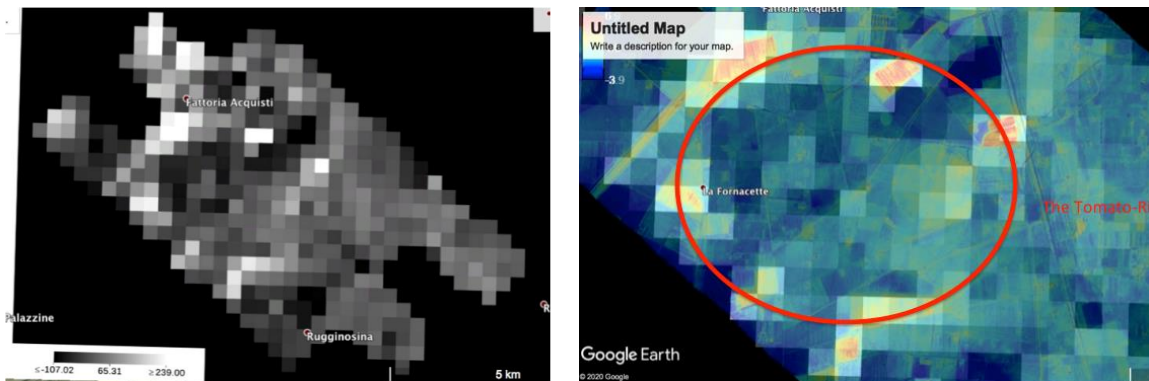


Figure 81: The left panel shows the *HyPlant* SIF-A image degraded to the FLEX satellite resolution and the right panel shows the overlap between the full spatial resolution and the degraded image (in transparency).

7.1.4 Comparison of reflectance-based indices and fluorescence metrics

Currently, at the field level, many efforts have been devoted to improving the estimation of fluorescence at the oxygen absorption bands and to computing the full spectra of fluorescence and a series of fluorescence metrics. But the way these quantities can bring additional information to sense vegetation dynamics have been poorly addressed. The perspective of exploiting the full SIF spectrum is relevant for future work on fluorescence in relation to different canopy species, chemical / physical variables, and the physiology of photosynthesis. Knowledge of the entire fluorescence spectrum may in fact be helpful to better quantify canopy re-absorption and to derive the respective PSI / PSII contributions and the fluorescence quantum efficiency. In this section, we present a preliminary comparison of different reflectance-based indices and fluorescence metrics with particular attention to the intensity of the far-red peak. Further details about the

	Doc.: Final Report		
	Date: 29 July 2021	Issue: 2	Revision: 1
	Ref.: ESA Contract No. 4000125402/18/NL/NA		Page: 116 / 288

behavior of fluorescence metrics are provided in the ATMOFLEX Report ([RD-09]) and will also be evaluated in the PhotoProxy activity.

Reflectance-based spectral indices and fluorescence metrics

Reflectance spectral indices correspond to R_{red} , $R_{red-edge}$ and R_{NIR} and were obtained averaging the SpecFit retrieved reflectance spectral values on the corresponding wavelengths intervals. The spectral bands used to evaluate spectral indices corresponds to 670 – 680 nm, 705 - 715 nm and 770 - 780 nm, respectively. Combining these wavebands, the $NDVI_{red-edge}$, $NIRv$, and CI_{red_edge} were computed, while the FloX GUI generated the PRI used in this framework. Conversely, the fluorescence metrics were derived directly from the SIF full spectrum. Specifically, the fluorescence magnitude was evaluated in correspondence to the O_2 absorption bands, at 760 nm and 687 nm (F_{760} and F_{687}) and at the two emission peaks in the red and far-red areas, respectively (F_{red} and $F_{far-red}$). Finally, the fluorescence full spectrum over the PAR spectral interval was also investigated (F_{INT}).

Firstly, the reflectance and fluorescence metrics have been analysed in time throughout the whole time series (from February up to July) along with the PAR values. Specifically, only the spectra acquired around the solar noon (± 10 minutes time interval) in the clear sky days have been selected to carry out the analysis at seasonal scale of all the crops together.

The reflectance-based indices were selected because they are strongly related to the crop-chlorophyll-content, biomass, and pigment-pool variations. For increasing PAR, all these indices show a common trend: lower values were typical of bare soil / sparse vegetation and an increase in agreement with the crop development stage. Finally, saturations values were reached in the crop maturation stage. This seasonal trend is clear at the forage site, characterized by the longest time series, while only four clear days were available for the corn and hence not enough to cover the complete growing season. Conversely, the alfalfa measurements were collected when the crop was already developed, so the indices did not show a large temporal variability. Similarly, this temporal behaviour was also observed for all the considered fluorescence metrics. Therefore, from a qualitative point of view, the reflectance and fluorescence metrics seem highly correlated at a seasonal scale. To investigate deeper the link between the reflectance and fluorescence metrics, the comparisons summarized in Figure 82 were carried out. In most of the analysed cases, forage and alfalfa trends result were coupled, while corn values lie below the other two crops. This is probably due to the different crop types (C3 and C4) and / or by the crop geometry (uniform and planophiles, rather than arranged in line and with a predominant vertical development). It is interesting to point out the $NIRv$ case. In general, the $NIRv$ index shows a linear relationship with both F_{760} and F_{INT} , regardless of the crop considered. Therefore, unlike the other reflectance-based indices, the $NIRv$ seems unaffected by the crop type and geometry; it is influenced only by the amount of chlorophyll within the canopy. This behaviour may indicate that, at least in unstressed canopies and at a temporal level, $NIRv$ can be used to infer the expected spatial variability of fluorescence in a generic FLEX pixel. This may open new opportunities for evaluating the spatial uncertainty in CAL / VAL schemes because this index can be computed from Sentinel-2. Since the $NIRv$ is related to the crop biomass, it could be used as a proxy for the APAR, a difficult parameter to obtain. Therefore, the ratio between F_{INT} and $NIRv$ may be linked to the fluorescence yield, a useful value for an estimation of GPP. Of course, this concept is valid only under unstressed conditions, in which all the energy not used for the photosynthetic processes is dissipated by fluorescence.

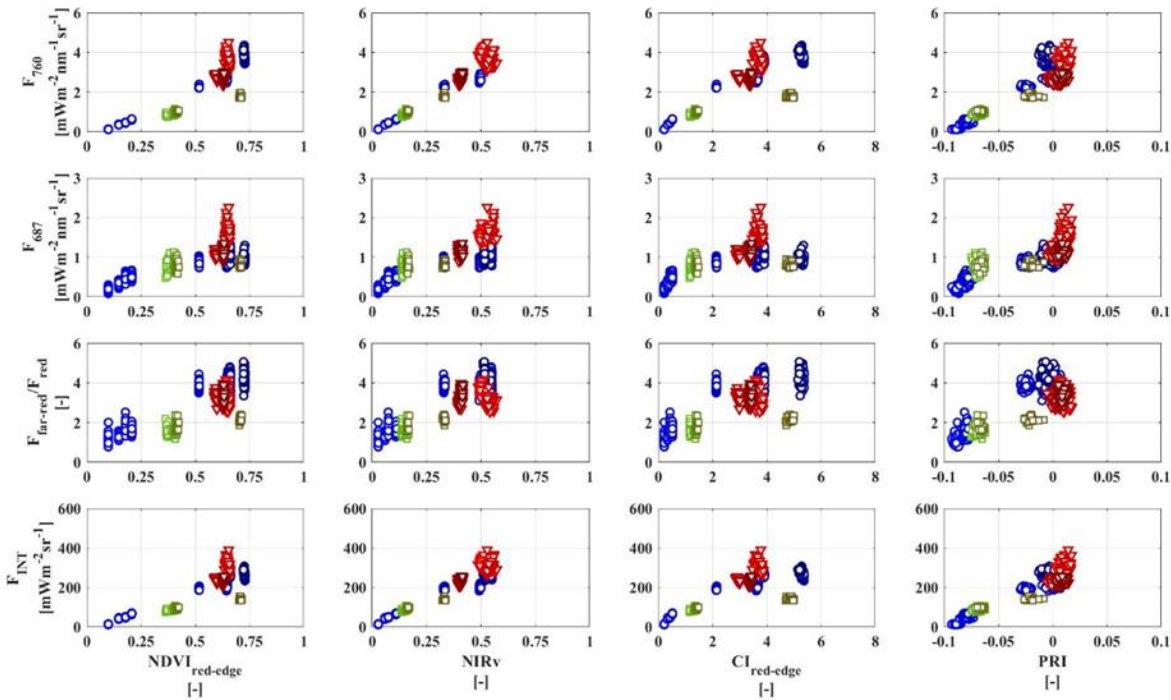


Figure 82: Reflectance-based index and fluorescence metrics. Blue dots correspond to the forage, red triangles to the alfalfa and green squares to the corn.

7.1.5 Variability in wavelength position of the red and far-red peaks

The FLEX mission concept shall provide estimates of maximum fluorescence emission of the two peaks including the wavelength position of the peaks. In this section, we show the results of a test aimed to evaluate the behavior of these peaks during the growing season. In principle, we expect that this position will change in time due to the mutual combination between reabsorption in red and emission in the far-red. However, the magnitude and its implications are not known. For this purpose, we conducted a simple analysis by considering both simulated data and field data.

The simulated high-resolution dataset was generated in the L2 project by identifying four land cover classes according differences in LAI: soil (S0), sparse (V1), medium (V2) and dense (V3) vegetation, and leaf chlorophyll content (LCC) values (Figure 83). Specifically, a synthetic image was generated giving as input for SCOPE around 10,000 different combinations of LAI and LCC in order to simulate several crops at different growing stages. The sun-target-sensor geometry, represented by means of the SZA, was kept fixed, together with the canopy fluorescence quantum yield and the crop type. The SpecFit algorithm was then applied on the simulated incoming and reflected radiances to retrieve the fluorescence and reflectance full spectra. In particular, the fluorescence emission wavelengths position (in the red and far-red) were estimated and plotted along with the spectral indices linked to the chlorophyll content (Figure 84).

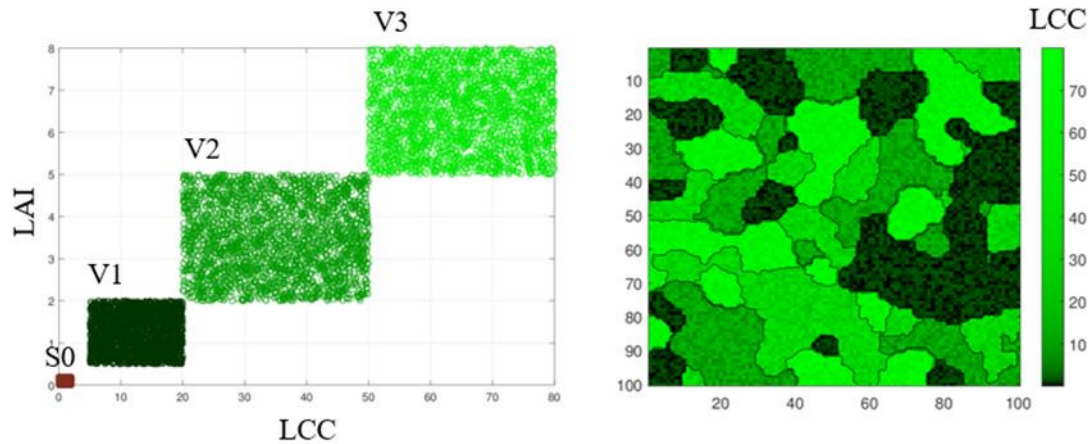


Figure 83: (left) data classes organized according to the LCC and LAI simulated values; (right) synthetic image used in this study (Courtesy L2 study).

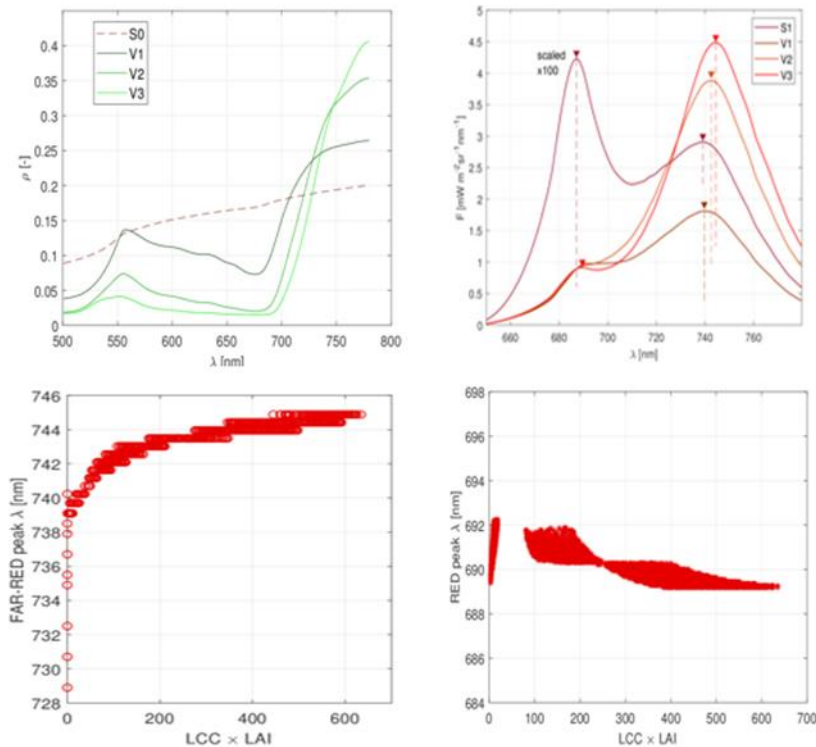


Figure 84: (top) Examples of reflectance and fluorescence simulated spectra. Dashed line in the reflectance corresponds to a soil target and the colors represent chlorophyll content levels; (bottom) wavelength position in the far-red and red.

For increasing LAI x LCC, we notice a clear shift of the $\lambda_{\text{far-red}}$ toward greater wavelengths, with a range in the order of 5 nm, excluding points corresponding to the bare soil case. This evolution, which can be considered as a red shift, stabilizes a wavelength maximum value around 745 nm. Conversely, the λ_{red} behavior is less clear compared with the far-red one. However, if we do not consider the values linked to the soil, we notice a subtle decline of the red-peak position of a few nanometers. Both these trends are linked to the fluorescence re-absorption at the canopy level. For LAI x LCC greater than 70, we observe the highest λ_{red} values (around 691 nm) and the lower $\lambda_{\text{far-red}}$. When the LAI x LCC increase, the re-absorption is expected to increase as well. The fluorescence in the red is then re-absorbed by the canopy. Furthermore, the

fluorescence emission always occurs at a greater wavelength compared with the absorbed one. For this reason, the emission in the far-red increases while the red contribution declines, resulting in a $\lambda_{\text{far-red}}$ red shift. When using field data, the $\lambda_{\text{far-red}}$ seasonal behavior is similar to the one observed in the simulation analysis (Figure 85). Unfortunately, we did not obtain a temporal series of LAI and LCC, so here we used a spectral index proxy of this product instead.

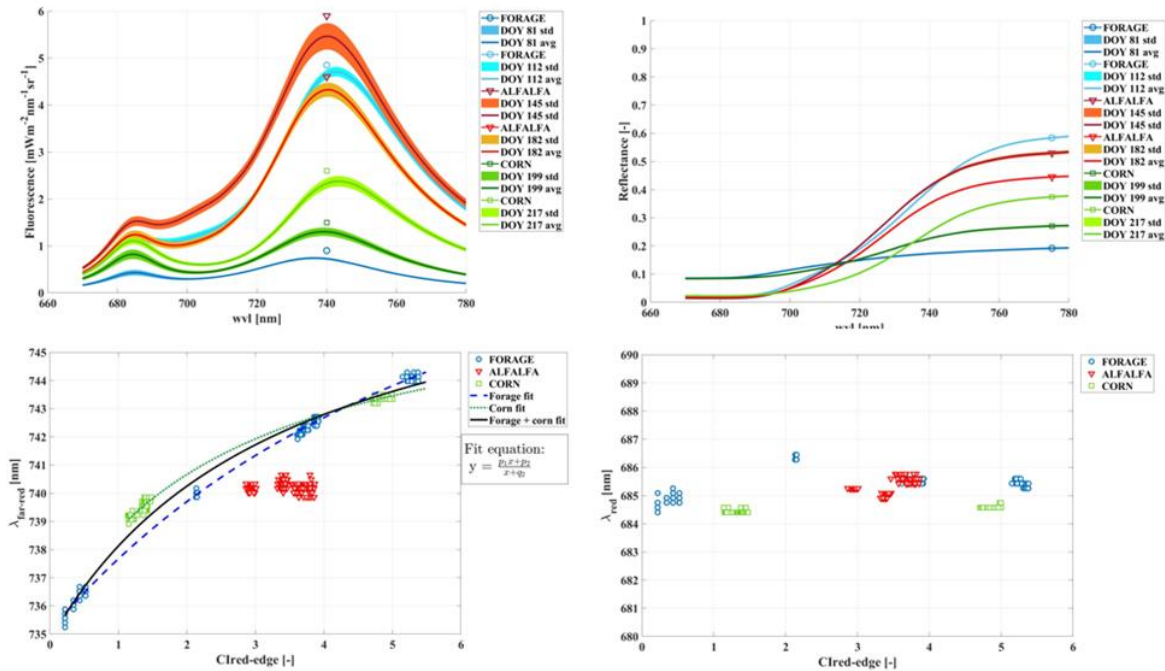


Figure 85: (top) Fluorescence and reflectance spectra averaged around midday. Darker colors correspond to emerging crops, while lighter color to mature stage; (bottom) peak wavelength position evolution in the far-red and red plotted vs the $Cl_{\text{red-edge}}$ spectral index.

A clear shift of the $\lambda_{\text{far-red}}$ was also observed from field measurements. Lower $Cl_{\text{red-edge}}$ values are linked to a bare soil condition. But if we exclude the points characterized by $Cl_{\text{red-edge}}$ lower than 1, the overall $\lambda_{\text{far-red}}$ shift toward greater wavelengths becomes clear. Specifically, forage and corn trend are very similar to simulation results, while alfalfa exhibits a different behavior. As previously assessed, the alfalfa measurements were acquired in a few close days on a crop already in a mature stage. Therefore, all the metrics evaluated show a small degree of time variability. The λ_{red} , by contrast, is almost stable in time. But the forage which accounts for the longer time series, shows a decreasing trend, consistent with the simulated cases. In general, a clear physiological explanation is missing, but it is beyond the scope of this analysis. Further studies are needed to better understand the role of these FLEX products.

7.1.6 Diurnal dynamics of airborne measured SIF and canopy temperature

On two particular days (18 and 20 July 2018), the weather conditions allowed a high concentration of flights. This permitted the creation of an almost complete daily cycle of both thermal (TASI) and hyperspectral (*HyPlant*) data for selected ROIs. They were focused either around fixed or ground transects measurements or on areas that were relevant from a land cover point of view (e.g. full vegetation cover, bare soil). The flight pattern for both sensors is presented in Figure 86.

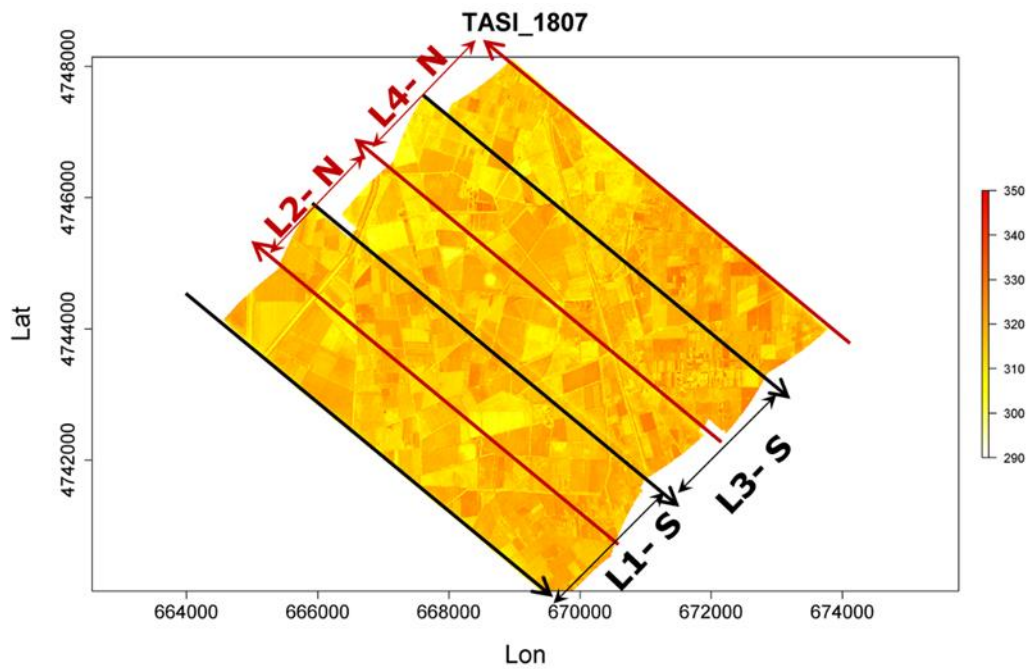


Figure 86: Flight pattern for TASI.

One daily course was built for a special case in the pivot area in an attempt to capture the water stress behavior of the vegetation because of the pivot malfunction (Figure 86 and Figure 87). As observable in the figures below, the thermal images clearly capture the differences in LST between the irrigated and the non-irrigated part of the pivot. By contrast SIF, measured by *HyPlant* did not show a clear difference between the irrigated and non-irrigated field. This may be the effect of a non-full vegetation fractional cover or the result of the soil component contributing to the differences in LST (Figure 87 - lower panels) but not being accounted for in the fluorescence signal (Figure 87– upper panels).

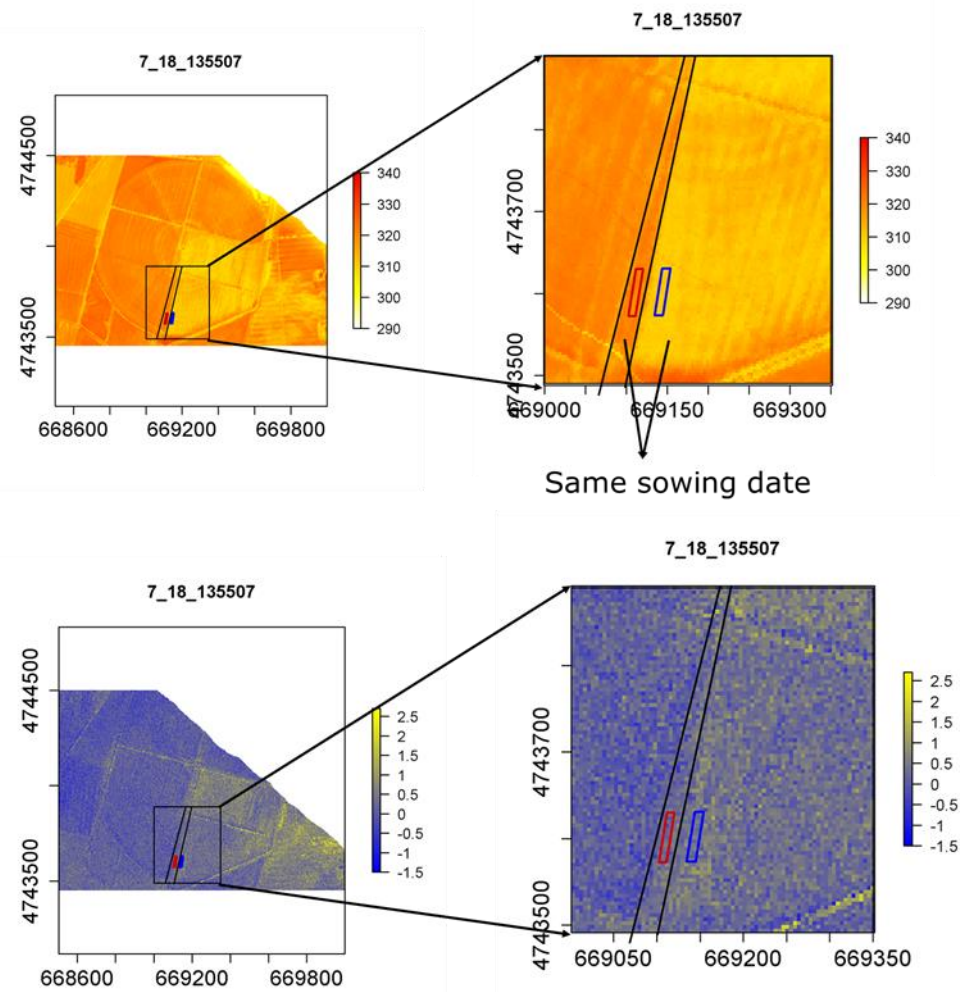


Figure 87: Selection of the ROIs in the pivot area overlapped on a TASI image from 18 July 2018 (upper panels) and over the *HyPlant* image for the 760 nm peak (lower panels) recorded during the same flight line.

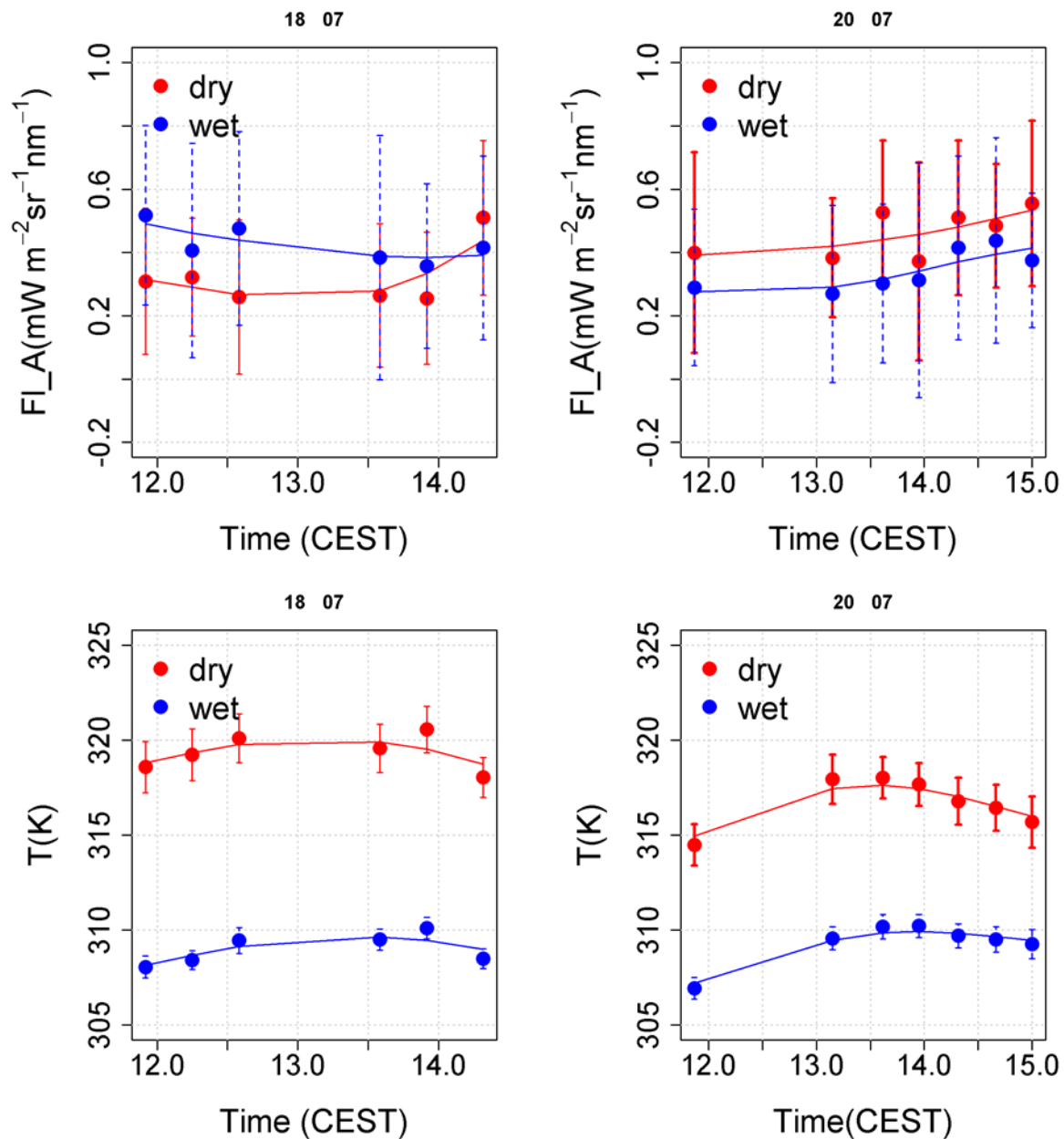


Figure 88: Mean values for the selected region of interest for 18 and 20 July 2018: SIF (at 760 nm measured with *HyPlant*) - upper panels, LST measured by TASI - lower panels. In both days, only scenes with no clouds or clouds shadows were considered.

All the flight lines reported here (for 18 and 20 July 2018) are part of SurfSense. A much more detailed analysis that includes LST and ET estimation, LST ground validation, or a sensitivity analysis of atmospheric correction on LST retrieval is included in the SurfSense final report([RD-04]). The following section provides a short summary of the results from the SurfSense campaign.

7.1.7 Outcomes of the SurfSense campaign 2018 in Grosseto, Italy (summary of main findings)

The content of this section is a summary of the main findings of the SurfSense campaign. More details can be found in the SurfSense final report ([RD-04]).

Objectives

The SurfSense campaign was done to collect LST in Grosseto, Italy ([RD-04]). The activity is embedded in the Copernicus Candidate High Spatio-Temporal Resolution Land Surface Temperature Monitoring (LSTM) mission to address water, agriculture and food security issues by monitoring variability of LST.

The campaign shall provide feedback to the Agency:

1. On the impact of the revisit period and the overpath time for specific priority applications including accuracy of daily ET estimates under partly cloudy and sunny conditions.
2. On the impact of spatial resolution by addressing relevant field.
3. On the impact of different number of bands and related impact on product accuracy.
4. In addition, the campaign will focus on the sensitivity to systematic and random errors separately (to correspond to the MRD) for the different applications.
5. For daily ET, the demonstration will focus on how accuracy decreases beyond acceptable level and the evaluation for the foreseen error limits per pixel, per land-use class, at field scale, etc.

Summary

The SurfSense campaign was successfully carried out during the intensive period of measurements recording a high quality in-situ and airborne data. Thermal in-situ measurements in Grosseto were taken for each flight pass over almost eight days in which an LSE characterization of different surfaces, including bare soils and vegetation covers, were provided. Continuous radiometric data measured by fixed station and through transects were also recorded. All the data are now available in the database; a quick summary is detailed in Table 17 and Table 18.

Table 17: Data summary.

No. LSE targets		10
No. LSE measurements		350
No. LST Transects		25
Total no. LST values acquired in the coincidence flight pass	Transects	> 1500
	Fixed stations	> 1000

Table 18: Summary of data acquisition flights for SurfSense.

Date	Registration	DEP	ARR	Flight Time	No. of S-3P Patterns	Front Inst.	Rear Inst.	Remark
17.7.2018	OK-CZG	10:30	11:25	0:55	0.5	HyPlant	TASI/Q780	lines 3 and 4
18.7.2018	OK-CZG	9:35	13:40	4:05	9	HyPlant	TASI/Q780	lines 3,4,1,4
19.7.2018	OK-CZG	10:30	11:13	0:43	1	HyPlant	TASI/Q780	
20.7.2018	OK-CZG	9:32	13:40	4:08	7	HyPlant	TASI/Q780	
21.7.2018	OK-CZG	12:40	13:28	0:48	1	HyPlant	TASI/Q780	
22.7.2018	OK-CZG	9:30	10:45	1:15	1	HyPlant	TASI/Q780	lines 2,3
24.7.2018	OK-CZG	12:18	13:03	0:45	1	HyPlant	TASI/Q780	

Different TIR bands configurations for TES algorithm application were compared in terms of LST. They showed minor discrepancies (around 0.5 K) mostly due to small differences in emissivity estimation. It is important to note that TES algorithm is designed to work over all kinds of natural surfaces and especially over areas with high spectral contrast, which is not the case for the Grosseto area. For that, it is more or less logical to expect similar results regardless of the number of TIR bands used because the emissivity effect is not important over these kinds of areas (Sobrino et al. 2008). Only 24 configuration bands for TES application were only selected in order to avoid the noisiest bands and to obtain smoother emissivity spectrum retrieval. Figure 89 shows an example of the radiosondes acquired on 18, 19 and 20 July 2018, air temperature and relative humidity vertical profiles were obtained at noon.

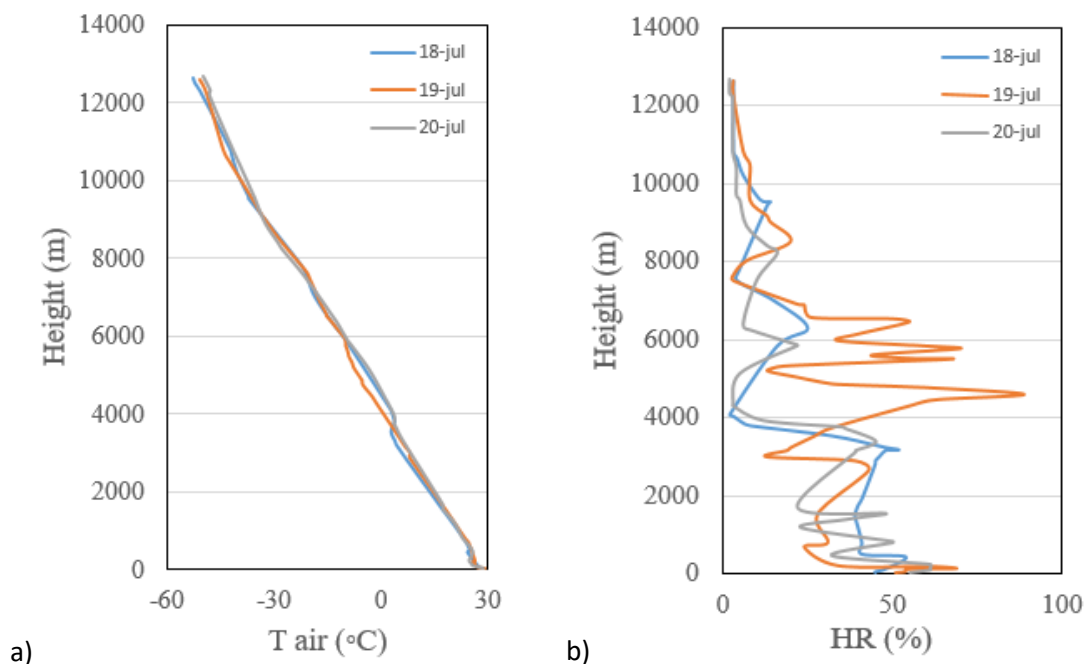


Figure 89: Air temperature (a) and relative humidity (b) on 18, 19 and 20 July 2018 were obtained at noon from the LIRE station.

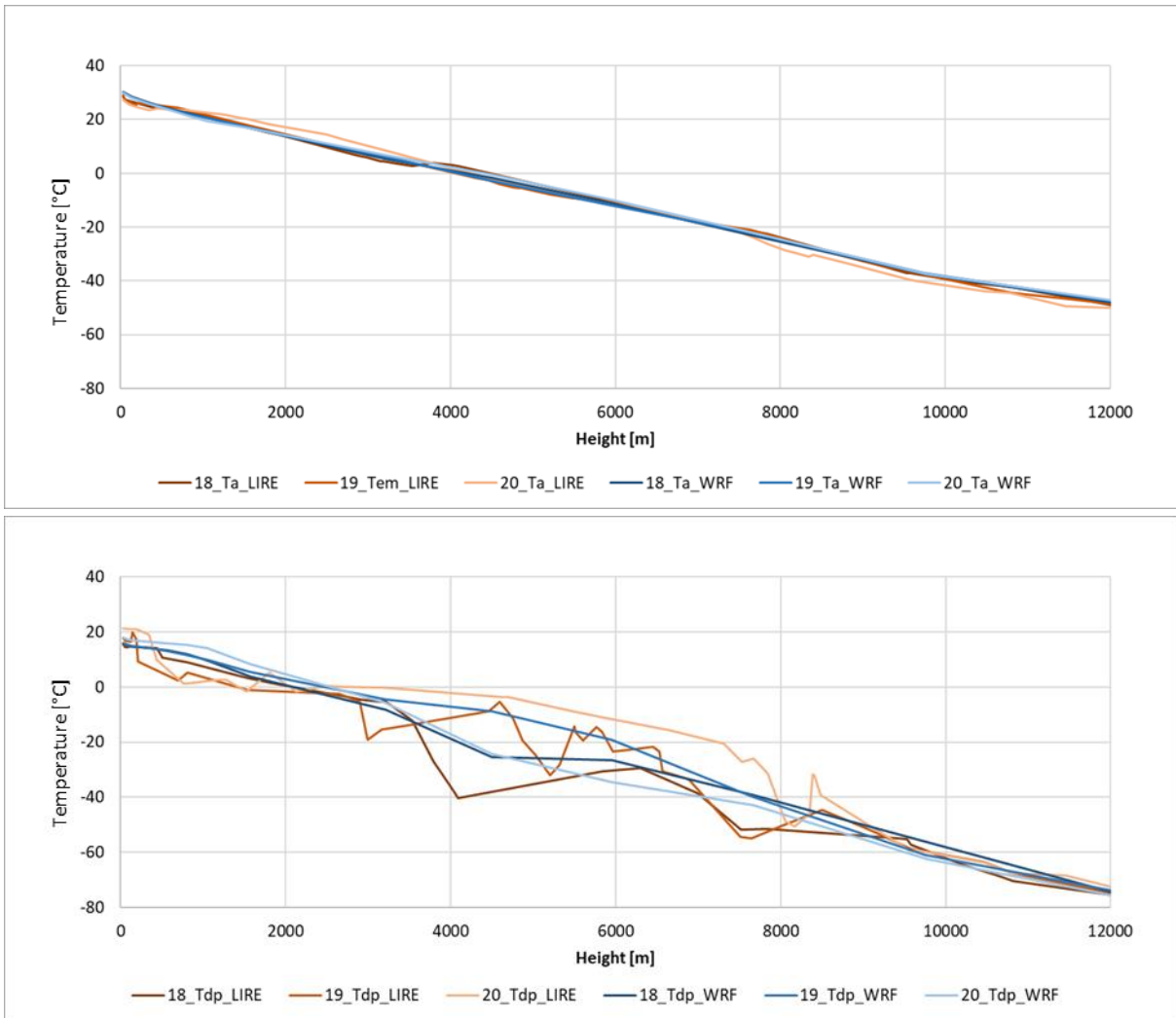


Figure 90: Profiles of air temperature (Ta) and dew point temperature (Tdp) on 18, 19, and 20 July 2018 for the LIRE station and WRF model.

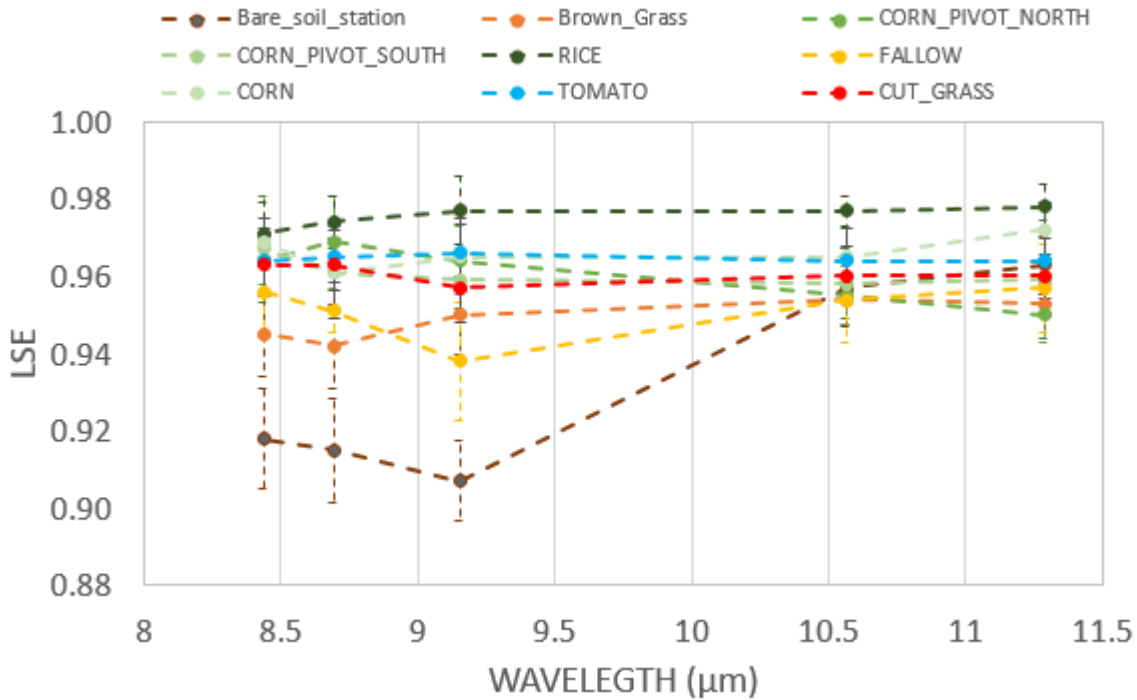


Figure 91: Emissivity of surfaces measured during the campaign.

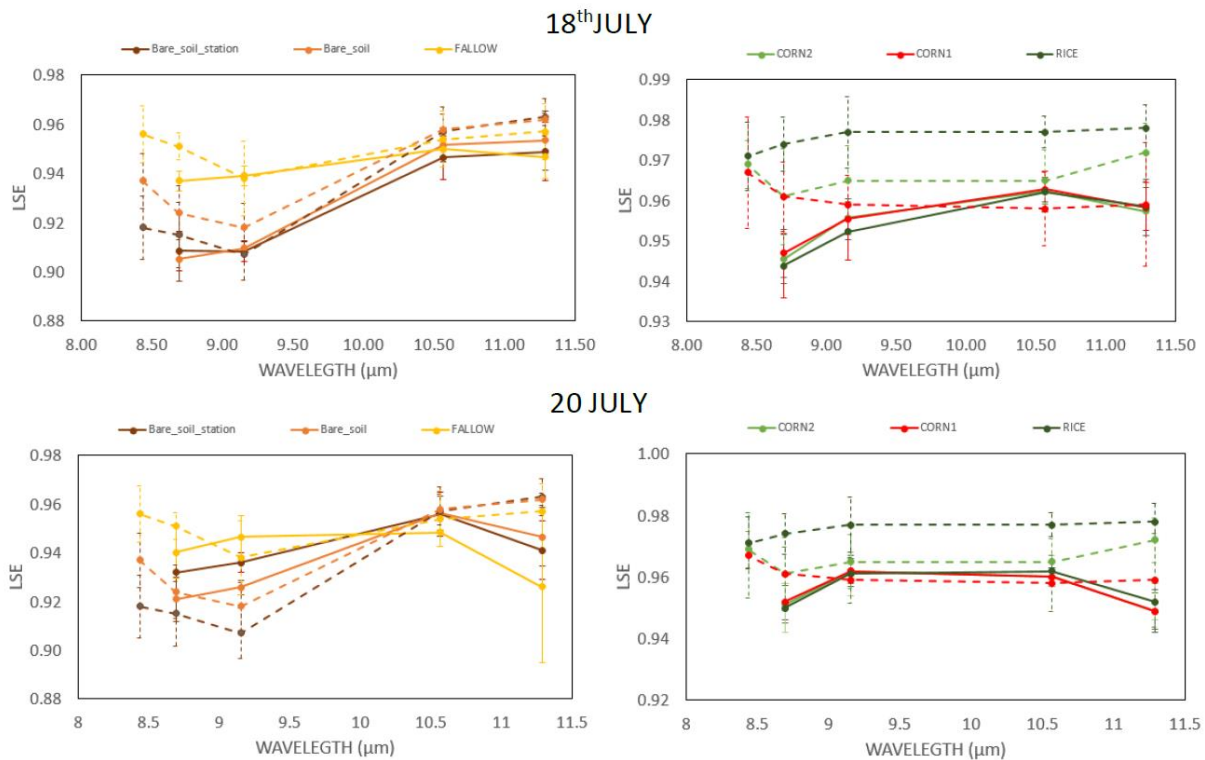


Figure 92: Comparison between emissivity retrieved with the TES algorithm (continuous line) and emissivity measured in-situ (dotted line) over three bare soils (left) and vegetated (right) samples. Uncertainties for emissivity are represented with vertical bars.

Using the in-situ database as a reference, TASI processed imagery was atmospherically corrected with LIRE sounding. The imagery showed a good correlation for vegetation and water (below 1.5 K) and higher discrepancies for bare soil areas (in some cases above 2.0°K, especially for 20 July 2018). Another atmospheric profile (WRF data) was used for LST and LSE estimation, which in some cases provide better accuracies for

bare soils but poor results for vegetated areas. This atmospheric indetermination is one of the main contributions in the LST uncertainties retrieved by TES algorithm. The study team recommend the use of in-situ radio soundings because the inaccuracy of atmospheric profile estimations can lead to important uncertainties. Different atmospheric profiles show LST estimation differences of 4 K on hot surfaces. Regarding LSE values, uncertainties of 0.01 - 0.02 have been retrieved. These values, in general, are within the errors of both, in-situ and airborne measurements.

Figure 93 represents the general schedule of in-situ measurements during the campaign. The map shows fixed stations, fixed CIMEL measurements, and transect data, which are represented by circles, triangles and arrows, respectively.

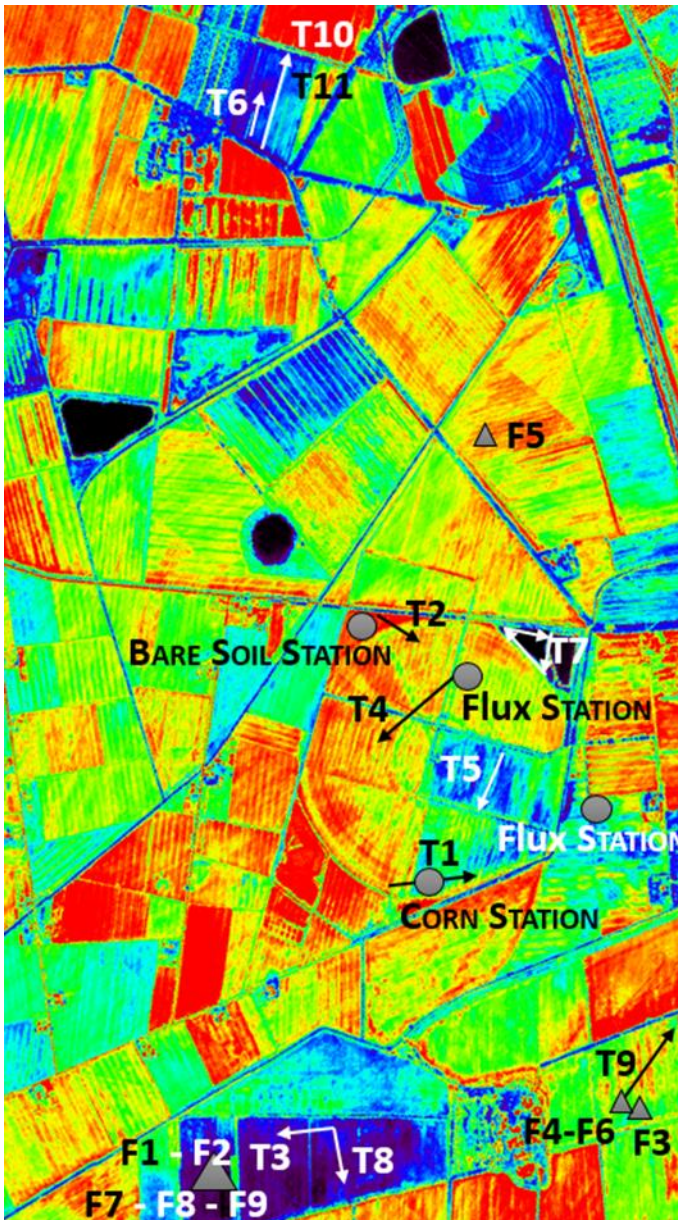


Figure 93: TASI thermal image of the Grosseto test site. Image shows transects (T) and fixed (F) measurements performed during the campaign.

Fix station data are represented in Figure 94 in UTC time. The acquisition data points are shown in Figure 93.

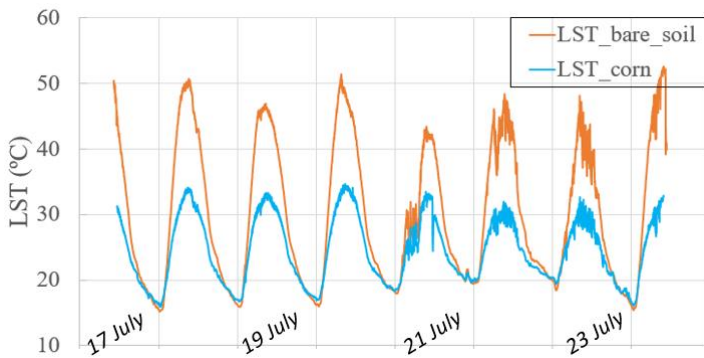


Figure 94: LST data acquired by fixed stations on bare soil and corn area. Location of stations is provided in Figure 93.

One main objective of the study was to provide an estimation of the energy balance budget for vegetated plots. TES estimations with LIRE atmospheric correction, which have shown a higher accuracy over these areas, were used for LE and energy balance estimations. The S-SEBI method has shown acceptable results with a RMSE of 50 Wm^{-2} when compared to in-situ EC measurements over alfalfa area. The stability of the method for different overlaps was tested over four vegetated points. It showed good results with mean differences below 40 Wm^{-2} . Differences are more important when clouds appear in the image, because the S-SEBI method makes use of all available pixels of the image. If a cloudy pixel is introduced in an LST-albedo scatterplot, which can be the case of some images, the precision of Λ estimation is affected and then differences can appear in LE estimation.

Figure 95 and Figure 96 present the LST validation for the two largest days of the campaign (18 and 20 July 2018). TASI values were obtained as the average value of a 3x3 m pixels window.

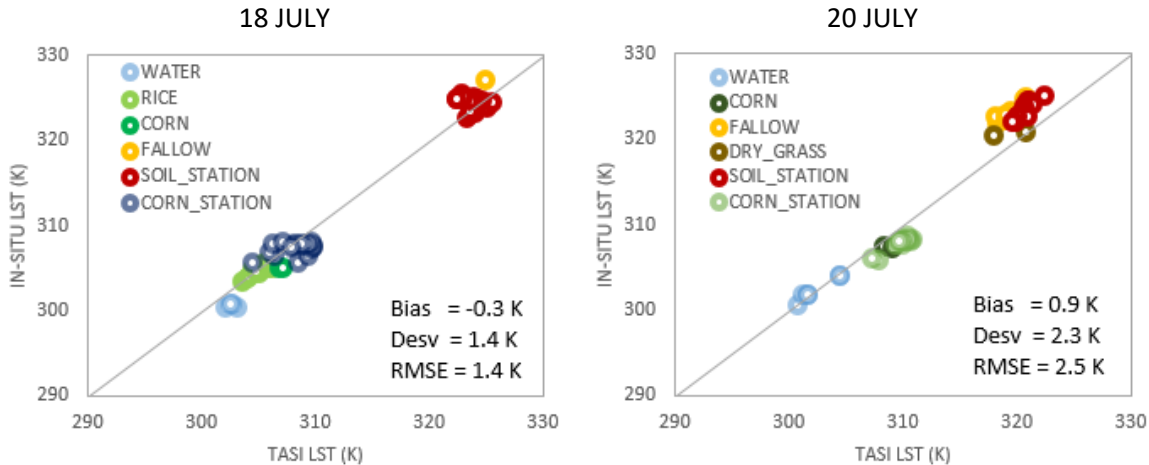


Figure 95: Assessment of LST retrieved with LIRE sounding versus the in-situ LST measured by UVEG.

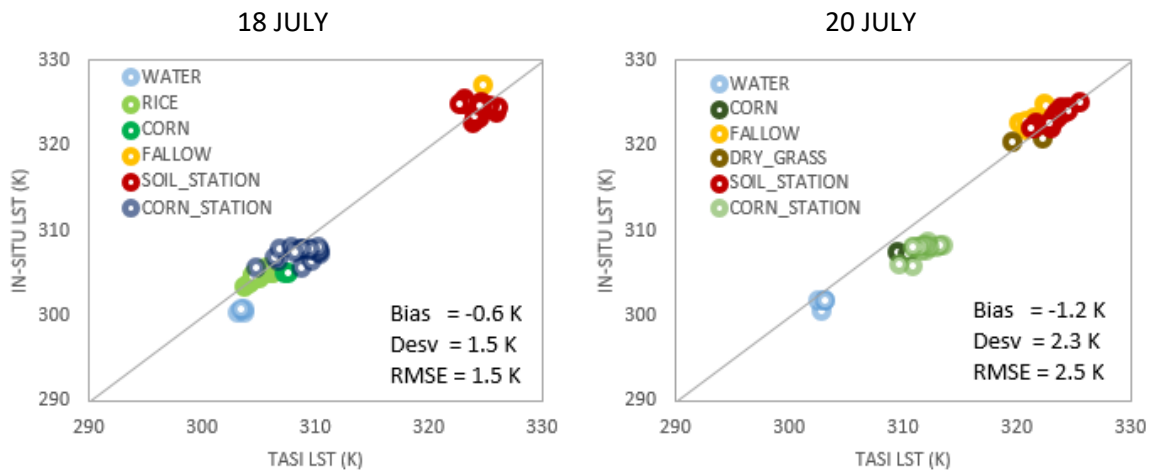


Figure 96: Assessment of LST retrieved with WRF profiles versus the in-situ LST measured by UVEG.

Regarding diurnal ET estimations, the time of image collection (between 10:00 and 14:00 UTC) seems not to be important for ET_d because similar results were obtained for all images from 18 July 2018. A standard deviation of 0.35 mm/day is retrieved over the same area mostly due to variations in instantaneous LE values during the day. The key factor for accurate ET_d estimations is the use of clear sky images. When cloudy pixels are introduced in the image (because of inaccurate cloud masking), lower daily ET estimations are obtained. Figure 97 shows an illustrative example of energy balance data outputs retrieved with S-SEBI. Images are a composite of four flights between 10:00-10:20 UTC. Results show instantaneous LE values of 350 - 550 Wm^{-2} for vegetated areas which, when transformed to daily ET values, range between approximately 4 and 6 mm per day depending on vegetation type.

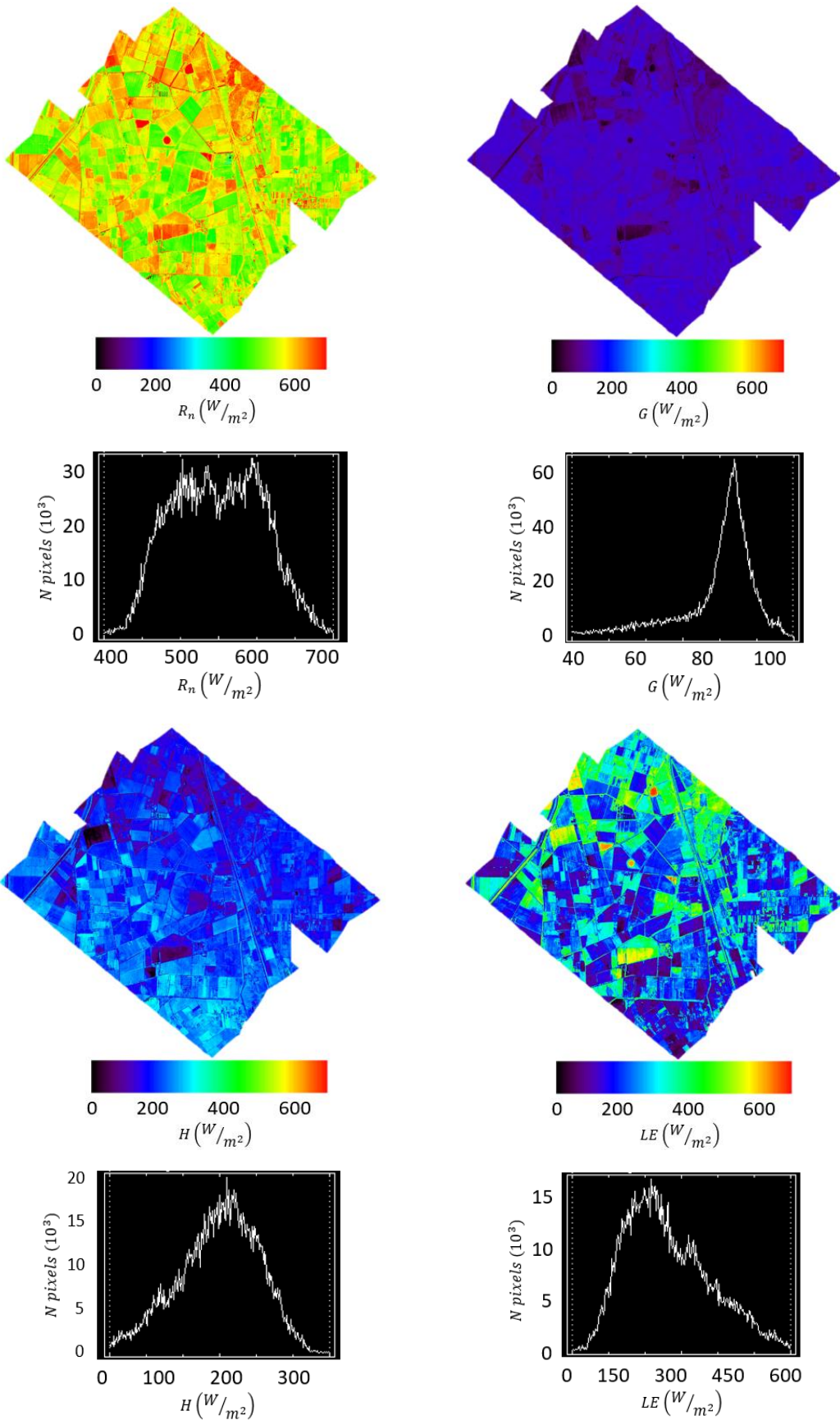


Figure 97: Net radiation (R_n), conduction flux in the soil (G), (H and LE including its histograms). The components of the energy balance equation were estimated for a composite of four flights between 10:00-10:20 UTC.

	Doc.: Final Report		
	Date: 29 July 2021	Issue: 2	Revision: 1
	Ref.: ESA Contract No. 4000125402/18/NL/NA		Page: 131 / 288

Finally, the use of 18 July 2018 data for energy balance appears more accurate because it shows better assessment for all data. 20 July 2018 imagery can be used with caution as validation shows an inaccuracy above 2°K for bare soils.

7.2 Selhausen and Jülich, Germany

Part of these data are used for a scientific publication. More details on the data and an extended scientific discussion can be found in this publication (Attachment 12.1).

Vila-Guerau de Arellan J., Ney P., Hartogensis O., de Boer H, van Diepen K., Emin D., de Groot G., Klosterhalfen A., Langensiepen M., Matveeva M., Miranda G., Moene A., Rascher U., Röckmann T., Adnew G., Brüggemann N., Rothfuss Y. & Graf A. (2020). CloudRoots: integration of advanced instrumental techniques and process modelling of sub-hourly and sub-kilometre land-atmosphere interactions. *Biogeosciences*, 17, 4375-4404

[50.87N, 6.45E]

The study sites near Jülich, Germany were initiated during the Transregional Collaborative Research Centre 32 (TR32 - Patterns in Soil-Vegetation-Atmosphere Systems). This interdisciplinary research consortium was funded by the German Research Foundation (DFG) 2007 – 2018. During these years, a highly instrumented long-term observation site was established with a focus on developing a better characterization of the spatio-temporal structures and patterns within the soil-plant-atmosphere continuum with the goal of generating a deeper qualitative and quantitative understanding of the soil vegetation atmosphere system. In this context, the consortium focused on the analysis of H₂O and CO₂ fluxes across a large range of space and time scales (Simmer et al. 2015). Even though the consortium ended in 2018, national and institutional funding is continuing to ensure a dense network of atmospheric and vegetation-monitoring systems, which in combination with a good knowledge of the agricultural management in the region, provides an excellent research area with high-quality data.

The Rur catchment is the central research area of the consortium. Covering an area of approximately 100 x 40 km, the site is an anthropogenically influenced area consisting of different ecosystems, including intensive agricultural, managed pine and mixed forest, natural grasslands, and swamp areas. The catchment of the Rur extends over 2354 km² and is mainly situated in Western Germany, with about 157 km² (6.7%) extending into Belgium and about 108 km² (4.6%) into the Netherlands (Figure 98; further information can be found at <http://tr32new.uni-koeln.de/> and in Simmer et al., 2015). The site is equipped with a dense network of meteorological measurement stations complemented by several eddy flux towers. Additionally, since 2012, the *HyPlant* sensor has mapped a core region (app. 15 x 10 km) of the study area every year ([RD-10]). The flight pattern was comparable in the past years and, in 2018, covered an area around Jülich as shown in Figure 99. This flight pattern covered various ground-based measurements of SIF, three EC stations, and a detailed soil and soil moisture mapping from the 2018 SARSense campaign ([RD-05]).



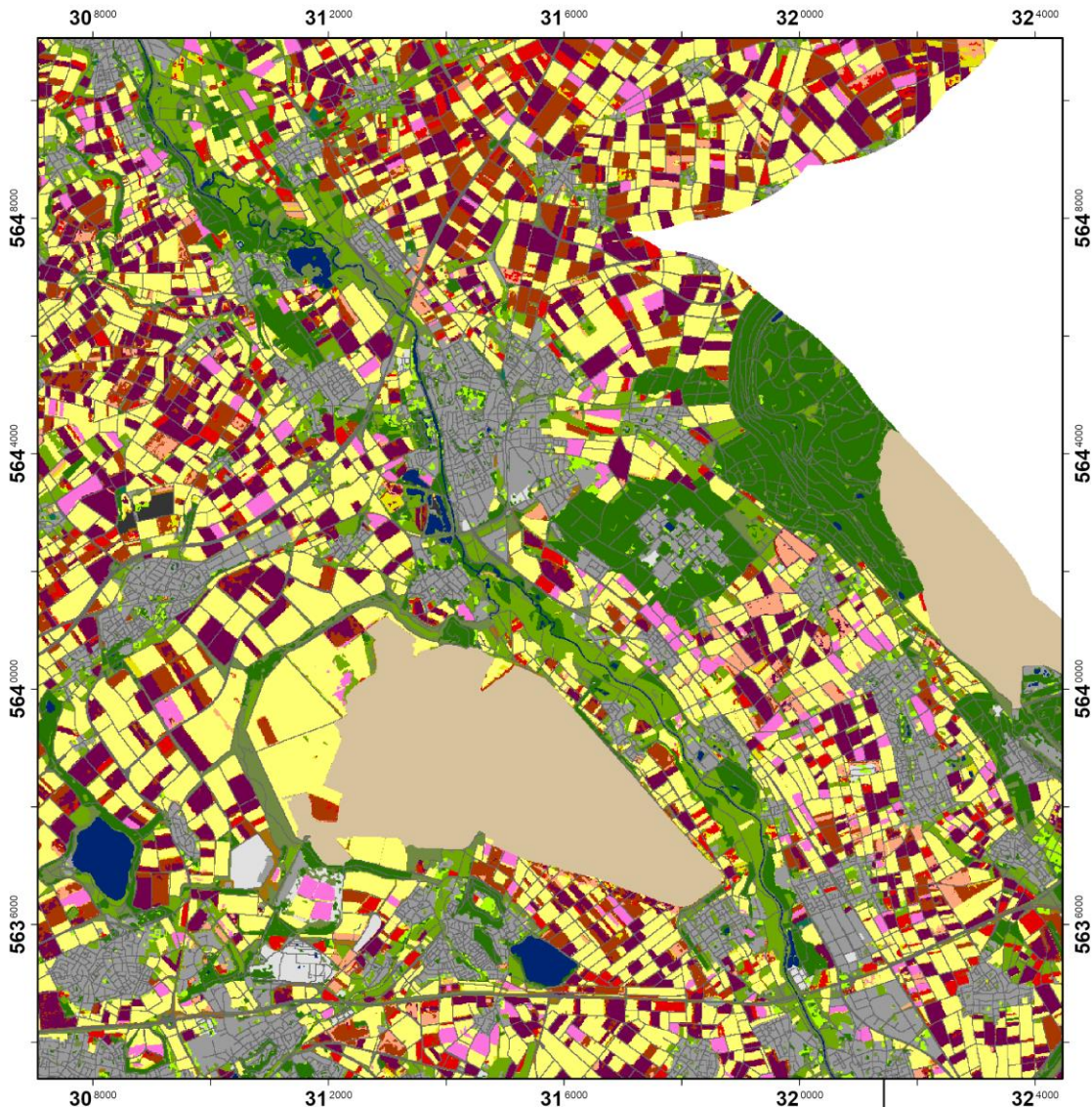
Figure 100: Flight lines to cover a central area around Selhausen (the core site with the ICOS eddy tower and a FloX system) with the airborne high-performance imaging spectrometer *HyPlant*. Flight lines were stitched to produce a 1-meter resolution map of this special focus area.

7.2.1 Mapping the spatial variability of sun-induced fluorescence and canopy traits in a large agricultural region

The study area around Jülich was mapped in previous campaigns. Data thus acquired were used to analyze the correlations between various vegetation indices and SIF (Matveeva et al. *in prep.* for submission). In these previous studies, we identified and classified the main agricultural crops (sugar beet, potatoes, and corn) and the forest area. Furthermore, we showed that the correlations between SIF and reflectance-based vegetation indices are greatly dependent on the crop type. In 2016, almost 650 single fields were analyzed and used to quantify heterogeneity in between fields.

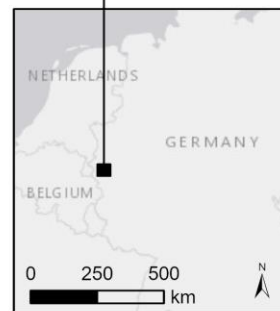
We repeated a similar flight pattern to cover the large dynamically changing agricultural area in order to facilitate, among other things, long-term evaluation of the dynamics of vegetation based remote sensing data in a representative agricultural region. The area was mapped on 26 June 2018 and the data were of high quality. All *HyPlant* products could be produced, i.e. the full set of vegetation indices from the DUAL module (Figure 103); the red- and far-red fluorescence products, which were for the first time generated by the two retrieval schemes, namely iFLD and SFM (Figure 104 and Figure 105); and a map of LST (Figure 106, left panel). These momentary measurements were complemented by a validated land-use classification (Figure 101) and a DEM, which was recorded simultaneously with the optical data (Figure 106, right panel).

From the visual inspection, it became clear that the whole study area was covered under clear and stable illumination conditions and the RGB composite gives a very clear impression of the study area where no patterns in illumination conditions are visible (Figure 102).



Legend

- | | |
|---|---|
|  Potato |  Forest |
|  Maize |  Water |
|  Sugarbeet |  Open-cast mine |
|  Cereals |  Urban green area |
|  Rapeseed |  Urban area |
|  Other crops |  Roads |
|  Grassland |  Power station, sewage treatment, waste disposal facility etc. |



Esri, HERE, Garmin, (c) OpenStreetMap contributors, and the GIS user community

Data source: Lussem, U., Herbrecht, M. (2019): Land use classification of 2018 for the Rur catchment. doi: 10.5880/TR32DB.38.

Cartography: U. Lussem, 2020-01-21

Figure 101: Land cover classification of 2018 for the Rur catchment. The land cover map was produced by Ulrike Lussem, University of Cologne⁸.

⁸ This map is not included in the data from this campaign and the map is copyrighted by Ulrike Lussem. Please contact her for access and usage permission.

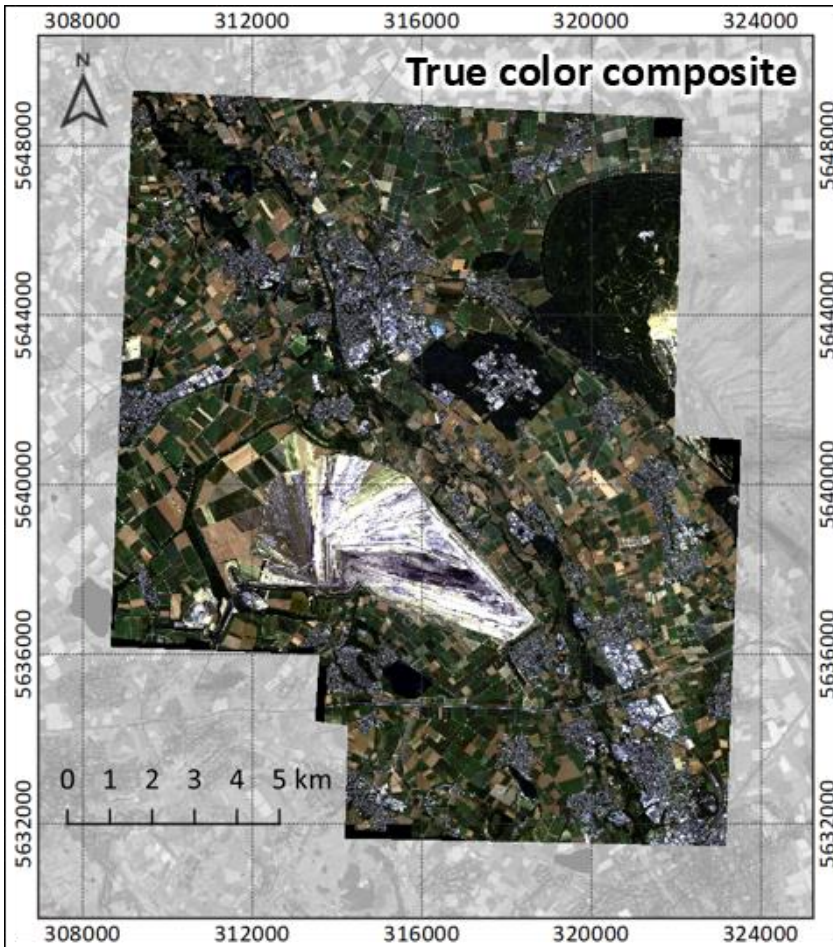


Figure 102: True color composite of the large study region demonstrating the good and stable measurement conditions. Data were acquired by 17 parallel north-south oriented flight lines on 26 June 2018.

Looking at the set of vegetation indices, it becomes clear that the different types of land-use in this agricultural area also produces a small-scale pattern of different fields and vegetation types (Figure 103). Different crop types are contrasted in different vegetation indices and the forested areas in the scene are also clearly separated and visible in the vegetation indices. The parallel evaluation of the selected vegetation indices demonstrates the complementary nature of greenness-based vegetation indices (SR, NDVI, EVI) on the one hand, and the more physiologically linked PRI.

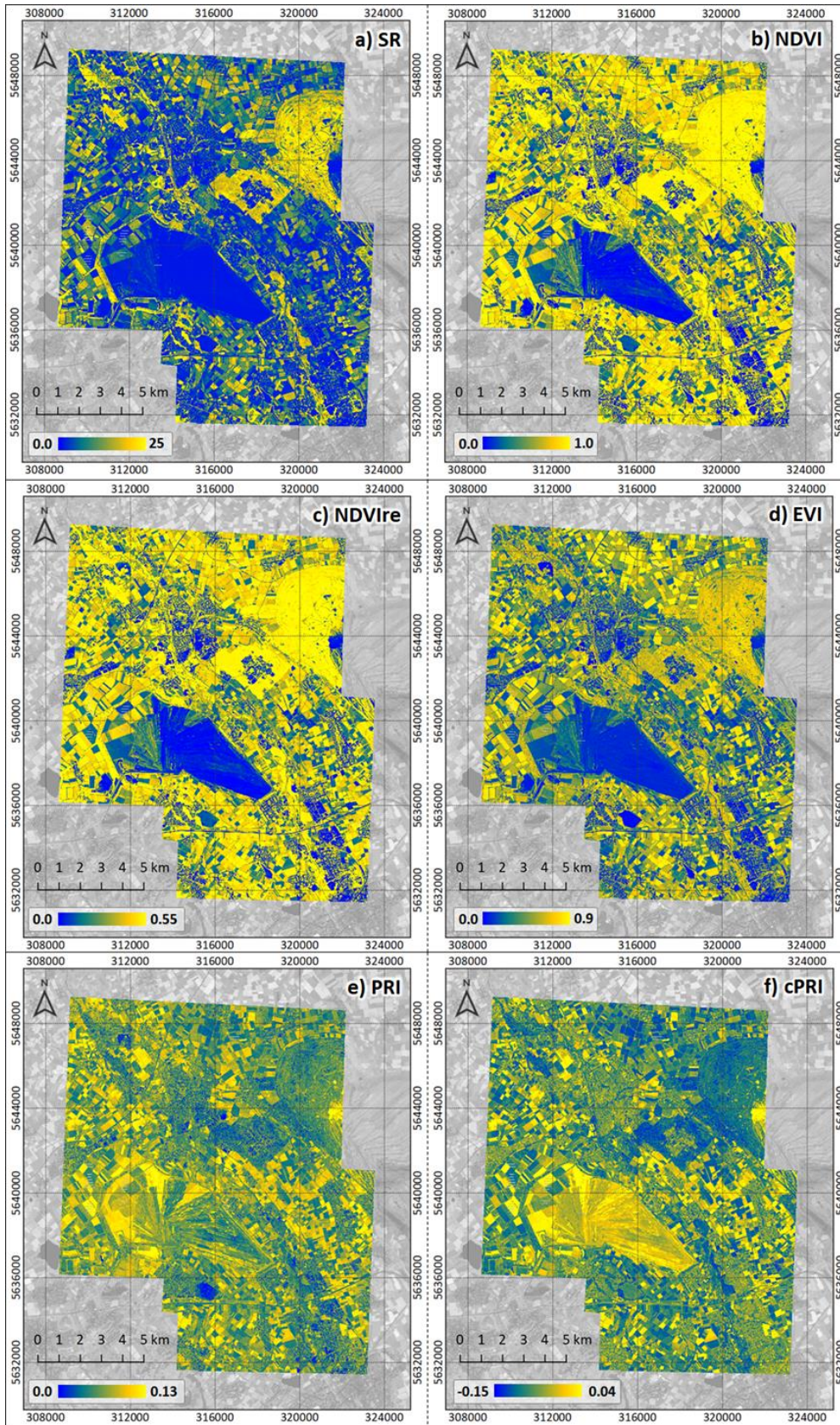


Figure 103 Maps of selected vegetation indices from the large agricultural map around Jülich. The vegetation indices were derived from *HyPlant* DUAL module for each single flight lines. Flight lines were then stitched together to produce the large map. a) SR, b) NDVI, c) NDVI_{re}, d) EVI, e) PRI and f) corrected PRI (cPRI).

The SIF maps show a different spatial pattern compared to the vegetation indices as already indicated visually by the different nature and information content of SIF and reflectance-based vegetation indices (Figure 104

and Figure 105 vs Figure 103). With the SIF maps, a clear difference between the central part of the study region and its east and west borders becomes visible, and, in general, higher fluorescence values are recorded in the center of the study region. This large-scale difference may be related to different soil types and thus different plant performance, or may be related to the slight elevation differences prevailing in the study region (Figure 106, right panel).

Another interesting option in this data set is the possibility to compare the regional patterns of red and far-red SIF and also to compare the results that are obtained by the iFLD and the SFM retrieval method. Comparing the results of the two retrieval methods, it is clear that the principal patterns in the study region are visible in both retrievals. However, after looking at single fields, clear differences also exist, and individual fields may show greatly different SIF values depending on the retrieval method. Additionally, the SFM method seems sharper, field borders are represented with greater clarity, and the results seem slightly more plausible. We currently take this as an indication that our new SFM retrieval approach performs at least as well as the iFLD method and that the SFM may even produce better results than the iFLD.

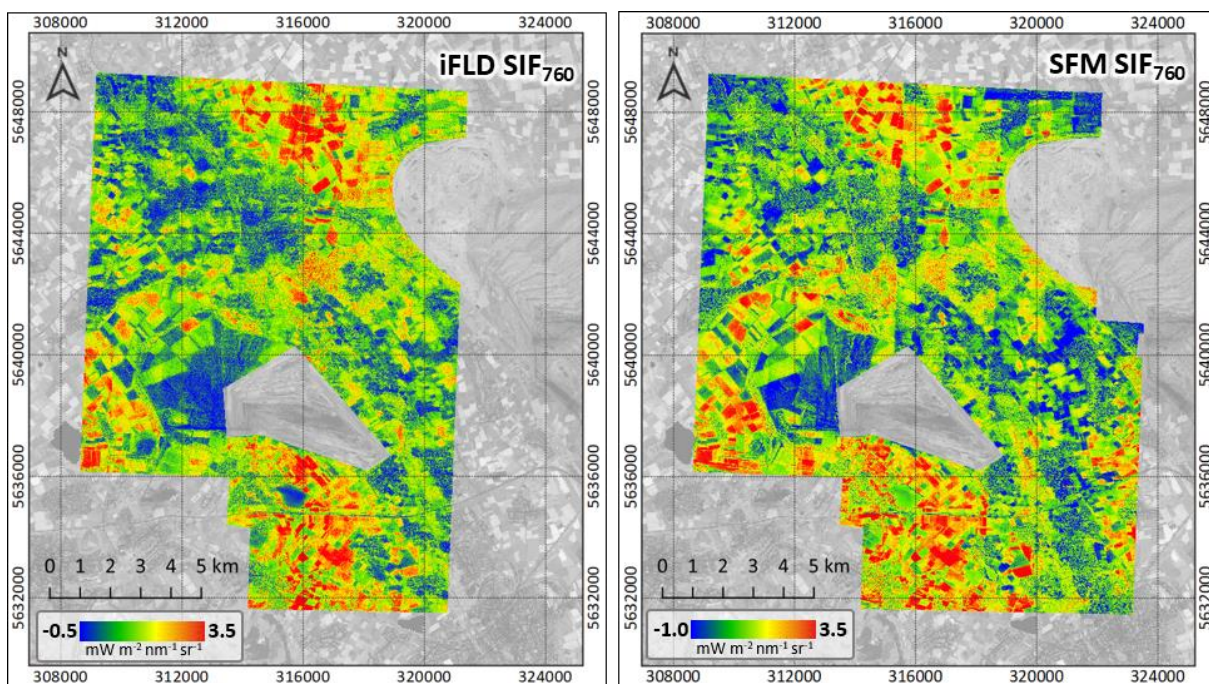


Figure 104: Map of SIF at 760 nm, which was calculated by the iFLD retrieval method (left) and the SFM (right). The map was composed of 17 parallel flight lines, which were processed individually and then registered to a large overview map with a pixel resolution of 3 x 3 m. The areas within the open brown-coal pit mines (several meter-deep holes) and the mine tailings (mountain on the upper right corner of the study region) were masked out in the SIF maps as the SIF retrieval is not yet adapted to derive valid SIF results in hilly terrain.

As already reported in previous studies, SIF₇₆₀ shows more contrast between different fields and land-use classes than SIF₆₈₇ (compare Figure 104 and Figure 105). The generally higher SIF values in the middle of the study region are also seen in SIF₆₈₇, but heterogeneity between single fields is less pronounced, even though different vegetation types can still be separated in the SIF₆₈₇ maps.

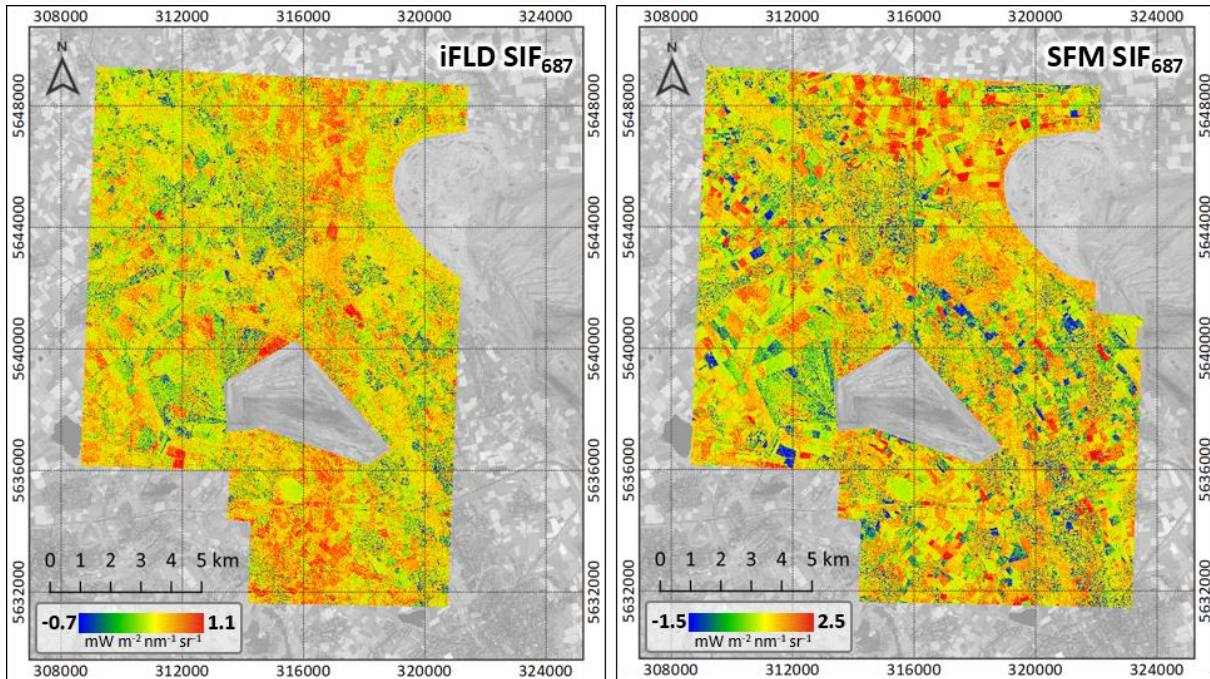


Figure 105: Map of SIF at 687 nm, which was calculated by the iFLD retrieval method (left) and the SFM (right). The map was composed of 17 parallel flight lines, which were processed individually and then registered to a large overview map with a pixel resolution of 3 x 3 m.

In addition to *HyPlant* data products, thermal images and LiDAR data are also available from all *HyPlant* overpasses. As surface structure does not change during the relatively short time window of this campaign, we only processed one set of LiDAR data and provide one DSM and one DEM with this data set. This data set was produced from the large map (TR-32 flight pattern) and thus covers the extended region around Jülich and Selhausen. Therefore, it also includes all study areas on the ground (Figure 106). LST was derived from the TASI instrument and LST was calculated according to standard settings for atmospheric correction and emissivity. A detailed assessment of the temperature products of the TASI sensor used during this campaign was performed in the frame of the SurfSense campaign activity and details can be found in the reports of this campaign ([RD-07]). However, this map from the Selhausen area is not validated since ground validation was only done at the Italian site. Nevertheless, we expect that relative temperature differences should be correct; however, absolute values may deviate up to 3°C.⁹

⁹ The TASI performance and data products were carefully evaluated during the SurfSense campaign, which took place during the same time window as the FLEXSense campaign. Main SurfSense activities (including ground validation) took place in Grosseto, Italy. Based on these activities, we know that absolute values of LST from TASI may show variations of up to 3°C depending on the atmospheric parameters. Relative values within the flight lines are stable, however. Thus, for the Jülich / Selhausen maps a bias of ± 3°C is possible.

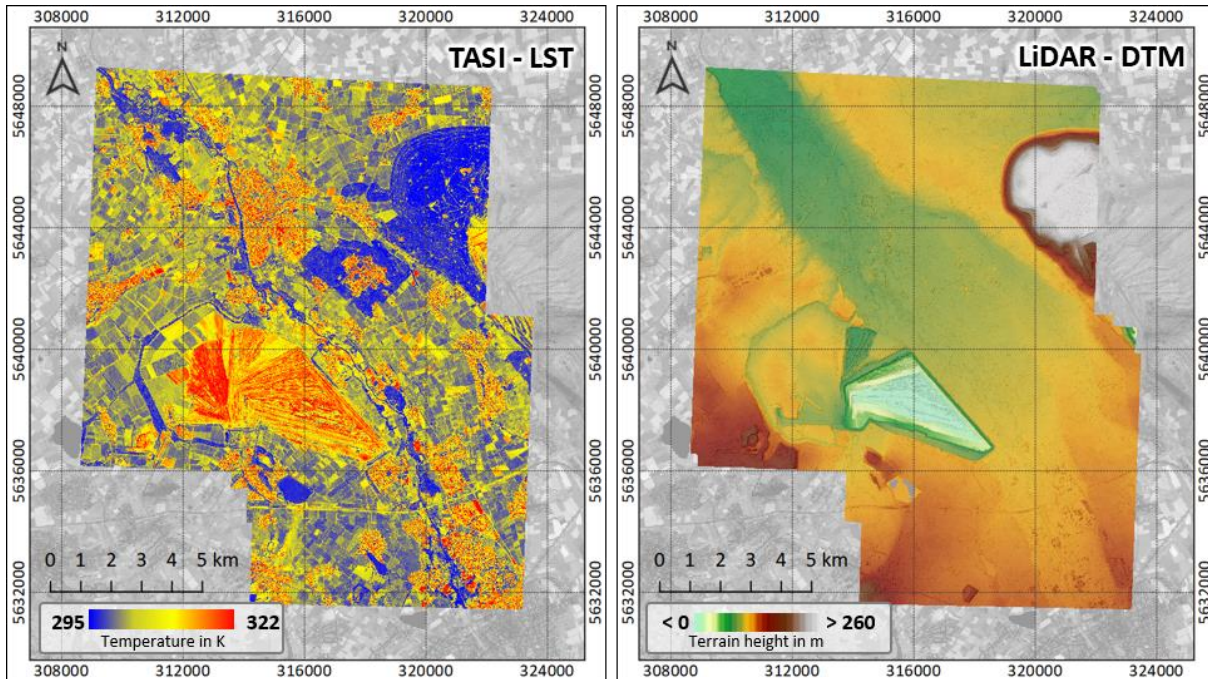


Figure 106: LST map that was calculated from the TASI hyperthermal imaging data (left) and a DTM that was recorded with the Rigel LiDAR scanner (right). The map was composed of 17 parallel flight lines, which were processed individually and then registered to a large overview map.

Recommendations for further analysis of this data set

The study area around Jülich was mapped in previous campaigns. The data thus acquired were used to analyze the correlations between various vegetation indices and SIF (Matveeva et al. *in prep.* for submission). In these previous studies, we identified and classified the main agricultural crops (sugar beet, potatoes, and corn) and forest areas. Furthermore, we showed that the correlations between SIF and reflectance-based vegetation indices is greatly dependent on the crop type. In 2016, almost 650 single fields were analyzed and used to quantify heterogeneity in and between fields. We currently analyze the 2018 campaign data with the aim of extracting general themes, which will finally be used to scale single field properties to large scale FLEX pixels. During this upscaling to 300 x 300 m pixels, various vegetation types need to be averaged, and it is currently being discussed which scaling approaches (linear or non-linear scaling properties) have to be used (Liu et al. 2019).

Based on visual inspection, it is already obvious that patterns of different vegetation indices and SIF patterns are associated with different vegetation types (Figure 101). However, more subtle differences can be expected. Accordingly, a more detailed correlation analysis between reflectance-based vegetation indices and SIF was undertaken using this data set. This allow us to compare 2016 to 2018 data and to identify common themes and environment-specific features. Synergies are also expected from the currently running PhotoProxy project as this data set was identified as core data set for the study ([RD-06]).

7.2.2 Understanding spatial heterogeneity of SIF from the single pixel to the field

During the 2018 campaign, two time periods provided the unique opportunity to have very complete data sets, including: (i) the biophysical properties of various fields including the within-field heterogeneity of plant traits, (ii) TOC measurements of carbon and water fluxes from EC systems, (iii) TOC spectra of canopy reflectance and SIF from a mobile FloX system and the unmanned aerial vehicle (UAV)-based spectroradiometer system AirSIF, (iv) high resolution maps of TOC reflectance and SIF from low-flying *HyPlant* overpasses, (v) larger maps of TOC reflectance and SIF from high-flying *HyPlant* overpasses, (vi) overpasses

of the Sentinel-3A and 3B tandem constellation, and (vii) regular Sentinel-2 and Sentinel-3 images. All of these optical remote sensing data are complemented by the detailed characterization of the atmospheric conditions, which is provided by the dense JOYCE network (Löhnert et al. 2015, [RD-09])¹⁰.

The two-time windows of interest were 26 June – 2 July and 1 and 2 August 2018. During these two-time windows, the majority of measurement systems were operational and delivered high-quality data (Table 19). These data will be described in more detail below and have the potential to be used as a core data set for future scientific studies because of their completeness.

Table 19: Overview on the different measurements across a wide range of spatial scales, which were taken at the two intensive measurement periods in the Jülich/Selhausen area.

	26 June – 2 July	1 and 2 Aug
Biophysical characterization of plant traits (i.e. LCC, leaf water content, LAI, canopy height, total biomass)	26 – 29 June: data from winter wheat, maize, potato, sugar beet	1 Aug: data from sugar beet, potato
Carbon and water fluxes from EC systems	Yes (30 min averages over whole time period from two eddy towers)	Yes (30 min averages over whole time period from two eddy towers)
TOC spectra of canopy reflectance and SIF	Several transects taken by the mobile FloX on June 26 – 29 UAV based AirSIF measurements on 2 July	
High-resolution maps (1 x 1 m) of reflectance and SIF from low-flying <i>HyPlant</i> overpasses	26 June: Selhausen flight pattern 15:30h 29 June: Selhausen flight pattern 12:00 and 15:30h	2 Aug: Selhausen flight pattern 12:30h
Larger maps (3 x 3 – 5 x 5 m) of reflectance and SIF from high-flying <i>HyPlant</i> overpasses	26 June: TR-32 flight pattern 13:00 – 15:00h 2 July: Sentinel-3 flight pattern 12:30h	2 Aug: Sentinel-3 flight pattern 12:00h
Overpasses of the Sentinel-3A and 3B tandem constellation ¹¹	2 July (GE1): Data of good quality based on atmospheric characterization	2 Aug (GE2): Data of highest quality based on atmospheric characterization
Regular Sentinel-2 images	27 + 29 June, 4 July, 2 Aug	
Regular Sentinel-3 images	6 + 7, 21, 28 – 30 June 2 + 3, 7, 13+14, 18+19, 21+22, 25+26· 30 July, 2 Aug	

Plant sampling was performed during the June / July and August time window and samples for vegetation traits were taken in the dominating crops, i.e. sugar beet (71 sample locations in four fields), maize (15 sample locations in three fields), potato (nine sample locations in one field), wheat (four sample locations in one field), and pea (23 locations in two fields) (Figure 108). The sampling was organized to coincide with the locations for mobile FloX measurements (see section 4.5.2, Figure 108).

To determine if there are simple correlations between the LCC and SIF₇₆₀ values, 3 m x 3 m ROIs around the chlorophyll measurements were drawn (Figure 107). Despite some trends, there is no obvious or conclusive

¹⁰ See also the ATMOFLEX activities report for a detailed description of the atmospheric data that were collected during the 2018 campaign window. The atmospheric data are also processed and provided with the ATMOFLEX reports. See ESA webpages for access to this data.

¹¹ Based on analysis by Neus Sabater and Univ. Helsinki, which were done as part of ATMOFLEX campaign.

correlation between these two parameters, indicating that there is no simple underlying correlation between LCC and canopy SIF signal.

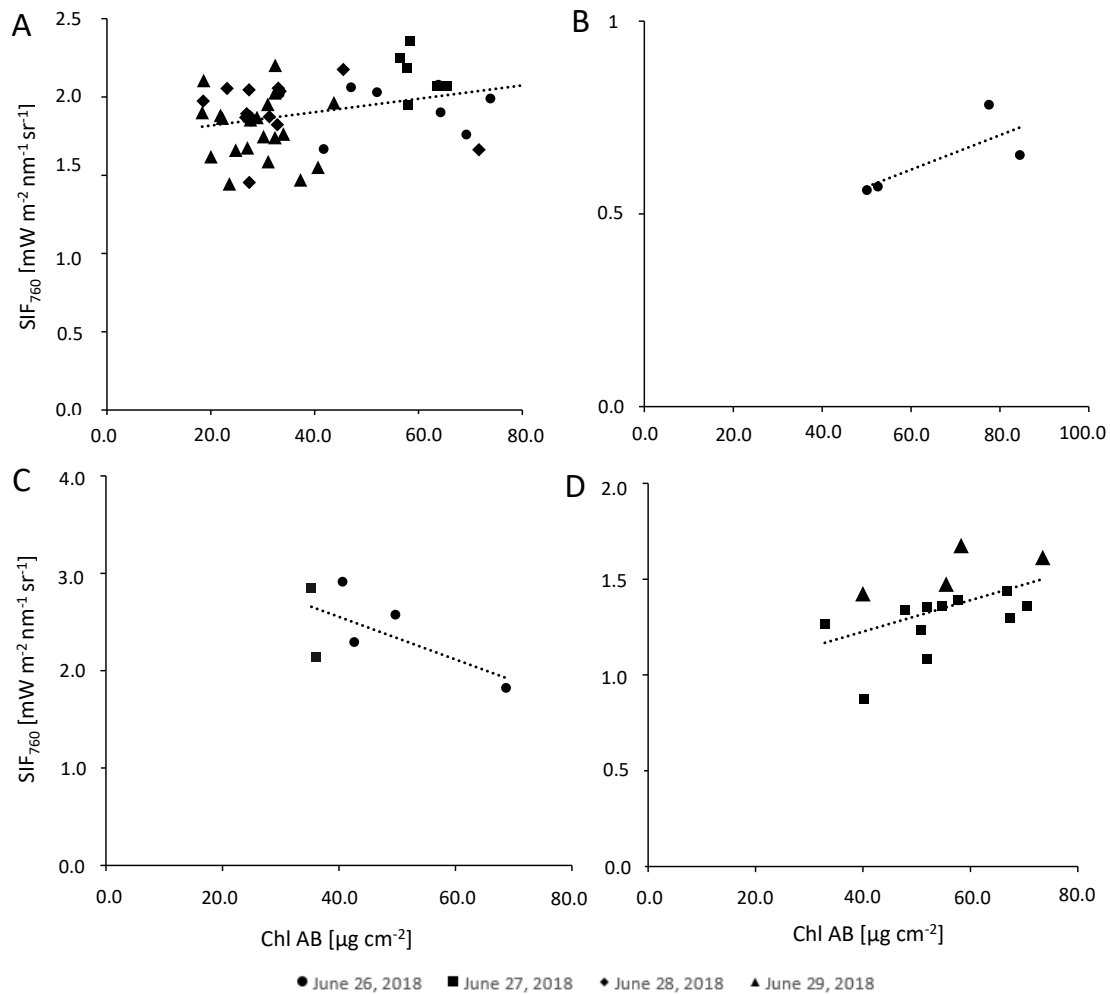


Figure 107: Correlation of chlorophyll A+B content and SIF₇₆₀. SIF₇₆₀ was calculated from *HyPlant* measurements using the iFLD method. 3 x 3-pixel windows around the chlorophyll measurements on the ground were extracted from the *HyPlant* iFLD SIF maps and averaged. The analysis was done for A) sugar beet, B) winter wheat, C) potato, and D) maize.

Quantifying within and between field heterogeneity by mobile TOC measurements of reflectance and fluorescence

During the campaign, two FloX systems were permanently installed for continuous measurements in the Selhausen area: One device near an ICOS tower and one - near a mobile EC-tower (red stars in Figure 108). The first FloX system measured a winter wheat field and the second one measured a sugar beet field. In addition to these stationary FloX systems, one mobile device was used for the first time to map the spatial heterogeneity within a single field and between fields (section 4.5.2, Figure 108).

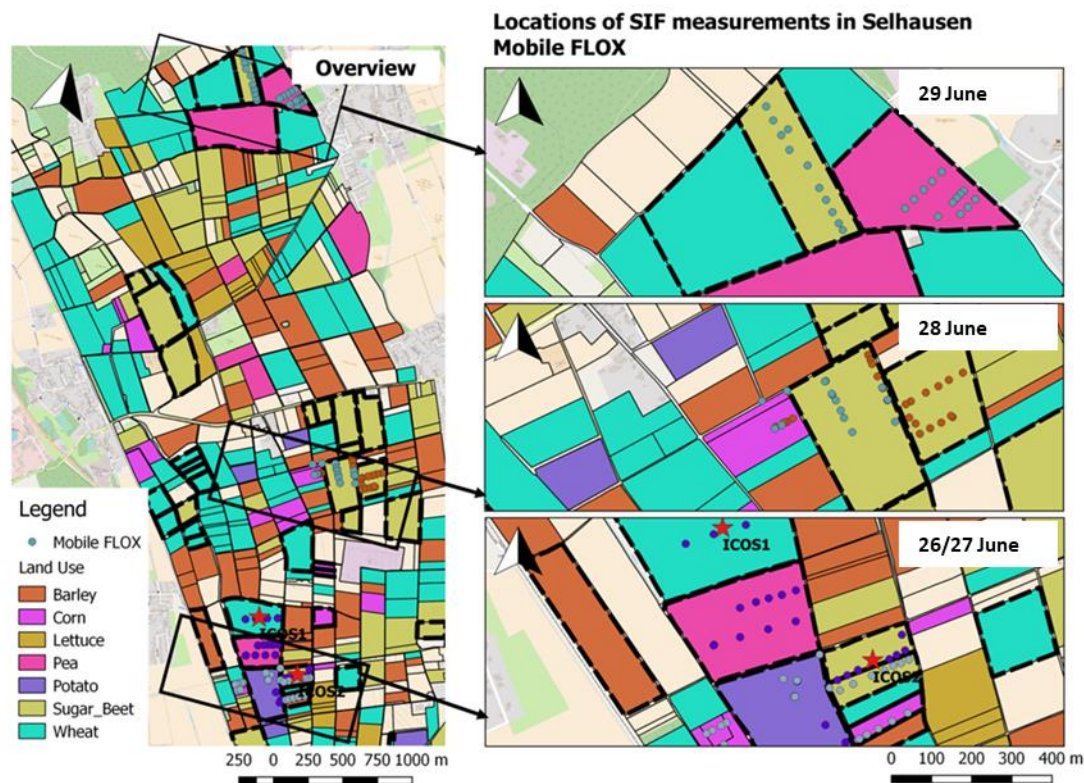


Figure 108: Core measurement site of Selhausen area. In this map, land-use / land cover classification is shown as well as the location of the two permanently operational ICOS eddy towers and the permanently working FloX systems (red stars). Additionally, measurement locations (mobile FloX system and determination of vegetation traits) are shown as dots.

Thanks to continuous TOC fluorescence measurements at a single spot within a field in combination with a cross-calibrated mobile FloX system, we could quantitatively compare the spatial variability of SIF measured across transects in a single field for the first time (Figure 109, Figure 110). Even though fields in Selhausen are managed homogeneously some spatial within-field heterogeneity in crop parameters is expected (Stadler et al. 2012). Single measurement spots along the within-field transect showed clear variations in F_{760} in comparison to the stationary measurement, which may be attributed to the inherent spatial heterogeneity of the sugar beet field or may be related to the measurement uncertainty of the mobile FloX system. (Figure 109, Figure 111).

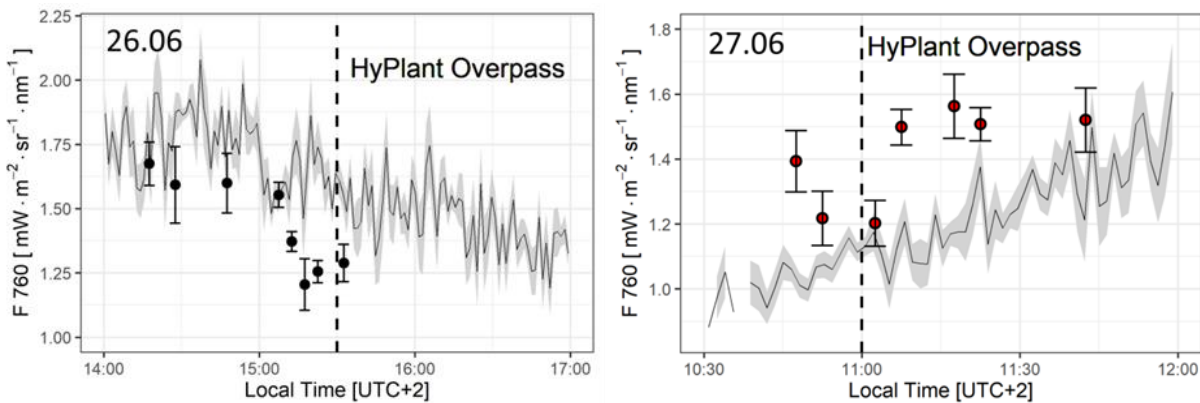


Figure 109: SIF(F_{760}) measured with the mobile FloX system at different locations along a transect in a single sugar beet field (dots) in comparison to continuous FloX measurements of the same field (line). The time of the *HyPlant* flyover is shown as a dashed line.

Further variability could be shown by measuring different crop types with the mobile FloX system (Figure 110). It becomes clear that there are species-specific differences, which can be seen, for example, in the comparable higher F_{760} values in potato and the lower values in corn and wheat. It is currently being analyzed how leaf level traits such as higher chlorophyll content or canopy structure influences these crop specific results. The data from this campaign may provide a good basis for further analyzing within-field, between-field as well as species-specific influences on TOC fluorescence. The data of this campaign may be the basis for SCOPE modelling studies or other empirical scaling studies to better understand the link between leaf level fluorescence emission and SIF canopy values.

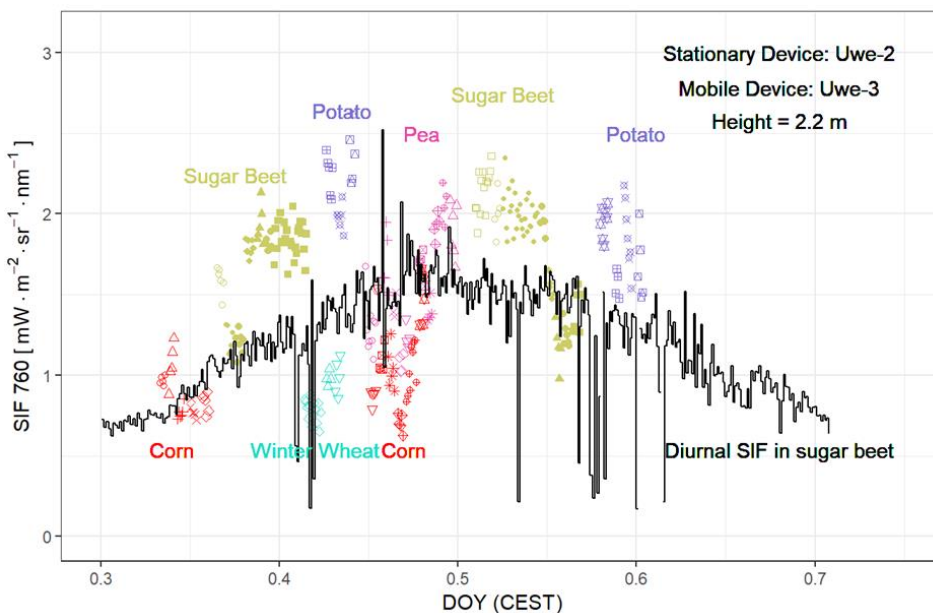


Figure 110: Mobile SIF at 760 nm measured by the mobile FloX device at different locations on various crop fields in comparison to continuous diurnal FloX measurements of the sugar beet field (26 and 27 June 2018). The iFLD retrieval was used.

Airborne reflectance and fluorescence measurements across scales

Various flight lines from different flight altitudes were recorded over the site in Selhausen / Jülich. On one day (26 June 2018) extensive ground-based measurements (see above) were performed in combination with *HyPlant* airborne acquisition from different flight altitude (680 m agl and 1600 m agl). This day in combination with other days was used to test the stability of the retrieval and to better understand spatial scaling and its impact on SIF. SIF was retrieved using the iFLD method as the SFM retrieval method was not yet operational at the time of this activity. The results are shown in the figures below (Figure 111 - Figure 117), which shall

provide a good basis for testing the stability of the retrieval and its sensitivity to different atmospheric conditions. In summary, we used three types of maps with different spatial resolutions based on different flight altitudes:

- 1 x 1 m resolution: derived from low-flying *HyPlant* overpasses (680 m agl) recorded on 26, 27, 29 June and 2 July 2018 (Figure 111 - Figure 117).
- 3 x 3 m resolution: derived from high-flying *HyPlant* overpasses (1600 m agl) recorded during the large map on 26 June 2018 (Figure 103 - Figure 105).
- 5 x 5 m resolution: derived from high-flying *HyPlant* overpasses (3050 m agl) recorded during the Sentinel-3 pattern. These flight lines were recorded in synchrony with the Sentinel-3A / 3B tandem constellation on 2 July and 2 August 2018 (Figure 111).

This unique data set allows detailed studies in scaling properties for SIF. As SIF is a novel remote sensing parameter, many scale related aspects still need to be understood and only a few pioneering studies are available thus far (see e.g. Pinto et al. 2017, Liu et al. 2019). The data set, which was acquired during the 2018 campaign and which is described in this section provides a unique nested data set, with data across different spatial scales were acquired during the same time period. All aircraft data were carefully georeferenced and thus allow the linkage and comparison of scaling properties in SIF. As a detailed analysis of all scaling properties is far beyond the scope of this campaign activity, we limit ourselves to a careful and detailed description of the different SIF products and the spatial consistency of the products.

In Figure 111, we give an overview of the core Selhausen study site showing the spatial heterogeneity of the two main SIF products in this region. This map is a composite of four spatially registered flight lines that cover a region of approx. 1.5 x 7 km. The region is dominated by various intensely managed fields (mainly sugar beet, summer and winter crops, potatoes, beans as well as some horticultural fields). Fields have rather homogeneous NDVI values and only some isolated fields show spatial differences in NDVI. Additionally, NDVI values can be used to clearly separate fields with different developmental stages, but it also becomes obvious that many fields have NDVI values close to saturation indicating the dense and green vegetation at this time of the year (Figure 111b).

The SIF maps show a more differentiated picture and more pronounced between-field differences become obvious, especially in the SIF₇₆₀ map. Different SIF₇₆₀ values are visible in fields that were not distinguishable in the NDVI map. These differences in SIF₇₆₀ can be seen as another indication for the distinguish power of the SIF measurements (Figure 111d). While the NDVI is solely sensitive to canopy chlorophyll and while NDVI measurements saturate in dense vegetation, the SIF maps are not prone to saturation and thus allow the differentiation of densely vegetated fields. Additionally, SIF is also likely to show differences in the functional performance of the plants, which may be related to management practices or potential environmental limitations and stress that may occur in some of the fields. This hypothesis can be related to the different soil water holding capacity prevalent in the study region, and which provides a good test bed for further scaling studies (von Hebel et al. 2018).

SIF₆₈₇ maps do not show clear difference in field heterogeneity but these maps are still associated with substantial pixel noise (Figure 111c). This noise is retrieval noise that is still inherent to the iFLD method, which is at its limit for retrieving SIF₆₈₇ values in an operational mode. Nevertheless, patterns can be seen in this map and to further exploit the red peak fluorescence information (SIF₆₈₇), we have calculated a more precise sub-set of SIF₆₈₇ by manually adjusting retrieval parameters for some selected sub-scenes (see Figure 115 for a manually optimized SIF₆₈₇ map).

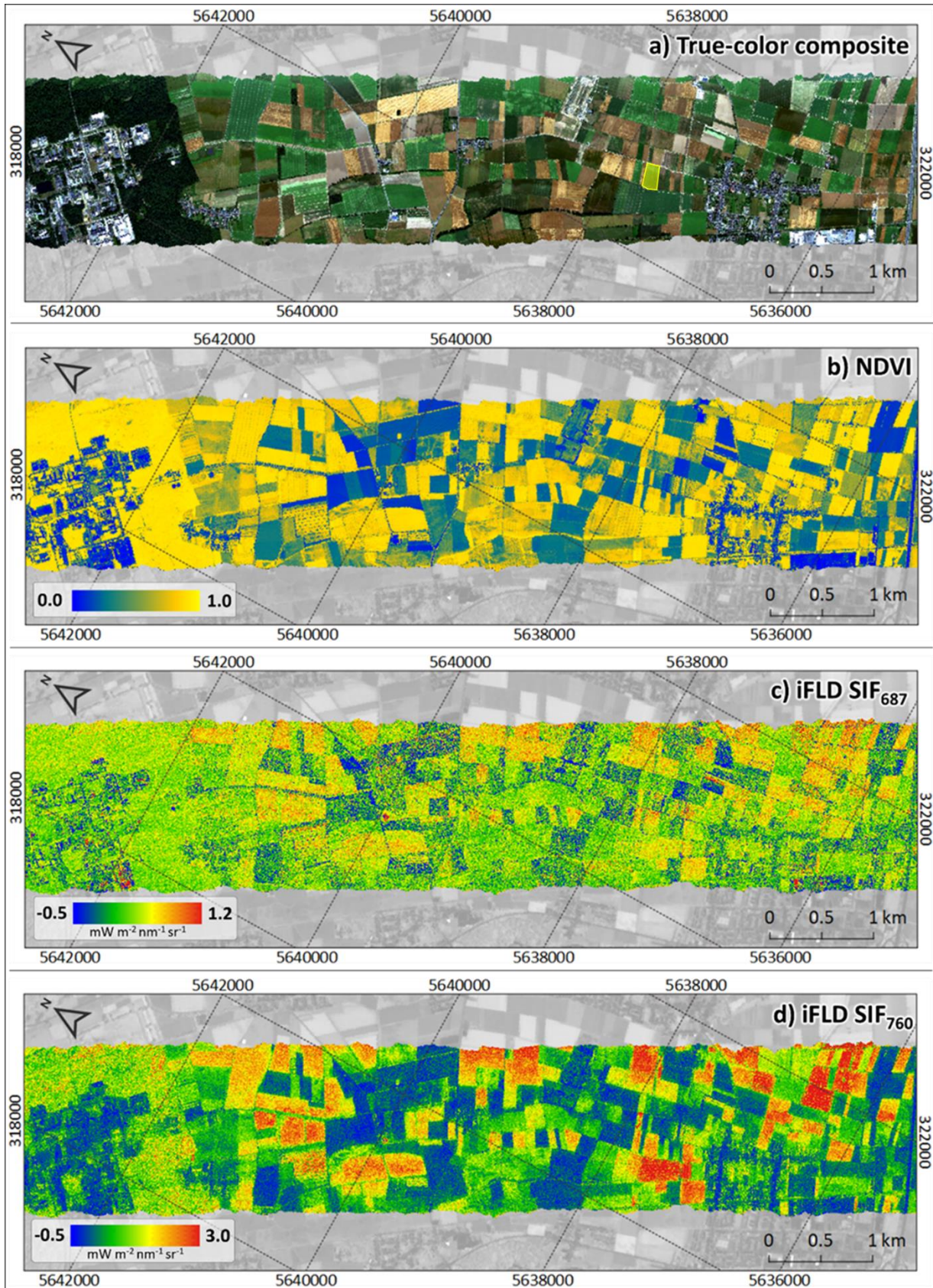


Figure 111: Overview of the Selhausen maps, measured during the *HyPlant* overpass on the 26 June 2018. These maps were produced by stitching together four parallel flight lines each with a resolution of 1 x 1 m. a) True-color composite / TOC reflectance, b) NDVI, c) SIF₆₈₇(iFLD) and d) SIF₇₆₀(iFLD). The field that was used for the mobile FloX measurements (see above from Figure 110) is marked as yellow ROI in (a) from this field also various biochemical parameters were sampled (see chapter 4.7).

	Doc.: Final Report		
	Date: 29 July 2021	Issue: 2	Revision: 1
	Ref.: ESA Contract No. 4000125402/18/NL/NA		Page: 146 / 288

Last but not least, we calculated SIF₇₆₀ and SIF₆₈₇ maps using the SFM from the high-altitude overpasses following the Sentinel-3 orbit (Figure 112). The SIF₇₆₀ maps derived for both acquisition days look a little bit blurry; specially, field borders (e.g., in the south of the map) and the edges of the forested area around the research center (in the middle of the map) are not that sharp. One reason for this effect could be the higher number of mixed pixels in comparison to lower altitude overpasses, where this effect is not visible. The higher number of mixed pixels makes the detection of bare soil pixels, which is one important part of the current SFM implementation, much more difficult and may lead to the 'blurry' SIF maps. SIF₆₈₇ maps are sharper, which in turn indicates that the detection of bare soil pixels also works for the high-altitude overpasses. In the future, we will use the SFM method as operational retrieval of *HyPlant* imagery and first quality performance checks of the SFM SIF results indicate that especially high-overpass images provide sharper results. Additionally, we may further optimize the PSF deconvolution algorithm based on the considerations from Sharr et al. (publication IV, chapter 12.4), which should additionally improve the contrast between adjacent pixels.

The lower SIF₇₆₀ and SIF₆₈₇ values derived from the image recorded on 2 July 2018 in comparison to the image recorded on 2 August 2018 are plausible because the earlier data acquisition took place at the beginning of the 2018 summer heat wave when the observed vegetation had a higher chlorophyll content and was not affected by drought stress. Furthermore, in the time between the two data acquisition days many fields were harvested so that much more bare soil was present in the observed area on 2 August 2018. This is clearly visible in the true color composites generated from the *HyPlant* DUAL module for both days shown in Figure 112a, b.

The high SIF₇₆₀ and SIF₆₈₇ values derived for the hill (Sophien Höhe) in the northeastern part of the area are not realistic. At the moment, one surface altitude is used in the SFM retrieval, which needs to be manually set. Since the focus was on the agricultural fields and the forest area around the research center, the used altitude was adapted to these parts of the scene. Including the surface altitude for each pixel separately within an image is another important topic for future improvements of the SFM to additionally enable the retrieval of reliable SIF maps for hilly terrain with significant altitude differences.

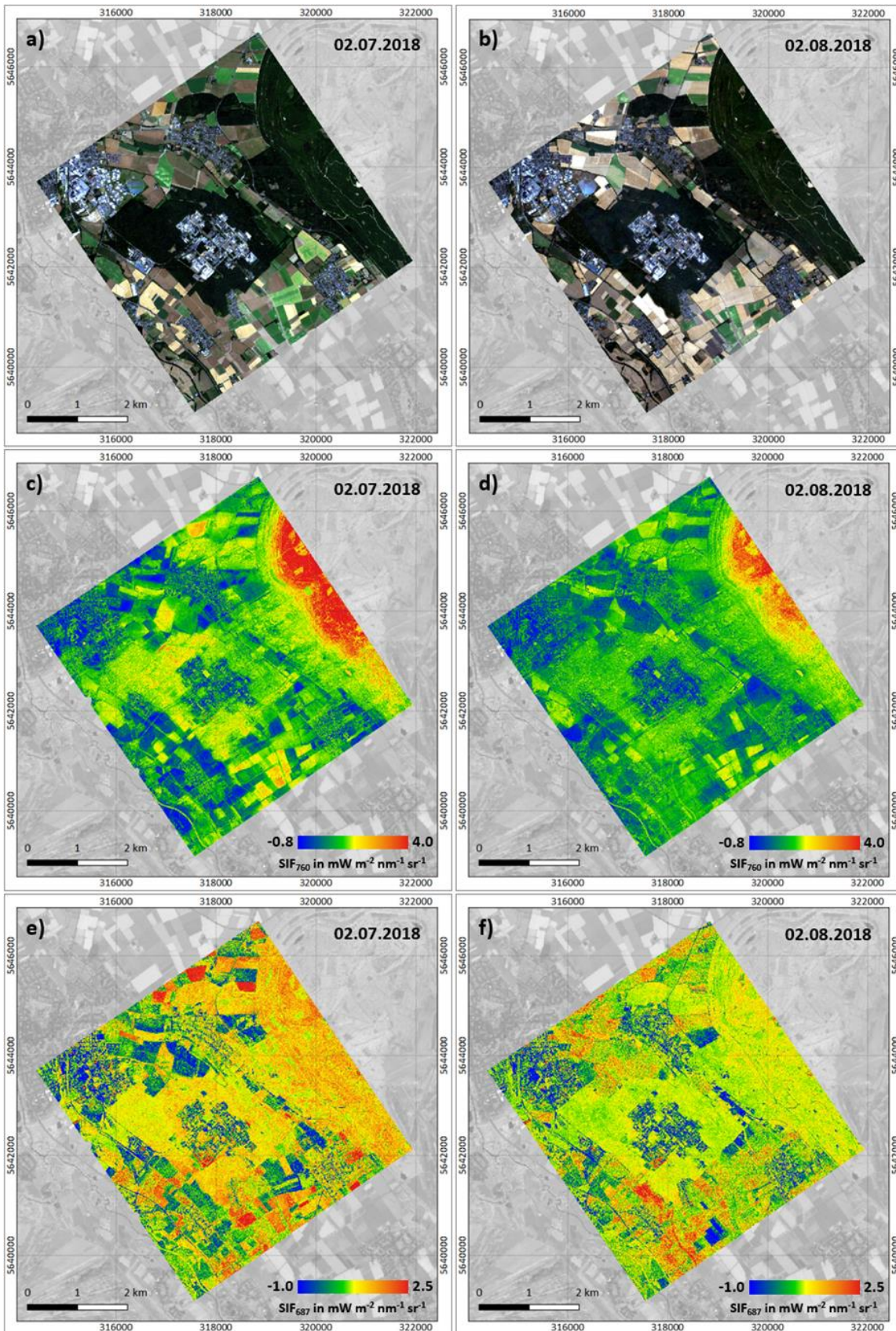


Figure 112: Sentinel-3 pattern acquired over the research center Jülich. *HyPlant* DUAL TOC reflectance true color composite recorded on 2 July 2018 (a) and 2 August 2018 (b). Derived SIF₇₆₀ maps using the SFM method on 2 July 2018 (c) and 2 August 2018 (d). Derived SIF₆₈₇ maps using the SFM method on 2 July 2018 (e) and 2 August 2018 (f).

Scaling and comparison to Sentinel satellite data

From June to August 2018, a total of nine Sentinel-2 and 22 Sentinel-3 images are available for the region covering Selhausen and CKA study sites (Figure 113a). The Sen2Cor plugin was used through the Sentinel application platform (SNAP) software to generate the level-2A product from the TOA level-1C data. The Sentinel-2 images are composed by twelve bands at three spatial resolutions. The RGB and NIR bands are 10 m Ground Sample Distance (GSD), while four red edge channels and two SWIR bands are 20 m GSD. The water vapor, coastal aerosol and SWIR-cirrus bands are 60 m GSD. Sentinel-2 images captured on 27 June, 7 July and 6 August are of particular importance due to their proximity to the *HyPlant* campaign dates (Figure 113b). Hyperspectral Sentinel-3 images of 300 m GSD are also available close to *HyPlant* overpasses (Figure 113c). Sentinel-3 imagery is composed by 21 spectral bands from 400 to 1020 nm with a spectral resolution varying from 2.5 nm (O₂-A) to 15 nm. The ninth band, at 673.75 with 7.5 nm width, allows the improvement of fluorescence retrievals and helps to address the ‘smile’ between the bands eight (665 nm, 10 nm width) and ten (681.25 nm, 7.5 nm width).

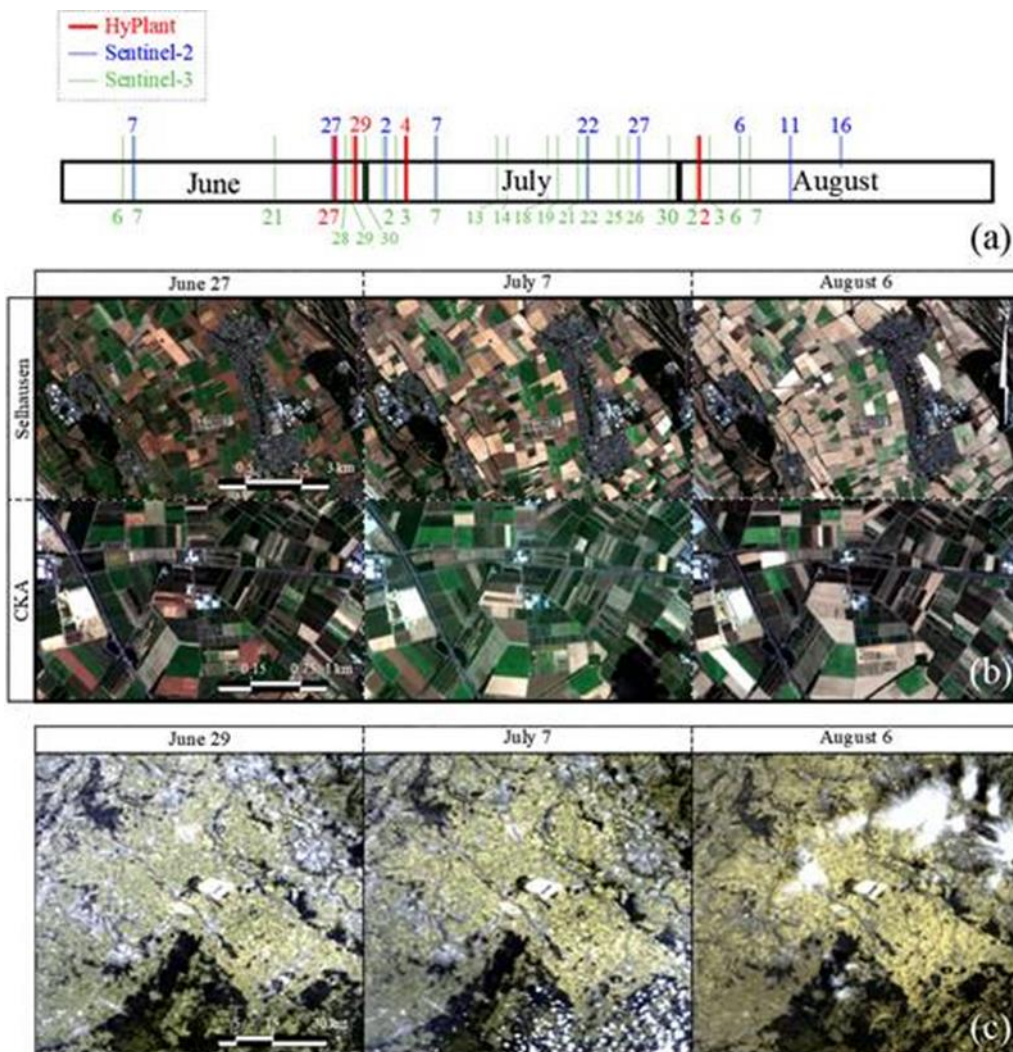


Figure 113: (a) Dates of *HyPlant*, Sentinel-2 and Sentinel-3 data availability from June to August 2018. (b) Sentinel-2 and (c) Sentinel-3 images captured close to *HyPlant* overpasses.

In addition to *HyPlant* and Sentinel-3 data products, thermal images and LiDAR data are also available from all *HyPlant* overpasses. This data set was produced from the large map (TR-32 flight pattern) and thus covers the extended region around Jülich and Selhausen (Figure 106). Especially the DEM data can be used for scaling studies, as the surface model did not change within the IOP. A more detailed analysis of this data set

	Doc.: Final Report		
	Date: 29 July 2021	Issue: 2	Revision: 1
	Ref.: ESA Contract No. 4000125402/18/NL/NA		Page: 149 / 288

was performed in the frame of the PhotoProxy study(see [RD-06] and the final Photosynthesis report of PhotoProxy for more details)

7.2.3 Linking eddy based GPP fluxes to SIF maps – determining the right spatial scale to register dynamically changing footprints of carbon fluxes to SIF

We have selected a sub-scene within the Selhausen study area and provide manually adjusted and optimized maps of all fluorescence products that can be derived from *HyPlant* using the iFLD method (Figure 114 - Figure 117). These maps were retrieved by manually selecting the best soil pixels and by optimizing all retrieval parameters. Thus, these maps can be seen as ‘ideal’ maps, which demonstrate the current performance of SIF retrieval of *HyPlant* imagery.

We additionally selected maps from three different campaign days to demonstrate the impact of seasonal changes on within- and between-field heterogeneity in this agricultural region. We are currently working on a scientific publication that makes use of this data set (Busch et al. *in prep.*). Another unique feature of this data set are the two eddy towers, which are located at the study site and which allow the analysis of the link between SIF data and GPP (see some analysis on this topic below).

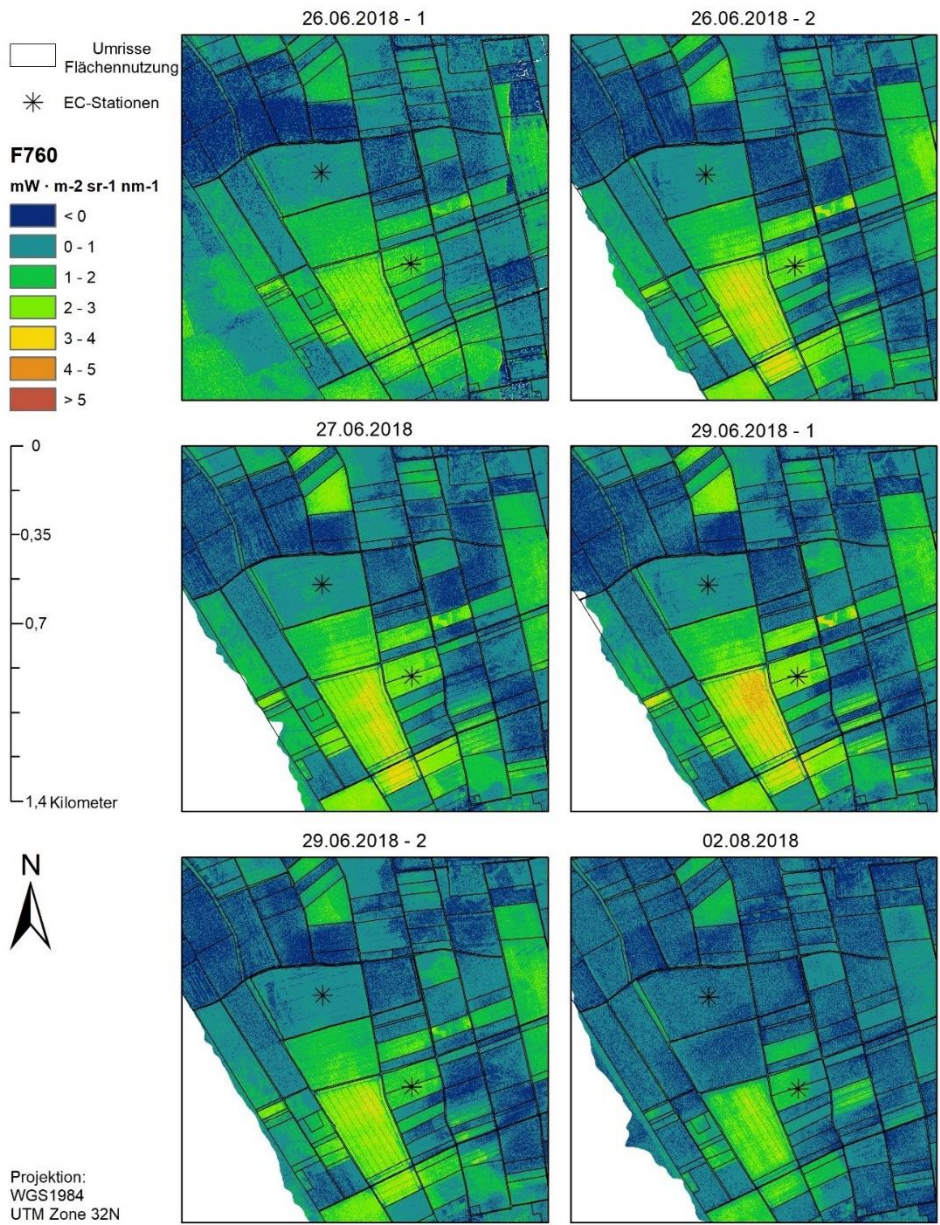


Figure 114: Maps of SIF (F_{760}) measured on the intensive observation days from the core area of Selhausen. SIF was retrieved from low-flying *HyPlant* data revealing a spatial resolution of 1 x 1 m. The asterisks shows the location of the two ICOS eddy flux towers.

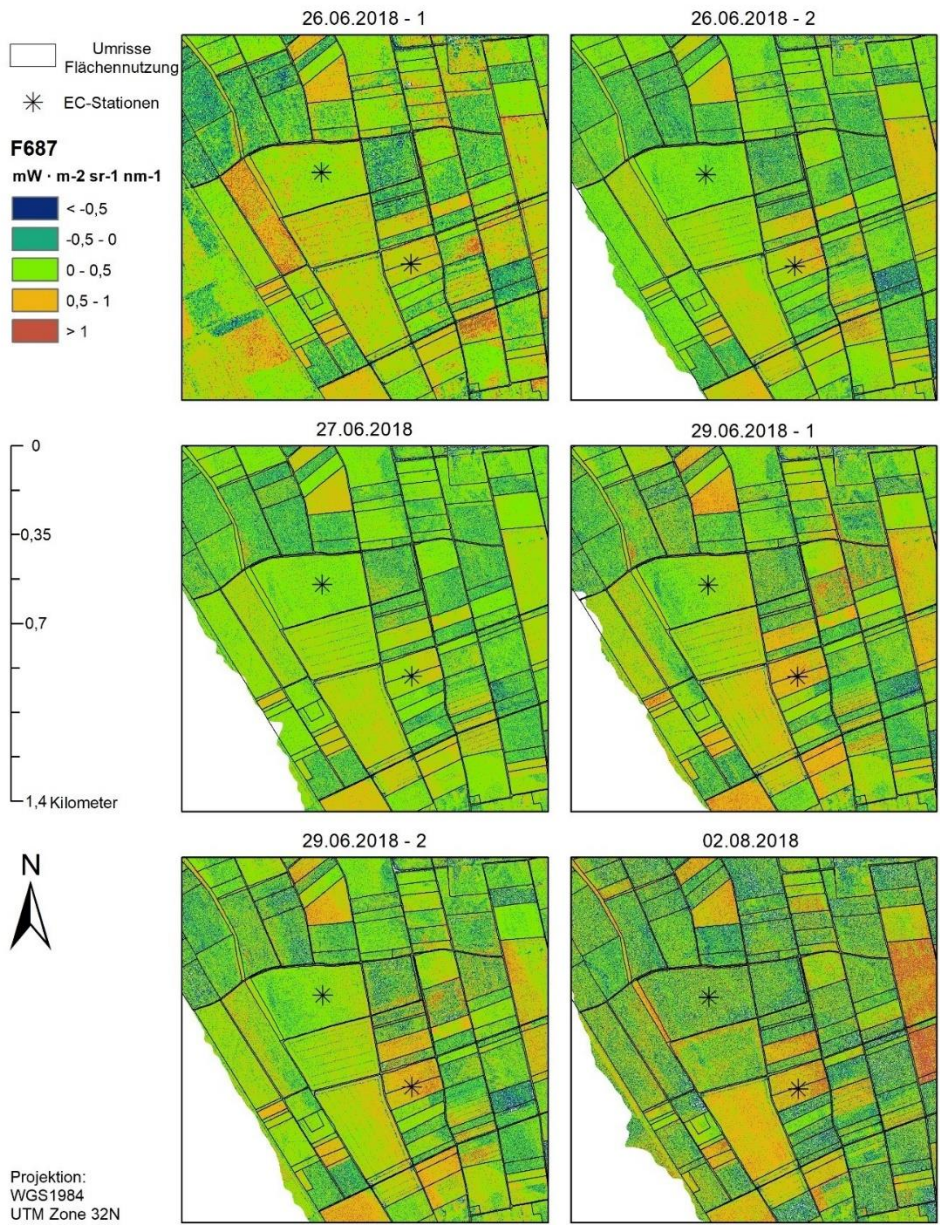


Figure 115: Maps of SIF (F_{687}) measured on the intensive observation days from the core area of Selhausen. SIF was retrieved from low-flying *HyPlant* data revealing a spatial resolution of 1 x 1 m. The asterisks shows the location of the two ICOS eddy flux towers.

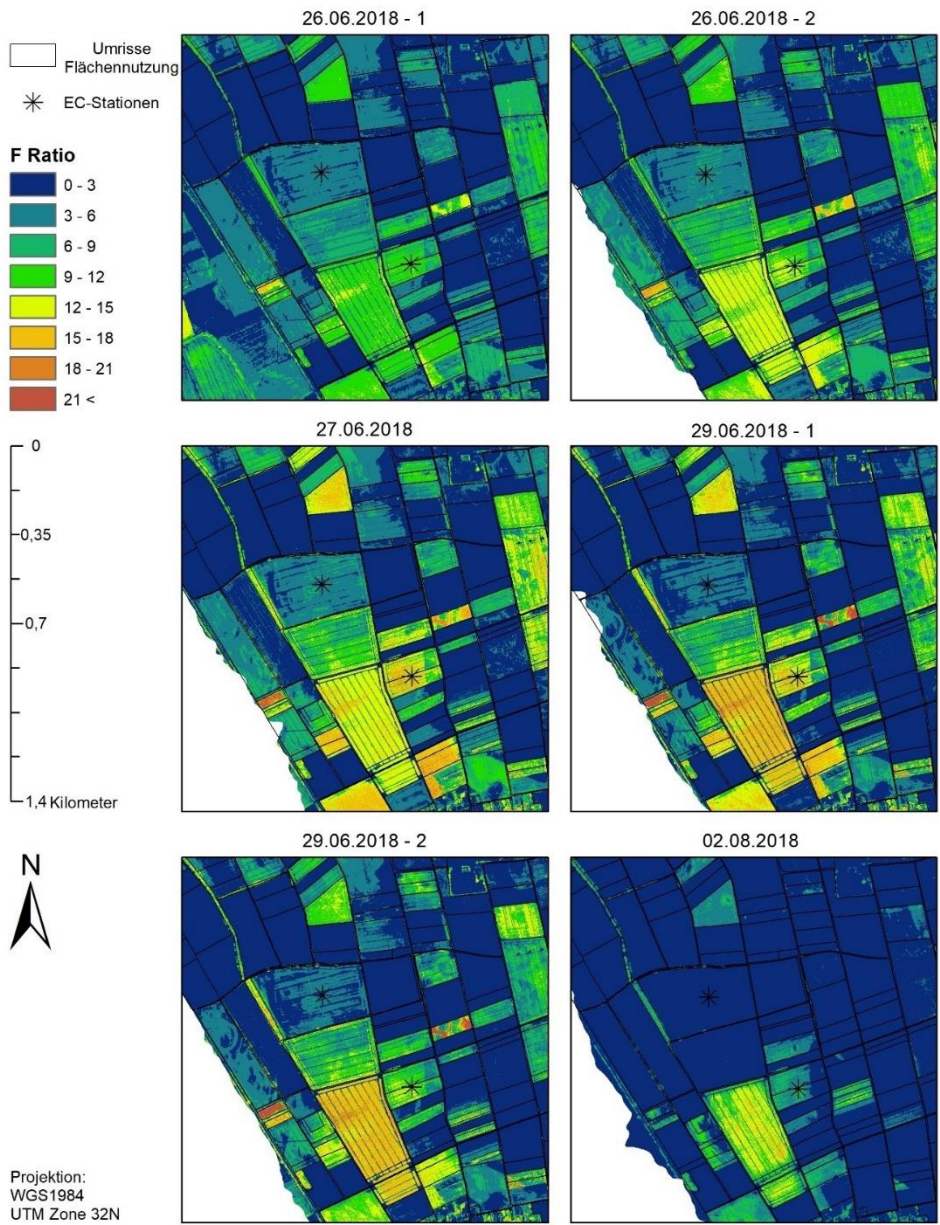


Figure 116: Maps of the ratio of both peaks of SIF ($F \text{ ratio} = F_{760} / F_{687}$) measured on the intensive observation days from the core area of Selhausen. SIF was retrieved from low-flying *HyPlant* data revealing a spatial resolution of 1 x 1 meters. The asterisks shows the location of the two ICOS eddy flux towers.

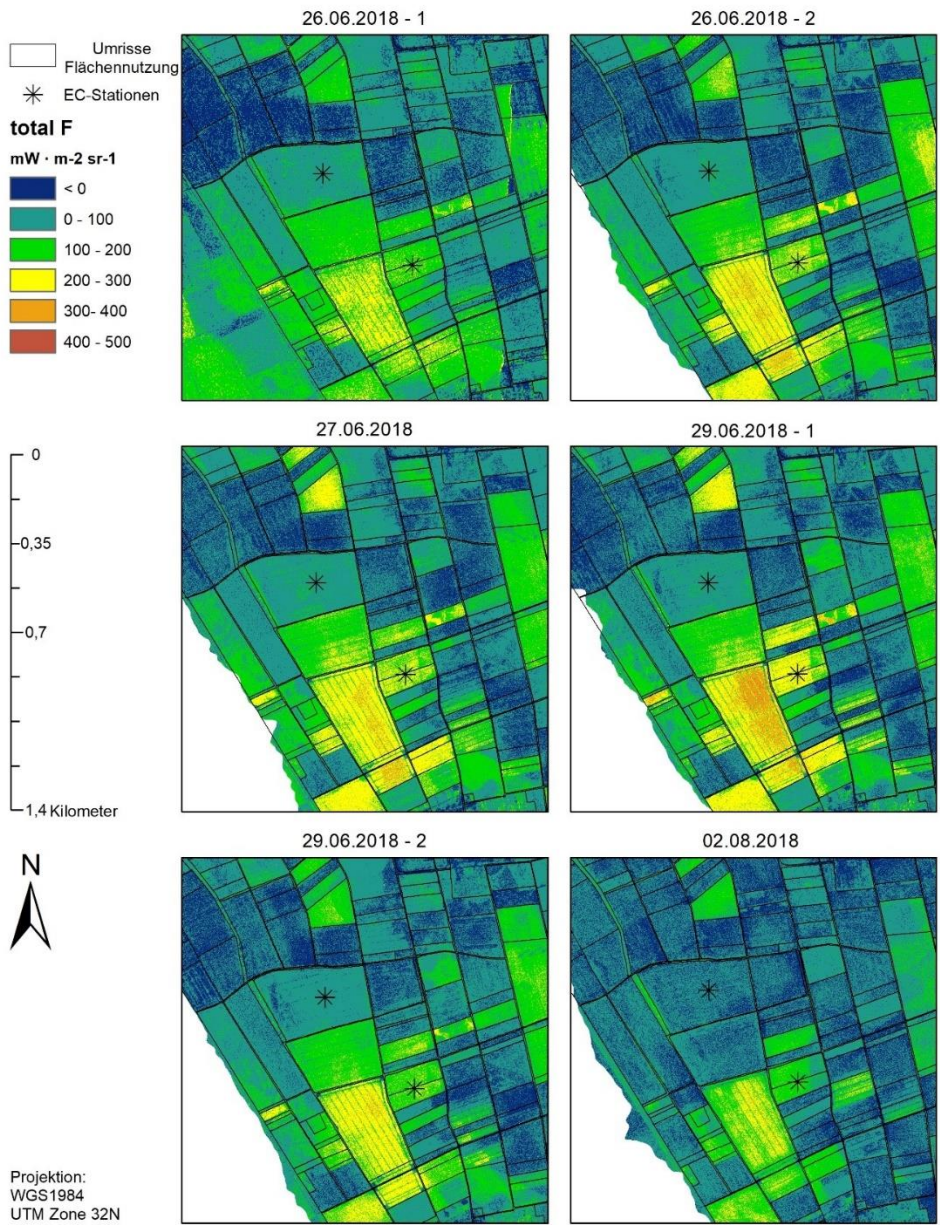


Figure 117: Maps of the total SIF (F_{tot}) measured on the intensive observation days from the core area of Selhausen. SIF was retrieved from low-flying *HyPlant* data revealing a spatial resolution of 1 x 1 m. Total fluorescence was extrapolated by using the height of the two peaks and using the empirical formula proposed by ESA 2015. The asterisks show the location of the two ICOS eddy flux towers.

Linking sun-induced fluorescence to GPP

Two EC towers were operational during the campaign window and continuous data on carbon and water fluxes were recorded (see Figure 108 for the location of the eddy towers). These eddy data show a decrease in NEE and GPP throughout the season (Table 20 and Table 21).

Table 20: NEE measurements and GPP calculations for the north EC tower in Selhausen during the overflights of *HyPlant* in 2018.

Day of the overflight	NEE [$\mu\text{molm}^{-2}\text{s}^{-1}$]	GPP [$\mu\text{molm}^{-2}\text{s}^{-1}$]
26 June, 1 m agl.	-16,82	21, 87
26 June, 3 m agl.	-14,81	20, 36
27 June, 1 m agl.	-7,48	12, 77
29 June, 1 m agl.	-4,4	9, 79
29 June, 3 m agl.	-2,01	7, 73
2 August, 1 m agl.	4,31	-1, 44

Table 21: NEE measurements and GPP calculations for the south EC tower in Selhausen during the overflights of *HyPlant* in 2018.

Day of the overflight	NEE [$\mu\text{molm}^{-2}\text{s}^{-1}$]	GPP [$\mu\text{molm}^{-2}\text{s}^{-1}$]
26 June, 1 m agl.	-32,16	35, 83
26 June, 3 m agl.	-18,79	22, 74
27 June, 1 m agl.	-27,35	31, 13
29 June, 1 m agl.	-20,56	24, 14
29 June, 3 m agl.	-10,55	14, 32
2 August, 1 m agl.	-6,8	11, 23

These NEE and GPP data were then related to airborne SIF measurements. As eddy measurements are integrated measurements covering a larger ‘footprint’, i.e. a larger area from which surface fluxes are collected. These foot prints are not stable, but their size and direction greatly depend on the prevailing wind and turbulence conditions. We used a forward model to compute a projected footprint area for the time of the *HyPlant* overpass and then calculated a spatially weighted mean of the SIF pixels within the foot print area (Table 22).

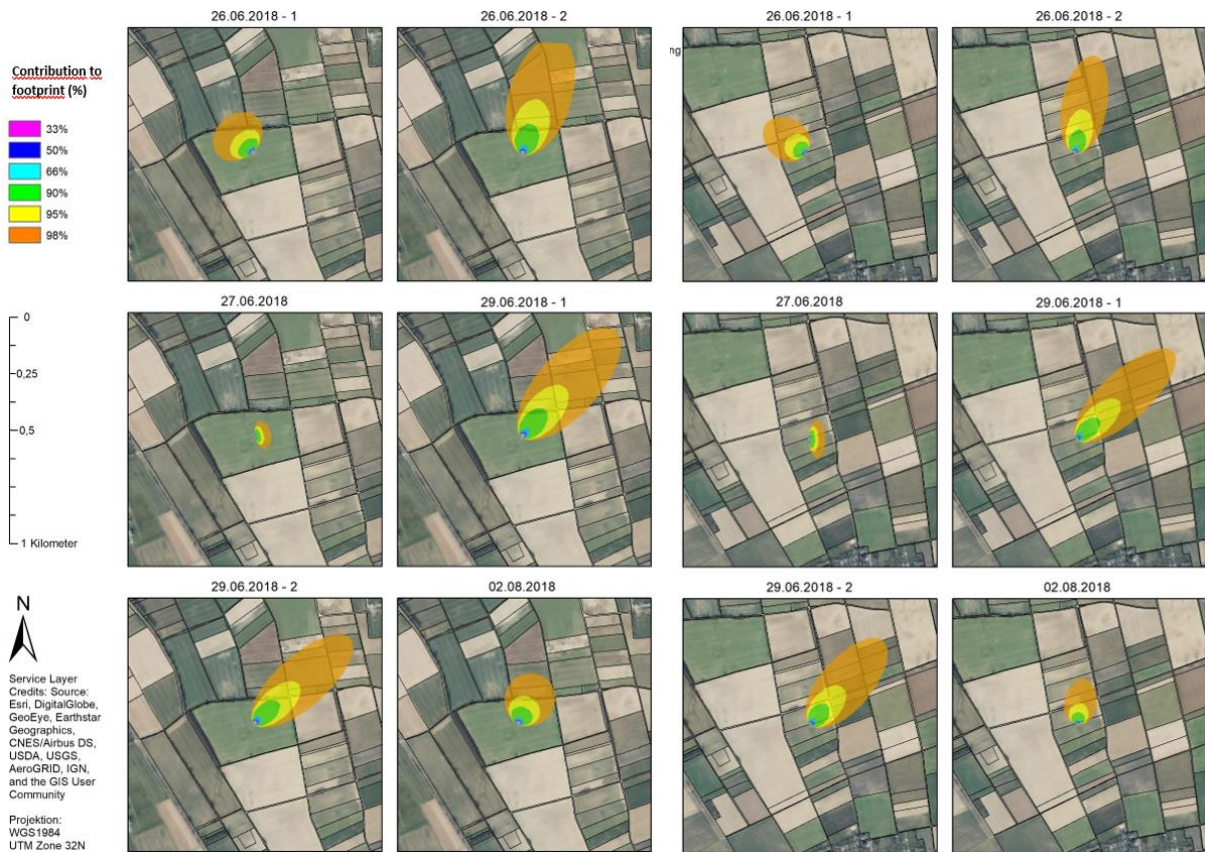


Figure 118: Calculation of the flux footprint from the two ICOS EC towers that are located in the Selhausen study site. The footprint calculation is based on the method of Kormann and Meixner (2001), which uses an analytical model of the lower boundary layer (Foken 2013). This footprint calculation is widely accepted in the community and thus provides a good a solid approximation of the footprint. Left maps: footprint calculation for the norther EC tower that was located on winter wheat; right maps, footprint calculation of the southern EC tower that was placed on the border of two sugar beet fields.

We want to point out that the data from Table 22 shall be handled with care as only a limited number of overpasses are included in this correlation analysis. However, it already becomes obvious that using a footprint that covers 50 - 90% of the area delivers the best results. Including the outer margins (95 and 98% of the footprint area) decreases the correlation between carbon fluxes and SIF. Additionally, we could demonstrate a clear correlation between SIF_{760} and SIF_{tot} and GPP, while we found no clear correlation between SIF_{687} and GPP. A detailed and statistically solid comparison and correlation of the SIF maps and the EC flux data would exceed the frame of this study would require more data covering different sites. We are currently working on a more detailed scientific publication on this topic. The data that are presented here provide the basic concept of how ground-based EC data can be aggregated via a footprint calculation and then related to airborne SIF estimates and vegetation indices that are acquired on different spatial scales (see the nested data above). We are confident that this describes a promising method for overcoming the sampling problem that arises when small-scale point measurements (e.g. from ground-based FloX systems) are related to larger scale satellite images (in the case of FLEX 300 x 300 m pixels).

Table 22: R^2 values of the comparison between SIF products and GPP for different aggregating of the footprint (red: 0 – 0.3; yellow: 0.3 – 0.7; and green: 0.7 – 1).

SIF product	Eddy station	Size of the footprint area					
		33%	50%	66%	90%	95%	98%
SIF ₆₈₇	Sugar beet & winter wheat	0.08	0.08	0.08	0.06	0.05	0.05
SIF ₇₆₀		0.33	0.34	0.35	0.35	0.33	0.32
SIF _{tot}		0.29	0.3	0.31	0.28	0.26	0.26
F _{Ratio}		0.4	0.41	0.44	0.46	0.44	0.39
SIF ₆₈₇	Winter wheat only	0.04	0.03	0.06	0.07	0.06	0.07
SIF ₇₆₀		1	1	0.98	0.85	0.72	0.61
SIF _{tot}		0.97	0.97	0.93	0.73	0.6	0.5
F _{Ratio}		0.95	0.94	0.91	0.76	0.64	0.5

7.3 Campus Klein-Altendorf, Germany

[50.62N, 6.99E]

The agricultural research CKA near Bonn comprises 181 ha for field trials and approximately 4,800 m² for greenhouse trials (Figure 119). At CKA, research can be conducted on all kinds of plants and crops, including small plants such as herbs; large crops such as maize; annual crops such as vegetables; and perennial plants such as Miscanthus and fruit trees. Plants can be grown in the experiments under practical conditions. Various groups from Bonn University and Forschungszentrum Jülich use the site. In past years, Forschungszentrum Jülich has invested greatly in the measurement capacities at the campus and now operates a network of modern, non-invasive field phenotyping sensors and positioning systems. These include a mini-plot facility and an automated phenotyping system to grow crops in field-like soil conditions in the greenhouse, a unique portfolio of imaging sensors for field phenotyping (hyperspectral systems, thermal camera for active and passive thermography, high-performance imaging spectrometers, stereo camera, and LiDAR systems), and various established hand-held instruments.

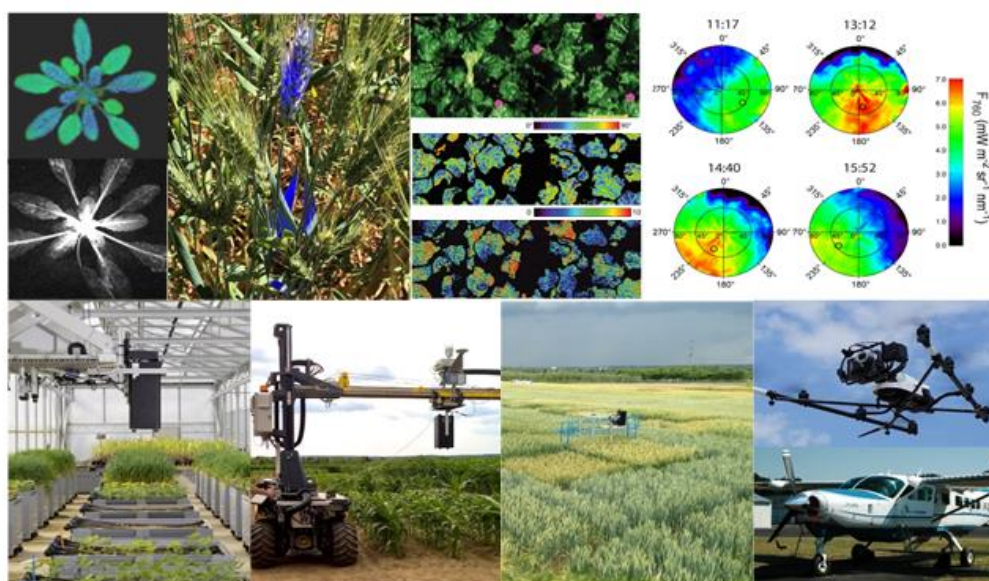


Figure 119: Snapshots of the CKA and selected field phenotyping instruments operating within the common experiment of Forschungszentrum Jülich. The plot design of the field traits provides a good test bed to link structural and functional properties of crops with remote sensing observations of SIF.

	Doc.: Final Report		
	Date: 29 July 2021	Issue: 2	Revision: 1
	Ref.: ESA Contract No. 4000125402/18/NL/NA		Page: 157 / 288

During the 2018 FLEXsense campaigns, various synergistic measurements and projects were ongoing at this research campus and the structural and functional response of selected crops types are quantified in detail. Thus, the research campus provides a selection of different crops and different breeding lines, the status of which was closely monitored during the campaign activity. We thus describe the most relevant data that are available for further analysis of the SIF data. All data described in the following sections can be made available upon request for further analysis. The following three sections are organized as follows:

- First, we describe the effects of elevated, future atmospheric CO₂ concentrations on the structural and functional traits of different wheat varieties and the link to active and passive fluorescence (section 7.3.1)
- We then perform a detailed evaluation of the diurnal dynamics of SIF from differently structured crop types and the option of scaling canopy fluorescence to the single leaf (section 7.3.2)
- Last, we describe of the functional diversity of different barley varieties and initial test measurements to quantify SIF from a UAV by using the novel and light weight AirSIF sensor (section 7.3.3)

7.3.1 Understanding the dynamics of photosynthesis of plants grown under future, elevated CO₂ concentrations using passive and active fluorescence approaches

BreedFACE is an experimental set-up, in which plants are grown in the field under elevated CO₂ conditions, thus simulating the atmospheric conditions we expect in 2040 (Figure 120). Elevated CO₂ will alter the capacity of plants to perform photosynthesis and we are investigating the functional and structural effects of our future climate in this large-scale field experiment. CO₂ enrichment rings which have a diameter of 20 m, are established in the field and used to cultivate wheat varieties. The structural and functional traits of the wheat varieties are closely monitored throughout the season.

The FACE system is an octagon of laser-drilled pipes that supplies CO₂ using an industrial PC-based control system. CO₂ released from the pipes flows over the vegetation in the direction of the wind to a set CO₂ level of about 550 - 590 ppm. CO₂ is supplied for the full growing season i.e. from seeding to harvest when plants are photosynthetically active.

The growth conditions for plants in the BreedFACE experimental set-up CKA is considered optimal in Germany, with an altitude of 186 m, a mean annual temperature of 9.6°C and a mean annual precipitation of 625 mm. The soil is a Haplic Luvisol derived from loess is a typical rich and well-watered soil for the region, and relevant for testing the effect of CO₂ under these growth conditions. However, additional effects such as nitrogen, drought and temperature are not included in the current set-up. Typically, barley, sugar beet, and rapeseed are grown in a rotation scheme in this area; cultivation options are limited by the site, but not to these species. In total, three octagons 18 m in diameter allow for 252 experimental plots of 1.5 x 3 m under elevated CO₂, and a large amount of area is reserved for growth at ambient [CO₂]. The plot size and thus number of genotypes that grow under elevated CO₂ can vary depending on the experimental design.

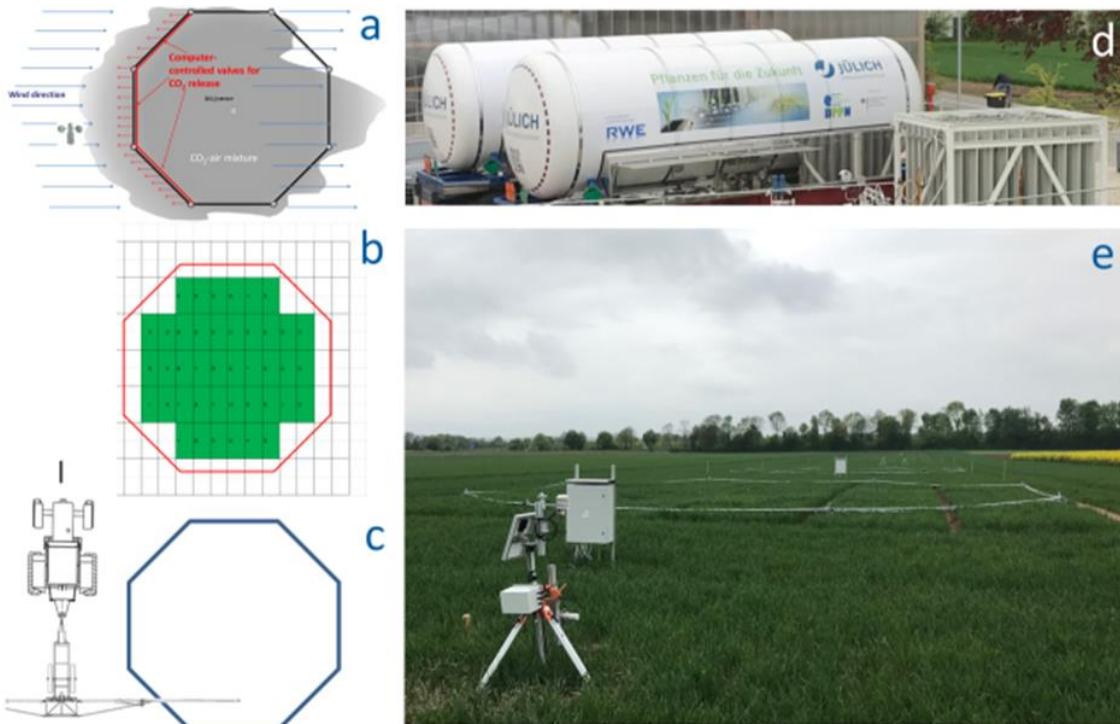


Figure 120: Drawing of CO₂ release against the wind to increase CO₂ in the octagon (a), distribution of plots in one octagon (b), example of positioning system covering half of the octagon (c), mobile CO₂ tanks for transport and storage of liquid CO₂ and vaporizer to produce CO₂ gas for the BreedFACE (d), overview of the BreedFACE with the octagons in the background and environmental station in the foreground (e).

The location benefits from the good agricultural practices of CKA and is integrated within the field phenotyping facilities of Forschungszentrum Jülich, including detailed environmental characterization as well as numerous phenotyping sensors for non-invasive assessment of above-ground traits such as plants structure, composition and photosynthesis. Specifically, depending on the research question, the sensors used could take the form of RGB and (hyper-)spectral and thermal cameras, stereo camera set-ups or the laser-induced fluorescence Transient (LIFT) instrument. The sensors are mounted on mobile platforms to obtain a medium- to high-throughput.

In line with most agricultural field experiments, the experiments are determined by the growing season of the crop, and during the season, multiple experiments can be performed with that crop. However, the FACE system will be installed once a year, and thus will allow one experiment per year, although different areas of elevated CO₂ can be considered (e.g., each ring could be placed over a different crop species).

In 2018, a historical winter wheat was grown in the BreedFACE set-up, and 12 genotypes were measured by the LIFT device mounted on the Field4Cycle together with the FloX to measure three replicates in control and elevated CO₂ conditions at a minimum level throughput (Figure 121).



Figure 121: Manual position system Field4Cycle modified for Breedface measurements, mounted with the LIFT and FloX device, (A) where FloX upwelling and downwelling fibers were placed such to avoid shading (B) and the blue light excitation area (approx. 3 cm in diameter) is shown in the shade covering multiple wheat leaves.

The LIFT measurements show for all genotypes a lower photosynthetic efficiency when grown and exposed to elevated CO₂ especially during the colder months. During shutdown of CO₂, an inverse pattern is observed (Figure 122).

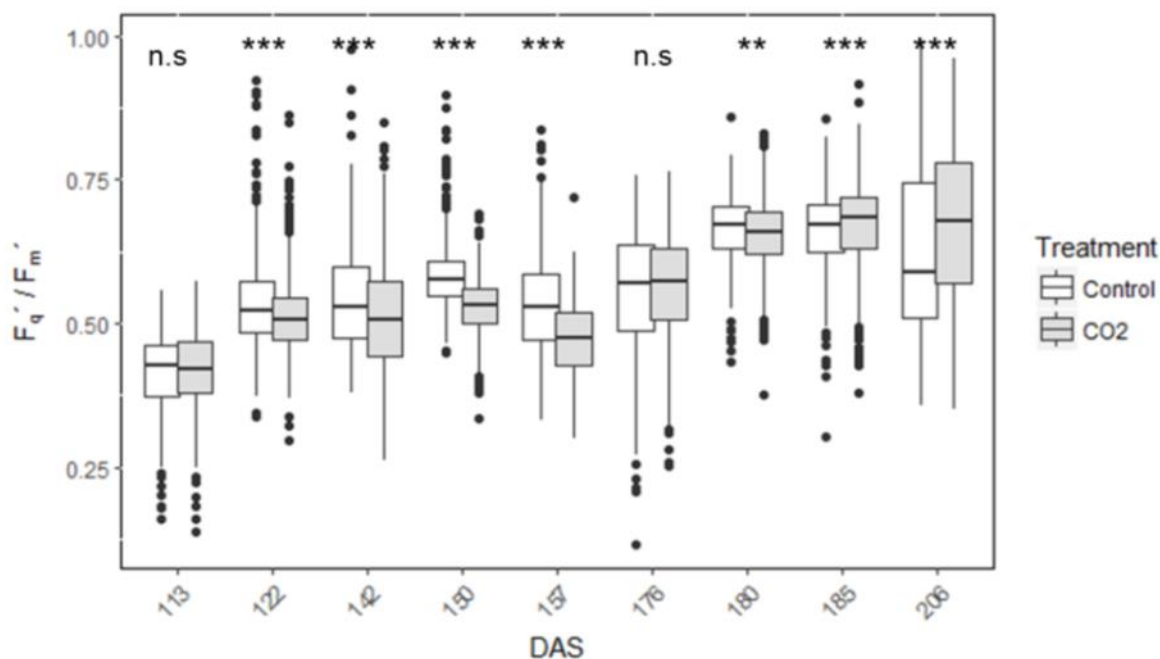


Figure 122: Photosynthetic efficiency of PSI (F_q' / F_m') determined by the LIFT instrument for 12 winter wheat genotypes pooled grown under elevated CO_2 (grey bars) or control (open bars) conditions in CKA. Winter wheat was sown on 16 October 2017. CO_2 was elevated to 600 ppm continuously from sowing with interruptions from 118 - 132, 167 - 170 and 180 - 204 days after sowing (DAS).

Between the selected genotypes that span 50 years of release dates of the different winter wheat varieties, no consistent pattern was shown over the different measurement dates (Figure 123). The decrease in F_q' / F_m' 157 days after sowing, when it was a relatively cold day, is shown for all varieties.

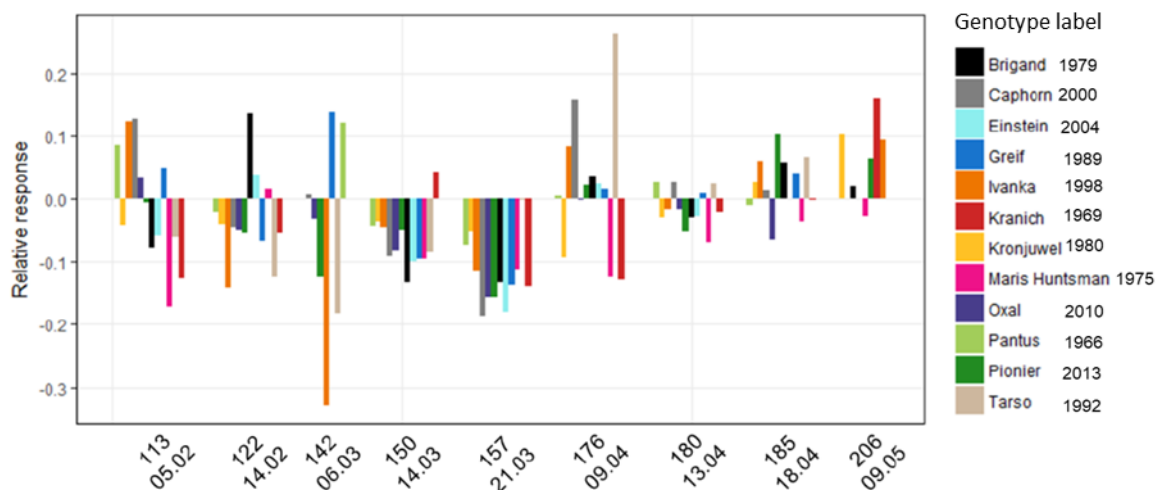


Figure 123: Relative response of F_q' / F_m' for the single genotype (eCO_2 -control / eCO_2) from February to May 2018. DAS after sowing are shown on top of the date. 12 different winter wheat varieties are labelled with different colors and in the figure ranked from early to recent release year (year shown behind the variety name).

SIF was measured with the FloX alongside LIFT measurements at 122, 185 and 206 DAS. Over the three measurement dates, the photosynthetic efficiency PSII (F_q' / F_m') measured by LIFT was highly correlated to SIF yield at 760 nm (Figure 124). Within each measurement day, only at 185 DAS was a significant correlation found (data not shown).

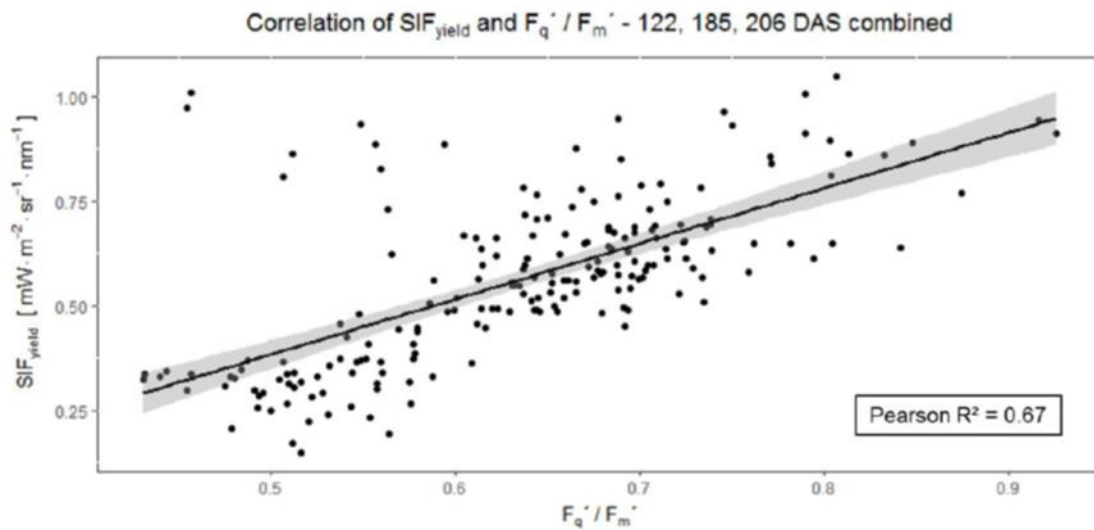


Figure 124: SIF yield versus F_q' / F_m' in winter wheat during three days in spring. SIF was retrieved at 760 nm with the iFLD method in the O₂-A band at 760 nm (Alonso et al. 2008, Meroni et al. 2009). Individual points indicate measurement of plot measurement comprising of one variety grown under elevated or control CO₂. SIF_{yield} was calculated with the QEPro spectrometer. The proxy for SIF_{yield} is depicted in the following formula: $SIF_{yield} = SIF_{ifld\ in\ O2-A\ band\ Incoming\ 760\ nm}$. We only used the incoming radiation at 760 nm as the nature of reflected light from the canopy is difficult to estimate (Pinto et al. 2016).

In addition to winter wheat, 12 soybean varieties (selected as part of the EU Horizon 2020 grant EPPN2020) were chosen and grown with 3 - 4 replications in one BreedFACE ring. LIFT measurement was done on all 12 genotypes in August 2018 and the plants were harvested in September. The seed yield per plant was higher under elevated than control CO₂ for the majority of genotypes. Additionally, the majority of genotypes showed a lower F_q' / F_m' under elevated CO₂ (Figure 125) similar to winter wheat (Figure 122).

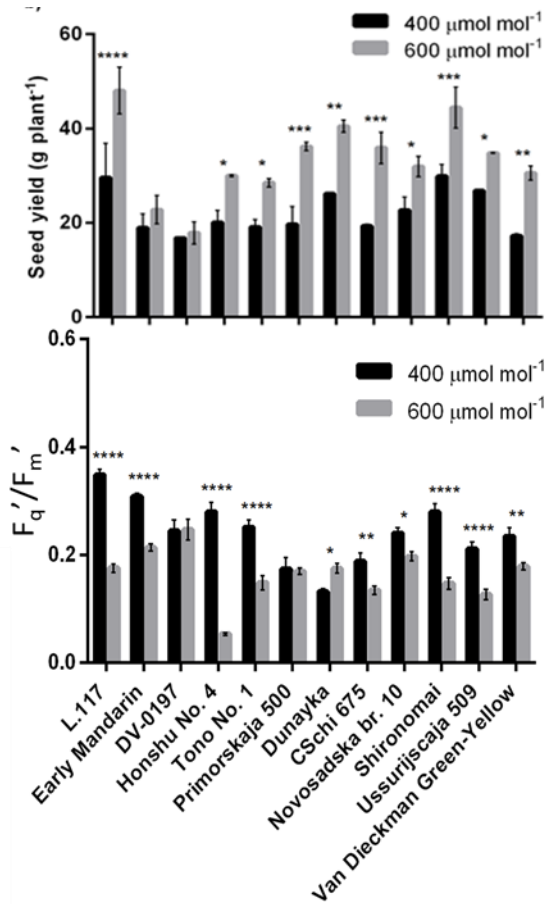


Figure 125: Seed yield and photosynthetic efficiency of PSI (F_q' / F_m') determined by the LIFT instrument for 12 soybean genotypes grown under elevated CO_2 (grey bars) or control (black bars) in September and July 2018, respectively. Asterisks indicate significant differences between control and elevated CO_2 .

Two soybean varieties, DV-0197 and Tono# No. 1, were selected for diurnal measurements of SIF by the FloX on 3 August 2018 (Figure 126). The SIF yield was higher under elevated CO_2 in the morning than in the control whereas in the evening the SIF yield did not differ. Over the day, SIF yield followed the solar diurnal pattern with lowest values at midday. The higher SIF yield in the morning is proposed to correlate to the higher biomass in soybean under elevated CO_2 , whereas the larger decrease in SIF yield under elevated CO_2 compared to the control is proposed to be related to stronger feedback inhibition, which may also explain the lower F_q' / F_m' for soybean as well as wheat.

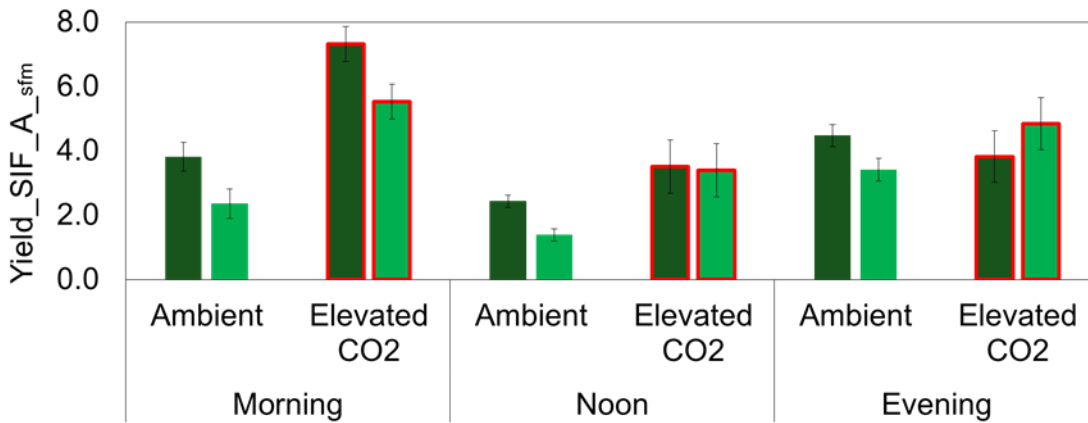


Figure 126: SIF measured by FloX shown SIF yield A derived by the SFM for the soybean varieties DV-0197 (dark green) and Tono # No. 1 (light green). Red borders indicate plants grown under elevated CO₂. Approximate times: Morning 9 am to 10 am, noon 12 pm to 1 pm, and evening 5 pm to 6 pm.

7.3.2 Mapping and understanding the diurnal dynamics of sun-induced fluorescence in agricultural plants

Some of these data are being used for a scientific publication that is under review at the time this report was submitted. More details on the data and an extended scientific discussion can be found in this publication (Attachment 12.3).

Siegmann B., Cendrero-Mateo M.P., Cogliati S., Damm A., Gamon J., Herrera D., Jedmowski C., Junker-Frohn L.V., Kraska T., Muller O., Rademske P., van der Tol C., Quiros-Vargas J., Yang P. & Rascher U. Downscaling of far-red solar-induced chlorophyll fluorescence of different crops from canopy to leaf level using a diurnal data set acquired by the airborne imaging spectrometer *HyPlant*. *Remote Sensing of Environment*, re-submitted after review.

At the end of June 2018, CKA was covered several times by *HyPlant* with 1-m spatial resolution. On 26 June, the campus was recorded in the late afternoon (17.15 CEST) and one day later on 27 June in the morning (10:10 CEST). After a day with cloudy conditions on 28 June, data acquisition was continued on 29 June. On that day, the campus was covered four times between 11.15 and 15.50 CEST. The six-recorded data sets together cover a complete day and allow investigation of the SIF diurnal changes in different crops. The data set was enriched through the additional acquisition of *HyPlant* DUAL, TASI hyperspectral thermal and Riegl LiDAR image data. Figure 127a and b show the *HyPlant* DUAL TOC reflectance of the 12.30 CEST overpass in the form of an RGB composite and the DSM of the campus derived from the Riegl LiDAR data. In addition, first LAI and LCC maps of the entire campus based on a PROSAIL inversion of the *HyPlant* DUAL TOC reflectance are presented in Figure 127c and d, respectively. Both maps provide an overview of these two important plant parameters, which were helpful in further data analysis and modeling.

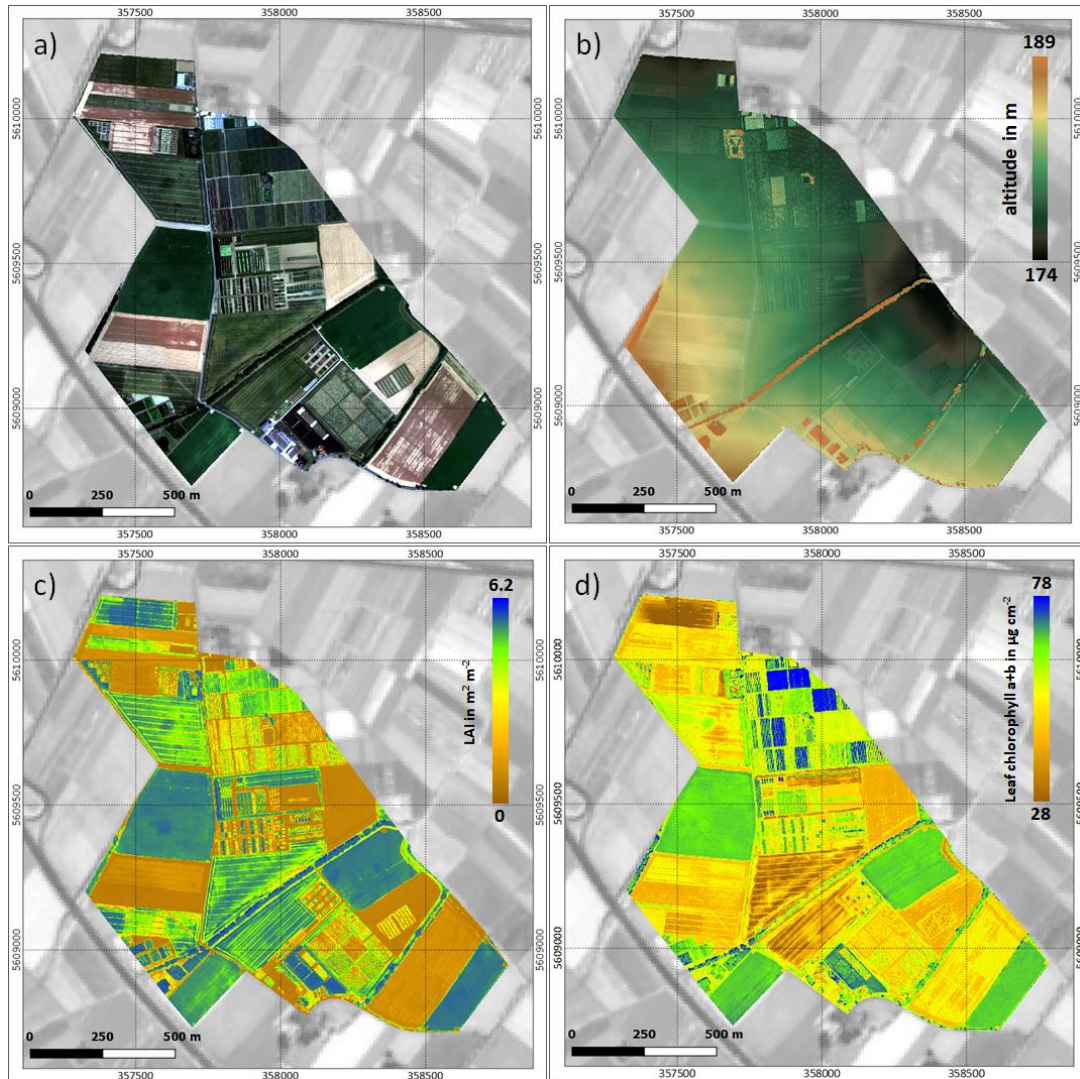


Figure 127: RGB composite of CKA (a) and the corresponding DSM (b) derived from the 12.30 CEST overpass on 29 June 2018. LAI (c) and LCC map (d) of the campus based on a PROSAIL inversion of the *HyPlant* DUAL TOC reflectance data.

While Table 23 gives an overview of the different dates and times of airborne data acquisition, Figure 128 provides information on temperature and PAR during data acquisition, as recorded at the weather station located in the northern part of the campus.

Table 23: Overview of the airborne data covering one diurnal cycle acquired over CKA in the period from 26 and 29 June 2018.

Acquisition date	Recording time (local)	<i>HyPlant</i>	TASI	LiDAR
26.06.2018	17:15	X	X	X
27.06.2018	10:10	X	X	X
29.06.2018	11:15	X	X	X
29.06.2018	12:30	X	X	X
29.06.2018	14:40	X	X	X
29.06.2018	15:50	X	X	X

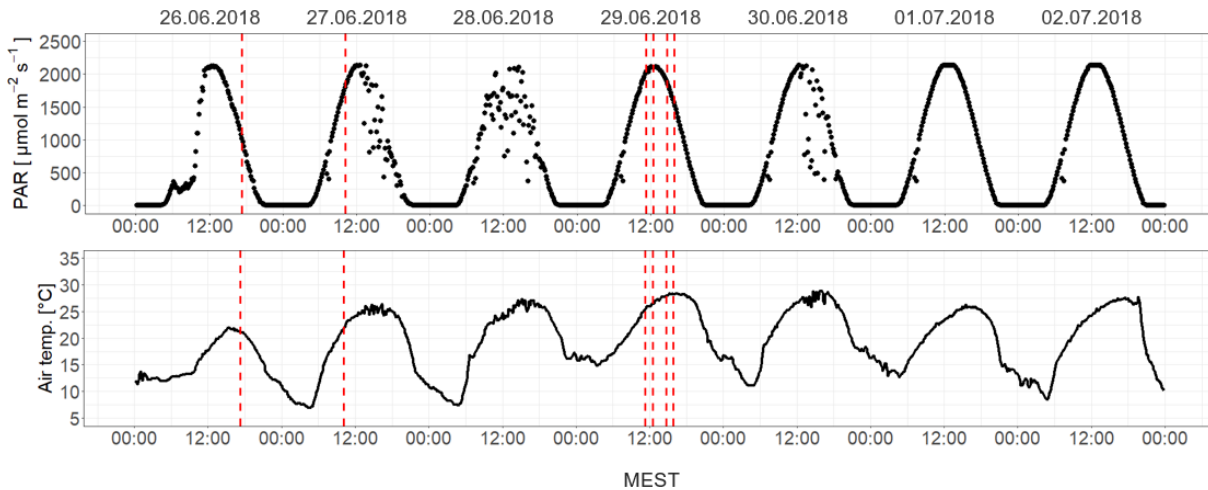


Figure 128: PAR and air temperature measured in 10-minute intervals at the weather station north at CKA from 26 June to 2 July 2018. The vertical red dashed lines indicate the six time points of *HyPlant*, TASI and Riegl LiDAR data acquisition.

Two main driving factors and their influence on SIF were investigated: Temperature and precipitation. It is clear that further parameters can have an impact on SIF, but in this experiment, we can assume that temperature and soil water availability (which is a factor of precipitation) are the primary environmental factors. Since the daily air temperature curves were comparable and there was no precipitation within the observation period, it was possible to combine the four airborne data sets recorded on 29 June with the data sets acquired on 26 and 27 June to investigate the diurnal changes in SIF derived from *HyPlant* FLUO image data. Figure 129 provides an overview of the averaged SIF_{760} , SIF_{687} and LST values for each of the six overpasses while only considering pixels having a NDVI higher than 0.3. Both SIF diurnal courses follow in shape the measured PAR curve with the highest values around local solar zenith (13.30 CEST local time), which is illustrated in Figure 130a. The shape of the SIF curves meets the expectations and show that *HyPlant* data can be used to investigate the diurnal changes in SIF for larger areas. The fact that SIF_{760} is 2 to 3 times higher than SIF_{687} , depending on the acquisition time, further verifies the validity of the SIF products derived from *HyPlant*, since similar ratios were also reported for crops in other studies (e.g., Rossini et al. 2016).

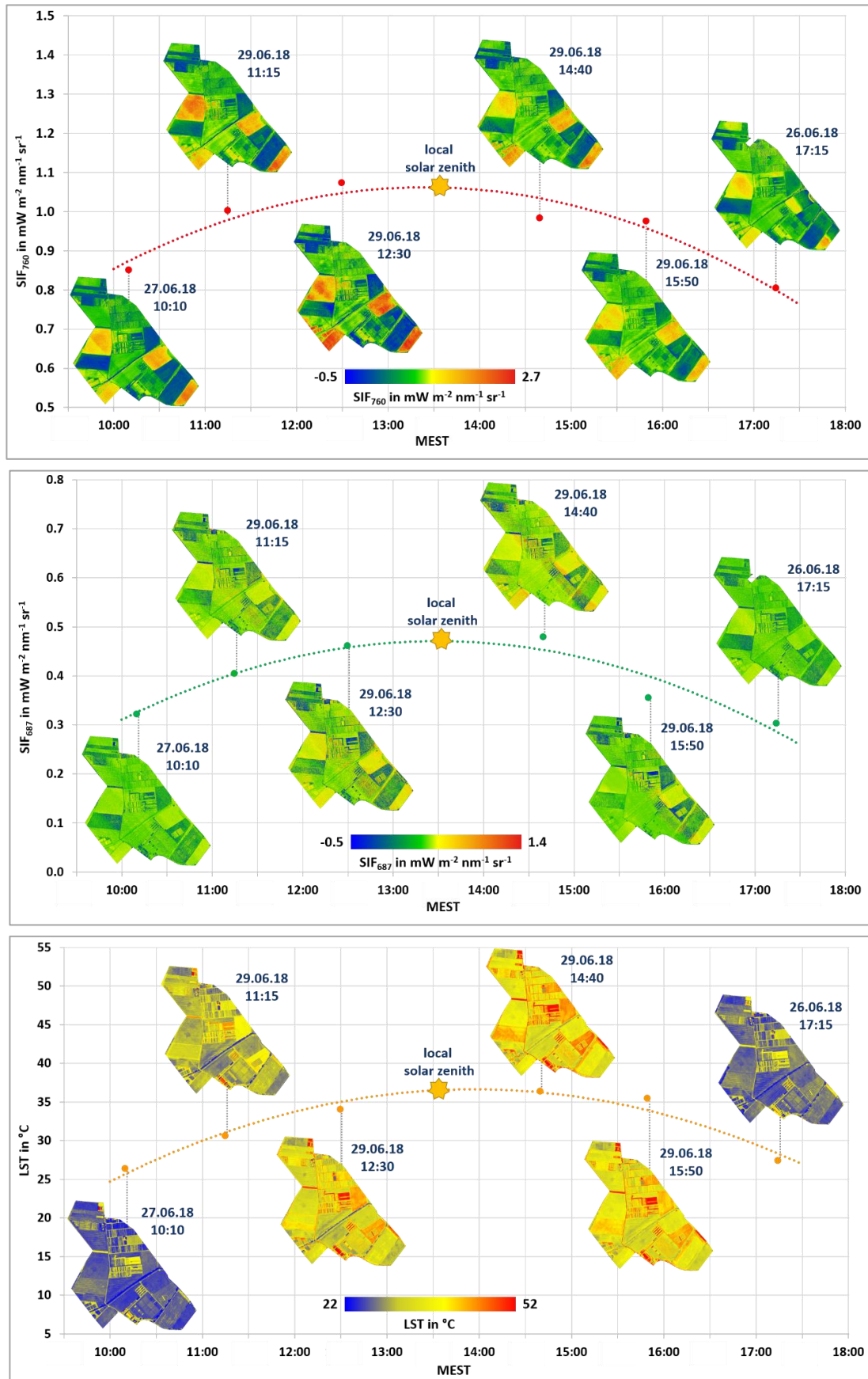


Figure 129: Diurnal course of iFLD SIF₇₆₀ (top), iFLD SIF₆₈₇ (middle) and LST (bottom) of CKA derived from HyPlant FLUO and TASI data acquired on 26, 27 and 29 June 2018. The dots attached to the maps represent the mean values of all vegetated pixels.

The diurnal course of TASI LST differs a bit from both SIF and the PAR curve and reaches its maximum half an hour after local solar zenith (Figure 130b). Figure 130c depicts how the curve of the vegetation index NIRv, which was recently developed by Badgley et al. (2017) as a proxy for far-red fluorescence, behaves in comparison to the SIF₇₆₀ curve. It can be seen that both curves have a similar shape. Since the NIRv was developed using a time series of satellite data, it needs to be investigated further whether this new vegetation index can also be used as a proxy for SIF₇₆₀ derived from *HyPlant* data covering a single day.

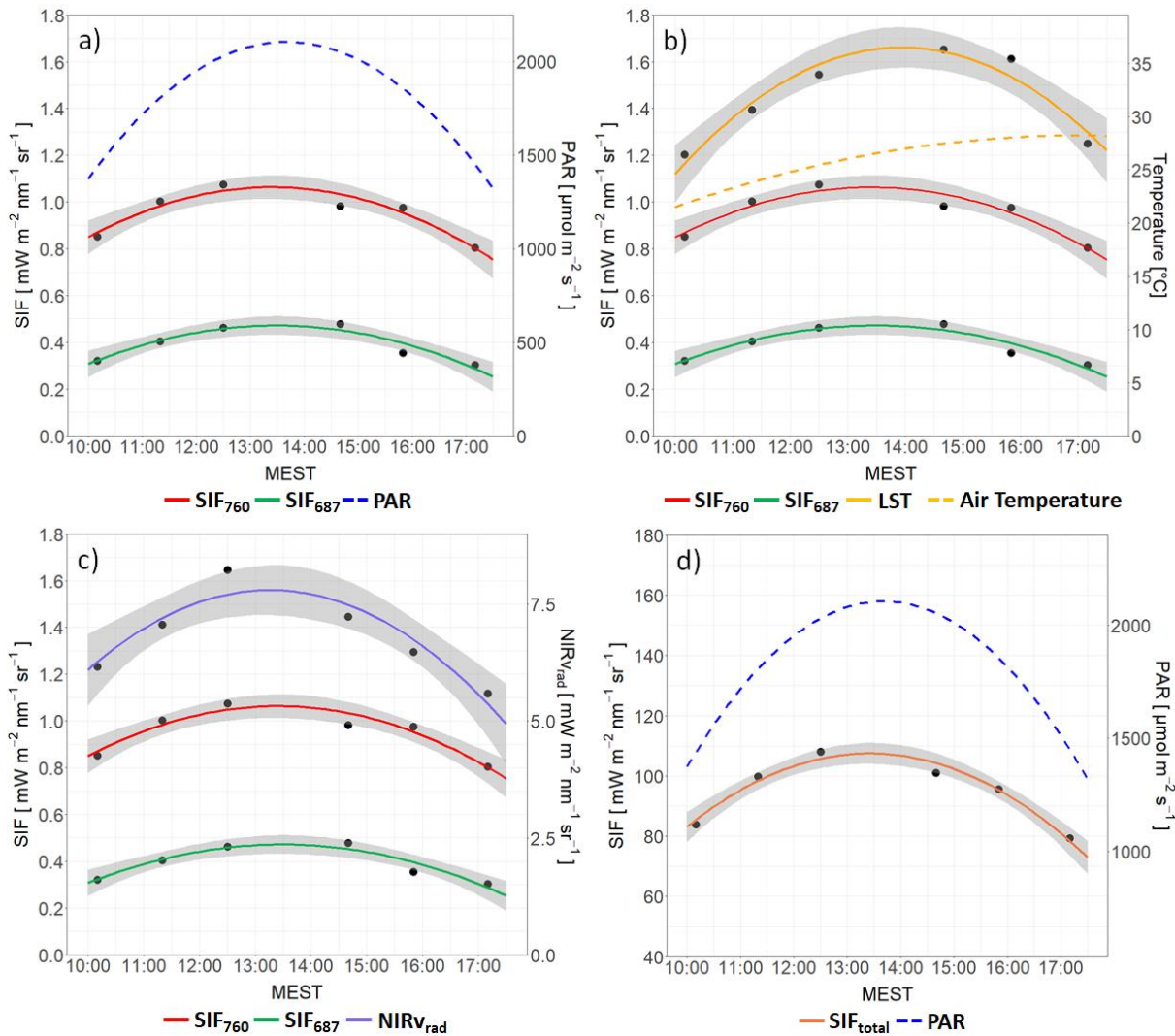


Figure 130: Comparison of the diurnal pattern of SIF₇₆₀ and SIF₆₈₇ with a) PAR, b) TASI LST and air temperature and c) NIRv_{rad}. d) comparison of SIF_{total} calculated according to ESA 2015 with PAR.

Since different crops were grown within the campus in 2018, Figure 131 depicts the diurnal course of SIF₇₆₀ (a), SIF₆₈₇ (b), SIF_{total} calculated according to ESA 2015 (c) and the LST derived from TASI image data for sugar beet, potato, winter wheat and fruit trees. It can be clearly seen that the different crops provided have comparably shaped diurnal curves but differ in absolute values. While the shape of the SIF₆₈₇ curves are similar to that obtained for the entire campus, as shown in Figure 130a, the SIF₇₆₀ curves show higher values in the morning and in general a less convex pattern. Especially, the potato curve differs from the curves of the other observed crops. In terms of absolute values, the order of the different crops is similar for the two SIF products. For both, potato provides the highest values followed by sugar beet, winter wheat and fruit trees. The diurnal curve derived for SIF_{total} is comparable to that one of SIF₇₆₀, since SIF_{total} consists to 90% of SIF₇₆₀. In contrast to the SIF products, the diurnal course of TASI LST shows a different shape and order for the different crops (Figure 131d). In the morning and the afternoon, the LST values of the different crops are

very similar. Around local solar noon, however, higher temperatures could be observed for potato and fruit trees. By contrast, sugar beet and winter wheat provide very similar diurnal curves at a distinctly lower LST level.

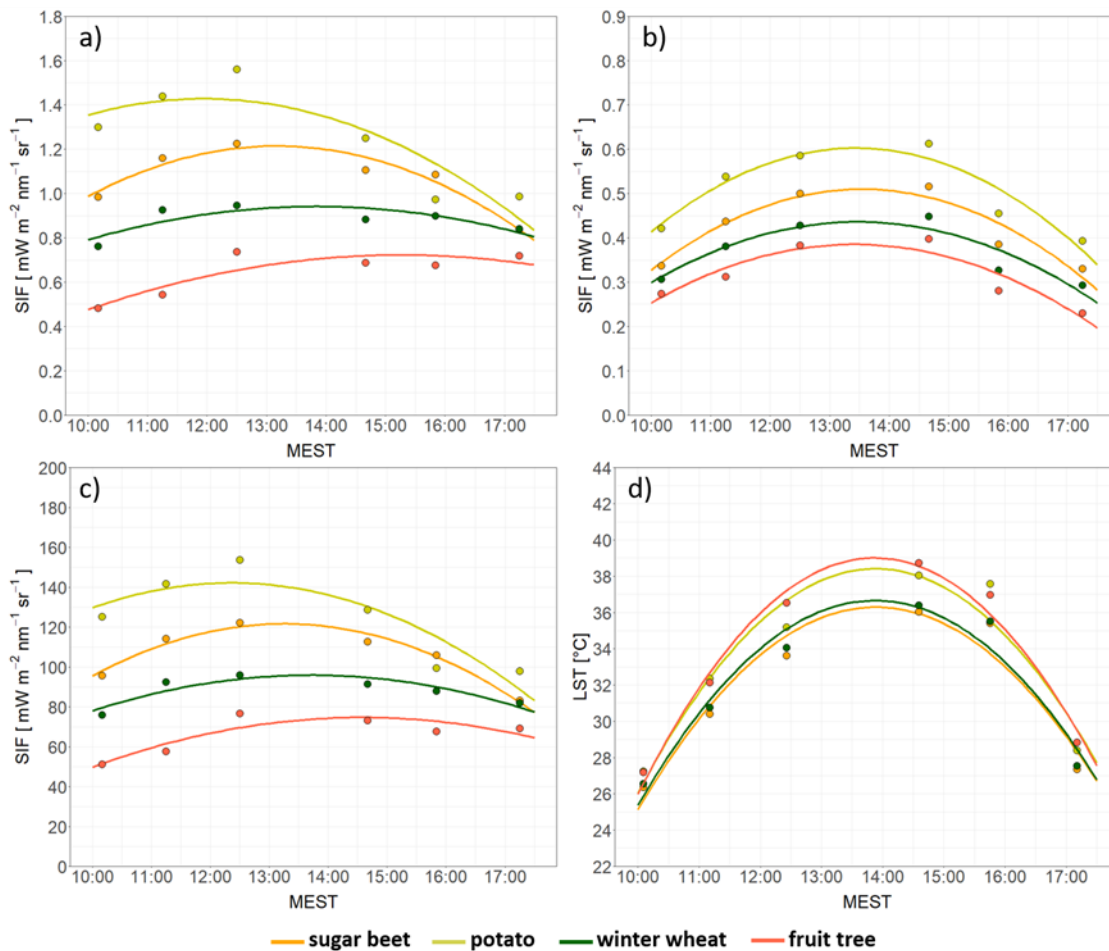


Figure 131: Comparison of the diurnal pattern of SIF₇₆₀ and SIF₆₈₇ with a) PAR, b) TASI LST and air temperature and c) NIRv_{rad}. d) comparison of SIF_{total} calculated according to ESA 2015 with PAR.

7.3.3 Measuring sun-induced fluorescence from a novel UAV-based SIF system

During the 2018 vegetation period, 10 barley varieties were planted in 3 x 6 m plots and measured once with LIFT for testing the speed of operation at the semi-automatic positioning system field cop (Figure 132). The same plots were used for testing UAV-based SIF measurements in comparison to ground SIF measurement with the FloX (Figure 133) (Quiros Vargas et al. 2020) and with *HyPlant* SIF observations.



Figure 132: Barley varieties from the DPPN collection planted in 3 x 6 m plots seen from above with barley in the center, maize on the left, rapeseed on the right and the field cop with the LIFT mounted in May 2018.

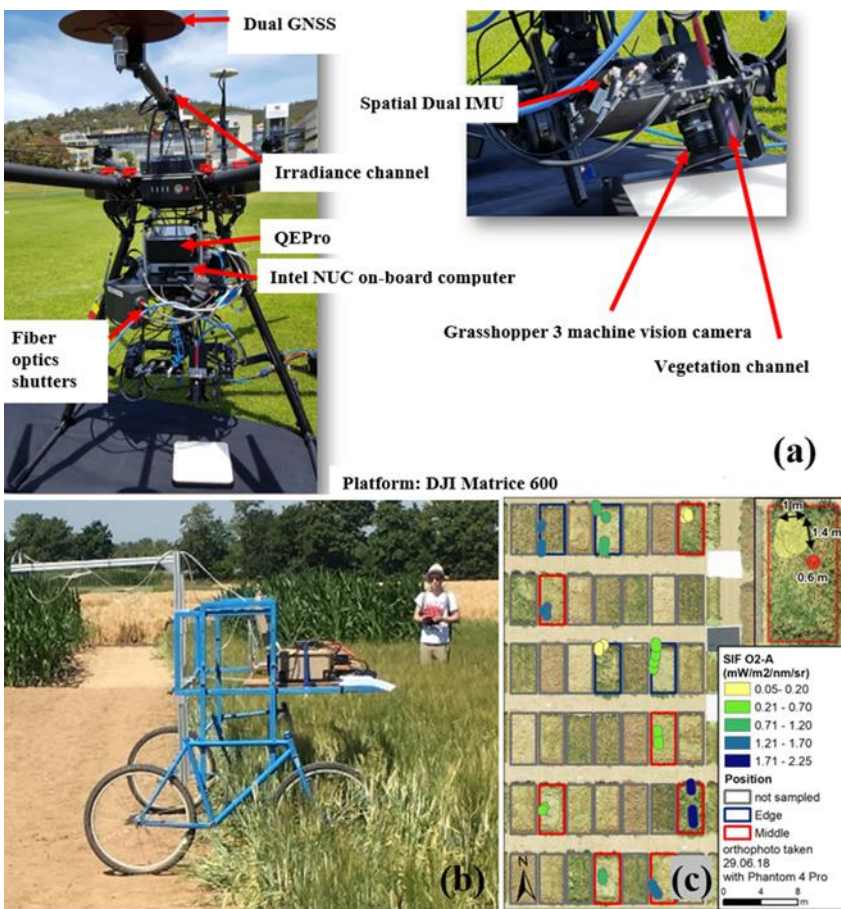


Figure 133: (a) AirSIF system components, (b) field bike used for ground FloX measurements and (c) footprints of the flight at 14:00 local time with their respective O₂-A SIF at edge (blue) and middle (red) sampled plots over the orthophoto derived from UAS photogrammetry.

UAV-borne SIF observations were acquired by the team from the University of Tasmania (Australia) on 29 June with the AirSIF instrument (Bendig et al. 2019, Gautam et al. 2020), followed by UAV-borne hyperspectral push broom scanner observations on 2 July (Lucieer et al. 2014). Flights were carried out over the common experiment (Figure 119) for barley and maize (SIF and hyperspectral radiance / reflectance), and wheat (hyperspectral radiance / reflectance only). Sample results for barley are depicted in Figure 134. The AirSIF instrument, a non-imaging high-spectral resolution spectroradiometer, was deployed four times on 29 June, aiming to match the *Hyplant* observations as closely as feasible. The results represent spatially precise point measurements of SIF₇₆₀ taken between 12:00 and 17:00 local time, mainly over the barley

experimental plots. The hyperspectral flight lines were acquired with the Headwall Micro-Hyperspec instrument (Headwall Photonics Inc.), configured with 162 spectral bands with FWHM of 5 nm (on average), and a GSD of 4 cm. The data was radiometrically calibrated to radiance and atmospherically corrected to reflectance. The NDVI image of the barely plots is shown by way of example, in Figure 134.

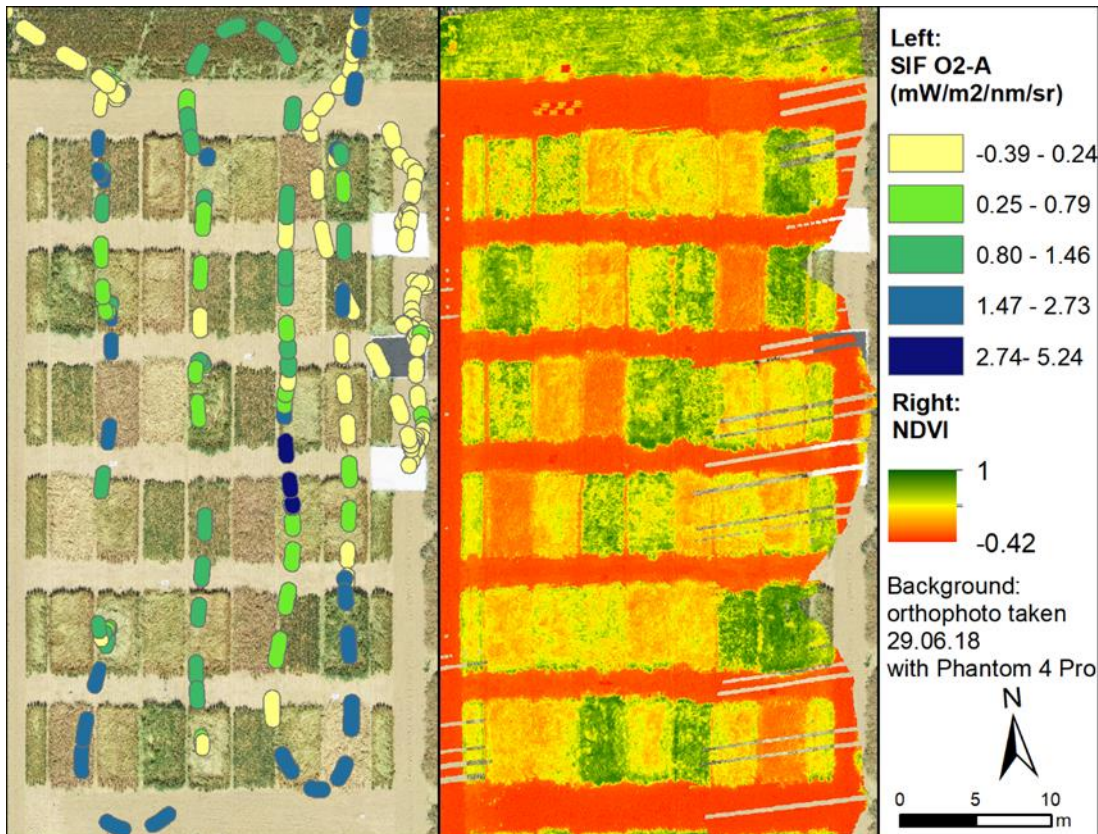


Figure 134: Left: SIF₇₆₀ in mWm⁻²nm⁻¹sr⁻¹ of barley, acquired from non-imaging spectroradiometer AirSIF (University of Tasmania), Right: NDVI mosaic retrieved from Headwall Micro-Hyperspec push broom scanner (University of Tasmania) at 4 cm GSD, Background: Orthophoto taken with DJI Phantom 4 Pro (courtesy of M. Dogotari and M. Prüm, Rhine-Waal University of Applied Sciences).

Values of SIF₇₆₀ footprints from the AirSIF system were compared with FloX and *HyPlant* SIF₇₆₀ acquired on the same day (29 June 2018) for the CKA common barley experiment. 10 of the 35 experimental plots were repeatedly sampled with AirSIF throughout the day. Figure 135 (left) shows SIF₇₆₀ radiance values for the mobile FloX, AirSIF and *HyPlant* per sampled plot and flight (n = 10). Morning values for FloX and AirSIF SIF₇₆₀ radiance were found to be relatively comparable. A similar general agreement was found between SIF₇₆₀ radiance of the AirSIF and *HyPlant* sensors, except the *HyPlant* values at 14:45 MEST that are significantly higher and form an obvious outlier in the boxplot. To enable a better comparison between the AirSIF and *HyPlant* sensors, and to compensate for the influence of apparent PAR and canopy structure impact within the different GSDs of SIF acquisitions, SIF₇₆₀ was normalized according to the approach suggested in Yang et al. (2020), by using the fluorescence correction vegetation index (FCVI) (Figure 135, right). Interpretation of the SIF₇₆₀ efficiency values reveals that all *HyPlant* flights conducted at 680 m agl, resulting in a larger pixel size of 1 x 1 m, produced significantly higher integrated values than the AirSIF and *HyPlant* observations carried out at the comparable GSDs. If we disregard the results of these three high agl overflights at 12:30, 14:45 and 16:00, one can say that the SIF₇₆₀ efficiencies of both sensors are fully comparable, with SIF₇₆₀ values steadily increasing from 11:15 until 14:00 and decreasing from 15:00 until 17:00, as well as showing a fast increase between 14:00 and 15:00 local time.

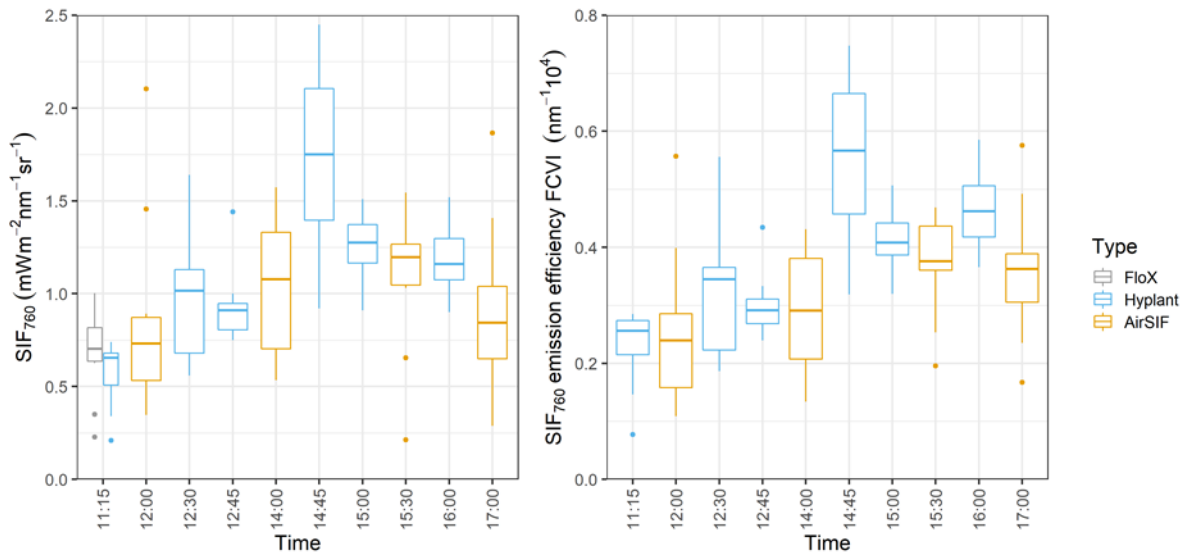


Figure 135: Left: SIF₇₆₀ of barley plots sampled by AirSIF in comparison with FloX and HyPlant values for all flights conducted on 29 June; times shown in MEST; SIF retrieval method is SFM. Right: SIF₇₆₀ emission efficiency for AirSIF and HyPlant observations calculated with the FCVI standardization approach (Yang et al. 2020). Note: HyPlant flights at 12:30, 14:45 and 16:00 local time were flown at 680 m agl resulting in a pixel size of 1 x 1 m. FCVI calculation for FloX was impossible due to the missing required spectral inputs.

7.4 Majadas de Tietar, Spain

[39.94N, 5.77W]

In Majadas de Tietar, Spain the ecosystem is a typical 'Iberic Dehesa', with an herbaceous stratum of native pasture and a tree layer of scattered oak trees, with 98% of the trees being *Quercus ilex* (Figure 136). The tree density is about 20 trees ha⁻¹ with a mean DBH of 46 cm and a canopy height of about 8 m. The canopy fraction of the trees is about 20%. The herbaceous layer consists mostly of various annual native species such as *Vulpia bromoides* (L.), *Vulpia geniculata* (L.), *Trifolium subterraneum* (L.), *Ornithopus compressus* (L.) with often more than 20 species within 4 m². The fractional cover of the three main functional plant forms within the pasture (grasses, forbs and legumes), varies spatially but also seasonally according to their phenological status (Perez-Priego et al. 2015). The LAI of the trees is around 0.35 m² m⁻² (1.5 - 2.0 m²m⁻² on a tree basis) while the spring peak green LAI of the herbaceous layer ranges between 2 - 4 m²m⁻² depending on the season. The savanna is managed and used for continuous grazing of extensive livestock with a low density of 0.3 cows ha⁻¹. During the driest summer months (July - Sept), most of the cattle is usually moved to nearby mountain grasslands. Mean annual temperature is 16.7 °C and annual precipitation is ca. 650 mm, with large inter-annual variability (El-Madany et al. 2018). The prevailing wind directions are West-Southwest and East-Northeast. The sampling scheme used during the FLEXsense campaign is reported in Figure 137.

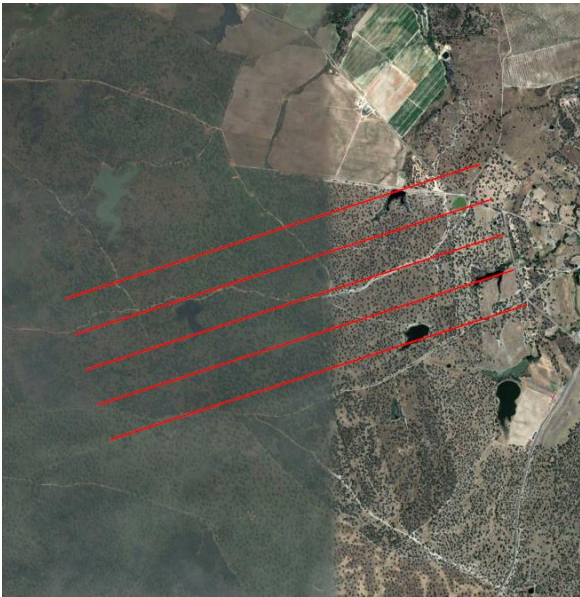


Figure 136: Flight lines for experimental site Majadas.

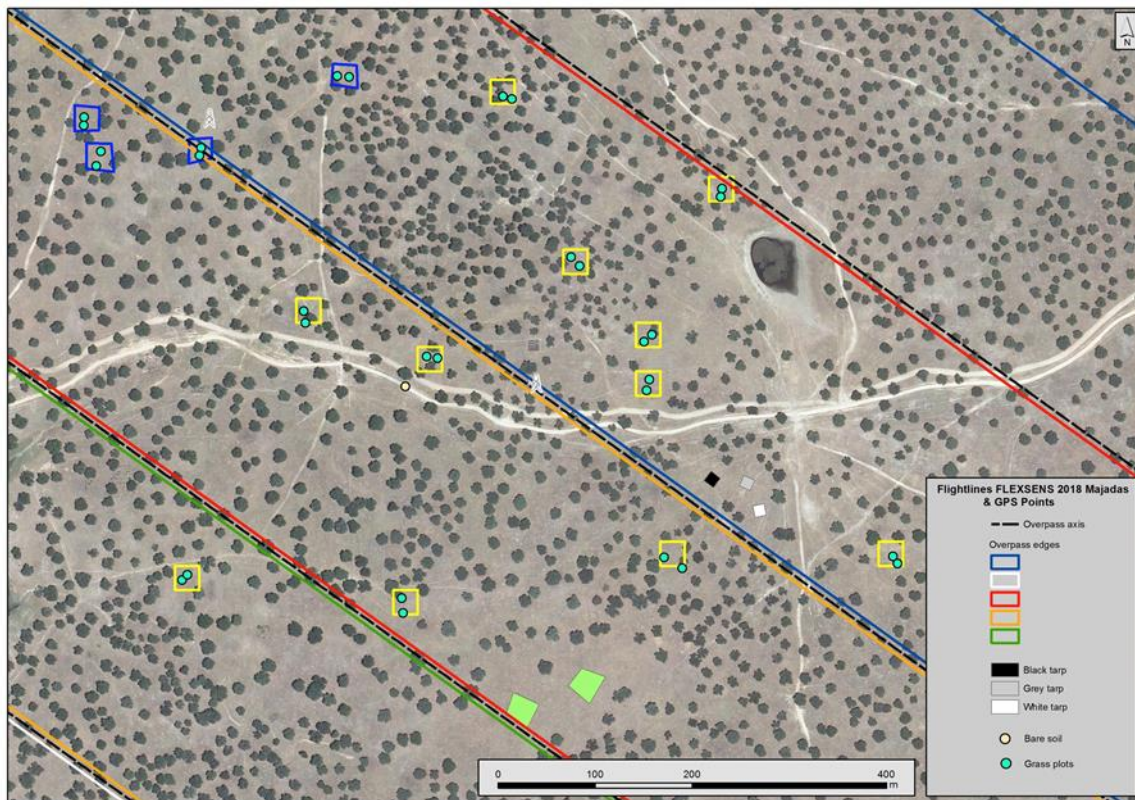


Figure 137: Flight lines and location of vegetation sampling and tarps during the campaign. Figure: Courtesy of Dr. Pilar Martin (CSIC).

7.4.1 Correlations between ground and airborne measured SIF of the herbaceous layers and the tree canopy

During the FLEXSense campaign, we deployed a series of instrument on the ground to measure ecosystem scale fluxes of CO₂, water and energy. To this end, we used six EC systems that cover a large amount of the spatial variability. Three FloX systems were deployed, two permanently installed on a boom that was

programmed to rotate in order to measure tree and grass every 15 minutes. The data coverage of the FloX system was very good, as shown in Figure 138. An additional system was used to sample the spatial variability of optical properties and fluorescence during the flight overpasses (Figure 139). The comparison between vegetation indices (NDVI, NIRv) and SIF estimates from two different retrievals are reported in Figure 140 and Figure 141. The results show a good agreement in terms of correlation between the *HyPlant* and FloX data for both flight patterns (low-altitude L, and high-altitude H). Comparing ground-based FloX measurements to airborne SIF data showed a good correlation between the NDVI and NIRv data as well as SIF data that were retrieved with the SFM. While none of the correlations were close to the 1:1-line, clear variability on the slopes and off-set of these correlations were found (Figure 140A - D). *HyPlant* SIF data that were derived with the iFLD were all very close to zero and showed no correlation to the corresponding ground-based FloX data (Figure 140A - D). This lack of correlation and the iFLD data that showed no variability can most likely be related to the very low number of soil pixels in these flight lines. During the visual inspection of these flight lines, it was already clear that the iFLD retrieval did not work well because of the low number of non-vegetated reference pixels. It thus is a promising indication that the SFM did reveal good (even though not-optimal) SIF data from these challenging flight lines. Some of the deviations between the ground-based FloX and airborne *HyPlant* data may also be related to a pronounced spectral shift, which was found in the FloX system.

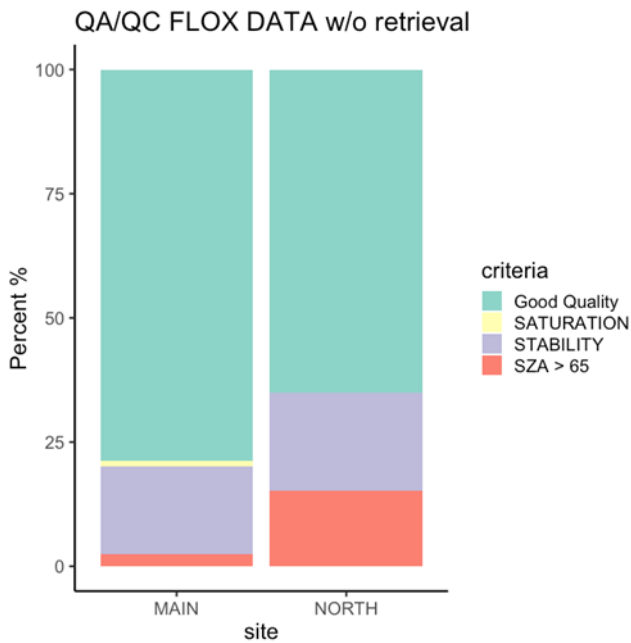


Figure 138: Overview of data quality. In light green, the data of good quality retained after filtering for the saturation and stability of the irradiance, and SZA.

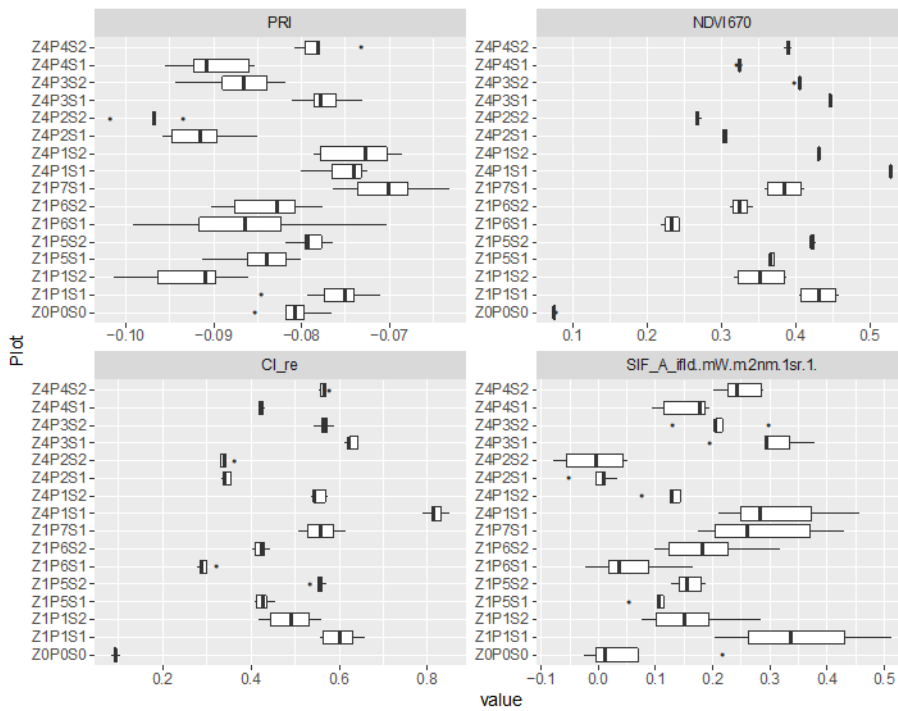


Figure 139: Boxplot of vegetation indices (PRI, NDVI and chlorophyll (CI)) and SIF retrieved with iFLD collected on the herbaceous layer. Different boxplots refer to multiple measurements collected in the sampling plots.

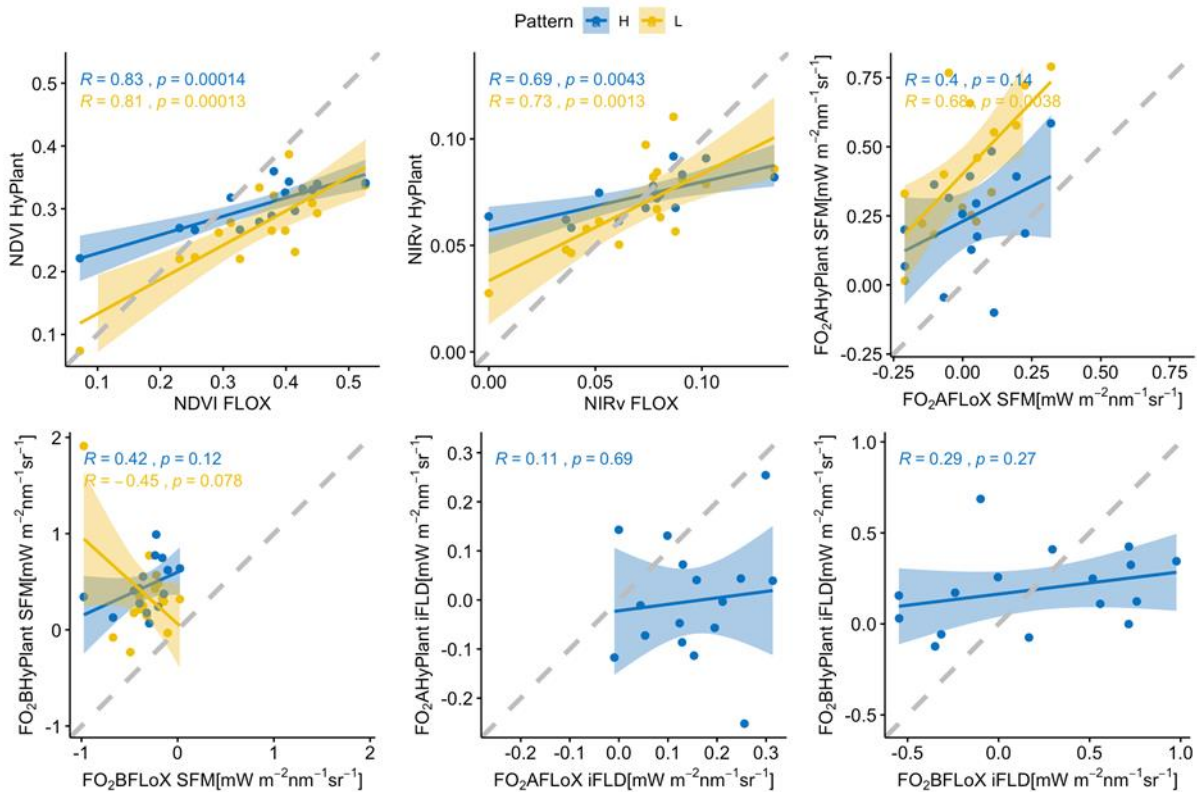


Figure 140: Comparison between vegetation indices (NDVI and NIRv) and different SIF metrics derived from the FloX at the ground and HyPlant.

The correlation analysis was repeated after removing the data from the bare soil plot, which had unexplainable values (Figure 141). The principal trends remained the same, but the correlation between the SIF values (derived by the SFM) was clearer and more consistent.

Additionally, the ground team characterized a series of plant traits and biophysical properties of both the herbaceous layers and the tree canopy (Table 24). Finally, terrestrial LiDAR scans were conducted in October 2018, few weeks after the flight, to characterize trees parameters (height, diameter at the breast height, crown area and clumping). In order to shed light on the structural and functional interplay in the diverse and complex ecosystem, all of these data were uploaded together with a readme file in the data repository.

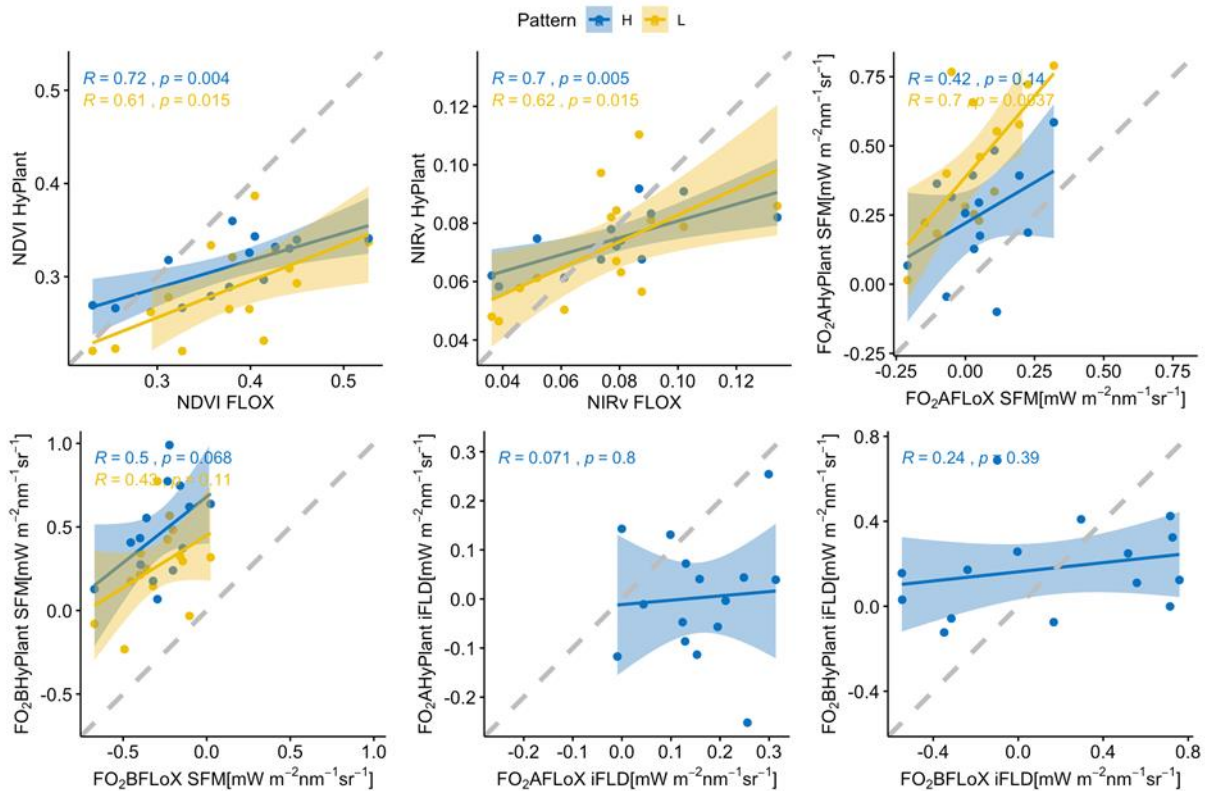


Figure 141: Comparison between vegetation indices (NDVI and NIRv) and different SIF metrics derived from the FloX at the ground and *HyPlant*. Compared to Figure 140, we removed the data from one bare soil plot (due to low NDVI and NIRv values).

Table 24: List of biophysical parameters sampled during the field campaign by the ground team.

Variables in Herbaceous Layer	
Fuel Moisture Content [-]	FMC
Canopy Water Content [g/cm ²]	CWC
Above Ground Biomass [g/m ²]	AGB
Green Above Ground Biomass [g/m ²]	AGB_v
Specific Leaf Weight [g/cm ²]	SLW
Green Specific Leaf Weight [g/cm ²]	SLW_v
Non-green Specific Leaf Weight [g/cm ²]	SLW_nv
Leaf Area Index [m ² /m ²]	LAI
Green Leaf Area Index [m ² /m ²]	
Non-green Leaf Area Index [m ² /m ²]	
Specific Leaf Area [cm ² /g]	SLA

Green Specific Leaf Area [cm ² /g]	SLA_v
Non-green Specific Leaf Area [cm ² /g]	SLA_nv
Leaf Water Content [-]	LWC
Green Leaf Water Content [-]	LWC_v
Non-green Leaf Water Content [-]	LWC_nv
Chlorophyl_a concentration per unit dry mass of green grass [mg/g]	Ca_dmass_v
Chlorophyl_b concentration per unit dry mass of green grass [mg/g]	Cb_dmass_v
Chlorophyl_a+b concentration per unit dry mass of green grass [mg/g]	Cab_dmass_v
Total Carotenoids concentration per unit dry mass of green grass [mg/g]	Cxc_dmass_v
Carbon concentration per unit dry mass of green grass [%]	C_perc_v
Nitrogen concentration per unit dry mass of green grass [%]	N_perc_v
Carbon concentration per unit dry mass of total grass [%]	C_perc
Nitrogen concentration per unit dry mass of total grass [%]	N_perc
Nitrogen allocated in chlorophylls per dry mass unit of green grass [mg/g]	N_Cab_dmass
Variables Tree Leaves	
Fuel Moisture Content [-]	FMC
Equivalent Water Thickness [g/cm ²]	EWT
Leaf Water Content [-]	LWC
Specific Leaf Weight [g/cm ²]	SLW
Specific Leaf Area [cm ² /g]	SLA
Plant Area Index [m ² /m ²]	PAI
Leaf age proportion visually estimated in the field [%]	fracYear
Chlorophyl-a content per leaf area [microgram/cm ²]	Ca_area
Chlorophyl-b content per leaf area [microgram/cm ²]	Cb_area
Chlorophyl-a+b content per leaf area [microgram/cm ²]	Cab_area
Total carotenoids content per leaf area [microgram/cm ²]	Cxc_area
Carbon concentration per unit dry mass of leaves [%]	C_perc
Nitrogen concentration per unit dry mass of leaves [%]	N_perc

7.4.2 The case study of the 2018 heat-wave in the Iberian Peninsula – heat stress effects on SIF and GPP

Some of these data are being used for a scientific publication that is under review at the time this report was submitted. More details on the data and an extended scientific discussion can be found in this publication (attachment 12.2).

Martini D., Sakowska K., Wohlfahrt G., Pacheco-Labrador J., van der Tol C., Porcar-Castell A., Magney T.S., Carrara A., Colombo R., El-Madany T., González-Cascón R., Martin M.P., Julitta T., Moreno G., Rascher U., Reichstein M., Rossini M. & Migliavacca M. Heat-wave breaks down the linearity between sun-induced fluorescence and gross primary production. *New Phytologist*, submitted 17 May 2021.

During summer 2018, a few weeks after the FLEXsense campaign, an intense heat wave hit the Iberian Peninsula, with unusually high air temperatures (T_{air}) and VPD. Figure 142a shows an increase in both T_{air} and decrease in GPP estimated during the period (1 Aug – 7 Aug 2018). Maximum T_{air} registered was 44.47°C and

the maximum VPD was 80.01 hPa (Figure 142b). Both the maximum, T_{air} and VPD were the highest ever registered in the last 12 years at the Majadas de Tietar site.

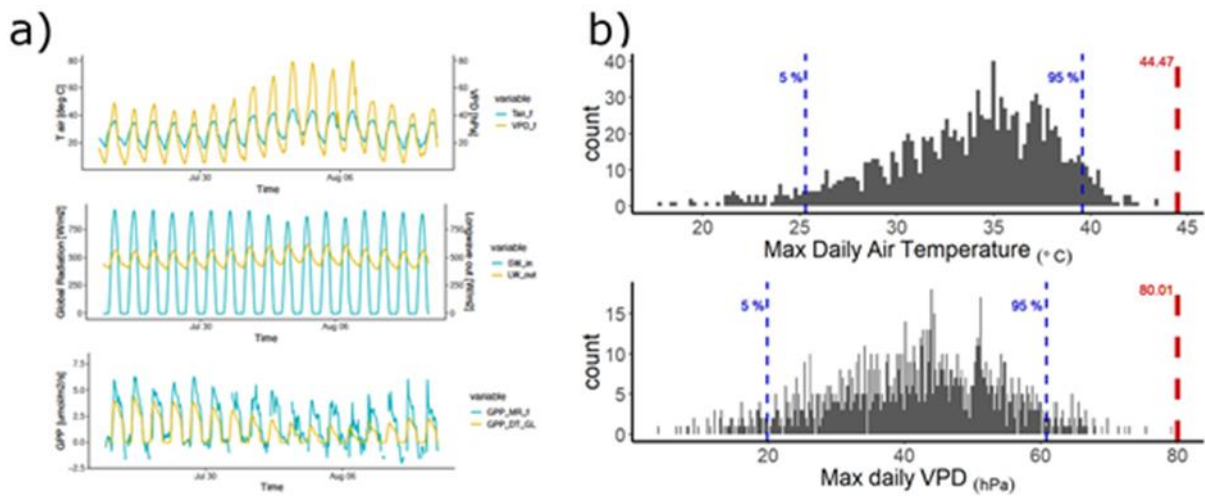


Figure 142: T_{air} , global radiation and GPP during the heat wave of 2018. a): Comparison of the maximum air temperature (44.47°C) and maximum VPD (80.01 hPa) during the 2018 heat wave with the maximum daily temperature and maximum daily VPD from 2004 to 2018 in the months of June, July and August. b): Maximum air temperature and VPD are represented with red dashed lines and the 95% and 5% of the distribution of maximum daily temperature and VPD are indicated with blue dashed lines.

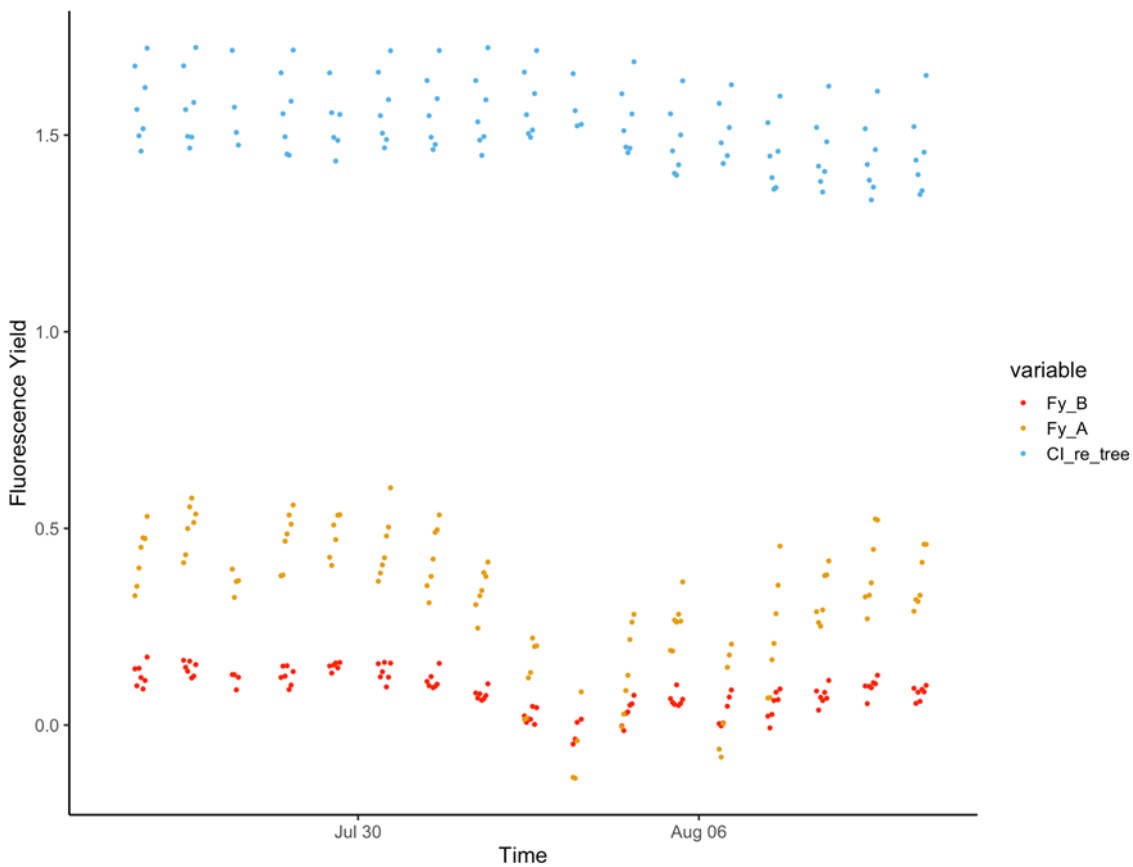


Figure 143: Time series for the Chlorophyll red edge index (Cl_{re}) and fluorescence yield on the O_2 -A (Fy_a) and O_2 -B (Fy_b) bands. The data plots are the hourly average of data of good quality and $SZA < 50^\circ$. Data were collected with the FloX for one individual Holm Oak.

GPP_{DT}, fluorescence on the O₂-A (below referred as “far-red SIF”) and fluorescence on the O₂-B (below referred as “red SIF”) declined significantly during the heat wave, while indices such as Cl_{re} (and others, including CCI, EVI, NDVI and NIRv) did not show significant differences. As the heat wave lasted only seven days and the Cl_{re} index, which is used to track changes in chlorophyll content was not affected by the extreme event, it is possible to conclude that no chlorophyll degradation took place during the heat wave, and that changes in SIF (both red and far-red) are mostly due to physiological regulation rather than changes in leaf or canopy structure.

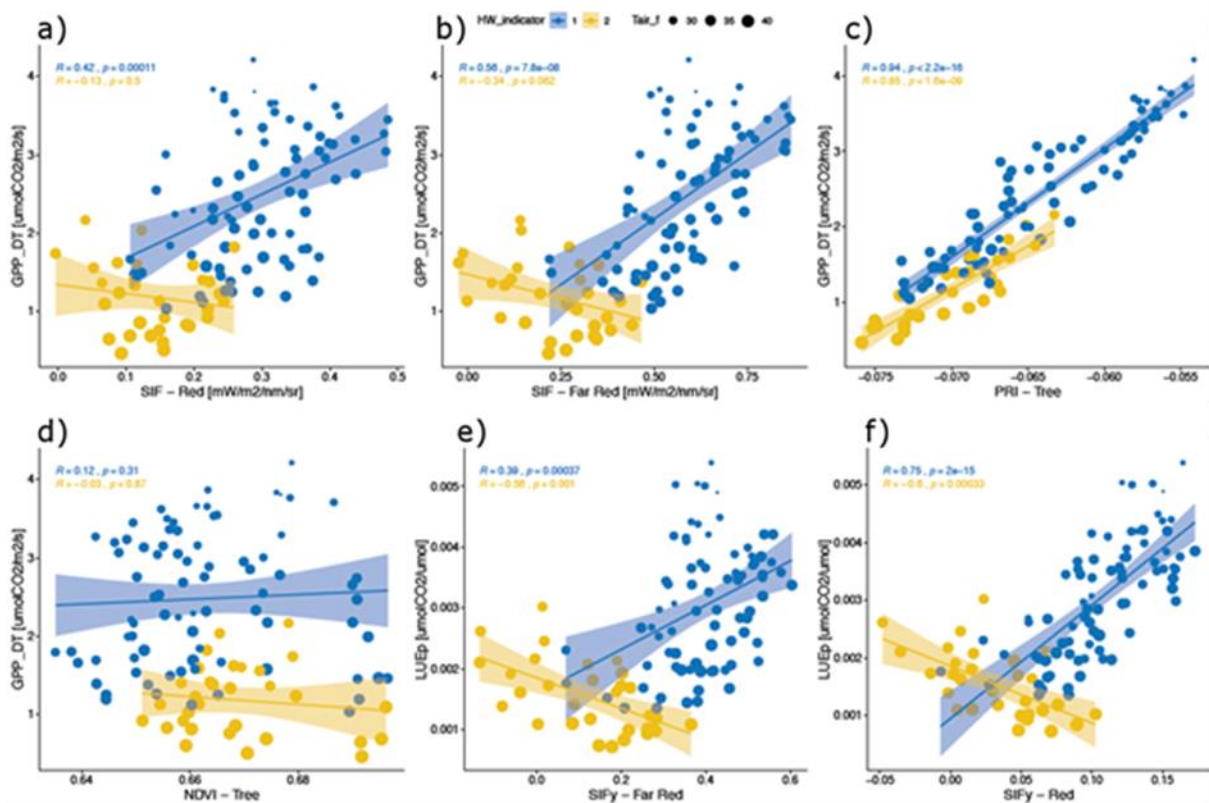


Figure 144: Relationship between GPP_{DT} and SIF at 680 nm (SIF-red) in a); Relationship between GPP_{DT} and SIF at 760 nm (SIF – far-red) in b); GPP_{DT} and PRI in c); GPP_{DT} and NDVI in d); relationship between light use efficiency of photosynthesis (LUEp), calculated as GPP / PAR and fluorescence yield at 760 nm (SIFy – far-red) calculated as F₇₆₀ / PAR in e); and relationship between LUEp and fluorescence yield at 680 nm (SIFy - Red) calculated as F₆₈₀/PAR in f); at the nitrogen fertilized tower in Majadas. Yellow dots indicate the heat wave period whereas blue dots indicate the days before and after the heatwave. GPP and LUEp are from the tall EC tower at the nitrogen-fertilized treatment, whereas SIF -Red, SIF –far-red, SIFy, NDVI and PRI are from one evergreen Q. ilex tree in the nitrogen-fertilized treatment.

The relationship between GPP_{DT} and fluorescence metrics (Figure 144a, b) is positive and significant before and after the heat wave (blue dots in Figure 144), but breaks down during the heat wave period (yellow dots). When normalizing by PAR both the GPP and the SIF, the contrast between the heatwave and the days before and after becomes even clearer. In Figure 144e and Figure 144f, the relationship between the LUEp and F₇₆₀ / PAR, and LUEp and F₆₈₀ / PAR becomes significantly negative during the heatwave (p < 0.01 in both cases). It is possible that in response to the extreme events, plants respond by shifting the allocation of absorbed PAR preferably to SIF that is reduced during the heatwave, but to a lesser extent compared to GPP. The best predictor of GPP during the heatwave was PRI (Figure 144c), indicating that during a heatwave the photosynthetic activity is highly controlled by xanthophyll cycle, which is tracked by PRI. Finally, NDVI fails to predict GPP both during the heatwave and in the days before and after (Figure 144d). These results, presented also in the report of the Photoproxy project, indicate the complexity of fluorescence – photosynthesis relationship, in particular during heat stress ([RD-06]).

7.4.3 Monitoring functional diversity with sun-induced fluorescence

In collaboration with the University of Milano Bicocca (G. Tagliabue and M. Rossini), we explored the possibility of using SIF at 760 nm (F_{760}) to estimate spatial patterns in the functional diversity of the herbaceous layer at the Majadas site.

In 19 plots, we sampled the vegetation layer (50 x 50 cm) and we measured for all the species in the plot. We estimated the abundance (fractional cover of the species) and a series of plant traits: specific leaf area (SLA), leaf length, leaf area, nitrogen content (N_{mass}) and ^{13}C leaf isotopic signature. Finally, we computed widely used functional diversity measurements such as functional divergence, functional dispersion and RAOQGROUND.

In each of the 19 plots, we calculated the RAOQRS metric from the *HyPlant* FO_2 -A data (low altitude patterns) as described by Tagliabue et al. (2019). Briefly, the RAOQRS is calculated on a 3 x 3 and 5 x 5-pixel window around the location of the ground plot and is based on the squared differences of all the combinations of the pixels in the windows. This metric represents the heterogeneity of the remote sensing signal within the window used for the calculation and it is supposed to be related to the functional diversity of the vegetation (e.g. Tagliabue et al. 2019).

The comparison between the functional diversity metrics derived in the field and the RAOQRS (from NDVI and F_{760}) show the better performance of F_{760} compared to NDVI to track spatial patterns of functional diversity (Figure 145). These results suggest fluorescence can be used to monitor functional diversity, and more research is needed to better understand the mechanism that links functional diversity and fluorescence.

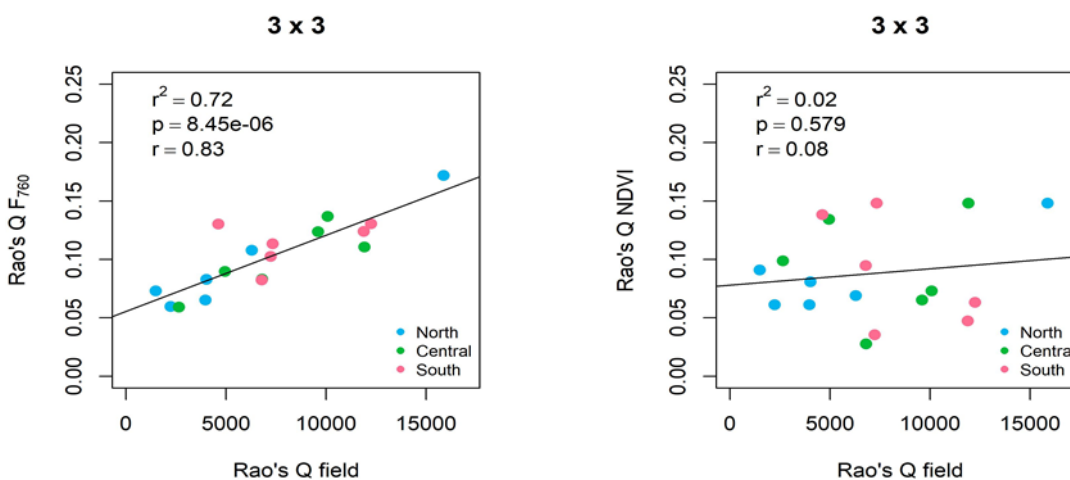


Figure 145: Evaluation of RAOQ metrics derived from NDVI, F_{760} and field-based functional diversity metrics.

7.5 OHP, France

[43.93N, 5.72E]

The overflight campaign in France covered a deciduous broadleaved forest dominated by Downy oak (*Quercus pubescens* WILLD) and had a footprint of approximately 1,700 km² (Figure 147). The site has a mean annual temperature of 11.3°C and a mean annual precipitation of 829 mm, with strong Mediterranean seasonality, including hot & dry summers and mild & humid winters. The canopy height is around 5 - 6 m, and the mean diameter of old forest stands (80-100 years) is around 10 cm, with a mean basal area of 29 m² ha⁻¹, a mean LAI of around 2 m² m⁻² and a canopy gap fraction of around 25%. Montpellier Maple (*Acer monspessulanum* L.) is co-dominant (25% of total leaf mass) with Downy oak. The undergrowth is frequently

dominated by large patches of European Smokebush (*Cotinus coggygria*) and has a high diversity of herbaceous and grass species. The forest cover is documented back to the 18th century, and has been anthropogenically exploited for firewood & charcoal. Typical silvicultural management is harvested by clear cutting, after which the trees re-sprout from their remaining root stools, initially forming a savannah-like bush cover.

Typically, this ecosystem is exposed to a long-lasting summer period without significant rainfall and thus the plants are well adapted physiologically to sustain this prolonged drought period. Also, in 2018 the last significant rainfall occurred in the middle of June. Soil water content then continuously decreased reaching low levels of soil available water on 10 June 2018 (Figure 146).

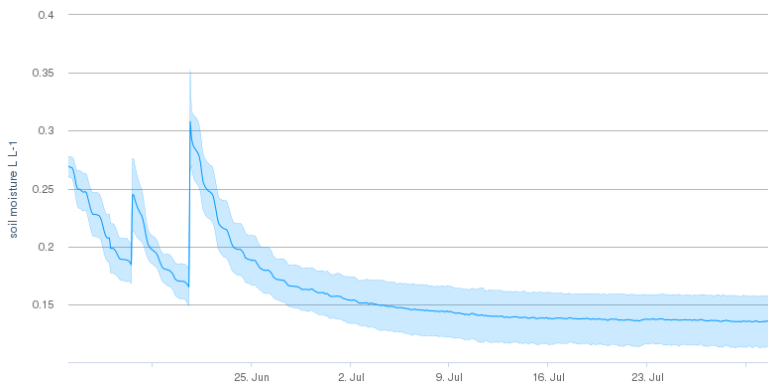


Figure 146: Volumetric soil moisture showing the impact of the last rain event in June and the drought conditions for the *HyPlant* overflight on 10 June 2018.

On the OHP premises, a FloX system was installed on an ICOS Atmosphere tower (100 m, Nov 2017 -Sept 2020) in cooperation with the University of Milano, and JB Hyperspectral. Atmospheric and ground-based measurements were provided by the Observatoire de Haute-Provence (main contributors: laboratories LATMOS (network: NDACC) and LOA (network: AERONET), ecological field site O₃HP, ACTRIS and ICOS research infrastructure).

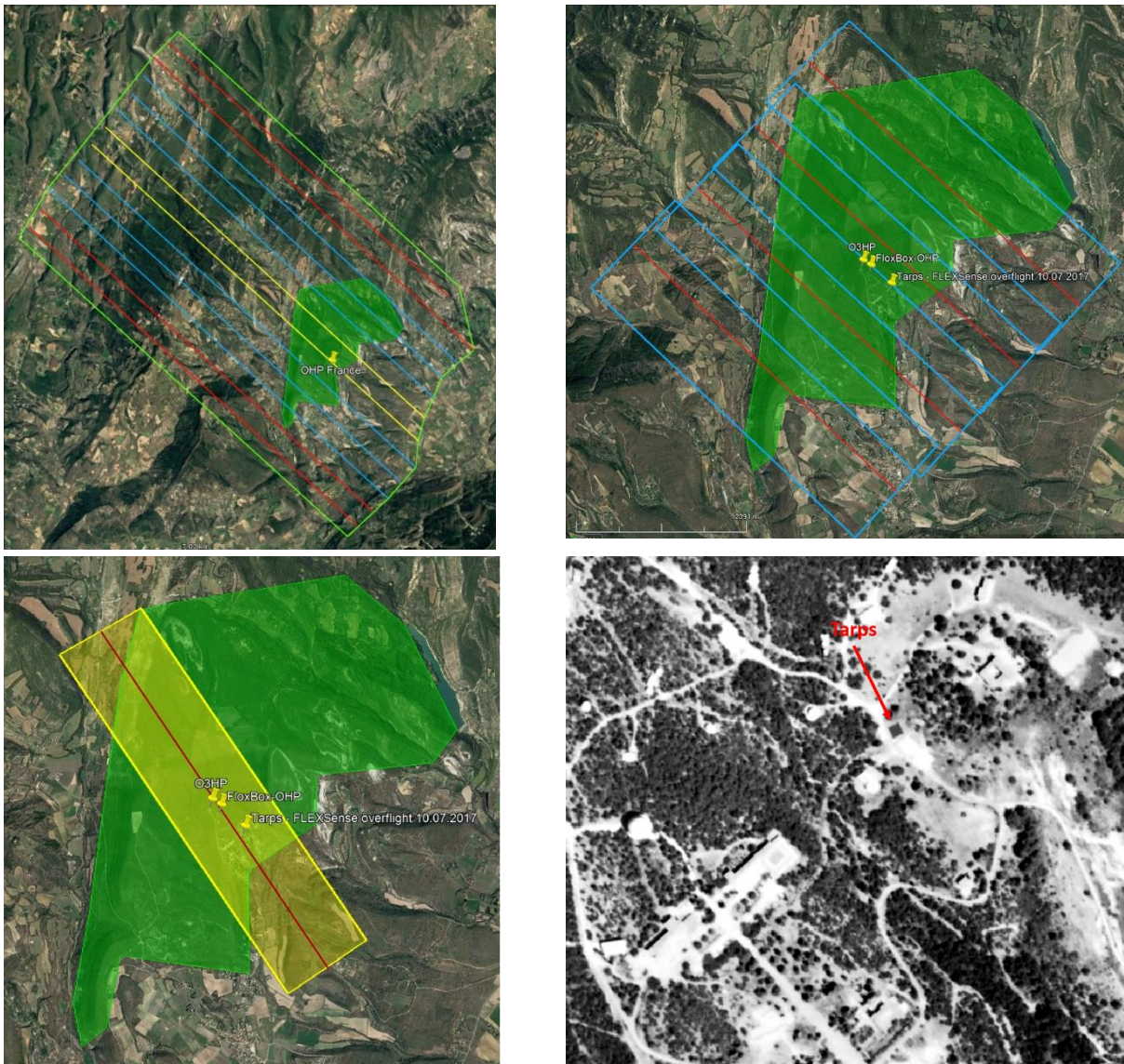


Figure 147: Flight lines of the three flight patterns for the OHP site, and tarp positions as identified from FLEXSense flyover imaging. The green surface denotes the forested OHP plateau. Top left: Flight lines to cover a large area around the OHP as to produce a 4.5-m resolution map. Top right: Flight lines to cover the plateau around the OHP site as to produce a 3-m resolution map. Bottom left: Flight lines to cover the main plots around the experimental field site O₃HP and the FloX footprint as to produce a 2-m resolution map. The three sets of flyovers all cover the reference tarp position.

For the overflight campaign, three tarps of black grey and white color were positioned on the OHP premises (Figure 148) and were covered by each overflight height. The hyperspectral reflectance was measured at each sub-plot using a portable ASD spectroradiometer (FieldSpec4 Standard-Res, Analytical Spectral Devices Inc., Boulder, CO, USA). The ASD is designed to record the signal from the spectral region ranging from 350 to 2500 nm with a sampling interval of 1.4 – 2 nm from 350 to 1050 nm and 1050 to 2500 nm, respectively. Measurements were obtained under cloudless conditions using a fiber optic probe with a 25° full conical angle. The probe was held vertically at approximately 1 m above the tarp in a nadir position. A Spectralon white reference panel was used to calibrate the spectroradiometer and to determine the reflected light percentages. The calibrations were carried out before and after the reflectance measurements for each sub-plot. Data were obtained from 10 to 12 am for the three tarps but additional measurement was acquired for the grey tarp (grey 2) at around 2 pm.

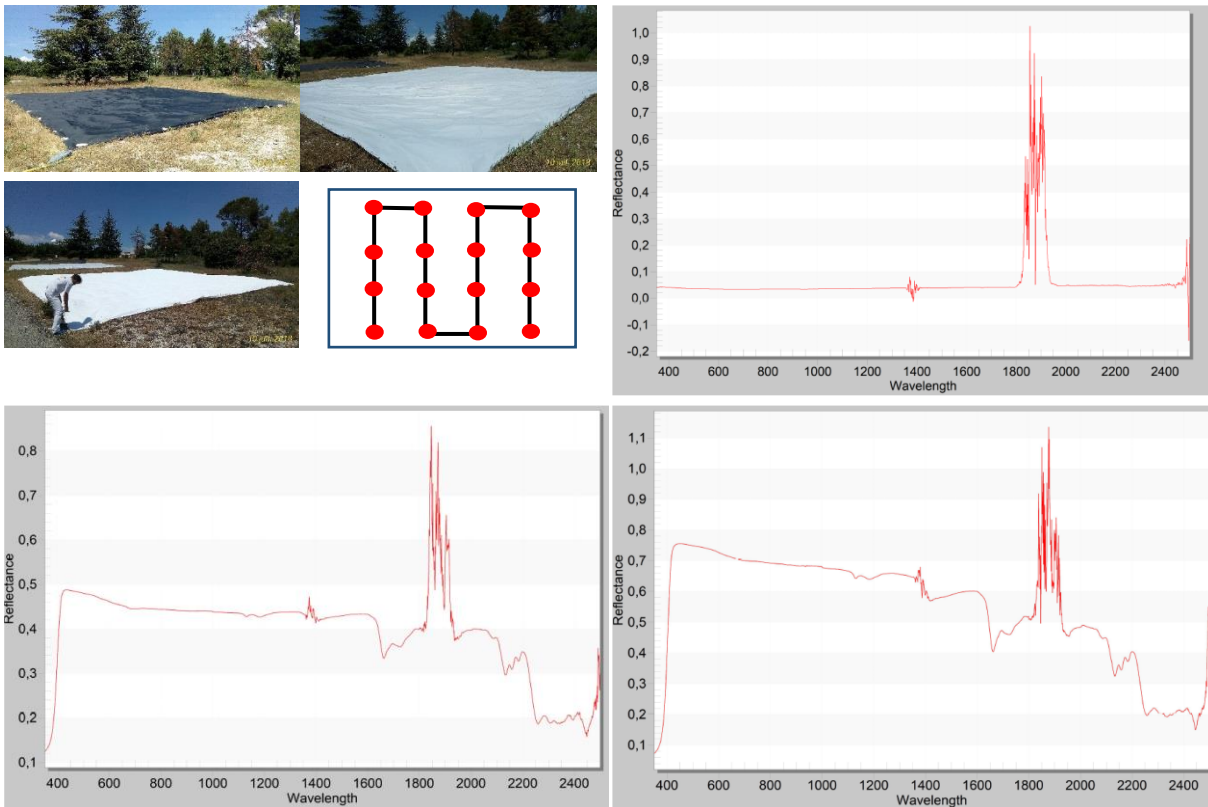


Figure 148 : Reflectance of reference tarps: Position *in-situ* and sampling positions on tarps (top left). Median reflectance spectra for black (top right), grey (bottom left) and white tarps (bottom right). The great spikes around 1900 nm are related to the water absorption band in this spectral window and thus these data shall be removed for further analysis.

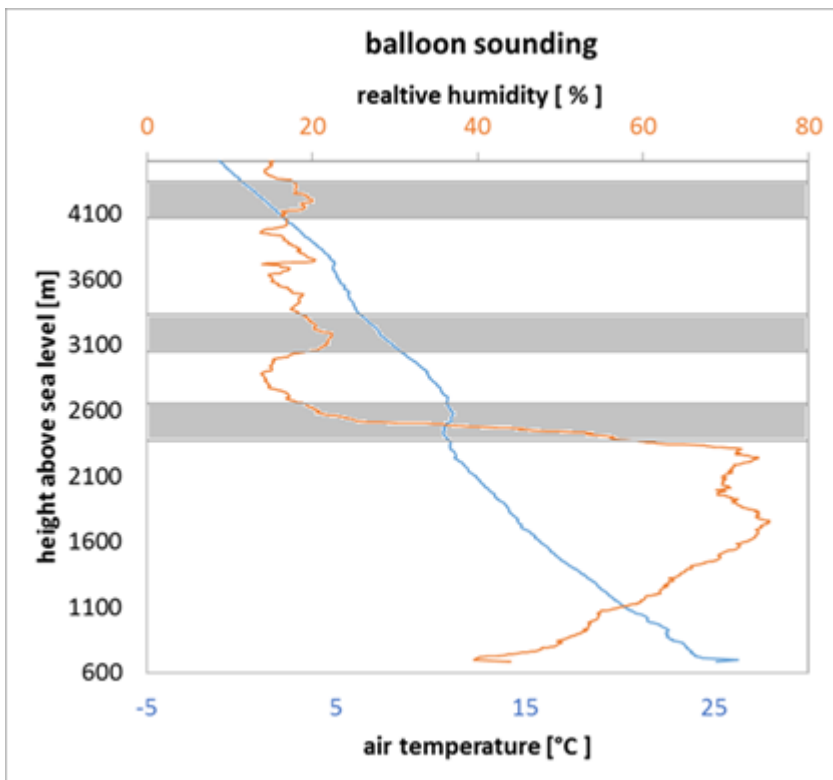


Figure 149: Vertical profiles of air temperature and relative humidity, measured via balloon sounding. Gray shading represents approximate overflight-heights of 1970 m (6470 ft), 2650 m (8693 ft) and 3665 m (12023 ft) agl. Pixel size of the imaging system corresponds to about 2 m, 3 m, and 4.5 m, i.e. a pixel area of 4 m², 9 m², and 20 m².

Balloon sounding around noon during the overflight day (Figure 149) shows that the upper two flight heights were well above the planetary boundary layer, whereas the lowest flight height was within the transition zone of the planetary boundary layer height.

7.5.1 Mapping of structural, bio-chemical and physiological traits of the ecosystem of the OHP Plateau

The plateau at the OHP and to the north is evenly sloped and evenly forested for a surface area that would cover several 300 m x 300 m pixels_{SIF} of the FLEX satellite. It has a surface area of about 11 km², comprising 4.5 km in the N-S extension and 3 km in the W-E extension, respectively. The area was mapped by the airborne *HyPlant* sensor with several parallel flight lines and airborne data were processed to reflectance-based vegetation indices, LST and DEM (Figure 150). Unfortunately, it has not yet been possible to calculate SIF maps for this area because of the strong elevation differences that characterize this study area. However, all level-1 products are available and SIF maps can be produced as soon as the elevation correction is implemented in the SIF retrieval of *HyPlant*.

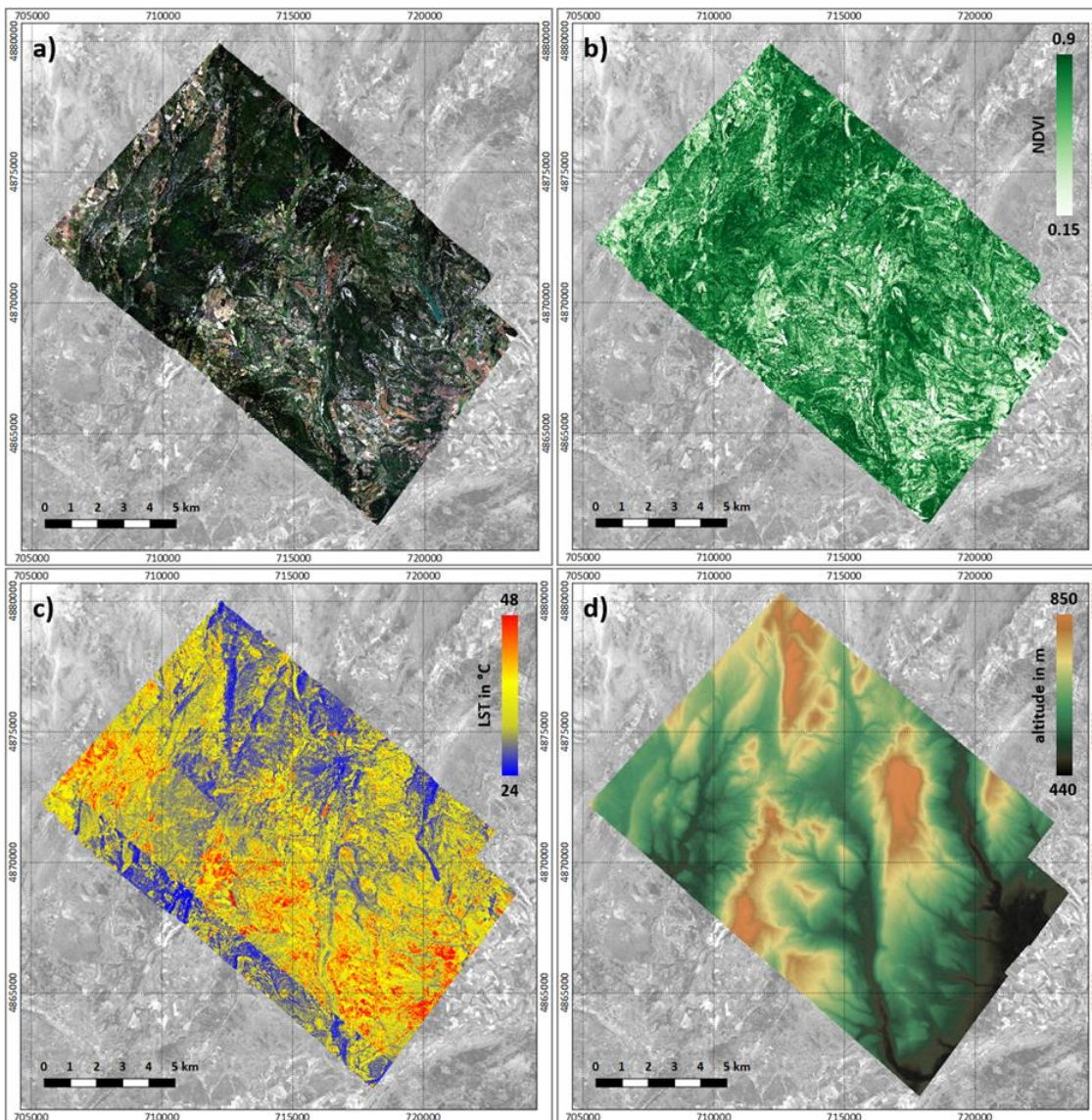


Figure 150 : Experimental site OHP a) *HyPlant* DUAL TOC reflectance true colour composite, b) NDVI calculated from *HyPlant* DUAL TOC reflectance, c) TASI LST, d) Riegli LiDAR DSM.

To interpret remote vegetation data, information on chlorophyll content per unit of projected ground surface area and information on other structural and functional vegetation traits is needed. The leaf physiology that drives LCC is adapted to the light environment in the strata of the trees' canopies and to environmental constraints, where water relations and availability play an important role. To have means to scale this, stand structure was characterized for the plateau, bringing together forest management, and their impact on tree height and leaf area development. Some heterogeneity of the local environment and human forest management add variability in stand structure to this otherwise quite homogeneous forest ecosystem.

Measurement-Map of the plateau Saint-Michel-l'Observatoire



Figure 151: Map of the OHP plateau. Blue markers denote where measurements were performed for Chl content, LAI, tree height and stand density (see section below).

Tree age since last clear-cut

The aboveground oak forest varies in age since the last clear-cut, which is the typical forest management practice (coppice) employed by the state and private owners, and is restricted to the size of their respective cadastral plots. As based on temporal series of aerial images (remonterletemps.ign.fr, geoportail.gouv.fr, Google Earth) clear-cuts were identified comparing one image to another. The approximate date since the last clear-cut was derived for each cadastral plot for the whole OHP plateau (Figure 152), as the mean date in between the image showing the clear-cut and the image closest in time before the clear-cut. For some plots (denoted in bluish colors), the date of the clear-cut could not be derived as no public images exist for that period. For the premises of the observatory (turquoise) no forest management was performed after acquisition by the CNRS in 1937. The age of a total of 609 cadastral plots was determined by this method.

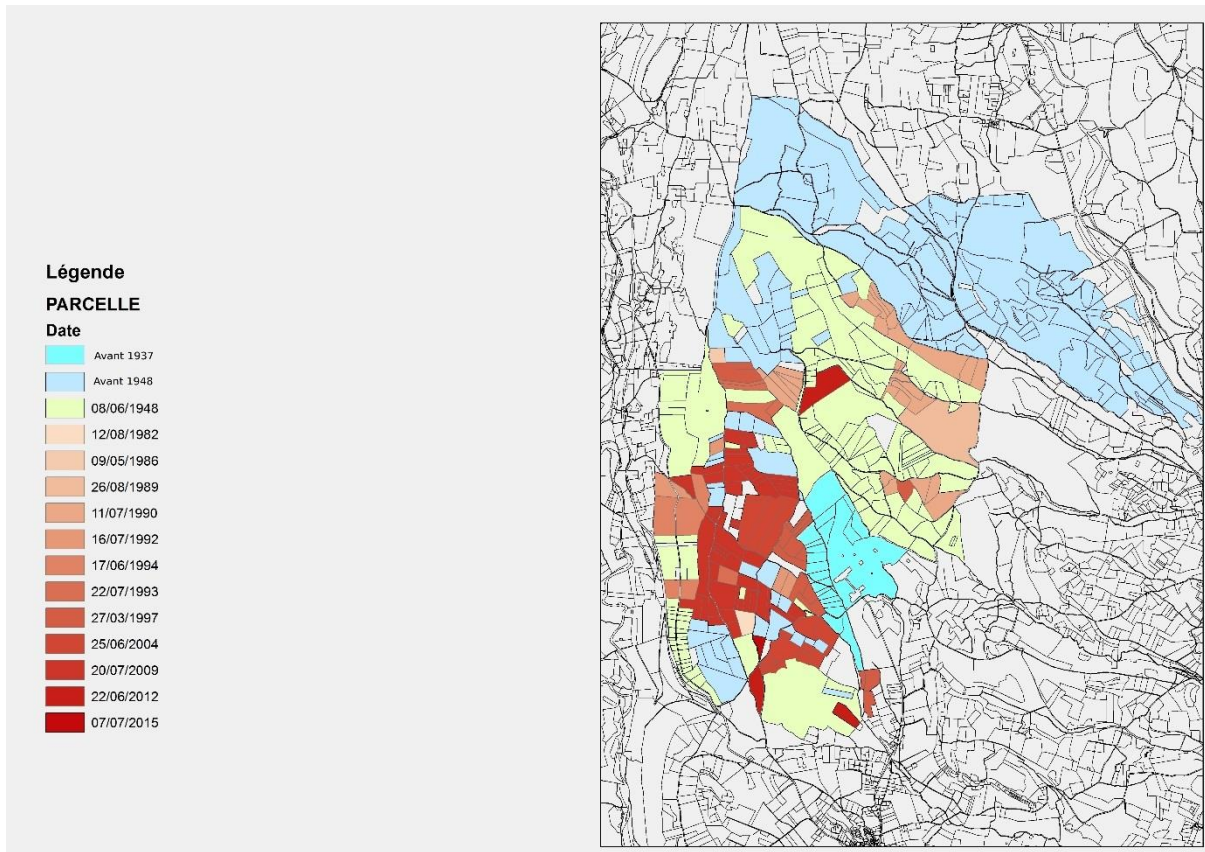


Figure 152: Date since last clear-cut of cadastral plots on the plateau around the OHP. Whereas many plots of the south-western part of the plateau had been harvested in the last 30 years, the northern and eastern part of the plateau is old-growth forest. The maximum N-S extension is about 4.5 km on this map (colored plots).

Tree height, leaf area index, and canopy gap fraction

Cadastral plots with forests of varying age were selected for detailed analyses of LAI and canopy gap fraction and tree height. For the determination of the LAI and the gap fraction, an optical sensor was used (LAI-2000, Li-cor, Lincoln, NE, USA). By choosing the appropriate restrictors and calculation procedures, the observed crown surface (projected) approximatively corresponded to the pixel size of the overflight imaging. LAI was measured non-overlappingly in terms of observed crown space as in order to avoid autocorrelation, i.e. in equidistant intervals along transects within the cadastral plot, so as to statistically correlate ground and aerial approaches. Tree height was measured with a hand-held, laser-based height meter (Häglof, Sweden).

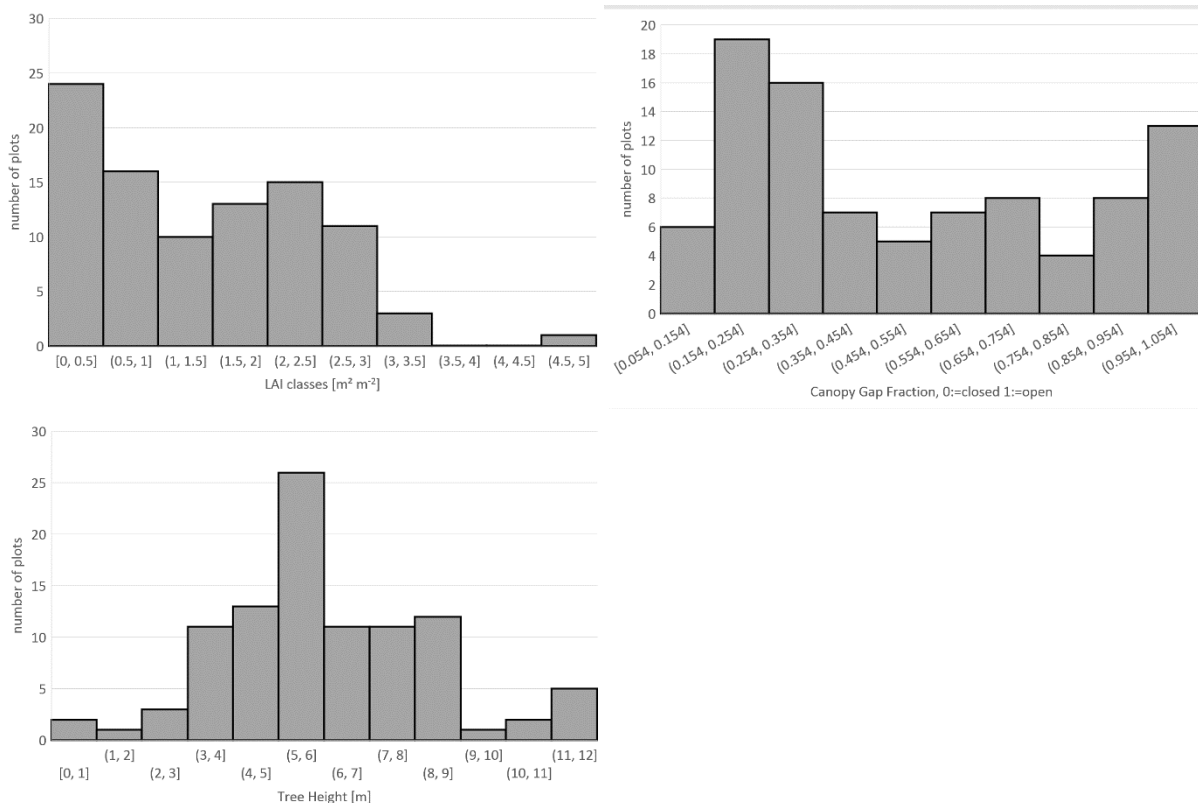


Figure 153: LAI (top left) saturated at about $3.5 m^2 m^{-2}$ and was mostly around $2 m^2 m^{-2}$ for mature stands, and lower for more recently cut stands. This is typical for the Mediterranean. Consequently, the canopy closure (top right) is quite low, leaving about 25% gaps for mature stands and being more open for developing stands. For most mature stands, tree height (bottom left) is around 5 m to 6 m, but quite a number of stands also show much higher trees.

Stand basal area

Basal area was determined by the Bitterlich-meter method. For the plots that had been cut recently, this method returns zero. About 30 plots were measured. The stand basal area explains about 65% of the variability of the LAI.

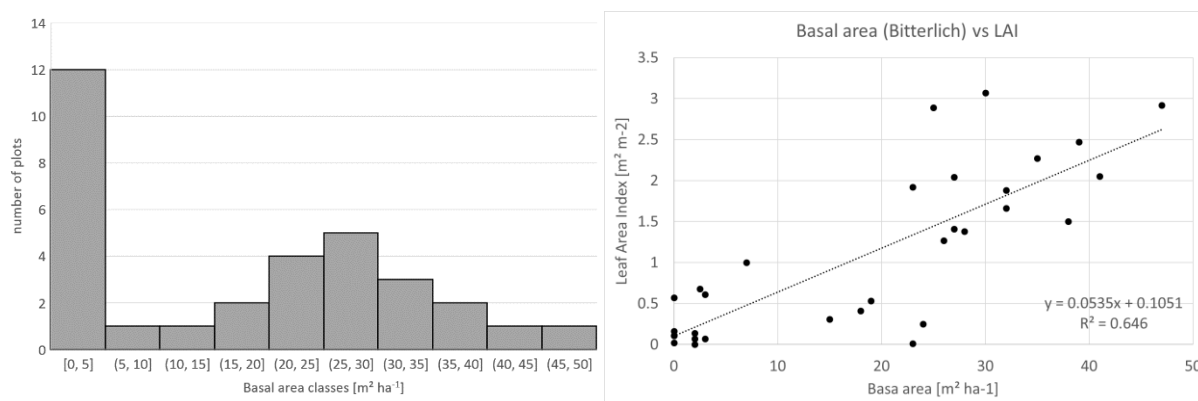


Figure 154: Basal area distribution (left) and its correlation to LAI (right). Basal area showed a normal distribution, when recently cut plots are excluded, however, the distribution is quite flat

Chlorophyll content of the upper sun crown

A series of transects were measured in order to cover most of the plateau (Figure 151), with one measurement per cadastral plot (or more for large plots). Leaves from the upper sun crown of three trees were analyzed per position ($n=282$ in total), covering 79 cadastral plots. We aimed at identifying how the relative chlorophyll content (SPAD) of leaves may scale with plant and stand characteristics (tree age, LAI,

	Doc.: Final Report		
	Date: 29 July 2021	Issue: 2	Revision: 1
	Ref.: ESA Contract No. 4000125402/18/NL/NA		Page: 187 / 288

canopy gap fraction, tree height, basal area), and geographically with the longitudinal and latitudinal position on the plateau.

Interestingly, the relative chlorophyll content of leaves from the upper tree crowns did not vary with plant and stand characteristics, nor with the geographical position (Figure 155). In conclusion, the chlorophyll content for leaves from the sun crown is very robust, from saplings to old-growth forests, irrespective of biological and geographical components. We can assume that the chlorophyll content per leaf surface area is very homogeneous across the entire plateau, and adjacent similar landscapes. Seeing that the distribution of the data looks normally distributed and not left-skewed, it does not seem that the measurement is saturated for high chlorophyll content. The manufacturer states that a specific hard-ware and software development efforts had been undertaken to overcome saturation issues.

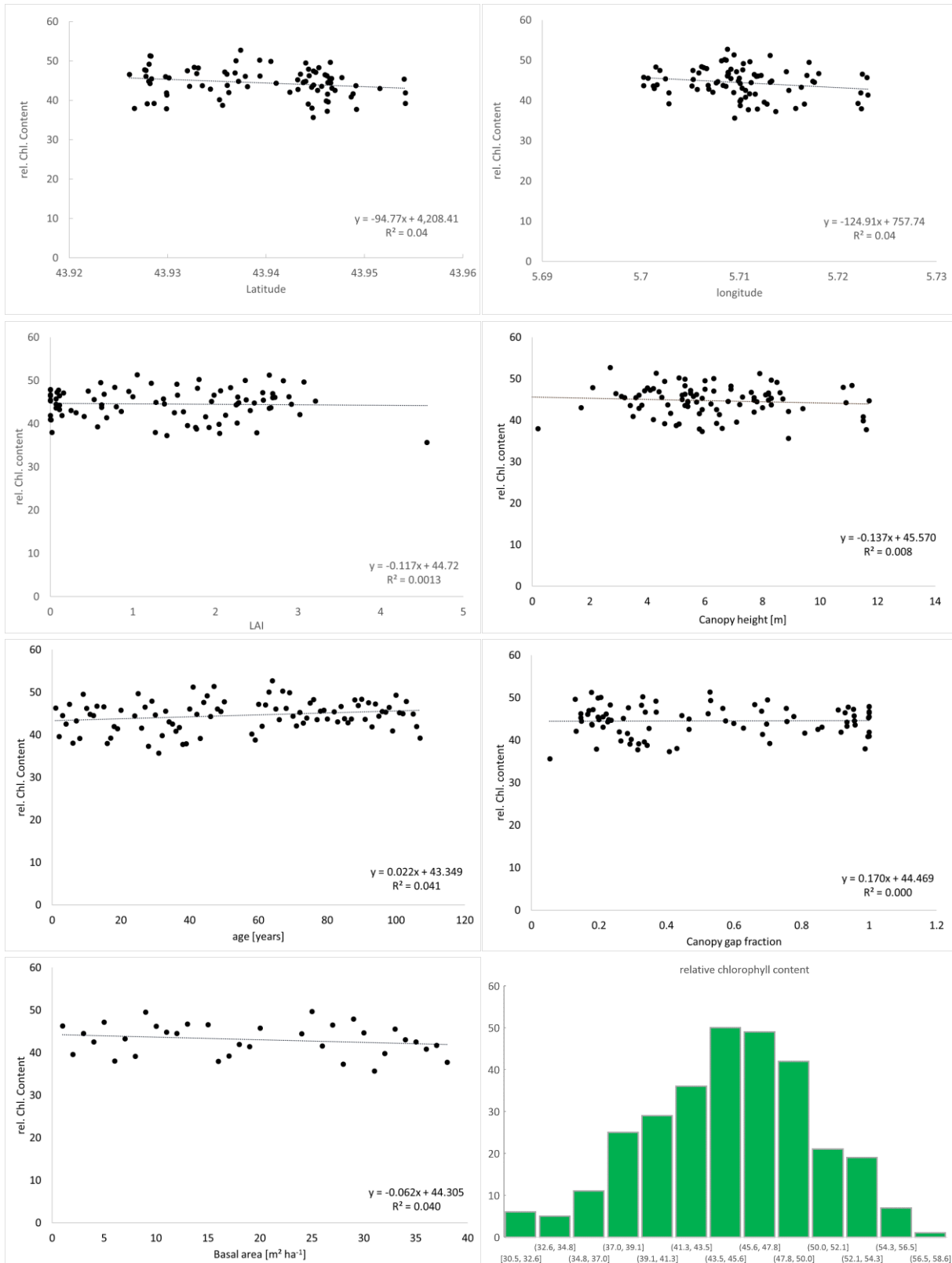


Figure 155: Relative chlorophyll content of the upper crown of Downy oak on the OHP plateau, in relation to stand characteristics measured at the same position: LAI (top left), canopy height (top right), approximate stand age (middle left), canopy gap fraction (middle right) and basal area (bottom left). Chlorophyll content for the upper sun crown was highly conservative and almost independent from stand characteristics. Relative chlorophyll content was normally distributed, bottom right. Downy oak (bottom right) n=302 mean=44.9 SD=5.4, Montpellier Maple (not shown) n=14 mean=41.2 SD=5.0. Relative chlorophyll content was determined with the MultispeyQ2 (manufacturer: Photosynq).

The main source for the variability of the relative chlorophyll content is likely attributable to a general variability among individuals. A contrasting example was found on one of the plots with very poor soil (almost no organic layer, high rock and gravel content) for two trees of similar habitus growing together at the same spot, but having very different relative chlorophyll content (see Figure 156). This indicates that the variability in the relative chlorophyll content data of the upper sun crown is real and not linked to methodological issues.



Figure 156: Two adjacent shrublike Downy oak trees of contrasting visual greenness and relative chlorophyll content, left tree 33.1, right tree 48.1, which cover the complete lower range of relative chlorophyll content data and 86% of the total range encountered on the plateau. Plants are situated on the northern part of the plateau on open ground with poor gravel-like soil.

In conclusion, the relative chlorophyll content data per unit leaf area are convincing in terms of the quality of the measurement, which means that the relative chlorophyll content distribution (bottom right in Figure 155) is realistic and statistically representative for the individual trees that form the canopy. To make the link to the pixels recorded by the *Hyplant* overflight would require the scaling of these chlorophyll contents to unit ground surface area via the LAI. Here, the clumping of the foliage has to be considered, i.e. depending on the degree of canopy closure, which is strongly related to LAI (Figure 158), the abundance of ground vegetation other than trees may ‘dilute’ or bias the above distribution estimates.

Chlorophyll content in the vertical profile

Chlorophyll content per unit leaf area may increase with decreasing light availability in the lower parts of the crown. We investigated this in the vertical profiles of trees at the O₃HP site, where we accessed the entire foliated crown (between 1 m and 5.5 m agl) of oak and maple trees using a scaffolding. Whereas the relative chlorophyll content of Montpellier maple does not scale with height, about 16% of the variability is explained by height in the canopy for the Downy oak (Figure 157). However, the relative chlorophyll content is merely 15% lower at the bottom of the shade crown as compared to the upper sun crown. Consequently, scaling the tree’s chlorophyll content on a leaf basis to a ground-based surface area is mainly determined by the LAI of the stand.

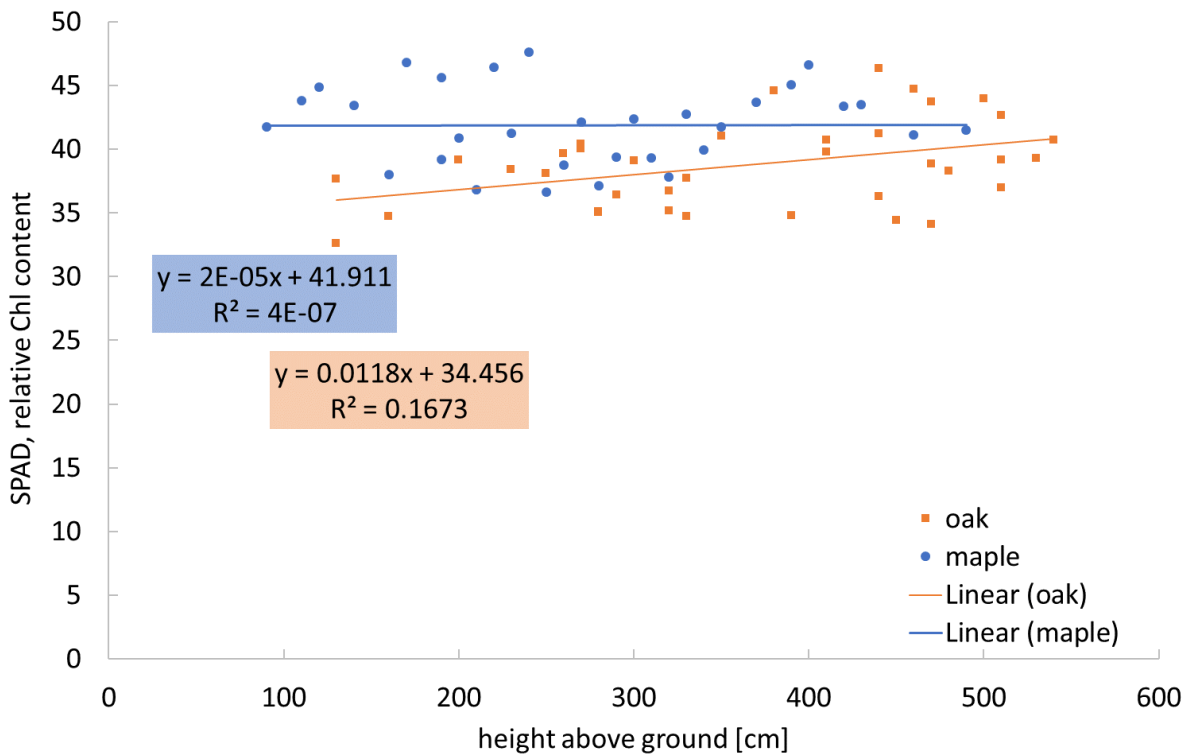


Figure 157: Relative chlorophyll content in the vertical profile of five Downy oak and three Montpellier maple trees from the experimental site O₃HP.

Nevertheless, some attention was addressed to crown development over the trees' lifespan. At the same LAI, older stands visually gave the impression of a more closed the canopy, and thus have a lower gap fraction with less leaf area density in the foliated crown space, i.e. in younger stands the leaf area seemed more clumped from a bird's eye view, than in old stands, which would potentially lead to a lower chlorophyll fluorescence signal at the same LAI. However, this was not confirmed by our measurements (Figure 158).

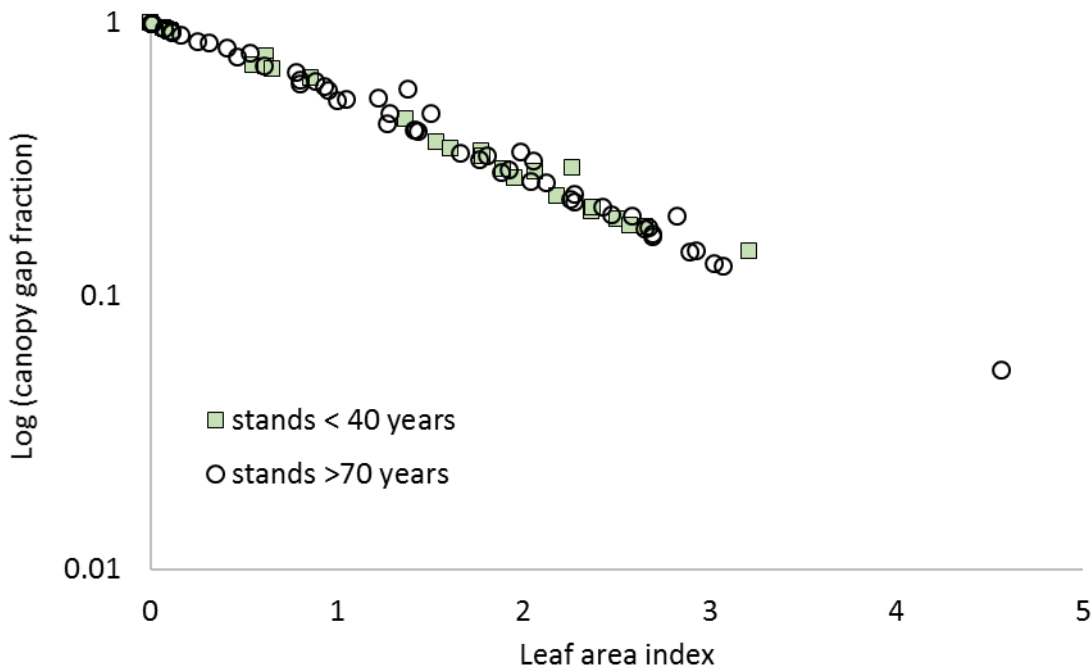


Figure 158: Relationship between gap fraction of the canopy cover and the LAI, illustrated for two age classes, for a range from open canopies (~1) to well closed canopies (~0.1), for a total of 85 cadastral plots.

Perspectives for the mapping of LAI over the OHP plateau

In situ ground measurements have shown substantial variation in the LAI for the forest stands, mainly related to their location on the plateau, and the period since the last clear-cut (Figure 151). Ground-based measurements are labor intensive. Remote sensing approaches are promising to facilitate the LAI mapping for the plateau.

A relevant dataset was elaborated in the framework of a national collaborate project at the O₃HP site ('CANOPEE', 2011-14, ANR-10-JCJC-0603): LiDAR measurements were performed from an ultralight-aircraft and by ground observations in a subproject headed by Patrick Chazette. This allowed estimates of tree height and clearly reproduced ground observations in a qualitative and quantitative way, i.e. showing up low canopy height after due to forest management and locally elevated tree heights (Figure 159, see Shang et al. 2016 for the approach). The dark blue patch west and adjacent to the O₃HP site, representing a low canopy height, is indeed the low canopy of a clear-cut after some years of regeneration (shrub-like canopy). The orange patch somewhat east of the O₃HP is a part of the forest with a high canopy up to 12 m at the bottom part of a slope. Even the rain exclusion structure above the canopy at the O₃HP itself was detected (Figure 159). In situ measurements correlated well with the LiDAR tree height estimates.

Using this approach, LAI was quantified for various forest types on the island La Réunion (Shang et al. 2016). It thus appears feasible that such remote-sensing LAI-products were developed from the Riegl LiDAR data from the FLEXsense overflight at the OHP, which could be intercompared with the Patrick Chazette's independent datasets above. A crucial point to consider is the clumping of the foliage and thus the quantification of the openness of the canopy by this method, e.g. whereas the overall LAI for the O₃HP plot is 2.0 - 2.2. The vertical profiles reveal LAIs of up to 4 within individual tree crowns. A parallel approach as based on satellite data (Chrysafis et al. 2020) would bear the potential to scale LAI over time, i.e. over the season (see comment on herbivory, mechanical, microbial and oxidative-stress-like damage below) and to follow-up interannual variation.

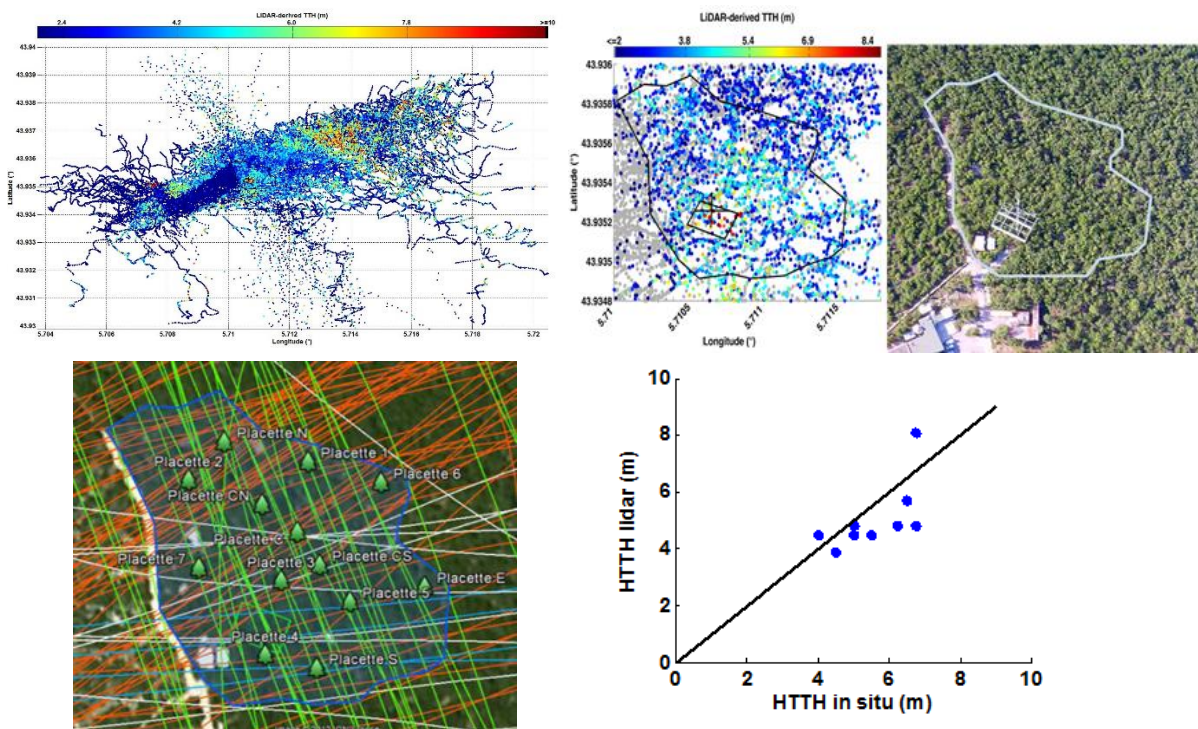


Figure 159: Top: Ultralight-aircraft flight lines in green and red, and positions of *in situ* tree height measurements. Bottom: Correlation of tree height measurements by LiDAR and *in-situ*. Images, courtesy of Patrick Chazette.

Biological/environmental impact on relative chlorophyll content per unit ground area

The leaves of oak and maple are almost flawless shortly after budburst and degrade thereafter due to herbivory, mechanical, microbial and oxidative-stress-like damage. Loss in leaf area can be detected by following the stand LAI with optical methods throughout the season. However, the degradation impact on chlorophyll content needs quantification. For the above determinations of relative chlorophyll content, healthy looking (or the most healthy-looking) leaves were chosen for measurements, which will lead to an overestimation of relative chlorophyll content, in the presence of degraded leaves, when scaled per unit of ground area.

Diurnal variations in chlorophyll fluorescence

Diurnal courses of SIF were measured by the FloX system that was installed at a height of 100 m above the Downy oak canopy (Figure 160). From this diurnal course, it becomes clear that SIF measurements are greatly influenced by atmospheric re-absorption processes and the negative values of SIF₇₆₀ during midday is attributed to the inaccurate correction of atmospheric processes. Thus, efforts are underway to develop an atmospheric correction procedure for ground FloX measurements, as atmospheric re-absorption of the atmospheric layer (which is between the FloX system and the vegetation canopy) greatly influences the projected top-of-canopy SIF values. More details of this topic are elaborated and presented in the ATMOFLEX report ([RD-09]).

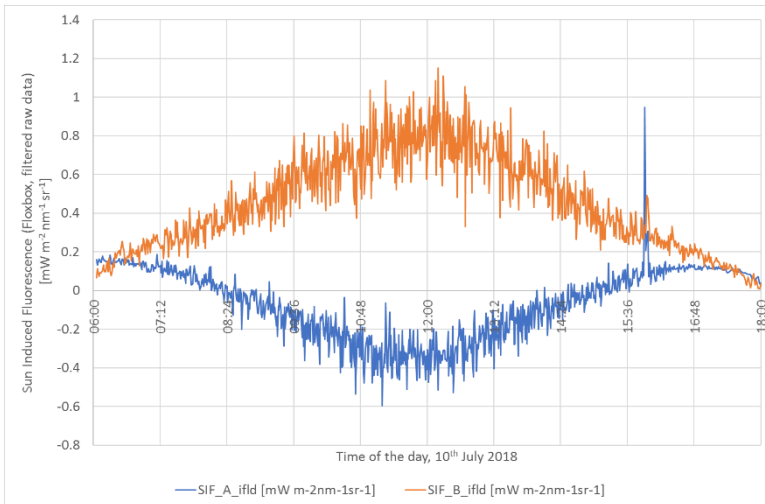


Figure 160: Diurnal course of SIF from Downy oak as measured from the FloX system 100 m above the canopy.

To quantitatively describe the diurnal dynamics of photosynthetic carbon and water fluxes as well as the leaf-level fluorescence parameters in this ecosystem, we performed diurnal leaf-level measurements by a combined chlorophyll fluorescence and CO₂ & H₂O gas exchange measurement system, reproducing ambient light by LED-light within a cuvette.

CO₂ and H₂O gas exchange were continuously measured in parallel to classical chlorophyll fluorescence measurements in an oak leaf in the sun crown, for the day of the overflight on 10 July 2018. CO₂ gas exchange showed strong daily dynamics: With high values in the morning, low values after midday, and an increase in the latter part of the afternoon. The overall pattern of net CO₂ assimilation is closely related to stomatal conductance (Figure 161)

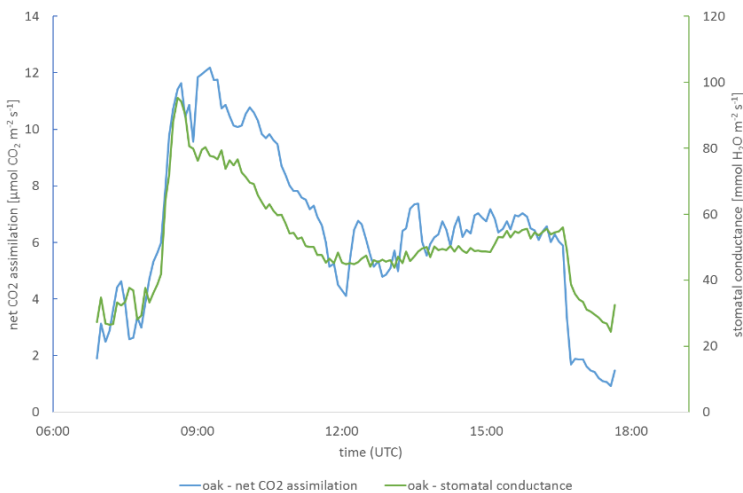


Figure 161: Diurnal course of CO₂ uptake rate and stomatal conductance of a representative oak tree at the day of the *HyPlant* overpass (10 June 2018).

A similar diurnal pattern was also shown in Montpellier maple and European smoke bush, which showed a pattern of high conductance in the morning hours and a reduction with stabilization, thereafter followed by an increase towards the end of the day (Figure 162). The increase towards the end of the day may not occur under more drought-stricken scenarios.

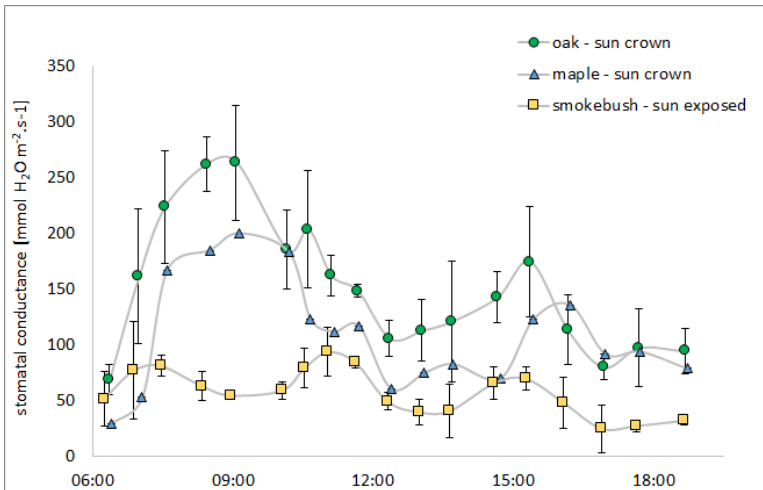


Figure 162: Stomatal conductance for Downy oak, Montpellier maple and European smoke bush in their respective sun crown for the overflight day 10 July 2018 for the O₃HP control plot. Data are shown is local time, UTC+ 2h.

7.5.2 Influence of variations in atmospheric CO₂ concentrations on plant performance

On the overflight day, a CO₂ plume was detected around 7:00 UTC and prevailed for 20 min raising ambient CO₂ by about 15 ppm. This was confirmed by three different instruments (Figure 163). Such plumes seem to occur regularly, and overall diurnal CO₂ variability was as high as 30 ppm during July 2018 (Figure 163, top left). Plants react to such CO₂ variability (Figure 164). In in-situ leaf gas-exchange experiments at the O₃HP from end of June to the beginning of July 2018, where we manipulated CO₂ concentrations in order to simulate CO₂ plumes, oak and maple reversibly decreased their conductance by about 20% to 30% when exposed to a +50 ppm and +100 ppm CO₂ increase. Net CO₂ assimilation was noisier, but in general increased in line with the rise in CO₂ partial pressure and on average settled to an about 5% increase in reaction to the plumes.

As a consequence, during such plumes we could expect the SIF signal to decrease as more radiation energy is transformed to chemical energy. With time, stomata should close again, diminishing this effect. However, on the overflight day, light intensity and photosynthesis were strongly increasing when the plume passed, making it impossible to reliably evaluate this phenomenon.

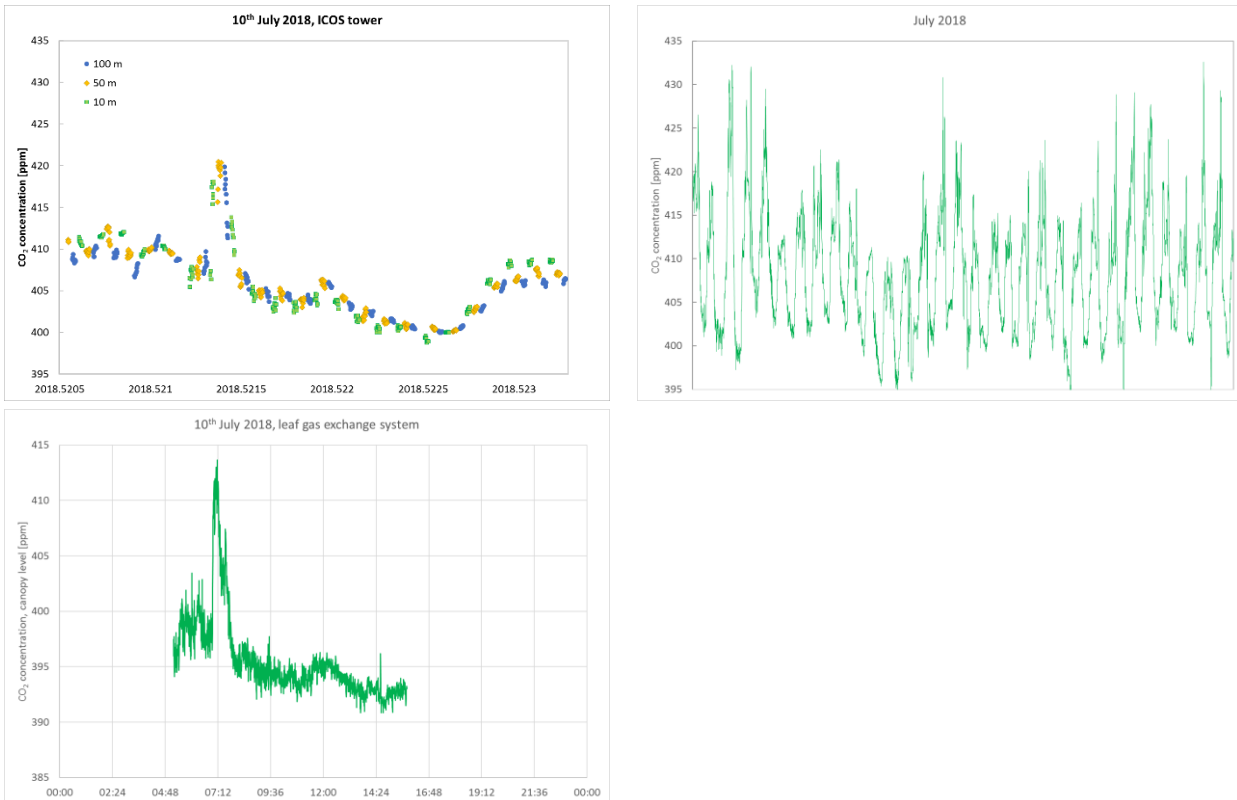


Figure 163: CO₂ concentrations, as measured along the ICOS tower installation in the diurnal course at three heights (Picarro, top left, ICOS Atmosphere research infrastructure, c/o Xueref-Remy) and for the whole of July at 10 m height (top right), as measured by a CO₂ & H₂O gas exchange cuvette, within the canopy (LI-6400 XT, top right), and as measured by a soil CO₂ efflux system with two automatized permanent chambers (LI-8100A, bottom left).

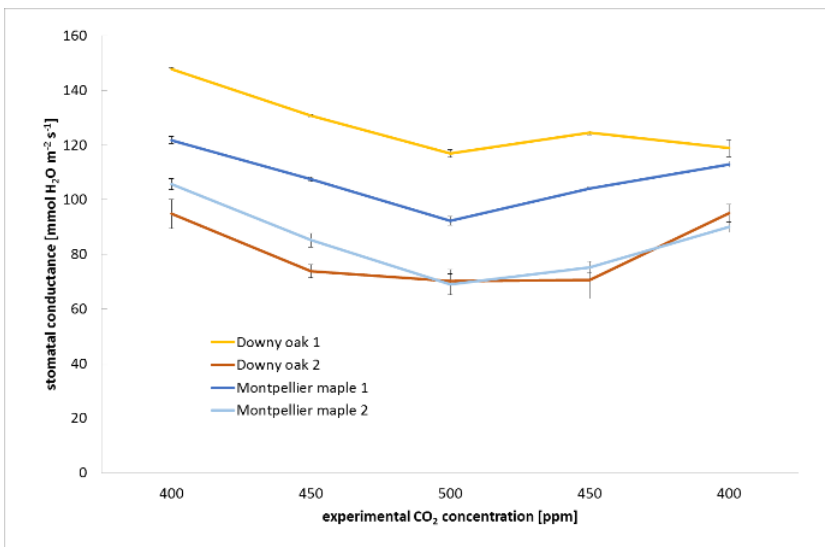


Figure 164: Stomatal conductance in Downy oak and Montpellier maple leaves changing in reaction to a simulated CO₂ plume of +50 ppm and +100 ppm. Plants were adapted to 400 ppm for about 45 minutes and then exposed to the subsequent CO₂ concentration (from left to right) giving 20 - 30 min time for each step, in order to attain stability for stomatal conductance. Note: This is a long in-situ experiment taking 2h - 3h over which environmental conditions and plant-internal status can change considerably.

7.6 Laegeren, Switzerland

[47.48N, 8.34E]

Scientific activities at the Laegeren site in Switzerland, aim to exploit FLEX mission like data for estimates of ecosystem functioning, in particular ecosystem evapotranspiration (ET). The FLEXense 2018 campaign intended to collect data to facilitate these activities. The following sections summarize the acquired data. Further, results derived in parallel activities (outside of the FLEXense 2018 project) are outlined that aid assessment of the importance and suitability of collected data in view of the scientific aim of moving towards a FLEX ET product.

7.6.1 Assessment of site data

Test site

The study site is temperate mixed deciduous forest area (47°28'42" N, 8°21'52" E) located on the south facing slope of the Laegeren mountain, northwest of the city of Zurich (Figure 165). The complex structured forest shows high species diversity (dominated by beech, ash, sycamore and spruce) (Eugster et al. 2007).

Core data acquisition activities in frame of the 2018 FLEXense campaign took place between June and September 2018 and included acquisitions with the *HyPlant* sensor and Sentinel-3, continuous in-situ radiometric measurements, and supporting ground observations (Figure 165). A synchronized data set was acquired between 13 and 14 July 2018 using the FloX, *HyPlant*, and Sentinel-3B. In addition, field spectroscopy using an ASD instrument complemented the acquisition.



Figure 165: Flight lines for the experimental site Laegeren – Zurich, Switzerland (left). Installed FloX system at the Laegeren tower (right), photograph by E. Paul-Limoges, 2018.

ASD measurements

ASD field spectrometer was acquired to support the evaluation of the radiometric accuracy and quality of the atmospheric correction. We sampled in total 18 targets in two days (i.e. on 13 July 2018 during *HyPlant* flights and on 14 July 2018 during Sentinel-3 flights). All measurements could be made under good conditions and cover a wide range of radiance-value cross wavelengths (Figure 167). This is particularly beneficial for vicarious calibration activities. A comparison between ASD and *HyPlant* data is pending: Due to the complex topography, *HyPlant* data have not yet been further processed; we are waiting for an upgrade on the SIF retrieval scheme (see section on *HyPlant* data).

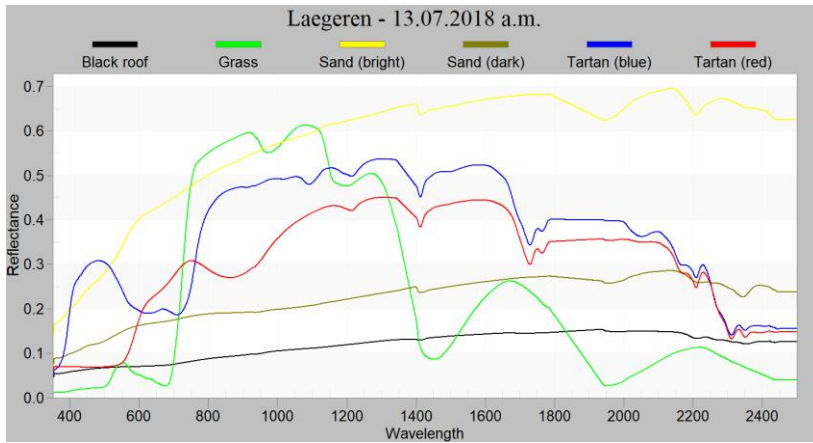


Figure 166: Example of pre-processed mean reflectance of reference targets measured at Laegeren site on the 13 July 2018 for the evaluation of *HyPlant* data.

FloX data

A FloX system was installed at the Laegeren tower and has been continuously measuring up and downwelling radiance between April 2018 and September 2018. This enabled us to look at the severe drought occurring in 2018. Visualizations of available FloX data are provided in Figure 167.

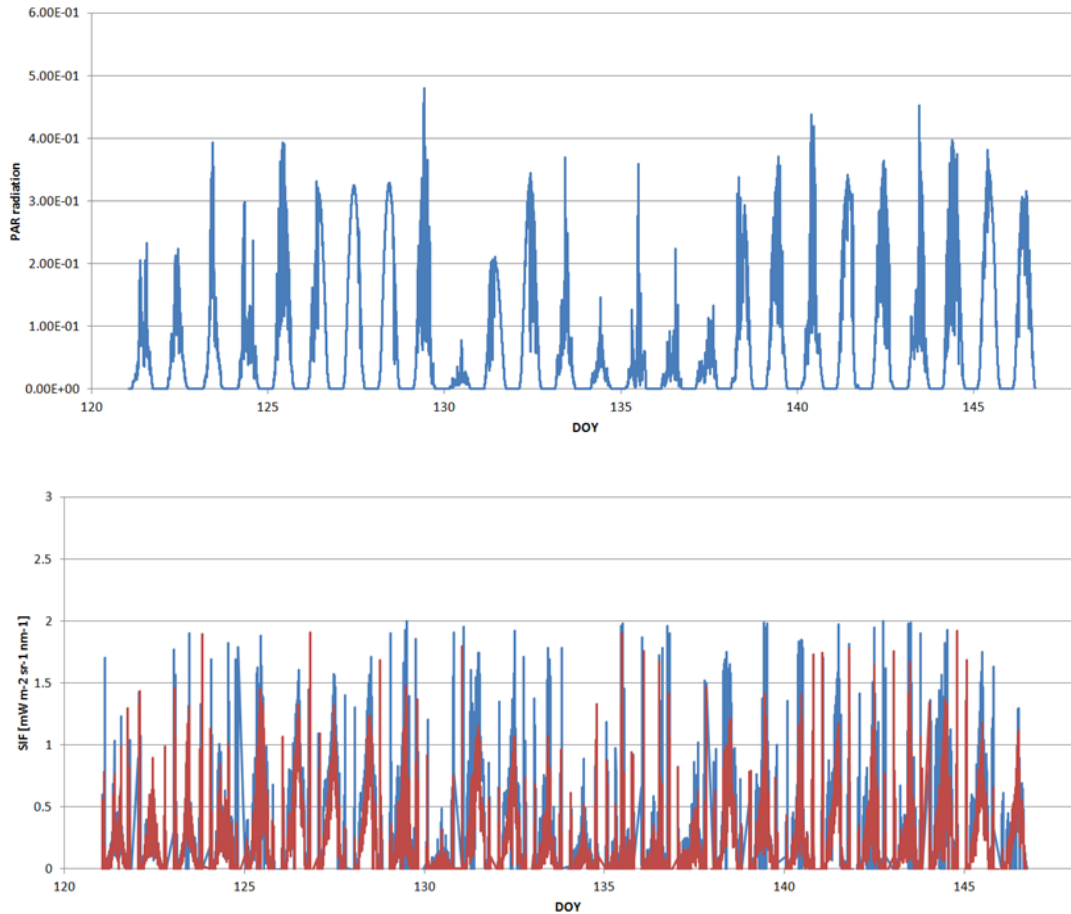


Figure 167: Time series of PAR (top) and derived SIF (O₂-A in blue; O₂-B in red, bottom) measured with the FloX system over the Laegeren temperate mixed forest.

HyPlant

HyPlant data were acquired under moderate to good weather conditions on 13 July 2018. The strong topography present at the site still complicates SIF retrievals. Accordingly, we have not yet used the acquired *HyPlant* data for further analysis as we are waiting for updated SIF retrieval algorithms.

Sentinel-3

Several Sentinel-3A data were acquired in the campaign window. We used the acquired FloX data to compare reflectance obtained from in-situ radiometric measurements (i.e. ratio between radiance and irradiance) with reflectance data derived Sentinel-3A (using a SNAP integrated atmospheric correction scheme). Working steps included a selection of corresponding data and the convolution of FloX retrieved reflectance data to mimic the band configuration of Sentinel-3. Given the substantially diverging spatial resolution of both sensors (i.e. 10 m for FloX and 300 m for Sentinel-3), the agreement is good and both data sources comparably capture reflectance changes due to phenological canopy changes (Figure 168). This comparison, however, also reveals differences in the spectral shape, possibly as result of a footprint mismatch between both sensors.

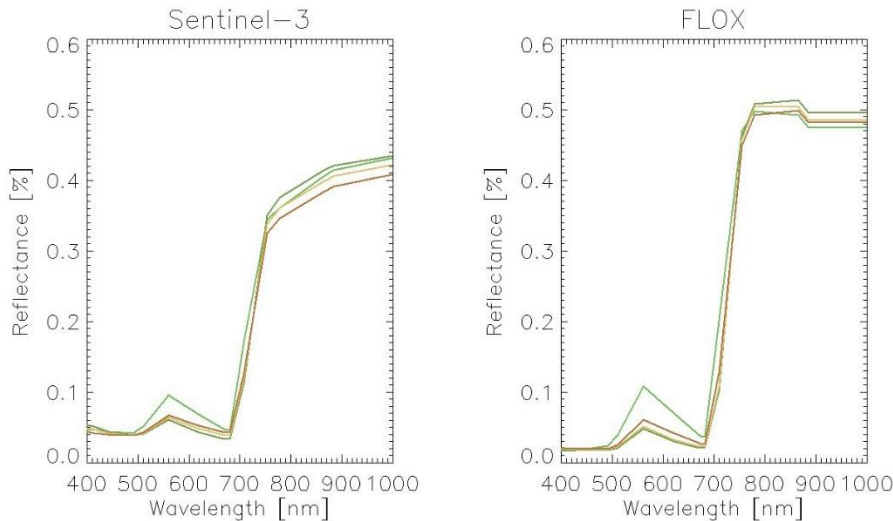


Figure 168: Comparison of reflectance obtained from FloX and Sentinel-3 radiance measurements between April and September 2018.

7.6.2 Contextual information to judge scientific suitability of collected data

Due to the complex topography, updates in the processing pipeline are needed to account for topography. No SIF retrieval for the Laegeren site is available so far. We therefore describe findings obtained in studies outside of the FLEXSense 2018 campaign that are relevant for judging the suitability of the collected data with a view to a possible development of a FLEX ET product.

An approach for partitioning EC based ET measurements in both component fluxes transpiration and evaporation was recently published (Paul-Limoges et al. 2020). This approach is suitable for providing in-situ reference measurements of transpiration, and it facilitates the validation of transpiration estimates obtained by techniques based on remote sensing. The approach uses EC measurements above and below the canopy and links both observations while considering micrometeorological constraints. Details of the approach can be found in Paul-Limoges et al. (2020).

This approach was applied to EC data measured at the Laegeren site and yielded interesting insights. Based on an assessment of the years 2014 and 2015, it can be stated that transpiration accounts for up to 90% of the total ET flux during canopy closure (June - September). During times with open canopy, the contribution of the transpired water flux compared to the total ET flux decreases below 50% (Paul-Limoges et al. 2020). Relevant to note is the possible range of T/ET ratios at the Laegeren site, relevant for plausibility checks of a possible FLEX ET. Further, the proposed approach might serve to provide reference transpiration estimates for the validation of possibly upcoming remote sensing products.

We could investigate the sensitivity of SIF measured at the Laegeren site to capture dynamics in transpiration. The results are expected to provide indications as to whether the development of a SIF-based transpiration assessment scheme is promising or not. In a first step, we compared the seasonal variation of transpiration (EC-based) with SIF (FloX-based) (Figure 169) and could identify common pattern and differences. A common pattern includes substantial fluctuations, particularly from June onwards when the canopy was closed. Diverging results were obtained from April to May, a time period dominated by an open canopy and stormy conditions.

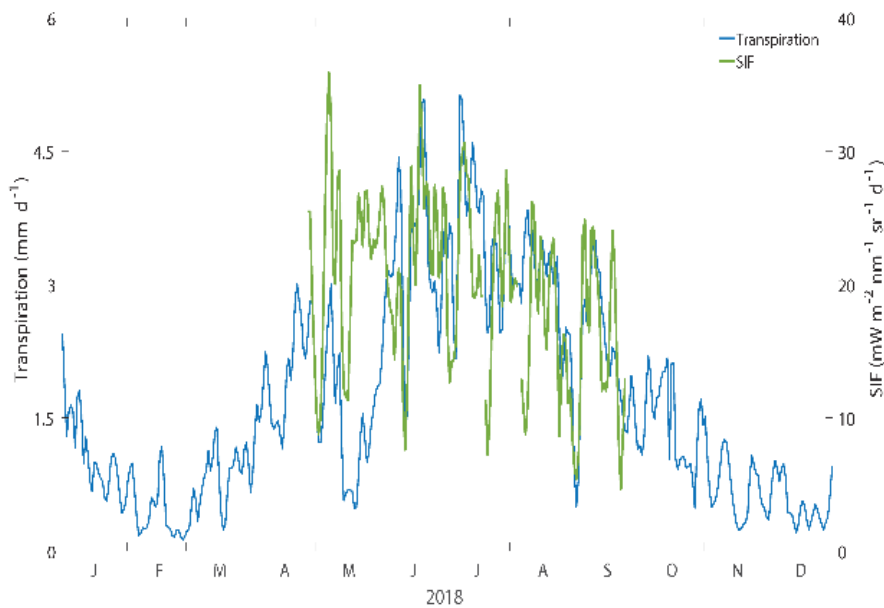


Figure 169: Comparison of SIF (flux-based) and transpiration (EC-based) during the year 2018 measured in the Laegeren forest. Courtesy of Eugenie Paul-Limoges, 2018.

These results indicate that the use of SIF for predicting transpiration is promising, which is in accordance with several recent papers (Lu et al. 2018, Maes et al. 2020, Shan et al. 2021). Divergence at certain times, however, indicate that additional measurements (i.e. energy and atmospheric constraints, plant physiological responses) are needed to provide robust estimates even under various conditions. In fact, a modelling experiment by Damm et al. (2021) indicates a co-variance between both, SIF and transpiration with net radiation and LAI, thus showing that SIF and transpiration are inherently linked to each other. Also, other parameters have effects either on SIF (air temperature, relative humidity) or SIF and transpiration (wind speed) and must be considered, alongside SIF to reliably estimate transpiration.

Another recent study evaluated the ET decline in 2018 due to the combined drought and heat wave. Based on their assessment of MODIS data, Ahmed et al. (2021) show that ET substantially declined in large parts of central and northern Europe where FLEXSense2018 campaign activities took place. This natural experiment was covered by campaign data and provides a suitable test bed to evaluate possible future developments of FLEX-like products for assessing ecosystem functions such as transpiration or GPP.

7.6.3 Concluding remarks

The multi-scale radiometric data acquired during the FLEXSense 2018 campaign are valuable, in terms of data quality and are also suitable for facilitating scientific activities.

Concerning data quality, a comparison between FloX and Sentinel-3 data indicates consistency between the acquired data, although retrieved reflectance data differ due to varying footprints. A more advanced data comparison requires harmonization strategies including a spectral-spatial convolution of available high-resolution data (FloX) to mimic low-resolution satellite data (Sentinel-3). An assessment of *HyPlant* data in this context is outstanding.

Concerning the suitability of acquired data for the scientific purpose of developing a possible FLEX ET product, the data can be judged highly interesting. During the 2018 campaign year, an extreme event with a combined drought and heat wave hit Europe and the acquired data captured the ecosystem response at that time. Furthermore, the Laegeren site shows a wide range of transpiration/ET ratios across the year. We also found promising similar dynamics of SIF (FloX) and T (EC) at the Laegeren site. All these aspects indicate that the

data set is an interesting test bed for elaborating possible future FLEX products that address ecosystem functions such as transpiration or GPP.

7.7 Greifensee, Switzerland and Tyrrhenian open water site

Data of this chapter have been used for a scientific publication. Thus, more details on the data and an extended scientific discussion can be found in this publication (attachment 12.2).

Di Cicco A., Gupana R., Damm A., Colella S., Angelini F., Fiorani L., Artuso F., Brando V.E., Lai A., Genangeli A., Miglietta F. & Santoleri R. (2021). "Flex 2018" Cruise: an opportunity to assess phytoplankton chlorophyll fluorescence retrieval at different observational scales. *8th International Symposium "Monitoring of Mediterranean Coastal Areas. Problems and Measurement Techniques"*, edited by L. Bonora, D. Carboni & M. De Vincenzi, pp. 688-697, doi: 10.36253/978-88-5518-147-1.68.

Greifensee: [47.36N, 8.67E]; Tyrrhenian open waters site: [42.65N, 10.99E]

In addition to the terrestrial sites, two water sites were included in the campaign activities to make first basic steps towards a possible FLEX phytoplankton SIF product: Greifensee [47.36N, 8.67E]; and the Tyrrhenian open waters site [42.65N, 10.99E]. The main objectives included i) evaluation of whether the signal stability of FloX and *HyPlant* data is sufficient to facilitate SIF retrievals in aquatic environments and ii) to investigate if SIF retrievals using common approaches are consistent across scales (i.e. in-situ, airborne and satellite).

7.7.1 Site characteristics

The inland water site Lake Greifensee is a pre-alpine lake (47°21'53.9"N 8°39'46.3"E) located south-east of Dübendorf, in close vicinity to the city of Zurich, Switzerland (Figure 170). The lake is characterized by a moderate level of eutrophication and a pronounced spatio-temporal variability in phytoplankton community structure. The lake is surrounded by agricultural fields to the south and an urban area and a wetland to the north-west.

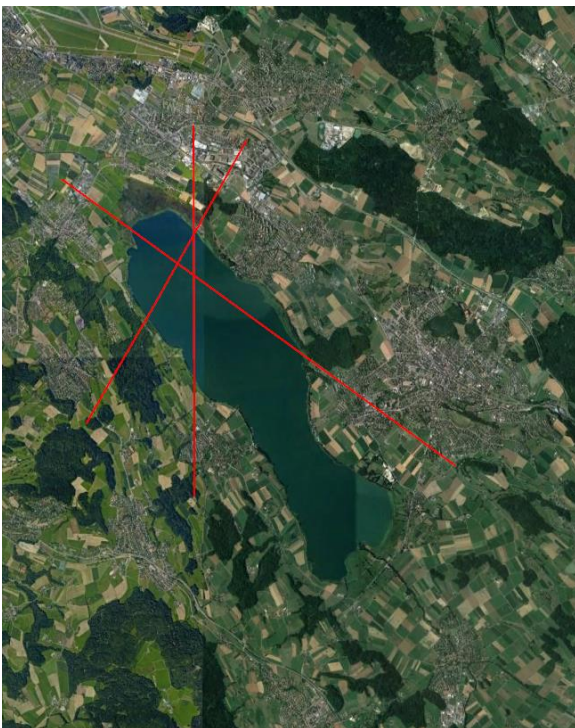


Figure 170: Flight lines for experimental site Greifensee, near Zurich, Switzerland.

The Tyrrhenian Sea is part of the Mediterranean Sea and loosely bounded by the western Italian peninsula as well as the islands of Corsica, Sardinia and Sicily (Figure 171). An oceanographic ship cruise, coordinated by Lia Santoleri (CNR-ISAC, Rome, I), during one week (4 to 8 June) of the 2018 campaign period supported a series of FlexSense measurements. The ship went from Livorno to Rome and basically rendered the full extent of the test area, while the core measurement region was close to Grosseto, Tuscany (Italy) (Figure 171).

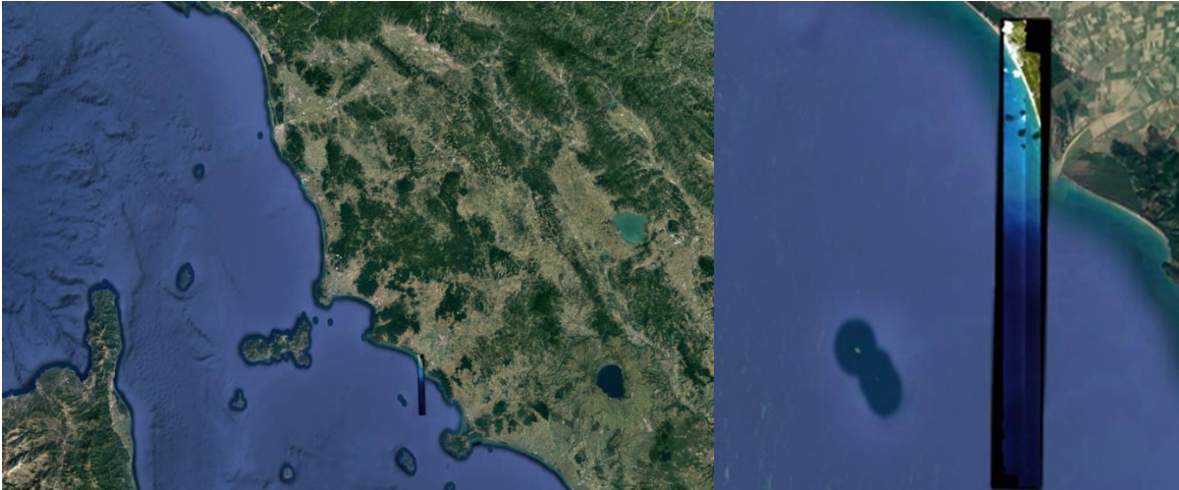


Figure 171: Tyrrhenian open water site: Starting point of the cruise was in Livorno (northern city). The cruise continued to a site between the island of Corsica and Elba, passed a site close Grosseto and ended in the harbor of Rome. *HyPlant* flights were made close to Grosseto (cf. small inlay on the left and enhanced picture on the right). The background picture was derived from Google Earth (2021 Google, Data SIO, NOAA U.S. Navy, NGA, GEBCO, Image Landsat/Copernicus).

FLEXSense 2018 related in-situ (FloX), airborne (*HyPlant*), and satellite (Sentinel-3) measurements aimed to exploit the capability to extract algae fluorescence across scales. For Greifensee, we used a WHISO and RAMSES spectrometer for in-situ radiometric measurements; *HyPlant* data were acquired on 13 July, and Sentinel-3B data on 14 July. At the Tyrrhenian site, a synchronized data set was acquired between 4 and 8, June 2018 using a FloX installed on a research vessel, *HyPlant*, and Sentinel-3B in the coastal area of Livorno and Rome. *HyPlant* flights were made along a gradient of river run-off, which generally causes some algae bloom (Figure 171).

7.7.2 First evaluation of radiometric measurements over aquatic sites

FloX system

The FloX system was used during the Mediterranean Sea campaign to obtain water-leaving reflectance. Given its specifications, in particular its spectral resolution and SNR, this instrument is a good candidate for measuring SIF emission from coastal areas and inland waters. However, the instrument should be reconfigured for aquatic purposes since three spectroradiometric measurements should be taken simultaneously for each target (that is, downwelling irradiance (E_d), upwelling radiance (L_u) and sky radiance (L_{sky})). Some results from the initial evaluation are given in Figure 172. While the E_d measurements for both high and low-resolution sensors correspond well with each other, the resulting remote sensing reflectance have discrepancies between both sensors. This may be attributable to the manual shifting of probes between measuring L_{sky} and L_u instead of doing all three measurements at the same time.

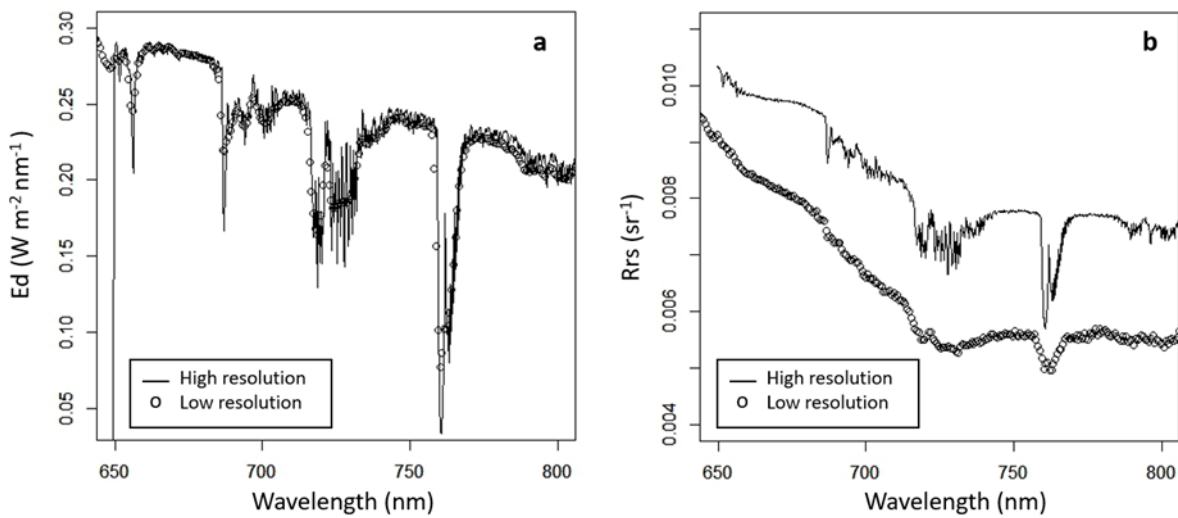


Figure 172: Sample measurement were recorded by the FloX. a) downwelling irradiance and b) remote sensing reflectance-based on manual shifting of probe to measure L_u and L_{sky} .

HyPlant

A spatial binning approach was conducted with *HyPlant* data for both the Mediterranean Sea and the Greifensee study area. This demonstration gives an idea of the range of values we are measuring for optically complex waters and how an “averaged” is obtained for one pixel. This evaluation is especially useful once the FLEX mission is operational to judge the representativeness of in-situ observation (or airborne reference acquisitions) for a satellite observation. Figure 173 shows sample measurements and their homogenous radiance values detected within adjacent regions.

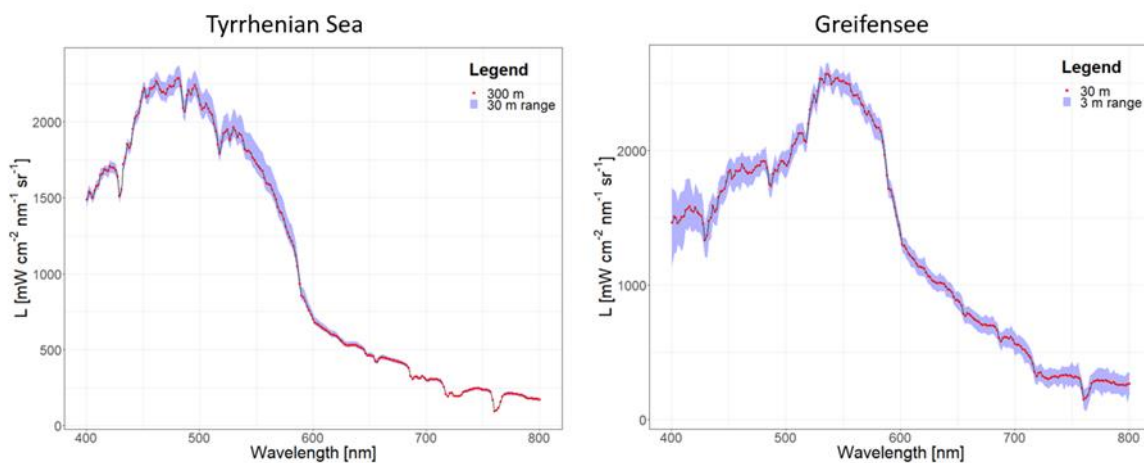


Figure 173: Sample of *HyPlant* upwelling radiance measurement from Tyrrhenian Sea and Greifensee that were spatially binned at 300 m and 30 m, respectively.

7.7.3 Retrieval of algal fluorescence from in-situ to airborne to satellite scale

A preliminary assessment of SIF retrieval consistency across scales was evaluated in both study areas using the commonly applied fluorescence line height (FLH) algorithm (Gower 1980). During a Sentinel-3 and *Hyplant* overpass, in-situ measurements were also taken for Tyrrhenian Sea and Greifensee. A summary of the results is presented in Figure 174. Overall, the range of FLH-based SIF values for airborne and space-borne measurement are within the same range and agree with each other. For the Tyrrhenian Sea, FLH-based SIF

was highest in the expected areas (near the coast and at the mouth of a river), with a generally decreasing trend as the distance to the coast increased. For Greifensee, we see a relatively homogenous distribution of FLH-based SIF values. This was expected since there is less turbulence and a homogenous distribution of optical properties (in contrast to larger lakes, which sometimes exhibit differing optical properties). More detailed and recent results for the Mediterranean site can be found in Di Cicco et al. (2020).

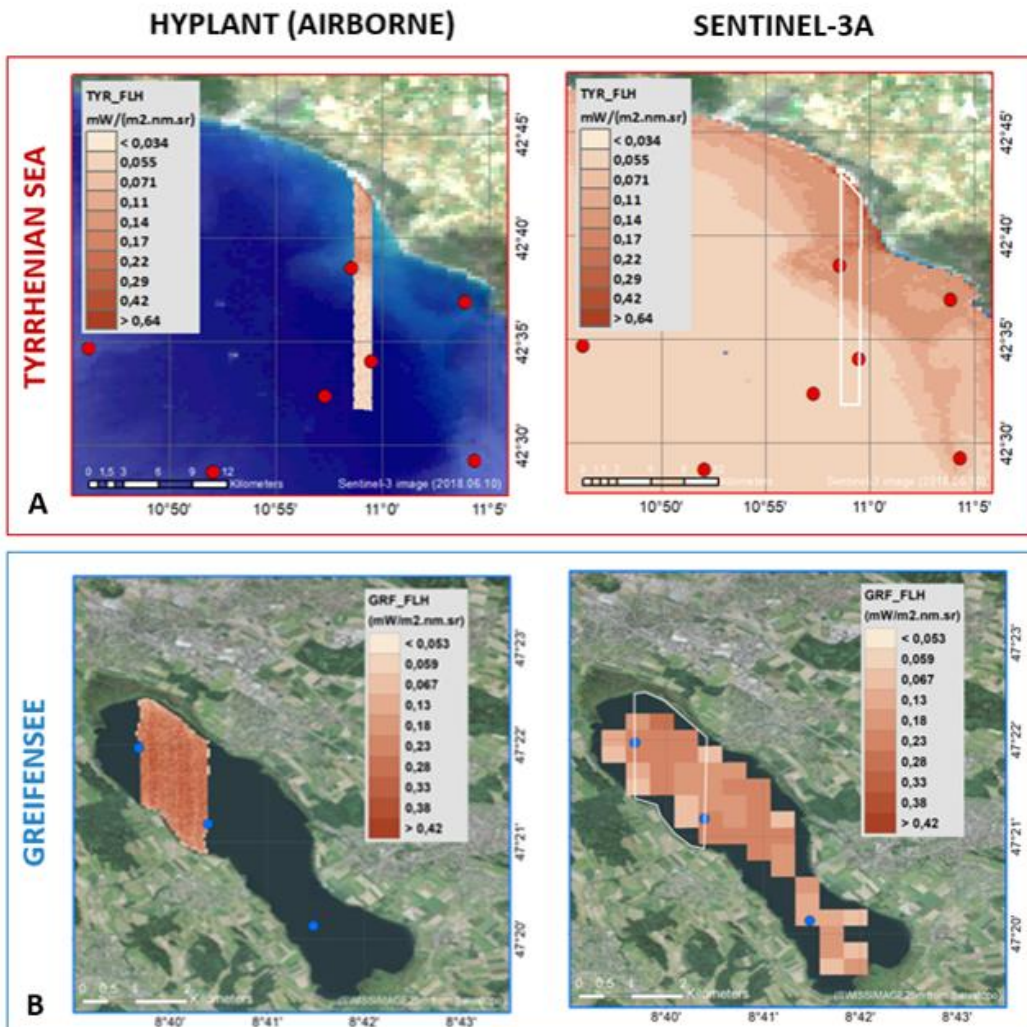


Figure 174: Comparison of SIF based on the fluorescence FLH retrieved from *HyPlant* and Sentinel-3A data for the Tyrrhenian Sea (A) and Greifensee site (B). Red and blue points indicate the location of in-situ sampling during *HyPlant* flights.

7.7.4 Follow up activities and concluding remarks

Based on the findings from the 2018 field campaign, we conducted a mesocosm experiment using the Eawag pond facility in July 2019. The objective is to have a better understanding of SIF dynamics in quasi-natural conditions (i.e. natural illumination, outdoor setting) while controlling nutrient input. In this experiment, we used two ponds filled with water obtained from Greifensee that contains the natural phytoplankton community found in the lake along with other in-water constituents. We infused one pond with nutrients to manipulate chlorophyll-a concentration while keeping the other pond as a control. Spectroradiometric measurements with the RAMSES instrument were obtained continuously during daytime to observe diurnal changes. Water was also sampled throughout the experiment period for later use in bio-optical modelling and algorithm validation.

First preliminary results of reflectance normalized against noontime measurements are shown in Figure 175 and Figure 176. The results provide insight on diurnal variation of SIF, while Pond 9B has lower chlorophyll-a concentration compared to Pond 9D. In general, it appears that reflectance at the SIF emission regions peaks under low light conditions but turns into a dip around solar noon (roughly 12 - 14 h). This could indicate photo adaptation processes ongoing due to high downwelling irradiance available in this period.

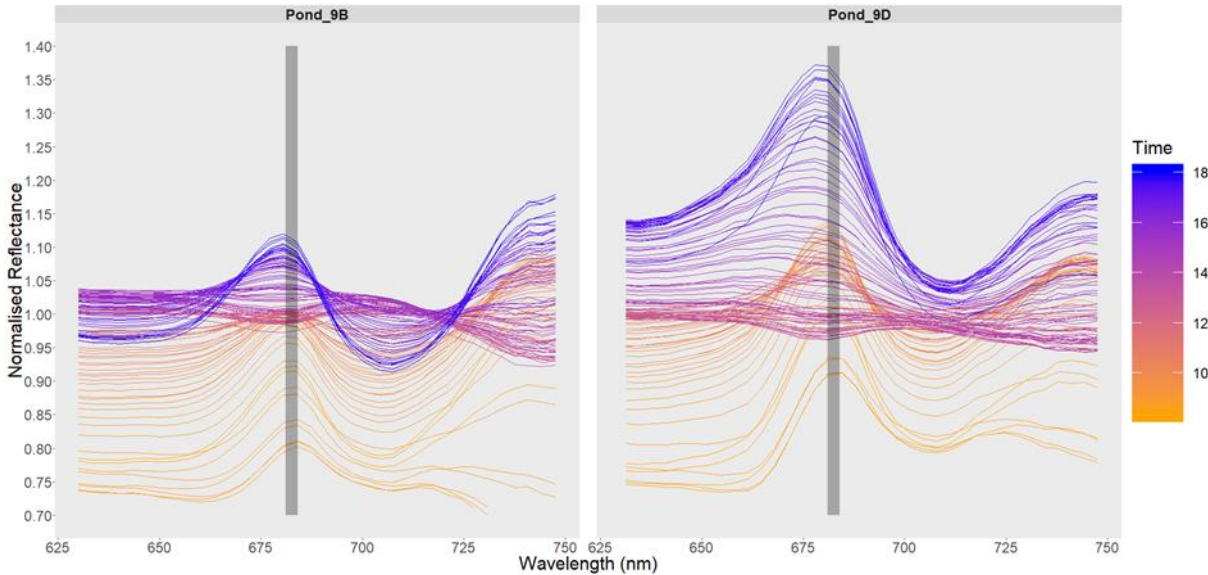


Figure 175: Diurnal cycle of noon time normalized reflectance measurements for two ponds with low (Pond 9B) and high (Pond 9D) nutrient concentration. Data were acquired on 16 July 2019.

Temporal changes in 683nm: normalised values (16 July 2019)

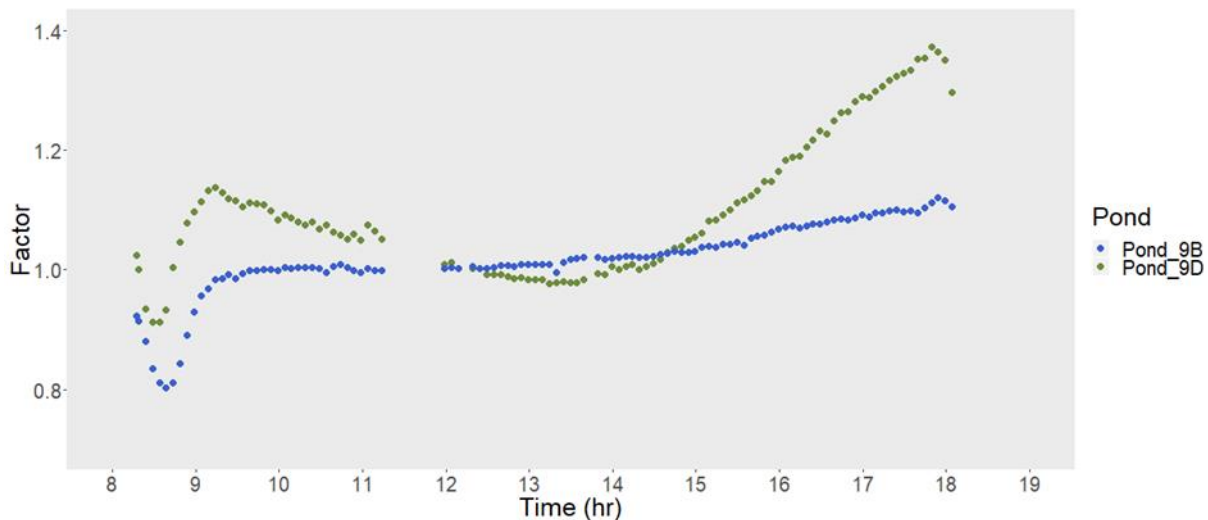


Figure 176: Diurnal cycle of normalized reflectance values at the SIF emission band (683 nm) for 16 July 2019 expressed as factor value. Diurnal cycles are presented for two ponds with low (Pond 9B) and high (Pond 9D) nutrient concentration factor values above one indicate situations when the SIF emission band shows a peak, factor values below one indicate situations when SIF emission shows a dip (possibly due to photo adaptation processes). The low factor values between 8 – 9 h could be attributed to a shadow effect from adjacent buildings; the gap between 11 - 12h is due to water sampling activity, which introduced noise to the data.

	Doc.: Final Report		
	Date: 29 July 2021	Issue: 2	Revision: 1
	Ref.: ESA Contract No. 4000125402/18/NL/NA		Page: 206 / 288

We conclude that multi-scale radiometric data acquired during the FLEXsense 2018 campaign in aquatic sites are valuable and a good base for future investigations.

Concerning data quality, a first look in FloX data indicates a possible SIF peak for the low-resolution detector. The measurement protocol for aquatic sites is different compared to land sites and further investigation on the impact of the applied sampling scheme on reflectance and SIF retrieval is needed. *Hyplant* data are promising and we could detect a similar coarse-scale SIF pattern compared to Sentinel-3A data for the Mediterranean site.

Future activities concern a need to understand SIF dynamics across the day and in different water types. We undertook a first attempt with a mesocosm experiment in 2019. Furthermore, a throughout experimental evaluation of SIF retrieval schemes applied to evaluated sensors is needed. A basis for possible retrieval schemes including aspects of concern, was recently developed and published by Gupana et al. (2021).

8 Synthesis of 2018 campaign data and recommendation for future use

In the 2018 campaign, we have recorded a very extensive data set of ground, airborne and satellite remote sensing measurements across contrasting vegetation types in Europe. On several days, we were able to collect complete data sets, including all elements, which according to our knowledge are needed for level-2 data product development and to develop FLEX Cal / Val concepts (see Table 1). In addition to high resolution radiance data in the optical domain (with an emphasis on the FLEX relevant spectral domains), we have collected thermal data, high-resolution surface and elevation data, detailed meteorological data and selected ground-based data on bio-physical vegetation properties and vegetation functioning. These data are anticipated to become relevant for meeting the technical and scientific objectives of the FLEX satellite mission.

In the following subsections, we briefly highlight the main outcomes of this campaign activity and give recommendations for future the steps going forward.

8.1 SIF retrieval: from SVD and iFLD to the Spectral Fitting Method (SFM) – the proposed retrieval method for the FLEX satellite mission

While the spectral fitting method was previously tested for airborne *HyPlant* imagery in past campaigns, the 2018 campaign activity was the first time we brought the SFM to an operational level. The SFM retrieval scheme for *HyPlant* was fundamentally improved and the processing of flight lines was brought to an operational level, which enabled us to (i) provide a consolidated version of the retrieval code and (ii) process all relevant flight lines of this campaign with the SFM method. The parallelization of code has substantially improved computation times, and are now within an operational range such that a flight line can be processed in less than 1 hour.

For future activities, we propose the following:

- The SFM (and also the iFLD) retrieval scheme needs to be extended that it is also operational in non-flat terrain and surfaces. To this end, a topographic correction needs to be included in the SIF retrieval. This correction must account for the different optical path length, which greatly affects the atmospheric parameterization of the fluorescence retrieval. We anticipate that the parameterization of the SFM SIF retrieval in non-flat terrain will be challenging because the retrieval needs to be parameterized for every single pixel of a flight line.
- For our data, the atmospheric absorption could not be defined accurately enough using solely atmospheric measurements. Accordingly, in our SFM SIF retrieval we needed to implement an additional constraint by non-vegetated surfaces. These findings should be further evaluated and we recommend determining whether this problem of non-sufficient atmospheric characterization for SFM SIF retrieval is solely related to airborne data or if it may also be a problem in satellite SIF retrievals.

8.2 Quality and uncertainties of airborne SIF products – current status and steps forward

With this campaign activity, we addressed for the first-time the quantification of uncertainties in the airborne SIF data products. We have thus developed a systematic approach to better understand uncertainties that are behind the *HyPlant* SIF products. For this report, we developed an operational method for flagging the

	Doc.: Final Report		
	Date: 29 July 2021	Issue: 2	Revision: 1
	Ref.: ESA Contract No. 4000125402/18/NL/NA		Page: 208 / 288

quality level of level-1c data (at-sensor radiance) that now is included in the operational processing pipeline of *HyPlant*. We have additionally undertaken initial consideration of quantitative criteria for evaluating the uncertainty of the level-2 SIF products, which provides a conceptual framework for how uncertainties in airborne SIF products can be derived. This may help as a first step towards an uncertainty estimate of *HyPlant* imagery. However, a full pixel-based uncertainty estimate, which might include a quantitative retrieval error, is very challenging, and cannot be reached within this activity.

For future activities, we propose the following:

- The development of a pixel-based error for the SIF products of *HyPlant* imagery would require substantial resources. However, such a quantitative error estimate for the level-2c SIF products would be desirable for future Cal / Val activities (providing that airborne imagery will be part of the Cal / Val concept of FLEX). Considering the complexity of developing a full error propagation for the processing of *HyPlant* imagery, we propose the following steps:
 - Develop a quantitative estimate of the SNR of the level-2c SIF products of *HyPlant*. With this report, we have developed an approach to give an SNR estimate for at-sensor-radiance measurements from single vegetation units. This approach can be transferred to level-2c SIF products and an empirical SNR estimate for fluorescence products should be developed and tested on existing campaign data.
 - In this campaign, we tested the correlation between ground-based FloX data and atmospherically corrected *HyPlant* data (Figure 42 and Figure 43). The results are encouraging and we recommend a similar comparison on campaign data from the years 2016, 2017, and 2019 to extend the test cases with more vegetation types and a wider variability of atmospheric conditions.
- A follow-up study / report to better understand the uncertainty of field and airborne instruments seems crucial and is highly recommended by the authors of this study. We recommend starting with the parameters that are to be validated for the FLEX satellite mission. We propose the definition of error metrics and the consideration of a Monte Carlo analysis for uncertainty and error propagation for the field and airborne instruments. We can follow the study by Białek et al. (2020) for ocean colour missions, adding the spatial representativeness. Within this follow-up study / report, one can start by considering TOC reflectance, radiance and fluorescence as the first parameters to be validated. In a second step, higher-level products, such as photosynthetic rates can be included. We anticipated that no new data need to be generated for this study, but that this exercise can be performed by using existing data gathered in previous projects. Such results shall be compared with the progress generated in the L2 project, to have the analysis at all levels.
- That also recommend development of best practice for the atmospheric correction of field data. Ground-based fluorescence reference data are crucial for the validation of the selected atmospheric corrections schemes. A procedure for the preprocessing of the fluorescence data at ground level (tower / drones) with field spectrometer should be developed. The installation of two FloX systems at different heights (similar to the procedure shown in sections 4.5.2 and 7.2.1) may be a promising path. Such FloX systems may be installed at existing towers or may be used on a crane. This may be a simple action that can be incorporated in the atmospheric correction study that is ongoing; we can also envision to a vertical acquisition by drone-based systems, which have shown great technical improvements in the recent years; we encourage a new campaign in this context (see also section 7.3.3).

8.3 SIF as an early stress indicator and its potential to improve forward modelling of gross primary productivity

In this campaign, we fundamentally improved our understanding of the correlation between GPP (measured by EC towers) and SIF maps. The relationship between GPP and SIF was re-examined for various ecosystems. Additionally, we could provide for the first-time quantitative data on the size of the footprint that should be taken into account when relating GPP and SIF data (chapter 7.2.3). With this campaign, which evaluates flux and SIF data from three different sites simultaneously, we could establish the following findings:

- Diurnal and seasonal dynamics were described and interpreted showing that a linear relationship between GPP and SIF only exists on aggregated seasonal data, when changes in canopy chlorophyll content determines GPP. Under stressful conditions, when photosynthesis operates below its potential maximum the linear relationship breaks down and SIF is one of the only remote sensing parameters that is able to track stress-induced down regulation of photosynthesis. Thus, we could establish that SIF is able to track physiological changes in photosynthesis, such as stomatal closure or heat related down-regulation of photosynthetic electron transport. Such changes are not seen in any reflectance-based vegetation index. This topic will be further evaluated in the PhotoProxy study, where data from this campaign were analyzed in more depth and will be picked up in the 2019 FLEXsense campaign by exploiting the results from the dedicated heat stress experiment.
- In section 7.4.2, we could clearly show that during the heat wave, which hit the Iberian Peninsula during our campaign activities, SIF reacted dynamically showing a clear and reversible decline during the days of extreme temperatures. The SIF signal readily recovered to pre-heat stress values as soon as air temperatures reached normal values again. Pigment related reflectance measurements did not track the heat wave effects. In this context, the data from the Iberian dehesa ecosystem proved very valuable as the time constants are recorded in this very well characterized field experiments. The temporal dynamics of natural stress events that can be covered by FLEX is still an open question that can only be revisited to a limited extent. Stress is a highly dynamic process and early stress responses develop and relax in the course of a few days. Accordingly, to better understand the potential of the FLEX satellite mission, it is important to determine which stress dynamics can be measured. In this context, the Spain experimental site, which provides a perfect ground monitoring of stress effects, has great potential, and we recommend the inclusion of this study site in further activities.
- Taking the results from this campaign activity and the associated campaign, we could confirm the capacity of SIF measurement to track heat stress induced physiological down regulation of photosynthesis before any signs of pigment degradation occur. This was previously hypothesized in a meta-analysis by Ac et al. (2015), and then experimentally confirmed by Yang et al. (2019) in crops and by Wohlfahrt et al. (2018) on the large satellite scale. With this report, we show that SIF tracks the physiological down regulation of photosynthesis during the heat wave in this agroforest system by tracking the dynamic behavior of SIF and GPP. This study additionally stresses the need to understand the temporal dynamics that govern the early stress responses of plants. SIF clearly has the potential to detect the immediate effects of a heat wave, which occur as instantaneous physiological effects that are tracked by SIF. We see clear proof of concept that heat stress (i.e. extreme high temperatures) can be readily tracked by SIF measurements.
- In addition, we have indications that drought leaves its signature in SIF. During the 2019 field activities, we acquired data from a dedicated drought stress experiment, the results of which will be presented in more detail in the 2019 campaign report. As a matter of fact, drought and heat in nature both often occur simultaneously and it is challenging to unravel the physiological nature of the two environmental constraints. To overcome this problem, we recommend to (i) reanalyze existing data in order to use existing measurements and advanced statistical methods to separate the causal

	Doc.: Final Report		
	Date: 29 July 2021	Issue: 2	Revision: 1
	Ref.: ESA Contract No. 4000125402/18/NL/NA		Page: 210 / 288

effects of drought and heat; and (ii) to evaluate the 2019 campaign data from the ‘Italian drought experiment’ and to potentially expand on these measurements.

- As mentioned above, we have the impression that the effects of drought and heat on SIF are becoming more and more established and the development of ‘heat and drought stress indicators’ are coming within reach. However, we have much less experimental knowledge on the specific effect of freezing, pests and nutrient limitation. Ac et al. (2015) show that SIF has some potential to detect early signs of freezing stress, the occurrence of pest, and also nutrient availability. It is becoming clear that ‘stress products’ for FLEX need to be more specific products, such as a ‘drought stress indicator’ or a ‘heat stress indicator’. Here our level of knowledge on a ‘freezing stress indicator’, an ‘infestation product’ or a ‘nutrient limitation indicator’ is still limited. If such products are to be developed for the FLEX mission, we recommend a data collection using a dedicated experimental design for each of these stress events.

8.4 Measuring and understanding SIF from open waters

Overall, the 2018 FLEXsense campaign in the Mediterranean Sea and at Greifensee provided insight into how SIF can be retrieved over optically complex waters. The major points that we can derive from this campaign are as follows:

- There is room for improving the spectrometers used for in-situ measurements. The FloX system can be reconfigured to allow simultaneous retrievals of Ed, Lu and Lsky.
- We are able to retrieve reasonable FLH values from in-situ, airborne and space borne data.
- We have demonstrated the potential of using FLEX for inland and coastal waters.

Recommended next steps are as follows:

- Apply other methods for retrieving SIF (e.g. inversion and other empirical techniques) while focusing on how best to disentangle elastic from inelastic scattering.
- Conduct more field campaigns while simultaneously retrieving in-water constituent concentrations as well as inherent and apparent optical properties on the ground.
- Assess atmospheric corrections suitable for inland and coastal waters.
- Investigate further PQ and NPQ mechanisms in phytoplankton and how this is reflected in SIF emissions, particularly in the quantum yield of fluorescence.

8.5 Towards a Cal / Val concept for the FLEX satellite mission

The activities, results and key findings obtained are presented in the ATMOFLEX-CCN report ([RD-11]). Here, we provide a summary of limitations and recommendations for future studies.

- **Selection of Cal / Val sites.** Although the five sites included in this campaign activity showed great potential for future Cal / Val sites, we propose the evaluation of additional sites across Europe for future FLEX Cal / Val activities. In particular, we propose searching for Cal / Val sites that (i) encompass simple, large homogeneous crop sites, (ii) provide good contrasts in seasonal SIF emission intensities by including different biomes and different plant functional types, and (iii) have two or three vegetation components with different seasonality. The two Cal / Val reports that have been developed by the FLEX MAG can still be considered a good basis. In future studies, it may be advisable to exploit Sentinel-2 data and to simulate spatial heterogeneity (GIS preparation, field polygons depiction, fractional cover, phenological cycles, spatial representativeness) to better understand if

	Doc.: Final Report		
	Date: 29 July 2021	Issue: 2	Revision: 1
	Ref.: ESA Contract No. 4000125402/18/NL/NA		Page: 211 / 288

proposed candidate sites are suitable FLEX Cal / Val sites. When FLEX is operational, we should have different sites serving the different needs of SIF product validation.

- **Instrumentation of the FLEX Cal / Val sites.** Some spatially homogeneous sites will be equipped for continuous acquisition of FloX-like data and to record the temporal (seasonal) dynamics of vegetation traits and SIF. Heterogeneous or two component sites will require the use of multiple radiometers (at least one for each end-member). More heterogeneous sites will be occasionally sampled by *HyPlant*-like systems (airborne SIF imagers) and others with drone-based acquisitions (point / image) to capture spatial variability concurrent with the satellite overpasses.
- **Reference Targets.** Both active and passive reference targets will be crucial for future Cal / Val activities and both concepts are to be further exploited. Even though if it turns out that large fluorescence reference targets that can be seen by the FLEX satellite mission prove to be infeasible, FLEX Cal / Val sites should be equipped with panels of limited size (e.g. 12 x 12 m). They will allow checking of fluorescence calibration before making the drone / airborne Cal / Val survey during FLEX overpasses as well as calibration of FloX data across different sites.
- **Sampling approach.** As outlined above and emphasized in the various documents, a Cal / Val concept for FLEX SIF data will be based on different measurement platforms. These systems will include ground and tower-based point spectrometers, UAV-based imaging and non-imaging spectrometers and high-performance airborne imaging systems. To integrate the different systems, we propose the development of guidelines for the comparison of SIF values from different measurements systems. One focus should be on the sampling approach from drone-based spectrometer system and tools that automatically define optimal UAV path planning for optimal fluorescence sampling. The number of necessary proximal sensing points that need to be sampled in order to achieve a certain spatial representativeness may be the basis for creating a planning scheme that seeks to maximize UAV coverage over the most variable areas for optimal fluorescence mapping. This will help to accomplish the direct validation approach in a bottom-up scheme. The ESU concept is not fully appropriate for FLEX and we do not have intermediate satellite products for upscaling purposes. Some first steps can be taken by re-using previously collected data (from this and other campaigns), but a combined campaign in which we combine *HyPlant* and drones-based SIF and reflectance measurements may be needed.
- **Indirect validation.** Until now, we have put our main focus on a direct comparison of airborne with in-situ measurements. We have also established a basis for other validation approaches. However, we believe that in the end, multiple validation methods and activities will be necessary to assess fluorescence compliance with specifications. Therefore, we also have to pursue an indirect validation through numerical RTMs, and this process should be applied to some of the sites defined above. If we properly parametrize a model to reproduce fluorescence in space and time, we may have an alternative way to evaluate the quality of the FLEX data. We may overcome the need for ground-based fluorescence data with high-resolution vegetation data (derived e.g. from Sentinel-2) and appropriate field parameters to simulate the expected (potential) fluorescence. Here, we suggest evaluating two focused overpasses with *HyPlant* for this specific aim (maybe in conjunction with the campaign activities mentioned above), in order to refine this approach. This would enable the use of well-characterized sites in terms of vegetation properties when ground-based SIF measurements are not available. Similar approaches have been tested by Sinha et al. (2020) for OCO-2, Yang et al. (2019), and recently by Bandopadhyay et al. (in press). For such an approach, we may use synergies from the Photoproxy project and the most relevant input parameter to correctly parameterize the RTM SCOPE model (i.e. LAI, Cab, mean tilt angle, Vcmax, and fqc).

	Doc.: Final Report		
	Date: 29 July 2021	Issue: 2	Revision: 1
	Ref.: ESA Contract No. 4000125402/18/NL/NA		Page: 212 / 288

- **Field network, processing chain and data delivery.** We suggest the improved definition of the overall FLEX field network and the consolidation of the processing chain with the implementation of a centralized system for data collection and processing (e.g. the FluoSpecchio platform). This will foster a collaborative use of the current FloX network, which is growing rapidly (with almost 40 FloX systems being employed worldwide). We also recommend exploring synergies with existing ecosystem monitoring networks, such as ICOS or SpecNet. Additionally, we recommend including the *HyPlant* processing chain, which is the most advanced processing chain for airborne fluorescence data, in addition to the inclusion of atmospheric data and auxiliary measurements at leaf level in such a data delivery framework.
- **Further considerations for the Cal / Val concept of FLEX.** In addition to the core Cal / Val concepts for the SIF data we recommend taking the following points into consideration:
 - For TOA radiance validation, we suggest using the RadCalnet scheme for the validation of level-1 products and accommodating FloX in a PICS monitored by RadCalnet.
 - Surface reflectance from reprogrammed OLCI bands should be further analyzed for their potential to be used in scaling. This could be part of a larger scaling exercise-based on FloX, *HyPlant* and Sentinel-3 data collected during the 2018 campaign. Until now, we have analyzed TOA radiances and a scientific publication on this topic being prepared (Celesti et al. *in prep.*). As next steps, we propose pursuing an atmospheric correction scheme and the generation of TOC radiance and reflectance. This data can then be used to generate a far-red fluorescence map from satellite data, which can be registered to 300 m aggregated *HyPlant* fluorescence maps. A spatial comparison could be an important milestone to go beyond the uncertainty characterization of Sentinel-3B “FLEX mode” data. In the end, we may use satellite fluorescence to evaluate the spatial pattern at the regional scale and to explore the possibility of sharing and comparing the results with those from the TROPOMI instrument.
 - We recommend initiating the development of a bidirectional fluorescence distribution function multitemporal library (BFDF) library. Simulation and measurements could be used to generate a BFDF multitemporal library for one or two CAL / VAL sites. For example, the directional response of fluorescence over several canopies has been characterized and simulated for some crops (e.g. see Biriukova et al. 2020), but this has never been done in the temporal domain to reflect the seasonality of vegetation.

9 References

- Ač A., Malenovský Z., Olejníčková J., Gallé A., Rascher U. & Mohammed G. (2015). Meta-analysis assessing potential of steady-state chlorophyll fluorescence for remote sensing detection of plant water, temperature and nitrogen stress. *Remote Sensing of Environment*, 168, 420-436.
- Ahmed K. R., Paul-Limoges E., Rascher U. and Damm A. (2021). A First Assessment of the 2018 European Drought Impact on Ecosystem Evapotranspiration. *Remote Sensing*, 13(16).
- Alonso L., Gómez-Chova L., Vila-Francés J., Amorós-López J., Guanter L., Calpe J., Moreno J. (2008). Improved Fraunhofer Line Discrimination method for vegetation fluorescence quantification. *IEEE Geosci. Remote Sens. Lett.*, 5, 620–624.
- Badgley G., Field C. B., Berry J. A. (2017). Canopy near-infrared reflectance and terrestrial photosynthesis. *Sci. Adv.* 3, e1602244.
- Bandopadhyay S., Rastogi A., Rascher U., Rademske P., Schickling A., Cogliati S., Julitta T., Mac Arthur A., Hueni A., Tomelleri E., Celesti M., Burkart A., Stróżecki M., Sakowska K., Gąbka M., Rosadziński S., Sojka M., Iordache M.-D., Reusen I., Van Der Tol C., Damm A., Schuettemeyer D., Juszczak R. (2019). Hyplant-Derived Sun-Induced Fluorescence—A New Opportunity to Disentangle Complex Vegetation Signals from Diverse Vegetation Types. *Remote Sensing*, 11(14):1691.
- Bandopadhyay S., Rastogi A., Cogliati S., Rascher U., Gabka M. & Juszczak R. (in press). Can spectral vegetation indices serve as proxies for potential Sun-Induced Fluorescence (SIF)? A fuzzy modelling approach on airborne imaging spectroscopy data. *Remote Sensing*, accepted 10. May 2021.
- Beckers J. M., Rixen M. (2003). EOF calculations and data filling from incomplete oceanographic datasets. *J Atmos Ocean Technol*, 20(12), 1839–1856.
- Bendig J., Malenovský Z., Gautam D., Lucieer A. (2019). Solar-Induced Chlorophyll Fluorescence Measured From an Unmanned Aircraft System: Sensor Etaloning and Platform Motion Correction. *IEEE Trans. Geosci. Remote Sensing*, 58, 3437-3444.
- Berk A., Anderson G. P., Acharya P. K., Bernstein L. S., Muratov L., Lee J., Fox M., Adler-Golden S. M., Chetwynd J. H., Hoke M. L., Lockwood R. B., Cooley T. W., Gardner J. A. (2005). MODTRAN5: A reformulated atmospheric band model with auxiliary species and practical multiple scattering option. *Proc. Soc. Photo Opt. Instrum. Eng.*, 5655, 662–667.
- Białek A., Douglas S., Kuusk J., Ansko I., Vabson V., Vendt R., & Casal T. (2020). Example of Monte Carlo Method Uncertainty Evaluation for Above-Water Ocean Colour Radiometry. *Remote Sensing*, 12(5), 780.
- Bielinis E., Jozwiak W., Robakowski P. (2015). Modelling the relationship between SPAD values and photosynthetic pigment content in *Quercus petraea* and *Prunus serotina* leaves. *Dendrobiology* 73:125-134.
- Biriukova K., Celesti M., Evdokimov A., Pacheco-Labrador J., Julitta T., Migliavacca M., Giardino C., Miglietta F., Colombo R., Panigada C., Rossini M. (2020) Effects of varying solar-view geometry and canopy structure on solar-induced chlorophyll fluorescence and PRI. *International Journal of Applied Earth Observation and Geoinformation*, 89, doi 10.1016/j.jag.2020.102069
- Buman B. Hueni A., Colombo R., Cogliati S., Celesti M., Julitta T., Burkhardt A., Siegmann B., Rascher U., Drusch M. & Damm A. (submitted). Towards consistent uncertainty assessments of in situ radiometric measurements for the validation of fluorescence satellite missions by using data exploitation platforms. *Remote Sensing of Environment*, submitted 3 June 2021.
- Campbell P. K. E., Huemmrich K. F., Middleton E. M., Ward L. A., Julitta T., Daughtry C. S. T., Burkart A., Russ A. L., Kustas W. P. (2019). Diurnal and Seasonal Variations in Chlorophyll Fluorescence Associated with Photosynthesis at Leaf and Canopy Scales. *Remote Sensing*, 11, 2072-4292.

	Doc.: Final Report		
	Date: 29 July 2021	Issue: 2	Revision: 1
	Ref.: ESA Contract No. 4000125402/18/NL/NA		Page: 214 / 288

- Cendrero-Mateo M. P., Wieneke S., Damm A., Alonso L., Pinto F., Moreno J., Guanter L., Celesti M., Rossini M., Sabater N., Cogliati S., Julitta T., Rascher U., Goulas Y., Aasen H., Pacheco-Labrador J., Arthur A. Mac. (2019). Sun-Induced Chlorophyll Fluorescence III: Benchmarking Retrieval Methods and Sensor Characteristics for Proximal Sensing. *Remote Sensing* 2019, Vol. 11, Page 962, 11(8), 962.
- Chang C. Y., Guanter L., Frankenberg C., Köhler P., Gu L., Magney T. S., Grossmann K., & Sun Y. (2020). Systematic assessment of retrieval methods for canopy far-red solar-induced chlorophyll fluorescence (SIF) using high-frequency automated field spectroscopy. *Journal of Geophysical Research: Biogeosciences*.
- Chrysafis I., Korakis G., Kyriazopoulos A. P. and Mallinis G. (2020). Retrieval of Leaf Area Index Using Sentinel-2 Imagery in a Mixed Mediterranean Forest Area. *ISPRS Int. J. Geo-Inf.* 2020, 9, 622.
- Cogliati S., Verhoef W., Kraft S., Sabater N., Alonso L., Vicent J., Moreno J., Drusch M., & Colombo R. (2015). Retrieval of sun-induced fluorescence using advanced spectral fitting methods. *Remote Sensing of Environment*, 169, 344–357.
- Cogliati S., Rossini M., Julitta T., Meroni M., Schickling A., Burkart A., Pinto F., Rascher U., Colombo R. (2015a). Continuous and long-term measurements of reflectance and sun-induced chlorophyll fluorescence by using novel automated field spectroscopy systems. *Remote Sensing of Environment*, 164, 270–281.
- Cogliati S. et al. (2018). Red and Far-Red Fluorescence Emission Retrieval from Airborne High-Resolution Spectra Collected by the Hyplant-Fluo Sensor.” *IGARSS 2018 - 2018 IEEE International Geoscience and Remote Sensing Symposium*, 3935-3938.
- Cogliati S., Celesti M., Cesana I., Miglietta F., Genesio L., Julitta T., Schuettemeyer D., Drusch M., Rascher U., Jurado P. & Colombo R. (2019). A spectral fitting algorithm to retrieve the fluorescence spectrum from canopy radiance. *Remote Sensing*, 11, 1840.
- Colombo R., Celesti M., Bianchi R., Campbell P.K.E., Cogliati S., Cook B.D., Corp L.A., Damm A., Domec J.C., Guanter L., Julitta T., Middleton E.M., Noormets A., Panigada C., Pinto F., Rascher U., Rossini M., Schickling A. (2018). Variability of sun-induced chlorophyll fluorescence according to stand age-related processes in a managed loblolly pine forest. *Glob Chang Biol.*, 24(7):2980-2996.
- Damm A., Guanter L., Laurent V.E., Schaepman M.E., Schickling A., Rascher U. (2014). FLD-based retrieval of sun-induced chlorophyll fluorescence from medium spectral resolution airborne spectroscopy data. *Remote Sensing Environment*, 147, 256–266.
- Damm A., Guanter L., Verhoef W., Schläpfer D., Garbari S., Schaepman M.E. (2015). Impact of varying irradiance on vegetation indices and chlorophyll fluorescence derived from spectroscopy data. *Remote Sensing Environment*, 156, 202–215.
- Damm A., Haghghi E., Paul-Limoges E. and Van der Tol C. (2021). On the seasonal relation of sun-induced chlorophyll fluorescence and transpiration in a temperate mixed forest. *Agricultural and Forest Meteorology*, 304: 108386.
- Desmons M., Wang P., Stammes P., and Tilstra L. G. (2019). FRESCO-B: a fast cloud retrieval algorithm using oxygen B-band measurements from GOME-2, *Atmos. Meas. Tech.*, 12, 2485–2498.
- Di Cicco A., Gupana R., Damm A., Colella S., Angelini F., Fiorani L., Artuso F., Brando V. E., Lai A., Genangeli A., Miglietta F., Santoleri R. (2020). “Flex 2018” Cruise: an opportunity to assess phytoplankton chlorophyll fluorescence retrieval at different observative scales. In: Bonora, Laura; Carboni, Donatella; De Vincenzi, Matteo. *Eighth International Symposium “Monitoring of Mediterranean Coastal Areas. Problems and Measurement Techniques”*. Firenze (Italy): Firenze University Press, 688-697.
- Drusch M. et al. (2017). The FLuorescence EXplorer mission concept - ESA’s Earth Explorer 8. *IEEE Transactions on Geoscience and Remote Sensing*, 55, 1273-1284.

	Doc.: Final Report		
	Date: 29 July 2021	Issue: 2	Revision: 1
	Ref.: ESA Contract No. 4000125402/18/NL/NA		Page: 215 / 288

- El-Madany T. S., Reichstein M., Pérez-Priego O., Carrara A., Moreno G., Pilar Martín M., Pacheco-Labrador J., Wohlfahrt G., Nieto H., Weber U., Kolle O., Yunpeng L., Carvalhais N., Migliavacca M. (2018). Drivers of spatio-temporal variability of carbon dioxide and energy fluxes in a mediterranean savanna ecosystem. *Agricultural and Forest Meteorology*, 262, 258-278.
- El-Madany T. S., Carrara A., Martín M. P., Moreno G., Kolle O., Pacheco-Labrador J., Weber U., Wutzler T., Reichstein M., Migliavacca M. (2020). Drought and heatwave impacts on semi-arid ecosystems' carbon fluxes along a precipitation gradient. *Philosophical Transactions of the Royal Society of London, Series B: Biological Sciences*, 375(1810): 20190519.
- ESA 2015. Report for Mission Selection: FLEX, ESA SP-1330/2 (2 volume series), European Space Agency, Noordwijk, The Netherlands.
- Eugster W., Zeyer K., Zeeman M., Michna P., Zingg A., Buchmann N. and Emmenegger L. (2007). Methodical study of nitrous oxide eddy covariance measurements using quantum cascade laser spectrometry over a Swiss forest. *Biogeosciences*, 4(5), 927-939.
- Foken T., Göckede M., Mauder M., Mahrt L, Amiro BD, Munger JW. (2004). Post-field data quality control. In *Handbook of micrometeorology: a guide for surface flux measurement and analysis* (eds. X. Lee, W Massman, B Law), 181–208. Dordrecht, the Netherlands: Kluwer Academic Publishers.
- Foken T. (2013). Application of footprint models for wind turbine locations. *Meteorologische Zeitschrift*, 22 (2), 111 – 115.
- Frankenberg C., Butz A., and Toon G. C. (2011). Disentangling chlorophyll fluorescence from atmospheric scattering effects in O₂ A-band spectra of reflected sun-light, *Geophys. Res. Lett.*, 38.
- Fu P., Li C., Xia Y., Ji Z., Sun Q., Cai W., & Feng D. D. (2014). Adaptive noise estimation from 687 highly textured hyperspectral images. *Applied Optics*, 53(30), 7059.
- Gamon J. A., Somers B., Malenovsky Z., Middleton E., Rascher U. & Schaepman M. (2019). Assessing vegetation function with imaging spectroscopy. *Surveys in Geophysics*, 40, 489-513.
- Gautam D., Lucieer A., Bendig J., Malenovský Z. (2020). Footprint Determination of a Spectroradiometer Mounted on an Unmanned Aircraft System. *IEEE Trans. Geosci. Remote Sens.*, 58, 3085-3096.
- Gerhards M., Schlerf M., Rascher U., Udelhoven T., Juszczak R., Alberti G., Miglietta F., & Inoue Y (2018). Remote sensing of water stress symptoms based on airborne optical and thermal images. *Remote Sensing*, 10, article no. 1139.
- Gillespie A., Rokugawa S., Matsunaga T., Cothorn J. S., Hook S., and Kahle A. B., (1998). A temperature and emissivity separation algorithm for advanced spaceborne thermal emission and reflection radiometer (ASTER) images. *IEEE Transactions on Geoscience and Remote Sensing*, 36, 1113-1126.
- Gower J. F. R. (1980). Observations of in situ fluorescence of chlorophyll-a in Saanich Inlet Boundary-Layer Meteorol., 18, pp. 232-245.
- Graf A. (2017). Gap-filling meteorological variables with Empirical Orthogonal Functions. EGU 2017 General Assembly, Vienna (Austria), 23 Apr 2017 - 28 Apr 2017, URL <https://juser.fz-juelich.de/record/829701>, [Accessed 25 January 2019].
- Guanter L., Frankenberg C., Dudhia A., Lewis P.E., Gómez-Dans J., Kuze A., Suto H., Grainger G. (2012). Retrieval and global assessment of terrestrial chlorophyll fluorescence from GOSAT space measurement. *Remote Sensing Environment*, 121, 236–251.
- Guanter L., Rossini M., Colombo R., Meroni M., Frankenberg C., Lee J.E., Joiner J. (2013). Using field spectroscopy to assess the potential of statistical approaches for the retrieval of sun-induced chlorophyll fluorescence from ground and spac. *Remote Sensing Environment*, 15, 52–61.
- Gupana R., Odermatt D., Cesana I., Giardino, Nedbal L. and Damm A. (2021). Remote sensing of sun-induced chlorophyll-a fluorescence in inland and coastal waters: current state and future prospects. *Remote Sensing of Environment*, 262, 112482.

	Doc.: Final Report		
	Date: 29 July 2021	Issue: 2	Revision: 1
	Ref.: ESA Contract No. 4000125402/18/NL/NA		Page: 216 / 288

- Helm L. T., Shi H., Lerdau M. T., Yang X. (2020). Solar-induced chlorophyll fluorescence and short-term photosynthetic response to drought. *Ecological Applications*, 30.
- Hornero A., North P. R. J., Zarco-Tejada P. J., Rascher U., Martíne M. P., Migliavacca M. & Hernández-Clemente R. (2021). Assessing the contribution of understory sun-induced chlorophyll fluorescence through 3-D radiative transfer modelling and field data. *Remote Sensing of Environment*, 253, article no. 112195.
- Jähne, B. *Digital Image Processing*, 6th ed.; Springer: Berlin/Heidelberg, Germany, 2005; pp. 463–500.
- Joiner J., Guanter L., Lindstrot C., Voigt M., Vasilkov A. P., Middleton E. M., Huemmrich K. F., Yoshida Y., Frankenberg C. (2013). Global monitoring of terrestrial chlorophyll fluorescence from moderate-spectral-resolution near-infrared satellite measurements: Methodology, simulations, and application to GOME-2. *Atmos. Meas. Tech.*, 6, 2803–2823.
- Jonard F., De Cannière S., Brüggemann N., Gentine P., Short Gianotti D. J., Lobet G., Miralles D.G., Montzka C., Pagán B.R., Rascher U. & Vereecken H. (2020). Value of sun-induced chlorophyll fluorescence for quantifying hydrological states and fluxes: current status and challenges. *Agricultural and Forest Meteorology*, 291, article no. 108088.
- Julitta T., Wutzler T., Rossini M., Colombo R., Cogliati S., Meroni M., Burkart A., Migliavacca M. (2017). An R Package for Field Spectroscopy: From System Characterization to Sun-Induced Chlorophyll Fluorescence Retrieval, poster presented on 17th – 19th January 2017 at the ESA workshop in ESRIN, Frascati (Rome), Italy.
- Kormann R., Meixner F. X. (2001). An Analytical Footprint Model For Non-Neutral Stratification. *Boundary-Layer Meteorology* 99, 207–224.
- Kromdijk J., Katarzyna Głowacka, Lauriebeth Leonelli, Stéphane T. Gabilly, Masakazu Iwai, Krishna K. Niyogi, Stephen P. (2016). Improving photosynthesis and crop productivity by accelerating recovery from photoprotection. *Long Science*, 857-861
- Lamquin N., Clerc S., Bourg L., Donlon C. (2020). OLCI A/B Tandem Phase Analysis, Part 1: Level 1 Homogenisation and Harmonisation. *Remote Sensing*, 12(11), 1804.
- Lasslop G., Reichstein M., Papale D., Richardson A. D., Arneth A., Barr A., Stoy P. & Wohlfahrt G. (2010). Separation of net ecosystem exchange into assimilation and respiration using a light response curve approach: critical issues and global evaluation. *Global Change Biology*, 16(1), 187–208
- Lichtenthaler H. K. (1987). Chlorophylls and carotenoids – pigments of photosynthetic biomembranes. In *Methods in Enzymology* Eds SP Colowick and NO Kaplan, 350-382. (Academic Press: Sydney).
- Lichtenthaler H. K. and Buschmann C. (2001). Current protocols in Food and Analytical Chemistry. F4.3.8-F4.2.4
- Liu X., Guanter L., Liu L., Damm A., Malenovsky Z., Rascher U., Peng. D., Du S., Gastellu-Etchegorry J.-P. (2019). Downscaling of solar-induced chlorophyll fluorescence from canopy level to photosystem level using a random forest model. *Remote Sensing of Environment*, 231, 110772.
- Löhnert U., Schween J.H., Acquistapace C., Ebell K., Maahn M., Barrera-Verdejo M., Hirsikko A., Bohn B., Knaps A., O’Connor E., Simmer C., Wahner A., and Crewell S. (2015). JOYCE: Jülich Observatory for Cloud Evolution. *Bull. Amer. Meteor. Soc.*, 96, 1157–1174.
- Lu X. L., Liu Z. Q., An S. Q., Miralles D. G., Maes W., Liu Y. L. and Tang J. W. (2018). Potential of solar-induced chlorophyll fluorescence to estimate transpiration in a temperate forest. *Agricultural and Forest Meteorology*, 252: 75.
- Lucieer A., Malenovský Z., Veness T., Wallace L., (2014). HyperUAS-Imaging Spectroscopy from a Multirotor Unmanned Aircraft System: HyperUAS-Imaging Spectroscopy from a Multirotor Unmanned. *J. Field Robot.* 31, 571–590.

	Doc.: Final Report		
	Date: 29 July 2021	Issue: 2	Revision: 1
	Ref.: ESA Contract No. 4000125402/18/NL/NA		Page: 217 / 288

- Maes W. H., B. R. Pagan B. R., Martens B., Gentine P., Guanter L., Steppe K., Verhoest N. E. C., Dorigo W., Li X., Xiao J. and Miralles D. G. (2020). Sun-induced fluorescence closely linked to ecosystem transpiration as evidenced by satellite data and radiative transfer models. *Remote Sensing of Environment*, 249.
- Marrs J. K., Reblin J. S., Logan B. A., Allen D. W., Reinmann A. B., Bombard D. M., Tabachnik D., Hutrya L. R. (2020). Solar-Induced Fluorescence Does Not Track Photosynthetic Carbon Assimilation Following Induced Stomatal Closure. *Geophysical Research Letters* 47, 1–11.
- Marrs J. K., Jones T. S., Allen D. W., & Hutrya L. R. (2021). Instrumentation sensitivities for tower-based solar-induced fluorescence measurements. *Remote Sensing of Environment*, 259, 112413.
- Martini D., Pacheco-Labrador J., Perez-Priego O., van der Tol C., El-Madany T.S., Julitta T., Rossini M., Reichstein M., Christiansen R., Rascher U., Moreno G., Martin M.P., Yang P., Carrara A., Guan J., González-Cascón R. & Migliavacca M. (2019) Nitrogen and phosphorus effect on sun-induced fluorescence and gross primary productivity in Mediterranean grassland *Remote Sensing*, 11, article no. 2562.
- Martini D., Sakowska K., Wohlfahrt G., Pacheco-Labrador J., van der Tol C., Porcar-Castell A., Magney T.S., Carrara A., Colombo R., El-Madany T., González-Cascón R., Martin M.P., Julitta T., Moreno G., Rascher U., Reichstein M., Rossini M. & Migliavacca M. (submitted). Heat-wave breaks down the linearity between sun-induced fluorescence and gross primary production. *New Phytologist*, submitted 17 May 2021.
- Meroni M., Rossini M., Guanter L., Alonso L., Rascher U., Colombo R. & Moreno J. (2009). RS of solar-induced chlorophyll fluorescence: Review of methods and applications. *RS of Environment*, 113(10), 2037-2051.
- Middleton E.M., Rascher U., Corp L.A., Huemmrich K.F., Cook B.D., Noormets A., Schickling A., Pinto F., Alonso L., Damm A., Guanter L., Colombo R., Campbell P.K.E., Landis D.R., Zhang Q., Rossini M., Schuettemeyer D., Bianchi R. (2017). The 2013 FLEX—US Airborne Campaign at the Parker Tract Loblolly Pine Plantation in North Carolina, USA. *Remote Sensing*, 9(6):612.
- Mohammed G. H., Colombo R., Middleton E. M., Rascher U., van der Tol C., Nedbal L., Goulas Y., Pérez-Priego O., Damm A., Meroni M., Joiner J., Cogliati S., Verhoef W., Malenovsky Z., Gastellu-Etchegorry J.-P., Miller J. R., Guanter L., Moreno J., Moya I., Berry J. A., Frankenberg C. & Zarco-Tejada P. J. (2019). Remote sensing of solar-induced chlorophyll fluorescence (SIF) in vegetation: 50 years of progress. *Remote Sensing of Environment*, 231, article no. 111177.
- Murchie E. H., Ruban A. V. (2020). Dynamic non-photochemical quenching in plants: from molecular mechanism to productivity. *Plant Journal* 101, 885–896.
- Nelson J. A., Carvalhais N., Cuntz M., Delpierre N., Knauer J., Ogée J., Migliavacca M., Reichstein M., Jung M. (2018). Coupling water and carbon fluxes to constrain estimates of transpiration: The TEA algorithm. *Journal of Geophysical Research: Biogeosciences*, 123, 3617– 3632.
- Paul-Limoges E., Damm A., Hueni A., Liebisch F., Eugster W., Schaepman M. E., Buchmann N. (2018). Effect of environmental conditions on sun-induced fluorescence in a mixed forest and a cropland. *Remote Sensing of Environment* 219, 310–323.
- Paul-Limoges E., Wolf S., Schneider F.D., Longo M., Moorcroft P., Gharun M., & Damm A. (2020). Partitioning water vapor fluxes with concurrent eddy covariance measurements in a mixed forest. *Agricultural and Forest Meteorology*, 280, 107786.
- Percival G. C., Keary I. P., Noviss K. (2008). The Potential of a Chlorophyll Content SPAD Meter to Quantify Nutrient Stress in Foliar Tissue of Sycamore (*Acer pseudoplatanus*), English Oak (*Quercus robur*), and European Beech (*Fagus sylvatica*). *Arboriculture and Urban Forestry* 34:89-100.

	Doc.: Final Report		
	Date: 29 July 2021	Issue: 2	Revision: 1
	Ref.: ESA Contract No. 4000125402/18/NL/NA		Page: 218 / 288

- Perez-Priego O. and Guan J. and Rossini M. and Fava F. and Wutzler T. and Moreno, G. and Carvalhais N., Carrara A., Kolle O., Julitta T., Schrumpf M., Reichstein M. and Migliavacca M. (2015). Sun-induced chlorophyll fluorescence and photochemical reflectance index improve remote-sensing gross primary production estimates under varying nutrient availability in a typical Mediterranean savanna ecosystem. *Biogeosciences*, 12, 6351-6367.
- Pinto F., Damm A., Schickling A., Panigada C., Cogliati S., Müller-Linow M., Ballvora A. & Rascher U. (2016). Sun-induced chlorophyll fluorescence from high-resolution imaging spectroscopy data to quantify spatio-temporal patterns of photosynthetic function in crop canopies. *Plant, Cell & Environment*, 39, 1500-1512.
- Pinto F., Müller-Linow M., Schickling A., Cendrero-Mateo M. P., Ballvora A. & Rascher U. (2017). Multiangular observation of canopy sun-induced chlorophyll fluorescence combining imaging spectroscopy and stereoscopy. *Remote Sensing*, 9, article no. 415, doi: 10.3390/rs9050415.
- Pinto F., Celesti M., Acebron K., Alberti G., Cogliati S., Colombo R., Juszczak R., Matsubara S., Miglietta F., Palombo A., Panigada C., Pignatti S., Rossini M., Sakowska K., Schickling A., Schüttemeyer D., Stróżecki M., Tudoroiu M. & Rascher U. (2020) Dynamics of sun-induced chlorophyll fluorescence and reflectance to detect stress-induced variations in canopy photosynthesis. *Plant, Cell & Environment*, 43, 1637-1654, doi: 10.1111/pce.13754.
- Quirós-Vargas J., Bendig J., Mac Arthur A., Burkart A., Julitta T., Maseyk K., Thomas R., Siegmann B., Rossini M., Celesti M., Schüttemeyer D., Kraska T., Muller O. & Rascher U. (2020). Unmanned Aerial Systems (UAS)-based methods for Solar Induced Chlorophyll Fluorescence (SIF) retrieval with non-imaging spectrometers: State of the art. *Remote Sensing*, 12, article no. 1624.
- Rascher U., Alonso L.; Burkhardt A., Cilia A., Cogliati S., Colombo R., Damm A., Drusch M., Guanter L., Hanus J., Hyvärinen T., Julitta T., Jussila J., Kataja K., Kokkalis P., Kraft S., Kraska T., Matveeva M., Moreno J., Muller O., Panigada C., Píkl M., Pinto F., Prey L., Pude, Rossini M., Schickling A., Schurr U., Schüttemeyer D., Verrelst J., Zemek F. (2015). Sun-induced fluorescence—A new probe of photosynthesis: First maps from the imaging spectrometer HyPlant. *Global Change Biology*, 21, 4673–4684.
- REddyProc Team (2014). REddyProc: Data processing and plotting utilities of (half-) hourly eddy covariance measurements. R package version 1.1.3. <https://www.bgc-jena.mpg.de/bgi/index.php/Services/REddyProcWebRPackage> [Accessed 25 January 2019].
- Reed R., Travis R. L. (1987). Paraheliotropic Leaf Movements in Mature Alfalfa Canopies 1. *Crop Science* 27, 301–304.
- Reichstein M., Falge E., Baldocchi D., Papale D., Aubinet M., Berbigier P., Bernhofer C., Buchmann N., Gilmanov T., Granier A., Grünwald T., Havránková K., Ilvesniemi H., Janous D., Knohl A., Laurila T., Lohila A., Loustau D., Matteucci G., Meyers T., Miglietta F., Ourcival J.-M., Pumpanen J., Rambal S., Rotenberg E., Sanz M., Tenhunen J., Seufert G., Vaccari F., Vesala T., Yakir D., Valentini R. (2005). On the separation of net ecosystem exchange into assimilation and ecosystem respiration: review and improved algorithm. *Glob. Change Biol.* 11, 1424–1439.
- Richardson A. D., Duigan S. P., Berlyn G. P. (2002). An evaluation of noninvasive methods to estimate foliar chlorophyll content. *New Phytologist* 153:185-194.
- Rossini M., Nedbal L., Guanter L., Ač A., Alonso L., Burkart A., Cogliati S., Colombo R., Damm A., Drusch M., Hanus J., Janoutova R., Julitta T., Kokkalis P., Moreno J., Novotny J. (2015). Red and far red Sun-induced chlorophyll fluorescence as a measure of plant photosynthesis. *Geophysical Research Letters*, 42, 1632-1639.

	Doc.: Final Report		
	Date: 29 July 2021	Issue: 2	Revision: 1
	Ref.: ESA Contract No. 4000125402/18/NL/NA		Page: 219 / 288

- Rossini M., Meroni M., Celesti M., Cogliati S., Julitta T., Panigada C., Rascher U., van der Tol C. and Colombo R. (2016). Analysis of Red and Far-Red Sun-Induced Chlorophyll Fluorescence and Their Ratio in Different Canopies Based on Observed and Modeled Data. *Remote Sensing*, 8, 412.
- Scharr H., Rademske P., Alonso L., Cogliati S. & Rascher U. (submitted). Spatio-spectral deconvolution for high resolution spectral imaging with an application to the estimation of sun-induced fluorescence. *Remote Sensing of Environment*, submitted 7 March 2021.
- Shan N., Zhang Y., Chen J. M., Ju W., Migliavacca M., Penuelas J., Yang X., Zhang Z., Nelson J. A. and Goulas Y. (2021). A model for estimating transpiration from remotely sensed solar-induced chlorophyll fluorescence. *Remote Sensing of Environment*, 252.
- Shang X, Chazette P, Totems J, Dieudonné E, Hamonou E, Duflot V, Strasberg D, Flores O, Fournel J, Tulet P. (2016). Tropical Forests of Réunion Island Classified from Airborne Full-Waveform LiDAR Measurements. *Remote Sensing*, 8(1):43.
- Siegmann B., Alonso L., Celesti M., Cogliati S., Colombo R., Damm A., Douglas S., Guanter L., Hanuš J., Kataja K., Kraska T., Matveeva M., Moreno J., Muller O., Píkl M., Pinto F., Quirós Vargas J., Rademsk P., Rodriguez-Morene F., Sabater N., Schickling A., Schüttemeyer D., Zemek F. & Rascher U. (2019). The high-performance airborne imaging spectrometer HyPlant – From raw images to top-of-canopy reflectance and fluorescence products: Introduction of an automatized processing chain. *Remote Sensing*, 11, article no. 2760.
- Simmer C., Thiele-Eich I., Masbou M., Amelung W., Crewell S., Diekkruieger B., Ewert F., Hendricks Franssen H.-J., Huisman A. J., Kemna A., Klitzsch N., Kollet S., Langensiepen M., Loehnert U., Rahman M., Rascher U., Schneider K., Schween J., Shao Y., Shrestha P., Stiebler M., Sulis M., Vanderborgh J., Vereecken H., van der Kruk J., Zerenner T., and Waldhoff G. (2015). Monitoring and Modeling the Terrestrial System from Pores to Catchments - the Transregional Collaborative Research Center on Patterns in the Soil-Vegetation-Atmosphere System. *Bulletin of the American Meteorological Society*, 96, 1765–1787.
- Sinha S.K., Padalia H., Patel N.R., and Chauhan P (2020) Estimation of seasonal sun-induced fluorescence dynamics of Indian tropical deciduous forests using SCOPE and Sentinel-2 MSI. *International Journal of Applied Earth Observation and Geoinformation*, 91, 102155
- Sobrino J. A., Jiménez-Muñoz J. C., Sòria G., Gómez M., Barella Ortiz A., Romaguera M., Zaragoza M., Julien Y., Cuenca J., Atitar M., Hidalgo V., Franch B., Mattar C., Ruescas A., Morales L., Gillespie A., Balick L., Su Z., Nerry F., Peres L. & Libonati R. (2008). Thermal remote sensing in the framework of the SEN2FLEX project: field measurements, airborne data and applications. *International Journal of Remote Sensing*, 29:17,4961 - 4991.
- Stadler A., Kupisch M., Langensiepen M., Ewert F. (2012). Field heterogeneity as a crucial factor for improving crop growth simulations. Poster. Fall Meeting of the American Geophysical Union (AGU), San Francisco, California, USA.
- Tagliabue G., Panigada C., Dechant B., Baret F., Cogliati S., Colombo R., Migliavacca M., Rademske P., Schickling A., Schüttemeyer D., Verrelst J., Rascher U., Ryu Y. & Rossini M. (2019). Exploring the spatial relationship between airborne-derived red and far-red sun-induced fluorescence and process-based GPP estimates in a forest ecosystem. *Remote Sensing of Environment*, 231, article no. 111272.
- Tagliabue G., Panigada C., Celesti M., Cogliati S., Colombo R., Migliavacca M., Rascher U., Rocchini D., Schüttemeyer D., Rossini M. (2020). Sun-induced fluorescence heterogeneity as a measure of functional diversity. *Remote Sensing of Environment*, 247: 111934.
- van Dijk A., Moene A. F., de Bruin H. A. R. (2004). The principles of surface flux physics: theory, practice and description of the ECPACK library. Internal Report 2004/1, Meteorology and Air Quality Group, Wageningen University, Wageningen, the Netherlands, 99.

- Vanlerberghe G. C., Martyn G. D., Dahal K. (2016). Alternative oxidase: a respiratory electron transport chain pathway essential for maintaining photosynthetic performance during drought stress. *Physiologia plantarum* 157, 322–337.
- Verhoef W., Bach H. (2003). Remote sensing data assimilation using coupled radiative transfer model. *Phys. Chem. Earth*, 28, 3–13.
- Verhoef W., Bach H. (2003a). Simulation of hyperspectral and directional radiance images using coupled biophysical and atmospheric radiative transfer model. *Remote Sensing of Environment*, 87, 23–41.
- Verhoef W., Bach H. (2007). Coupled soil-leaf-canopy and atmosphere radiative transfer modeling to simulate hyperspectral multi-angular surface reflectance and TOA radiance data. *Remote Sensing of Environment*, 109, 166–182.
- Verhoef W., Bach H. (2012). Simulation of Sentinel-3 images by four-stream surface–atmosphere radiative transfer modeling in the optical and thermal domains. *Remote Sensing of Environment*, 120, 197–207, ISSN 0034-4257.
- Verhoef W., van der Tol C.; Middleton E.M. (2018). Hyperspectral radiative transfer modeling to explore the combined retrieval of biophysical parameters and canopy fluorescence from FLEX—Sentinel-3 tandem mission multi-sensor data. *Remote Sensing of Environment*, 204, 942–963.
- Vila-Guerau de Arellan J., Ney P., Hartogensis O., de Boer H, van Diepen K., Emin D., de Groot G., Klosterhalfen A., Langensiepen M., Matveeva M., Miranda G., Moene A., Rascher U., Röckmann T., Adnew G., Brüggemann N., Rothfuss Y. & Graf A. (2020). CloudRoots: integration of advanced instrumental techniques and process modelling of sub-hourly and sub-kilometre land-atmosphere interactions. *Biogeosciences*, 17, 4375-4404.
- von Hebel C., Matveeva M., Verweij E., Rademske P., Kaufmann M. S., Brogi C. Vereecken H., Rascher U. & van der Kruk J. (2018) Understanding soil and plant interaction by combining ground-based quantitative electromagnetic induction and airborne hyperspectral data. *Geophysical Research Letters*, 45, 7571-7579.
- Wang P., Stammes P., van der A R., Pinardi G., and van Roozendaal M. (2008). FRESCO+: an improved O2 A-band cloud retrieval algorithm for tropospheric trace gas retrievals, *Atmos. Chem. Phys.*, 8, 6565–6576.
- Wieneke S., Ahrends H., Damm A., Pinto F., Stadler A., Rossini M. & Rascher U. (2016). Airborne based spectroscopy of red and far-red sun-induced chlorophyll fluorescence: Implications for improved estimates of gross primary productivity. *Remote Sensing of Environment*, 184, 654-667.
- Wieneke S., Burkart A., Cendrero-Mateo M. P., Julitta T., Rossini M., Schickling A., Schmidt M. & Rascher U. (2018). Linking photosynthesis and sun-induced fluorescence at sub-daily to seasonal scales. *Remote Sensing of Environment*, 219, 247-258.
- Wohlfahrt G., Gerdel K., Migliavacca M., Rotenberg E., Tatarinov F., Müller J., Hammerle A., Julitta T., Spielmann F. M., Yakir D. (2018). Sun-induced fluorescence and gross primary productivity during a heat wave. *Scientific Reports*, 8, 2045-2322, doi.org/10.1038/s41598-018-32602-z.
- Wutzler T., Lucas-Moffat A., Migliavacca M., Knauer J., Sickel K., Šigut L., Menzer O., Reichstein M. (2018). Basic and extensible post-processing of eddy covariance flux data with REdDyProc. *Biogeosciences* 15, 5015–5030.
- Wyber R., Osmond B., Ashcroft M. B., Malenovský Z. and Robinson S. A. (2018). Remote monitoring of dynamic canopy photosynthesis with high time resolution light-induced fluorescence transients. *Tree Physiology*, 38(9), 1302-1318.
- Yang P., van der Tol C., Verhoef W., Damm A., Schickling A., Kraska T., Muller O. & Rascher U. (2019). Response of crops to a heat wave: Insights from airborne based reflectance and chlorophyll fluorescence measurement. *Remote Sensing of Environment*, 231, article no. 110996.

 JÜLICH Forschungszentrum	Doc.: Final Report		
	Date: 29 July 2021	Issue: 2	Revision: 1
	Ref.: ESA Contract No. 4000125402/18/NL/NA		Page: 221 / 288

Yang P., van der Tol C., Campbell P. K. E. & Middleton E. M. (2020). Fluorescence Correction Vegetation Index (FCVI): A physically based reflectance index to separate physiological and non-physiological information in far-red sun-induced chlorophyll fluorescence. *Remote Sensing of Environment*, 240, 111676.

10 Data storage and organization

Since a large number of measurements and datasets were collected at the different test sites within the campaign period, we set up a hierarchical data structure to organize the information in a clear manner. This enables a rapid overview of all data collected during the campaign and as well as quick identification of data sets of interest.

In the following, we explain the data storage structure in detail. This is supported by examples from the German test site Klein-Altendorf to provide insight into how the data are organized at the different levels.

The entire data storage structure consists of six levels:

- Level 1 – Campaign
- Level 2 – Country/test site
- Level 3 – Type of data (scale)
- Level 4 – Acquisition date
- Level 5 – Type of device
- Level 6 – Acquired data

Level 1 only consists of the campaign name “FLEXSense”. This will allow the data storage structure to be expanded for future campaigns. In level 2, the different test sites / countries where data was recorded during the campaign are introduced.

- 01_Italy_Coast
- 02_Italy_Grosetto
- 03_France_OHP
- 04_Germany_CKA
- 05_Germany_Selhausen
- 06_Germany_Kermeter
- 07_Spain_Majadas
- 08_Switzerland_Laegeren
- 09_Switzerland_Greifensee

In level 3, each test site is further subdivided into the type of data. In this case, this refers to the different spatial scales of data recording.

- 01_Field_data
- 02_UAV_data
- 03_Airborne_data
- 04_Satellite_data

Field data include all data acquired direct on the ground (e.g. measured plant traits, D-FloX measurements, ASD measurements) or acquired in closer proximity to the ground (e.g. tower measurements).



Figure 177: First three levels of the FLEXSense data storage structure.

In level 4, the different dates are listed when data were measured in the different sites from different scales. In the following level 5, the measurements devices used to collect data from the different scales on the different dates are listed. Figure 178 provides an overview of the measurement dates at the CKA test site in Germany.

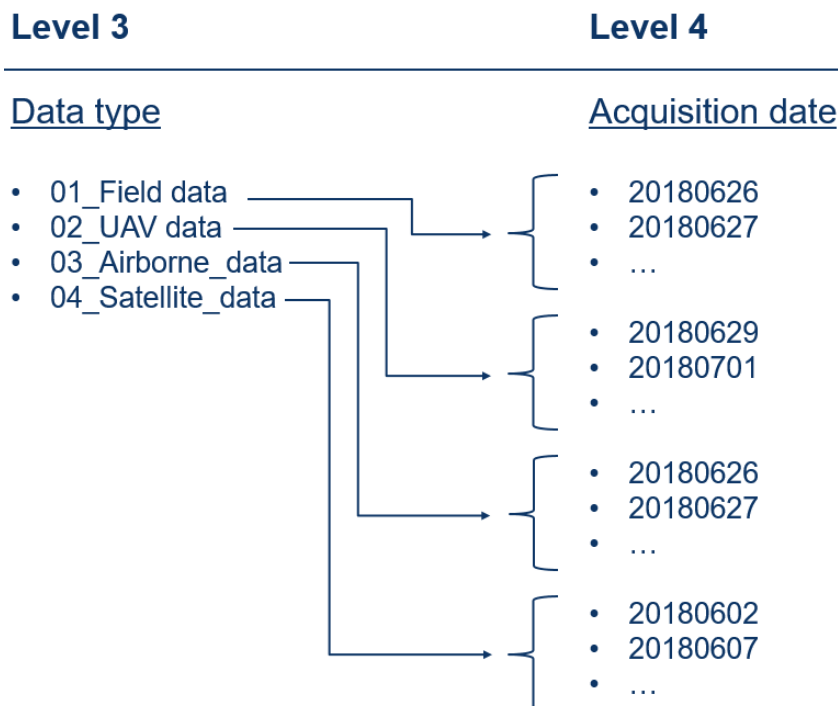


Figure 178: Level 3 and 4 of the FLEXSense data storage structure for the test site CKA.

Subsequently, in the final level 6 the data acquired with the different devices from level 5 are further subdivided into products (the location of real data products), measurement protocols, calibration files and metadata. The organization of the data from level 4 to 6 is illustrated in Figure 179 using one of the D-FloX devices employed at CKA as an example.

Level 4

Level 5

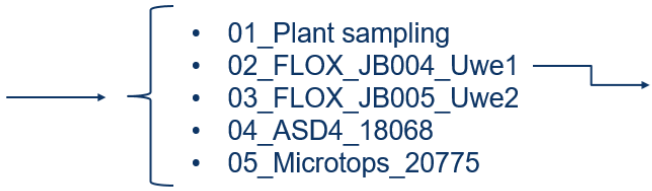
Level 6

Acquisition date

Type of device

Acquired data

- 20180626
- 20180627
- 20180629
- 20180630
- 20180701
- 20180702
- 20180703
- 20180802



- 01_Plant sampling
- 02_FLOX_JB004_Uwe1
- 03_FLOX_JB005_Uwe2
- 04_ASD4_18068
- 05_Microtops_20775

- 01_Products
- 02_Protocols
- 03_Calibration_File
- 04_Metadata

Figure 179: Level 4 to 6 of the FLEXSense data storage structure for the CKA test site using data from one D-FloX device as an example.

	Doc.: Final Report		
	Date: 29 July 2021	Issue: 2	Revision: 1
	Ref.: ESA Contract No. 4000125402/18/NL/NA		Page: 225 / 288

11 Quality Flags

Here, we present the processing reports of two exemplary flight lines. One flight line was chosen as 'high quality' example and was recorded on 2 July 2018, the second flight line was chosen as a 'low quality' example and was recorded on 28 June 2018.

HyPlant FLUO - Processing Report

21-Jun-2021

1 Quick look: At sensor radiance

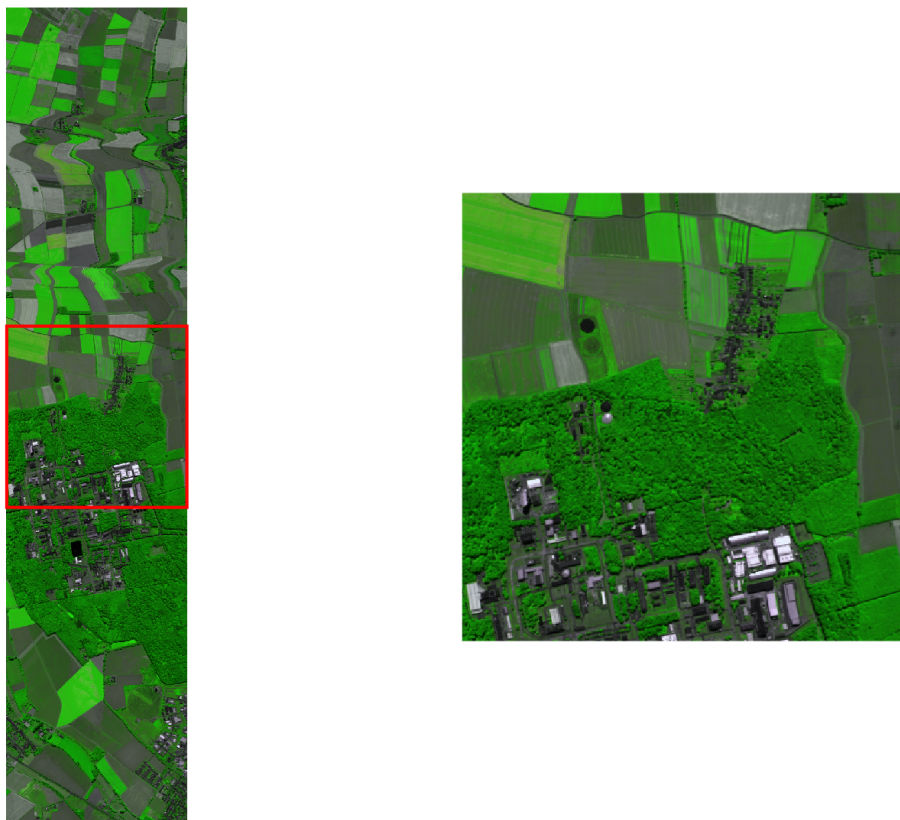


Figure 1: Non-georectified false color composites of the at-sensor radiance.

Table 1: Flight line meta information.

Name	20180702-S3GER-1223-3050-L2-N-FLUO
Acquisition date	02.07.2018
Acquisition time (local time)	12:23
Acquisition time (GMT)	10:26:7
Study site	S3GER
Flight direction	N
Ground sampling distance [m]	4.5

2 Quality Flags

Sun zenith angle (SZA) [°]	31
Cloud cover [%]	0
Mode surface elevation [m]	96
90th Percentile surface elevation [m]	102
10th Percentile surface elevation [m]	83
SNR 680 nm	116
SNR 687 nm	102.3
SNR 750 nm	186.7
SNR 760 nm	73.72

3 Cloud cover

Cloud cover is not provided as the current cloud mask algorithm based on the O2-A absorption features is not operational under clear sky conditions.

4 Actual Signal to Noise Ratio (SNR)

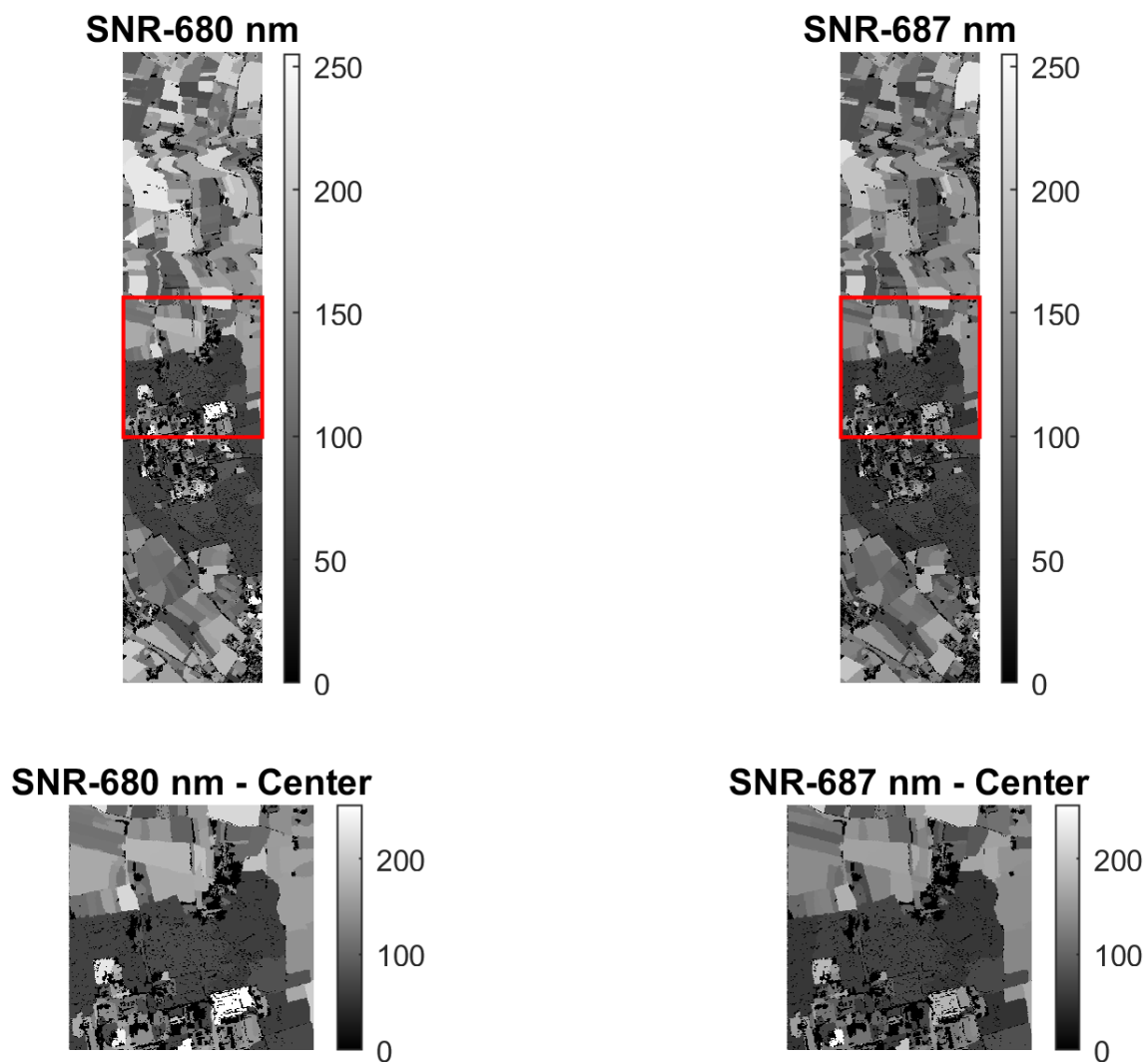


Figure 2: Signal to Noise ratio of bands outside (680 nm) and inside (687 nm) the O2B absorption feature.

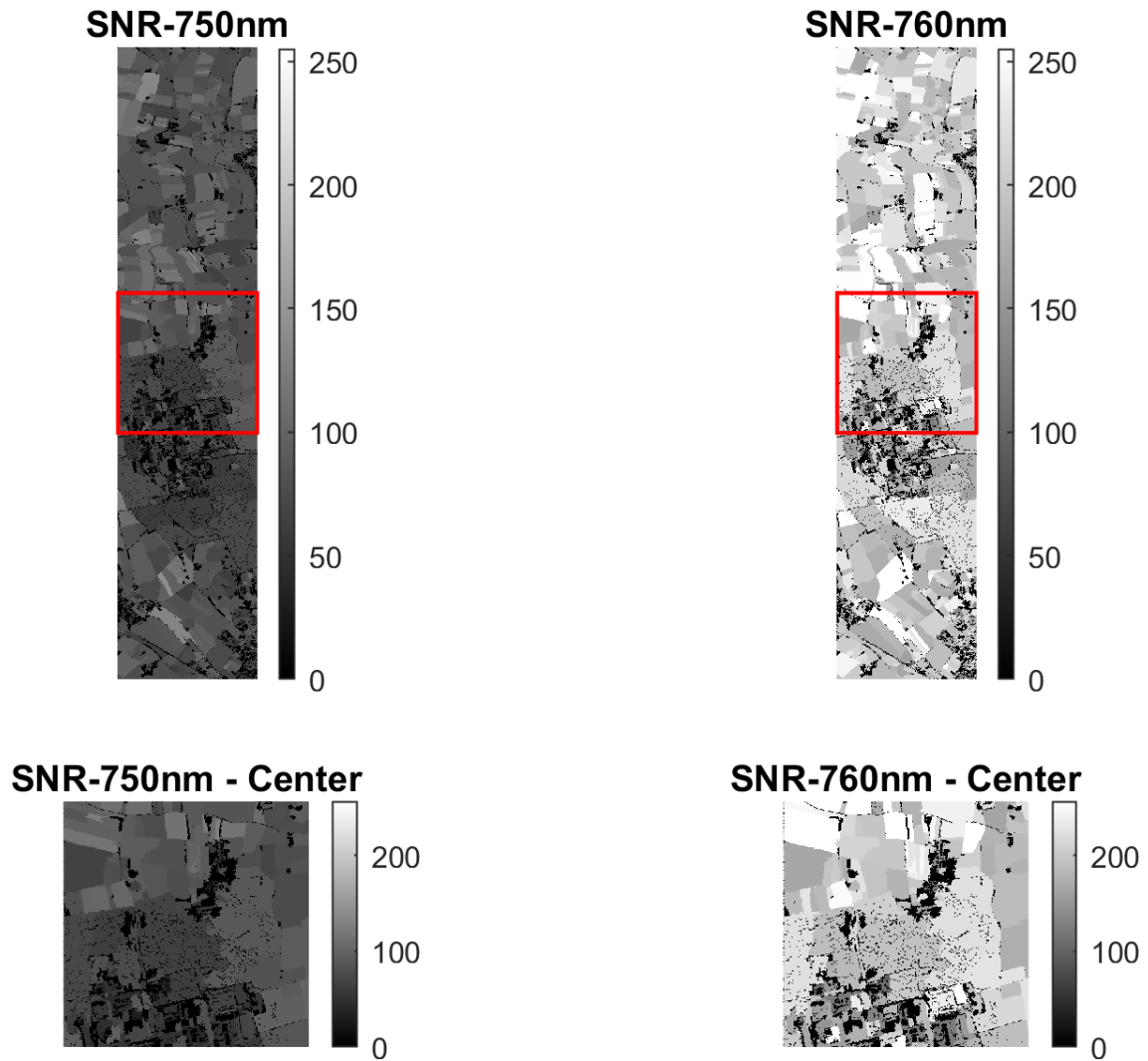


Figure 3: Signal to Noise ratio of bands outside (750 nm) and inside (760 nm) the O2A absorption feature.

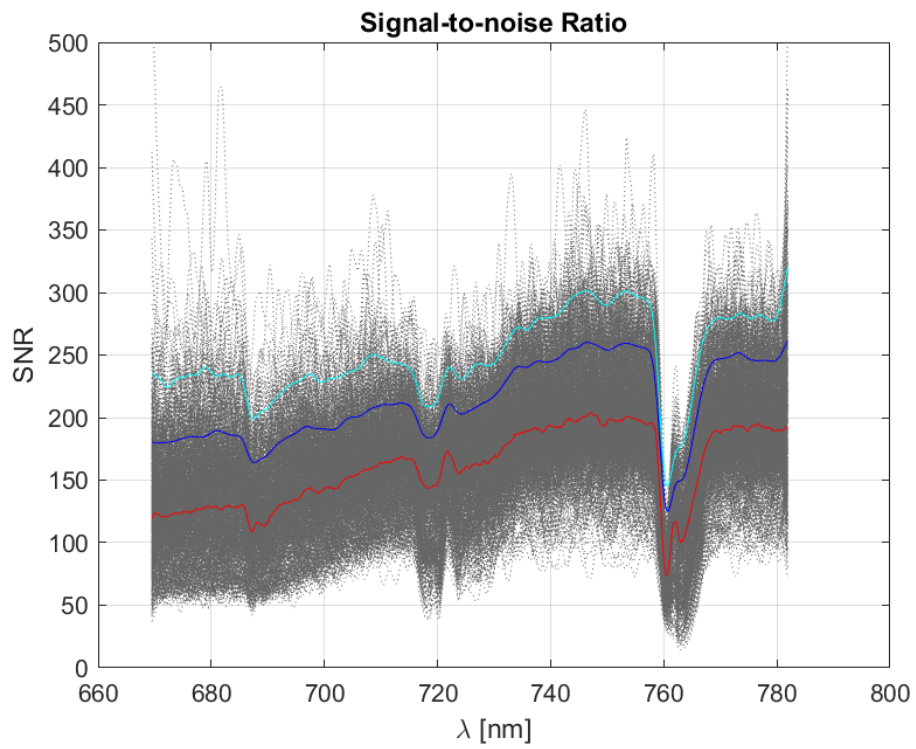


Figure 4: Signal to Noise ratio of flight line with plotted mean (red), 10 percent quantile (blue) and 2 percent quantile (cyan).

5 View Zenith Angle

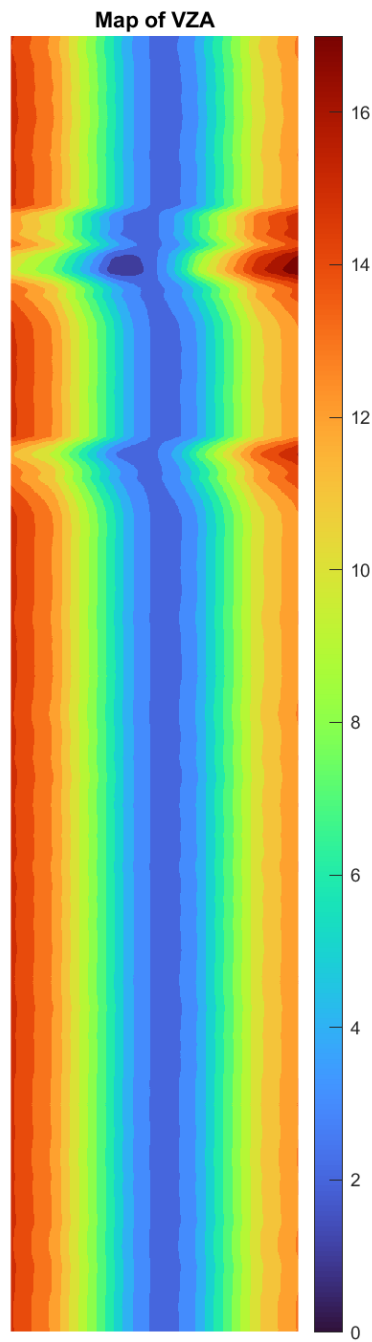


Figure 5: View Zenith Angle of flight line.

6 Elevation

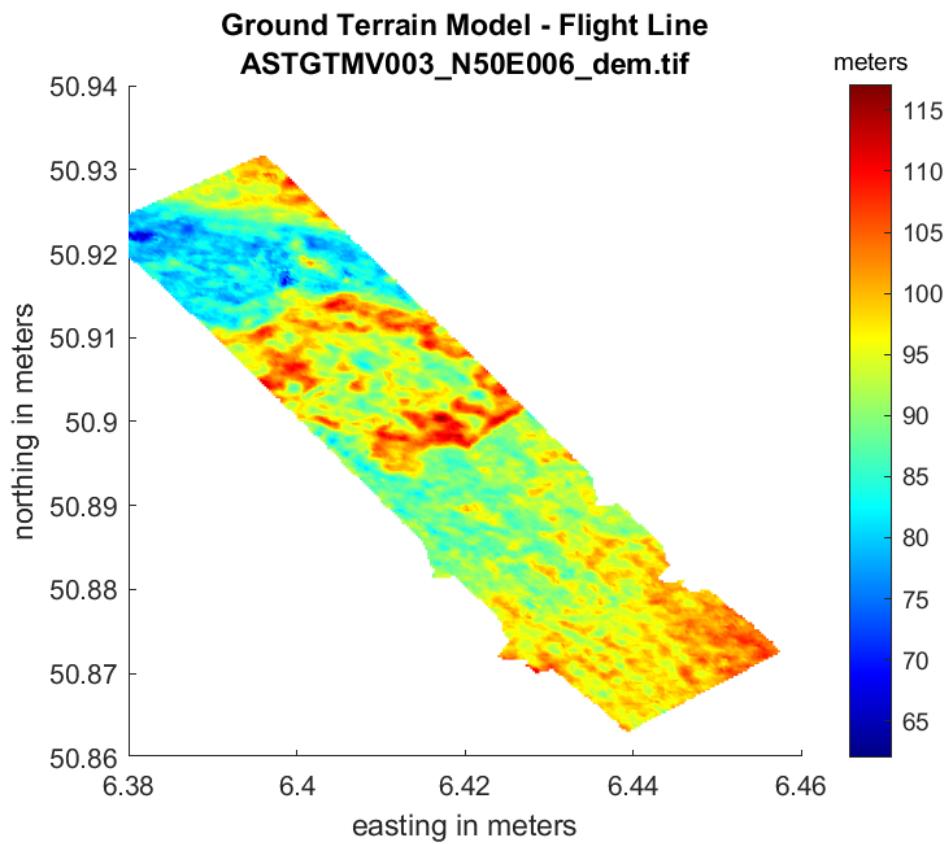


Figure 6: Digital Surface Model of georectified flight line.

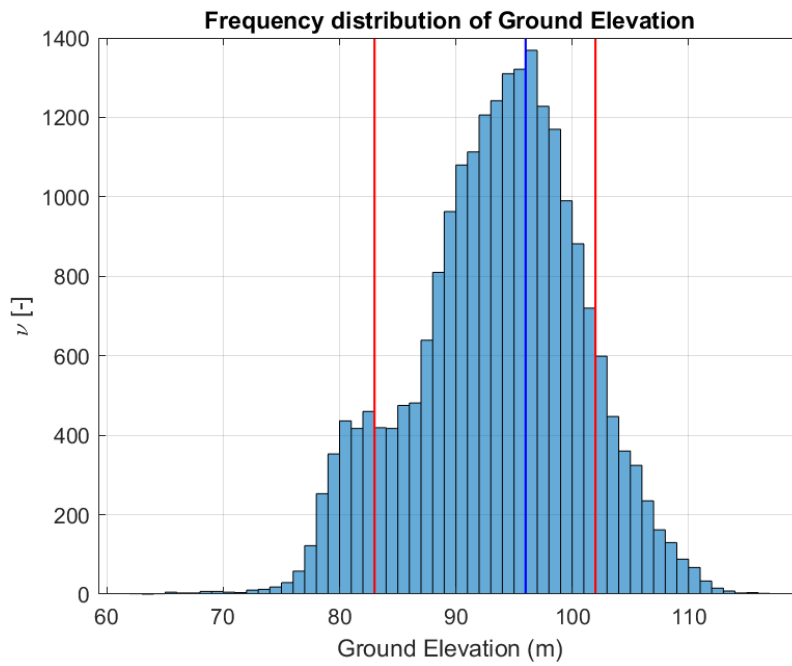


Figure 7: Distribution of elevation. Red lines indicate 10th (83 m) and 90th (102 m) percentile, Blue line shows the mode elevation (96 m) over the flight line.

HyPlant FLUO - Processing Report

21-Jun-2021

1 Quick look: At sensor radiance

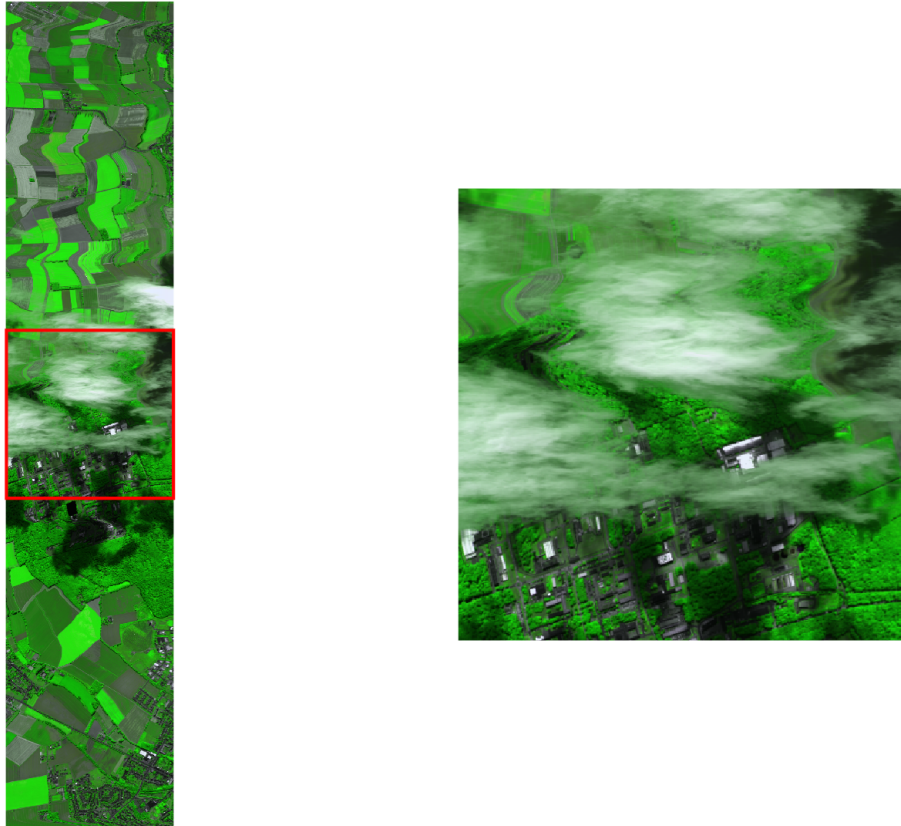


Figure 1: Non-georectified false color composites of the at-sensor radiance.

Table 1: Flight line meta information.

Name	20180628-S3GER-1217-3050-L2-N-FLUO
Acquisition date	28.06.2018
Acquisition time (local time)	12:17
Acquisition time (GMT)	10:19:40
Study site	S3GER
Flight direction	N
Ground sampling distance [m]	4.5

2 Quality Flags

Sun zenith angle (SZA) [°]	31
Cloud cover [%]	14
Mode surface elevation [m]	96
90th Percentile surface elevation [m]	102
10th Percentile surface elevation [m]	83
SNR 680 nm	105.1
SNR 687 nm	90.07
SNR 750 nm	172
SNR 760 nm	69.87

3 Cloud cover

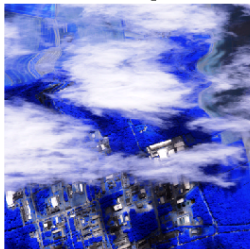
O2-A Band Depth



Cloud Mask



O2-A Band Depth - Center



Cloud Mask - Center

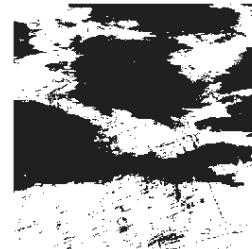


Figure 2: O2-A band depth (left) and cloud cover (right) of flight line. Black areas represent clouds (14 %).

4 Actual Signal to Noise Ratio (SNR)

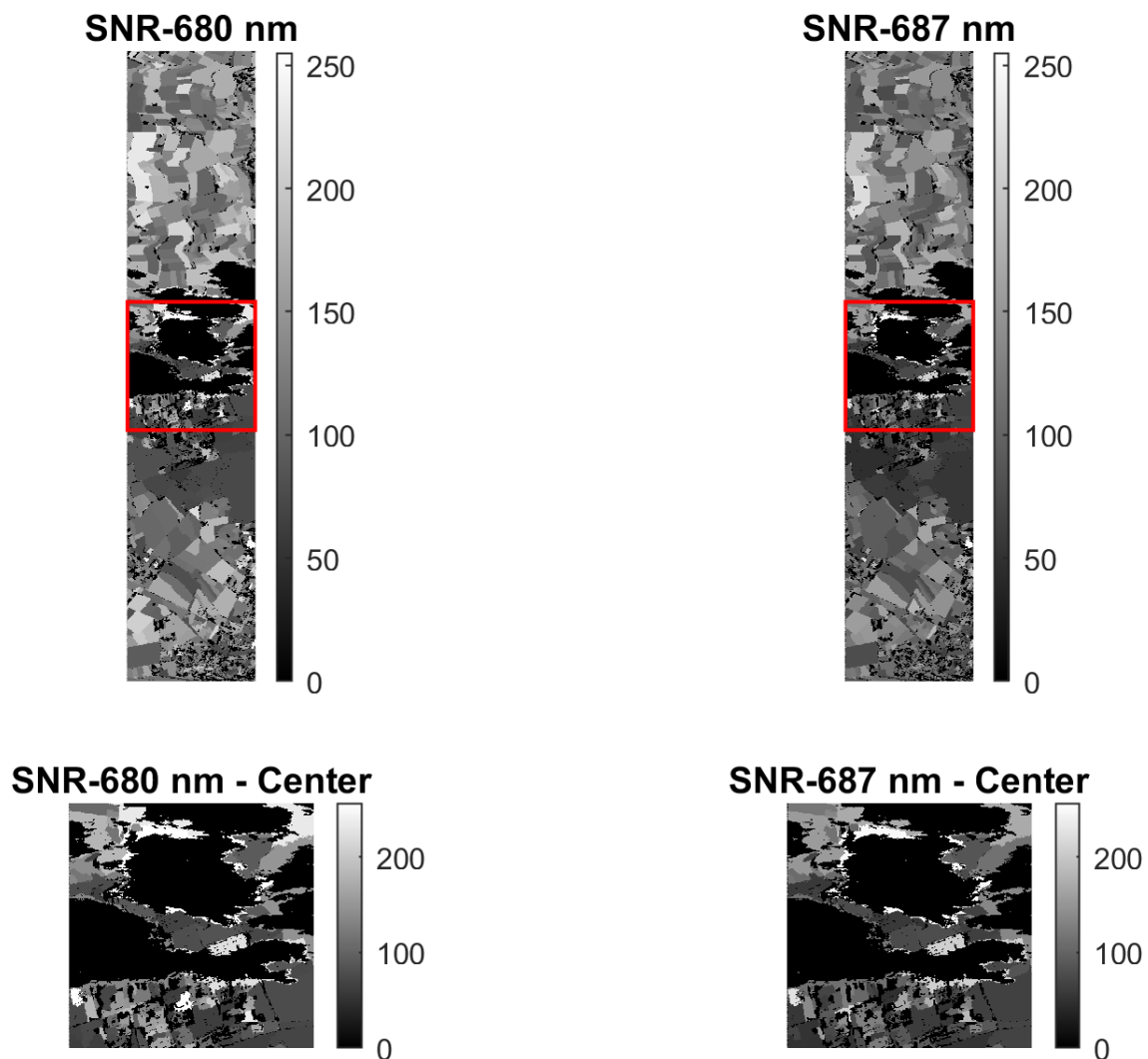


Figure 3: Signal to Noise ratio of bands outside (680 nm) and inside (687 nm) the O2B absorption feature.

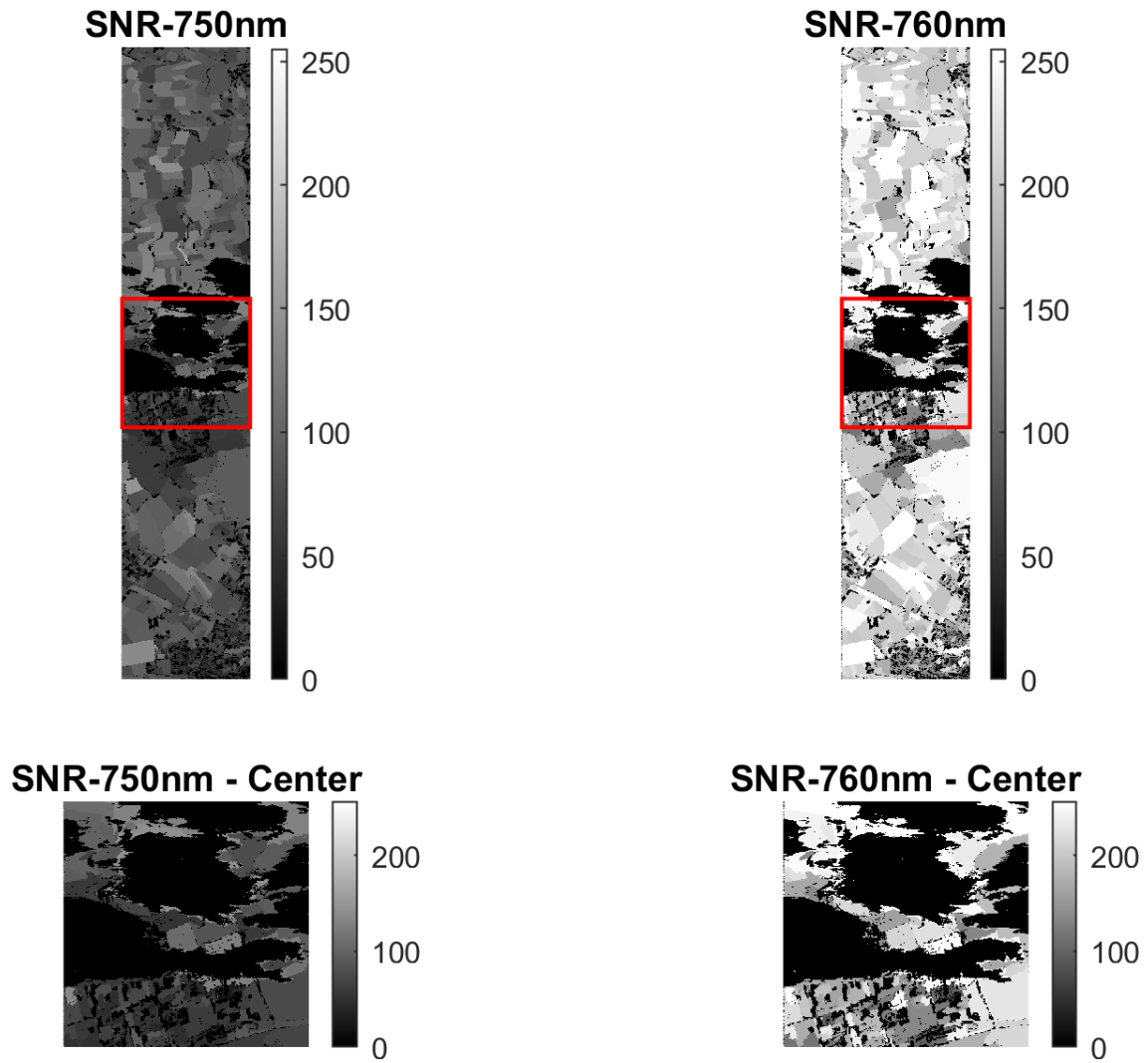


Figure 4: Signal to Noise ratio of bands outside (750 nm) and inside (760 nm) the O2A absorption feature.

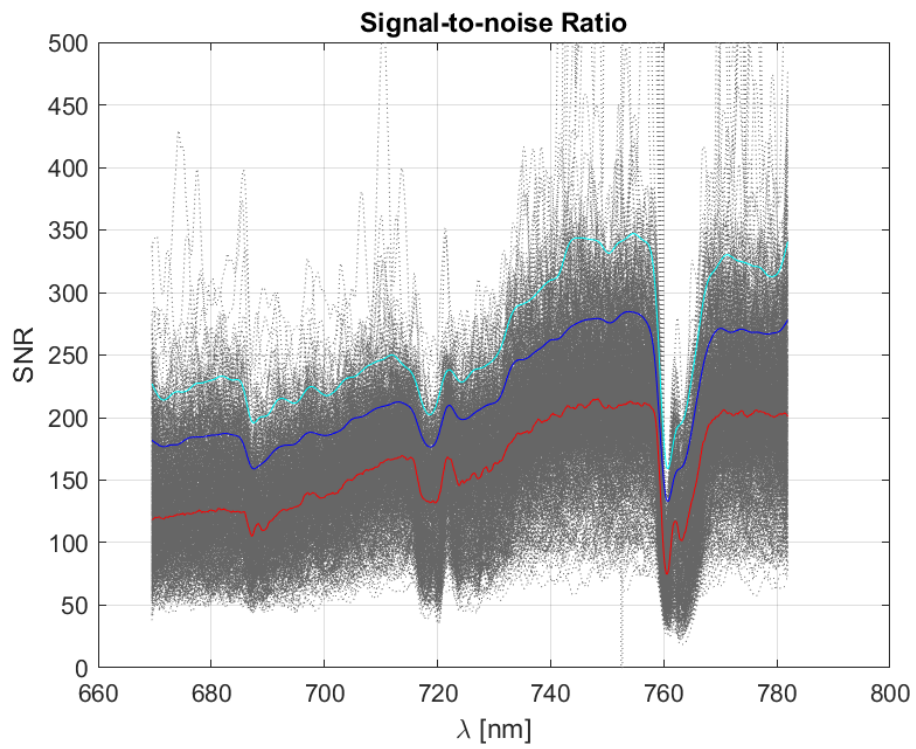


Figure 5: Signal to Noise ratio of flight line with plotted mean (red), 10 percent quantile (blue) and 2 percent quantile (cyan).

5 View Zenith Angle

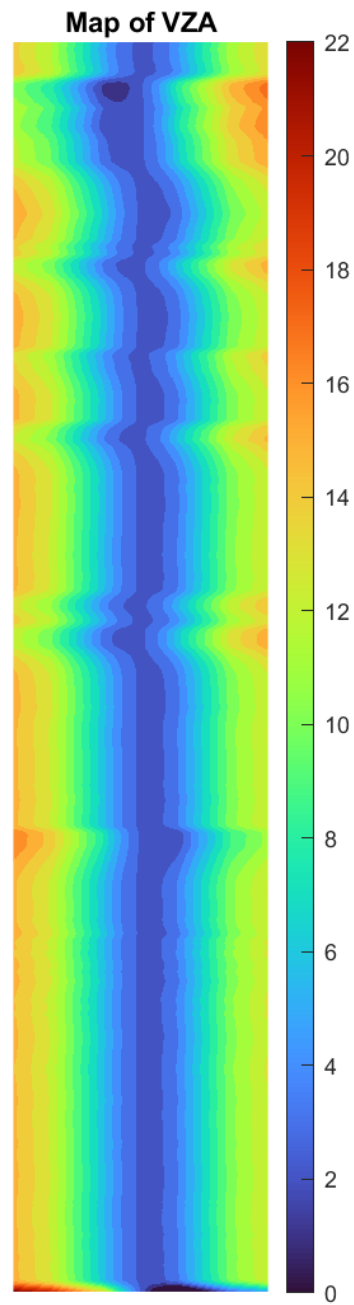


Figure 6: View Zenith Angle of flight line.

6 Elevation

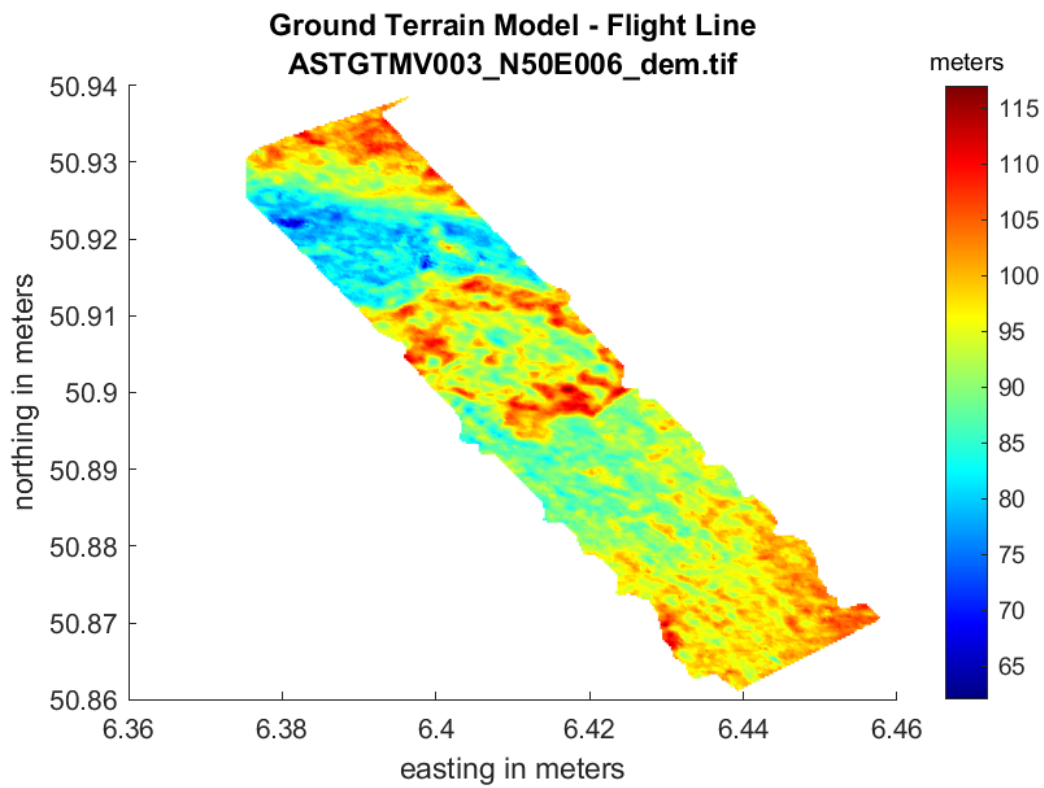


Figure 7: Digital Surface Model of georectified flight line.

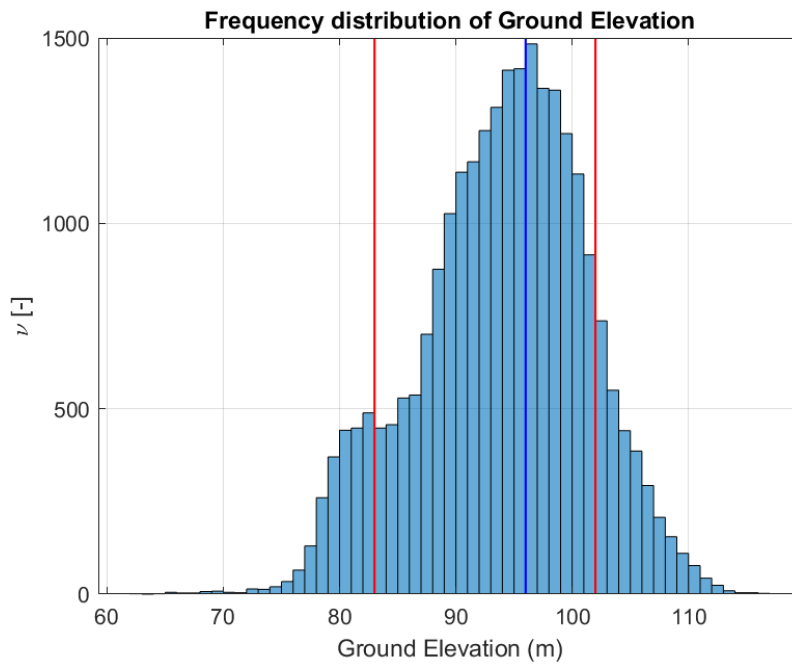


Figure 8: Distribution of elevation. Red lines indicate 10th (83 m) and 90th (102 m) percentile, Blue line shows the mode elevation (96 m) over the flight line.

	Doc.: Final Report		
	Date: 29 July 2021	Issue: 2	Revision: 1
	Ref.: ESA Contract No. 4000125402/18/NL/NA		Page: 243 / 288

12 Scientific publications that resulted from this campaign

Data from this campaign activity have been used in various scientific publications. As this report was submitted, these publications were at different stages of the scientific review process. We agreed with ESA to include scientific publications as annexes to this report whenever possible. As not all publications are available as open access reprints (open access publications with DOI number) at the time this report was submitted, we agreed with ESA on the following approach:

- We provide a short summary of the main findings in the report and reference the scientific publication that is being submitted.
- We provide a placeholder for the publication that does not compromise the scientific review process. In most cases this is a copy of the title page of the scientific publication (as it had been sent for review at the time of submission of this report).
- This placeholder will be replaced with the open access publication after it is available and a DOI is assigned.

	Doc.: Final Report		
	Date: 29 July 2021	Issue: 2	Revision: 1
	Ref.: ESA Contract No. 4000125402/18/NL/NA		Page: 244 / 288

12.1 Publication I: Vila-Guerau de Arellan et al. (2020) - CloudRoots: integration of advanced instrumental techniques and process modelling of sub-hourly and sub-kilometre land-atmosphere interactions

Citation of this publication

Vila-Guerau de Arellan J., Ney P., Hartogensis O., de Boer H, van Diepen K., Emin D., de Groot G., Klosterhalfen A., Langensiepen M., Matveeva M., Miranda G., Moene A., Rascher U., Röckmann T., Adnew G., Brüggemann N., Rothfuss Y. & Graf A. (2020) CloudRoots: integration of advanced instrumental techniques and process modelling of sub-hourly and sub-kilometre land-atmosphere interactions. *Biogeosciences*, 17, 4375-4404, doi: 10.5194/bg-17-4375-2020.

Link to this campaign activities

The CloudRoots field experiment took place in synchrony with the FLEXSense 2018 campaign and was designed to obtain a comprehensive observational dataset that includes soil, plant, and atmospheric variables to investigate the interaction between a heterogeneous land surface and its overlying atmospheric boundary layer at the sub-hourly and subkilometre scale. Our findings demonstrate the need to include measurements at leaf level to better understand the relations between stomatal aperture and ET during the growing season at the diurnal scale.

The data of this publication exploited the rich data set of atmospheric data, soil moisture measurements and airborne remote sensing that took place in summer 2018 in the Selhausen region around Jülich. The teams used the synergy between the CloudRoots and the FLEXSense campaigns and translated the *HyPlant* SIF maps (see section 7.2) to estimates of ecosystem ET (see Fig. 13a and Fig. 14 in the above-mentioned publication).



CloudRoots: integration of advanced instrumental techniques and process modelling of sub-hourly and sub-kilometre land–atmosphere interactions

Jordi Vilà-Guerau de Arellano^{1,2}, Patrizia Ney³, Oscar Hartogensis¹, Hugo de Boer⁴, Kevin van Diepen¹, Dzhaner Emin⁵, Geiske de Groot¹, Anne Klosterhalfen⁶, Matthias Langensiepen⁷, Maria Matveeva⁵, Gabriela Miranda-García¹, Arnold F. Moene¹, Uwe Rascher⁵, Thomas Röckmann⁸, Getachew Adnew⁸, Nicolas Brüggemann³, Youri Rothfuss³, and Alexander Graf³

¹Meteorology and Air Quality Section, Wageningen University Research, 6708 PB Wageningen, the Netherlands

²Atmospheric Chemistry Department, Max Planck Institute for Chemistry, 55128 Mainz, Germany

³Institute of Bio- and Geosciences, IBG-3: Agrosphere, Forschungszentrum Jülich GmbH, 52425 Jülich, Germany

⁴Department of Environmental Sciences, Faculty of Geosciences, Utrecht University, 3508 TA Utrecht, the Netherlands

⁵Institute of Bio- and Geosciences, IBG-2: Plant Sciences Forschungszentrum Jülich GmbH, 52425 Jülich, Germany

⁶Department of Forest Ecology & Management, Swedish University of Agricultural Sciences, 90183 Umeå, Sweden

⁷Faculty of Agriculture, University of Bonn, 53115 Bonn, Germany

⁸Institute of Marine and Atmospheric Research Utrecht University, 3584 CC Utrecht, the Netherlands

Correspondence: Jordi Vilà-Guerau de Arellano (jordi.vila@wur.nl)

Received: 17 April 2020 – Discussion started: 6 May 2020

Revised: 15 July 2020 – Accepted: 20 July 2020 – Published: 31 August 2020

Abstract. The CloudRoots field experiment was designed to obtain a comprehensive observational dataset that includes soil, plant, and atmospheric variables to investigate the interaction between a heterogeneous land surface and its overlying atmospheric boundary layer at the sub-hourly and sub-kilometre scale. Our findings demonstrate the need to include measurements at leaf level to better understand the relations between stomatal aperture and evapotranspiration (ET) during the growing season at the diurnal scale. Based on these observations, we obtain accurate parameters for the mechanistic representation of photosynthesis and stomatal aperture. Once the new parameters are implemented, the model reproduces the stomatal leaf conductance and the leaf-level photosynthesis satisfactorily. At the canopy scale, we find a consistent diurnal pattern on the contributions of plant transpiration and soil evaporation using different measurement techniques. From highly resolved vertical profile measurements of carbon dioxide (CO₂) and other state variables, we infer a profile of the CO₂ assimilation in the canopy with non-linear variations with height. Observations taken with a laser scintillometer allow us to quantify the non-steadiness of the surface

turbulent fluxes during the rapid changes driven by perturbation of photosynthetically active radiation by cloud flecks. More specifically, we find 2 min delays between the cloud radiation perturbation and ET. To study the relevance of advection and surface heterogeneity for the land–atmosphere interaction, we employ a coupled surface–atmospheric conceptual model that integrates the surface and upper-air observations made at different scales from leaf to the landscape. At the landscape scale, we calculate a composite sensible heat flux by weighting measured fluxes with two different land use categories, which is consistent with the diurnal evolution of the boundary layer depth. Using sun-induced fluorescence measurements, we also quantify the spatial variability of ET and find large variations at the sub-kilometre scale around the CloudRoots site. Our study shows that throughout the entire growing season, the wide variations in stomatal opening and photosynthesis lead to large diurnal variations of plant transpiration at the leaf, plant, canopy, and landscape scales. Integrating different advanced instrumental techniques with modelling also enables us to determine variations of ET that

depend on the scale where the measurement were taken and on the plant growing stage.

1 Introduction

Evapotranspiration (ET), the net exchange of water vapour between the land and the atmosphere, remains an elusive process to be measured, quantified, and represented in models because it depends on the interaction of multiple processes that act in a wide range of scales (Katul et al., 2012). ET is a key variable in the exchange of heat, moisture, and carbon dioxide at the surface, and it strongly depends on how radiation and energy are partitioned into latent and sensible heat (Moene and Dam, 2014; Monson and Baldocchi, 2014). The amounts of direct and diffuse radiation reaching the leaves depend on the transfer of radiation that is strongly perturbed by clouds and aerosols and on its subsequent penetration into the canopy. Triggered by ambient light conditions, the stomatal responses coupled to the surface and boundary layer dynamics is the main driver that regulates how the net available radiative energy is partitioned between the turbulent sensible and latent heat fluxes (van Heerwaarden and Teuling, 2014). However, due to the highly non-stationary nature of atmospheric radiation (van Kesteren et al., 2013b) and turbulent nature of the meteorological fluctuations, we still lack a fundamental understanding of the two-way feedback between stomatal control and cloud radiation perturbations across scales and land and atmosphere conditions (Katul et al., 2012; Sikma et al., 2018).

The bidirectional link between surface processes and boundary layer clouds as described above is what we refer to as the CloudRoots concept, where boundary layer dynamics and clouds are rooted in or coupled to the surface and vice versa (Vilà-Guerau de Arellano et al., 2014). The degree of coupling depends on soil, plant, and weather conditions characterized by the diurnal variability of wind, temperature, and specific humidity (Sikma et al., 2018). To fully comprehend this system requires inclusion of all necessary parameters at the required spatial scales, from the size of the stomata (10–100 μm) to the depth of the boundary layer and cloud top (~ 3 km), as well as temporal scales from seconds to daily and seasonal cycles and across disciplines, bringing together experts from diverse fields from ecophysiology to turbulence. This can only be obtained by integrating experimental and modelling efforts. Here we describe and show the first results of the CloudRoots field experiment aimed at obtaining new understanding about the interaction between the soil, vegetation, and the clear–cloudy boundary layers at these sub-hourly and sub-kilometre scales, i.e. on spatio-temporal scales smaller than the characteristic grid resolution scales of the weather (typical resolution ranging from 1 to 10 km) and climate (typical resolution ranging from 20 to 100 km) models. In that respect, the CloudRoots field campaign continues

the tradition of experiments that connect land surface properties with boundary layer dynamics but now instead by using advanced instrumental techniques and by modelling the coupling between the essential processes. Two examples of such previous campaigns are the First ISLSCP Field Experiment (FIFE) (Hall et al., 1989) and the Boreal Ecosystem–Atmosphere Study (BOREAS) (Sellers et al., 1995).

Thanks to their high-quality routine measurement programme (Franz et al., 2018; Rebmann et al., 2018), ICOS sites lend themselves as anchors for additional experiments. Here, we describe the CloudRoots campaign near the agricultural site “Selhausen” (ICOS site DE-RuS) and the Jülich Observatory for Cloud Evolution – Core Facility (JOYCE, <http://joyce.cloud>, last access: 21 August 2020) in Germany during spring 2018 (Löhnert et al., 2015). In order to quantify all the necessary scales of interest (leaf, canopy, and landscape), we complemented the existing radiation, flux, and soil measurements of the ICOS site by scintillometry, microlysimeters, sap flow and leaf-level flux measurements, quasi-instantaneous vertical profiles, and spectroscopic measurements of vegetation indices and sun-induced fluorescence (SIF). Scintillometers provided minute-scale turbulent fluxes enabling us to connect stomatal responses to the energy, moisture and carbon dioxide (CO_2) fluxes at this timescale. Microlysimeters, soil flux chambers, sap flow, leaf-level chambers, and canopy-resolving profiles all have the ability to distinguish vegetation from soil CO_2 and water vapour (H_2O) fluxes in contrast to the eddy covariance technique that provided net fluxes from the two sources combined. The remote sensing measurements of boundary layer dynamic evolution and cloud properties made at JOYCE provided evidence on diurnal variations of the boundary layer depth, the role of entrainment, and cloud diurnal variability. A key aspect of the research strategy of CloudRoots is the integration of all these measurements in a land–atmosphere conceptual model CLASS (Vilà-Guerau de Arellano et al., 2015). This model has been specially developed to support the interpretation of measurements at the sub-hourly scales (Vilà-Guerau de Arellano et al., 2019).

To this end, we study the following five facets of the diurnal interactions between the land and the atmosphere: (i) observational validation at leaf level of the mechanistic model representation of the stomatal aperture and photosynthesis, (ii) the diurnal variability of H_2O – CO_2 flux partition due to the soil and plant contributions at the canopy level, (iii) the non-steadiness of these fluxes due to the influence of clouds, (iv) the spatial heterogeneity of ET inferred from the SIF measurements, and (v) the integration of the observations in the conceptual model CLASS to quantify the influence of land–surface heterogeneity and advection. We finally obtain a daily estimation of ET and discuss differences with respect to the observational or modelling techniques.

The paper is organized as follows. In Sect. 2 we give a detailed overview of the field experiment with special emphasis on the instrumentation used that serve the overall

goals of our CloudRoots concept. The results in Sect. 3 are organized into the five topics outlined below. First, at leaf level, we validate a photosynthesis–conductance mechanistic model that is commonly used in large-eddy simulations (Pedruzo-Bagazgoitia et al., 2017; Sikma et al., 2018) and the global numerical model prediction system ECMWF-IFS (Boussetta et al., 2013). This allows us to assess the need to revisit currently used constants in the mechanistic model representing photosynthesis. This part is completed by comparing leaf transpiration rate with tiller-level measurements of sap flow at different stages of the growing season. Second, and in order to scale up to the canopy level, we analyse the soil and plant partitioning of the net ET and net ecosystem exchange (NEE) based on the inversion of observed high-resolution vertical concentration profiles (Warland and Thurtell, 2000; Santos et al., 2011). Third, in analysing the impact of clouds on ET, we measure the potential effectiveness of diffuse radiation in enhancing ET and NEE (Kanniah et al., 2012). Extending previous work by van Keesteren et al. (2013b), we quantify the time lag between fluctuations in incoming shortwave radiation and ET in the field. These real-world measurements are an essential addition to time lag of plant responses to radiation changes studied in laboratory experiments (Vico et al., 2011). Fourth, we infer the spatial variability of ET around the CloudRoots site using SIF remote sensing observations. Fifth, all of these observations are then integrated into several numerical experiments made by CLASS with special emphasis on the treatment and role of how to include surface heterogeneity and heat and moisture advection to improve the interpretation of the observations. Finally, in the discussion in Sect. 4 we bring together and discuss all CloudRoots methodologies by comparing their daily ET estimates. Conclusions are given in Sect. 5.

2 Description of the CloudRoots field experiment and modelling effort

2.1 Site description

The CloudRoots field campaign was carried out at the Terrestrial Environmental Observatory (TERENO) Selhausen, which is located in the southern part of the lower Rhine embayment in western Germany (50°52′09″ N, 6°27′01″ E, 104.5 m altitude) in a region largely dominated by agriculture (Fig. 1). In 2011, the site was equipped with micrometeorological measurement devices for long-term monitoring of energy and carbon exchange. Since 2015, the station has been extended in accordance with ICOS standards for Level 1 sites (ICOS site code DE-RuS) (Ney et al., 2020). For this campaign, a further IRGASON eddy covariance (EC) system with an open-path gas analyser (see Sect. 2.3.7) was placed on the test field and used for additional flux measurements presented here.

The test field covered 9.8 ha and was surrounded by other croplands (Ney and Graf, 2018). As Fig. 1 shows, these cultivated areas are mainly comprised of winter wheat, winter barley, sugar beet, rapeseed, maize, potatoes, and peas, whereby the various field sizes and locations of crops has led to small-scale heterogeneity in the vegetation cover. An agricultural road, mainly used by farm machinery, passes by the northern edge of the field. The next inhabited settlement is located 500 m to the west (Fig. 1a). There are two lignite open-cast mines in the wider surrounding of the study site, located 6 km northeast (extension of 4400 ha with a maximum depth of 470 m b.g.l.) and 6 km west (extension of 1400 ha with a maximum depth of 200 m b.g.l.). In general, the land surface at the study site is flat and has a slope less than 4°. A loess layer with a thickness of about 1 m covers Quaternary sediments, which were mainly built up from fluvial deposits of the Rur river system. The overlying soil is an Orthic Luvisol according to the USDA classification (IUSS Working Group WRB, 2006), whose texture is silt loam with a mixture of 20 % clay, 67 % silt, and 13 % sand.

The local climate is classified as temperate maritime with an annual mean air temperature of 10.3 °C and an annual mean precipitation of 718 mm (reference period 1981–2010, with data taken from the DWD climate station of the Forschungszentrum Jülich 5.3 km from the test site). The observation period from the beginning of May until the end of June 2018 was characterized by a 2.9 °C higher mean air temperature (17.5 °C) and 46 % less precipitation in comparison to the long-term average. Figure 1b shows the heterogeneity quantified by the sensible heat fluxes measured at the CloudRoots site and a bare soil field nearby. In consequence and as shown by Fig. 1c, in CloudRoots we aim to integrate horizontal and vertical scales in the analysis of ET and its relation to boundary layer dynamics.

The field campaign covered the main growing phases (booting, heading, and maturity stages) of winter wheat. During the observation period, we did three intensive observation periods (IOP). During these IOPs the following complementary instruments and measurements were added: microlysimeters, leaf-level measurements, SIF measurements on canopy and regional scale, and vertical profiles of state variables and CO₂ within and above the canopy were performed. Figure 2 shows a timeline of the deployment of the campaign-specific measurement setup (see Sect. 2.2 and 2.3) that includes the IOPs on 7 May (IOP 1), 15 June (IOP 2), and 28 June 2018 (IOP 3). The main meteorological and biometric conditions are summarized in Table 1. The test field was cultivated with a crop rotation cycle typical of the region (Ney et al., 2020). The rotation prior to the observation period was beet, potatoes, and winter wheat (catch-crop) and sugar beet. Residues of the harvest of sugar beet were left on the site and ploughed in before the cultivation cycle started with the sowing of winter wheat (*Triticum aestivum* L.; variety Premio) in October 2017. The field was fertilized with mineral nitrogen (N) once in March, April, and May

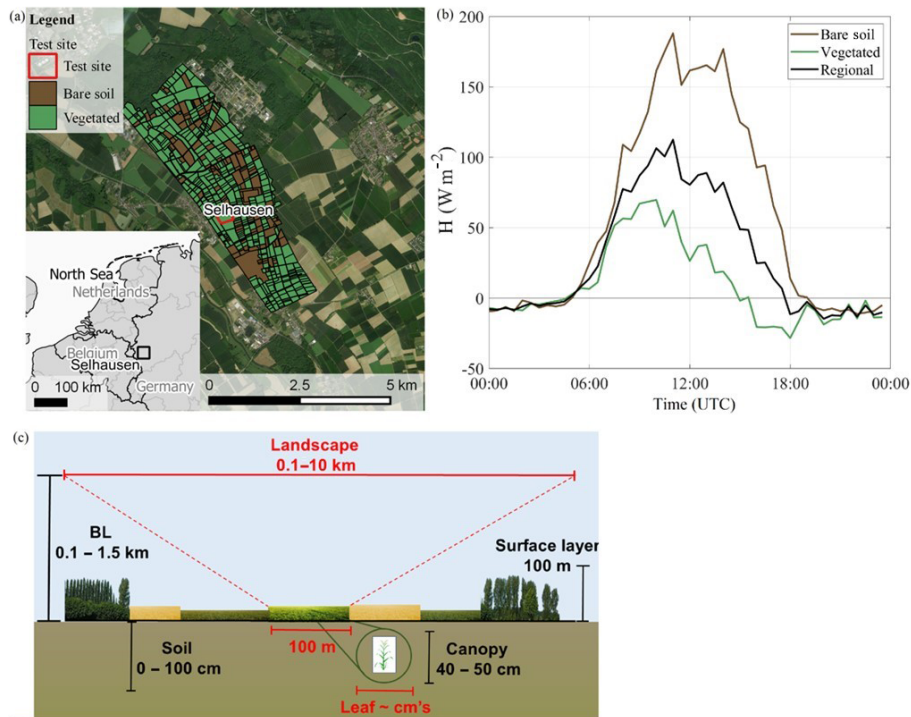


Figure 1. (a) Aerial view (Bing Maps, © 2019 Microsoft Corporation © 2019 DigitalGlobe © CNES (2019) Distribution Airbus DS) of the observation area. The ICOS Selhausen test site is located in the middle of the 10×10 km map section. The surrounding agricultural area was classified into the categories bare soil (including “late crops” following Table 3) and vegetated (“early crops”, forest and grassland following Table 3) during the IOP 1. (b) Corresponding sensible heat flux (H) during IOP 1, whereby H of bare soil and vegetated area were measured and the regional average was estimated as weighted average (60 % and 40 % for vegetated and bare soil, respectively). (c) Schematic sketch of horizontal (red) and vertical (black) length scales influencing the measurements. The larger indicated horizontal and vertical scales indicate the spatial scales of boundary layer dynamics. Horizontally, the 100 m scale is the size of the field hosting the ICOS test site.

2018 (81.6, 39.2, and 50 kg N ha^{-1} , respectively). The wheat was harvested on 17 July 2018 with a yield of 92 dt ha^{-1} . A detailed overview of the field management practices before, during, and after the campaign is given in the Appendix (Table A1).

2.2 Weather and crop description during the IOPs

The weather situation during all three IOPs was mainly characterized by an anticyclonic pressure pattern over central Europe (IOP 1 and IOP 2), extending up to northern Europe during IOP 3, which led to high 2 m temperatures up to 24 to 26°C during IOP 1 and IOP 2 and 28°C during IOP 3 (Table 1). Cloudiness and temperature inversion heights at the top of the atmospheric boundary layer were different. While weak subsidence motions during IOP 1 led to a slightly rising temperature inversion layer between 1200 and 2000 m above ground level (a.g.l.) with clear conditions during the whole period (mean daytime global radiation $S \downarrow$ of 514 W m^{-2}), a weak cold front passed the measuring site from the northwest in the early morning of IOP 2 (mean daytime $S \downarrow$ of 311 W m^{-2}). Diurnal heating caused the replacement of a layer of stratocumulus at a height of 1800 m a.g.l.

in the morning, followed by the appearance of scattered towering cumulus clouds. Light showers occurred only in the vicinity of the site. During IOP 3, a few shallow cumulus and cirrus clouds appeared, despite the existence of a small upper-air low that passed the area around the edge of a larger cut-off, although it was located above southeastern Europe. The mixed boundary layer was topped at a height of around 1700 m a.g.l.

The persistent high-pressure weather conditions resulted in a drought during the entire observation period. Ongoing dryness led to a reduction in the soil water content at 20 cm depth (Table 1) from 27 vol % during IOP 1 to 15 vol % at IOP 3. Maturity occurred 14 d earlier than in previous years. The leaf area index (LAI) ranged from $4.5 \text{ m}^2 \text{ m}^{-2}$ (green growing stage) in IOP 1 to $5.5 \text{ m}^2 \text{ m}^{-2}$ in IOP 2 (green/yellow ripening stage). No changes in LAI were observed between IOP 2 and IOP 3 (yellow senescence stage).

2.3 Instrument description

Table 2 summarizes all the variables measured and modelled during CloudRoots, together with specific nomenclature and information on units and scales.

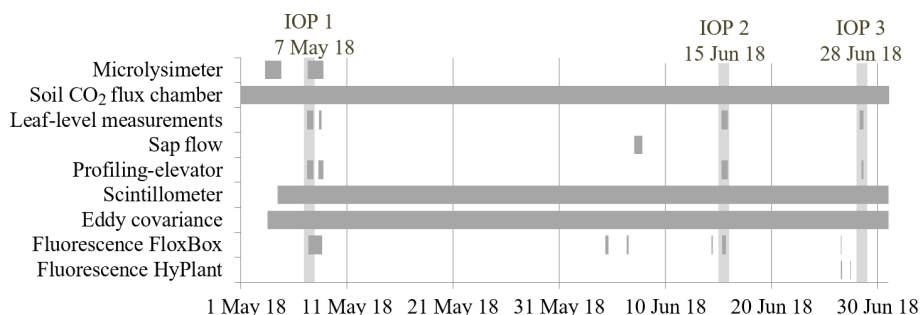


Figure 2. Campaign-specific measurement setup and temporal developments from May to June 2018, including three intensive operation periods (IOP).

Table 1. Meteorological and biometric conditions during the intensive operation periods on 7 May (IOP 1), 15 June (IOP 2), and 28 June 2018 (IOP 3). Global radiation, water vapour–pressure deficit (VPD), photosynthetically active radiation (PAR), and soil water content (SWC) are daily averages. The meteorological variables were measured at the height 2.4 ± 0.1 m (see Sect. 2.3.7 for details).

	IOP 1	IOP 2	IOP 3
Meteorological conditions			
Cloud cover (okta; full cloud cover: 8)	0–1	3–6	0–4
Temperature range (°C)	7.0–25.4	13.2–23.9	10.1–27.6
Wind range (m s ⁻¹)	0.1–2.1	0.06–1.5	0.2–3.3
Global radiation* (W m ⁻²)	514	311	462
Biometric conditions			
Canopy height (m)	0.45	0.80	0.78
LAI (m ² m ⁻²)	4.5	5.5	5.5
VPD / VPD _{max} (hPa)	11.7/20.9	7.6/14.9	16.0/23.6
PAR* (μmol m ⁻² s ⁻¹)	768	475	741
SWC 5, 20, 50 cm (vol %)	0.20/0.27/0.30	0.17/0.19/0.22	0.12/0.15/0.21

* Daily averages calculated from sunrise to sunset.

2.3.1 Microlysimeters

For direct measurements of soil evaporation (E_{lys}), four microlysimeters were installed at a number of locations around the EC-station (one in each cardinal direction) at the beginning of every observation period. In order to obtain an undisturbed soil monolith for each microlysimeter, an SDR-35 polyvinyl chloride (PVC) collar with an inner diameter of 0.2 m, a wall thickness of 0.005 m, and a depth of 0.11 m was pushed carefully into the ground. Afterwards the collar including the soil column was retrieved, its outside was cleaned, and the bottom of each lysimeter was sealed with an acrylic glass disc, which prevented percolation and capillary rise from or into the microlysimeter. The microlysimeters were then weighed initially and returned to their original positions. We made sure that the lysimeters were levelled with the soil surface, their walls were fully surrounded by soil, and that the crop was affected and destroyed as little as possible, so that the general conditions and characteristics of the field site could still be maintained (e.g., regarding heat flux, shading). All four microlysimeters were subsequently

collected, cleaned, weighed, and distributed again every 60 or 90 min. A scale with a precision of 0.1 g (equivalent to 0.00318 mm evaporation) was used. The scale was enclosed in a box to avoid wind effects during the measurements. Finally, the measured weight differences were converted to the standard units of the surface energy balance (W m⁻²) by means of the lysimeters surface area, the time periods between weighing, and the latent heat of vaporization (Quade et al., 2019).

2.3.2 Soil CO₂ flux chambers

Soil respiration (R_s) was observed with an automated soil CO₂ gas flux system (Li-8100, Li-Cor Inc. Biosciences, Lincoln, Nebraska, USA), connected to four long-term soil flux chambers. The chambers were installed close to the EC-station (one in each cardinal direction) on top of PVC soil collars with a diameter of 0.2 m and a total height of 0.07 m, from which 0.05 m was inserted into the soil. Each chamber was closed at 30 min intervals for 90 s during flux measurements, while CO₂, water vapour concentration, and cham-

Table 2. List of symbols, description, units, and the representative scale.

Symbol	Description	Unit	Scale represented
A	photosynthesis rate	$\mu\text{mol m}^{-2} \text{s}^{-1}$, $\text{mg m}^{-2} \text{s}^{-1}$	landscape
A_{leaf}	leaf-level photosynthesis rate	$\mu\text{mol m}^{-2} \text{s}^{-1}$, $\text{mg m}^{-2} \text{s}^{-1}$	leaf
A_{m}	maximum light-saturated photosynthesis	$\mu\text{mol m}^{-2} \text{s}^{-1}$, $\text{mg m}^{-2} \text{s}^{-1}$	landscape
$A_{\text{m,max298}}$	maximum leaf-level photosynthesis rate	$\mu\text{mol m}^{-2} \text{s}^{-1}$, $\text{mg m}^{-2} \text{s}^{-1}$	leaf
E	evaporation	mm , W m^{-2}	several
E_{lysi}	evaporation from microlysimeters	W m^{-2}	landscape
E_{p}	evaporation profile based	W m^{-2}	leaf
E_{sap}	sap flow	$\mu\text{mol tiller}^{-2} \text{s}^{-1}$	leaf
ET	evapotranspiration	mm , W m^{-2}	several
ET _{ec}	evapotranspiration eddy-covariance	W m^{-2}	canopy
g_{sw}	stomatal conductance of water vapour	$\text{mol m}^{-2} \text{s}^{-1}$	leaf
$S \downarrow$	global radiation	W m^{-2}	landscape
h	height	m	boundary layer
h_{c}	landscape	m	canopy
L	Obukove lenght	m	canopy
$L_{\text{v}}E$	latent heat flux	W m^{-2}	several
LAD	leaf area density	$\text{m}^2 \text{m}^{-3}$	canopy
LAI	leaf area index	$\text{m}^2 \text{m}^{-2}$	canopy
NEE	net ecosystem exchange	$\mu\text{mol m}^{-2} \text{s}^{-1}$, $\text{mg m}^{-2} \text{s}^{-1}$	canopy
NEE _{ec}	net ecosystem exchange eddy covariance	$\mu\text{mol m}^{-2} \text{s}^{-1}$, $\text{mg m}^{-2} \text{s}^{-1}$	canopy
NPP / NPP _{canopy}	net primary production	$\mu\text{mol m}^{-2} \text{s}^{-1}$, $\text{mg m}^{-2} \text{s}^{-1}$	canopy
NPP _p	net primary production inferres profile	$\mu\text{mol m}^{-2} \text{s}^{-1}$, $\text{mg m}^{-2} \text{s}^{-1}$	canopy
PAR	photosynthetically active radiation	$\mu\text{mol m}^{-2} \text{s}^{-1}$, W m^{-2}	leaf/canopy
Q^*	net radiation	W m^{-2}	leaf/canopy
R_{d}	CO ₂ dark respiration	$\text{mg m}^2 \text{s}^{-1}$	landscape
R_{s}	soil respiration	$\mu\text{mol m}^{-2} \text{s}^{-1}$	landscape
$R_{\text{s,ch}}$	soil respiration measured by chamber	$\mu\text{mol m}^{-2} \text{s}^{-1}$	landscape
$R_{\text{s,p}}$	soil respiration inferred from profile	$\mu\text{mol m}^{-2} \text{s}^{-1}$	landscape
H	sensible heat flux	W m^{-2}	canopy/landscape
T	temperature	$^{\circ}\text{C}$, K	several
T_{air}	air temperature	$^{\circ}\text{C}$, K	landscape
$T_{\text{air,p}}$	air temperature from vertical profile meas.	$^{\circ}\text{C}$, K	leaf/canopy
Tr_{p}	transpiration, profile-based	W m^{-2}	leaf/canopy
u	wind speed	m s^{-1}	landscape
u_{p}	wind speed from vertical profile meas.	m s^{-1}	landscape
u_*	friction velocity	m s^{-1}	landscape
VPD	water vapour-pressure deficit	kPa	leaf/canopy
α	light use efficiency	mg J^{-1}	landscape
α_0	initial value of light-use efficiency	mg J^{-1}	landscape
$\chi_{\text{H}_2\text{O}}$	mole fractions of H ₂ O concentration	$\mu\text{mol mol}^{-1}$	leaf/canopy
χ_{CO_2}	mole fractions of CO ₂ concentration	$\mu\text{mol mol}^{-1}$	leaf/canopy

ber headspace temperature were recorded at a sampling rate of 1 Hz. The CO₂ concentration was standardized to dry air and a constant temperature to eliminate effects of changes in air density and water vapour dilution during closure time. R_{s} was subsequently calculated by adjusting a linear regression fit to the final 60 s of the measurement before reopening.

2.3.3 Leaf-level measurements

Leaf gas exchange was measured using a Li-Cor LI-6400XT portable photosynthesis system with a 6400-02B LED light source. Leaf-level measurements included instantaneous stomatal conductance to water vapour (g_{sw}) and photosynthesis (A_{leaf}), maximum light-saturated photosynthesis (A_{max}) is the maximal primary productivity under high light conditions, CO₂-response curves, and light-response

curves. Measurements of g_{sw} and A_{leaf} were performed during the three IOPs, starting at sunrise and ending when measurements of g_{sw} indicated that stomata had nearly closed ($g_{sw} < 0.05 \text{ mol m}^{-2} \text{ s}^{-1}$). For measurements of g_{sw} and A_{leaf} , tillers were picked randomly in the field and immediately mounted in the leaf chamber for measurements. Initial tests showed no difference in g_{sw} between excised and attached tillers. Settings of leaf chamber photosynthetically active radiation (PAR) and CO_2 followed the diurnal variability measured in the field. For comparison with other observations, measurements of g_{sw} and A_{leaf} were binned and averaged at 30 min intervals. A_{max} was measured during the three IOPs, as well as on 8 May between 10:00 and 12:00 UTC. For measurements of A_{max} , the light intensity (PAR) was set to $1500 \mu\text{mol m}^{-2} \text{ s}^{-1}$ and the leaf was equilibrated under a reference CO_2 concentration of $450 \mu\text{mol CO}_2 \text{ mol}^{-1}$ air. CO_2 response curves were measured during IOP 1 and IOP 3, prescribing CO_2 concentrations in the following order: 0, 50, 100, 150, 250, 350, 450, 600, 800, and $1200 \mu\text{mol CO}_2 \text{ mol}^{-1}$ air. All CO_2 -response curves were measured using a light intensity (PAR) of $1500 \mu\text{mol m}^{-2} \text{ s}^{-1}$. Light-response curves were measured on IOP 1 only and used a reference CO_2 concentration of $450 \mu\text{mol CO}_2 \text{ mol}^{-1}$ air. PAR values were changed in the following order: 0, 25, 50, 100, 200, 400, 800, 1200, and $1500 \mu\text{mol m}^{-2} \text{ s}^{-1}$. The stomatal conductance to water vapour ($g_{sw} \text{ mol m}^{-2} \text{ s}^{-1}$) of the curves that relate A and PAR (A -PAR) in between 0 and $200 \mu\text{mol m}^{-2} \text{ s}^{-1}$ for the three repetitive experiments within the PAR range were (average and standard deviation in brackets): 0.49 (0.13), 0.12 (0.02), and 0.34 (0.06). Leaves were allowed to equilibrate to leaf chamber conditions in terms of gas exchange (approximately 1–2 min) but not in terms of stomatal aperture. For all measurements, leaf chamber temperature was set between 20 and 25 °C. Relative humidity in the leaf chamber was set between 60 % and 75 %. Measurements of A_{max} , CO_2 -response curves and light-response curves were performed on attached tillers.

2.3.4 Sap flow

Sap flow in wheat tillers was measured with the heat balance method (Sakuratani 1981; Baker and van Bavel, 1987). A total of 24 tillers were selected at random, diameters measured with an electronic calliper, and SGA3-type sap-flow sensors installed at the lowest possible internodes following the procedure recommended by the manufacturer (Dynamax, 2007, 2017). Sensors were connected with electrically shielded wire to AM 16/32 multiplexers controlled and scanned by CR1000 data loggers (Campbell Scientific, Logan, Utah, USA). Energy supply to the stem heaters was carefully regulated to the highest permissible level in order to obtain a strong heat signal. We employed the dual voltage regulators (Dynamax AVRDC) which were parts of wired measurement, control, and extension units assembled and tested by the heat balance sensor manufacturer (Flow32 1K A and

B models, Dynamax Inc., Houston, Texas, USA). Data were processed according to the calculation procedure of Dynamax (2007) with adaptations to wheat (Langensiepen et al., 2014) to obtain reliable data on the convective stem heat flow generated by sap flow. Here we take the evolution of the tiller densities from 480 tillers per square metre (IOP 1 and IOP 2) to 370 tillers per square metre (IOP 3) into account.

2.3.5 Profiling elevator

Vertical profiles H_2O and CO_2 expressed as mole fractions $\chi_{\text{H}_2\text{O}}$ and χ_{CO_2} (mole of substance per mole of moist air), temperature ($T_{\text{air,p}}$) and wind speed (u_p) from the soil surface to the surface layer above the crop canopy were measured with a portable elevator system. The elevator moved continuously up and down the measuring sensors attached to an extension arm over a total profile height of 2 m. A sampling tube connected to a differential gas analyser (LI-7000, Li-Cor Inc. Biosciences, Lincoln, Nebraska, USA) collected $\chi_{\text{H}_2\text{O}}$ and χ_{CO_2} at a frequency of 20 Hz. $T_{\text{air,p}}$ and u_p were measured at the same frequency by a ventilated fine-wire thermocouple (FW3, Campbell Scientific, Logan, Utah, USA) and a hot-wire anemometer (8455-075-1, TSI, Shoreview, Minnesota, USA). All measurements were duplicated as a continuous fixed-height measurement at the top of the profile. During the data post-processing, the temporal and vertical resolution of the mean profiles was set to a time-averaging block of 30 min with a vertical resolution of 0.025 m. Time delays in each variable with respect to the position caused by response times of the sensors, electronic delays, and the tube transport of the gas samples were adjusted by a hysteresis minimization algorithm. Detailed information on the profile measurement setup and the processing of the data profile is given in Ney and Graf (2018). The measured concentration profiles were then used to determine the vertical source profiles of H_2O and CO_2 , with the aim of providing an independent, non-invasive partitioning between above-ground net primary production (NPP) and R_s or evaporation (E) and transpiration (Tr_p). To estimate source profiles and flux partitioning, we used an analytical dispersion Lagrangian technique introduced by Warland and Thurtell (2000) and further developed by Santos et al. (2011). Other than in the above-mentioned literature, a simple optimization method (Nelder and Mead, 1965) was used to fit four parameters: soil source, canopy source, and shape parameters p and q of a beta distribution, which describes the vertical source distribution within the canopy.

2.3.6 Scintillometer

The receiver of a displaced-beam laser scintillometer, hereafter referred to as DBLS (SLS-20, Scintec, Rottenburg, Germany), was placed 9 m southeast of the EC station (Fig. 1). The scintillometer measurements height was 1.95 m a.g.l. The path length towards the instrument transmitter was

86.8 m. It was pointed along a transect from northwest to southeast. The DBLS measures the scintillation intensity of two displaced laser beams (wavelength of 670 nm and separation distance of ~ 2.7 mm). The structure parameter of temperature (C_T^2) and dissipation rate of turbulent kinetic energy (ε) are determined from the log variance of one beam and log covariance between the beams. The general equation that links the scintillometer measurements to fluxes is given by

$$F_x = \rho K_x \left(u_*, \frac{z}{L} \right) z^{\frac{1}{3}} \sqrt{C_x^2}, \quad (1)$$

where F_x is defined as the turbulent flux of the transported variable x , C_x^2 is the structure function parameter of x , and K_x represents the turbulent exchange coefficient that links F_x to C_x^2 . K_x is a function of the friction velocity, u_* , and the Obukhov length, L . Finally, ρ is the air density, and z is the measurement height above the surface. For the sensible heat flux $H = F_T$, x represents temperature (T) and appropriate constants need to be added to convert Eq. (1) to energy fluxes. H , u_* , and L are solved iteratively as a function of the DBLS-measured C_T^2 and ε (Thiermann, 1992; Hartogensis et al., 2002). The Monin–Obukhov Similarity Theory (MOST) functions that define K_x were taken from Kooijmans and Hartogensis (2015). For our purpose, however, the exact shape of the MOST functions is of minor importance as we are primarily interested in the dynamic temporal behaviour of the fluxes rather than an accurate description of their quantitative values. We are aware that advective contributions can lead to the violation of MOST. However, advection did not influence our measurements for two reasons. First, the scintillometer transmitter and receiver are far enough from the edges of the CloudRoots field given the height of the sensor (1.95 m), the wind speed and direction during the IOPs, and the stability conditions. All of these mean that the footprints are small enough to fit within the field. The typical footprint length (90 % footprint contribution) for the 3 IOPs yields IOP 1 (85 m), IOP 2 (30 m), and IOP 3 (75 m). Second, the scintillometer has a path weighting function that is at its maximum in the middle of the path and near-zero at the transmitter and receiver positions, i.e. the major contribution occurs at the farthest point of the field edge.

The added value of DBLS fluxes over the traditional EC method is that they converge to statistically stable flux estimates at much shorter flux averaging times of 1 min or less, while the EC technique typically requires flux averaging times of 10 to 30 min (Hartogensis et al 2002; van Kesteren et al., 2013b). The essence behind this is that the flux estimate is based on structure parameters that are defined in the inertial range of the turbulent spectrum. As such, the flux estimates rely on a limited range of the turbulent scales that contribute to the flux rather than all of them as is the case with the EC method.

We also adopted the combination technique introduced by van Kesteren et al. (2013a, b) to obtain fluxes of H_2O and CO_2 at these short timescales. This technique combines structure parameters of H_2O and CO_2 that are obtained from H_2O and CO_2 time series from an Infra-Red Gas Analyser (IRGASON system; see Sect. 2.3.7) with an exchange coefficient defined by the DBLS fluxes to finally calculate flux estimates of H_2O and CO_2 . In other words, with u_* and L solved with the DBLS, Eq. (1) can be evaluated using structure parameters of trace gases x , where in this case x represents the specific density, q_x , of H_2O or CO_2 .

2.3.7 Eddy covariance and ancillary micrometeorological measurements

A continuously running EC system was operated in the middle of the field (Fig. 1), comprising a three-dimensional sonic anemometer (Model CSAT-3, Campbell Scientific, Inc., Logan, Utah, USA) and an open-path infrared gas analyser (Model LI-7500, Li-Cor, Inc., Biosciences, Lincoln, Nebraska, USA). The sensors height was 2.34 m a.g.l. Raw data were sampled in 20 Hz mode and fluxes and averages were calculated as 30 min block averages using the TK3.11 software package developed at the University of Bayreuth, including corrections and quality control as given in Mauder and Foken (2011). Missing values in the calculated turbulent fluxes were filled with the marginal distribution sampling (MDS) method following Reichstein et al. (2005) which is implemented in the REddyProc software package (Wutzler et al., 2018). The station also included measurements of all components of the radiation budget (NR01, Hukseflux, Delft, the Netherlands), PAR (LI-190R, Li-Cor Inc. Biosciences, Lincoln, Nebraska, USA, and BF5, Delta-T Devices, Cambridge, UK), air temperature (T_{air}), and humidity (HMP45C, Vaisala Inc., Helsinki, Finland) at 2.4 m, and precipitation (Thies Clima type tipping bucket, distributed by Ecotech, Bonn, Germany) at 1.0 m a.g.l. Radiation measurements were taken at 2.5 m. Soil heat flux, temperature, and moisture were measured next to the station, more specifically, this was performed using the following parameters: 3 times HFP01SC at 3 and 8 cm, Hukseflux, the Netherlands; 3 times TCAV, Campbell Scientific, Logan, USA; and 1 cm, 5 cm, and 2 to 65 cm layer average, 2 times CS616, Campbell Scientific, Logan, USA, 2 to 6 cm layer average. In addition, we measured at five points distributed across the field using the wireless SoilNet sensor system (Bogena et al., 2010). One SoilNet point was placed next to the station, while the other four were placed next to the soil CO_2 efflux chambers described above. Each SoilNet point comprised a single soil heat flux measurement at 5 cm (HFP01SC, see above) and combined temperature and soil water content measurements in depths of 1, 5, 10, 20, 50, and 100 cm (SMT100, Truebner GmbH, Neustadt, Germany).

A second mobile EC station with instruments heights of 1.93 m a.g.l. was deployed in the immediate vicinity of

the continuously monitoring station during the measurement campaign. The system comprised an IRGASON EC system (SN1185 Irgason EC150, Campbell Scientific, Inc., Logan, Utah, USA; PTB101B pressure sensor, Vaisala Inc., Helsinki, Finland) with an additional LI-7500 sensor (same manufacturer). Here, fluxes were processed with the LiCor EddyPro v6.2.2 software. Radiation (CM11 for global and CG2 for long-wave radiation, Kipp & Zonen B.V., Delft, Netherlands), ground heat flux (4× HFP01SC at 5 cm depth, Hukseflux, the Netherlands), and temperatures at depths of 2 cm (4×) and 8 cm (2×) were also measured at this station.

2.3.8 Canopy-level measurements of reflectance and sun-induced fluorescence (SIF): FloxBox

A field spectroscopy system was used (FLOX, JB Hyper-spectral Devices UG, Düsseldorf, Germany) for canopy-level measurements of reflectance and SIF. FLOX is constructed for high temporal frequency acquisition of continuous top-of-canopy optical properties with a focus on sun-induced chlorophyll fluorescence. The system is equipped with two spectrometers: an Ocean Optics FLAME S, covering the full range of Visible and Near-Infrared (VIS-NIR) and an Ocean Optics QEPro, with a high spectral resolution (Full Width at Half Maximum, FWHM, of 0.3 nm) in the 650–800 nm range of the fluorescence emission. The optical input of each spectrometer is split between two fibre-optic cables that lead to a cosine receptor that measures solar irradiance and a bare fibre bundle that measures the target-reflected radiance. Spectrometers are housed in a Peltier thermally regulated box to keep the internal temperature lower than 25 °C in order to reduce dark current drift. The signal is automatically optimized for each channel at the beginning of each measurement cycle, and two associated dark spectra are collected as well. Metadata such as spectrometer temperature, detector temperature and humidity, Global Positioning System (GPS) coordinates, and time are also simultaneously stored in the secure digital memory of the system. More detailed information about the system can be found in Wohlfahrt (2018) and in Campbell (2019).

2.3.9 Regional level measurements of reflectance and sun-induced fluorescence (SIF): HyPlant

An airborne high-performance imaging spectrometer (HyPlant) was used for regional-level measurements of the same quantities. Several flight lines over the 15 km × 15 km study site with 1–3 m pixel resolution were used. HyPlant is a hyperspectral imaging system for airborne and ground-based use, developed as a cooperative effort between Forschungszentrum Jülich GmbH (Germany) and the company SPECIM (Oulu, Finland). It consists of two sensor heads, named DUAL and FLUO. The DUAL module is a line-imaging push broom hyperspectral sensor, which provides contiguous spectral information from 370 to 2500 nm

in a single device that utilizes a standard objective lens with 3 nm spectral resolution in the VIS-NIR spectral range and 10 nm spectral resolution in the SWIR spectral range. The FLUO module measures the vegetation fluorescence signal with a separate push broom sensor that produces data at high spectral resolution (0.25 nm) in the spectral window between 670 and 780 nm. The position and altitude sensor (GPS/INS sensor) provides, synchronously with the image data, aircraft position and altitude data for image rectification and geo-referencing. Both imagers are mounted in a single platform with the mechanical capability to align the field of view (FOV). A more detailed description of the sensor is given in Rascher et al. (2015).

Sun-induced fluorescence (F_{687} and F_{760}) was retrieved in the two oxygen absorption bands according to the improved Fraunhofer Line Discrimination (iFLD) method. The iFLD method was initially proposed by Alonso et al. (2008) and was adapted to allow SIF retrievals from the FLUO module of the HyPlant sensor (Rascher et al., 2015). Surface reflectance and vegetation indices were calculated after an atmospheric correction using the MODTRAN software package was applied. The atmospheric correction was performed using the MODTRAN software package (for an overview of the data processing of HyPlant, see Siegmann et al., 2019). For the reason of easier comparison of SIF values with other methods of this paper, the commonly used SIF units ($\text{mW m}^{-2} \text{sr}^{-1} \text{nm}^{-1}$) were replaced by a substitute ($\text{nmol m}^{-2} \text{sr}^{-1} \text{s}^{-1}$) using conversion factors of 6.35 for and 5.74 for F_{687} and F_{760} , respectively.

2.3.10 Boundary layer and cloud remote sensing measurements

The JOYCE remote sensing facility (Löhnert et al., 2015) (located at a distance of 5 km from the test site) provided continuous information about boundary layer and cloud characteristics. Specifically, microwave and lidar measurements were used to compare the CLASS model results (see Sect. 2.4) with the inferred boundary layer depth. This comparison was completed by vertical profiles measured by the routine radio soundings at Essen (station ID EDZE/10410 at a distance of 75 km).

2.4 Modelling from leaf to landscape scales: CLASS

The Chemistry Land-surface Atmosphere Soil Slab (CLASS, <https://classmodel.github.io/>, last access: 21 August 2020) is a model that couples the soil–vegetation–atmospheric processes and is used to interpret the observations and analyse the interaction of scales (Vilà-Guerau de Arellano, et al., 2015). It contains a leaf-level representation of photosynthesis and stomatal aperture (leaf resistance). By upscaling this leaf resistance to the canopy level (surface canopy resistance), it connects with the soil processes and boundary layer diurnal dynamics. In Sect. 2.4.1 and 2.4.2, we will

subsequently discuss the two main modules of CLASS that we will target in this paper, i.e. the leaf level photosynthesis module and the mixed-layer module.

2.4.1 Modelling leaf-level photosynthesis

Leaf-level photosynthesis was modelled using the representation of photosynthetic biochemistry, as included in CLASS (Vilà-Guerau de Arellano et al., 2015), which was originally developed by Goudriaan (1986) and further adapted to meteorological applications by Jacobs and de Bruin (1997). As this model describes the relationship between stomatal conductance (g_s) and photosynthesis (A), it is usually referred to as the A - g_s sub-model. In short, plant transpiration and CO_2 assimilation as part of the surface energy balance model are represented by a two-big-leaves model, one for sunlit leaves and one for shaded leaves (Jacobs and de Bruin, 1997; Pedruzo-Bagazgoitia et al., 2017). The exchange at the leaf surface depends on the gradient of atmospheric CO_2 and an internal leaf CO_2 concentration, which depends on the water vapour deficit and leaf conductance. The CO_2 exchange is upscaled to the canopy level by integrating over the leaf area index (LAI).

Available field measurements were used for improving the model settings at the leaf level. The parameters representing the initial value of the light use efficiency (α_0) and the temperature-normalized maximum leaf-level photosynthesis rate ($A_{m,\max298}$) were fitted using light-response curves (Fig. 5) and CO_2 -response curves (Fig. 3b) collected on 8 May 2018 (1 d after IOP 1). Table 3 summarizes the optimized values used in the A - g_s (sub)model to simulate the leaf-level photosynthesis. The A -PAR curves contain only the lower light intensity values (0 – $200 \mu\text{mol m}^{-2} \text{s}^{-1}$) for which the light response is near linear and not limited by CO_2 diffusion into the leaf. As leaf-level measurements of A_{\max} indicated a decline in photosynthetic capacity in the course of the growing season (Fig. 5c), we performed additional measurements of $A_{m,\max298}$ to represent the observed seasonal decline for IOP 2 and IOP 3. The impacts on these optimized values are shown and discussed in the Supplement.

2.4.2 Modelling the diurnal variability of landscape surface fluxes and boundary layer dynamics

The fundamental assumption of the mixed-layer model is that under convective conditions the atmospheric boundary layer (ABL) dynamics lead to profiles of the meteorological state variables that are uniform (well-mixed) with height. As a result, these state variables are governed by horizontally averaged 0-dimensional slab equations: one equation for the evolution through time of the slab variable and another for the difference between the residual layer (in the morning transition) and the free tropospheric values and the slab value, i.e. the jump at the interface between residual layer and ABL. The ABL dynamics are governed by the mixed-layer

equations of potential temperature (heat), specific humidity (moisture), CO_2 , and two horizontal wind momentum components. In addition, there is an equation that governs the boundary layer growth, which depends on the buoyancy flux at the surface and the jump in the virtual potential temperature at the interface between the atmospheric boundary layer and the free troposphere.

A key feature of the model is its representation of the sub-daily variability of the land–atmosphere interactions (van Heerwaarden et al., 2010; Vilà-Guerau de Arellano et al., 2015). The net ecosystem exchange is calculated as a result of the assimilation of CO_2 by plants and the CO_2 soil efflux. We calculate the assimilation rate from photosynthesis and the stomatal aperture measurements at leaf level (see Sect. 2.4.1), upscaled to canopy level (Ronda et al., 2001). This model depends on the diurnal variability of PAR, temperature (T_{air} and $T_{\text{air,p}}$), and the water vapour deficit (VPD). The two-big-leaves approach is used (sunlit and shaded) to take the different contributions of direct and diffuse radiation into account (Pedruzo-Bagazgoitia et al., 2017). The soil efflux is calculated as a function of the soil temperature and moisture. Other relevant physical processes include a radiation transfer model, the Penman–Monteith equation included in the surface energy balance, and the possibility of adding large-scale forcings such as vertical subsidence motions and large-scale advection of momentum, heat, moisture, and CO_2 . Within the context of CloudRoots, it is important to mention that the model assumes a horizontal homogeneous surface. While the experimental field itself is quite homogeneous, it is surrounded by other land use types at a spatial scale that will affect the boundary layer. In that respect, and in setting the initial and boundary conditions for the numerical case, we assume that the boundary layer dynamic is governed by a sensible heat flux that is an aggregate of all the fields shown in Fig. 1b.

3 Results: integrating spatio-temporal scales from leaf to boundary layer

This section is structured following the five facets of the diurnal interactions between the land and the atmosphere outlined in the introduction.

3.1 Leaf-level exchange of H_2O and CO_2 : observations and modelling

We combine leaf-level and sap flow measurements of tiller assimilation and transpiration with leaf-level assimilation modelled by CLASS, A - g_s representation, to study their variation during the growing season and the impact of unsteady PAR due to the presence of clouds.

Table 3. Parameters representing the maximum leaf-level photosynthesis rate ($A_{m,max298}$) and the initial value of light-use efficiency (α_0) under low light, as adjusted in the original $A-g_s$ model to represent plant-specific photosynthesis characteristics for winter wheat (ww). $A_{m,max298}$ was initially fitted using the $A-C_i$ curves and α_0 is fitted using the $A-PAR$ curves taken during IOP 1 (Fig. 5). For IOP 2 and IOP 3, $A_{m,max298}$ values were fitted only on leaf-level measurements of A_{max} . The values of IOP 1 were used as numerical settings for the CLASS model runs (Fig. 16). The equivalence to typical values of the commonly used in the Farquhar–Berry–von Caemmerer (FBvC) model of leaf photosynthesis (Farquhar et al., 1980) is given in Table S1 at the Supplement.

Fitted model variable	Default value (for C3 plants)	Fitted ww IOP 1	Fitted ww IOP 2	Fitted ww IOP 3
Mesophyll conductance at 298 K (mm s^{-1})	7.0	10.0	10.0	10.0
Maximum leaf-level photosynthesis rate ($A_{m,max298}$) ($\text{mg m}^{-2} \text{s}^{-1}$)	2.2	1.926	1.0	0.2
light-use efficiency (α_0) (mg J^{-1})	0.017	0.0053	0.0053	0.0053

3.1.1 Stomatal conductance and sap flow

Our leaf-level measurements revealed clear diurnal patterns in g_{sw} during all the IOPs (Fig. 3). The observed daily maximum g_{sw} decreased over the growing season. This daily maximum g_{sw} occurred at an earlier time during each IOP. Specifically, the 30 min average daily maximum g_{sw} declined from $0.84 \text{ mol m}^{-2} \text{ s}^{-1}$ (around 10:00 UTC, 12:00 LT) during IOP 1 and $0.83 \text{ mol m}^{-2} \text{ s}^{-1}$ (around 10:00 UTC) during IOP 2 to $0.30 \text{ mol m}^{-2} \text{ s}^{-1}$ (between 05:30 and 06:30 UTC) during IOP 3. The weather during IOP 2 was characterized by large cumulus clouds passing over the field site, which were made visible in the large fluctuations in PAR (Figs. 3b, 11 and 12). The cloud-related changes in light intensity induced consistent stomatal opening–closing responses during IOP 2. The relatively low g_{sw} observed during IOP 3 probably reflects the continuing drought that characterized the 2018 growing season in combination with the relatively high VPD and high temperatures. Sap flow measurements were performed during IOP 2 and IOP 3 (Fig. 3b and c) and one earlier non-IOP day (7 June) (Fig. 4). Measurements of sap flow revealed clear diurnal patterns for all measurement days and consistent responses to cloud-induced changes in light intensity during IOP 2 (Fig. 3b). These responses were comparable to the observed responses in g_{sw} during IOP 2. Interestingly, the notable decline in leaf-level g_{sw} between IOP 2 and IOP 3 was neither reflected in the measurements of sap flow nor in the ET measurements with the eddy covariance. For IOP 3, the ET measured by the eddy covariance had still maximum values of 300 W m^{-2} . Thereafter, the decrease in ET started 1 week afterwards (5 July) with values lower than 100 W m^{-2} . This discrepancy could partly be explained by increases in VPD and wind speed between IOP 2 and IOP 3. The more probable causes are senescence effects on physiological control of transpiration and the physical reactions to heat of the wheat tillers, which were noticeably wilting between IOP 2 and IOP 3. This observation has so far not been reported in the literature. Further studies of the relationships between senescence and simultaneously occurring changes

in the heat and physical properties of wheat tillers are needed to explain this phenomenon.

3.1.2 Observed versus modelled leaf-level photosynthesis

One of the main aims in CloudRoots is to improve the mechanistic modelling of photosynthesis and stomatal aperture. To this end, we calibrate the constants of the $A-g_s$ model using systematic in situ field observations. Figure 5 shows the dependencies of leaf-level photosynthesis of A_{leaf} on PAR (Fig. 5a) and the leaf-internal CO_2 concentration (Fig. 5b) and the long-term decline in maximum light-saturated photosynthesis (Fig. 5c). Our observations indicate the need to calibrate the model depending on the functional type of the plant, in particular the dependence of A_{leaf} on PAR, during the field campaign. Table 2 summarizes the new constant values used in the $A-g_s$ model adjusted to the winter wheat crop conditions.

Figure 6 shows a comparison of the model results of A_{leaf} using the new constants and the measurements of A_{leaf} and NPP together with the diurnal variation in PAR and VPD during the three IOPs. Our measurements and model results of A_{leaf} showed clear diurnal patterns during each IOP, and a consistent decline over the three IOPs. The decline in A_{leaf} was comparable to the decline in A_{max} (Fig. 5c) and probably reflects a combination of seasonal decay in photosynthetic capacity and increasing stomatal limitations owing to persistent drought, especially during IOP 3. The magnitude of the seasonal decline in A_{leaf} was comparable to the seasonal decline in NPP derived from EC data. Cloud-induced changes in PAR during IOP 2 also induced changes in A_{leaf} . The $A-g_s$ model reproduced the diurnal patterns in A_{leaf} during each IOP, as well as the cloud-induced changes in A_{leaf} during IOP 2. The agreement is very satisfactory during IOP 1, which was characterized by cloudless conditions and the maturity of winter wheat. The model underestimated A_{leaf} during IOP 3, which was a result of the strong stomatal limitations that influenced the measurement of A_{max} on which the

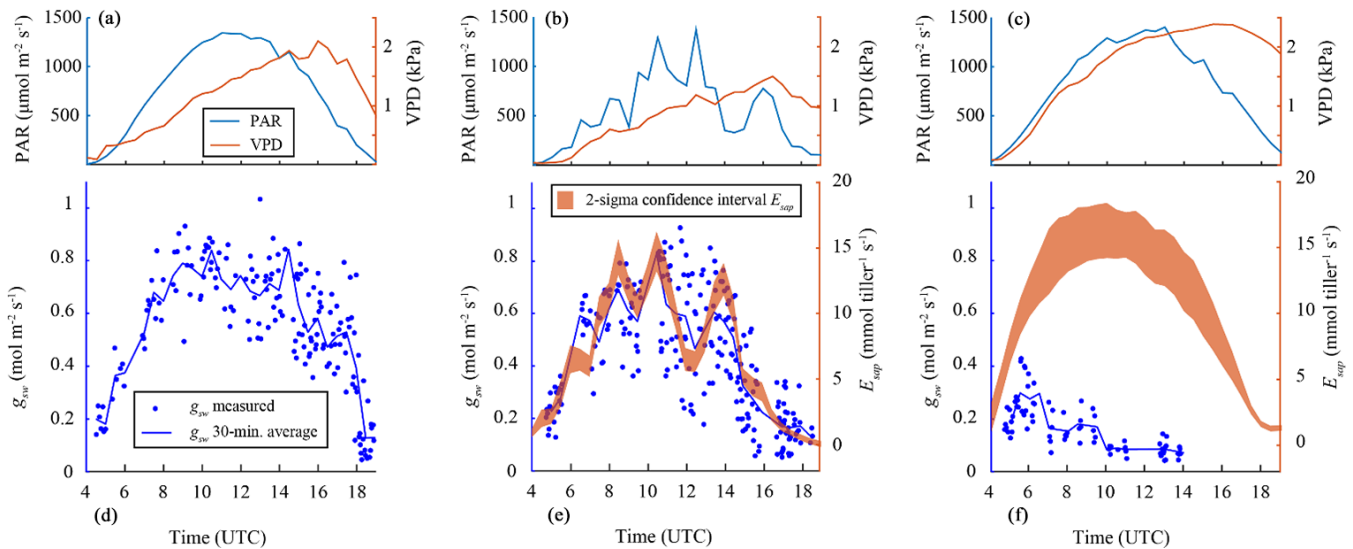


Figure 3. Diurnal changes in photosynthetically active radiation (PAR) and vapour pressure deficit (VPD) measured for (a) IOP 1, (b) IOP 2, and (c) IOP 3. Leaf-level measurements of stomatal conductance of water vapour (g_{sw}) in (b) and (c) compared to tiller-level measurements of sap flow (E_{sap}). Leaf-level measurements of g_{sw} (blue markers) were averaged over 30 min intervals (blue line). Sap flow measurements represent the 1 SD confidence interval (shaded region) of measurements on 24 tillers averaged over 30 min timescales.

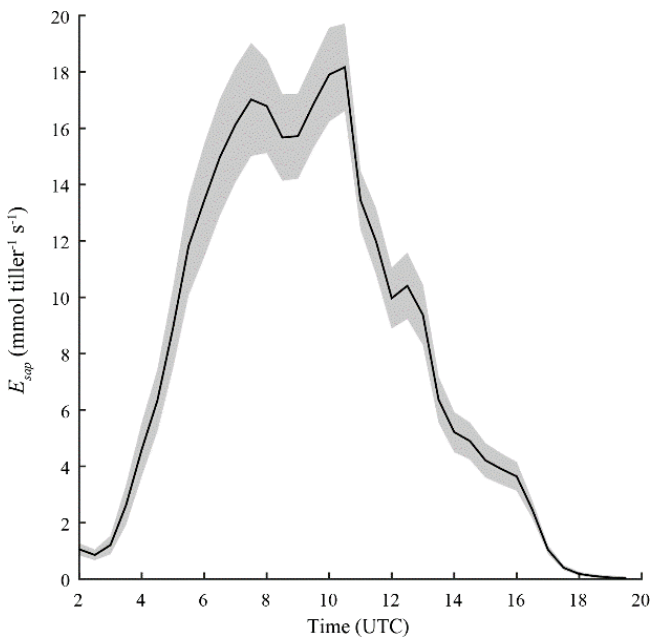


Figure 4. Sap flow measured using the heat balance method for 7 June 2018 (non-IOP day).

model parameterization from IOP 3 was based. The model furthermore overestimates the decline in A_{leaf} between 14:00 and 19:00 UTC, which probably reflects a misrepresentation of the temperature and VPD sensitivity of *Triticum aestivum*.

3.2 Canopy-level partitioning of the net H_2O and CO_2 fluxes between soil and plant processes

Moving from leaf to canopy scale, we analyse the detailed profiles of micrometeorology and carbon dioxide collected using the elevator and infer vertical assimilation profiles and the diurnal variability in the surface contributions to ET and NEE.

3.2.1 Concentration profiles of H_2O and CO_2 , temperature and wind speed

Figure 7 shows selected 30 min mean profiles of χ_{H_2O} and χ_{CO_2} , temperature, and wind speed versus height (z) above ground level during IOP 1 and IOP 2. Over the diurnal cycle, χ_{CO_2} concentrations fell between 08:00 and 13:00 UTC from 370 to 360 $\mu\text{mol mol}^{-1}$ in the mid-canopy during IOP 1 but stagnated slightly below 370 $\mu\text{mol mol}^{-1}$ during IOP 2. This seasonal reduction in CO_2 uptake was also observed in measured A_{leaf} , i.e. see the decrease of the maximum values in Fig. 6. The lowest values were observed during local noon, simultaneous with the highest PAR values (Fig. 5b). χ_{CO_2} minima were located in the upper third of the canopy during IOP 1 and during the middle third during IOP 2. The highest χ_{CO_2} values were found near the soil surface due to soil respiration, lower light intensity caused by shadowing, and a low amount of photosynthetic organs in the stems. Maximum χ_{CO_2} concentrations were measured in the morning and evening hours and peaked at about 475 and 420 $\mu\text{mol mol}^{-1}$ during IOP 1 and IOP 2, respectively. The photosynthetic CO_2 uptake by plants is highly related to plant transpiration. Consequently, χ_{H_2O} in the canopy space was higher than in

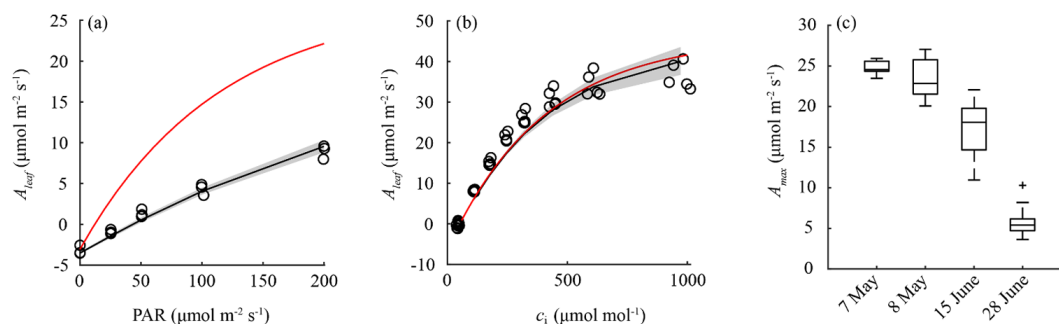


Figure 5. Measurements of leaf-level photosynthesis (A_{leaf}) as a function of photosynthetically active radiation (PAR) (a) and leaf interior CO_2 concentrations (c_i) (b). These results were used to parameterize the A - g_s model for IOP1, as indicated by the black line and shaded 1 SD confidence interval. The red line indicates the model response using the default parameter values. (c) Observed and modelled seasonal decline in maximum light-saturated photosynthesis (A_{max}). Boxes indicate the variability in observed values in A_{max} ; red markers indicate the modelled net photosynthesis rate using fitted values for $A_{m,max298}$. Fitted and default A - g_s model parameter values are indicated in Table 3.

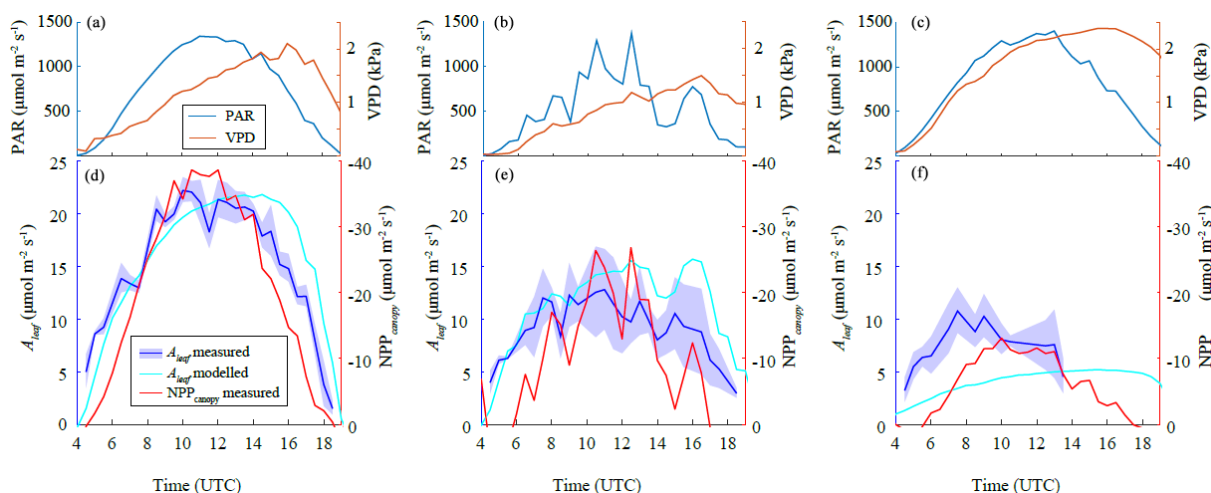


Figure 6. Measured leaf-level photosynthesis (A_{leaf}) compared to modelled A_{leaf} using the A - g_s model and canopy-level net primary productivity (NPP_{canopy}) for (a) IOP 1, (b) IOP 2, and (c) IOP 3. Measurements of A_{leaf} were plotted as 30 min averages (blue line) and their 1 SD confidence interval (shaded region). Panels (d), (e), and (f) show diurnal changes in photosynthetically active radiation (PAR) and vapour pressure deficit (VPD) measured for each IOP.

the air above the canopy. The highest values were found directly above the soil surface and were caused by evaporation and due to plant transpiration within the canopy.

The highest temperatures appeared near the canopy top (Fig. 7d, e, j and l). In the late morning of IOP 2, the temperature reached a distinct maximum just below the canopy top (Fig. 7j). This phenomenon has been reported in previous studies (Ney and Graf, 2018) and is caused by the changing solar incidence angle. A low angle of incidence in the morning and afternoon limited the heating to an area just below the canopy surface. Previous studies have shown that the presence of such a pronounced temperature maximum has the potential to increase thermal stability within the canopy and thus inhibit the vertical turbulent exchange of sensible heat (Gryning et al., 2001; Ney and Graf, 2018; Sikma et al., 2020). It can be assumed that the sensible heat flux

within the dense plant stand was largely determined by the entire canopy. In other words, during the day, mixing near the soil surface was impeded by stable temperature stratification, while in the evening cooling expanded upwards from the soil surface (Fig. 7f). In general, the processes described above were more pronounced during IOP 2 with its greater canopy height than with the lower canopy during IOP 1. The vertical wind profile showed consistently low wind speeds within the dense canopy ($<0.5 \text{ m s}^{-1}$). Above the canopy layer, the wind speed increased in a log-like profile up to a maximum of 2 m s^{-1} .

3.2.2 Profiles of gross primary production

The detailed profile observations presented in the previous section enable us to calculate height-resolved estimates of

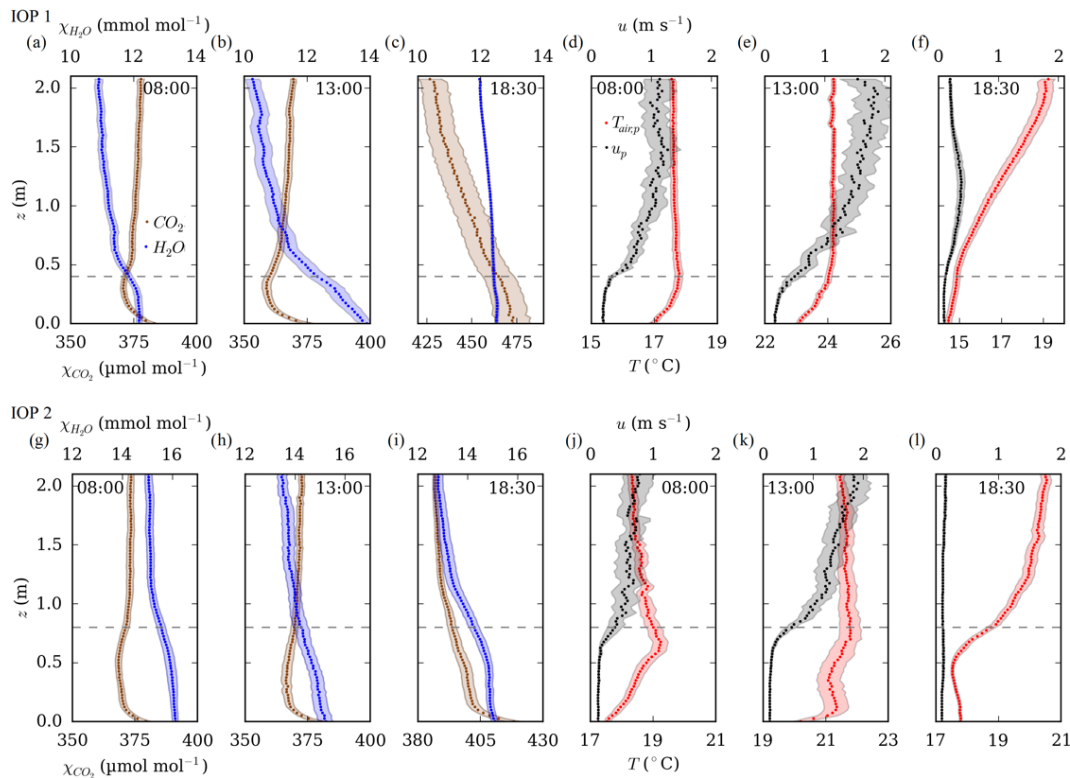


Figure 7. Selected (08:00, 13:00 and 18:30 UTC) 30 min mean profiles of the H_2O and CO_2 mole fractions ($\chi_{\text{H}_2\text{O}}$, χ_{CO_2}), wind speed (u_p), and temperature ($T_{\text{air,p}}$) measured at high vertical resolution during IOP 1 (upper row) and IOP 2 (lower row). Shaded areas indicate the 95 % confidence interval resulting from the standard deviation between individual profiles sampled within a 30 min average interval. The dashed lines indicate the canopy heights.

gross primary production A . Using the 30 min averages of the vertical profiles for temperature, moisture, and CO_2 in the canopy, A is determined using the A - g_s model (Jacobs et al., 1997; Ronda et al., 2001). A ($\text{mg m}^{-2} \text{s}^{-1}$) is calculated as follows:

$$A = \text{LAD} (A_m(h) + R_d(h)) \left[1 - \exp\left(\frac{-\alpha \text{PAR}(h)}{A_m(h) + R_d(h)}\right) \right], \quad (2)$$

where LAD ($\text{m}^2_{\text{leaf}} \text{m}^{-3}$) is the leaf area density, $A_m(h)$ is the CO_2 primary productivity ($\text{mg m}^2_{\text{leaf}} \text{s}^{-1}$) as a function of height h , $R_d(h)$ ($\text{mg m}^2_{\text{leaf}} \text{s}^{-1}$) is the CO_2 dark respiration as a function of h , α (mg J^{-1}) is the light use efficiency, and $\text{PAR}(h)$ ($\text{W m}^{-2}_{\text{leaf}}$) is the amount of available photosynthetically active radiation within the canopy. Solar-zenith-angle-related variation in PAR intrusion and differences between atmospheric and skin values for temperature, moisture, and CO_2 are neglected. Figure 8a shows the winter wheat LAD applied in the calculation.

Figure 8b shows that the entire canopy contributes to the photosynthetic activity but with maximum A at $h/h_c = 0.7$ (h_c : canopy height). This is primarily caused by the extinction of PAR within the canopy and reduced leaf density distribution close to the ground (Fig. 8a). Maximum diurnal

productivity is found at around $h/h_c = 0.7$, with the diurnal maximum at 12:00 UTC. Integration over the canopy shows minor discrepancies with respect to the bulk A - g_s model calculation, as the profile data allows for a more precise evaluation of photosynthetic activity. The profile measurements combined with Eq. (2) therefore allows for an improved modelling of the photosynthetic CO_2 uptake of vegetation depending on height and the understanding of mechanisms. More accurate estimates of CO_2 gross primary production still require improved knowledge of plant canopy micrometeorology (Drewry et al., 2014).

3.2.3 Profile-based partitioning of H_2O and CO_2

Figure 9 shows the measured fluxes of latent heat, NEE, and soil respiration, as well as their partitioning based on the inversion of vertical high-resolution concentration profiles into the soil evaporation and plant transpiration and the R_s and NPP components. In this section, positive values indicate a flux from the surface and plants into the atmosphere and vice versa. During IOP 1, measured latent heat flux ($L_v E$, hereafter referred to as ET_{ec}) showed a typical daily pattern under clear sky conditions (Fig. 9a) with maximum ET_{ec} at noon (345 W m^{-2}). Evaporation E of both methods dis-

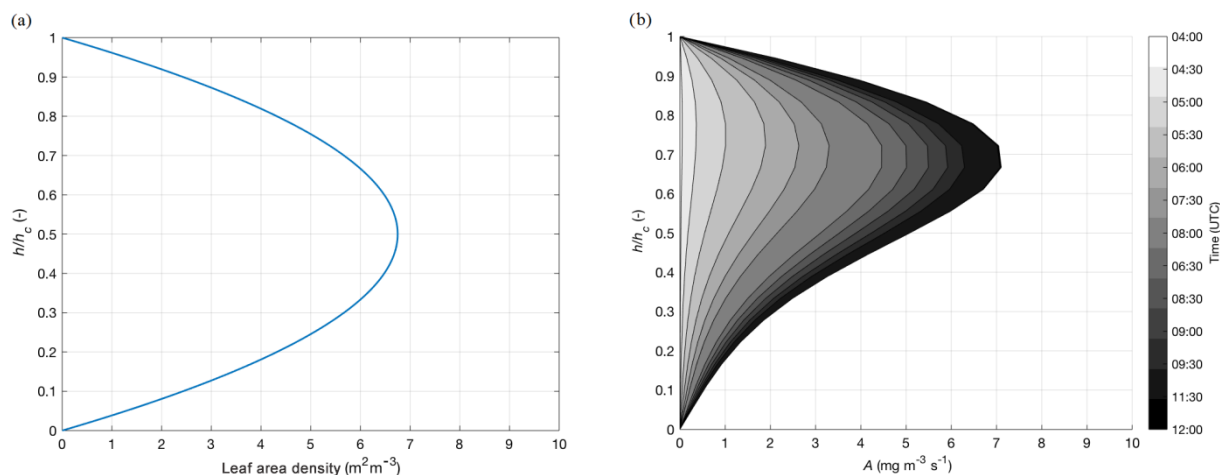


Figure 8. (a) Leaf area density ($\text{m}^2_{\text{leaf}} \text{m}^{-3}$) on 7 May 2018 as a function of height (h) normalized to the maximum canopy h (h_c). The profile is typical for winter wheat, as defined by Olesen et al. (2004). (b) Time evolution of CO_2 gross primary production A ($\text{mg m}^{-3} \text{s}^{-1}$) on 7 May 2018 as function of h normalized to h_c . The profile is obtained using the profile measurements and using Eq. (2).

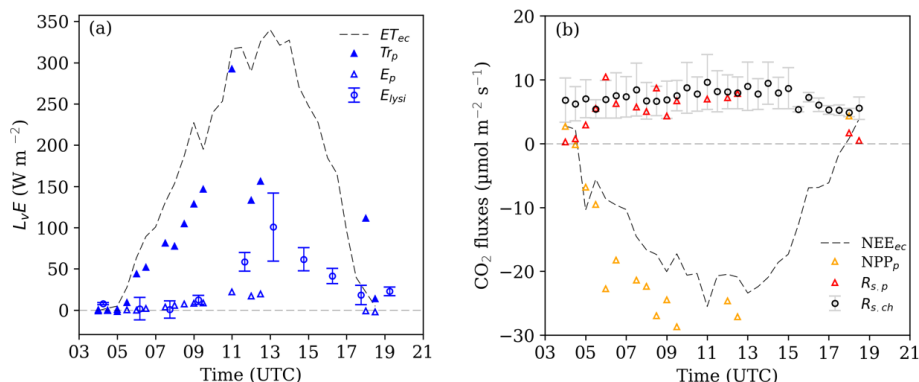


Figure 9. Source partitioning results for (a) H_2O and (b) CO_2 fluxes for IOP 1. Dashed grey lines show the measured latent heat flux (ET_{ec}) and net ecosystem exchange (NEE_{ec}) in half-hourly time steps. Values with subscript index p indicate estimates based on inversed profile concentration measurements (Sect. 3.4). Error bars for evaporation calculated from microlysimeters (E_{lysi}) and soil respiration measurements ($R_{s,ch}$) indicated to 1 SD. (ET_{ec} : evapotranspiration measured as latent heat flux $L_v E$ by the eddy covariance system; E : evaporation; Tr_p : transpiration; NPP_p : above-ground net primary production; R_s : soil respiration).

played comparable values in the morning and evening but differed at midday. In the morning, the evaporation estimated using the profile measurements and method (E_p) and the lysimeter observations (E_{lysi}) both consistently suggested low E/ET fractions with E below 10 W m^{-2} . Towards noon, E_p increased to 25 and E_{lysi} to 60 W m^{-2} , and in the afternoon E_{lysi} reached a maximum of $101 \pm 41 \text{ W m}^{-2}$ (no E_p available). Estimated Tr_p increased to about 290 W m^{-2} at 11:00 UTC, this being the highest diurnal proportion of ET. Lower Tr_p levels around 12:00 UTC are probably due to a sub-optimal performance of the profile-based partitioning at this particular time. For example, none of the available inversion methods, including the algorithm by Santos et al. (2011) used here, include the effect of local thermal stability varying with height. Figure 7 demonstrates that thermal stability increased from the canopy top towards the ground around noon

of IOP 1 (Fig. 7e), which may have contributed to the large increase of humidity towards the surface (Fig. 7b) due to the lack of mixing.

Variations in CO_2 fluxes NEE , NPP , and R_s during IOP 1 are shown in Fig. 9b. NEE_{ec} followed a typical diurnal cycle, with strong negative fluxes during the day and slightly positive values (carbon source) during transition times. The highest NEE was observed before noon ($-25 \mu\text{mol m}^{-2} \text{s}^{-1}$). NPP_p followed the graph of NEE_{ec} , with higher values ($-26 \mu\text{mol m}^{-2} \text{s}^{-1}$) in the morning hours than during the afternoon under comparable PAR values. This behaviour coincides with the photosynthesis rate observed at leaf level in Fig. 6a and provides further evidence that carbon uptake by plants was limited due to stomatal occlusion caused by the increase in VPD (Fig. 6a) and/or T_{air} in the afternoon. Profile-based $R_{s,p}$ ranged between 0.5 and $6 \mu\text{mol m}^{-2} \text{s}^{-1}$

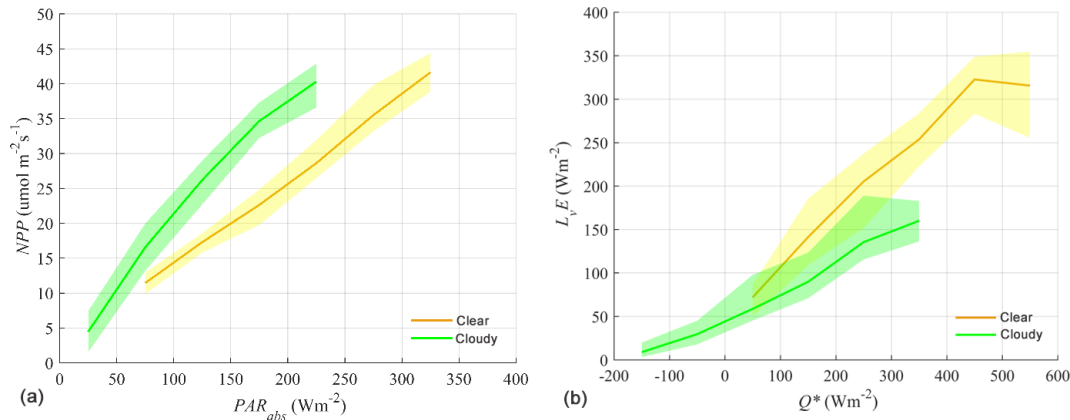


Figure 10. (a) Net primary production (NPP) versus photosynthetic active radiation (PAR). (b) Latent heat ($L_v E$) versus net radiation (Q^*). In both figures, the observation period encompasses clear and cloudy skies during a 2-week period starting on 7 May 2018 at 03:30 UTC (sunrise) and ending on the 20 May 2018 at 19:40 UTC (sunset). The solid line represents the median of the data. The lower and upper boundaries of the shaded area are the 25th and 75th percentiles of the data, respectively.

with higher values around noon. Compared to measured $R_{s,ch}$, $R_{s,p}$ lay within the standard deviations of $R_{s,ch}$, though $R_{s,p}$ was significantly lower during the morning and evening hours.

3.3 Effects of clouds on surface turbulent fluxes

3.3.1 Cloud-induced diffuse fertilization effect on evapotranspiration

One of the main aims of CloudRoots was to obtain observational evidence of the effects of clouds on the CO_2 assimilation and ET. Figure 10 shows the net primary production (NPP) (Fig. 10a) and $L_v E$ (Fig. 10b), both measured using the eddy covariance, observed under a wide range of clear and cloudy skies as a function of PAR and compared to Q^* at the top of the canopy (van Diepen and Moene, 2019). We analyse a 2-week period of observations, between 7 and 20 May 2018. The effect of the different direct and diffuse radiation due to cloud perturbations is distinguishable with an enhancement of NPP under clear conditions whereas $L_v E$ is reduced. Clouds affect plant photosynthesis by increasing the fraction of diffuse solar radiation that arrives at the top of the canopy (Kanniah et al., 2012). With a larger contribution of diffuse solar radiation and within the canopy, the radiation spreads more equally over all leaves and thereby increases the light-use efficiency of a canopy (Farquhar and Roderick, 2003). At a constant level of radiation at the top of the canopy, the increased light-use efficiency results in enhanced canopy photosynthesis, which is known as the diffuse fertilization effect (Roderick et al., 2001). This phenomenon is especially noticeable for canopies with a high LAI (Knohl and Baldocchi, 2008; Dengel and Grace, 2010). In CloudRoots and due to the high values of LAI (values between 4.5 and 5.5 m^{-2}), we expect situations in which diffuse fertilization occurs, but here the question is how it influences

$L_v E$. Previous large-eddy simulation modelling studies by Pedruzo-Bagazgoitia et al. (2017) have shown that under conditions dominated by clouds with a small optical depth, i.e. thin clouds, $L_v E$ is enhanced with respect to its clear-sky values at the same radiation level.

We find that the observed $L_v E$ is higher rather than lower during clear conditions (less diffuse light) than under more diffused cloudy conditions. At constant Q^* , the median of $L_v E$ is always higher under clear skies than for cloudy skies. The diffuse fraction plays a minor role and the decrease on $L_v E$ under cloudy conditions is mainly due to the reduction in the incoming shortwave radiation. Our observations indicate that $L_v E$ is driven by the partitioning of direct and diffuse radiation but also other effects such as diurnal variations of temperature, and the link to VPD may partially compensate for the different distribution of direct and diffuse radiation caused by clouds. The higher VPD values during the day partly offset the more optimal PAR conditions and therefore cause a closing of the stomatal that leads to decreases in $L_v E$. For both clear and cloudy skies, the shaded area below the median represents conditions before 11:30 UTC and the shaded area above the median represents conditions after 11:30 UTC, i.e. implying a hysteresis loop (Zhang et al., 2014). This spread in $L_v E$ at a constant level of Q^* is caused by a difference in VPD between morning (before 11:30 UTC) and afternoon (after 11:30 UTC). This is because on a clear day the VPD raised rapidly due to its non-linear dependence on temperature relative to a cloudy day. In a typical clear day at CloudRoots, the value of 200 W m^{-2} for Q^* is crossed twice: once in the morning and once in the afternoon. When 200 W m^{-2} is crossed in the morning, the VPD is around 1000 Pa and reaches a value of 2000 Pa in the afternoon. On the other hand, on a cloudy day with similar values of around 200 W m^{-2} the VPD remains almost constant through the entire day and with a value of 1000 Pa at 11:30 UTC.

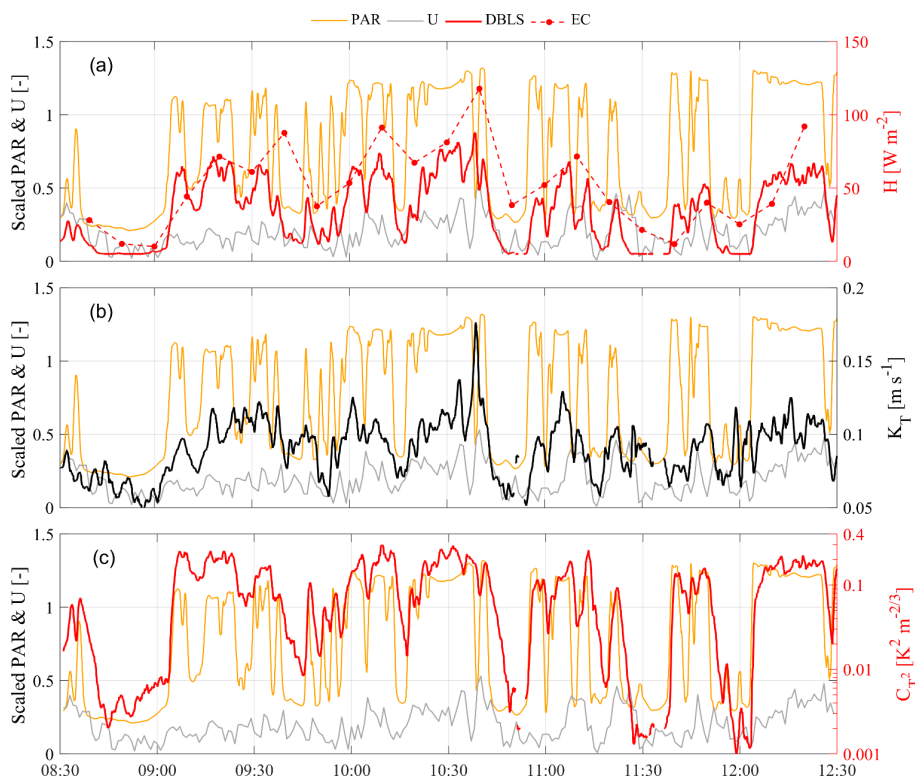


Figure 11. IOP 2 (15 June 2018) time series of (a) sensible heat flux (H) at 1 min intervals with a displaced-beam laser scintillometer (DBLS) and at 10 min intervals with an eddy covariance system (EC), combined with scaled time series of photosynthetically active radiation (PAR, scaled by $1500 \mu\text{mol m}^{-2} \text{s}^{-1}$) and wind speed (U , scaled by 6 m s^{-1}); (b) turbulent exchange coefficient K_T ; and (c) structure parameter of temperature, C_T^2 , that together make up H in the DBLS method following Eq. (1).

The influence of VPD on $L_V E$ also has the effect that the diurnal cycles of Q^* and $L_V E$ are out of phase due to its dependence on leaf temperature. Q^* is primarily a function of incoming shortwave radiation and VPD of air temperature at the leaf surface. As a result, Q^* and VPD peak at different times of the day. Q^* peaks at maximum incoming shortwave radiation (local noon is at 11:30 UTC), and near-surface VPD times when air temperature peaks, which is around the time at which $Q^* = 0$ (17:00 UTC). The diurnal cycle of the sun implies there is a short period around 11:30 UTC when Q^* does not change. On the contrary, air temperature increases almost linearly around 11:30 UTC due to the approximately constant Q^* , as does VPD. Therefore, peak values for $L_V E$ are found between the moments of maximum Q^* and of maximum VPD. For this dataset, the peak of $L_V E$ is around 12:00 UTC for both clear and cloudy skies, although the peak for cloudy skies is less distinct due to the more fluctuating daily cycle of Q^* . Because Q^* and $L_V E$ are out of phase, the highest values for $L_V E$ do not occur in the bin with the highest net radiation, but rather in the bin of $400\text{--}500 \text{ W m}^{-2}$ (which roughly contains data from 11:00 UTC and after 12:00 UTC).

3.3.2 Cloud-induced radiation perturbations and response by turbulent fluxes

The short interval fluxes (1 min) of the double-beam laser scintillometer (DBLS) technique enable us to study the vegetation response to rapid radiation perturbations due to changes in cloud cover. The goal here is to illustrate this potential by discussing selected time series under changing cloud conditions during IOP 2. The morning of IOP 2 was characterized by rapidly changing cloud conditions due to the overpass of a shallow cumulus cloud deck. A breakdown of the 1 min DBLS sensible heat flux in terms of contributions from turbulent exchange (K_T) and the measure for temperature fluctuations (C_T^2) is given in Fig. 11. This figure also depicts, on the same axes, scaled time series of wind speed and PAR that can be regarded as proxies that fuel mechanically induced turbulence (wind speed) and buoyancy turbulence (radiation in general) as well as photosynthesis (PAR).

First of all, the 1 min DBLS fluxes of H closely follow the cloud cover induced radiation changes, but with a time-lag of 45–120 s (Fig. 11a). This is similar to those reported by van Kesteren et al. (2013b). H fluxes measured with EC techniques even when estimated over the relatively short interval of 10 min, which is not a standard output, are not capable of

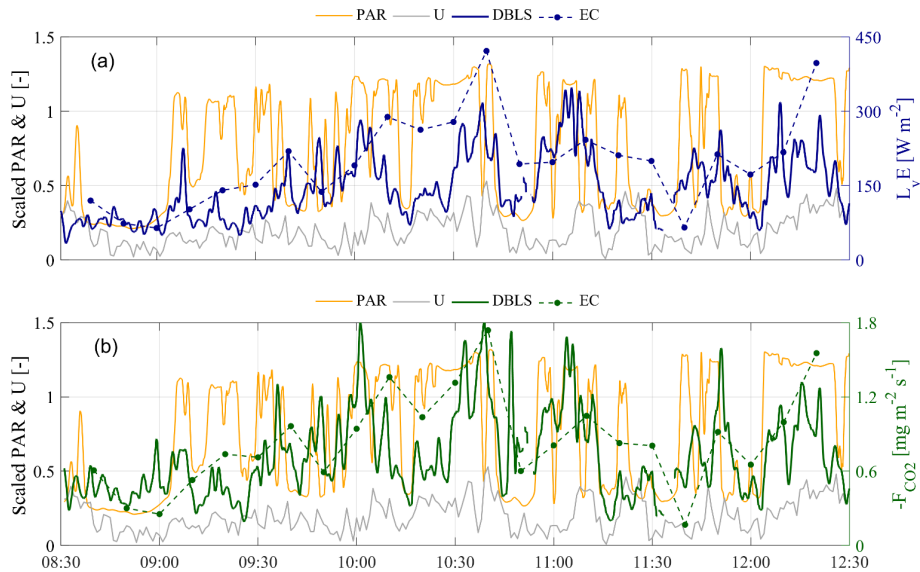


Figure 12. IOP 2 (15 June 2018) time-series of (a) latent heat fluxes (L_v) at 1 min intervals with a displaced-beam laser scintillometer (DBLS) and at 10 min intervals with an eddy covariance system (EC) combined with scaled time series of photosynthetically active radiation (PAR, scaled by $1500 \mu\text{mol m}^{-2} \text{s}^{-1}$) and wind speed (U , scaled by 6 ms^{-1}). Panel (b) is the same as (a) but for the CO_2 flux (F_{CO_2}).

capturing such rapid dynamic behaviour of the flux regime (Fig. 11a). The dynamic behaviour in the DBLS H is mainly governed by fluctuations in T expressed by C_T^2 (Fig. 11c) and to a lesser extent by changes in the exchange coefficient K_T (Fig. 11b). Note that it is impossible to fully distinguish the three variables H , K_T , and C_T^2 from each other as they are all interconnected, e.g. K_T is defined in terms of the Obukhov length L , which in turn depends on H and u_* . Nevertheless, our high-time-resolution observations demonstrate that changes in PAR induce very fast responses of the transported quantity T (Fig. 11c). Even in the absence of strong wind-induced variations in K_T , these T variations lead to approximately similar dynamic behaviour of H . On top of this, the additional but smaller wind-induced fluctuations in K_T are also reflected in H and lead to “noise” in the variability of H compared to the cloud-induced on–off behaviour of PAR.

Next we examine how soon the fluxes of H_2O and CO_2 respond to the cloud induced radiation changes. Figure 12 demonstrates that there is indeed a fast response, and the 1 min resolution fluxes of H_2O and CO_2 allow us to precisely determine a delay time of approximately 2 min for the increases in CO_2 uptake and transpiration of H_2O relative to the changes in PAR. The delay is once again undetectable with the standard 30 min eddy covariance results (Fig. 12). This behaviour is in line with what was concluded about the state of the vegetation observed at leaf level (Sect. 3.1). As the vegetation is not water-stressed and is at a stage of development at which it is still actively growing, it will react rapidly to changes in radiation, i.e. it is in a radiation-limited regime. Under the conditions of our study, stomata appear to have reacted only slowly or remained constantly

open because leaves were unstressed or reacting only slowly to cloud-induced changes. Moreover, the timescale of a light-induced stomatal response (maximum values of 20 min; Van Kesteren, 2013b) is normally larger than the timescale of most fluctuations in radiation. Our suggested explanation is that the 1 to 2 min delay time observed between radiation and turbulent fluxes is due to processes associated with the inertia of the leaf in addition to turbulent transport between the leaf and laser path due to, e.g. the small but not negligible storage of heat, H_2O and CO_2 in the canopy layer. However, we need further evidence to disentangle the separation in delays between H_2O and CO_2 fluxes.

3.4 Sun-induced fluorescence (SIF) measurements: temporal variability

Studying spatial and seasonal variabilities in ET during plant growth was one of the key goals of CloudRoots. To this end, we analysed SIF observations measured on time and on space. The top-of-canopy measurements of SIF were carried out in two ways: (i) diurnal courses from a single representative location were recorded from a stationary FLOX system, and (ii) mobile measurements covering several locations within a field were recorded from a FLOX system that was housed in a backpack. To ensure reproducible measurements, the two fibre optics of the system were attached to a gimbal and were placed with a movable tripod 2 m above ground. Diurnal curves were acquired on 7 May, 4 June, and 14 June (only morning hours due to cloudy conditions in afternoon); mobile measurements (with change of measurement locations during the day) on 6 and 26 June. As SIF measurements should be performed under clear-sky conditions only, records

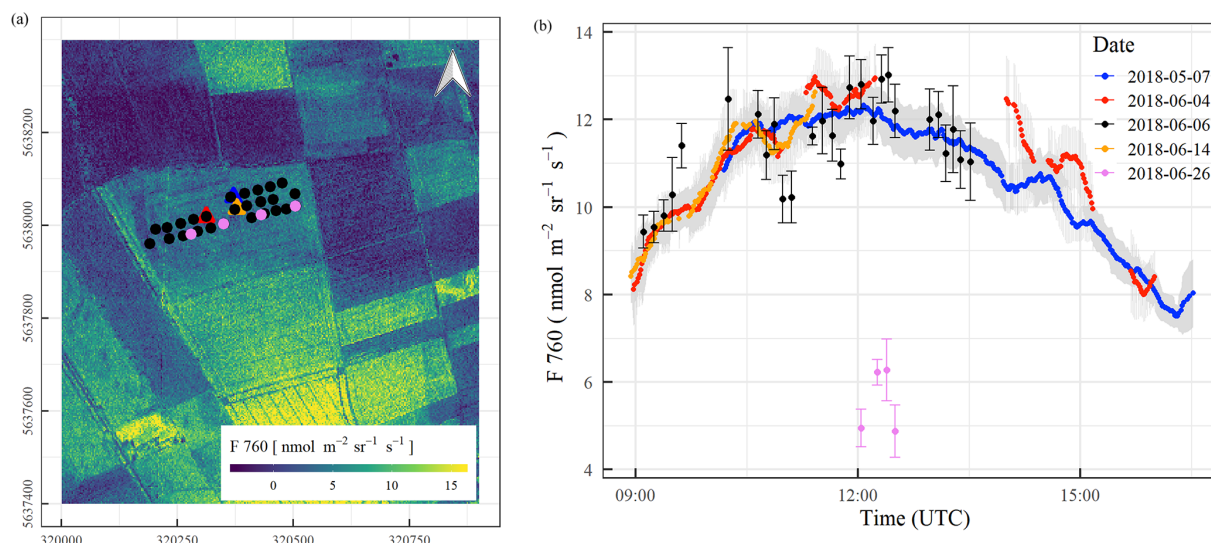


Figure 13. (a) Aerial map of F_{760} on 26 June 2018 with measurement locations used to combine with mobile (circles) and stationary (triangles) measurements. (b) Diurnal changes in F_{760} on different days of the campaign as 5 min measurement averages depicted in the same colours as observation locations in (a).

affected by clouds were carefully removed. Aerial maps of SIF were acquired with the high-resolution imaging spectrometer HyPlant. Figure 13a shows the aerial map of F_{760} acquired on 26 June, suggesting homogeneous canopy properties within the winter wheat study field, while great differences can be seen between different fields. The same image identifies the FloxBox measurement locations in the same colour code that reconstruct the diurnal temporal variability of F_{760} during the entire CloudRoots campaign in Fig. 13b.

Diurnal changes in photosynthetic activity are clearly visible in F_{760} . Measurements made at different locations generally follow the same diurnal pattern, especially within the period 7 May to 14 June, further confirming the hypothesis that ET spatial heterogeneity within the winter wheat field was small. The seasonal changes are also traced by F_{760} : from 7 May until 14 June, the winter wheat canopy was photosynthetically active in a transition stage from booting (7 May) until grain filling (14 June), as is reflected by high SIF values. At the end of June, however, the canopy approached senescence and the reduction in photosynthesis was documented by greatly reduced fluorescence levels (see Fig. 13b, see pink values after 12:00 UTC). This photosynthesis reduction is also corroborated by the normalised difference vegetation index (NDVI), which was calculated as the normalized difference between far-red to red reflectance (see Supplement for details). The green dense canopy has a NDVI value close to 1, and the decrease in NDVI is caused by the yellowish colour of the winter wheat canopy (see Fig. S2 at the Supplement).

3.5 Connecting SIF and evapotranspiration flux at the landscape scale

It is difficult to directly quantify spatial variations in the ET flux with the currently available in-situ equipment due to the necessity of installing a large number of measurement stations. Recently, some promising concepts have been published that exploit the relationship between SIF and plant water relations (Damm et al., 2018; Jonard et al., 2020). Following these concepts, we studied the connections between ET to regional measurements of SIF in two steps, which were recorded on this scale by the airborne sensor HyPlant (see Fig. 13a). First, to obtain an estimation of the spatial variability ET at CloudRoots, we used the $15 \text{ km} \times 15 \text{ km}$ map acquired by the HyPlant sensor on 26 June 2018 and a land use classification of the region (Lussem, 2018). ET cannot directly be measured, thus, it was predicted using different coefficients (K_c) that depend on the land use categories around CloudRoots. We define K_c as the ratio of ET over a particular crop relative to the ET of potential grass used as reference (Allen et al., 1998; Bogaen et al., 2010). For this analysis, the regional land use map that consisted of 32 different land use classes was translated to a reduced classification scheme of 9 land use classes, which covered most of the vegetation types in the study region (Table 4). Roads were excluded from the analyses, as we assumed that their effect is negligible on the $15 \text{ m} \times 15 \text{ m}$ grid.

For the estimation of K_c coefficients to calculate ET, we used the plant developmental stage at the CloudRoots site at the end of June. For the main regional crops, namely sugar beet, winter wheat, winter barley, and potatoes, local measurements of evapotranspiration by EC towers were used.

Table 4. Estimated K_c coefficients for different land use classes that are dominant in the study area. The land use classes were calculated using a more detailed land use classification that consisted of 32 classes. For this study several classes that have similar transpiration rates were combined.

	Land use class	K_c	Main surface types included
1.	Impervious	0.0	Roads, urban areas, industrial areas
2.	Bare soil	0.2	Bare fields, incl. harvested fields with rapeseed harvest residuals
3.	Needle forest	0.5	Managed spruce and pine forest
4.	Broadleaf forest	0.7	Broadleaf forest, scrubs
5.	Early crops (senescence)	0.6	Winter barley
6.	Early crops (approaching senescence)	0.7	Winter wheat
7.	Grassland	0.8	Natural grasslands, urban grasslands
8.	Late crops	1.1	Sugar beet, potato
9.	Maize	1.2	Maize

These data have been collected over several years and weekly averaged. This enabled us to compute K_c from measured and potential ET averaged over the last 2 weeks of June. In the particular cases of winter wheat and winter barley especially, the K_c coefficient changes rapidly at this time of the year, in extreme cases from 1.0 to 0.3 within 2 weeks, due to the onset of senescence. Therefore, the coefficients for these two crops shall be used with care. In absence of eddy covariance data, we calculate the characteristic values of K_c for each crop type and the developmental stage were taken from Allen et al. (1998). All estimated K_c coefficients for different crops can be found in Table 4. To estimate the ET over a specific area occupied by particular crop on a given day and time, the land use map was transferred to the map of K_c coefficients according to Table 4 and then multiplied by the potential ET, using the ET grass as a reference value (ET_{grass}), specific to that moment in time. Figure 14 shows the spatial variability of predicted ET for the IOP 3 inferred from the K_c coefficients and the value of potential grass reference averaged between 09:00 and 14:00 UTC. The area is a 1 km × 1 km square, characterized by a mean of 5.76 mmol m⁻² s⁻¹ and a standard deviation of 1.86 mmol m⁻² s⁻¹. Figure 14 shows that this method can provide plausible information on the variability of ET at the sub-kilometre scale, and it points out to the need to introduce this sub-grid ET variability information in modelling studies. In the second step of the procedure, we compared this estimated ET to the SIF measurements (F_{760}). Figure 15 shows the correlation between estimated ET and solar-induced fluorescence F_{760} for 26 June (Julian day 177) for the different land covers. The correlation between mean F_{760} values and predicted ET values is $R^2 = 0.61$ with larger ET and F_{760} values for crops and grass compared to the forest conditions. It is calculated from the comparison pixel by pixel of the SIF (Fig. 13a) and ET (Fig. 14). As the HyPlant overflight was carried out at noon in order to acquire the maximal SIF values and minimize the influence of changing sun angle, we also used the maximal value of ET grass, measured at midday on 26 June. The large

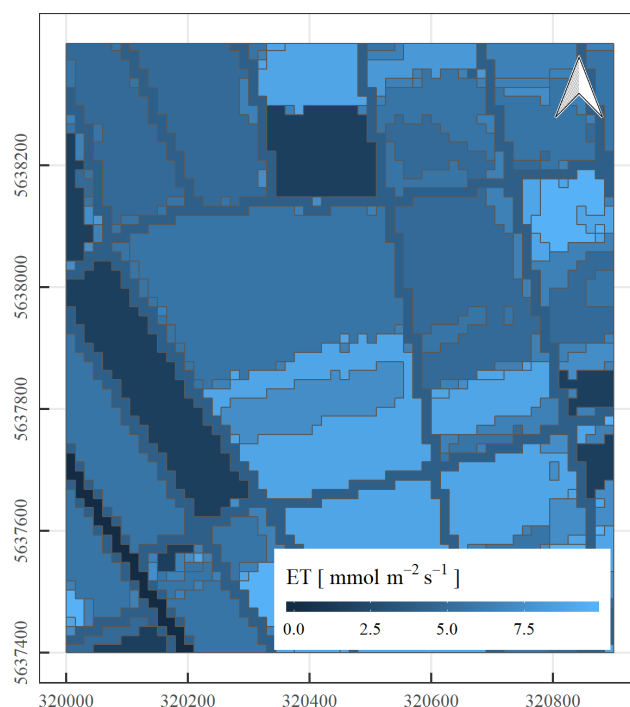


Figure 14. Spatial variability of evapotranspiration inferred from combining K_c coefficients with the value of potential grass reference ET_{grass}. The x and y axes represent the geographical coordinates of the CloudRoots site in metres (50°52′09″ N, 6°27′01″ E).

range of values of ET, F_{760} , and F_{687} from the different land use categories corroborate the large variability of ET around the CloudRoots field.

3.6 Boundary layer integrated dynamics over heterogeneous landscapes

To integrate and improve the interpretation of our observations, we used CLASS to model the cloudless day 7 May 2018 (IOP 1). Our specific aims, related to the scales

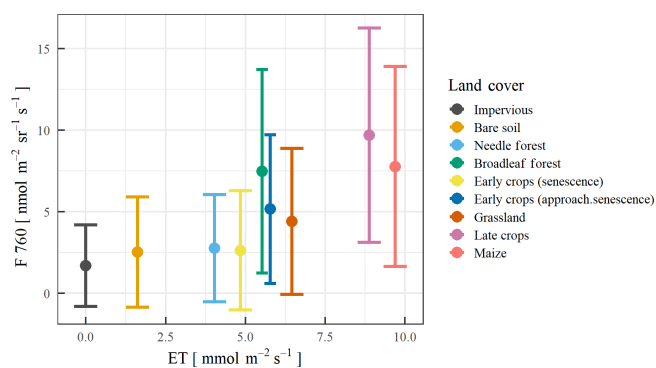


Figure 15. Relation between evapotranspiration (ET) and fluorescence F_{760} , including the standard deviation for the nine land use categories defined in Table 4. The data were collected on 26 June 2018.

and processes under study, are (i) at leaf level to make use of the new constants in the mechanistic $A-g_s$ model obtained from the observations (Fig. 5 and Table 3), (ii) at a landscape scale to represent the sensible heat flux in a heterogeneous landscape, and (iii) to estimate the potential impact of advection (heat) on the diurnal evolution of surface and boundary layer variables. Table A2 summarizes all initial and boundary conditions, constrained by the observations, which are employed in the modelling of the surface and atmospheric variables. Figure 16 compares the model results with the surface and upper-air observations. Focusing first on Fig. 16a, we found that the modelled H largely overestimates the observations taken at the CloudRoots. However, comparing our modelled H with the estimate of the regional flux shown in Fig. 1b, we found a satisfactory agreement in terms of magnitude and diurnal variability between this regional observed flux and CLASS model calculation. Note that here, and compared to Table 4, we oversimplified the land surface into two categories: “bare soil” and “vegetated”. To complete this evaluation, we show in Fig. S1 the impact of the optimized $A-g_s$ constants presented in Table 3 (CloudRoots) versus the default ones. Both the evolution of surface fluxes and boundary layer height are in better agreement with the observations. Similar impacts on how leaf processes (rice) can influence the meteorology were reported by Ikawa et al. (2018). There the boundary layer temperature changed by up to 0.5 K depending on the constants used in the leaf photosynthesis model.

Our explanation of the improved comparison between the observations and the CLASS results using the aggregated sensible heat flux is the following: in a heterogeneous landscape such as the location of CloudRoots (Fig. 1a), each surface type contributes its own latent and sensible heat fluxes. It is the landscape aggregate of heat fluxes (named regionally and shown with triangles in Fig. 16a and introduced in Fig. 1b) and more specifically the sensible heat flux that governs the boundary layer evolution in terms of height, po-

tential temperature, specific humidity, and atmospheric constituents. Only by using this higher H do we obtain satisfactory agreement with the observed boundary layer height evolution, which reaches its maximum values at around 1500 m in the afternoon (Fig. 8b). This further emphasizes that the H measured with the EC instrument during CloudRoots is only representative of the specific measurement site (leaf and canopy scales). The landscape average is an aggregate of values of H made up of the mosaic of surfaces as shown in Fig. 1. As a consequence, it is this composite H rather than a local value of H that is the main driver of the boundary layer development (boundary layer scales). With regard to ET, the model results are in good agreement with the local CloudRoots observations. This indicates the secondary and more local role played by ET in the dynamics of boundary layer development. For studies focusing on the regional values of ET, it will be necessary to calculate landscape-scale aggregate following the same procedures as H , while for studies at the leaf and canopy scales the local observations of ET are representative. Focusing now on Fig. 16b, we found a satisfactory agreement between the modelled boundary layer height and the three independent observations made with three different instruments. In Fig. 16b, it is interesting to note that the ABL height (75 km) inferred by the radio sounding measurement collected more than 100 km from of the Cloud Roots site has values similar to those collected by the lidar located within a radius of 5 km from the CloudRoots site. We attribute these similar values to a boundary layer that is characterized by being spatially homogeneous and with a similar temporal evolution on the larger regional scale.

CLASS, besides solving the diurnal variability of the boundary layer dynamics and the state variables, offers the possibility of adding a large-scale contribution that represents the advection of heat and/or moisture (see Vilà-Guerau de Arellano et al., 2015). We have performed a sensitivity analysis to determine the role played by heat advection for the surface fluxes and the boundary layer development. In the specific case that is modelled on 7 May, we relate this advection of heat or moisture to the diurnal evolution of H contrast between the measurement site and its adjacent fields, i.e. horizontal transport of heat, moisture, or momentum is driven by secondary circulations induced by the different thermal characteristics of the fields around the CloudRoots site (Fig. 1a). More specifically, we prescribe an advective heat contribution to represent the horizontal transport of heat due to the thermal variability of the surface conditions. This term follows an exponential function (Table A2 in Appendix A) with maximum positive values of advection equal to 0.9 K h^{-1} at midday. This advective term is imposed only on the mixed layer and not on the free troposphere. Figure 16 shows how this advection of warm air to the CloudRoots site influences the boundary layer height. Starting with H , warm advection leads to higher mixed-layer temperatures that reduce the gradient between the temperature at the surface and the atmosphere, and thus reduce H . We find an opposite effect

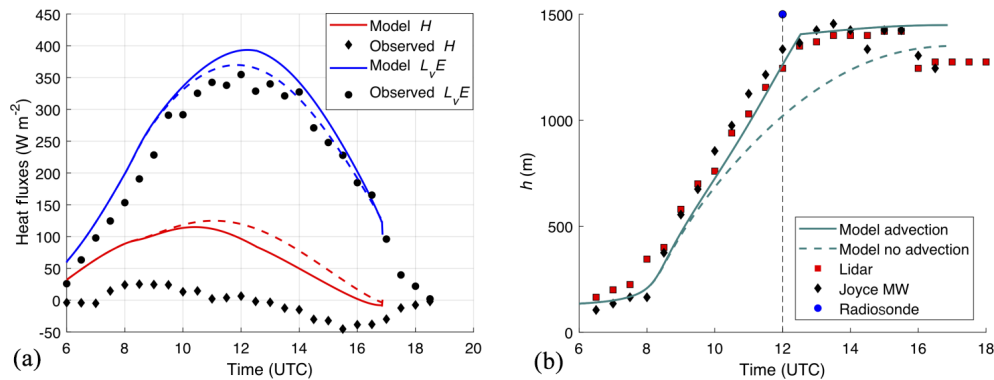


Figure 16. Comparison of the model and observed results of 7 May 2018: (a) surface fluxes and (b) boundary layer depth. The regional H , an aggregate that combines the vegetated and bare soil surfaces around the CloudRoots site as shown in Fig. 1b, is also included. For the boundary layer depth estimations, we used three different observational techniques. The lidar and microwave (MW) techniques were located at the JOYCE site facility. Solid and dashed lines represent the model results of surface fluxes and boundary layer height with and without imposing the advection of heat, respectively (Table A2), for completing the information on initial and boundary conditions.

on ET. The increase in temperature by advection of warm air leads to an increased atmospheric demand, and therefore enhances ET. With regard to the boundary layer height, we might suppose that a drop in H would lead to a decrease of the boundary layer growth. However, the modelled boundary layer height displays the opposite behaviour. This is because the lower H is partly offset by a decrease in the thermal inversion at the interface between the boundary layer and the free troposphere. Lower values of the difference in θ_v between the free troposphere and the mixed layer enable boundary layer air parcels to be more easily transported into the free troposphere, resulting in faster growth of the boundary layer. This is because of the virtual potential temperature between the environment and the parcel is effectively reduced. The CLASS model results show that this process is more important than the decrease in H at the surface, and it allows the boundary layer to grow deeper than in the numerical experiment in which the warm advection is omitted. These numerical sensitivity experiment analyses enable us to quantify how non-local processes, in particular the effects of the regional average H and of warm advection, influence the observations at the measurement site.

4 Discussion

CloudRoots offers an integrated methodology that combines field experiments across spatial scales (from leaf to landscape) closely linked to the modelling of the diurnal variability of the soil–plant–atmosphere continuum. To frame the discussion and link all our observations at the various scales and modelling efforts, we present in Fig. 17 all the different estimates of ET obtained during the three IOPs, averaged between 09:00 and 14:00 UTC in order to avoid the morning and afternoon transitions. Plotted alongside the ET estimates, we showed the leaf-level measurement of g_{sw} to indicate the

control of vegetation on canopy-level ET. The four instrumental techniques are sap flow, eddy covariance (EC), scintillometer (averaged over 30 min and 1 min), ET inferred by the profile lift measurements, and ET infrared from the SIF observations. The ET modelled by CLASS is also included for IOP 1.

In comparing ET from the three IOPs, we find significant differences in magnitude from different techniques. In general, the highest values of ET are observed during IOP 1. The three IOPs were characterized by differences in the stages of growth, from very active vegetation to senescent vegetation, and influenced by a range of weather conditions: IOP 1 cloudless, IOP 2 scattered and thick clouds, and IOP 3 shallow cumuli. It is surprising that the decay in the vegetation activity as quantified by the measurements of leaf conductivity (Fig. 3d, e, f) is less evident in differentiating IOP 3 (senescent stage) from the more active vegetation at IOP 1 and 2. Furthermore, we observed, moving from IOP 1 to IOP 3, a much stronger decline in g_{sw} , suggesting that stomatal closure compensated for increased atmospheric moisture demand.

Several conclusions can be drawn from this intercomparison of ET observations using different techniques. Firstly, we might expect that the EC and scintillometer measurements, both with larger footprint and the inclusion of the soil evaporation contribution, show a net total ET that is similar to or higher than that obtained by the sap flow measurements. Secondly, we observed a far more pronounced response in declining g_{sw} compared to all ET measurements. These results point to the need to more accurately measure the leaf energy balance to take the penetration of radiation in the canopy under clear and cloudy conditions into account. This would also require a revision of scaling procedure from the leaf to the canopy level. Secondly, it is known that the EC flux measurements normally underestimate the sensible and latent heat

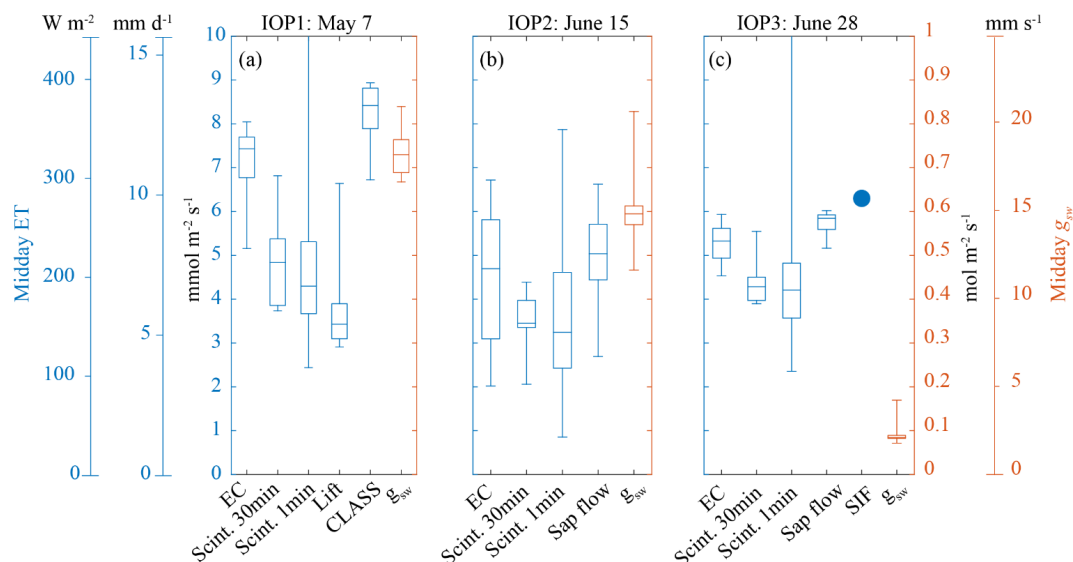


Figure 17. Summary of midday evapotranspiration collected using different instrumental techniques during (a) IOP 1, (b) IOP 2, and (c) IOP 3. ET fluxes (left y axis) and g_{sw} (right y axis) reflect the period from 09:00 to 14:00 UTC. Box plots denote the variability in 30 min measurement intervals, except for the 1 min scintillometer measurements. The central mark of each box indicates the median, and the bottom and top edges of the box indicate the 25th and 75th percentiles, respectively. The acronyms are eddy covariance (EC), scintillometer (Scint) with 30 min and 1 min averages, ET inferred from the lift profiles (Lift), sap flow, ET calculated with the CLASS model, and ET inferred from the sun-induced fluorescence (SIF).

fluxes because the EC flux measurements filter out the low frequencies (Foken et al., 2008; Gao et al., 2017). This underestimation is difficult to determine, but as a first guess and related to Fig. 17, the underestimation might range between 10 % and 15 %.

Although the contribution of soil evaporation is small compared to plant transpiration due to the high vegetation cover, we need to stress that EC and scintillometer observations are similar to or smaller than the ET observed or inferred from the other techniques (Fig. 17). This highlights the difficulty of estimating ET due to the need to include and quantify the contributions of the four fundamental processes: soil evaporation, upscaled leaf transpiration, evaporation related to the sap flow and the two non-local processes, entrainment of dry air, and horizontal advection of heat and moisture. Here, the modelling of ET, taking into account for and integrating all these processes, enables us to discriminate among these processes and calculate the budget of ET as a function of these local and non-local contributions. In that respect, the CLASS model is a tool capable of efficiently combining observations and model results that integrate surface and boundary layer dynamics. The averaged modelled ET is at the higher range of the ET observed estimations during IOP 1.

With respect to the differences between the 1 min and 30 min series measured by the scintillometer, their median is very similar in the three IOPs. However, differences become larger at smaller timescales due to the non-steadiness of ET under the presence of clouds. Here, the 1 min flux calculated

from the scintillometer can capture the rapid and large fluctuations by clouds (Fig. 12) and the maximum values in particular. In order to obtain more definitive conclusions on how ET varies under cloud conditions, we need to analyse other situations characterized by different diurnal cloud cycles in more detail and systematically relate ET to key cloud characteristics such as the cloud optimal depth to determine how cloud thickness influences ET and the timescale of the cloud passage.

Regarding the quantification of the different processes contributing to ET, Fig. 9 illustrates the need to continue to test analytical techniques to identify the individual contributions of soil and plants to determine the diurnal ET budget. A possibly useful tracer would be the stable isotopic composition of water vapour and carbon dioxide (Lee et al., 2009; Griffis 2013) and, combined with isotope signals, for modelling the surface and boundary layer dynamics with the carbon and water exchanges. To further discriminate between soil and plant sources and sinks under unsteady conditions due to radiation and dynamic perturbations by cloud shading, these high-frequency stable isotope measurements should go beyond the typical average time of eddy covariance (30 min). As van Keesteren et al. (2013) showed and is further corroborated in this work, the scintillometer technique combined with high-frequency observations of H_2O and CO_2 enable us to quantify the response time of ET and CO_2 assimilation to these intermittent radiation fluctuations or cloud flecks (Kaiser et al., 2018).

Finally, the integration of all processes in the CLASS model shows the challenges in interpreting the measurements taken at the sub-kilometre scales and adequately representing the surface turbulent fluxes. Although the measurements indicate that the day selected for the modelling displayed a very homogeneous boundary layer depth over an area with a radius of 100 km², the sensible heat flux measured at the CloudRoots facility was not representative of it. Therefore, we recommend extending the number of stations by means of a multi-tower approach that would also include detailed observations of the soil and plant conditions. In addition to obtaining a more representative field sensible heat flux that is better related to the development of the boundary layer, a denser network of spatial observation stations is also necessary to estimate the role of hectometre-scale heterogeneity-induced circulations and their relationships with the local advection of heat and moisture more accurately (Mauder et al., 2010).

5 Conclusions

Our main findings, organized from the smaller to the larger scales observed and modelled, are summarized as follows:

At leaf scale, we find that stomatal conductance and gross primary production decrease in line with the increasing senescence of the plant. The tiller-level measurements of the sap flow are virtually constant throughout the growing period. Underlying causes need to be further investigated under controlled conditions. The successful modelling of the leaf stomatal conductance and the photosynthesis assimilations required the relevant constants used in the mechanistic model ($A-g_s$) in the field to be measured. Modelled leaf-level photosynthesis compares better with the measurements during the mature growing period than during senescence. For future field experiments, we recommend including leaf-level measurements in meteorological campaigns to improve calculations related to the water–carbon leaf and canopy exchanges.

At canopy scale, the high-frequency vertical profiles – measured in and above the canopy – of wind speed, potential temperature, specific humidity, and carbon dioxide prove to be very valuable in obtaining profiles of gross primary production in the canopy and as a function of height. By inverting these observed profiles, we obtain an estimate of the contributions of soils and plants to the net evapotranspiration and CO₂ ecosystem exchange. The validation against individual measurements of these components gives better results for the net ecosystem exchange than those for the net evapotranspiration. We argue that for evapotranspiration the dependence on temperature and water vapour deficit plays a more important role than for CO₂ assimilation, the latter being mainly controlled by the partitioning between direct and diffuse radiation.

Under cloud conditions, we show that the perturbation by clouds of direct and diffuse radiation create large fluctuations in evapotranspiration and the CO₂ assimilation with opposite signs for evapotranspiration and CO₂ exchange. A cloudy boundary layer reduces evapotranspiration, whereas it enhances plant assimilation of CO₂. The 1 min turbulent fluxes acquired by the scintillometer demonstrate the relevance of flux measurements observed at higher frequencies for improving quantification of the impact of clouds on the photosynthetically active radiation. With these fast turbulent fluxes, we quantify delays of the turbulent fluxes with respect to the photosynthetically active radiation. These delays are on the order of minutes. Comparing these 1 min flux estimates with the standard 30 min average measured with the eddy covariance technique, we find a lower median and a large increase in the variability of the net evapotranspiration. This information can be useful in determining the impact of rapid fluctuations driven by the impact of clouds on evapotranspiration and its impact on the closure of the surface energy balance.

At landscape and boundary layer integrated scales, the modelled sensible heat flux correlates better with the area-weighted average flux than the local flux estimates. The area-weighted flux integrates in a simple manner a composite of bare soil and vegetated surfaces at regional scale (kilometres). This aggregate regional flux is representative of an area that is larger than the CloudRoots site (100 m × 100 m). Therefore, a model setup that represents the boundary layer evolution well only needed to be informed by the area-weighted average of two main surface types, bare soil, and vegetated areas. The variations of ET due to surface heterogeneity were also measured and inferred from airborne sun-induced fluorescence observations. Our findings corroborate the large heterogeneity of ET at the sub-kilometre scales with values ranging from forest (about 2.5 mmol m⁻² s⁻¹) to late crops such as potato or sugar beet (8–10 mmol m⁻² s⁻¹).

The comparison of all the ET measurements at the various scales show that there are still large differences in observing ET among the different observing techniques, the modelling of ET and their relation to stomatal aperture during the entire growing season. These ET observations do not show a clear pattern related to the scale at which they were measured.

The modelling and scale integration of this comprehensive observational dataset enables us to study the carbon and water exchange at leaf, canopy, and landscape levels. It also allows us to quantify how horizontal advection of heat within the mixed layer influences the surface fluxes and the growth of the atmospheric boundary layer. We show, for instance, that the horizontal advection of heat leads to deeper boundary layer depths. This numerical experiment thus paves the way to more complete modelling studies, for instance using large-eddy simulation numerical experiments, on how the surface and the overlaying atmosphere interact on sub-diurnal and sub-kilometre scales.

Appendix A: Construction of light and radiation response curves under clear and cloudy conditions

For the construction of the light and radiation response curves in Fig. 10, the data were divided into bins of PAR and Q^* . For Fig. 10a, we divided the data points in bins of incoming total PAR. Each bin covers a range of 50 W m^{-2} , starting at $0\text{--}50 \text{ W m}^{-2}$ and presumably ending at around $350\text{--}400 \text{ W m}^{-2}$ (maximal intensity for incoming direct PAR). For Fig. 10b and the variable Q^* , each bin covers a range of 100 W m^{-2} , starting at -200 to 100 W m^{-2} for cloudy skies and at 0 to 100 W m^{-2} for clear skies. In both figures, for each data point the diffuse fraction of PAR is determined by combining measurements of incoming total PAR and incoming diffuse PAR. Subsequently, a data point is labelled “clear” for diffuse fractions <0.3 and labelled “cloudy” for diffuse fractions >0.8 . We choose these boundaries to balance a distinct difference between clear and cloudy skies with a large enough sample size for each bin. For clear skies, the first two bins are missing. This is due to the fact that under clear skies low levels of Q^* are the result of the sun being close to the horizon, and as a result solar radiation has to travel a long distance through the atmosphere before reaching the surface. In those cases, most of the solar radiation reaches the surface as diffuse radiation due to Rayleigh scattering and scattering by aerosols, and therefore does not meet the criteria to be labelled “clear”. For cloudy skies, bins are missing for high levels of Q^* . Clouds attenuate solar radiation through absorption and backscattering, and thereby reduce Q^* to a level lower than it would be for a clear sky.

Table A1. Management activities on the test site over the winter wheat cultivation cycle before, during, and after the observation period of the CloudRoots campaign.

Date	Management	Product
25 Oct 2018	sowing crop seeds (weight of seeds)	156 kg ha^{-1} winter wheat (Premio)
8 Mar 2018	fertilization	$81.6 \text{ kg N ha}^{-1}$
9 Apr 2018	herbicide treatment	200 g ha^{-1} Broadway
9 Apr 2018	herbicide treatment	1 L ha^{-1} CCC720
22 Apr 2018	fertilization	$39.2 \text{ kg N ha}^{-1}$
2 May 2018	fungicide treatment	1 L ha^{-1} Capalo
2 May 2018	fungicide treatment	0.3 L ha^{-1} Corbel
2 May 2018	herbicide treatment	0.3 L ha^{-1} CCC720
16 May 2018	fertilization	50 kg N ha^{-1}
19 May 2018	fungicide treatment	1.5 L ha^{-1} Adexar
19 May 2018	fungicide treatment	0.5 L ha^{-1} Diamant
19 May 2018	insecticide treatment	0.3 L ha^{-1} Bulldock
16 Jul 2018	harvesting	winter wheat, 92 dt ha^{-1}
19 Jul 2018	straw pressed and removed	
25 Aug 2018	ploughing	
18 Sep 2018	harrowing	

Table A2. Initial and boundary conditions prescribed in CLASS to reproduce IOP 1 (7 May 2018).

Mixed-layer model parameters		
Parameter (units)	Value	Source
Time steps (s)	60	–
Runtime (s)	50 400	–
Residual-layer starting height (z_{i0})	135	Joyce microwave
Surface layer top height (m)	1400	radiosonde
Surface pressure (Pa)	100 600	EC pressure gauge
Large-scale wind divergence (s^{-1})	0	default
f_c ($m s^{-1}$)	1.10^{-4}	latitude
Coriolis parameter (–)	0.2	default
Potential temperature		
Initial mixed-layer temperature (K)	286.2	profile data and radiosonde
Jump in potential temperature from boundary layer to free troposphere (K)	4	radiosonde
Jump in potential temperature from boundary layer to residual layer (K)	4.4	radiosonde
Free troposphere lapse rate for potential temperature ($z_{i0} < 1400$ m) (K)	4.9×10^{-3}	radiosonde
Free troposphere lapse rate for potential temperature ($z_{i0} > 1400$ m) (K)	6.2×10^{-3}	radiosonde
Advection of heat into the mixed layer ($K s^{-1}$)	$2.5 \times 10^{-4} e^{-\frac{t[UTC]-12}{5}}$	
Specific humidity		
Initial function mixed-layer specific humidity ($kg kg^{-1}$)		0.0067–0.0004 ($t[UTC]-6.5$)
Residual-layer lapse rate for specific humidity ($kg kg^{-1} m^{-1}$)	-1.4×10^{-3}	radiosonde
Free troposphere lapse rate for specific humidity ($z_{i0} < 1400$ m) ($kg kg^{-1} m^{-1}$)	-2.7×10^{-6}	radiosonde
Free troposphere lapse rate for specific humidity ($z_{i0} > 1400$ m) ($kg kg^{-1} m^{-1}$)	-9.0×10^{-6}	radiosonde
Advection of specific humidity into the mixed layer ($kg kg^{-1} m^{-1}$)	0	default
Carbon dioxide		
Initial mixed-layer CO_2 ($\mu mol CO_2 mol^{-1} air$)	400	profile measurements
Jump in CO_2 at the inversion layer ($\mu mol CO_2 mol^{-1} air$)	–44	profile measurements
Free troposphere lapse rate for CO_2 ($\mu mol CO_2 mol^{-1} air m^{-1}$)	0	default
Advection of CO_2 into the mixed layer ($\mu mol CO_2 mol^{-1} air s^{-1}$)	0	default
Wind		
Initial wind speed in the longitudinal direction ($m s^{-1}$)	1.75	profile measurements
Jump in longitudinal wind velocity at the inversion layer ($m s^{-1}$)	3	profile measurements
Free troposphere lapse rate for longitudinal wind velocity ($m s^{-1} m^{-1}$)	-1.8×10^{-3}	profile measurements
Advection of longitudinal wind into the mixed layer ($m s^{-1} s^{-1}$)	0	default
Wind speed in the latitudinal direction ($m s^{-1}$)	0	default
Jump in latitudinal wind velocity at the inversion layer ($m s^{-1}$)	0	default
Free troposphere lapse rate for latitudinal wind velocity ($m s^{-1} m^{-1}$)	0	default
Advection of latitudinal wind into the mixed layer ($m s^{-1} s^{-1}$)	0	default
Roughness length for momentum (m)	0.02	canopy height
Roughness length for scalars (m)	0.002	canopy height
Geographical coordinates and radiation		
Latitude ($^\circ$)	50.9	geographical location
Longitude ($^\circ$)	6.4	geographical location
Julian day of year (d) (7 May 2018)	127	data selected case
Start time (hours UTC)	6.0	–
Cloud cover fraction (–)	0	camera
Cloud-top radiative divergence ($W m^{-2}$)	0	camera

Table A2. Continued.

Mixed-layer model parameters		
Parameter (units)	Value	Source
Soil		
Soil moisture top soil layer ($\text{m}^3 \text{m}^{-3}$)	0.177	soil measurements
Soil moisture deep soil layer ($\text{m}^3 \text{m}^{-3}$)	0.286	soil measurements
Vegetation cover fraction (–)	0.98	visual inspection, camera
T top soil layer (K)	285.5	soil measurements
T deep soil layer (K)	284	soil measurements
Clapp and Hornberger parametre a (–)	0.219	soil composition
Clapp and Hornberger parametre b (–)	5.3	soil composition
Clapp and Hornberger parametre p (–)	4	soil composition
Saturated soil conductivity for heat (–)	3.56×10^{-6}	soil composition
Saturated volumetric water content (–)	0.472	soil composition
Field capacity volumetric water content (–)	0.3	soil composition
Wilting point volumetric water content (–)	0.154	soil composition
Parameter to calculate top layer soil moisture tendency (–)	disabled	soil composition
Parameter to calculate top layer soil moisture tendency (–)	disabled	soil composition
LAI (–)	4.5	on-site determination
Correction factor transpiration for VPD for high vegetation (–)	0	vegetation height
Minimum soil resistance (s m^{-1})	50	default
Albedo (–)	0.2	radiation measurements
Surface temperature (K)	286.3	profile measurements
Thickness of water layer on wet vegetation (m)	0.0002	default
Equivalent water layer depth for wet vegetation (m)	0.0001	on-site observations
Thermal conductivity skin layer	5.9	default
A- g_s model parameters		
CO_2 compensation concentration (mg m^{-3})	68.5	C3 reference value
Function parameter to calculate CO_2 compensation (–)	1.5	C3 reference value
Mesophyll conductance (m s^{-1})	10.0	leaf gas exchange
Maximum assimilation rate for CO_2 at 298 K ($\text{mg m}^{-2} \text{s}^{-1}$)	1.926	leaf gas exchange
Reference temperature to calculate mesophyll conductance (K)	278	C3 reference value
Reference temperature to calculate mesophyll conductance (K)	301	C3 reference value
Function parameter to calculate maximal primary productivity (–)	2.0	C3 reference value
Reference temperature to calculate maximal primary productivity (K)	281	C3 reference value
Reference temperature to calculate maximal primary productivity (K)	311	C3 reference value
Maximum value of the ratio between the leaf and external (–)	0.89	C3 reference value
Regression coefficient to calculate the ratio between the leaf and external CO_2 concentration (–)	0.07	C3 reference value
Initial low-light conditions use efficiency for CO_2 (mg J^{-1})	0.0053	leaf gas exchange
Extinction coefficient PAR (m m^{-1})	0.7	C3 reference value
Minimum cuticular conductance (mm s^{-1})	2.5×10^{-4}	C3 reference value

Data availability. All CloudRoots observations are archived at <https://www.tr32db.uni-koeln.de> (last access: 21 August 2020), using the search term “cloudroots”. Only CRC/TR32 participants are allowed to apply for an account. Please contact the TR32DB admin for further information. The CLASS model (Python and Fortran versions) is freely available at <http://classmodel.github.io/> (last access: 21 August 2020).

Supplement. The supplement related to this article is available online at: <https://doi.org/10.5194/bg-17-4375-2020-supplement>.

Author contributions. JVGdA designed the CloudRoots study and approach. OH and AG designed and coordinated the CloudRoots field experiment. The individual measurements were gathered by OH (scintillometer); HB (stomatal aperture/photosynthesis); AK, AG, and PN (microlysimeters and elevator profiles); ML (sap flow); MM and DE (SIF); and TR, GA, NB, and YR (stable carbon and water vapour isotopes). HdB integrated the observations to be connected with the modelling efforts. GdG, GM, HdB, and JVGdA performed the numerical experiments with CLASS. PN and JVGdA wrote the paper with key contributions from all the authors: OH, HdB, KvD, DE, GdG, AK, ML, MM, GMG, AFM, UR, TR, and GA.

Competing interests. The authors declare that they have no conflict of interest.

Acknowledgements. The authors wish to thank Bernhard Pospichal and Tobias Marke for contributing measurements on boundary layer properties. These data were provided by the Jülich Observatory for Cloud Evolution (JOYCE-CF), a core facility funded by DFG via grant DFG LO 901/7-1. Hubert Hüging and Huu Thuy Nguyen from the INRES Crop Science Group of Bonn University for operating the sap-flow equipment.

Financial support. This study was financed by the Deutsche Forschungsgemeinschaft (DFG) Collaborative Research Centre 32 (TR32) “Patterns in Soil-Vegetation-Atmosphere System”. The contribution of AG and deployment of the profile elevator, microlysimeter and part of the isotope measurements were financed by the German Federal Ministry of Education and Research (BMBF) within the framework of the project “IDAS-GHG” (Grant: FKZ 01LN1313A). Airborne acquisition and data analysis with the HyPlant sensor were financed by the European Space Agency (ESA) in the frame of the FLEXsense campaign (ESA Contract No. ESA RFP/3-15477/18/NL/NA). The contribution of PN to the analysis were financed by the European Space Agency (ESA) within the project PhotoProxy (Grant. ESA RFP/3-15506/18/NL/NF). The ancillary hardware and its maintenance were supported by TERENO (<https://www.tereno.net>, last access: 21 August 2020). These data were provided by the Jülich Observatory for Cloud Evolution (JOYCE-CF), a core 40 facility funded by DFG via grant DFG LO 901/7-1.

The article processing charges for this open-access publication were covered by the Max Planck Society.

Review statement. This paper was edited by Ivonne Trebs and reviewed by Dennis Baldocchi and one anonymous referee.

References

- Allen, R., Pereira, L., Raes, D., and Smith, M.: Crop evapotranspiration: Guidelines for computing crop water requirements. Food and Agriculture Organization of the U.N. Irrigation and Drainage Paper 56, 300 pp., 1998.
- Alonso, L., Gómez-Chova, L., Vila-Francés, J., Amorós-López, J., Guanter, L., Calpe, J., and Moreno, J.: Improved Fraunhofer Line Discrimination method for vegetation fluorescence quantification, *IEEE Geosci. Remote Sens. Lett.*, 5, 620–624, 2008.
- Baker, J. M. and van Bavel, C. H.: Measurement of mass flow of water in the stems of herbaceous plants, *Plant Cell Environ.*, 9, 777–782, 1987.
- Bogena, H., Herbst, M., Huisman, J., Rosenbaum, U., Weuthen, A., and Vereecken, H.: Potential of Wireless Sensor Networks for Measuring Soil Water Content Variability, *Vadose Zone J.*, 9, 1002–1013, 2010.
- Boussetta, S., Balsamo, G., Beljaars, A., Panareda, A., Calvet, J.-C., Jacobs, C., van den Hurk, B., Viterbo, P., Lafont, S., Dutra, E., Jarlan, L., Balzarolo, M., Papale, D., and van der Werf, G.: Natural land carbon dioxide exchanges in the ECMWF Integrated Forecasting System: Implementation and offline validation, *J. Geophys. Res.-Atmos.*, 118, 5923–5946, 2013.
- Campbell, P., Huemmrich, K., Middleton, E., Ward, L. A., Julitta, T., Daughtry, C. S. T., Burkart, A., Russ, A. L., and Justas, W. P.: Diurnal and Seasonal Variations in Chlorophyll Fluorescence Associated with Photosynthesis at Leaf and Canopy Scales, *Remote Sens.*, 11, 488–515, 2019.
- Damm, A., Paul-Limoges E., Haghghi E., Simmer C., Morsdorf F., Schneider F. D., van der Tol C., Migliavacca M., and Rascher U.: Remote sensing of plant-water relations: An overview and future perspectives, *J. Plant Physiol.*, 227, 3–19, <https://doi.org/10.1016/j.jplph.2018.04.012>, 2018.
- Dengel, S. and Grace, J.: Carbon dioxide exchange and canopy conductance of two coniferous forests under various sky conditions, *Oecologia*, 164, 797–808, 2010.
- Drewry, D. T. Kumar, P., and Long, S. P.: Simultaneous improvement in productivity, water use, and albedo through crop structural modification, *Glob. Change Biol.*, 20, 1955–1967, 2014.
- Dynamax: Dynagage Sap Flow Sensor User Manual, available at: http://dynamax.com/images/uploads/papers/Dynagage_Manual.pdf (last access: 29 July 2019), 2007.
- Dynamax: Flow32-1K Sap Flow Monitoring System Installation & Operation Manual, available at: http://www.dynamax.com/images/uploads/papers/Flow32-1K_Manual.pdf (last access: 21 August 2020), 2017.
- Farquhar, G. D. and Roderick, M. L.: Pinatubo, diffuse light, and the carbon cycle, *Science*, 261, 1997–1998, 2003.
- Farquhar, G. D., von Caemmerer, S., and Berry, J. A.: A biochemical model of photosynthetic CO₂ assimilation in leaves of C₃ species, *Planta*, 149, 78–90, 1980.

- Franz, D., Acosta, M., Altimir, N., et al.: Towards long-term standardised carbon and greenhouse gas observations for monitoring Europe's terrestrial ecosystems: a review, *Int. Agrophys.*, 32, 439–455, 2018.
- Foken, T.: The energy balance closure problem: an overview, *Ecol. Appl.*, 18, 1351–1367, 2008.
- Gao, G., Liu, H., Katul, G. G., and Foken, T.: Non-closure of the surface energy balance explained by phase differences between vertical velocity and scalars of a large atmospheric eddies, *Environ. Res. Lett.*, 12, 034025, <https://doi.org/10.1088/1748-9326/aa625b>, 2017.
- Goudriaan, J.: A simple and fast numerical method for the computation of daily totals of crop photosynthesis, *Agr. Forest Meteorol.*, 38, 2249–2254, 1986.
- Griffis, T. J.: Tracing the flow of carbon dioxide and water vapor between the biosphere and atmosphere: A review of optical isotope techniques and their application, *Agr. Forest Meteorol.*, 174/175, 85–109, 2013.
- Gryning, S. E., de Bruin, H., and Batchvarova, E.: Energy balance of a sparse coniferous high-latitude forest, *Bound.-Lay. Meteorol.*, 99, 465–488, 2001.
- Hall, F. G., Sellers, P. J., MacPherson, I., Kelly, R. D., Verma, S., Markham, B., Blad, B., Wang, J., and Strebel, D. E.: FIFE: Analysis and results: a review, *Adv. Space Res.*, 9, 275–293, 1989.
- Ikawa, H., Chen, C.P., Sikma, M., Yoshimoto, M., Sakai, H., Tokida, T., Usui, Y., Nakamura, H., Ono, K., Maruyama, A., Watanabe, T., Kuwagata, T., and Hasegawa, T.: Increasing canopy photosynthesis in rice can be achieved without a large increase in water use—A model based on free-air CO₂ enrichment, *Glob. Change Biol.* 24, 1321–1341, 2018.
- IUSS Working Group WRB: World Reference Base for Soil Resources 2006, FAO Rome: World Soil Resources Reports 103, 145 pp., 2006.
- Jacobs, C. M. and de Bruin, H. A.: Predicting regional transpiration at elevated atmospheric CO₂: influence of the PBL–vegetation interaction, *J. Appl. Meteorol.*, 36, 1663–1675, 1997.
- Kaiser, E., Morales, A., and Harbinson, J.: Fluctuating Light Takes Crop Photosynthesis on a Rollercoaster Ride, *Plant Physiol.*, 176, 977–989, 2018.
- Kanniah, K. D., Beringer, J., North, P., and Hutley, L.: Control of atmospheric particles on diffuse radiation and terrestrial plant productivity: A review, *Prog. Phys. Geogr.*, 2, 209–237, 2012.
- Katul, G. G., Oren, R., Manzoni, S., Higgins, C., and Parlange, M. B.: Evapotranspiration: A process driving mass transport and energy exchange in the soil-plant-atmosphere-climate system, *Rev. Geophys.*, 50, RG3002, <https://doi.org/10.1029/2011RG000366>, 2012.
- Jonard, F., De Cannière, S., Brüggemann, N., Gentine, P., Short Gianotti, D. J., Lobet, G., Miralles, D. G., Montzka, C., Pagán, B. R., Rascher, U., and Vereecken, H.: Value of sun-induced chlorophyll fluorescence for quantifying hydrological states and fluxes: current status and challenges, *Agr. Forest Meteorol.*, 291, 108088, <https://doi.org/10.1016/j.agrformet.2020.108088>, 2020.
- Knohl, A. and Baldocchi, D. D.: Effects of diffuse radiation on canopy gas exchange processes in a forest ecosystem, *J. Geophys. Res.*, 113, G02023, <https://doi.org/10.1029/2007JG000663>, 2008.
- Langensiepen, M., Kupisch, M., Graf, A., Schmidt, M., and Ewert, F.: Improving the stem heat balance method for determining sap-flow in wheat, *Agr. Forest Meteorol.*, 186, 34–42, 2014.
- Lee, X., Griffis, T. J., Baker, J. M., Billmark, K. A., Kim, K., and Welp, L. R.: Canopy-scale kinetic fractionation of atmospheric carbon dioxide and water vapor isotopes, *Global Biogeochem. Cy.*, 23, GB1002, <https://doi.org/10.1029/2008GB003331>, 2009.
- Löhnert, U., Schween, J., Acquistapace, C., Ebell, K., Maahn, M., Barrera-Verdejo, M., Hirsikko, A., Bohn, B., Knaps, A., O' Connor, E. O., Simmer, C., Wahner, A., and Crewell, S.: JOYCE: Jülich Observatory for Cloud Evolution, *B. Am. Meteorol. Soc.*, 96, 1157–1174, 2015.
- Lussem, U.: Land use classification of 2018 for the CRC/TR32 measurement region Selhausen/Merken/Merzenhausen, preliminary results, CRC/TR32 Database (TR32DB), <https://doi.org/10.5880/TR32DB.32>, 2018.
- Mauder, M. and Foken, T.: Documentation and instruction manual of the eddy-covariance software package TK3, Internal Report 43, Department of Micrometeorology, University of Bayreuth, Bayreuth, Germany, 60 pp., <https://epub.uni-bayreuth.de/342/1/ARBERG046.pdf> (last access: 21 August 2020), 2011.
- Mauder, M., Desjardins, R. L., Pattey, E., and Worth, D.: An attempt to close the daytime surface energy balance using spatially-averaged flux measurements, *Bound.-Lay. Meteorol.*, 136, 175–191, 2010.
- Mauder, M., Cuntz, M., Graf, A., Rebmann, C., Schmidt, H., and Steinbrecher, R.: A strategy for quality and uncertainty assessment of eddy-covariance measurements, *Agr. Forest Meteorol.*, 169, 122–135, 2013.
- Moene, A. F. and Van Dam, J. C.: Transport in the atmosphere-vegetation-soil continuum, Cambridge, Cambridge University Press, 436 pp., 2014.
- Monson, R. and Baldocchi, D.: Terrestrial Biosphere-Atmosphere Fluxes, Cambridge, Cambridge University Press, 487 pp., 2014.
- Nelder, J. A. and Mead, R.: A simple method for function minimization, *Comput. J.*, 4, 308–313, 1965.
- Ney, P. and Graf, A.: High-resolution vertical profile measurements for carbon dioxide and water vapour concentrations within and above crop canopies, *Bound.-Lay. Meteorol.*, 166, 449–473, 2018.
- Ney, P., Graf, A., Schmidt, M., and Vereecken, H.: The carbon budget of a 4-year crop rotation: using three different non-linear regression CO₂ flux partitioning approaches, in preparation, 2020.
- Olesen, J., Hansen, P., Berntsen, J., and Christensen, S.: Simulation of above-ground suppression of competing species and competition tolerance in winter wheat varieties, *Field Crop. Res.*, 89, 263–280, 2004.
- Pedruzo-Bagazgoitia, X., Ouwensloot, H. G., Sikma, M., van Heerwaarden, C. C., Jacobs, C. M., and Vilà-Guerau de Arellano, J.: Direct and diffuse radiation in the shallow cumulus–vegetation system: enhanced and decreased evapotranspiration regimes, *J. Hydrometeorol.*, 6, 1731–1748, 2017.
- Quade, M., Klosterhalfen, A., Graf, A., Brüggemann, N., Hermes, N., Vereecken, H., and Rothfuss, Y.: In-situ monitoring of soil water isotopic composition for partitioning of evapotranspiration during one growing season of sugar beet (*Beta vulgaris*), *Agr. Forest Meteorol.*, 165, 114–126, 2019.
- Rascher, U., Alonso, L., Burkart, A., et al.: Sun-induced fluorescence – a new probe of photosynthesis: First maps from the imag-

- ing spectrometer HyPlant, *Glob. Change Biol.*, 12, 4673–4684, 2015.
- Rebmann, C., Aubinet, M., Schmid, H., et al.: ICOS eddy covariance flux-station site setup: a review, *Int. Agrophys.*, 32, 471–494, 2018.
- Reichstein, M., Falge, E., Baldocchi, D., et al.: On the separation of net ecosystem exchange into assimilation and ecosystem respiration. Review and improved algorithm, *Glob. Change Biol.*, 11, 1424–1439, 2005.
- Roderick, M. L., Farquhar, G. D., Berry, S. L., and Noble, I. R.: On the direct effect of clouds and atmospheric particles on the productivity and structure of vegetation, *Oecologia*, 1, 21–30, 2001.
- Ronda, R. J., De Bruin, H. A., and Holtslag, A. A.: Representation of the canopy conductance in modeling the surface energy budget for low vegetation, *J. Appl. Meteorol.*, 40, 1431–1444, 2001.
- Sakuratani, T.: A heat balance method for measuring water flux in the stem of intact plants, *J. Agr. Meteorol.*, 1, 9–17, 1981.
- Santos, E. A., Wagner-Riddle, C., Warland, J., and Brown, S.: Applying a Lagrangian dispersion analysis to infer carbon dioxide and latent heat fluxes in a corn canopy, *Agr. Forest Meteorol.*, 151, 620–632, 2011.
- Sellers, P., Hall, F., Margolis, H., Kelly, R., Baldocchi, D., den Hartog, G., Cihlar, J., Ryan, M. G., Goodison, B., Crill, P., Ranson, K. J., Lettenmaier, D., and Wickland, D. E.: The Boreal Ecosystem–Atmosphere Study (BOREAS): An Overview and Early Results from the 1994 Field Year, *B. Am. Meteorol. Soc.*, 76, 1549–1577, 1995.
- Siegmann B., Alonso L., Celesti M., Cogliati S., Colombo R., Damm A., Douglas S., Guanter L., Hanuš J., Kataja K., Kraska T., Matveeva M., Moreno J., Muller O., Píkl M., Pinto F., Quirós Vargas J., Rademske P., Rodríguez-Moreno F., Sabater N., Schickling A., Schüttemeyer D., Zemek F., and Rascher U.: The high-performance airborne imaging spectrometer HyPlant – From raw images to top-of-canopy reflectance and fluorescence products: Introduction of an automatized processing chain, *Remote Sens.*, 11, 2760, <https://doi.org/10.3390/rs11232760>, 2019.
- Sikma, M., Ouwersloot, H., Pedruzo-Bagazgoitia, X., Van Heerwaarden, C., and Vilà-Guerau de Arellano, J.: Interactions between vegetation, atmospheric turbulence and clouds under a wide range of background wind conditions, *Agr. Forest Meteorol.*, 255, 31–43, 2018.
- Sikma, M., Ikawa, H., Heusinkveld, B.G., Yoshimoto, Y., Hasegawa, T., Groot Haar, L. T., Anten, N. P. R., Nakamura, H., Vilà-Guerau de Arellano, J., Sakai, H., Tokida, T., Usui, Y., and Evers, J. B.: Quantifying the feedback between rice architecture, physiology and microclimate under current and future CO₂ conditions, *J. Geophys. Res.-Bioge.*, 125, e2019JG005452, <https://doi.org/10.1029/2019JG005452>, 2020.
- van Diepen, K. and Moene A.F.: Canopy photosynthesis under clear and cloud conditions, MSc thesis at Meteorology and Air Quality, Wageningen University, 39 pp., 2019.
- van Heerwaarden, C. C. and Teuling, A. J.: Disentangling the response of forest and grassland energy exchange to heatwaves under idealized land–atmosphere coupling, *Biogeosciences*, 11, 6159–6171, <https://doi.org/10.5194/bg-11-6159-2014>, 2014.
- van Heerwaarden, C. C., Vilà-Guerau de Arellano, J., Gounou, A., Guichard, F., and Couvreur, F.: Understanding the daily cycle of evapotranspiration: A method to quantify the influence of forcings and feedbacks, *J. Hydrometeorol.*, 11, 1405–1422, 2010.
- van Kesteren, B., Hartogensis, O. K., van Dinter, D., Moene, A.F., De Bruin, H. A., and Holtslag, A. A.: Measuring H₂O and CO₂ fluxes at field scales with scintillometry: Part II–Validation and application of 1-min flux estimates, *Agr. Forest Meteorol.*, 178, 88–105, 2013.
- Vico, G., Manzoni, S., Palmroth, S., and Katul, G.: Effects of stomatal delays on the economics of leaf gas exchange under intermittent light regimes, *New Phytol.*, 192, 640–652, 2011.
- Vilà-Guerau de Arellano, J., Ouwersloot H. G., Baldocchi D., and Jacobs C. M. J.: Shallow cumulus rooted in photosynthesis, *Geophys. Res. Lett.*, 41, 1796–1802, 2014.
- Vilà-Guerau de Arellano, J., van Heerwaarden, C. C., Van Stratum, B. J., and Van den Dries, K.: Atmospheric boundary layer: Integrating air chemistry and land interactions, Cambridge, Cambridge University Press, 279 pp., 2015.
- Vilà-Guerau de Arellano, J., Koren, G., Ouwersloot, H. G., van der Velde, I., Röckmann, T., and Miller, J. B.: Sub-diurnal variability of the carbon dioxide and water vapor isotopologues at the field observational scale, *Agr. Forest Meteorol.*, 275, 114–135, 2019.
- Warland, J. S. and Thurtell, G. W.: A Lagrangian solution to the relationship between a distributed source and concentration profile, *Bound.-Lay. Meteorol.*, 96, 453–471, 2000.
- Wohlfahrt, G., Gerdel, K., Migliavacca, M., Rotenberg, E., Tatarinov, F., J. Müller, J., Hammerle, A., Julitta, T., Spielmann F. M., and Yakir D.: Sun-induced fluorescence and gross primary productivity during a heat wave, *Sci. Rep.*, 8, 14169, <https://doi.org/10.1038/s41598-018-32602-z>, 2018.
- Wutzler, T., Lucas-Moffat, A., Migliavacca, M., Knauer, J., Sickel, K., Šigut, L., Menzer, O., and Reichstein, M.: Basic and extensible post-processing of eddy covariance flux data with REddyProc, *Biogeosciences*, 15, 5015–5030, <https://doi.org/10.5194/bg-15-5015-2018>, 2018.

	Doc.: Final Report		
	Date: 29 July 2021	Issue: 2	Revision: 1
	Ref.: ESA Contract No. 4000125402/18/NL/NA		Page: 275 / 288

12.2 Publication II: Martini et al. (submitted to *New Phytologist*) - Heat wave effect on SIF and GPP on the Iberian dehesa ecosystem

Main Manuscript for:

Heat-wave breaks down the linearity between sun-induced fluorescence and gross primary production

David Martini^{1,4}, Karolina Sakowska², Georg Wohlfahrt³, Javier Pacheco-Labrador¹, Christiaan van der Tol⁴, Albert Porcar-Castell⁵, Troy S Magney⁶, Arnaud Carrara⁷, Roberto Colombo⁸, Tarek El-Madanay¹, Rosario González-Cascón⁹, Maria Pilar Martin Isabel¹⁰, Tommaso Julitta¹¹, Gerardo Moreno Marcos¹², Uwe Rascher¹³, Markus Reichstein¹, Micol Rossini⁸ and Mirco Migliavacca¹

- 1- Max Planck Institute for Biogeochemistry, Hans Knöll Straße, 10, D-07745, Jena, Germany
- 2- Institute of BioEconomy, National Research Council (IBE-CNR), Via Biasi 75, 38010 San Michele all'Adige (TN), Italy
- 3- Department of Ecology, University of Innsbruck, Sternwartestrasse 15, 6020 Innsbruck, Austria
- 4- Faculty of Geo-Information Science and Earth Observation (ITC), University of Twente, 7500 AE Enschede, the Netherlands
- 5- Optics of Photosynthesis Laboratory, Institute for Atmospheric and Earth System Research (INAR/Forest Sciences) and Viikki Plant Science Center, 00014 University of Helsinki, Finland
- 6- Department of Plant Sciences, University of California, Davis, CA, USA
- 7- Centro De Estudios Ambientales Del Mediterráneo, 46980 Valencia, Spain
- 8- University of Milano Bicocca, 20126 Milan, Italy
- 9- Department of Environment, National Institute for Agriculture and Food Research and Technology (INIA), 28040 Madrid, Spain
- 10- Environmental Remote Sensing and Spectroscopy Laboratory (SpecLab), Spanish National Research Council (CSIC), 28037 Madrid, Spain
- 11- JB hyperspectral devices, 33 – 40225 Düsseldorf, Germany
- 12- Universidad de Extremadura, 10600 Plasencia, Spain
- 13- Institute of bio- and geosciences, IBG-2, Plant Sciences, Forschungszentrum Jülich, Jülich, Germany

12.3 Publication III: Siegmann et al. (submitted to *Remote Sensing of Environment*) - Dynamics of diurnal courses of SIF in agricultural systems

Downscaling of far-red solar-induced chlorophyll fluorescence of different crops from canopy to leaf level using a diurnal data set acquired by the airborne imaging spectrometer HyPlant

Bastian Siegmann^{a,*}, Maria Pilar Cendrero-Mateo^b, Sergio Cogliati^c, Alexander Damm^d, John Gamon^{e,f}, David Herrera^a, Christoph Jedmowski^a, Laura Verena Junker-Frohn^a, Thorsten Kraska^g, Onno Muller^a, Patrick Rademske^a, Christiaan van der Tol^h, Juan Quiros-Vargas^a, Peiqi Yang^h, Uwe Rascher^a

^a Institute of Bio- and Geosciences, IBG-2: Plant Sciences, Forschungszentrum Jülich GmbH, Wilhelm-Johnen-Straße, 52428 Jülich, Germany

^b Image Processing Laboratory, University of Valencia, C/Catedrático José Beltrán 2, E-46980 Paterna, Valencia, Spain

^c Remote Sensing of Environmental Dynamics Lab., DISAT, University of Milano-Bicocca, Piazza della Scienza 1, 20126 Milano, Italy

^d Department of Geography, University of Zurich, Winterthurerstrasse 190, 8057 Zurich, Switzerland

^e Department of Earth and Atmospheric Sciences and Department of Biological Sciences, University of Alberta, 11335 Saskatchewan Drive, Edmonton, AB T6G 2E3, Canada

^f Center for Advanced Land Management Information Technologies, School of Natural Resources, University of Nebraska–Lincoln, 3310 Holdrege Street, Lincoln, NE 68583, USA

^g Field Lab Campus Klein-Altendorf, Faculty of Agriculture, University of Bonn, Campus Klein-Altendorf 1, 53359 Rheinbach, Germany

^h Faculty of Geo-Information Science and Earth Observation (ITC), University of Twente, Hengelosestraat 99, Enschede 7500 AE, The Netherlands

12.4 Publication IV: Scharr et al. (submitted to *Remote Sensing of Environment*) - Effect of the point-spread function of SIF retrieval

Spatio-spectral deconvolution for high resolution spectral imaging with an application to the estimation of sun-induced fluorescence

Hanno Scharr^{a,*}, Patrick Rademske^a, Luis Alonso^b, Sergio Cogliati^c, Uwe Rascher^a

^a*Institute of Bio- and Geosciences (IBG), IBG-2: Plant Sciences
Forschungszentrum Jülich GmbH, D-52425 Jülich, Germany*

^b*Image Processing Laboratory, University of Valencia, Valencia, Spain*

^c*Remote Sensing of Environmental Dynamics Lab., DISAT
University of Milano-Bicocca, P.zza della Scienza 1, 20126, Milano, Italy*

Abstract

We propose a signal deconvolution procedure for imaging spectrometer data, where a measured point spread function (PSF) is deconvolved itself before being used for deconvolution of the signal. Imaging spectrometers are well established instruments for remote sensing. When used for scientific purposes these instruments are usually calibrated on a regular basis. In our case the point spread function of the optics is measured in an elaborate procedure with a tunable monochromator point light source. PSFs are measured at different pixel positions of the imaging sensor, i.e. at different spatio-spectral locations, and averaged in order to get an as accurate PSF as possible. We investigate error sources in this calibration process by simulating the procedure in silico. Averaging as well as the spectral and spatial width of the point source introduce some smoothness in the measured PSF. We propose corrective measures, i.e. deconvolution of the PSF itself and median instead of mean averaging, leading to a set of sharper PSFs. We test the performance of these PSFs in deconvolving simulated as well as hyperspectral images. For deconvolution we test a set of well-known, off the shelf deconvolution algorithms. Quantitatively in terms of PSNR (Peak signal to Noise Ratio) a combination of Wiener filtering and sharpened PSFs yields strongest improvements, while using Wiener filtering with non-sharpened PSFs even deteriorates the signal. Comparing deconvolution results of the simulated data with results of real data reveals, that visually very similar effects can be observed. This well supports the assumption, that our findings are also valid for real spatio-spectral data. Surprisingly, the choice of PSF sharpened or not is of little effect for estimation of sun-induced fluorescence (SIF) with

	Doc.: Final Report		
	Date: 29 July 2021	Issue: 2	Revision: 1
	Ref.: ESA Contract No. 4000125402/18/NL/NA		Page: 278 / 288

12.5 Publication V: Di Cicco et al. (2020) - “Flex 2018” Cruise: an opportunity to assess phytoplankton chlorophyll fluorescence retrieval at different observational scales

Citation of this publication

Di Cicco A., Gupana R., Damm A., Colella S., Angelini F., Fiorani L., Artuso F., Brando V.E., Lai A., Genangeli A., Miglietta F. & Santoleri R. (2020) “Flex 2018” Cruise: an opportunity to assess phytoplankton chlorophyll fluorescence retrieval at different observational scales. *8th International Symposium “Monitoring of Mediterranean Coastal Areas. Problems and Measurement Techniques”*, edited by L. Bonora, D. Carboni & M. De Vincenzi, pp. 688-697, doi: 10.36253/978-88-5518-147-1.68.

Link to this campaign activities

This publication covers the main results and findings from the FLEXsense measurements from open waters (chapter 7.7). This publication thus can be considered to be a concise and reviewed summary of the results that are also presented in this report.

“FLEX 2018” CRUISE: AN OPPORTUNITY TO ASSESS PHYTOPLANKTON CHLOROPHYLL FLUORESCENCE RETRIEVAL AT DIFFERENT OBSERVATIVE SCALES

Annalisa Di Cicco¹, Remika Gupana^{2,3}, Alexander Damm^{2,3}, Simone Colella¹, Federico Angelini⁴, Luca Fiorani⁴, Florinda Artuso⁴, Vittorio Ernesto Brando¹, Antonia Lai⁴, Andrea Genangeli⁵, Franco Miglietta⁶, Rosalia Santoleri¹

¹CNR – Istituto di Scienze Marine (ISMAR), Via del Fosso del Cavaliere, 100 - 00133 Rome (Italy)
phone +39 06 49934508, e-mail: annalisa.dicicco@artov.ismar.cnr.it

²Eawag - Swiss Federal Institute of Aquatic Science and Technology, Duebendorf (Switzerland)

³Department of Geography, University of Zurich, Zurich (Switzerland)

⁴Italian National Agency for New Technologies, Energy and Sustainable Economic Development (ENEA), Frascati - Rome (Italy)

⁵University of Florence (UniFi), Florence (Italy)

⁶CNR – Istituto per la BioEconomia (IBE), Florence (Italy)

Abstract – In frame of the European Space Agency’s (ESA) “FLEXSense Campaign 2018” and the Copernicus Marine Environment Monitoring Service (CMEMS) project, the Global Ocean Satellite monitoring and marine ecosystem study group (GOS) of the Italian National Research Council (CNR) organized the oceanographic cruise “FLEX 2018”. The CNR research vessel “Dallaporta” provided a ground station for several bio-optical instruments to investigate the coastal waters of the Tyrrhenian Sea (central Italy) in June 2018. The field measurements were performed in time synchrony with spaceborne (i.e. Sentinel 3A and Sentinel 3B satellites) and airborne (i.e. HyPlant airborne imaging spectrometer) observations, with the intent to contribute to calibration/validation activities for existing and future space mission developments. Particularly, active and passive fluorescence were investigated at different scales in aquatic ecosystems, to support preparatory activities of the FLuorescence EXplorer (FLEX) satellite mission to be launched in 2022. Results provide new insight on the sensitivity of Solar Induced Fluorescence (SIF) retrievals for atmospheric disturbances and other scale related aspects, and will eventually facilitate the implementation of robust retrieval schemes for the FLEX mission products. In addition, active fluorescence signals acquired from a LIDAR fluorosensor show a good agreement with SIF pattern retrieved by HyPlant and Sentinel-3 Ocean and Land Colour Instrument (OLCI). Our results demonstrate that the combination of active and passive fluorescence, together with the synergistic measurements from integrated platforms, is a promising approach to support the retrieval and interpretation of SIF in aquatic environments.

Introduction

Chlorophyll fluorescence is a fundamental proxy to provide physiological information and estimates of photosynthetic energy conversion efficiency. Long exploited in laboratory and field, the interest of the scientific community in remote sensing based fluorescence observations increased over the last years. Instruments adopting the Light Induced Fluorescence (LIF)

FUP Best Practice in Scholarly Publishing (DOI 10.36253/fup_best_practice)

Annalisa Di Cicco, Remika Gupana, Alexander Damm, Simone Colella, Federico Angelini, Luca Fiorani, Florinda Artuso, Vittorio Ernesto Brando, Antonia Lai, Andrea Genangeli, Franco Miglietta, Rosalia Santoleri., “Flex 2018” Cruise: an opportunity to assess phytoplankton chlorophyll fluorescence retrieval at different observational scales, pp. 688-697, © 2020 Author(s), CC BY 4.0 International, DOI 10.36253/978-88-5518-147-1.68

technique to remotely monitor actively stimulated fluorescence from dissolved and particulate sea water constituents have been widely employed for marine environment monitoring. [1]. In the recent years, large steps have been made also in the retrieval of passive Sun-Induced chlorophyll Fluorescence (SIF). In the framework of its Earth Observation Envelope Programme, the European Space Agency (ESA) is currently implementing the FLuorescence EXplorer (FLEX) satellite mission, the first mission specifically designed to monitor the photosynthetic activity of terrestrial vegetation. FLEX is scheduled to be launched in 2022 and comprises two spectrometers, the FLuorescence Imaging Spectrometer measuring in low (FLORIS-LR) and in high resolution (FLORIS-HR). Both sensors together cover the spectral range between 500 nm and 780 nm and provide a varying spectral sampling interval and resolution of up to 0.1 nm and 0.3 nm respectively, particularly in the Oxygen absorption bands (O₂B and O₂A) [2]. Considering the complexity of the targeted photosynthetic process, FLEX will be ESA's first mission designed as "tandem concept", flying in tandem with the Copernicus Sentinel - 3 satellite. This allows measuring all relevant data to facilitate subsequent estimates of photosynthesis [2].

Measurement campaigns providing detailed in situ observations from integrated platforms at different scales play a crucial role to develop, calibrate and validate data products of current and future satellite missions [3]. In this context, ESA organized the "FLEXsense campaign" in 2018 to facilitate preparatory activities for FLEX, particularly addressing the development of retrieval schemes and atmospheric correction approaches. The campaign specifically focused on the collection of hyperspectral data over monitoring sites in vegetation ecosystems such as agricultural and forest sites, and aimed to evaluate the potential applicability of FLEX data to assess coastal marine environments.

SIF retrieval in aquatic ecosystems has a great ecological value considering its potential in discriminating phytoplankton diversity and in improving productivity estimates. Particularly, in optically complex waters, characterized by active constituents with very different dynamics compared to open waters, the retrieval of SIF is a major challenge. McKee et al. [4] explored coastal waters with CDOM and TSM ranging from 0 m⁻¹ to 1 m⁻¹ and from 0 g m⁻³ to 10 g m⁻³ respectively, and found that increasing concentrations of CDOM and minerals can reduce the water-leaving SIF per unit chlorophyll by over 50 %. This suggests caution in the interpretation of SIF signals from coastal waters [4] and highlights the crucial role of the in-situ bio-optical characterizations for SIF retrievals and validation activities in aquatic ecosystems in general and coastal waters in particular. In this context, CNR-ISMAR organized in frame of the FLEXsense campaign the oceanographic cruise "FLEX 2018". The CNR research vessel "Dallaporta" provided a ground station for several bio-optical instruments that investigated the coastal waters of the Tyrrhenian Sea (central Italy) in June 2018. All the Apparent and Inherent Optical Properties (AOPs and IOPs) were estimated in addition to various physical ancillary data. These detailed in-situ measurements were complemented with concurrent radiometric observations acquired using the high-resolution airborne imaging spectrometer HyPlant [5] and both Sentinel - 3A and - 3B satellites.

The aim of this work is to assess whether SIF can be consistently retrieved using a simple retrieval scheme for in-situ, airborne and spaceborne measurements and if, in the framework of this integrated approach, TChla active fluorescence, less affected at 680 nm by other constituents, can be useful to improve the retrieval of passive fluorescence and the understanding of its behavior.

Materials and Methods

The “FLEX 2018” cruise took place between 5th and 7th of June 2018 in the Tyrrhenian Sea. Figure 1 shows the sampling plan of the cruise in the investigated area. The sampling strategy was optimized to facilitate the objectives of the “FLEXSense Campaign”.

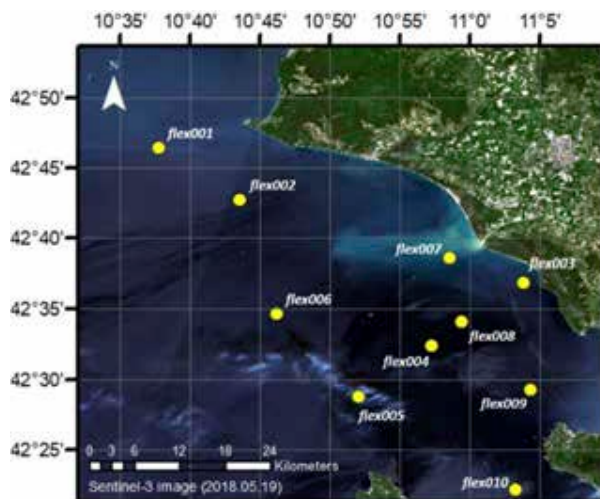


Figure 1 - FLEX 2018 in-situ sampling plan. Yellow circles indicate stations intensively characterized by in situ sensors. The background true color image was obtained by Sentinel-3.

For each measurement station, in-situ data for the determination of CDOM, algal and non-algal absorption coefficients (a_{CDOM} , a_{phy} and a_{NAP} respectively) and phytoplankton pigments and Total Suspended Matter (TSM) concentration were collected at the surface. Water was sampled by a horizontal hand Van Dorn bottle. For all parameters except CDOM, water was pre-filtered by a net with a mesh of 250 μm to eliminate the zooplankton component and different water volumes, dependent on the optical properties, were vacuum filtered through Whatmann GF/F glass microfiber filter (nominal porosity 0.7 μm). Samples for particle absorption and pigment concentration were stored in liquid nitrogen, while those for TSM were stored at -20 °C. CDOM filtrations were carried out by low pressure through 0.2 μm Nylon filters. Filtered water was stored in black Pyrex bottles at -4 °C until measurements have been performed in laboratory. With regard to the instruments and analysis methods, pigment concentrations were estimated by High Performance Liquid Chromatography (HPLC, Agilent 1260) implementing the method of [6]. The absorption measurements were carried out by a dual beam Lambda 19 Spectrophotometer (Perkin-Elmer), equipped with a 50 mm integrative sphere for the particulate only. Methods of [7] and [8] were adapted for estimates of dissolved and particulate material absorption respectively. The analysis of TSM concentration were carried out by a gravimetric method following the protocol of [9].

Continuous LIF measurements were carried out using a LIDAR fluorosensor system developed by the ENEA agency in collaboration with the INSIS company in frame of the Italian Regional Project “RIMA” and installed on the ship. The light source is a frequency-tripled Nd:YAG laser (355 nm) and the detection system combines a telescope, wavelength dependent beam splitters, interference filters and Avalanche PhotoDiodes (APDs) being more compact and robust than photomultiplier tubes. LIF data are corrected with respect to the solar background and normalized to the Raman signal collected at 405 nm (Raman Unit, R. U), making it insensitive to instrumental variations [1]. The fluorescence signal has also been calibrated as TChla and compared with TChla data obtained from VIIRS (Visible Infrared Imaging Radiometer Suite) on 8th June, the first satellite data available due to cloud cover on campaign days and retrieved by applying the regional MedOC4 algorithm [10].

Above water surface radiometric measurements were collected in 8 of the 10 stations sampled using the in-situ fluorescence spectrometer FLOX (jb-hyperspectral.com). Sampling activities took place in concurrence with HyPlant and Sentinel-3 scene acquisitions. The spectral characteristics of the three systems in terms of sampling interval and resolution are comparable (cf. jb-hyperspectral.com, [2], [5]). FLOX comprises two sensors to measure irradiance and radiance in high and low spectral resolution, comparable to HyPlant and FLEX sampling schemes, making this instrument a good candidate for the multi-scale assessment of SIF retrieval accuracy in coastal areas. However, the instrument needs to be reconfigured to facilitate the simultaneous acquisition of downwelling irradiance (E_d), upwelling radiance (L_u) and sky radiance (L_{sky}), the three quantities required by specific protocols for spectroradiometric observation in aquatic systems.

HyPlant data were acquired over a coastal area near the Ombrone River in a North-South oriented flight path up to roughly 20 km from the coastline on 6th of June. The original HyPlant spatial resolution (3 m) was resampled to 300 m to facilitate the comparison with Sentinel-3 data. Since Sentinel-3B data acquired during the cruise day was substantially cloud covered, we used Sentinel-3 L1A data from 10th of June 2018 instead.

SIF was retrieved from in-situ, airborne and spaceborne measurements in SNAP using the Fluorescence Line Height (FLH) algorithm, an established empirical algorithm that exploits radiances at and around the SIF emission in three spectral bands (for this work 665 nm, 681 nm and 709 nm). For more details on the algorithm approach, its general formula and the selected spectral bands see [11], [12], [13]. The FLH method is typically used in the open ocean since low signal from elastic scattering provides good resulting baseline curves [14], [15]. High TChla and TSM concentrations in optically complex waters could significantly affect FLH results due to a peak from the elastic reflectance overlapping with the fluorescence signal and therefore potentially contaminating fluorescence retrieval [11].

Results

The compositional variability of the IOPs in each station is shown in Figure 2 using ternary plots, which feature a_{CDOM} , a_{phy} and a_{NAP} at four characteristic wavelengths, 443 nm, 560 nm, 620 nm and 680 nm [16].

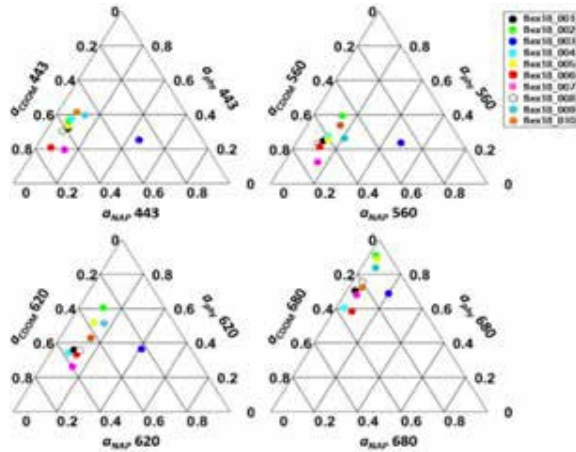


Figure 2 - Ternary plot showing the compositional variability of the IOPs in each station.

At 443 nm, where all three components absorb significantly, data show that in general the absorption budget is dominated by CDOM. Low values of a_{NAP} were found also at 560 nm (band usually governed by NAP absorption), except for station 3. The ternary plots at 620 nm and 680 nm indicate stations 2, 5 and 9 as the most characterized by phytoplankton absorption, also in terms of phycocyanin absorption (typical at 620 nm and proxy for cyanobacteria). All over the cruise, TChla and TSM concentrations range from 0.08 mg m^{-3} to 0.31 mg m^{-3} and from 0.13 g m^{-3} to 1.65 g m^{-3} , respectively. The relations between TChla and TSM and a_{CDOM} highlighted a more coastal feature for stations 3 and 7 (data not shown).

The relation between TChla concentration derived from HPLC measurements and FLH based – SIF values derived from FLOX (performed in 8 of the 10 stations) is shown in Figure 3 (left panel). On the right panel in Figure 3, the same relation but using LIF data detected from LIDAR in-situ acquisition is illustrated.

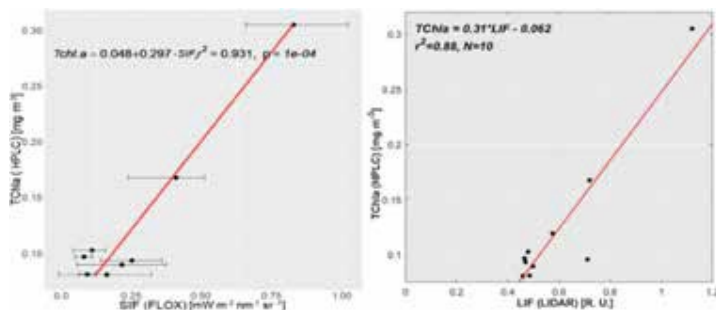


Figure 3 - In-situ estimates of TChl-a vs SIF (FLOX) and LIF (LIDAR).

For both in-situ instruments, derived fluorescence and TChla concentrations show a good agreement (i.e. $r^2 = 0.93$ and 0.88 , respectively). It must be noted that the correlation for the LIDAR is slightly lower due to the TChla value in station 10, while no FLOX measurements are available for this station.

FLH based SIF retrieved from HyPlant and Sentinel-3 data is shown in Figure 4.

When comparing the SIF data obtained from airborne and spaceborne in the corresponding swath, similar spatial patterns can be observed. Figure 5 (left panel) shows a comparison of SIF dynamics obtained from both sensors along a coast to offshore transect (black line in Figure 4). However, the range of SIF values calculated from HyPlant and Sentinel-3 differs significantly. In particular, SIF derived from Sentinel-3 FLH processing resulted in numerous negative values.

The spatial SIF pattern of from HyPlant and Sentinel-3 OLCI along the coast to offshore transect was also compared with the LIF signal (Figure 5, right panel), using the data overlapping with the airborne track (Figure 6, left). LIF signal shows a behavior comparable

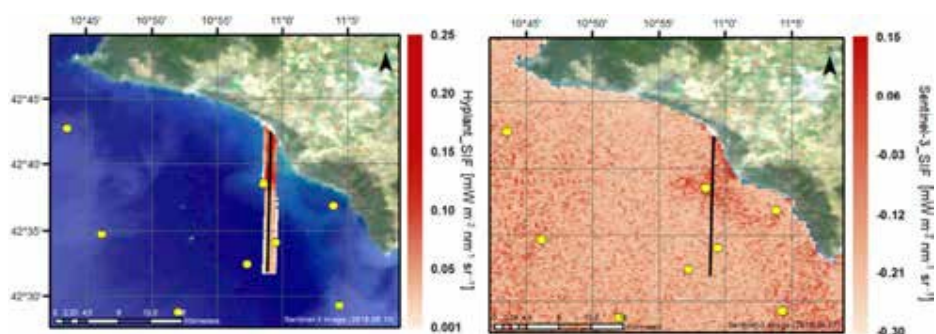


Figure 4 - SIF values calculated for the study area from HyPlant (left) and Sentinel-3A (right). The black N-S line indicates a transect used in Figure 5 (left panel).

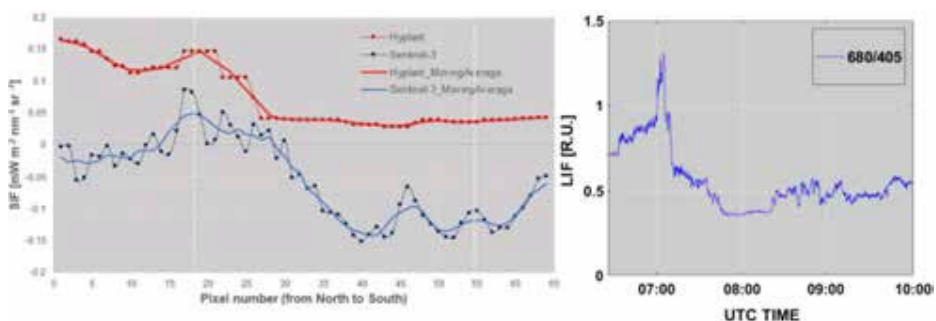


Figure 5 - SIF from HyPlant and Sentinel-3 OLCI from coast to offshore (dashed line with points) and smoothed profiles using a moving average approach. White dotted lines enclosed the pixels where HyPlant and LIDAR acquisition overlap (left). The corresponding LIF signal is shown to the right.

with the SIF obtained from the other two sensors, with increasing values in proximity of station 7 closer to the coast that gradually decrease and then stabilizes offshore. In the right panel of Figure 6, the LIDAR data collected during the whole cruise and calibrated in TChla is shown with respect to VIIRS TChla data.

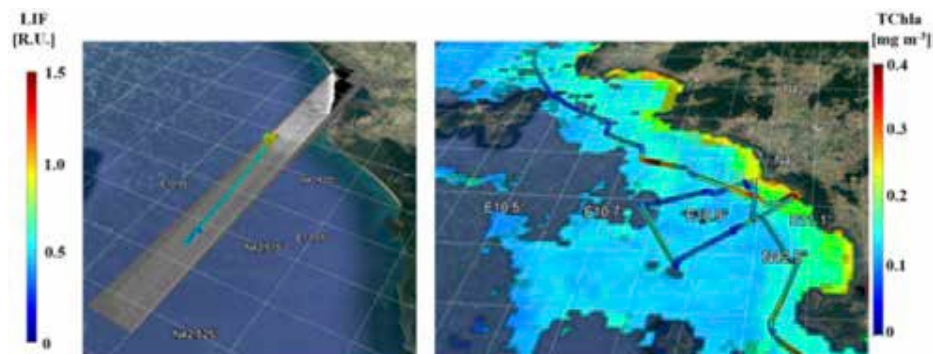


Figure 6 - On the left, LIDAR LIF data overlapping the HyPlant track and used in Figure 5. On the right, LIDAR data acquired over the all cruise (05 – 07 June) calibrated in TChla concentration and shown with respect to VIIRS TChla data related to the 8th of June.

Discussion

Based on the relative contribution of the three active constituents (i.e. phytoplankton, yellow substances, suspended material) to the total absorption, all investigated stations can be classified as complex waters dominated by yellow substances [17], except station 3 that is dominated by NAP. The ranges found for TChla and TSM concentrations and a_{CDOM} , suggest that the SIF retrieval based on the FLH approach could yield good results in this type of water. The evaluation of in situ SIF and LIF with TChla measurements (Figure 3) indicates a good positive correlation between both quantities. This finding corresponds with the known fact that higher phytoplankton biomass leads to higher fluorescence emissions. However, we only had a few sampling locations with most points dominated by low TChla concentrations and the linear regression is mainly driven by two points with higher fluorescence and TChla values. Future analysis would require more measurements and a sampling following gradients of chlorophyll concentrations, preferably closer to the shoreline, to properly account for the heterogeneity in this dynamic region. Further, only the upwelling radiance measurements from the FLOX were used for the FLH based SIF retrieval. It would be important to assess the impact of this configuration on the SIF-retrieval and advantageous to improve the FLOX design to facilitate standard aquatic measurement protocols.

SIF values derived from FLOX and HyPlant have similar magnitudes and trends but the SIF maximum from FLOX is four times that from HyPlant. This divergence can be possibly, among other effects, attributed to a missing atmospheric correction of HyPlant data. We also observe comparable spatial pattern between the airborne and spaceborne based SIF retrievals, with a coast to offshore gradient (Figure 4 and Figure 5, left). The same gradient

is also evident in the LIF data (Figure 5, right and Figure 6, left). This expected behavior is caused by the gradient in biomass that decreases with the distance from the coast. This is also confirmed by the TChla values found in the two sampling stations that fall into the HyPlant acquisition area, station 7 (more coastal) and 8. SIF and LIF values were also affected by the discharge coming from Ombrone River, which coincides with the higher FLOX based SIF values calculated especially near the river delta and the peak in SIF and LIF values between 15-25 pixels in Figure 5. The influx of additional constituents, particularly of algae and nutrients, contributes to an increased biomass concentration and thus a higher SIF and LIF signal in coastal waters surrounding the river outflow and in correspondence with station 3, the most coastal station, where the highest in-situ SIF and LIF values and TChla concentrations were obtained. Despite the common spatial pattern, however, the range of SIF values calculated from HyPlant and Sentinel-3 data substantially differ (Figure 5). The numerous negative values from Sentinel-3 FLH retrieval is likely due to the relatively low TChla concentrations in the study area. Perhaps the main reason for the difference in HyPlant and Sentinel-3 SIF results is the detection limit of Sentinel-3 OLCI due to its SNR combined with unfavourable atmospheric conditions. A similar study [18], using FLH in oligotrophic waters, showed good results for field data set but negative values from MERIS. The authors attributed this result to MERIS detection limited which appears to also be applicable for Sentinel-3 OLCI in this case. It must be noted that we did not account for effects of optically shallow waters, adjacency effects and stray light in our calculations, which could also affect the results obtained.

Conclusion

We conclude that the FLH approach is effective in measuring SIF in our study area, but further investigations to assess the general suitability of this method for different water types is important, e.g. by extending our approach to a wider range of optically complex waters that are typical of coastal regions. Particularly, at higher TChl-a concentrations (5 mg m^{-3} to 7 mg m^{-3} [4], [19]) and TSM concentrations, the apparent SIF peak observed at 685 nm appears to “shift” to a longer wavelength due to overlapping of SIF emission region and strong elastic scattering in the NIR [20]. Since such elevated concentrations are common in coastal and inland waters, especially during algal bloom events in spring and summer, refinements of the standard FLH approach are possibly needed to avoid a violation of method inherent assumptions. We suggest to consider more sophisticated retrieval schemes based on high spectral resolution data to possibly define more robust strategies to disentangle SIF from non-SIF signals.

Our results indicate that consistent SIF retrievals from in situ to airborne and satellite platforms are possible in relative terms and obtained spatial pattern are expected for coastal areas [21], [22]. Absolute differences in retrieved SIF across scales, however, require further investigations. Our approach allows to set priorities for the refinement of further pre-processing (e.g. implementation of more sophisticated atmospheric correction schemes) and to understand possible future limitations of retrieving SIF due to SNR.

The good agreement between active LIF signals from LIDAR fluorosensor and passive SIF values retrieved from FLOX, HyPlant and Sentinel-3, demonstrates how the connection between active and passive fluorescence, combined with measurements from integrated platforms, can be a promising approach supporting the development and evaluation of SIF retrieval approaches and contributing to phytoplankton fluorescence interpretation.

Acknowledgments

HyPlant data acquisition was funded by the European Space Agency in frame of the FlexSense project (No. ESA RFP/3-15477/18/NL/NA). We would like to thank the HyPlant team (PI Prof. Dr. Uwe Rascher, Research Centre Julich) for operating the instrument, acquiring and pre-process data. We thank the team of JB-Hyperspectral for providing a FLOX spectrometer system and Paul Nätke for assistance in installing the FLOX instrument on the research vessel. We also want to thank all the CNR researchers, technicians and students involved in the “FLEX 2018” cruise organization and in the field sampling activities.

References

- [1] Palucci, A., Nuvoli, M., Colao, F., Angelini, F., & Fiorani, L. (2018) - *Laser radars for marine monitoring*. In 22nd International Symposium on High Power Laser Systems and Applications, HPLS and A 2018 (Vol. 11042). SPIE.
- [2] Drusch, M., Moreno, J., Del Bello, U., Franco, R., Goulas, Y., Huth, A., ... & Nedbal, L. (2016) - *The fluorescence explorer mission concept—ESA's earth explorer 8*. IEEE Transactions on Geoscience and Remote Sensing, 55(3), 1273-1284.
- [3] Cendrero-Mateo, M. P., Wieneke, S., Damm, A., Alonso, L., Pinto, F., Moreno, J., ... & Cogliati, S. (2019) - *Sun-induced chlorophyll fluorescence III: Benchmarking retrieval methods and sensor characteristics for proximal sensing*. Remote Sensing, 11(8), 962.
- [4] McKee, D., Cunningham, A., Wright, D., & Hay, L. (2007) - *Potential impacts of nonalgal materials on water-leaving Sun induced chlorophyll fluorescence signals in coastal waters*. Applied optics, 46(31), 7720-7729.
- [5] Rascher, U., Alonso, L., Burkart, A., Cilia, C., Cogliati, S., Colombo, R., ... & Hyvärinen, T. (2015) - *Sun-induced fluorescence—a new probe of photosynthesis: First maps from the imaging spectrometer HyPlant*. Global change biology, 21(12), 4673-4684.
- [6] Wright, S. W., Jeffrey, S. W., Mantoura, R. F. C., Llewellyn, C. A., Björnland, T., Repeta, D., & Welschmeyer, N. (1991) - *Improved HPLC method for the analysis of chlorophylls and carotenoids from marine phytoplankton*. Marine ecology progress series, 183-196.
- [7] Tassan, S., & Ferrari, G. M. (2002) - *A sensitivity analysis of the 'Transmittance–Reflectance' method for measuring light absorption by aquatic particles*. Journal of Plankton Research, 24(8), 757-774.
- [8] Ferrari, G. M. (2000) - *The relationship between chromophoric dissolved organic matter and dissolved organic carbon in the European Atlantic coastal area and in the West Mediterranean Sea (Gulf of Lions)*. Marine Chemistry, 70(4), 339-357.
- [9] Van der Linde, D. W. (1998) - *Protocol for determination of total suspended matter in oceans and coastal zones*. JRC Technical Note I., 98, 182.
- [10] Volpe, G., Santoleri, R., Vellucci, V., d'Alcalà, M. R., Marullo, S., & d'Ortenzio, F. (2007) - *The colour of the Mediterranean Sea: Global versus regional bio-optical algorithms evaluation and implication for satellite chlorophyll estimates*. Remote Sensing of Environment, 107(4), 625-638.
- [11] Gilerson, A. A., & Huot, Y. (2017) - *Bio-optical Modeling of Sun-Induced Chlorophyll-a Fluorescence*. In Bio-Optical Modeling and Remote Sensing of Inland Waters (pp. 189-231). Elsevier.

- [12] Gower, J. F., Brown, L., & Borstad, G. A. (2004) - *Observation of chlorophyll fluorescence in west coast waters of Canada using the MODIS satellite sensor*. Canadian Journal of Remote Sensing, 30(1), 17-25.
- [13] Abbott, M. R., & Letelier, R. M. (1999) - *Algorithm theoretical basis document chlorophyll fluorescence (MODIS product number 20)*. NASA (<http://www.modis.gsfc.nasa.gov/data/atbd>).
- [14] Huot, Y. (2005) - *Sun-induced fluorescence of phytoplankton in the ocean: Linking physiology and remote sensing*.
- [15] IOCCG (2006) - *Remote Sensing of Inherent Optical Properties: Fundamentals, Tests of Algorithms, and Applications*. Lee, Z.-P. (ed.), Reports of the International Ocean-Colour Coordinating Group, No. 5, IOCCG, Dartmouth, Canada.
- [16] Ogashawara, I., Mishra, D. R., & Gitelson, A. A. (2017) - *Remote sensing of inland waters: background and current state-of-the-art*. In Bio-optical modeling and remote sensing of inland waters (pp. 1-24). Elsevier.
- [17] IOCCG (2000) - *Remote Sensing of Ocean Colour in Coastal, and Other Optically-Complex, Waters*. Sathyendranath, S. (ed.), Reports of the International Ocean-Colour Coordinating Group, No. 3, IOCCG, Dartmouth, Canada.
- [18] Gons, H. J., Auer, M. T., & Effler, S. W. (2008) - *MERIS satellite chlorophyll mapping of oligotrophic and eutrophic waters in the Laurentian Great Lakes*. Remote Sensing of Environment, 112(11), 4098-4106.
- [19] Moreno-Madrinán, M. J., & Fischer, A. M. (2013) - *Performance of the MODIS FLH algorithm in estuarine waters: a multi-year (2003–2010) analysis from Tampa Bay, Florida (USA)*. International journal of remote sensing, 34(19), 6467-6483.
- [20] Gilerson, A., Zhou, J., Hlaing, S., Ioannou, I., Schalles, J., Gross, B., ... & Ahmed, S. (2007) - *Fluorescence component in the reflectance spectra from coastal waters. Dependence on water composition*. Optics Express, 15(24), 15702-15721.
- [21] Gilerson, A., Zhou, J., Hlaing, S., Ioannou, I., Gross, B., Moshary, F., & Ahmed, S. (2008) - *Fluorescence component in the reflectance spectra from coastal waters. II. Performance of retrieval algorithms*. Optics express, 16(4), 2446-2460.
- [22] Gower, J., & King, S. (2007) - *Validation of chlorophyll fluorescence derived from MERIS on the west coast of Canada*. International Journal of Remote Sensing, 28(3-4), 625-635.